



Editor, **YOGESH JALURIA** (2010)
Assistant to the Editor, **S. PATEL**

Associate Editors

Yutaka Asako, Tokyo Metropolitan University, Japan (2010)
Cho Lik Chan, The University of Arizona (2010)
Louis C. Chow, University of Central Florida (2010)
Frank J. Cunha, Pratt & Whitney (2011)
Ali Ebadian, Florida International Univ. (2011)
Ofodike A. Ezekoye, Univ. of Texas-Austin (2011)
Srinivas Garimella, Georgia Institute Technology (2012)
Kenneth Goodson, Stanford University (2012)
Satish G. Kandlikar, Rochester Inst. of Tech. (2010)
Sung Jin Kim, KAIST, Korea (2010)
Giulio Lorenzini, University of Bologna (2012)
Jayathi Y. Murthy, Perdue University (2010)
Pamela M. Norris, Univ. of Virginia (2011)
Patrick H. Oosthuizen, Queens University, Canada (2012)
Patrick E. Phelan, National Science Foundation (2011)
Roger R. Schmidt, IBM Corporation (2010)
S. A. Sherif, University of Florida (2010)
Heping Tan, Harbin Institute of Technology (2011)
Wen Q. Tao, Xi'an University, China (2012)
Wei Tong, Danaher Corporation (2012)
Peter Vadasz, Northern Arizona University (2010)
Walter W. Yuen, Univ. of California—Santa Barbara (2011)

Past Editors

V. DHIR
J. R. HOWELL
R. VISKANTA
G. M. FAETH
K. T. YANG
E. M. SPARROW

HEAT TRANSFER DIVISION
Chair, **V. CAREY**
Past Chair, **CHANG OH**

PUBLICATIONS COMMITTEE
Chair, **BAHRAM RAVANI**

OFFICERS OF THE ASME
President,
AMOS E. HOLT
Executive Director,
THOMAS G. LOUGHLIN
Treasurer,
WILBUR MARNER

PUBLISHING STAFF
Managing Director, Publishing
PHILIP DI VIETRO
Manager, Journals
COLIN McATEER
Production Coordinator
JUDITH SIERANT

Transactions of the ASME, Journal of Heat Transfer (ISSN 0022-1481) is published monthly by The American Society of Mechanical Engineers, Three Park Avenue, New York, NY 10016. Periodicals postage paid at New York, NY and additional mailing offices.
POSTMASTER: Send address changes to Transactions of the ASME, Journal of Heat Transfer, c/o THE AMERICAN SOCIETY OF MECHANICAL ENGINEERS, 22 Law Drive, Box 2300, Fairfield, NJ 07007-2300.
CHANGES OF ADDRESS must be received at Society headquarters seven weeks before they are to be effective. Please send old label and new address.

STATEMENT from By-Laws. The Society shall not be responsible for statements or opinions advanced in papers or ... printed in its publications (B7.1, Para. 3).
COPYRIGHT © 2009 by The American Society of Mechanical Engineers. For authorization to photocopy material for internal or personal use under those circumstances not falling within the fair use provisions of the Copyright Act, contact the Copyright Clearance Center (CCC), 222 Rosewood Drive, Danvers, MA 01923, tel: 978-750-8400, www.copyright.com.
Request for special permission or bulk copying should be addressed to Reprints/Permission Department.
Canadian Goods & Services Tax Registration #126148048

Journal of Heat Transfer

Published Monthly by ASME

VOLUME 131 • NUMBER 8 • AUGUST 2009

PHOTOGALLERY

- 080901 Heat Transfer Photogallery
Kenneth D. Kihm
- 080902 Computational Simulation of Swirl Enhanced Flow and Heat Transfer in a Twisted Oval Tube
F. Bishara, M. A. Jog, and R. M. Manglik
- 080903 Computational Analysis of Binary-Fluid Heat and Mass Transfer in Falling Films and Droplets
Vishwanath Subramaniam and Srinivas Garimella
- 080904 Visualization of Thermally Actuated Pumping in the Leidenfrost Regime by Surface Asymmetry
Vinod Narayanan, Heiner Linke, and Mike Taormina
- 080905 Experimental Visualization of the Thermoacoustic Effect
C Herman and M Pirtini Çetingül
- 080906 Thin-Film Evaporation in an Evaporating Droplet
H. K. Dhavaleswarapu, C. P. Migliaccio, S. V. Garimella, and J. Y. Murthy
- 080907 Unveiling Hidden Complex Cavities Formed by Evaporative Nanofluidic (Al_2O_3) Self-Assembly
Iltae Kim and Kenneth D. Kihm
- 080908 Condensation of Sodium Vapor and High-Temperature Reaction With Quartz Pore Inner Surface
Kenneth D. Kihm, David M. Pratt, and Andrew D. Swanson

RESEARCH PAPERS

Experimental Techniques

- 081601 Novel Two-Dimensional Transient Heat Conduction Calculation in a Cooled Rotor: Ventilation Preheating—Blow-Down Flux
J. P. Solano and G. Paniagua

Forced Convection

- 081701 An Experimental Investigation of the Cold Mass Fraction, Nozzle Number, and Inlet Pressure Effects on Performance of Counter Flow Vortex Tube
Volkan Kirmaci and Onuralp Uluer

Heat Exchangers

- 081801 A Bejan's Constructal Theory Approach to the Overall Optimization of Heat Exchanging Finned Modules With Air in Forced Convection and Laminar Flow Condition
Giulio Lorenzini and Simone Moretti

Heat Transfer Enhancement

- 081901 Convective Heat Transfer Enhancement in a Circular Tube Using Twisted Tape
Zhi-Min Lin and Liang-Bi Wang
- 081902 Characterization and Pool Boiling Heat Transfer Studies of Nanofluids
R. Kathiravan, Ravi Kumar, Akhilesh Gupta, and Ramesh Chandra

(Contents continued on inside back cover)

This journal is printed on acid-free paper, which exceeds the ANSI Z39.48-1992 specification for permanence of paper and library materials. ©™
♻️ 85% recycled content, including 10% post-consumer fibers.

Heat and Mass Transfer

- 082001 Magnetohydrodynamic Convective Heat and Mass Transfer Flow Due to a Rotating Disk With Thermal Diffusion Effect
Kh. Abdul Maleque

Heat Transfer in Manufacturing

- 082101 Interactions Between Electromagnetic and Thermal Fields in Microwave Heating of Hardened Type I-Cement Paste Using a Rectangular Waveguide (Influence of Frequency and Sample Size)
P. Rattanadecho, N. Suwannapum, and W. Cha-um

Jets, Wakes, and Impingement Cooling

- 082201 Full-Field Flow Measurements and Heat Transfer of a Compact Jet Impingement Array With Local Extraction of Spent Fluid
Andrew J. Onstad, Christopher J. Elkins, Robert J. Moffat, and John K. Eaton

Melting and Solidification

- 082301 Heat Transfer and Thermodynamic Analyses of Some Typical Encapsulated Ice Geometries During Discharging Process
David MacPhee and Ibrahim Dincer

Micro/Nanoscale Heat Transfer

- 082401 Modeling Electron-Phonon Nonequilibrium in Gold Films Using Boltzmann Transport Model
Arvind Pattamatta and Cyrus K. Madnia

Natural and Mixed Convection

- 082501 Natural Convection Heat Transfer From Horizontal Rectangular Inverted Notched Fin Arrays
Sanjeev D. Suryawanshi and Narayan K. Sane
- 082502 Flow and Heat Transfer of Natural Convection in Horizontal Annulus With a Heating Element on Inner Cylinder
C. S. Yang, D. Z. Jeng, U. H. Tang, and C. Gau

Porous Media

- 082601 Effect of Wick Characteristics on the Thermal Performance of the Miniature Loop Heat Pipe
Randeep Singh, Aliakbar Akbarzadeh, and Masataka Mochizuki

Radiative Heat Transfer

- 082701 Experimental Determination and Modeling of the Radiative Properties of Silica Nanoporous Matrices
Sylvain Lallich, Franck Enguehard, and Dominique Baillis

Two-Phase Flow and Heat Transfer

- 082901 Correlations of Wave Characteristics for a Liquid Film Falling Down Along a Vertical Wall
Yasuo Koizumi, Ryou Enari, and Hiroyasu Ohtake

The ASME Journal of Heat Transfer is abstracted and indexed in the following:

Applied Science and Technology Index, Chemical Abstracts, Chemical Engineering and Biotechnology Abstracts (Electronic equivalent of Process and Chemical Engineering), Civil Engineering Abstracts, Compendex (The electronic equivalent of Engineering Index), Corrosion Abstracts, Current Contents, E & P Health, Safety, and Environment, Ei EncompassLit, Engineered Materials Abstracts, Engineering Index, Enviroline (The electronic equivalent of Environment Abstracts), Environment Abstracts, Environmental Engineering Abstracts, Environmental Science and Pollution Management, Fluidex, Fuel and Energy Abstracts, Index to Scientific Reviews, INSPEC, International Building Services Abstracts, Mechanical & Transportation Engineering Abstracts, Mechanical Engineering Abstracts, METADEX (The electronic equivalent of Metals Abstracts and Alloys Index), Petroleum Abstracts, Process and Chemical Engineering, Referativnyi Zhurnal, Science Citation Index, SciSearch (The electronic equivalent of Science Citation Index), Theoretical Chemical Engineering



**Journal of
Heat Transfer**

Heat Transfer Photogallery

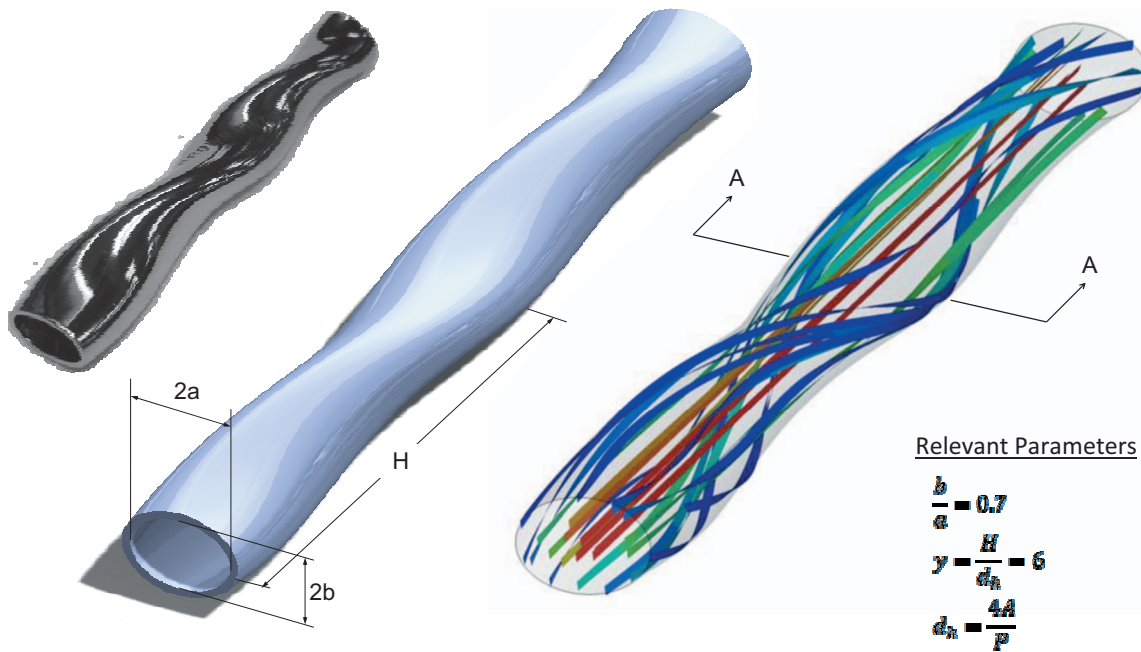
The Thirteenth Heat Transfer Photogallery was sponsored by the K-22 Heat Transfer Visualization Committee for the 2008 International Mechanical Engineering Congress and Exhibition (IMECE) held in Boston, Massachusetts, on October 31–November 6, 2008. The peer-reviewed evaluation process for the presented entries identified the seven entries for production in the ASME *Journal of Heat Transfer* August issue of 2009.

The purpose of publishing these entries is to draw attention to the innovative features of optical diagnostic techniques and aesthetic qualities of thermal processes. To focus on visualization images and schematics, the text is kept to a minimum and further details should be found directly from the authors. My wish is that the journal readers enjoy viewing these collections, acquire knowledge of the state-of-the-art features, and also promote their participation in the 2009-IMECE Photogallery [<http://www.asmeconferences.org/Congress09>].

The **Call for Photogallery for 2009-IMECE** is also announced in this issue of *Journal of Heat Transfer*.

Kenneth D. Kihm

Department of Mechanical, Aerospace,
and Biomedical Engineering,
University of Tennessee
Knoxville, TN 37996-2210

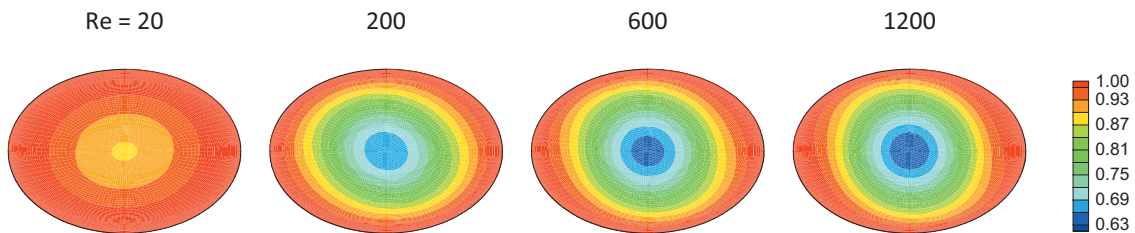


Relevant Parameters

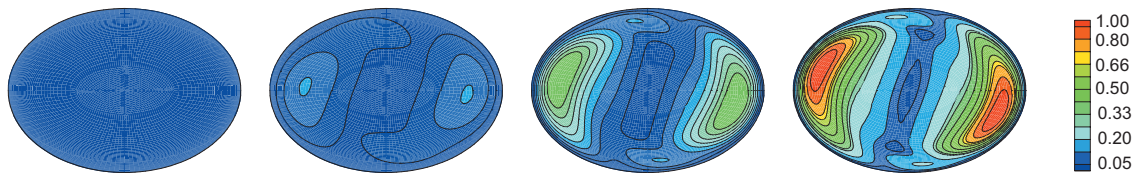
$$\frac{b}{a} = 0.7$$

$$\gamma = \frac{H}{d_h} = 6$$

$$d_h = \frac{4A}{P}$$



Temperature Distribution (Pr = 3.0) at Section A—A



In-Plane Velocity Magnitude ($\sqrt{u^2 + v^2}$) at Section A—A

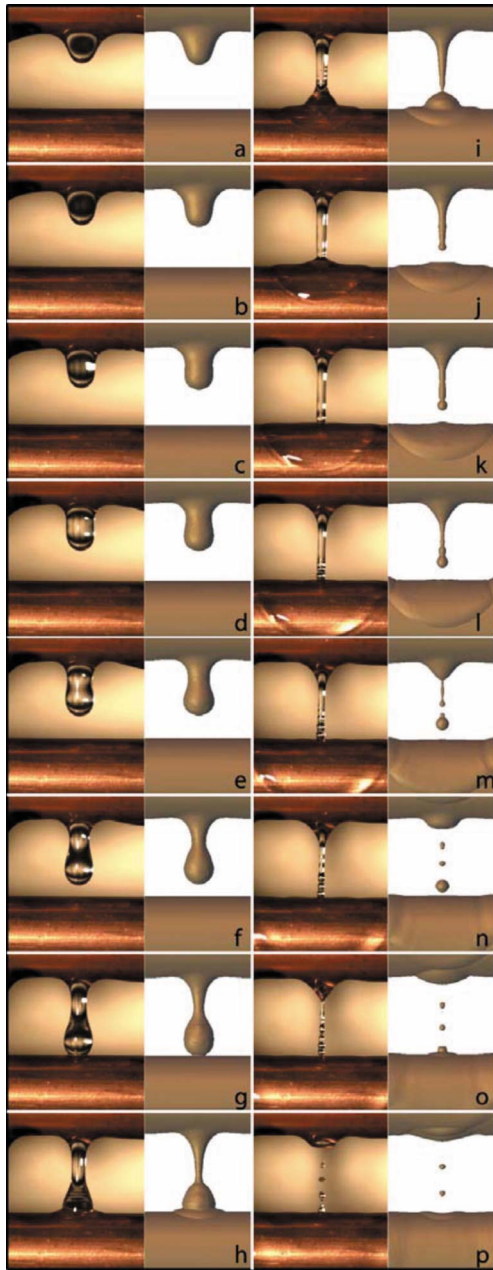
Computational Simulation of Swirl Enhanced Flow and Heat Transfer in a Twisted Oval Tube

F. Bishara, M. A. Jog and R. M. Manglik

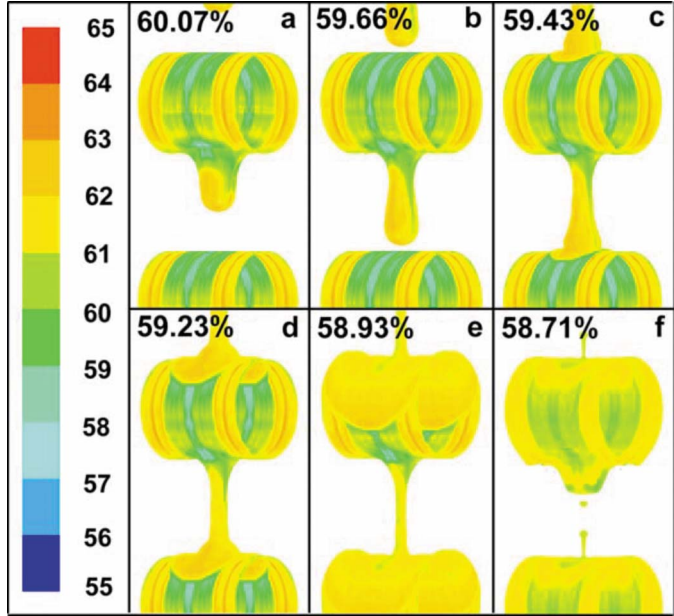
Department of Mechanical Engineering, University of Cincinnati, Cincinnati, OH 45221

Fully developed swirling flow in a twisted tube with an oval cross section is considered. The results shown here are for a tube with an elliptical cross section with a twist ratio of 6 and an aspect ratio of 0.7 (see equations above). The wall of the tube is held at a constant temperature. The secondary flows induced by the tube twist promote mixing in the plane normal to the bulk flow direction. This mixing works to maintain a high temperature gradient close to the tube wall and in turn increase the Nusselt number relative to that in a straight tube of the same cross section. The temperature plots show that it is indeed the case that the in-plane mixing is effective in maintaining the temperature gradient near the tube wall. The isometric view shows flow streamlines (ribbons represent adjacent streamlines) to illustrate the swirling nature of the flow.

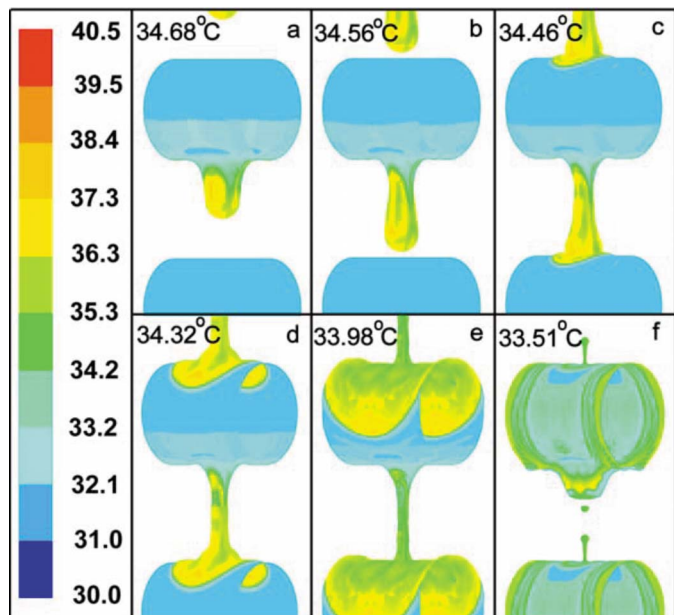
Flow Patterns: Experiments and Computations



LiBr-H₂O Solution Concentration Distribution (LiBr Weight %)



LiBr-H₂O Solution Temperature Distribution (°C)



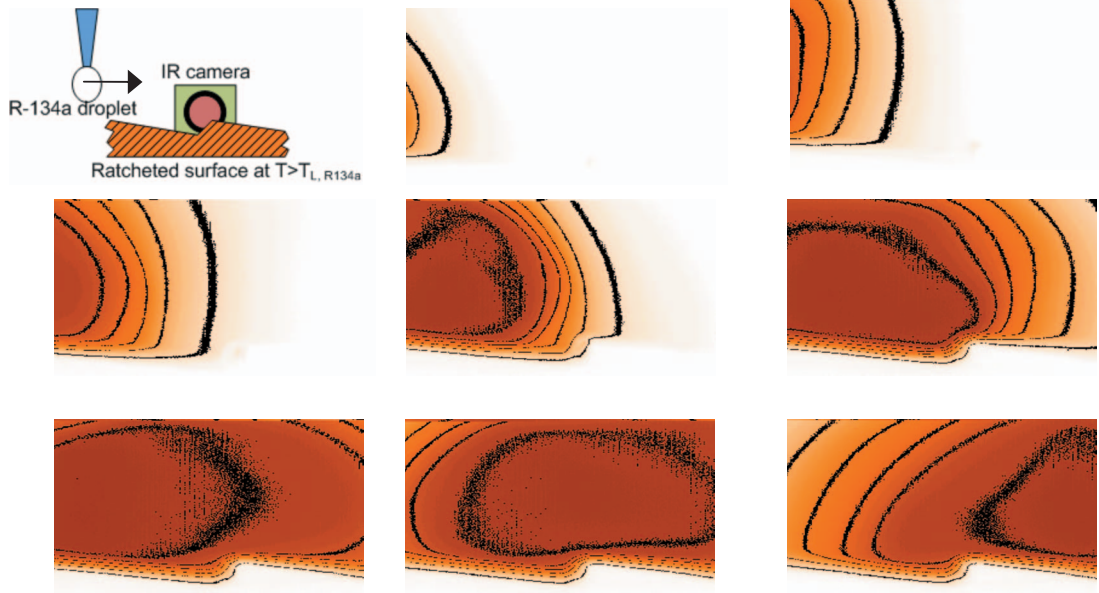
Computational Analysis of Binary-Fluid Heat and Mass Transfer in Falling Films and Droplets

Vishwanath Subramaniam and Srinivas Garimella

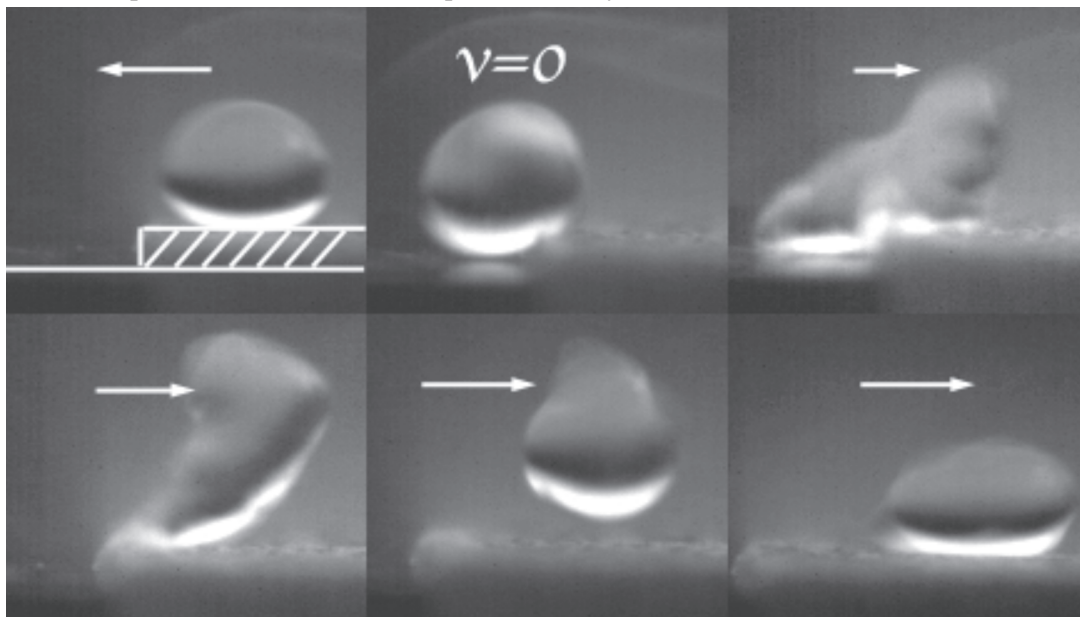
Sustainable Thermal Systems Laboratory, GWW School of Mechanical Engineering
Georgia Institute of Technology, Atlanta, GA

Heat and mass transfer models in the literature on horizontal-tube absorbers make simplistic assumptions about fluid flow patterns. High-speed flow visualization was used to show that inter-tube flow occurs as droplets, and the formation and detachment of these droplets and their impact on the tube have significant effects on heat and mass transfer. Most models neglect these flow modes and assume the solution to flow as a uniform film. The present study numerically models heat and mass transfer in the absorber taking the realistic drop-wise and wavy film flow mechanisms into consideration. The impact of droplets on the tube causes the lithium bromide solution film on the tube to mix and present newer regions of the solution for vapor absorption. The impact also gives rise to waves that propagate axially over the liquid film on the tube. The mixing effect and the waves caused by droplet impact play a very important role in the heat and mass transfer. Results obtained from this study will lead to better understanding of the vapor absorption process, and yield more efficient and optimal absorber designs.

Sustained droplet propulsion by repeated asymmetric surface patterns



Local droplet acceleration due to step discontinuity



VISUALIZATION OF THERMALLY ACTUATED PUMPING IN THE LEIDENFROST REGIME BY SURFACE ASYMMETRY

Vinod Narayanan*, Heiner Linke**, Mike Taormina**

*Mechanical Engineering

**Physics Department

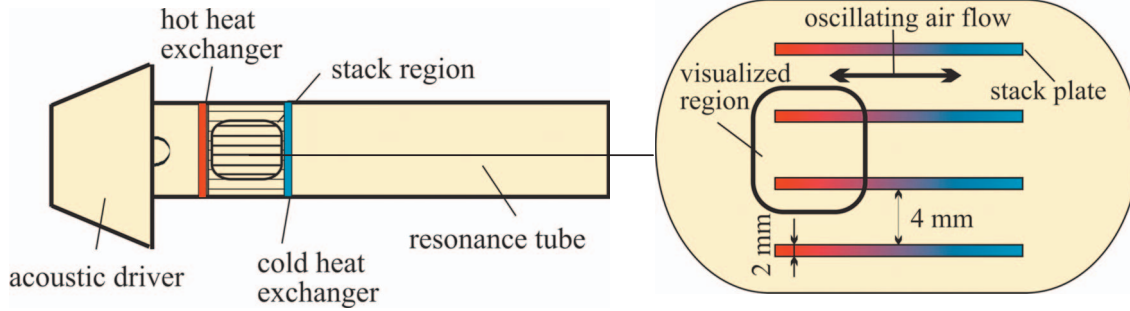
Oregon State University

University of Oregon

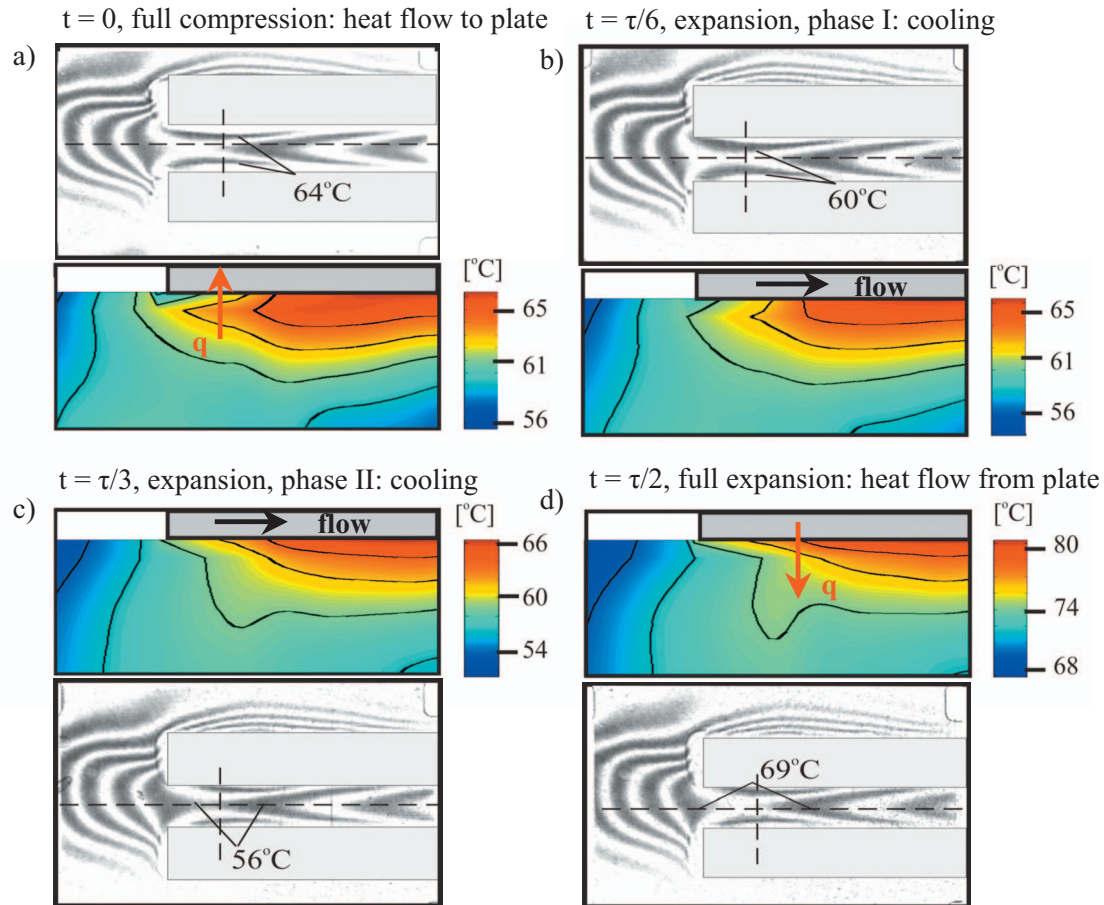
The propulsion of film boiling (Leidenfrost) liquid droplets that encounter a surface asymmetry has been observed. Repeated pattern of surface asymmetries, such as the saw-tooth ratchet illustrated in the top video sequence, have been shown to provide sustained droplet propulsion. On the other hand, isolated surface asymmetries such as a step change in height of the surface provides a local droplet acceleration that is illustrated in the bottom figure. Such heat-actuated pumping has been observed for a wide variety of fluids, two of which are illustrated in this photo gallery exhibit.

The sequence of images on the top panel is that of a film boiling droplet of R134a ($T_b = 246.6$ K) on a room-temperature brass ratchet. This sequence was recorded using an infrared camera. The time interval between the frames is 8 ms. On the bottom panel is a video sequence of a liquid nitrogen droplet that is introduced with an initial momentum towards the left. Upon encountering a step, the droplet reverses direction. The fifth frame shows that the droplet gains sufficient energy to momentarily detach from the substrate.

Thermoacoustic refrigerator



Experimentally visualized temperature fields by holographic interferometry and temperature distributions reconstructed from interferometry images (color plots)

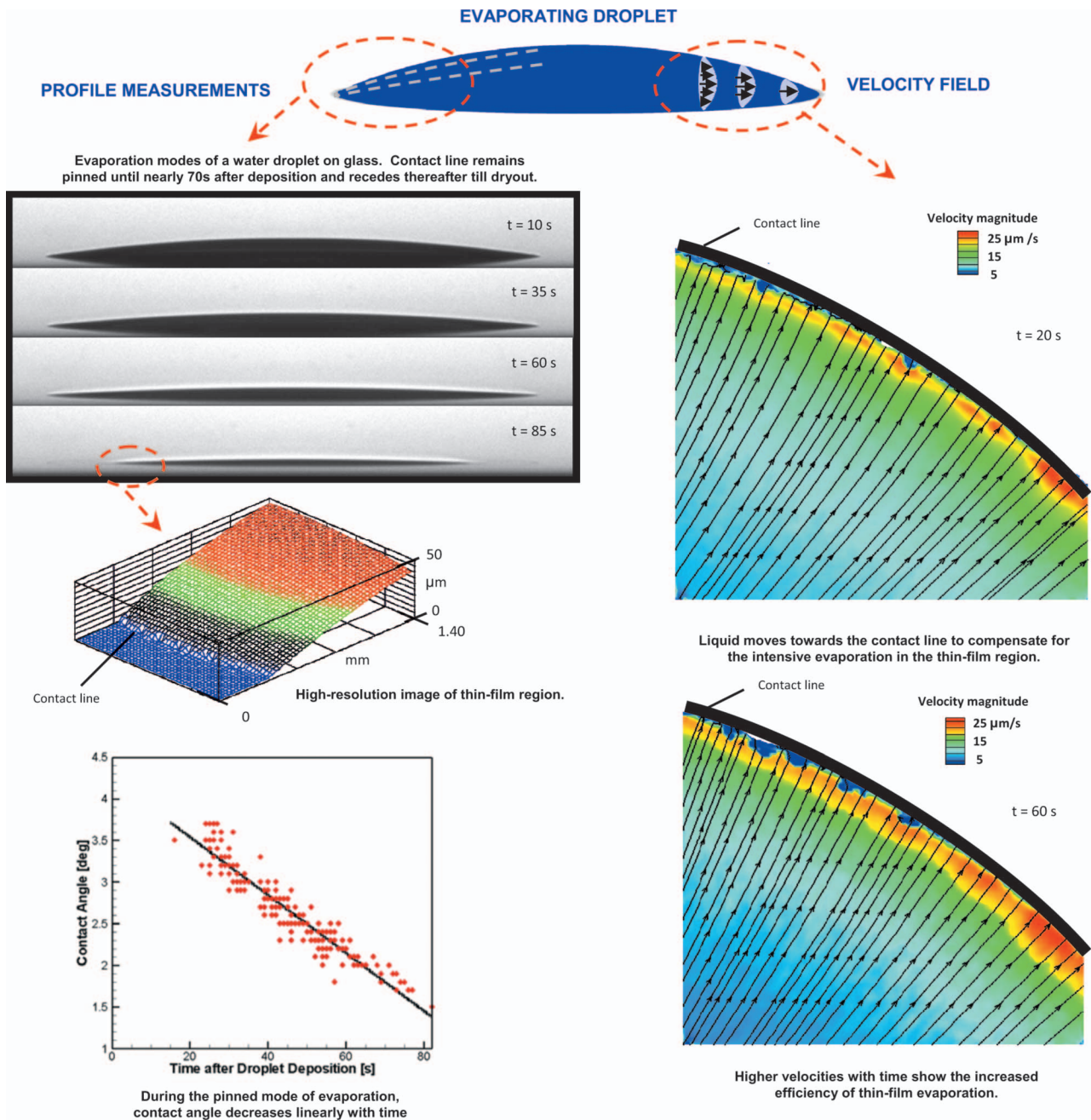


Experimental visualization of the thermoacoustic effect

C. Herman, M. Pirtini Çetingül

Department of Mechanical Engineering, Johns Hopkins University, Baltimore, MD 21218

A thermoacoustic refrigerator uses sound energy to transport heat. Using a sound source such as a loudspeaker, a standing wave is formed in a tube filled with noble gas. As the wave travels back and forth (oscillates) in the resonator, the gas compresses and expands. To exploit this effect for heat pumping, a “thermoacoustic core”, consisting of a densely packed stack of plates, is placed in the tube. In the compression phase of the cycle, the gas heats up, transferring heat to the plates (a). Then, as the gas gradually expands and cools down (b,c), it absorbs heat from the plates (d). This sets up an overall temperature gradient along the plates, effectively pumping heat from the cold side to the hot side of the core. When heat exchangers are attached to the thermoacoustic core, this device becomes a useful refrigerator. Four image pairs, showing one half of the acoustic cycle ($t = 0, \tau/6, \tau/3$ and $\tau/2$), are the first experimental visualization of the thermoacoustic effect on two stack plates. Fringe patterns are generated by holographic interferometry and color images are reconstructed temperature distributions based on experimental data.



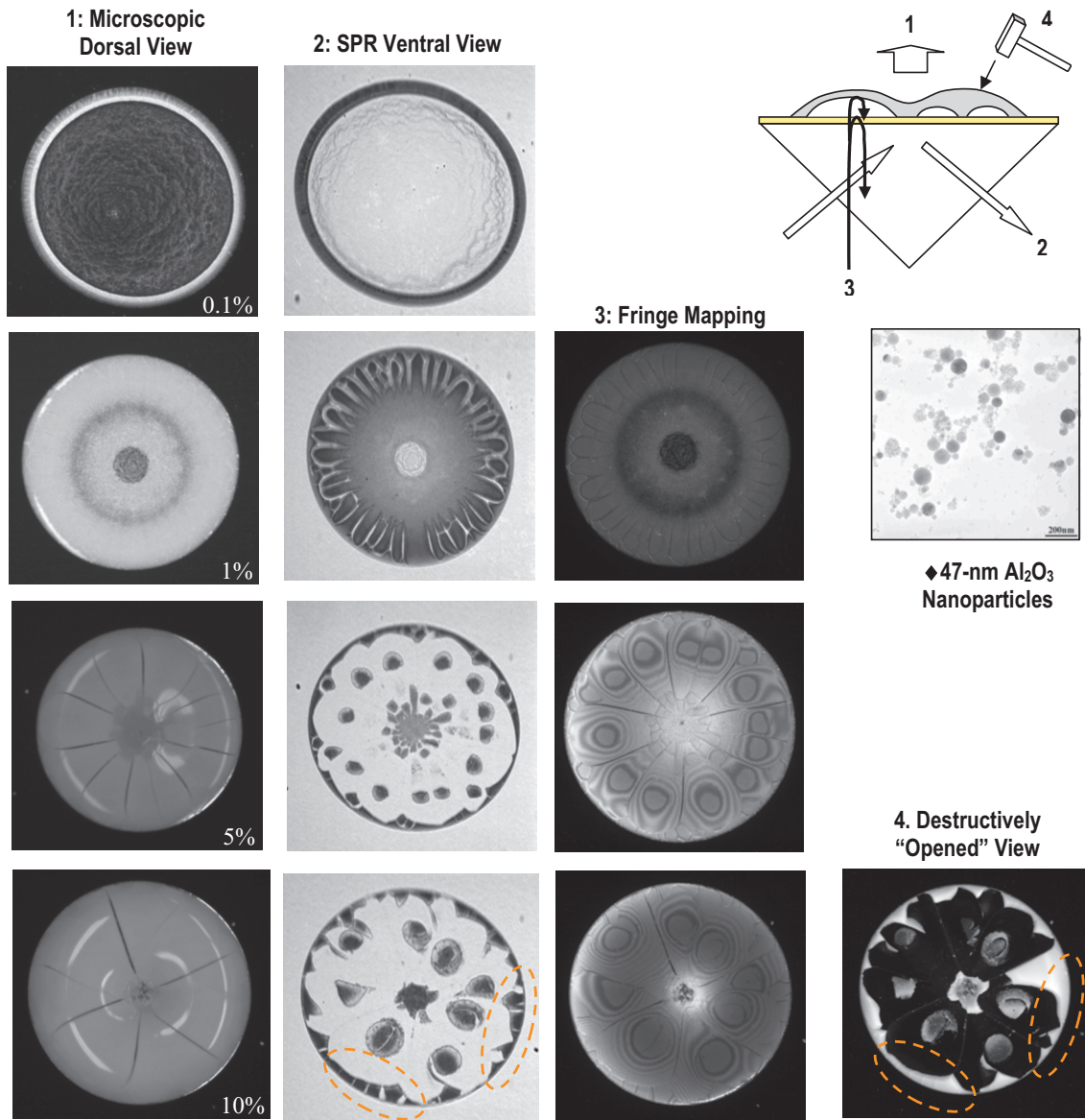
Thin-film Evaporation in an Evaporating Droplet

H. K. Dhavaleswarapu, C. P. Migliaccio, S. V. Garimella, and J. Y. Murthy

NSF Cooling Technologies Research Center

School of Mechanical Engineering, Purdue University, West Lafayette, Indiana

Thin-film evaporation – the evaporation taking place near a solid-liquid-vapor junction – has long been believed to be the dominant mode of heat transfer in two-phase heat transfer systems. Evaporation of droplets is important in many applications such as coating, printing, spraying and dropwise condensation. Small ($0.5 \mu\text{l}$) water droplets evaporating on glass slides are studied. Three distinct modes of evaporation are observed: (1) the contact line remains pinned and the contact angle decreases progressively (4.5 to 0.7 deg), (2) the contact line recedes suddenly, and (3) complete dryout occurs. A high-resolution optical interferometer (0.1 nm in z -direction) is used to resolve the transient droplet profiles in the thin-film region. Micro-particle image velocimetry measurements of the flow field generated near the thin-film region are obtained. The liquid flows from the center of the droplet to the thin-film region to replenish the evaporating liquid.



Unveiling Hidden Complex Cavities Formed by Evaporative Nanofluidic (Al_2O_3) Self-Assembly

Iltai Kim and Kenneth D. Kihm

Department of Mechanical, Aerospace, and Biomedical Engineering
University of Tennessee, Knoxville, Tennessee

The hidden complex cavity structures are first unveiled for nanofluidic self-assembly when $2\text{-}\mu\text{l}$ aqueous droplets containing 47-nm diameter Al_2O_3 nanoparticles are evaporated and crystallized. The microscopic dorsal images (1) show dramatically different crystallized surface shapes and textures depending on the nanoparticle concentrations. The nonintrusive fingerprints by Surface Plasmon Resonance (SPR) imaging* (2) clearly evidence the existence of the hidden hollow cavity structures. Note that each cell bounded by crack lines is crystallized to form a single anchoring onto the substrate. The interference fringe mapping (3) can lead to reconstruct quantitative dimensions of the ventral inner cavity surfaces. The destructive image taken with the roof shattered (4) confirms the SPR fingerprints, but lacks the details particularly in the self-pinned edge regions.

* I. T. Kim and K. D. Kihm, "Label-Free Visualization of Microfluidic Concentration Fields Using a Surface Plasmon Resonance (SPR) Imaging," *Experiments in Fluids* Vol. 41, No. 6, pp. 905-916, 2006.



Condensation of Sodium Vapor and High-Temperature Reaction with Quartz Pore Inner Surface

Kenneth D. Kihm

Department of Mechanical, Aerospace, and Biomedical Engineering
University of Tennessee, Knoxville, Tennessee

David M. Pratt and Andrew D. Swanson

Structures Division, Air Vehicles Directorate
United States Air Force Research Laboratory, WPAFB, Ohio

Sudden boiling of liquid sodium (b.p. = 1156 K at 1 atm) inside the all quartz-made smelting/evaporation chamber results in condensation and high-temperature reaction of sodium vapor with the inner wall surface. The attack and reaction becomes more aggressive with increasing vapor temperature. The condensation "fingerprints" express different color bands from **silver, metallic, milky, brown, orange, red, and black** with increasing level of the sodium attack and reaction on the surface.

Novel Two-Dimensional Transient Heat Conduction Calculation in a Cooled Rotor: Ventilation Preheating—Blow-Down Flux

J. P. Solano

G. Paniagua

Department of Turbomachinery and Propulsion,
von Karman Institute for Fluid Dynamics,
Chaussée de Waterloo,
72 B1640 Rhode-Saint-Genèse, Belgium

This contribution presents an alternative to classical data reduction techniques to measure the heat transfer using thin-film gauges. A finite-element model of the two-dimensional unsteady heat conduction equation is solved in the cross-sectional area of a metallic airfoil bounded with a polyamide sheet on which thermal sensors are deposited. This novel methodology allows capturing all 2D heat conduction effects that are irretrievably neglected with the 1D data reduction technique. The application of this technique in a compression tube facility allows an exact evaluation of the initial wall heat flux into cooled rotor blades. During the spinning-up period, the rotor is spun up to nearly its nominal speed (from 0 rpm to 6200 rpm) resulting in preheating due to drag losses. The long duration of this experiment (~ 450 s) and the magnitude of the wall temperature increase result in significant 2D conduction effects that are not accounted for using the 1D approach. In addition, short-duration experiments confirm the existence of 2D effects at smaller time scales (~ 0.5 s), as well as the influence of the initial nonuniform temperature distribution in the rotor blade. The resulting flux with such an initial condition appears to be the superposition of the wall heat flux at the end of the spinning up before the test and the flux due to the blow-down itself. [DOI: 10.1115/1.3122777]

Keywords: gas turbines, thin-film gauges, convective heat flux

1 Introduction

Thin-film gauges are used in short-duration facilities for gas turbine aerothermal research since the 1970s. These resistive temperature detectors provide the surface temperature evolution of an instrumented airfoil during blow-down tests. This information allows computing the wall heat flux around the blade and subsequently the Nusselt number distribution. This is especially useful at the design stages of cooling schemes in turbine blades and also yields essential experimental data regarding the boundary layer status, transition, turbulent spot growth, and speed. Single layer and double layer substrates constitute the technical solutions usually employed to implement thin-film sensors onto airfoils in transient tunnels. The single layer thin-film gauges used at the von Karman Institute consist of platinum thin-film gauges fired onto a ceramic substrate. The entire blade might be manufactured in ceramic for cascade testing [1], or inserts could be fitted into metallic blades in the case of measurements on the rotor of a turbine stage [2–4]. A faster and more flexible implementation was possible after the intensive development of the two-layered thin-film gauge carried out at MIT [5] and University of Oxford [6]. In the most recent applications at the von Karman Institute [7], the sensor arrays were deposited on a polyamide sheet wrapped around the airfoil with a double-sided adhesive.

The two-sided sensor proposed by Epstein et al. [5] consists of two thin-film sensors mounted on either sides of the first insulating substrate, resulting in simpler data reduction requirements. Piccini et al. [8] proposed to place a thermocouple between the insulating layer and the metallic layer. However, this dual-sided technique required the monitoring of two temperature signals at each measurement location.

The data reduction associated to both single-sensor one-layered and two-layered thin-film gauges has traditionally relied on semi-infinite, flat plate heat conduction. This so-called 1D approach is especially appropriate in single layer configurations due to the low thermal diffusivity of the ceramic substrate and the short duration of the test [1]. Moreover, the thickness of the ceramic insert justifies the assumption of semi-infinite substrate during the test duration [3]. Various approaches have been proposed to account for the presence of multilayered substrates [9–11] but all of them rely on the semi-infinite assumption on a flat plate.

Diverse solutions may be utilized to correct the curvature effects in unsteady heat transfer data from thin-film gauges [12–14]. In the noteworthy methodology proposed by Buttsworth and Jones [15], radial heat conduction modeling allows constructing analytical corrections for the thin-film measurements. Such corrections could be easily implemented in the routine 1D data analysis. However, none of the proposed methods account for the presence of a multilayered system, where the existence of a metallic substrate under the insulating coating promotes 2D diffusion effects once the thermal wave penetrates the polyamide substrate. Even though curvature effects could be successfully accounted for, lateral heat conduction phenomena are neglected.

Complete details of a new data processing methodology are provided in the present work. The direct solution of the 2D unsteady heat conduction equation in the airfoil section results in the inherent ability to capture curvature effects, furthermore without requiring the semi-infinite assumption. This numerical tool was successfully applied to compute and analyze in detail the heat flux in a cooled rotor geometry tested in a short-duration facility. The airfoils are cooled internally with two radial cooling ducts. This technique retrieves the temperature distribution inside the multilayered substrate due to viscous heating related to drag losses during the turbine pretest rotation (~ 450 s) prior to the actual test. Then, the influence of this nonuniform initial temperature distribution in the subsequent experiment was assessed in a com-

Contributed by the Heat Transfer Division of ASME for publication in the JOURNAL OF HEAT TRANSFER. Manuscript received September 16, 2008; final manuscript received January 13, 2009; published June 3, 2009. Review conducted by Sai C. Lau.

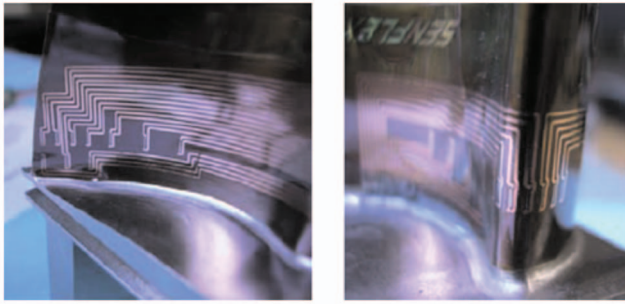


Fig. 1 Thin-film gauges at 15% rotor blade height

plex geometry, highlighting the presence of important 2D effects. Finally the convective heat flux on the rotor airfoil is presented. In the course of this investigation an interesting superposition effect was identified and validated, which serves to simplify the heat transfer data processing.

2 Experimental Apparatus

2.1 Rotor Cooled Airfoil. The rotor blades are representative of state-of-the-art of transonic single-stage high pressure turbines. The cooled airfoils were designed by Avio with a maximum turning of 105 deg to limit the secondary flows. Figure 1 shows the rotor blade instrumented with a thin-film gauge array at 15% height. The heat transfer gauges were calibrated in a controlled temperature oven. To avoid spurious effects due to electronic drift in the measurement chain components, the gauges are recalibrated for every test. The slope of the calibration is conserved from the oven calibration, while the intercept is corrected for every test in an automated way.

2.2 Compression Tube Facility. The von Karman Institute compression tube rotating rig is the world's largest short-duration compression tube facility. Figure 2 displays the test section located between an upstream pressurized cylinder (compression tube) and the downstream dump tank at vacuum. Therefore, the Reynolds number and Mach number can be adjusted independently. When the initially closed shutter valve opens, hot gas flows across a cold turbine, simulating the heat transfer of a hot engine. In the current measurement campaign the temperature ratios are $T_{\text{metal}}/T_{\text{gas}}=0.70$ and $T_{\text{coolant}}/T_{\text{gas}}=0.64$. The mass flow

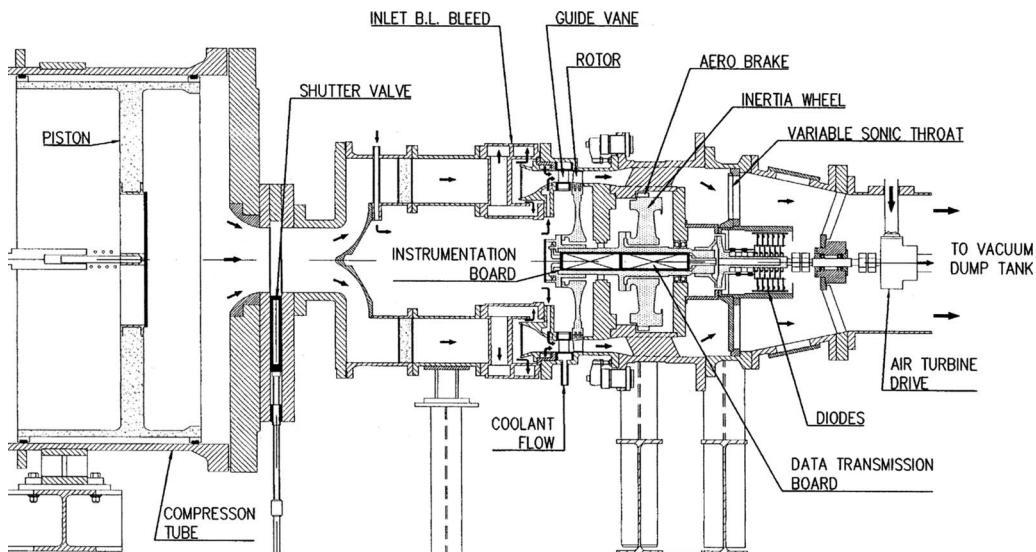


Fig. 2 Meridional view of the turbine facility

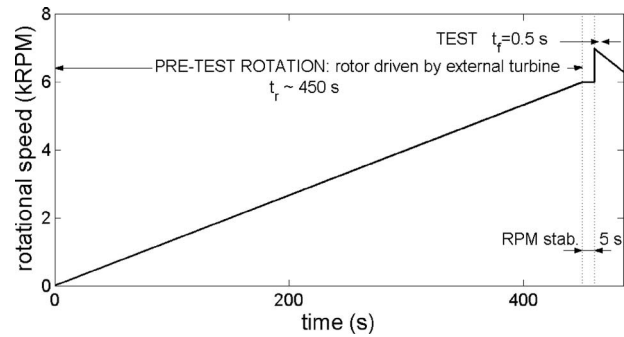


Fig. 3 Typical testing sequence

through the stage is controlled by opening a variable sonic throat located in between the test section and the dump tank. The nominal turbine power is 1 MW at $Re=10^6$, with supersonic vane outlet conditions $M_2=1.07$, while the rotor has transonic conditions $M_3=0.89$.

2.3 Typical Test Cycle. Initially, with the shutter valve closed, the pressure in the upstream tube is set to a value that will allow attaining the required pressure and temperature at the end of the quasi-isentropic compression. By means of a vacuum system the pressure level in the test section and dump tank is set equal to about 30 mbars. The rotor is then spun up to almost its design speed from 0 rpm to 6200 rpm in around 7 min, as displayed in Fig. 3. After the pretest rotation, air in the tube is compressed by the piston, which is driven by the high pressure line. Once the required pressure in the tube is obtained, a fast acting valve opens the shutter. As the piston continues the compression a choked sonic throat (downstream of the test section) keeps constant the design conditions for about 400 ms.

Regarding the spinning-up period Traupel [16] indicated that the friction loss is a combination of different mechanisms, mainly windage and ventilation. Both loss mechanisms contribute to heat generation that is then transferred into the still air existing in the test section. In the vicinity of the rotor blades, air is being swirled due to viscous forces. This mechanism is called ventilation and the generated loss is equal to $P_{\text{ventilation}} = \rho \cdot 5.571 \times 10^{-7} \text{ rpm}^3$, which at 6000 rpm results in 5.8 kW. Windage losses are due to the drag that the flow exerts on the rotor disk. This loss is a power law of the speed and function of density. The exact values of the

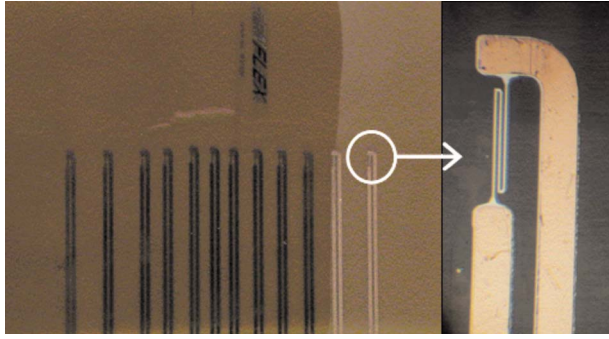


Fig. 4 Two-layered substrate thin-film gauges

equation were obtained from deceleration tests performed in the same turbine rotor between 6500 rpm and 5000 rpm at different levels of pressure [17]: $P_{\text{windage}} = \rho \cdot 6.44 \times 10^{-6} \text{ rpm}^{2.3881}$, i.e., 0.3 kW at 6000 rpm. Part of the heat is being dissipated by convection into the turbine end walls, and a significant part is transformed into temperature increase in the test section.

2.4 Double-Layered Thin-Film Sensors. The thin-film temperature gauges consist of a 2.5 mm serpentine nickel thin-film with a resistance of 60 Ω deposited on an Upilex-S polyamide sheet (produced by TAO Systems, Hampton, VA). This instrumented plastic thin layer is glued on the blade surface with a double-sided adhesive sheet. The sensing element of the thin-film acts as a variable resistance thermometer, whose resistance variation is monitored by a Wheatstone bridge. The use of copper paths allows performing connections with a negligible resistance (Fig. 4).

3 Data Processing Methodology

3.1 1D Processing. The classical data reduction technique used for double-layered thin-film gauges comprises the resolution of the 1D unsteady heat conduction equation in a multilayered substrate:

$$\frac{1}{\alpha} \frac{\partial T}{\partial t} = \frac{\partial^2 T}{\partial x^2} \quad (1)$$

To solve this equation, a set of initial and boundary conditions is needed: The wall temperature evolution measured with the thin-film gauge is imposed $T_w(0, t)$. Assuming that the last substrate is semi-infinite, a second boundary condition is obtained: $T(x \rightarrow \infty, t) = T_0$. This assumption is valid as long as the test duration is sufficiently short. The duration of the test and the heat penetration depth are correlated with the following expression [3]:

$$L_\infty = 3.648 \sqrt{\alpha t} \quad (2)$$

In the case of multilayer substrates, an additional boundary condition ought to be imposed at the interface between each substrate, namely, the heat flux continuity:

$$-k_1 \left. \frac{\partial T}{\partial x} \right|_{x=L^-} = -k_2 \left. \frac{\partial T}{\partial x} \right|_{x=L^+} \quad (3)$$

A Crank–Nicholson numerical discretization is employed to solve the 1D unsteady heat conduction equation. It provides the temperature field in the substrate at every time step and, subsequently, the wall heat flux at the gauge location:

$$\dot{q}_w = -k_1 \left. \frac{\partial T}{\partial x} \right|_{x=0} \quad (4)$$

The local convective heat transfer coefficient is then computed as

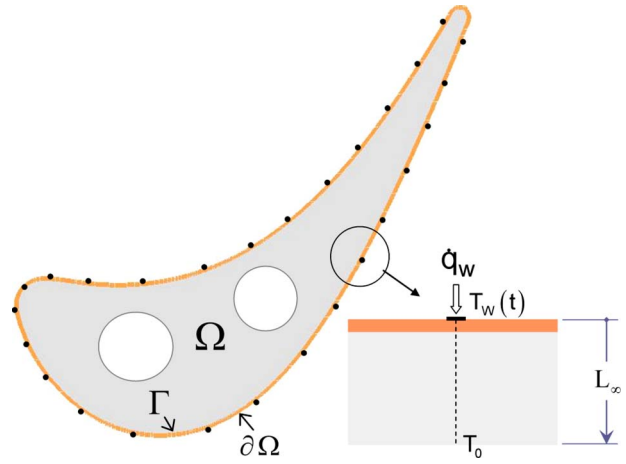


Fig. 5 Computational domain for the 1D approach

$$h = \frac{\dot{q}_w(t)}{T_{\text{gas}} - T_w(t)} \quad (5)$$

where the gas temperature T_{gas} is measured with microthermocouple probes [18], and the wall temperature evolution $T_w(t)$ is monitored by the thin-film gauge (Fig. 5).

3.2 2D Novel Unsteady Heat Calculation. By contrast to the previously presented 1D procedure, the current technique is able to accurately determine the wall heat flux distribution regardless of the complex airfoil geometry. The current method consists of directly solving the 2D unsteady heat conduction equation in the double-layered cross-sectional area of the tested airfoil. The initial temperature distribution, together with the reconstructed temperature history provided by the thin-film gauges around the airfoil, is necessary to solve the problem:

$$\frac{1}{\alpha} \frac{\partial T}{\partial t} = \frac{\partial^2 T}{\partial x^2} + \frac{\partial^2 T}{\partial y^2}$$

$$T(x, y, 0) = T_0(x, y), \quad x, y \in \Omega \quad (6)$$

$$T(x, y, t) = T_w(x, y, t), \quad x, y \in \partial\Omega, \quad 0 < t \leq t_f$$

A weighted residual (Galerkin) approach is used to derive the finite-element equations from the governing differential equation, Eq. (6). The solution of the resulting algebraic system provides the time-dependent temperature distribution inside the body and subsequently the normal heat flux to its external boundary [19]:

$$\dot{q}_w(x, y, t) = -k_1 \cdot \mathbf{n} \cdot \nabla T, \quad x, y \in \partial\Omega \quad (7)$$

The conservative property of the Galerkin approach ensures the continuity of the heat flux in the interface between the polyamide sheet and the metallic substrate:

$$-k_1 \cdot \mathbf{n} \cdot \nabla T = -k_2 \cdot \mathbf{n} \cdot \nabla T, \quad x, y \in \Gamma \quad (8)$$

The two-layered cross-sectional area of a cooled rotor blade is discretized with a 170,000 element mesh, as shown in Fig. 6.

The internal layer of the substrate is the metallic blade itself, and the external layer is the polyamide sheet (Upilex) over which the thin-film is deposited (thickness $\approx 150 \mu\text{m}$). The finite-element model of the 2D unsteady heat conduction is then employed to compute the time-dependent temperature distribution in the numerical domain.

The external layer was meshed with triangular, structured elements, while the internal layer presents an unstructured mesh. A careful sensitivity analysis was carried out to optimize the thickness of the elements adjacent to the external Upilex surface. The low thermal product ratios of the first and second layers,

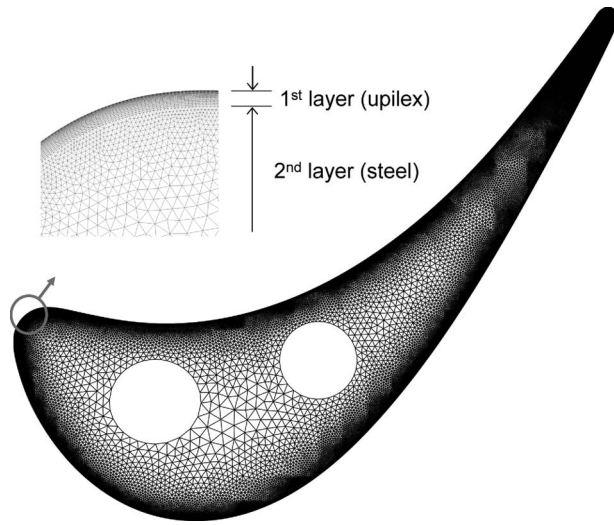


Fig. 6 FEM mesh of the two-layered rotor blade

$\sqrt{\rho_1 C_1 k_1} / \sqrt{\rho_2 C_2 k_2}$, indicate that large temperature gradients will appear in the Upilex wall at every time step [20]. A wall element thickness of $1.8 \mu\text{m}$ proved to accurately capture these wall temperature gradients. Elements with a length 20 times bigger than their thickness permitted decreasing the total size of the mesh without any loss of computation accuracy. A detail of the fine mesh built in the first layer is depicted in Fig. 6.

The resulting stiffness matrix, sparse and sized 87,000, needs to be solved with the efficient generalized minimal residual (GMRES) method [21]. Despite the increased computational cost, compared with 1D discretizations, computer capabilities permit nowadays a fast solution of the present problem. The computational time of the current calculation takes about 15 min in a Pentium IV processor. Considering that the rotor airfoil contains 22 thermal gauges, each local wall heat flux derivation involves around 40 s of computational time.

4 Results and Discussion

4.1 2D Effects in Actual Turbine Profiles. Two-dimensional heat conduction effects are traditionally neglected in the processing of short-duration heat transfer measurements. However, the experimental correlations or analytical corrections to account for radial heat conduction in curved regions do not consider the lateral phenomena induced by the nonuniform temperature field in the vicinity of the gauge under study. The semi-infinite assumption, which implies the extension of the 1D domain to a certain depth, is conversely not satisfied in the trailing edge region and the vicinity of cooling ducts.

To highlight the shortcomings of a purely 1D approach, the heat flux along the airfoil profile was computed prescribing as temperature evolution the analytical variation in a flat plate corresponding to a step of heat flux, therefore discarding any lateral heat conduction phenomenon. The temperature law, obtained by Doorly and Oldfield [10] for a 1D, semi-infinite double-layered substrate, is linked to a wall heat flux step \dot{q}_w :

$$T_w(t) = \frac{2\dot{q}_w}{\sqrt{\rho_1 C_1 k_1}} \left[(t/\pi)^{1/2} + 2 \sum_{n=1}^{\infty} A^n \left\{ (t/\pi)^{1/2} \exp \left[\frac{-n^2 L_1^2}{\alpha_1} \right] - \frac{n L_1}{\sqrt{\alpha_1}} \text{erf}(n L_1 / (\alpha_1 t)^{1/2}) \right\} \right] \quad (9)$$

where

Table 1 Properties of the double-layered domain

	ρ (kg/m ³)	C (J/kg K)	k (W/m K)
First layer	1470	1130	0.288
Second layer	7900	460	18

$$A = \frac{\sqrt{\rho_1 C_1 k_1} - \sqrt{\rho_2 C_2 k_2}}{\sqrt{\rho_1 C_1 k_1} + \sqrt{\rho_2 C_2 k_2}}$$

This equation was evaluated for a substrate with a first layer thickness $L_1 = 150 \mu\text{m}$ and thermal properties defined in Table 1. The imposed wall heat flux step is $\dot{q}_w = 30,000 \text{ W/m}^2$. The resulting time-dependent temperature evolution, with a duration of 0.5 s, is depicted in Fig. 7 together with the reconstructed wall heat flux. These conditions are representative of short-duration experiments in the compression tube facility.

The problem is solved in the cross-sectional area of the rotor blade under study with a time step corresponding to the sampling frequency and the next initial and boundary conditions

$$T(\Omega, 0) = 0 \text{ } ^\circ\text{C}$$

$$T(\partial\Omega, t) = T_w(t), \quad 0 < t_f(s) \leq 0.5$$

Temperature distribution in the cross-sectional area of the blade is shown in Fig. 8(a), with the determination of four control points. Wall heat flux distribution at the end of the test ($t_f = 0.5 \text{ s}$) is represented in Fig. 9(a). The associated error, depicted in Fig. 9(b), is defined as

$$\varepsilon(\%) = 100 \times \frac{\dot{q}_{1D} - \dot{q}_{2D}}{\dot{q}_{1D}} \quad (10)$$

The expected heat flux step \dot{q}_w is reconstructed in wide regions of the pressure side and suction side during the whole test duration, proving that these regions fulfill the 1D hypothesis. However, the wall heat flux evolution around the leading edge and trailing edge does not behave as a step function: The initial $30,000 \text{ W/m}^2$ heat flux reconstruction decays shortly after the commencement of the test (see locations 1 and 3 in Fig. 8(b)). This is due to the presence of curvature effects, mainly in the leading edge, and the failure of the semi-infinite assumption, which is predominant in the trailing edge.

The corrected wall heat flux in the leading edge can be computed with the analytical correction proposed by Buttsworth and Jones [15] for cylinders:

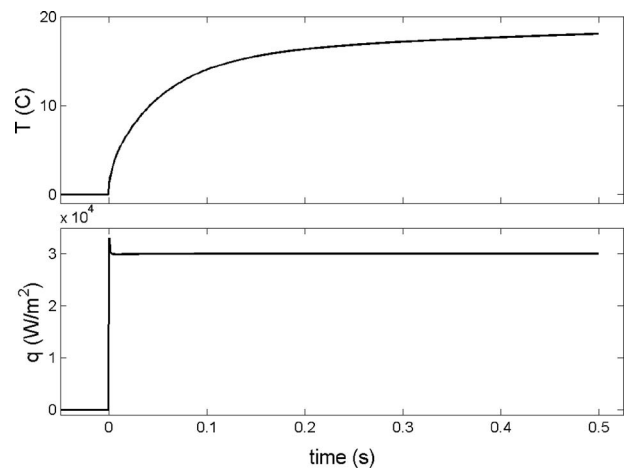


Fig. 7 Analytical temperature evolution and wall heat flux reconstruction under 1D semi-infinite assumptions

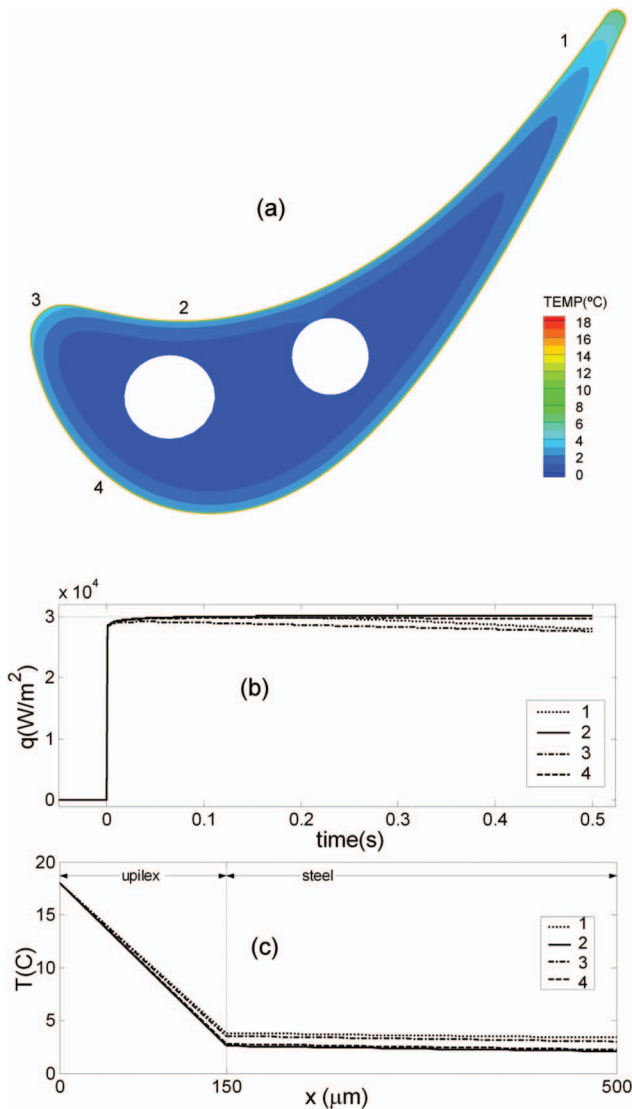


Fig. 8 (a) Temperature field in the cross-sectional area of the two-layered rotor blade at $t_f=0.5$ s, (b) wall heat flux evolution in four control points, and (c) temperature profile in the four control locations at $t_f=0.5$ s

$$\dot{q}_R = \dot{q}_{1D} - \frac{k_1}{2R}(T_w - T_0) \quad (11)$$

The application of this equation, being $R=24 \times 10^{-3}$, and $(T_w - T_0)$ the temperature of the analytical law depicted in Fig. 7(a) at $t_f=0.5$ s, yields a decrease of 4% of the resulting wall heat flux with respect to the 1D solution, i.e., $\dot{q}_{1D}=30,000$ W/m². These results do not agree with the wall heat flux computed with the 2D approach in the leading edge, which results in a value 8% lower than the 1D solution (see Fig. 9(b)).

4.2 Effects of Pretest Rotation. In spite of the relatively low levels of pressure during the rotor speed up, ventilation losses cause considerable blade heating. As a result of this process, the rotor blade presents a nonuniform wall temperature profile at the end of the pretest rotation (at about ~ 450 s). The experimental temperature profile around the rotor blade is depicted in Fig. 10(a). Similar trends for an uncooled rotor were evidenced with ceramic inserts [3]. Such distribution of external temperature results in a nonhomogeneous internal temperature map impossible to predict by means of 1D routines. The computation of this tem-

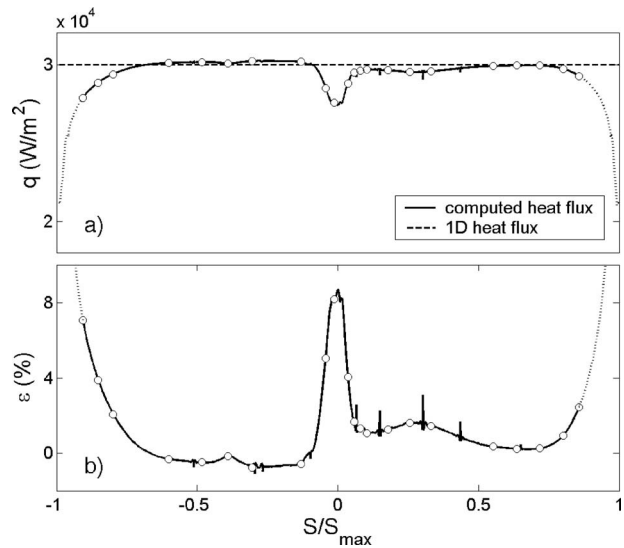


Fig. 9 (a) Wall heat flux distribution at $t_f=0.5$ s in the rotor blade submitted to uniform 1D boundary conditions and (b) local error distribution with respect to expected 1D solution

perature field, and the surface heat flux associated, is of utmost importance to determine the influence of this initial distribution in the subsequent blow-down test.

The surface temperature evolution during the rotor speed-up process can be approximated to a parabolic law, as depicted in Fig. 10(b). Data acquisition during a conventional test can be concentrated on the blow-down process if the temperature evolution in the gauge locations during the turbine pretest rotation are fitted with the law

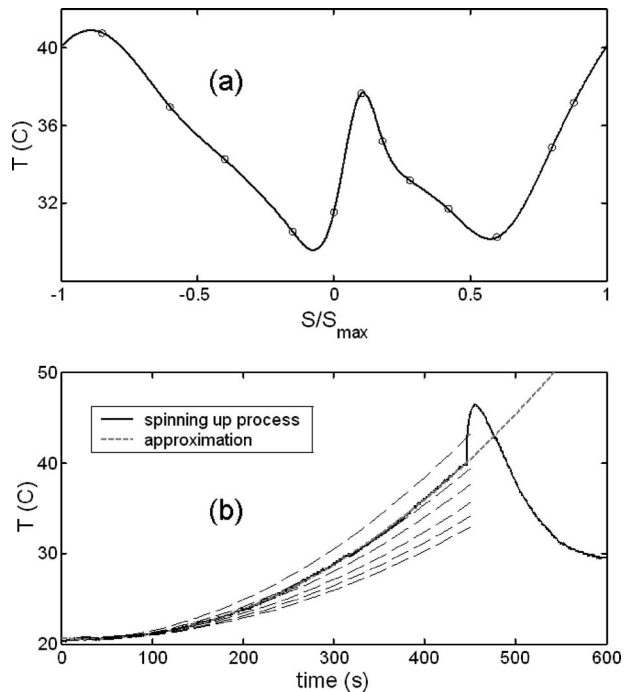


Fig. 10 (a) Temperature distribution at the end of the turbine pretest rotation ($t_f=450$ s) and (b) parabolic fitting of the temperature evolution during the pretest rotation

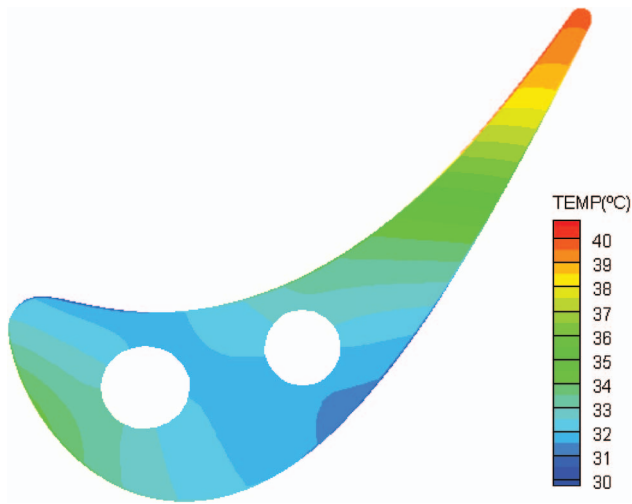


Fig. 11 Temperature field in the cross-sectional area of the two-layered rotor blade at $t_r=450$ s

$$T(x,y,t) = T_0 + K(x,y) \cdot t^2, \quad x,y \in \partial\Omega \quad (12)$$

where T_0 is the acquired initial temperature before the pretest rotation, considered uniform in the cross-sectional area of the blade. $K(s)$ is a constant value for each gauge location, so as to fit the local temperature measured at 6200 rpm.

The surface temperature in each external wall node is computed at every time step with a cubic spline interpolation algorithm. Thus, the necessary boundary conditions for the solution of the 2D unsteady heat conduction problem are imposed, together with the uniform initial temperature distribution

$$T(\Omega,0) = T_0$$

$$T(\partial\Omega,t) = T_{\text{pretest rotation}}(S/S_{\text{max}},t), \quad 0 < t_r(s) \leq 450$$

Figure 11 shows the temperature field across the rotor blade at the end of the pretest rotation ($t_r=450$ s). Wall heat flux distribution, prior to the blow-down test, is represented in Fig. 12 (dashed lines).

In both pressure and suction sides there exist regions where heat exits the blade ($q > 0$) and where heat enters the blade. This is a consequence of the nonuniform heating of the blade during the spinning-up process. Temperature distribution in the cross-sectional area of the blade (Fig. 11) justifies the existence of this pattern. This solution can be employed as initial condition in the processing of a characteristic blow-down test.

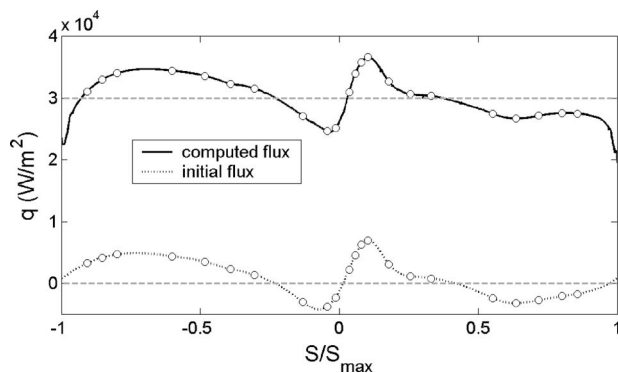


Fig. 12 Wall heat flux distribution at the end of the nonuniform analytical blow-down ($t_r=0.5$ s) versus initial wall heat flux distribution ($t_r=450$ s)

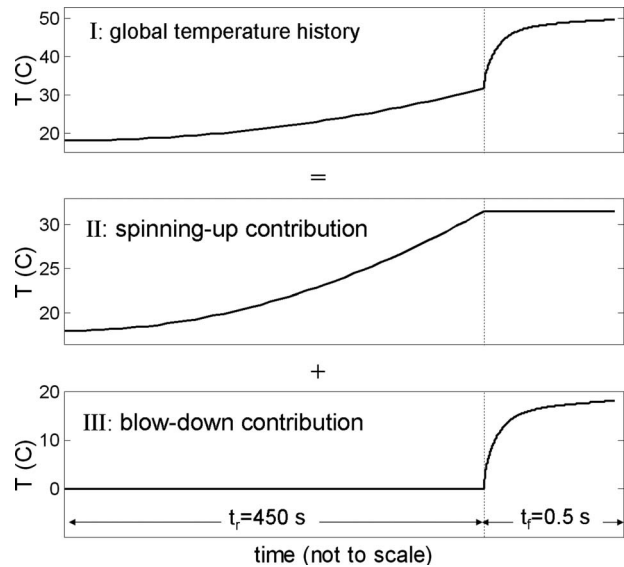


Fig. 13 Temperature history decomposition

4.3 Blow-Down Flux With an Initial Temperature Distribution. The effect of an initial temperature distribution prior to the actual test is studied by means of analytical temperature evolutions. Let us consider that each gauge is submitted to an external heat flux step of $30,000 \text{ W/m}^2$. Considering that the blade would behave as a semi-infinite flat plate, the temperature evolution is the one given by Eq. (9) plus a temperature shift dictated by the temperature at the end of the pretest rotation (see Fig. 10(a)). Hence, the 2D unsteady heat conduction problem is solved in the cross-sectional area of the coated rotor blade with the next initial and boundary conditions

$$T(\Omega,0) = T_{\text{pretest rotation}}(x,y,450)$$

$$T(\partial\Omega,t) = T_w(S/S_{\text{max}},t), \quad 0 < t_f(s) \leq 0.5$$

Figure 12 represents the surface heat flux reconstructed in the blade wall and the initial heat flux to the blade at the commencement of the blow-down. The influence of this initial heat flux distribution on the solution is clearly observed, compared with the wall heat flux obtained in the previous test case (Fig. 9(a)).

4.4 Superposition. The surface heat flux reconstructed in Fig. 12 is intrinsically associated with the global temperature history experienced by the blade during the spinning-up process followed by the short-duration test. This evolution is depicted as law (I) in Fig. 13 and can be decomposed into two independent temperature evolutions: law (II), which accounts for the pretest rotation heating, and law (III), which accounts for the blow-down process.

Therefore, the resulting heat flux could be computed as the superposition of the heat flux at the end of law (II) and the heat flux at the end of law (III). Considering the blow-down contribution (III), the wall heat flux derived at $t_r=450$ s is obviously zero, and the wall heat flux decrease in the short straight step ($t_r < t(s) < t_r+t_f$) of the spinning-up contribution (II) may easily be negligible. Then, it is clear that the surface heat flux at the end of the global temperature history can be computed as the addition of the initial heat flux to the blade (due to the pretest rotation heating) and the heat flux obtained in the solution of the blow-down with a uniform initial temperature distribution.

This conclusion is shown in Fig. 14(a), where surface heat flux computed with the presented superposition principle is compared with the solution of the heat flux associated with the global temperature history. Divergences between both solutions are negligible, and the resulting relative error of the superposition is, in

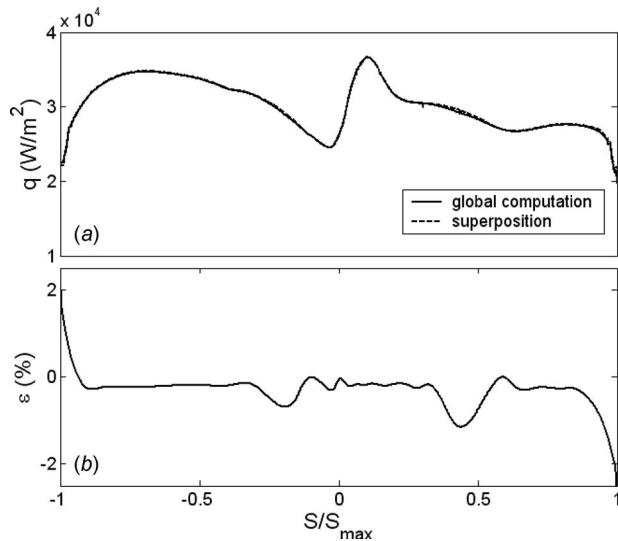


Fig. 14 (a) Comparison of two approaches for the computation of wall heat flux distribution: global computation and superposition of separate solutions and (b) relative error of the superposition procedure with respect to the global computation

any case, not higher than 1%, as shown in Fig. 14(b).

It is therefore admissible to sum up both separate solutions, which is of great importance for the simplification of the data processing methodology. The computation of the initial heat flux due to the pretest rotation, and the analysis of the short-duration test, can be solved independently. This principle provides the data processing routine with high flexibility. In problems where 2D heat conduction effects can be neglected, the final local heat flux can be obtained as the result of superimposing the initial wall heat flux (computed with the 2D approach) and the wall heat flux during the blow-down (computed with 1D assumptions). For the sake of simplicity, a 1D test was performed to account for the temperature profile inside the substrate during the global process (pretest rotation+blow-down). Temperature evolution corresponding to the leading edge of the rotor blade during the pretest rotation yields the wall heat flux evolution depicted in Fig. 15(a).

The solution derived at the end of the process is completely

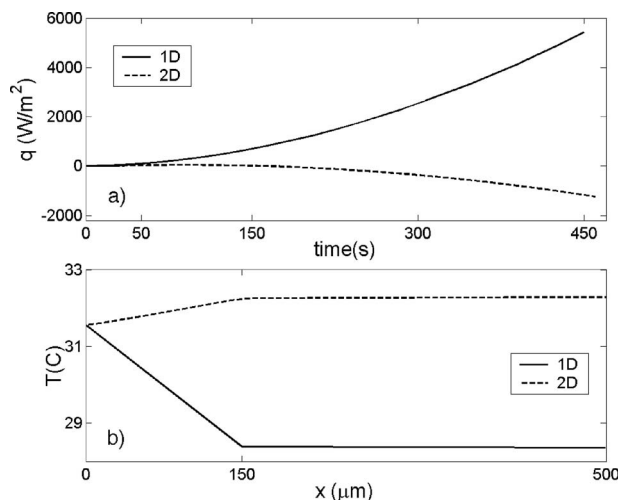


Fig. 15 (a) Wall heat flux evolution in the leading edge during the pretest rotation and (b) temperature distribution inside the leading edge substrate at the end of the pretest rotation ($t_r = 450$ s)

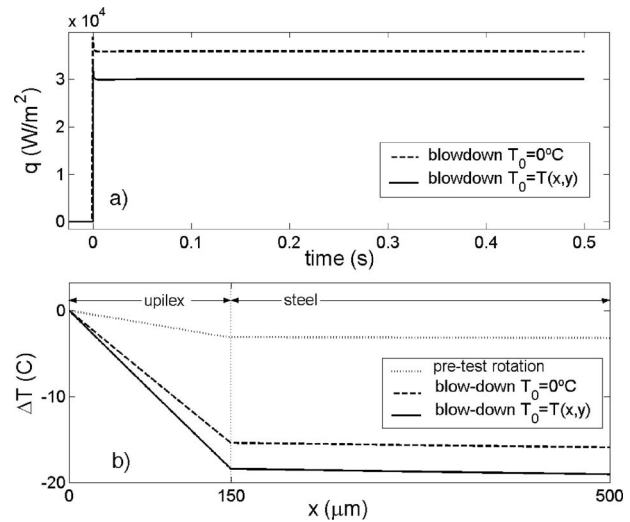


Fig. 16 (a) Wall heat flux evolution during a 1D blow-down for different initial temperature distributions and (b) shifted temperature profiles at the end of the pretest rotation and blow-down processes

different from the corresponding local wall heat flux to the blade computed with the 2D approach. It confirms again that 2D diffusion effects are dominant during the turbine pretest rotation. The corresponding temperature profile inside the substrate at the end of the pretest rotation, $t_r = 450$ s, is depicted in Fig. 15(b).

Wall heat fluxes during an analytical blow-down have been computed with initial uniform condition, imposing the 1D temperature profile of Fig. 15(b). It is clear in Fig. 16(a) that the wall heat flux derived from nonuniform initial conditions corresponds to the superposition of the analytical wall heat flux ($30,000$ W/m²) and the wall heat flux at the end of the spinning-up period (6120 W/m²).

Temperature profiles at the end of the blow-down with both initial conditions are shown in Fig. 16(b). It can be observed that the slope difference of both profiles is equal to the slope (and indirectly the wall heat flux) at the end of the pretest rotation.

4.5 Experimental Wall Heat Flux Distribution. The presented 2D methodology is next assessed with experimental data from a blow-down test. Figure 17 compares the heat flux derived with the 2D methodology with uniform initial temperature distribution ($T_0 = 0^\circ\text{C}$) and the result of applying the superposition principle over this solution (thus adding the initial heat flux of Fig. 12). The relative error defined as

$$\varepsilon(\%) = 100 \times \frac{q_{2D70(x,y)} - q_{\text{test}}}{q_{2D70(x,y)}} \quad (13)$$

is, in some regions, of the order of $\pm 20\%$ due to the neglect of the initial heat flux due to the spinning-up heating.

Classical 1D methodology was also employed [7], and the derived distribution was added to the initial heat flux that results from the pretest rotation. The comparison between the 1D and 2D superimposed distributions is shown in Fig. 18. Higher discrepancies exist in the leading edge and trailing edge region, as expected from the results obtained in the analytical test derived in Fig. 9.

Figure 19 shows the comparison between the corrected 1D data, using Eq. (11), and the results of the 2D computation. Although the corrections applied to the 1D data bring both solutions closer, still there are discrepancies in the leading edge region. The origin of these differences, of the order of 4%, can be found on the fact that Eq. (11) applies for cylinders, while the leading edge of the rotor blades does not present a constant curvature radius.

Moreover, the 2D diffusion promoted in the steel substrate once

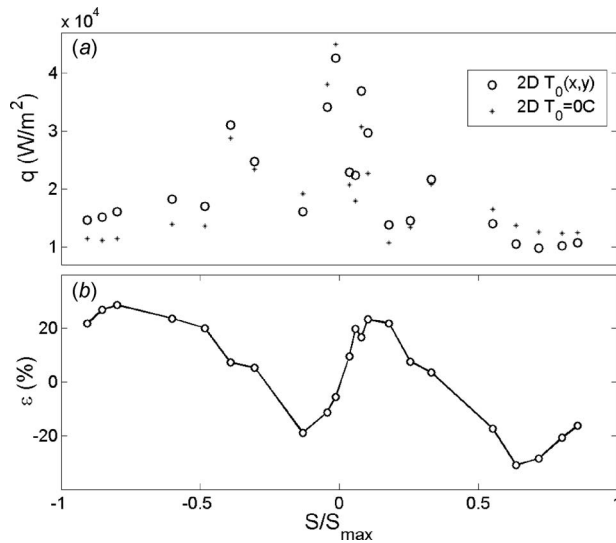


Fig. 17 (a) Experimental wall heat flux computation for uniform and nonuniform initial temperature distributions and (b) local error distribution referenced to uniform initial conditions

the thermal wave penetrates the Upilex steel interface is not taken into account, nor is the lateral heat conduction phenomena induced in the leading edge due to the observed temperature gradient. Similar trends were found in the analytical study depicted in Fig. 9. On the other hand, there are no expressions available to correct 1D experimental data in the trailing edge region.

5 Conclusions

An innovative methodology for processing transient heat transfer experiments with double-layered thin-film gauges was developed. The technique consists of solving the 2D unsteady heat conduction equation in the double-layered cross-sectional area of a turbine airfoil with finite-element discretization. The method was successfully employed to prove the existence of 2D heat conduction phenomena in short-duration heat transfer experiments. Under analytical boundary conditions for 1D models, it was demonstrated that the leading edge and the trailing edge of the airfoil do not fulfill the requirements for the classical 1D postprocessing

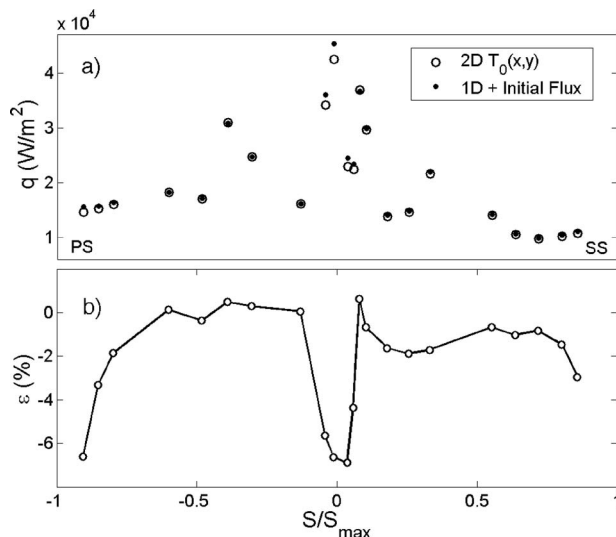


Fig. 18 (a) Wall heat flux computation with two approaches: 2D and 1D and (b) local error distribution referenced to 1D results

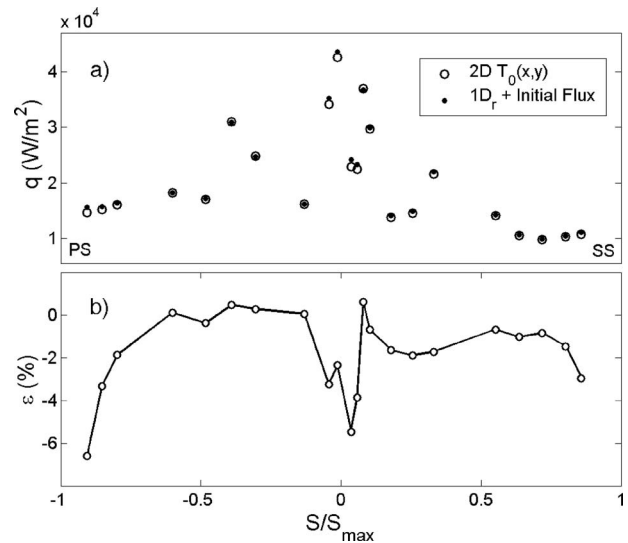


Fig. 19 (a) Wall heat flux computed with 2D approach and 1D approach corrected with Buttsworth and Jones' [15] analytical expressions and (b) local error distribution referenced to 1D corrected results

assumptions: 2D heat conduction phenomena appear, as a result of the curvature of the geometry and the absence of a semi-infinite substrate.

The temperature distribution and wall heat flux to the blade at the end of the pretest rotation in rotating facilities, as a result of ventilation preheating, were also assessed. The important contribution of this nonuniform wall heat flux in the subsequent short-duration test was determined. Experimental data were processed with the novel methodology and with classical 1D models combined with analytical expressions to account for the radial heat conduction in the leading edge. These 1D corrections do not reproduce faithfully the solution obtained with the 2D methodology due to the failure of the restrictive assumptions of their analytical derivation.

The superposition principle proved to be a powerful tool for data processing routines. The separate solutions of the initial heat flux after the pretest rotation heating, and the blow-down test, can be added to yield the final surface heat flux distribution.

The large potential of the technique makes possible its extension to the heat transfer data processing of other techniques (such as infrared thermography and liquid crystal). Furthermore this procedure can be used as a design tool for optimizing airfoil heat transfer instrumentation.

Acknowledgment

The authors would like to thank Rémy Denos who initiated this research. Special thanks to Andrés de la Loma and Bertrand Haguenaer for their devotion to the physical understanding of the heat transfer phenomena in our rotating rig. Likewise, they are grateful to Terence Boeyen for the implementation of the sensors, acquired from TAO Systems. The authors wish to acknowledge the financial support of the European Commission and industrial partners involved in "Turbine Aero-Thermal External Flows 2" (TATEF2).

Nomenclature

- C = specific heat at constant pressure (J/(kg K))
- h = heat transfer coefficient (W/(m² K))
- k = thermal conductivity (W/(m K))
- L = layer thickness (m)
- M = Mach number
- n = vector normal to the blade wall (m)

Nu = Nusselt number (hD/k)
 P = power (W)
 \dot{q} = heat flux (W/m^2)
 R = curvature radius (m)
 T = temperature (K)
 t = time (s)

Greek Symbols

α = thermal diffusivity (m^2/s)
 ρ = density (kg/m^3)
 ε = error
 Ω = 2D numerical domain
 Γ = substrate interface
 $\partial\Omega$ = external boundary

Subscripts

0 = initial condition
 1 = index for the first layer
 2 = index for the second layer
 ∞ = semi-infinite
 w = wall
 r = time at spinning-up process
 f = time at blow-down process

References

- [1] Arts, T., and Lambert de Rouvroit, M., 1992, "Aero-Thermal Performance of a Two-Dimensional Highly Loaded Transonic Turbine Nozzle Guide Vane: A Test Case for Inviscid and Viscous Flow Computations," *ASME J. Turbomach.*, **114**, pp. 147–154.
- [2] Dunn, M. G., 1985, "Measurement of Heat Flux and Pressure in a Turbine Stage," *ASME J. Eng. Gas Turbines Power*, **107**, pp. 76–83.
- [3] Dénos, R., 1996, "Aerothermal Investigation of the Unsteady Flow in the Rotor of a Transonic Turbine Stage," Ph.D. thesis, University of Poitiers, France.
- [4] Didier, F., Dénos, R., and Arts, T., 2002, "Unsteady Rotor Heat Transfer in a Transonic Turbine Stage," *ASME J. Turbomach.*, **124**(4), pp. 614–622.
- [5] Epstein, A. H., Guenette, G. R., Norton, R. J. G., and Yuzhang, C., 1986, "High-Frequency Response Heat-Flux Gauge," *Rev. Sci. Instrum.*, **57**(4), pp. 639–649.
- [6] Doorly, J. E., and Oldfield, M. L. G., 1986, "New Heat Transfer Gages for Use on Multilayered Substrates," *ASME J. Turbomach.*, **108**, pp. 153–160.
- [7] Iliopoulou, V., Dénos, R., Billiard, N., and Arts, T., 2004, "Time-Averaged and Time-Resolved Heat Flux Measurements on a Turbine Stator Blade Using Two-Layered Thin-Film Gauges," *ASME J. Turbomach.*, **126**, pp. 570–577.
- [8] Piccini, E., Guo, S. M., and Jones, T. V., 2000, "The Development of a New Direct-Heat-Flux Gauge for Heat-Transfer Facilities," *Meas. Sci. Technol.*, **11**, pp. 342–349.
- [9] Schultz, D. L., and Jones, T. V., 1973, "Heat Transfer Measurements in Short Duration Facilities," AGARDograph Report No. 165.
- [10] Doorly, J. E., and Oldfield, M. L. G., 1987, "The Theory of Advanced Multi-Layer Thin Film Heat Transfer Gauges," *Int. J. Heat Mass Transfer*, **30**(6), pp. 1159–1168.
- [11] Billiard, N., Iliopoulou, V., Ferrara, F., and Dénos, R., 2002, "Data Reduction and Thermal Product Determination for Single and Multi-Layered Substrates Thin-Film Gauges," *Proceedings of the 16th Symposium on Measuring Techniques*, Cambridge, UK.
- [12] Smith, M., and Kueth, A., 1966, "Effects of Turbulence on Laminar Skin Friction and Heat Transfer," *Phys. Fluids*, **9**, pp. 2337–2344.
- [13] Kestin, J., and Wood, R., 1971, "The Influence of Turbulence on Mass Transfer From Cylinders," *Trans. ASME, Ser. C: J. Heat Transfer*, **93**, pp. 321–327.
- [14] Lowery, G. W., and Vachon, R. I., 1975, "The Effect of Turbulence on Heat Transfer From Heated Cylinders," *Int. J. Heat Mass Transfer*, **18**, pp. 1229–1242.
- [15] Buttsworth, D. R., and Jones, T. V., 1997, "Radial Conduction Effects in Transient Heat Transfer Experiments," *Aeronaut. J.*, **101**, pp. 209–212.
- [16] Traupel, W., 1958, *Thermische Turbomaschinen*, Vol. 1, Springer, Göttingen, Heidelberg.
- [17] Dénos, R., Paniagua, G., Yasa, T., and Fortugno, E., 2006, "Determination of the Efficiency of a Cooled HP Turbine in a Blow-Down Facility," ASME Paper No. GT-2006-9046.
- [18] Paniagua, G., Dénos, R., and Oropesa, M., 2002, "Thermocouple Probes for Accurate Temperature Measurements in Short Duration Facilities," ASME Paper No. GT-2002-30043.
- [19] Rao, S. S., 1989, *The Finite Element Method in Engineering*, 2nd ed., Pergamon, New York.
- [20] Incropera, F. P., and DeWitt, D. P., 2002, *Introduction to Heat Transfer*, 4th ed., Wiley, New York.
- [21] Saad, Y., and Schultz, M. H., 1986, "GMRES: A Generalized Minimal Residual Algorithm for Solving Nonsymmetric Linear Systems," *SIAM (Soc. Ind. Appl. Math.) J. Sci. Stat. Comput.*, **7**, pp. 856–869.

An Experimental Investigation of the Cold Mass Fraction, Nozzle Number, and Inlet Pressure Effects on Performance of Counter Flow Vortex Tube

Volkan Kirmaci

Faculty of Engineering,
Mechanical Engineering Department,
Bartın University,
74100 Bartın, Turkey
e-mail: volkankirmaci@gmail.com

Onuralp Uluer

Faculty of Technical Education,
Department of Mechanical Education,
Gazi University,
Teknikokullar,
06503 Ankara, Turkey

This paper discusses the experimental investigation of vortex tube performance as it relates to cold mass fraction, inlet pressure, and nozzle number. The orifices have been made of the polyamide plastic material. Five different orifices, each with two, three, four, five and six nozzles, respectively, were manufactured and used during the test. The experiments have been conducted with each one of those orifices shown above, and the performance of the vortex tube has been tested with air inlet pressures varying from 150 kPa to 700 kPa with 50 kPa increments and the cold mass fractions of 0.5–0.7 with 0.02 increments. The energy separation has been investigated by use of the experimentally obtained data. The results of the experimental study have shown that the inlet pressure was the most effective parameter on heating and the cooling performance of the vortex tube. This occurs due to the higher angular velocities and angular momentum conservation inside the vortex tube. The higher the inlet pressure produces, the higher the angular velocity difference between the center flow and the peripheral flow in the tube. Furthermore, the higher velocity also means a higher frictional heat formation between the wall and the flow at the wall surface of the tube. This results in lower cold outlet temperatures and higher hot outlet temperatures. [DOI: 10.1115/1.3111259]

Keywords: counter flow vortex tube, cold mass fraction, heating, cooling

1 Introduction

The vortex tube, also known as Ranque vortex tube, Hilsch vortex tube, and Ranque–Hilsch vortex tube, is a device that enables the separation of hot and cold air as pressurized air flows tangentially into the vortex chamber through inlet nozzles [1–5]. Vortex tube was first discovered in 1933 by metallurgist and physicist Ranque, and the German physicist Hilsch improved the design [6]. A vortex tube consists of one or more inlet nozzles, a vortex chamber, a cold-end orifice, a hot-end control valve, and a tube [7]. Specially designed vortex chamber's internal configuration, combined with the effect of the pressure, accelerates the air to a high rate of rotation (over a million rpm) [8].

A high pressure gas stream enters into the vortex tube, tangentially, and there it splits into two lower pressure streams: one hot and one cold temperature streams. Cold gas stream leaves the tube through a center orifice near the entrance nozzle, while the hot gas stream flows toward control valve and leaves the tube there [4,9]. Centrifugal separation of the two split flow elements, and their adiabatic expansion causes the energy separation in the vortex tube system.

The vortex tube can be used in many industrial applications such as cooling equipment of computer numerical control (CNC) machine tools, refrigerators, cooling suits, heating processes, etc., because it is simple, compact, light, and quiet. Since it has no moving parts, it does not cause to break or wear the unit and therefore it requires little maintenance [7,10]. There are two types of flow in vortex tubes, such as parallel flow and counter flow

[4,11]. The working principle of the counter flow can be defined as follows: A compressible fluid, which is tangentially introduced into the vortex tube from nozzles, starts to make a circular movement inside the vortex tube at high speeds, caused by the cylindrical structure of the tube, depending on its inlet pressure and speed. A pressure difference occurs between the tube wall and the tube center caused by the friction of the fluid circling at high speeds, though the radial pressure gradient also is partially responsible for the separation of the two streams. The speed of the fluid near the tube wall is lower than the speed at the tube center due to the effects of wall friction. As a result, the fluid in the center region transfers energy to the fluid at the tube wall, depending on the geometric structure of the vortex tube. The cooled fluid leaves the vortex tube by moving against the main flow direction after the stagnation point, whereas the heated fluid leaves the tube in the main direction [12]. In Figs. 1 and 2 the schematic representations of the parallel flow and counter flow vortex tubes are shown. In this study, the counter flow vortex tube was elected. The energy separation in counter flow vortex tube is shown in Fig. 3.

Ahlborn et al. [13] carried out measurements in the vortex tubes to support their models for calculating limits of temperature separation. They also attributed the heating to the conversion of kinetic energy into heat and the cooling to the reverse process. Ahlborn et al. [14] identified the temperature splitting phenomenon of a Ranque–Hilsch vortex tube in which a stream of gas divides itself into a hot and a cold flow as a natural heat pump mechanism, which is enabled by a secondary circulation.

Lewins and Bejan [15] suggested that the angular velocity gradients in the radial direction give rise to frictional coupling between different layers of the rotating flow resulting in a migration of energy via shear work from the inner layers to the outer layers. Trofimov [16] verified that the dynamics of internal angular mo-

Contributed by the Heat Transfer Division of ASME for publication in the JOURNAL OF HEAT TRANSFER. Manuscript received September 11, 2008; final manuscript received February 26, 2009; published online June 5, 2009. Review conducted by Ali Ebadian.

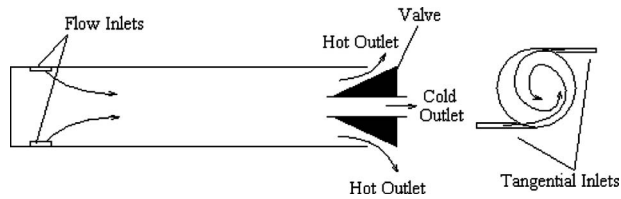


Fig. 1 The schematic representation of a parallel flow vortex tube principle [11]

mentum leads to this effect. Saidi and Valipour [17] presented information data on the classification of the parameters affecting vortex tube operation. In their study, the thermophysical parameters such as inlet gas pressure, type of gas and cold gas mass ratio, moisture of inlet gas, and the geometrical parameters, i.e., diameter and length of main tube diameter of the outlet orifice and shape of the entrance nozzle, were designated and studied. Singh [18] reported the effect of various parameters such as cold mass fraction, nozzle, cold orifice diameter, hot outlet of the tube, and L/D ratio on the performance of the vortex tube. Dincer et al. [12] investigated the effect of control valve tip angle on the performance of Ranque–Hilsch vortex tube using different inlet pressures ($P_i=200\text{--}420$ kPa) and different nozzle numbers ($N=2,4,6$).

Cockerill [11] studied the vortex tubes for use in gas liquefaction and mixture separation as applied to uranium enrichment for determining the basic performance characteristics, and the relationship between cold air temperature versus hot air temperature, and cold mass fraction, and the variation in the hot discharge tube wall temperature with a hot tube length. Cockerill also reported a mathematical model for the simulation of a compressible turbulent flow in a vortex tube. Promvong and Eiamsa-ard [19] experimentally studied the energy and temperature separations in the vortex tube with a snail entrance. Depending on their experimental results, the use of a snail entrance could help increase the cold air temperature drop and improve the vortex tube efficiency when compared with those of original tangential inlet nozzles. Promvong and Eiamsa-ard [20] furthermore reported the effects of the number of inlet tangential nozzles, the cold orifice diameter, and the tube insulations on the temperature reduction and isentropic efficiency of the vortex tube. Aydın and Baki [21] investigated experimentally the energy separation in a counter flow vortex tube having various geometrical and thermophysical parameters.

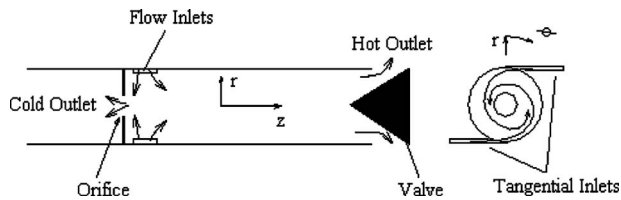


Fig. 2 The schematic representation of a counter flow vortex tube principle [11]

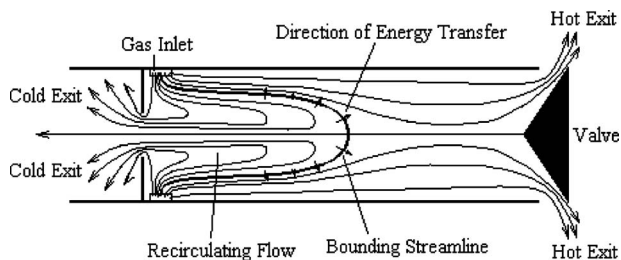


Fig. 3 Energy separation of counter flow vortex tube [11]

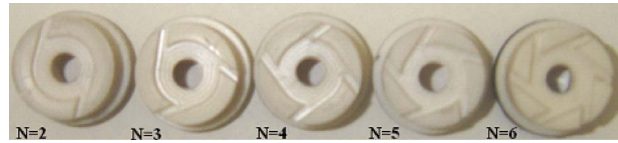


Fig. 4 Orifices used in the experiments

In this study, the performance of a counter flow type vortex tube is determined in regard to the measured cold outlet temperature and the hot outlet temperature gradient. The difference of this study from the previous studies is to determine the performance of the counter flow type vortex tube (L/D ratio is 15) by use of the processing conditions such as inlet pressure in a large pressure scale with very small increments, cold mass fraction with small increments, and nozzle numbers from 2 to 6 together.

2 Experimental Study

In this study, a counter flow type vortex tube with L/D ratio equal to 15 was used. Five different orifices with different nozzle numbers (2–6) have been manufactured and used in the experiments, as shown in Fig. 4. Polyamide plastic was used as an orifice material. The thermal conductivity of polyamide plastic is 0.25 W/m $^{\circ}$ C, the specific heat is 4400 J/kg $^{\circ}$ C, and its density is 1173 kg/m 3 . Each one of the nozzles has the same constant rectangular cross section (2×2 mm 2). The schematic of the experimental setup is shown in Fig. 5.

The inlet pressures and the hot and cold outlet pressures of the vortex tube have been measured by use of a pressure gauge (precision tolerance of ± 0.01 bar), as shown in Fig. 5. The mass flow rates at the cold and hot outlets of the vortex tube have been measured by use of a rotameter with ± 0.02 m 3 /h precision tolerance. The temperatures of the pressurized air at the inlet and the cold and hot outlets were measured by use of a digital thermometer with $\pm 0.5^{\circ}$ C precision tolerance, and the obtained temperature values have been converted into kelvins. Temperature probes of the digital thermometer were placed into the $\varnothing 1$ mm hole, which was drilled at the center of the vortex tube and 1 cm away from the cold and the hot outlets. The cavities between the probes and the hole were filled with silicon in order to prevent the leakage. A control valve has been mounted on the hot outlet of the tube in order to adjust the mass flow rate of the hot air. With the help of this valve, cold mass fraction (μ_c) was being adjusted from 0.50 to 0.70 in 0.02 increments. Before starting the experimental studies, the control valve on the hot outlet was kept in

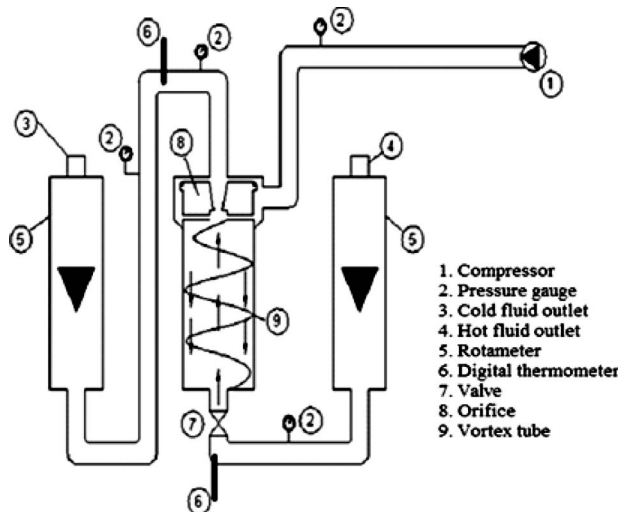


Fig. 5 The schematic of the experimental setup

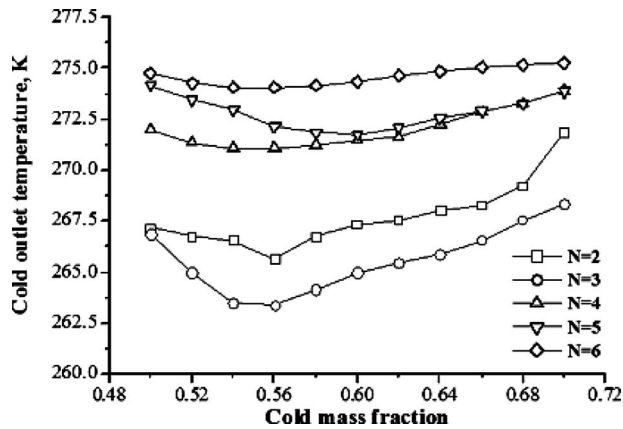


Fig. 6 Cold outlet temperatures versus cold mass fractions at $P_i=700$ kPa inlet pressure

fully open position. And then the air compressor was started and by use of the valve placed on the vortex tube inlet side, the beginning pressure value of 150 kPa was reached. Until the constant temperature values have been reached at the cold outlet and at the hot outlet of the vortex tube, the compressed air flow is continued. And during this stage, the mass flow rates and pressures of the air at the cold outlet and hot outlet were measured by using rotameters and pressure gauges, respectively. This experimental cycle was made three times for the entire inlet pressures selected (150–700 kPa with 50 kPa increments) and for the cold mass fractions (0.50–0.70 with 0.02 increments) with the different orifices selected (with two, three, four, five, and six nozzle numbers). The mean values of the measured results have been used to obtain the energy separation.

3 Results and Discussion

In this study the performance of the vortex tube with $L/D=15$ and $N=2,3,4,5,6$ was tested under the $P_i=150-700$ kPa and $\mu_c=0.50-0.70$ conditions with compressed air. The cooling (ΔT_c) and the heating (ΔT_h) effects of the vortex tube are defined as follows, respectively:

$$\Delta T_c = T_i - T_c \quad (1)$$

$$\Delta T_h = T_h - T_i \quad (2)$$

In general, the performance of the vortex tube was defined as the difference between the heating effect and the cooling effect [18,20]. Subtracting Eq. (1) from Eq. (2) gives the vortex tube performance equation as follows:

$$\Delta T = T_h - T_c \quad (3)$$

The cold mass fraction is one of the important parameters since it indicates the vortex tube performance and the energy separation inside the vortex tube. Cold mass fraction is defined as the percentage of the pressurized air input to that released through the cold end of the tube and can be calculated by using Eq. (4). The cold mass fraction can be controlled by the cone valve, which is placed at the hot end of the tube. This can be expressed as follows:

$$\mu_c = \frac{\dot{m}_c}{\dot{m}_i} \quad (4)$$

where \dot{m}_i and \dot{m}_c are the mass flow rates at the inlet of the vortex tube and at the cold outlet, respectively [22]. For each of the nozzles used in the experiments, the minimum cold outlet temperature value was measured when $\mu_c \cong 0.56$ and $P_i=700$ kPa. The measured minimum cold outlet temperatures of the air at 700 kPa inlet pressure are shown in Fig. 6.

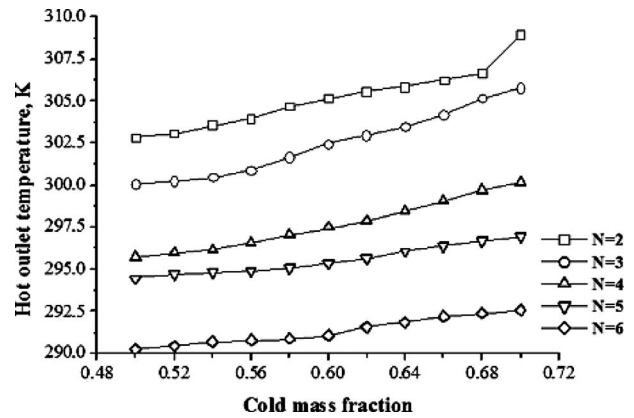


Fig. 7 Hot outlet temperatures versus cold mass fractions at $P_i=700$ kPa inlet pressure

As shown in Fig. 6, for each one of the nozzles used when the μ_c was adjusted to 0.56 with $N=2,3,4,5,6$ the cold outlet temperatures were measured as follows: 265.66 K, 263.36 K, 271.06 K, 272.16 K, and 274.06 K, respectively. For each one of the nozzles used in the experiments, maximum hot outlet temperature values have been measured when $\mu_c \cong 0.7$ and $P_i=700$ kPa. The measured maximum hot outlet temperatures of the air at 700 kPa inlet pressure are shown in Fig. 7.

As shown in Fig. 7, when the μ_c was adjusted to 0.70 for each one of the nozzles of $N=2,3,4,5,6$ the hot outlet temperatures were measured as follows: 308.96 K, 305.76 K, 305.76 K, 296.96 K, and 292.56 K, respectively. The cold mass fraction is the maximum cold mass fraction ratio used in this study. But, as shown in Fig. 7, increasing the cold mass fraction ratio also shows an increasing tendency of the hot outlet temperature. And this means that in order to obtain a higher hot outlet temperature the cold mass fraction ratio is to be increased.

When we look at Figs. 6 and 7 again, the hot outlet temperature values changing from maximum to minimum have been obtained for the nozzle numbers of 2, 3, 4, 5, and 6, respectively, while the cold outlet temperature values varying from minimum to maximum have been obtained for the nozzle numbers of 3, 2, 4, 5, and 6, respectively.

For testing the performance of the vortex tube the temperature gradient was used, and the performances are shown in Figs. 8–12 according to cold mass fraction and inlet pressure for each of the orifices. Increasing the orifice nozzle number has decreased the cold and the hot outlet temperature gradient. But, if the nozzles are considered separately, the increase in the pressure also increases the temperature gradient. As shown in Figs. 8–12, increasing the vortex tube inlet pressure has also increased the temperature gradient between the cold and the hot outlets. However, increasing the orifice nozzle number has decreased the cold and the hot outlet temperature gradient. For testing the performance of the vortex tube the temperature gradient was used, and the performances are shown in Figs. 8–12 according to cold mass fraction and inlet pressure for each one of the orifices. It is understood from the graphics that the inlet pressure is the most effective parameter for heating and cooling performances.

As shown in Figs. 8–12, the temperature gradient between the cold and hot outlets is decreased when we consider the effects of the nozzle numbers. But, if we consider the nozzles separately the increase in the pressure increases the temperature gradient.

4 Conclusion

In this study, the experimental data for a counter flow type vortex tube with $L/D=15$ have been tested by using the compressed air and five different orifices with different nozzle numbers ($N=2,3,4,5,6$) under the processing conditions of 150–700

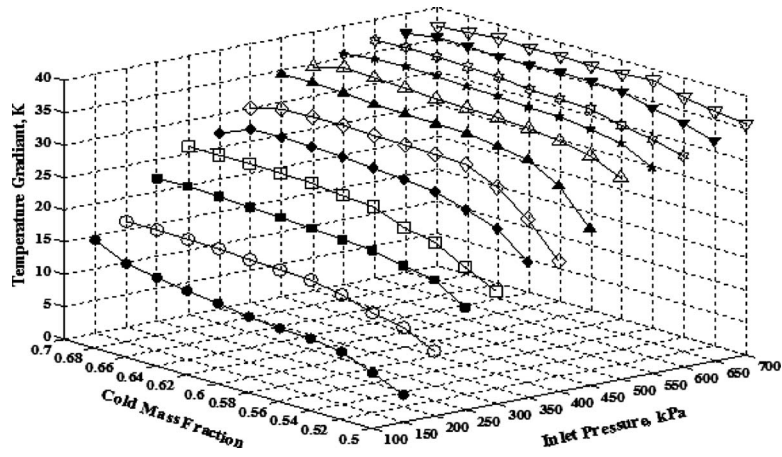


Fig. 8 The temperature gradient versus cold mass fractions and inlet pressures ($N=2$)

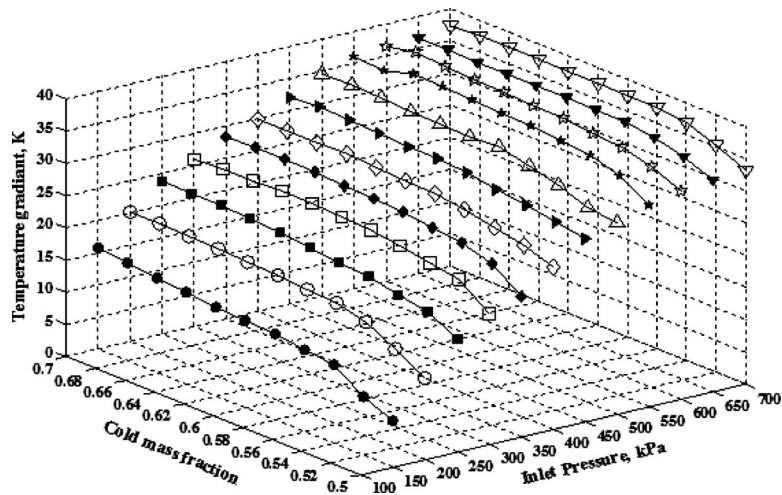


Fig. 9 The temperature gradient versus cold mass fractions and inlet pressures ($N=3$)

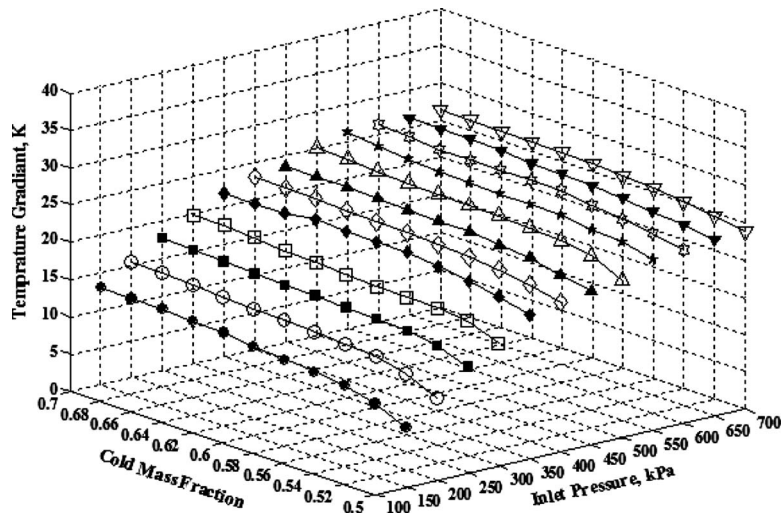


Fig. 10 The temperature gradient versus cold mass fractions and inlet pressures ($N=4$)

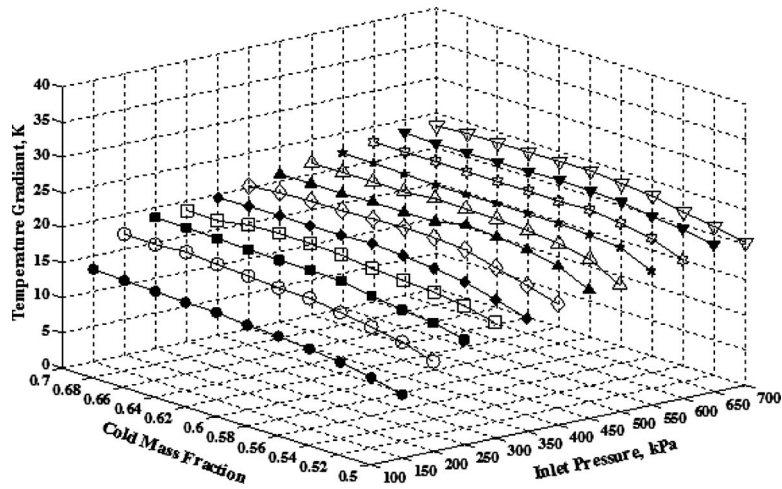


Fig. 11 The temperature gradient versus cold mass fractions and inlet pressures ($N=5$)

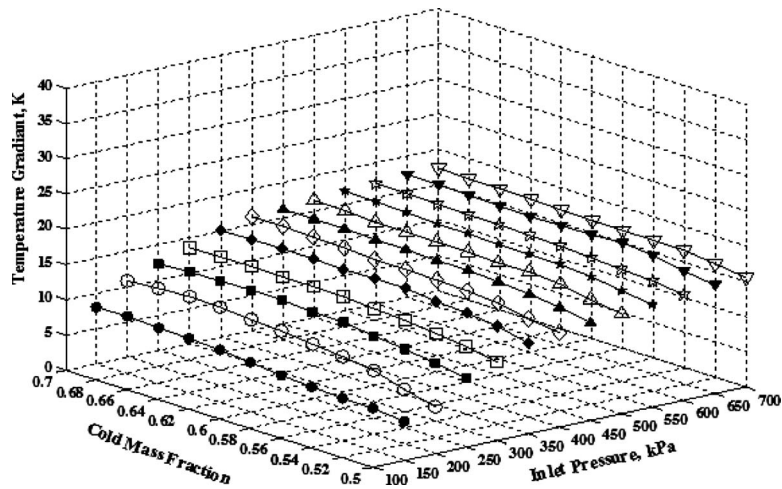


Fig. 12 The temperature gradient versus cold mass fractions and inlet pressures ($N=6$)

kPa with 50 kPa increments and cold mass fractions of 0.5–0.70 with 0.02 increments to obtain the vortex tube performance. To do so, the difference between the heating effect and the cooling effect is used as the performance metric. According to the experimental results, the temperature gradient between the cold and hot outlets is decreased when we take into account the effects of the nozzle numbers. But, if we consider each nozzle separately the increase in the pressure increases the temperature gradient. Furthermore, it appears that as the nozzle number increases, the temperature gradient becomes less sensitive to the inlet pressure. The maximum temperature gradient between the cold and hot outlets is obtained when the orifice number is 2. This can be explained by the flow rate variations. For a fixed mass flow rate, when the nozzle number is increased it means that the total flow area increases and the orifice exit velocity decreases, as shown in Fig. 13.

Increasing the vortex tube inlet pressure, the temperature gradient between the cold and the hot outlets was increased. Increasing the orifice nozzle number has decreased the cold and the hot outlet temperature gradient. Furthermore, the minimum cold outlet temperature was measured when μ_c was 0.56 and P_i was 700 kPa, and the maximum hot outlet temperature was measured when μ_c was 0.70, which is the last tested maximum cold mass fraction in this study and then P_i was 700 kPa. This means that under those high pressure conditions, high cold mass fractions give

greater air flow, but they do not possibly give the lowest temperatures. The combination of high cold mass fraction of air flow and cold outlet temperature produces the maximum cooling capacity. A low cold mass fraction means that a smaller volume of air comes out, which is very cold. In short, the less the air is released,

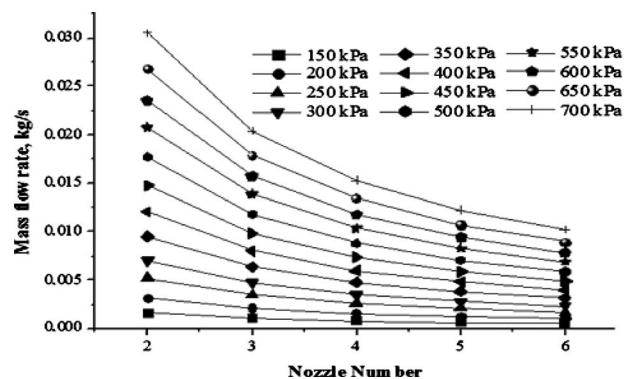


Fig. 13 Mass flow rate variation according to the nozzle number

the colder the air will be. For cooling applications such as spot cooling needs, cooling of the cutting tools in manufacturing processes, etc., for a fixed mass flow rate, the minimum cold mass fraction has to be chosen, and for heating applications such as melting the glues, softening the plastics, humidifying the ambient air, etc., for a fixed mass flow rate, the cold mass fraction ratio has to be increased.

Nomenclature

- \dot{m} = mass flow rate, kg/s
 P = pressure, kPa
 T = temperature, K
 ΔT = temperature gradient, K
 μ_c = cold mass fraction

Subscripts

- i = inlet
 c = cold outlet
 h = hot outlet

References

- [1] Khodorkov, L., Poshernev, N. V., and Zhidkov, M. A., 2003, "The Vortex Tube-A Universal Device for Heating, Cooling, Cleaning, and Drying Gases and Separating Gas Mixtures," *Chem. Petrol. Eng.*, **39**, pp. 409–415.
- [2] Wu, Y. T., Ding, Y., Ji, Y. B., Ma, C. F., and Ge, M. C., 2007, "Modification and Experimental Research on Vortex Tube," *Int. J. Refrig.*, **30**, pp. 1042–1049.
- [3] Lewins, J., and Bejan, A., 1999, "Vortex Tube Optimization Theory," *Energy*, **24**, pp. 931–943.
- [4] Eiamsa-ard, S., and Promvong, P., 2008, "Review of Ranque-Hilsch Effects in Vortex Tubes," *Renewable Sustainable Energy Rev.*, **12**, pp. 1822–1842.
- [5] Aljuwayhel, N. F., Nellis, G. F., and Klein, S. A., 2005, "Parametric and Internal Study of the Vortex Tube Using a CFD Model," *Int. J. Refrig.*, **28**, pp. 442–450.
- [6] Ranque, M. G., 1933, "Experiences sur la detente avec production simultanees d'un echappement d'air chaud et d'un echappement d'air froid," *J. Phys. Radium*, **4**, pp. 112–115.
- [7] Chengming, G., 2005, Technische Universiteit Eindhoven, p. 151.
- [8] Hilsch, R., 1947, "The Use of the Expansion of Gases in a Centrifugal Field as Cooling Process," *Rev. Sci. Instrum.*, **18**, pp. 108–1113.
- [9] Gao, C. M., Bosschaart, K. J., Zeegers, J. C. H., and de Waele, A. T. A. M., 2005, "Experimental Study on a Simple Ranque-Hilsch Vortex Tube," *Cryogenics*, **45**, pp. 173–183.
- [10] Kirmaci, V., and Uluer, O., 2008, "The Effects of Orifice Nozzle Number on Heating and Cooling Performance of Vortex Tubes: An Experimental Study," *Instrum. Sci. Technol.*, **36**, pp. 493–502.
- [11] Cockerill, T., 1995, "Thermodynamic and Fluid Mechanics of Ranque-Hilsch Vortex Tube," MS thesis, University of Cambridge, Cambridge, England.
- [12] Dincer, K., Baskaya, S., Uysal, B. Z., and Ucgul, I., 2009, "Experimental Investigation of the Performance of a Ranque-Hilsch Vortex Tube With Regard to a Plug Located at the Hot Outlet," *Int. J. Refrig.*, **32**, pp. 87–94.
- [13] Ahlborn, B., Keller, J. U., Staudt, R., Treitz, G., and Rebhan, E., 1994, "Limits of Temperature Separation in a Vortex Tube," *J. Phys. D: Appl. Phys.*, **27**, pp. 480–488.
- [14] Ahlborn, B., Keller, J. U., and Rebhan, E., 1998, "The Heat Pump in a Vortex Tube," *J. Non-Equilib. Thermodyn.*, **23**, pp. 159–165.
- [15] Lewins, J., and Bejan, A., 1999, "Vortex Tube Optimization Theory," *Energy*, **24**, pp. 931–943.
- [16] Trofimov, V. M., 2000, "Physical Effect in Ranque Vortex Tubes," *JETP Lett.*, **72**, pp. 249–252.
- [17] Saidi, M. H., and Valipour, M. S., 2003, "Experimental Modeling of Vortex Tube Refrigerator," *Appl. Therm. Eng.*, **23**, pp. 1971–1980.
- [18] Singh, P. K., Tathgir, R. G., Gangacharyulu, D., and Grewal, G. S., 2004, "An Experimental Performance Evaluation of Vortex Tube," *J. Inst. Eng. (India), Part MC*, **84**, pp. 149–153.
- [19] Promvong, P., and Eiamsa-ard, S., 2004, "Experimental Investigation of Temperature Separation in a Vortex Tube Refrigerator With Snail Entrance," *ASEAN J. Science & Technol Development*, **21**, pp. 297–308.
- [20] Chengming, G., 2005, "Experimental Study on the Ranque-Hilsch Vortex Tube," Technische Universiteit Eindhoven, Proefschrift.
- [21] Aydin, O., and Baki, M., 2006, "An Experimental Study on the Design Parameters of a Counter Flow Vortex Tube," *Energy*, **31**, pp. 2763–2772.
- [22] Dincer, K., Baskaya, S., and Uysal, B. Z., 2008, "Experimental Investigation of the Effects of Length to Diameter Ratio and Nozzle Number on the Performance of Counter Flow Ranque-Hilsch Vortex Tubes," *Heat Mass Transfer*, **44**, pp. 367–373.

A Bejan's Constructal Theory Approach to the Overall Optimization of Heat Exchanging Finned Modules With Air in Forced Convection and Laminar Flow Condition

Giulio Lorenzini¹

e-mail: giulio.lorenzini@unibo.it

Simone Moretti

Department of Agricultural Economics and Engineering,
Alma Mater Studiorum-University of Bologna,
viale Fanin no. 50,
40127 Bologna, Italy

Optimizing ever smaller heat exchangers determines two opposite needs: augmenting performances, on the one hand; removing heat in excess to reduce failures, on the other. This numerical study, modeled thanks to Bejan's Constructal theory, researches the overall optimization of finned modules, differently shaped and combined, cooled by air in laminar flow and forced convection condition: Losses of pressure, together with heat removed, contribute to the final assessment made through a novel idea of performance based on the so called overall performance coefficient. [DOI: 10.1115/1.3109996]

Keywords: Bejan's Constructal theory, heat removal, fins, numerical methods, optimization

1 Introduction

Modern technology requires more powerful and heat generating components to be utilized. The easiest solution would be that of using bigger heat exchangers, but volume occupation is also a problem. So optimizing shape and flow conditions in a heat exchanger is now compulsory. Numerical codes can help in such purpose, saving time and money with respect to experimental approaches. In scientific literature manifold contributes analyze thermal performance trends of extended surfaces with different boundary conditions superimposed. Among them, Refs. [1,2] offer useful experimental results in relation to air cooled finned heat exchangers. Moreover, in Ref. [3], one can observe the performances in the air side of the same exchangers. Other studies, mainly theoretical-numerical ones, offer a more complete vision of the processes analyzed. Among the most relevant ones one can quote Refs. [4–6], analyzing the performance of a few finned heat exchanging devices in relation to their geometry. There are also papers, such as Ref. [7], facing this problem for each single fin. Such approach fully matches that employed in the present paper. Here, starting from the root of the problem (i.e., the fin), it is investigated how to affect the behavior of the whole heat exchanger. Other researches, as in Refs. [8,9], provide, instead, a comparative analysis among different kinds of finned shapes utilized in a modular context. The present investigation derives from such approaches and from the subsequent developments made by the same authors of this paper. The importance of simple shapes is confirmed by many papers in literature, as in Refs. [10,11], where we can find an interesting example of performance optimization in differently shaped metal cavities wetted by a coolant. The investigation performed here is based on a numerical approach to evaluate the performances of finned heat exchangers. The advantages of an enhanced and optimized geometry is an already ac-

quired datum in the scientific panorama and many papers faced this phenomenon, which presently represents the “bottle neck” limiting further technological developments [12–21]. The researches recently performed by the authors of the present paper and published in Refs. [22–25] utilized a commercial finite element method (FEM) computational fluid dynamics (CFD) code called COMSOL MULTIPHYSICS and were all based on Bejan's Constructal theory, a very powerful modeling approach. In particular, in Ref. [26] Bejan and Almgöbel faced the problem of optimizing T-shaped fins to get the highest conductance possible through the fin root. Many applications proving the effectiveness of the Constructal theory are easily available in literature, in a large number of fields. A useful example is that in Ref. [27], analyzing the geometrical evolution of droplets impact against a solid plane wall, in function of their final velocity. In Ref. [23] Lorenzini and Moretti tested the accuracy of the numerical code, via the method adopted, by analyzing the same geometry and boundary conditions of [26]: The performance results were in extremely good agreement with the reference study. Successively the challenge shifted to the research of new fin geometries able to further improve the thermal removing ability of the extended surface systems considered. So, in Ref. [22], the case of Y-shaped fins was studied, which were designed starting from the optimized T-shaped ones obtained in Ref. [23]. This was made possible by the introduction of new morphological parameters such as the angle between the two horizontal arms of the fin and the fin encumbrance. Once determined which kind of fins could determine which kind of heat removal advantage, a further step was that of investigating multifin modules. This was made in Refs. [24,25] with the aim of designing a device to be applied in an industrial production context. It was so achieved an interesting outcome: clarifying which multifin system can assure the best performance. However, as in Ref. [26], the boundary condition superimposed at the interface fin—local environment, in all the studies performed [22,25], was that of ideally forced convection with infinite velocity of the coolant sweeping the fins along their sides (or, in other words, a pure conductive model), i.e., constant convection coefficient. This, of course, denotes the particular condition of a fluid,

¹Corresponding author.

Contributed by the Heat Transfer Division of ASME for publication in the JOURNAL OF HEAT TRANSFER. Manuscript received July 24, 2008; final manuscript received December 10, 2008; published online June 3, 2009. Review conducted by Yogesh Jaluria.

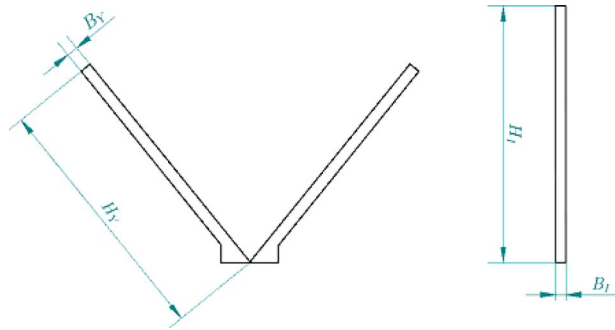


Fig. 1 I fin and Y fin

which is not affected by the contact heating because of its infinite velocity, but cannot cope with the entire amount of technical cases possible. So it was necessary to do further research concerning actual forced convection with variable heat exchange coefficients. This condition, novel for what relates a Bejan's Constructal theory approach to this kind of problems, is one of the challenges of the present paper. As anticipated, the models onto which this investigation is based represent the technological context in a very accurate way. The practical aim of the study is so evident; in fact, both the flow and the thermal fields inside the coolant (air) are fully considered to solve the general problem called conjugate heat transfer. In more detail, attention has been put to the study of different layouts of fins, in order to identify which configurations, intended as flow conditions and mutual location of the profiles examined, perform better in specific applications. In particular, this study focuses on a laminar flow condition with a Reynolds number of less than 1500. Therefore the process of optimization takes into account not only the thermal flux removed by the finned extensions, but also the losses of pressure within the coolant, which is the pumping power required by the heat exchanger to work in that particular way. Such choice implied the necessity of defining a criterion able to identify univocally this "convenience": This is also a goal of the present publication. It has, in fact, been defined a parameter, called overall performance coefficient, considering both aspects into account for a final decision about the most convenient heat exchanger, depending on the application required.

2 Systems and Conditions Investigated

The geometrical models employed in this research can be referred to two different roots. The first root is that of the classic I shape (see Fig. 1), very common in heat exchangers for electronic applications. The second root is that of the Y profiles (see Fig. 1) already optimized in Refs. [22,24,25]. The characteristic dimensions of these fins, defined in Fig. 1, are B_I (m) and H_I (m), for the former shape, and B_Y (m) and H_Y (m), for the latter. They satisfy the following condition:

$$H_I = H_Y; \quad B_I = B_Y \quad (1)$$

The optimal Y fin and module were determined for certain geometrical ratios: (fin base thickness/fin arm thickness)=5 and (fin base length/fin arm length)=0.07. The intention was to optimize the evaluation parameter, i.e., the dimensionless conductance q^* , defined as [26]

$$q^* = \frac{q_L}{k(T_R - T_\infty)} \quad (2)$$

where q_L ($W m^{-1}$) is thermal power per unit length through the root of the heat exchanging profile; k ($W m^{-1} K^{-1}$) is thermal conductivity; T_R (K) and T_∞ (K) are the fin root temperature and the undisturbed one (that is the undisturbed flow inlet temperature), respectively. The reference studies focused on thermal con-

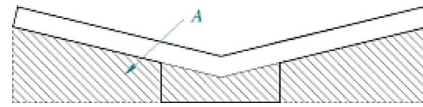


Fig. 2 Example of A in a Y fin

duction, with the convection coefficient h ($W m^{-2} K^{-1}$) being constant. That parameter was defined in function of the geometry of the fin [26]

$$h = \frac{a^2 k}{2\sqrt{A}} \quad (3)$$

where a is a number dependent on thermal convection, k ($W m^{-1} K^{-1}$) is thermal conductivity, A (m^2) is the surface subtended by the horizontal arms of the fins, as Fig. 2 displays. The assumptions adopted in Refs. [22–25] approximate the process of a refrigerant fluid flowing in the z -direction (see Fig. 3) with "infinite" velocity. In the present study, instead, the attention has been drawn by the "actual" phenomenon of forced convection; the thermal fluid dynamics within the refrigerant fluid (air, $Pr \approx 0.71$) flowing along the x -axis (see Fig. 3) was also numerically simulated. As Fig. 4 shows, the geometrical model utilized in the simulations performed is composed of a duct of fixed length, chosen after suitable tests and the superimposition of an inlet parabolic flow profile. The parameter L (m) displayed in Fig. 4 represents the length of the multifin module, which gives the pitch of the periodical structure of a multimodule (with Y fins) heat exchanger [24,25]. Its multiple $3 \times L = L_D$ (m) was a fundamental parameter here, which has been kept constant throughout the research, while H (m), the height of the duct considered, varied through the variation in the dimensionless duct shape ratio θ

$$\theta = \frac{H}{L_D} \quad (4)$$

On the whole, four geometrical models have been analyzed. Each model was characterized by a particular shape, as their name will recall from now on. These shapes, from A to D, are displayed in Figs. 5–8. As the four geometries considered prove, the study puts in relation the Y shape with the "classic" I one, comparing the two. As explained above, the cross-sectional area of the I profile is half of the Y one; this justifies a 1:2 comparison, where five Y fins are compared with ten I fins, and each one of the four shapes investigated have the same cross-sectional area. Moreover, in all the tests performed for this study, the length (horizontal direction) devoted to a heat exchanging module has been always kept constant and equal to L_D (m), both in the case of fins concentrated on the bottom surface of the duct and in the case of fins distributed

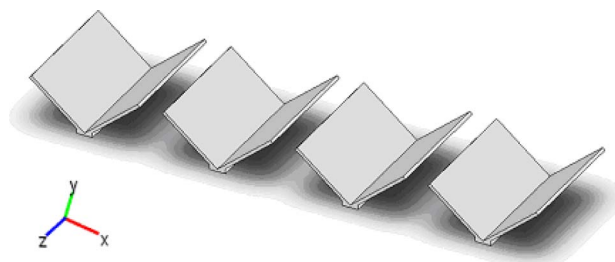


Fig. 3 Heat exchanging module with Y fins



Fig. 4 Example of geometrical model simulated (duct) and its characteristic dimensions

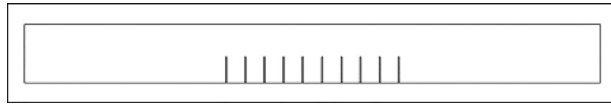


Fig. 5 Shape A: I fins just at the bottom surface

both on the bottom and on the top surfaces. Then, to focus on a specific problem once the geometrical parameters involved in the study have been fully defined, it was also superimposed a condition of laminar flow acting on the inlet flow, with the Reynolds number never exceeding 1500, defined as

$$Re = u\rho D\eta^{-1} \quad (5)$$

where u ($m\ s^{-1}$) is the x -component of the channel inlet velocity (see Fig. 3), ρ ($kg\ m^{-3}$) is the volumic mass of the refrigerant fluid at its inlet temperature, η [$kg\ m^{-1}\ s^{-1}$] is the dynamic viscosity of the refrigerant fluid at its inlet temperature, and D (m) is the characteristic length of the duct, computed starting from the idea of equivalent diameter

$$D = \frac{4S}{P_{cs}} \quad (6)$$

where P_{cs} (m) is the duct cross sectional perimeter “wetted” by the refrigerant fluid and S (m^2) is the duct cross-sectional area. As a consequence of the geometry adopted, the characteristic length D (m) is equal to $2H$ (m), double the duct height. As clearly anticipated, this investigation aims at creating a novel tool for the correct choice of the suitable heat exchanger in each particular application. The answer the industry gives to such a problem is related to which of the two following needs is more important: either to remove more elevated heat fluxes per unit surface, so requiring compact heat exchangers with high performance, or to reduce, as possible, the pumping power requested by the forced convection process involving the refrigerant fluid. The latter draws attention on the losses of pressure, which, by the way, tend to be inversely proportional to the heat removing performances. Such a variable, fundamental for the present evaluation, has been computed as the difference between the mean inlet pressure p_{in} and the mean outlet pressure p_{out} , made dimensionless by dividing it by the atmospheric pressure $p_0 = 1.013 \times 10^{-1}$ MPa:

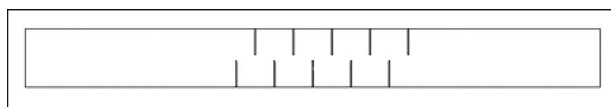


Fig. 6 Shape B: I fins both at the bottom and at the top surfaces

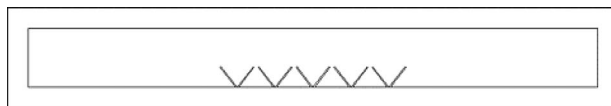


Fig. 7 Shape C: Y fins just at the bottom surface

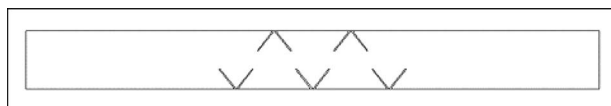


Fig. 8 Shape D: Y fins both at the bottom and at the top surfaces

Table 1 Grid refinement depending on shape ratio θ

Geometry	Shape ratio			
	$\theta=0.1$	$\theta=0.15$	$\theta=0.2$	$\theta=0.25$
Shape A	8060	10,364	12,428	14,604
Shape B	8186	10,554	12,592	14,834
Shape C	8933	11,135	13,285	15,565
Shape D	9247	11,437	13,555	15,753

$$\Delta p^* = \frac{p_{in} - p_{out}}{p_0} \quad (7)$$

So, the final challenge faced here is that of finding an overall optimization criterion for the heat exchanging extended profiles, as a consequence not only of heat removing issues, as generally done, but also of more general evaluations of the process occurring. The boundary conditions applied to all the models investigated (issue treated in Sec. 3 of this paper) are partially in common with those in Refs. [22–25]: T_R (K) is equal to 373.15 K and T_∞ (K) is equal to 297.15 K. These values, dimensional, are arbitrary but they do not limit the general applicability of the study, as the parameter investigated (and to be optimized) is the dimensionless conductance q^* , as defined in Eq. (2). Moreover, for what concerns the material which the fins are made of, aluminum was chosen, which has a thermal conductivity k ($W\ m^{-1}\ K^{-1}$) equal to $200\ W\ m^{-1}\ K^{-1}$. This choice, again, is arbitrary even if typical of the field, but through the definition of Eq. (2), it does not affect the generality of the treatment. It was then superimposed a null duct outlet pressure, typical in numerical modeling, so as to obtain an inlet backward value equal to the actual difference in pressure between inlet and outlet. Obviously, volumic mass and viscosity, necessary for the correct punctual computation of the flow and temperature fields within the domain, were initially computed at a pressure value p_0 (Pa). The relations employed for viscosity and volumic mass are [28]

$$\eta(T) = (-7.887 \times 10^{-12}) * (T^2 + 4.427 \times 10^{-8}) * (T + 5.204) \times 10^{-6}$$

$$\rho(p, T) = (28.8p \times 10^{-3})T/8.314$$

3 Method and Tests Performed

The finite element CFD code employed was COMSOL MULTIPHYSICS Version 3.3. Specific details are available in the manuals [28]. The grid refinement was the object of a first preliminary investigation aimed at determining the least number of elements able to provide a grid-independent solution. Such number is, obviously, strictly related to the particular geometry considered and to the shape ratio θ , as Table 1 shows, quoting the values of θ investigated in the present study. An example of the meshing results obtained can be observed in Fig. 9 for the case of $\theta=0.15$.

4 Results and Preliminary Discussion

The performances of the different models examined have been evaluated under two different points of view. Initially four differ-

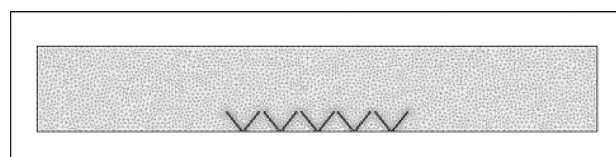


Fig. 9 Example of meshing (case $\theta=0.15$)

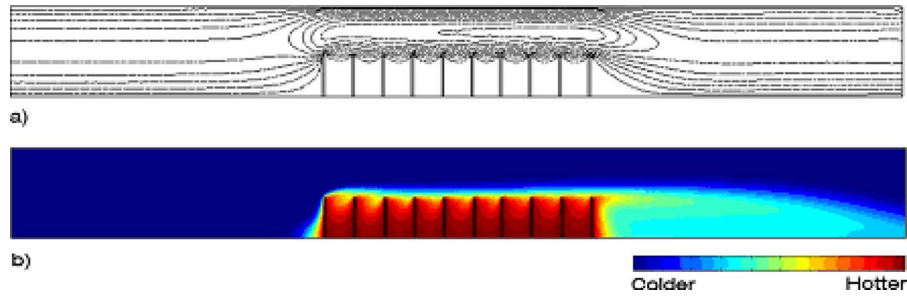


Fig. 10 Example of velocity (a) and temperature (b) fields (shape A; $\theta=0.1$)

ent cases were defined, characterized by incremental values of θ . Then, for every given value of θ , Re was varied up to 1500.

4.1 Case 1: $\theta=0.1$. This model is characterized by a height of the duct considered H (m), which is 1/10 of its length L_D (m). As a consequence the fins strongly hamper the refrigerant fluid in its flow. The friction between fluid and solid walls enhances thermal removal up to a very significant level, but, on the contrary, elevated losses of pressure affect significantly the overall performance of the model by lowering it. The numerical elaboration of the models provided temperature and velocity distributions within the computational domain: obviously the results varied from case to case with Re, but qualitatively they can be represented by the examples in Figs. 10–13, one for each shape considered in this

investigation. A performance analysis of the different modules, based on the previously defined dimensionless parameters, i.e., thermal conductance and loss of pressure between inlet and outlet, can be made starting from the functional trends represented in Figs. 14 and 15. As the aforementioned figures clearly display, when the duct height is so small, as in case 1, the model that maximizes the thermal power removed is shape D, which is the one with Y fins distributed both at the bottom and at the top sides of the duct. The optimal value of dimensionless thermal conductivity for Re=1500, found for shape D, is equal to $q^* = 1.2389338 \times 10^{-2}$, while the worst case, which is shape B, resulted in $q^* = 2.008769 \times 10^{-3}$. For what pertains to the losses of pressure, fundamental in case pumping power has to be econo-

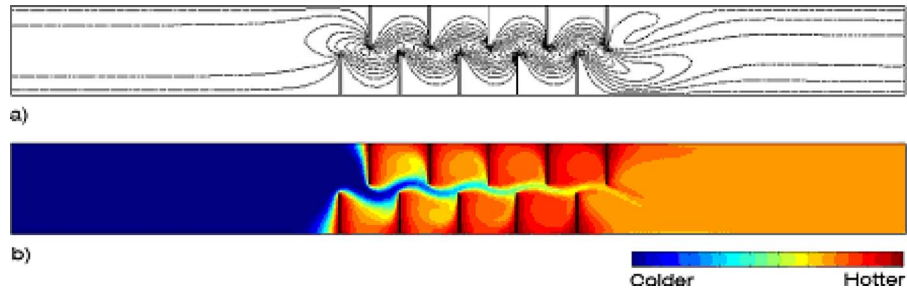


Fig. 11 Example of velocity (a) and temperature (b) fields (shape B; $\theta=0.1$)

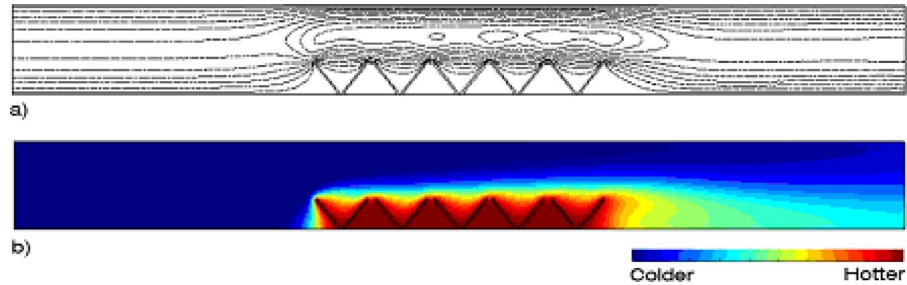


Fig. 12 Example of velocity (a) and temperature (b) fields (shape C; $\theta=0.1$)

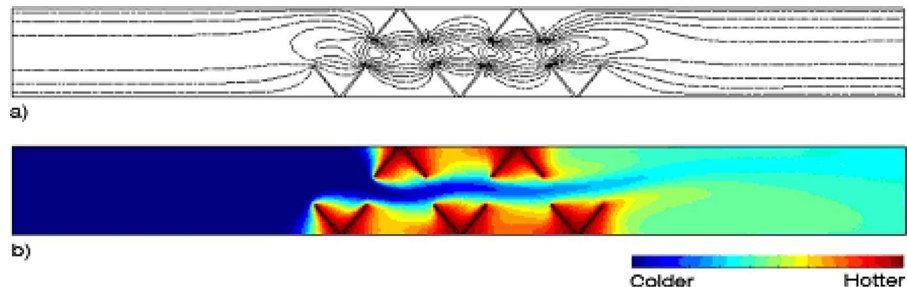


Fig. 13 Example of velocity (a) and temperature (b) fields (shape D; $\theta=0.1$)

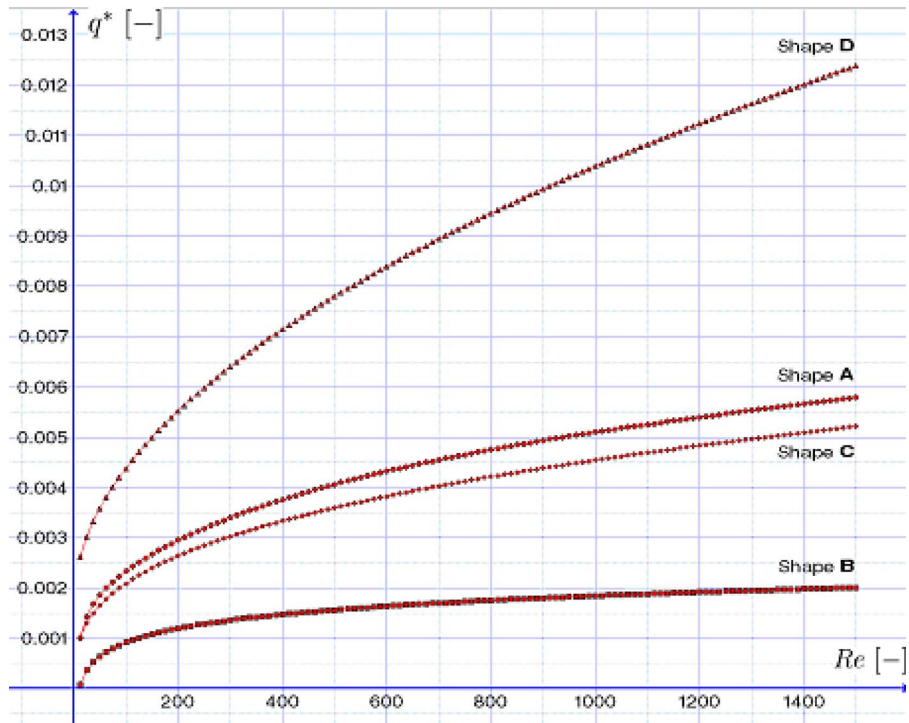


Fig. 14 Dimensionless conductance q^* in function of the Reynolds number Re : case $\theta=0.1$

mized for the refrigerant flow, it is advisable to use a shape C heat exchanger. This is the one with Y fins located just at the bottom side of the duct. In such case and still for $Re=1500$, in fact, one obtains a dimensionless loss of pressure between inlet and outlet equal to $\Delta p^*=5.09563 \times 10^{-8}$; in the worst case, instead, i.e., for shape B, it was found that $\Delta p^*=6.05452 \times 10^{-7}$.

4.2 Case 2: $\theta=0.15$. In this second case study the enhancement of the duct cross-sectional area affects the parameters involved in the simulation: The characteristic qualitative trends of flow and temperature fields in this case can be observed in the Figs. 16–19. As it can be inferred by looking at Fig. 20, the best performing heat exchanging module in terms of the heat flux re-

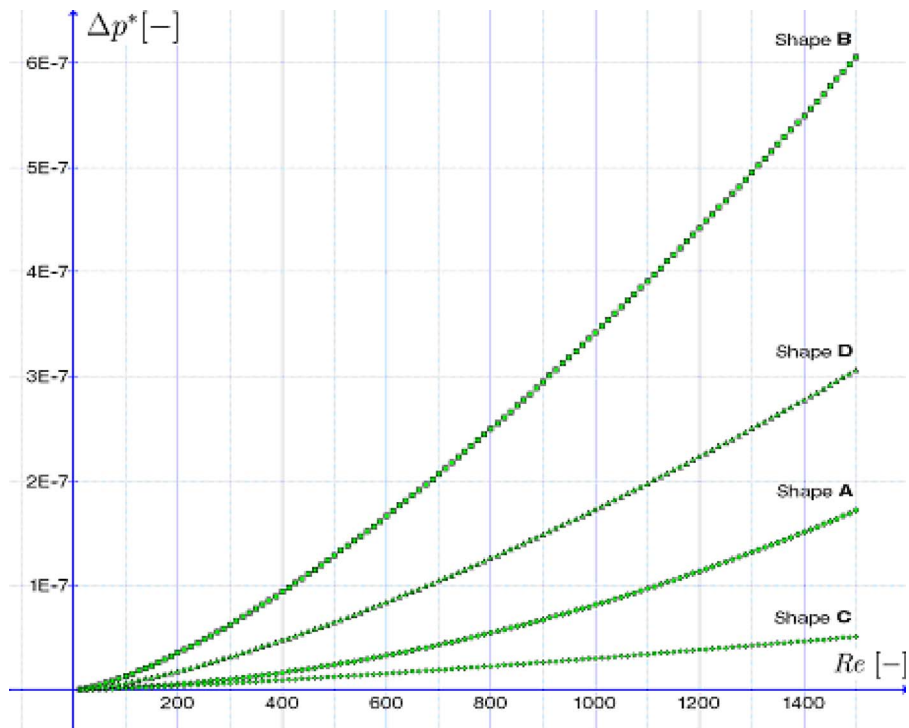


Fig. 15 Dimensionless loss of pressure Δp^* in function of the Reynolds number Re : case $\theta=0.1$

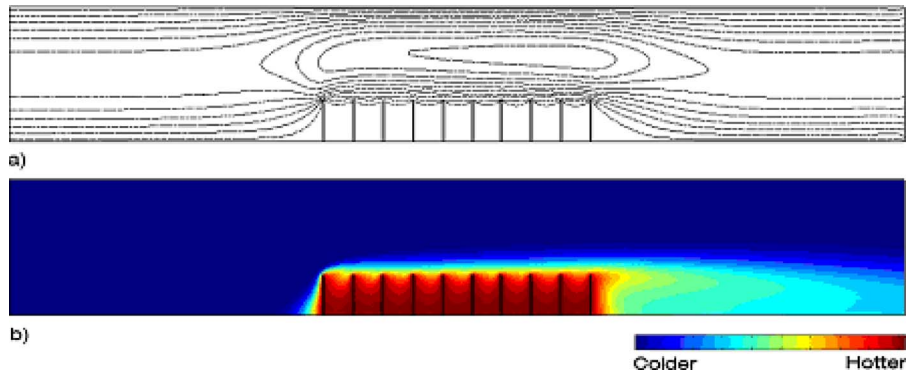


Fig. 16 Example of velocity (a) and temperature (b) fields (shape A; $\theta=0.15$)

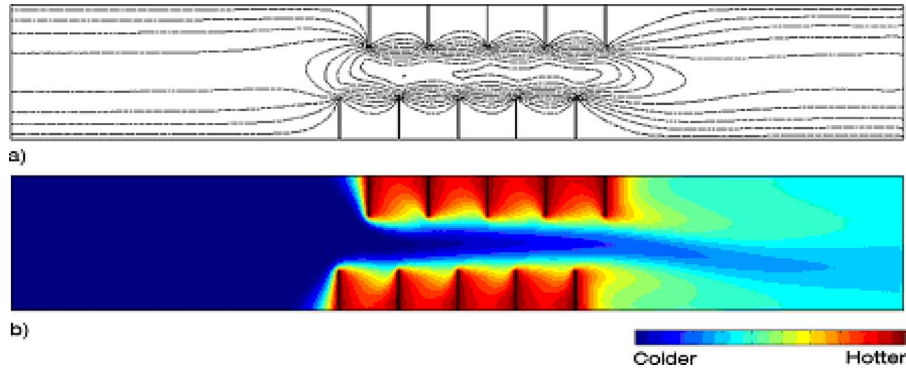


Fig. 17 Example of velocity (a) and temperature (b) fields (shape B; $\theta=0.15$)

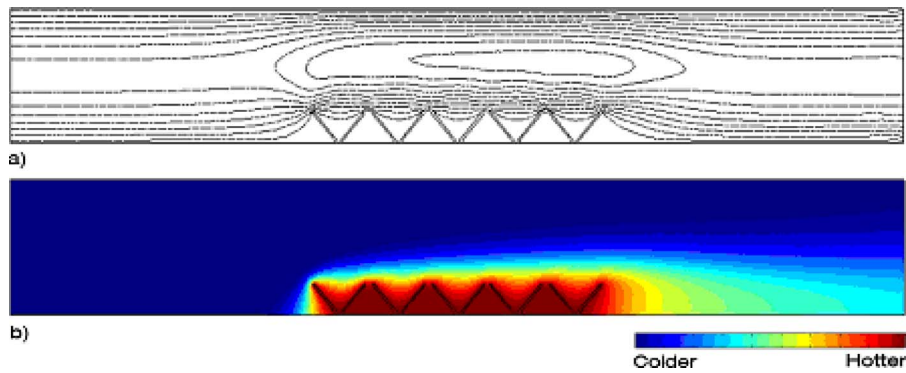


Fig. 18 Example of velocity (a) and temperature (b) fields (shape C; $\theta=0.15$)

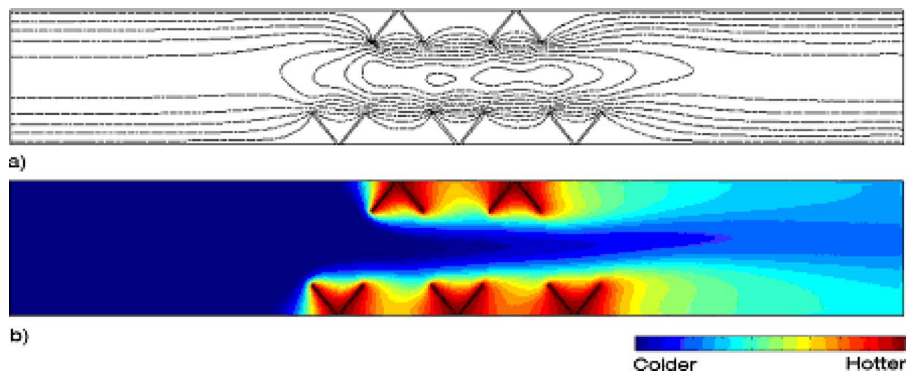


Fig. 19 Example of velocity (a) and temperature (b) fields (shape D; $\theta=0.15$)

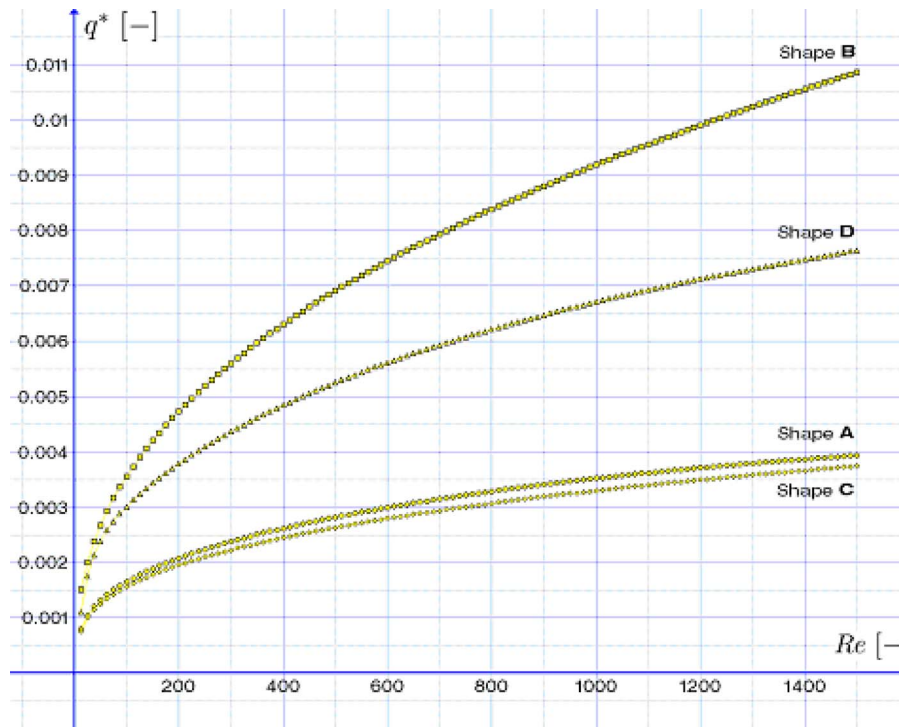


Fig. 20 Dimensionless conductance q^* in function of the Reynolds number Re : case $\theta=0.15$

moved is that corresponding to shape B, i.e., to the module with I fins distributed both at the top and at the bottom surface of the duct. For this optimal module and for $Re=1500$, it is determined a conductance of $q^*=1.0864816 \times 10^{-2}$. The worst performing module for what pertains to q^* is that with a shape C, showing for $Re=1500$ a dimensionless conductance of 3.748029×10^{-3} . Furthermore, it is important to observe that the performances of the

heat exchanging modules with shape A present a very similar trend with respect to those with shape C. Such trend can be observed in the whole range of Re analyzed here, and this makes the two systems almost equivalent in relation to their heat removing attitude. For what relates to the losses of pressure in this case study, from the trends in Fig. 21, it can be evicted that the best performing profile is shape C (Y fins just at the bottom surface of

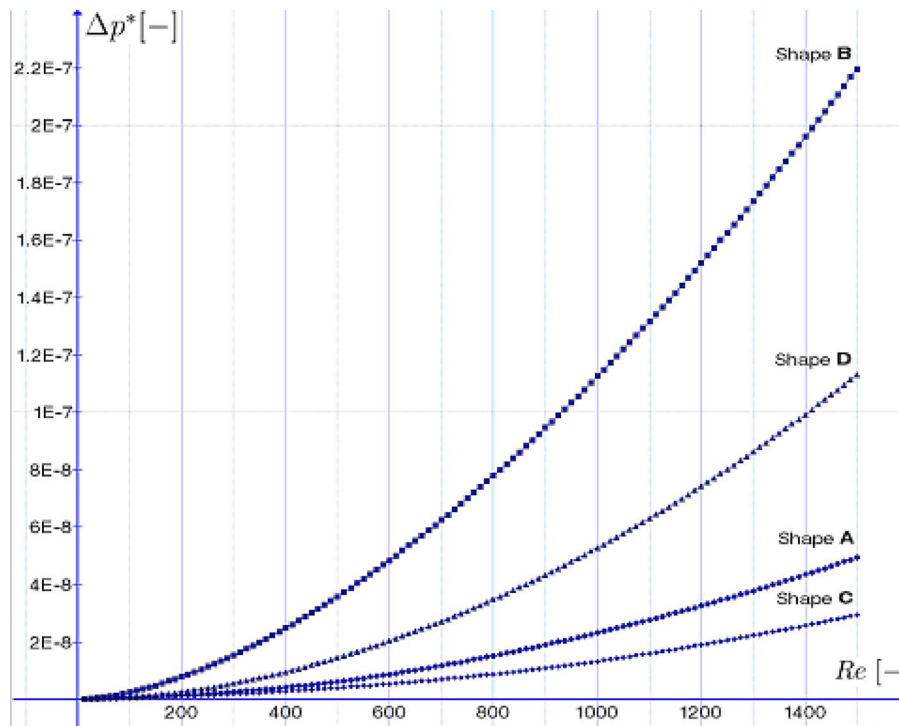


Fig. 21 Dimensionless loss of pressure Δp^* in function of the Reynolds number Re : case $\theta=0.15$

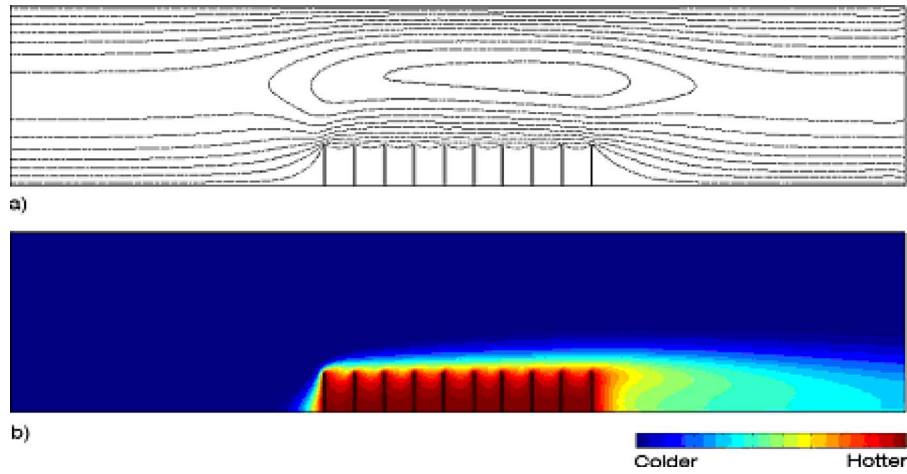


Fig. 22 Example of velocity (a) and temperature (b) fields (shape A; $\theta=0.2$)

the duct), in the sense that it affects the fluid flow less severely than the other options. In case 2 the dimensionless loss of pressure for $Re=1500$ assumed values between $\Delta p^*=2.950619052 \times 10^{-8}$ in the optimal case (shape C) and $\Delta p^*=2.19689 \times 10^{-7}$ in the worst case (shape B).

4.3 Case 3: $\theta=0.2$. Case 3 is characterized by a duct height, which is double with respect to case 1. The qualitative results for velocity and temperature fields within the numerical domain are reported in Figs. 22–25. The trends obtained with the different shapes investigated are similar to those of the previous case. In

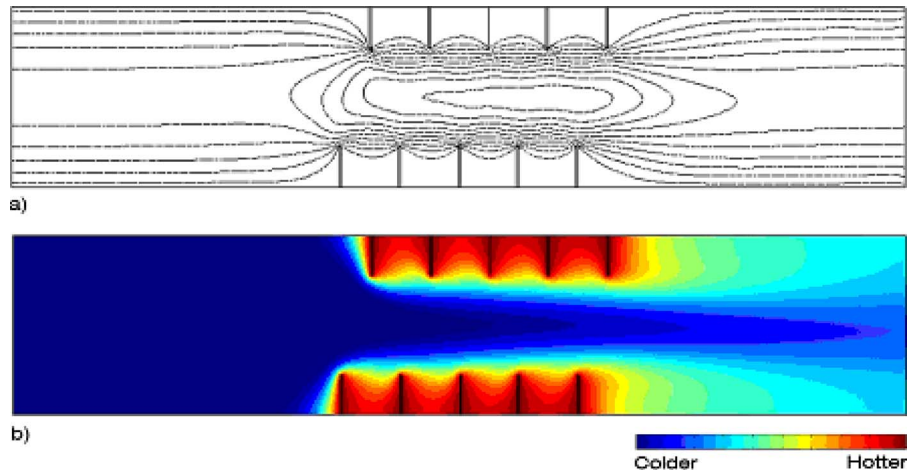


Fig. 23 Example of velocity (a) and temperature (b) fields (shape B; $\theta=0.2$)

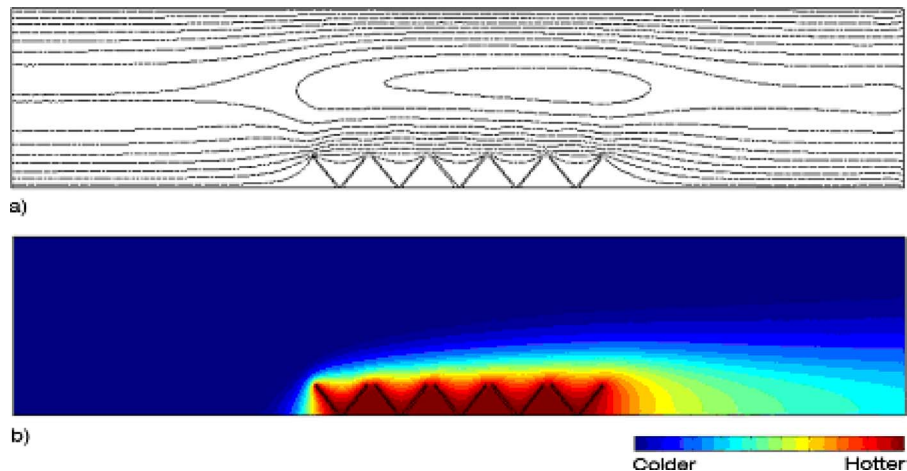


Fig. 24 Example of velocity (a) and temperature (b) fields (shape C; $\theta=0.2$)

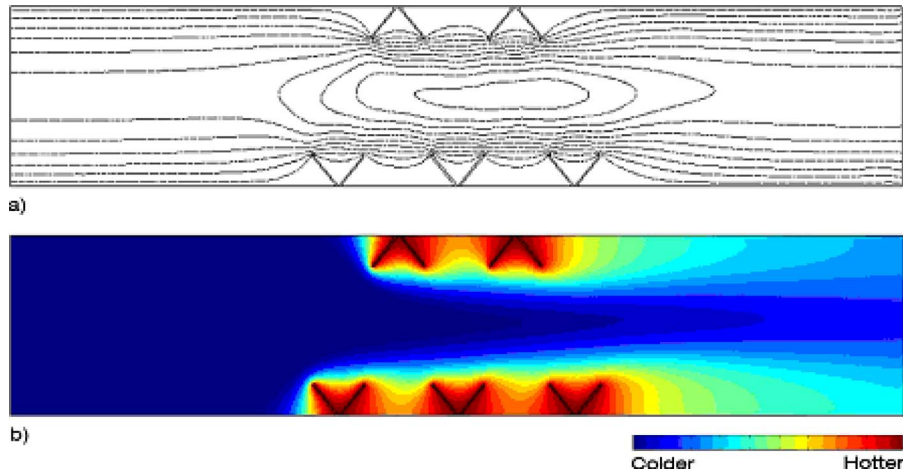


Fig. 25 Example of velocity (a) and temperature (b) fields (shape D; $\theta=0.2$)

particular, the highest value of dimensionless conductance for a fixed Reynolds number is reached when a shape B module (I fins distributed both at the top and at the bottom surface of the duct) is employed. Figures 26 and 27 report the results. Analyzing in more detail the variable dimensionless conductance, for $Re=1500$, it can be inferred that the value of q^* is included in the range $q^* = 7.465938 \times 10^{-3}$ (optimal case, shape B) to $q^* = 3.123738 \times 10^{-3}$ (worst case, shape C). Examining the losses of pressure data (between inlet and outlet) shows a trend inversion with respect to what was stated about dimensionless conductance. Shape C (Y fins just at the bottom surface of the duct) now becomes the best performing module, as, for $Re=1500$, it shows a $\Delta p^* = 1.22719 \times 10^{-8}$. Shape B, on the other hand, is the worst performing profile, with $\Delta p^* = 7.32821 \times 10^{-8}$, again for $Re=1500$. Another consideration, extremely important, concerns the similar trends of dimensionless conductance shown by shape A and shape

C modules: From a heat removing attitude point of view, they are, consequently, almost equivalent. From a requested pumping power point of view, instead, shape C proves to be more effective than shape A at the same Re value.

4.4 Case 4: $\theta=0.25$. In the present case the value of H (m) is equal to $1/4$ of L_D (m). This proves that, going from case 1 to case 4, we move to less hampered cooling flows. The qualitative distribution of velocity and temperature fields in the four shapes examined is reported in Figs. 28–31. The trends of the evaluation parameters are, instead, available in the curves of Figs. 32 and 33, for what concerns q^* and Δp^* in function of the shape and Re. The results obtained in terms of dimensionless conductance performance tend to worsen slightly with respect to the previous case, as the thermal boundary layer varies proportionally to the duct height. As a consequence the optimal value of dimensionless con-

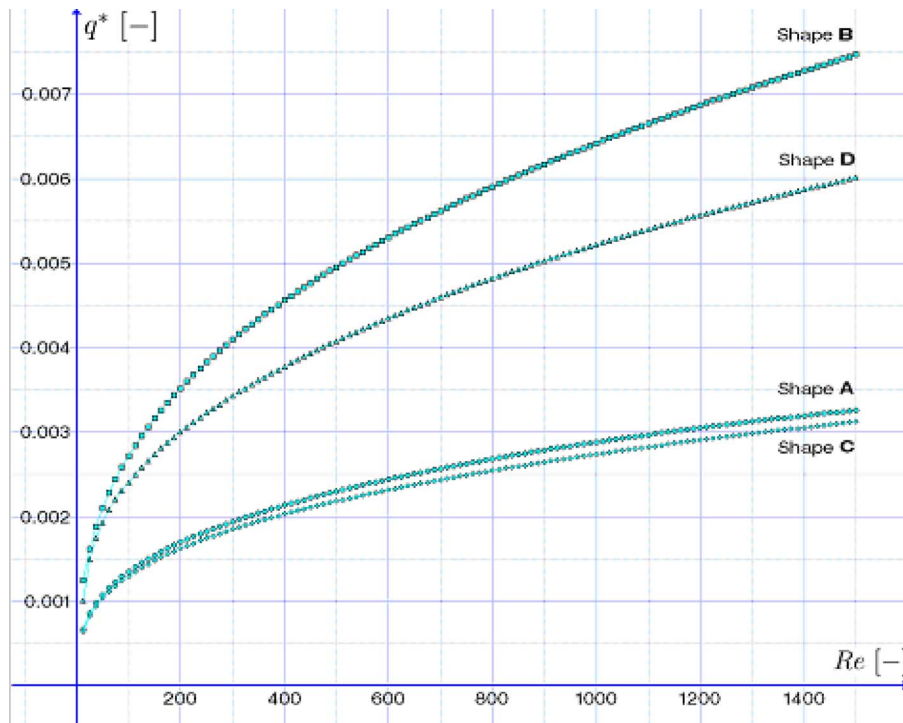


Fig. 26 Dimensionless conductance q^* in function of the Reynolds number Re: case $\theta=0.2$

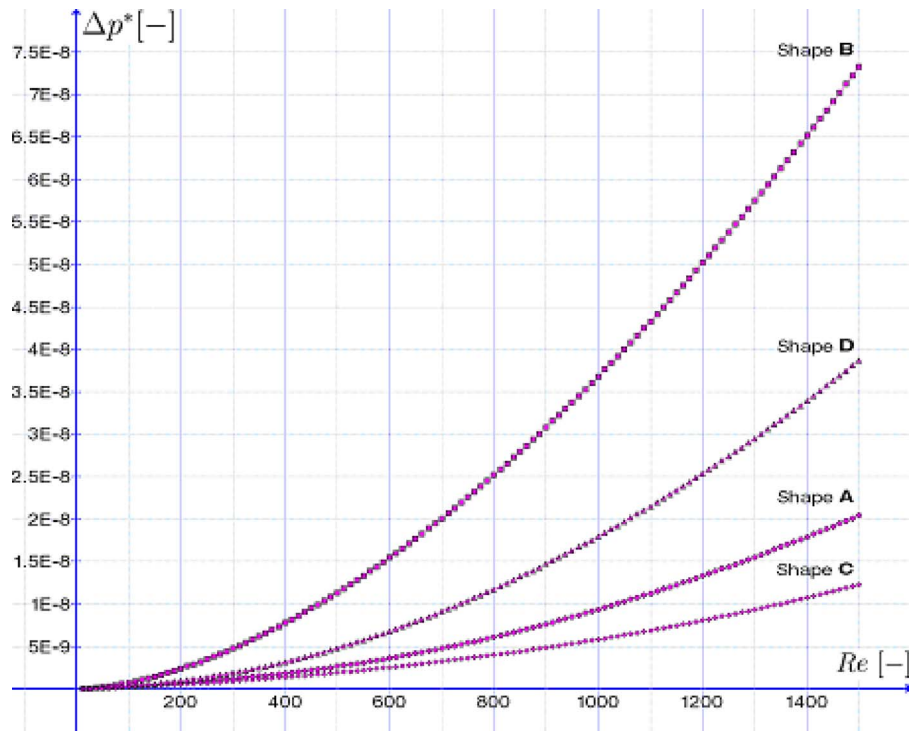


Fig. 27 Dimensionless loss of pressure Δp^* in function of the Reynolds number Re ; case $\theta=0.2$

ductance, encountered for shape B, is $q^* = 6.059234 \times 10^{-3}$; the lowest value, encountered for shape C, is $q^* = 2.725890 \times 10^{-3}$, both computed for a flow characterized by a Reynolds number of 1500. About the losses of pressure, it can be observed a general decrease between inlet and outlet (with respect to the other cases study) due to the different section of the duct. In relation to the flow, then, the optimal performance is that of shape C (Y fins just at the bottom surface of the duct), with $\Delta p^* = 6.75242 \times 10^{-9}$. The least performing one is shape B (I fins distributed both at the top and at the bottom surface of the duct) with a loss of pressure

between the two reference locations $\Delta p^* = 3.26172 \times 10^{-8}$.

5 The Overall Optimization

Table 2 summarizes the results obtained, highlighting the best and worst models for each case study. These data introduce a sort of split situation, as one model may be thermally but not dynamically performing or the exact contrary. Consequently, we need an overall performance evaluation criterion helping in the choice of the optimal heat exchanging profiles and taking into account, with

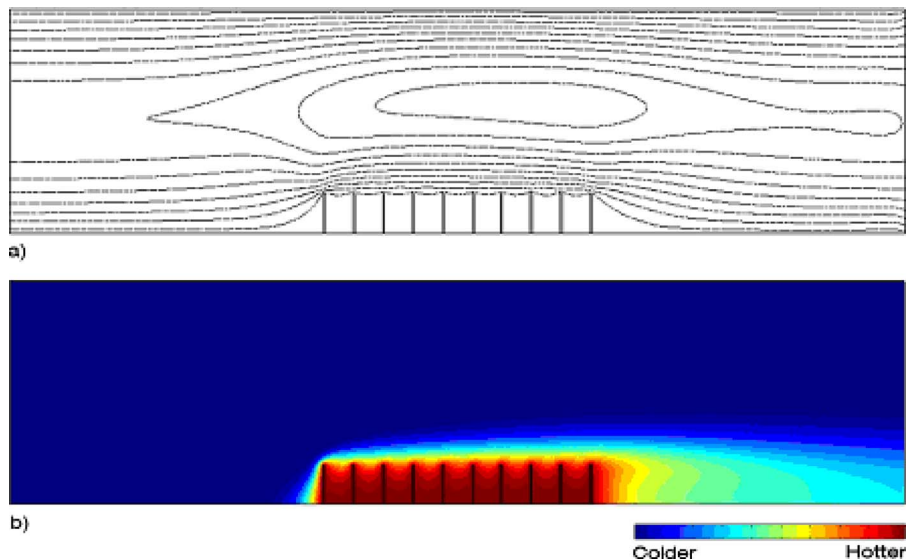


Fig. 28 Example of velocity (a) and temperature (b) fields (shape A; $\theta=0.25$)

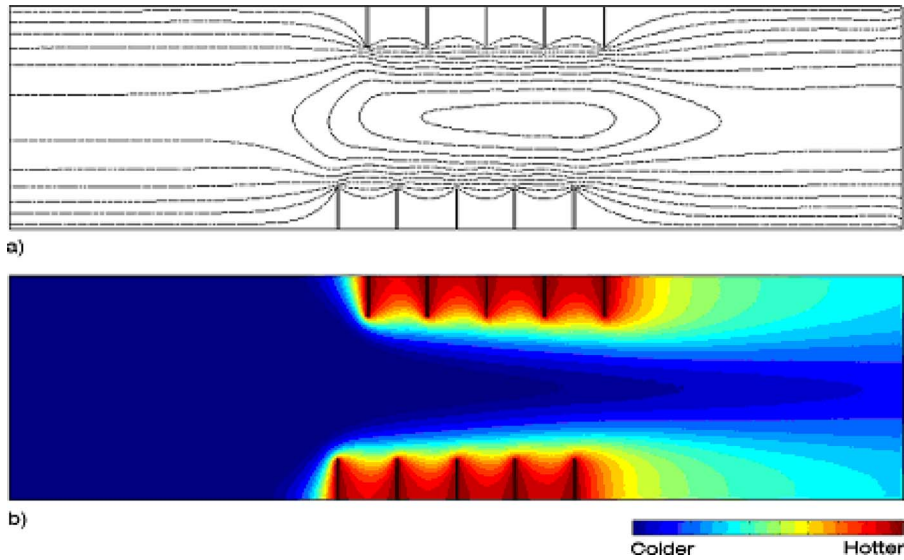


Fig. 29 Example of velocity (a) and temperature (b) fields (shape B; $\theta=0.25$)

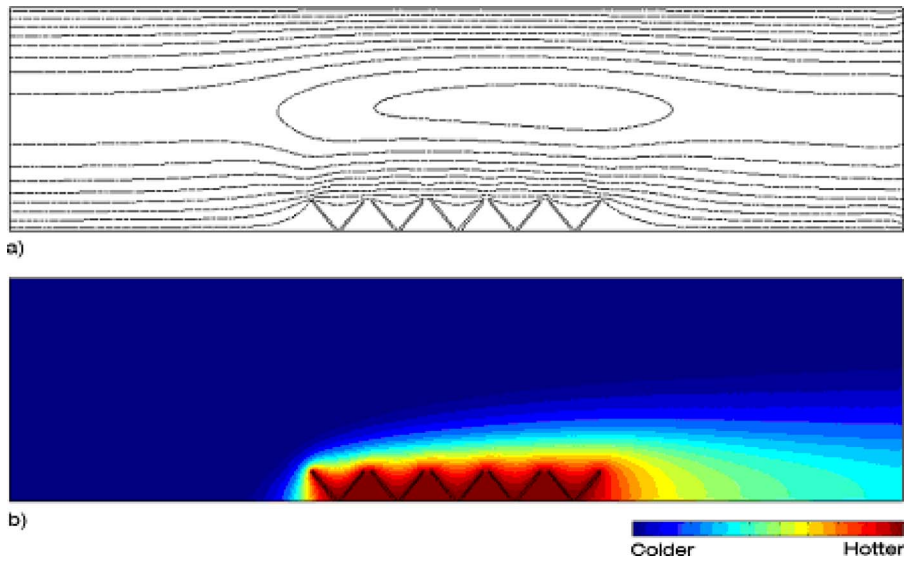


Fig. 30 Example of velocity (a) and temperature (b) fields (shape C; $\theta=0.25$)

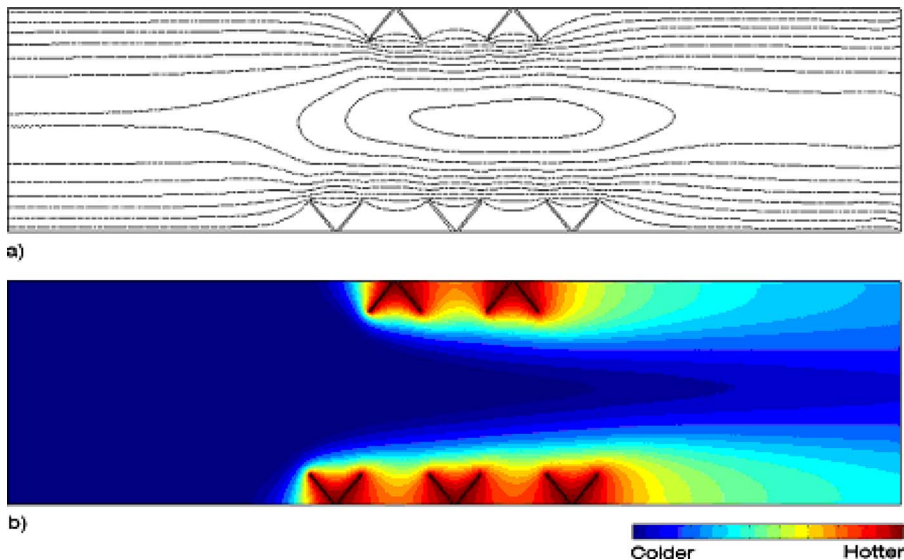


Fig. 31 Example of velocity (a) and temperature (b) fields (shape D; $\theta=0.25$)

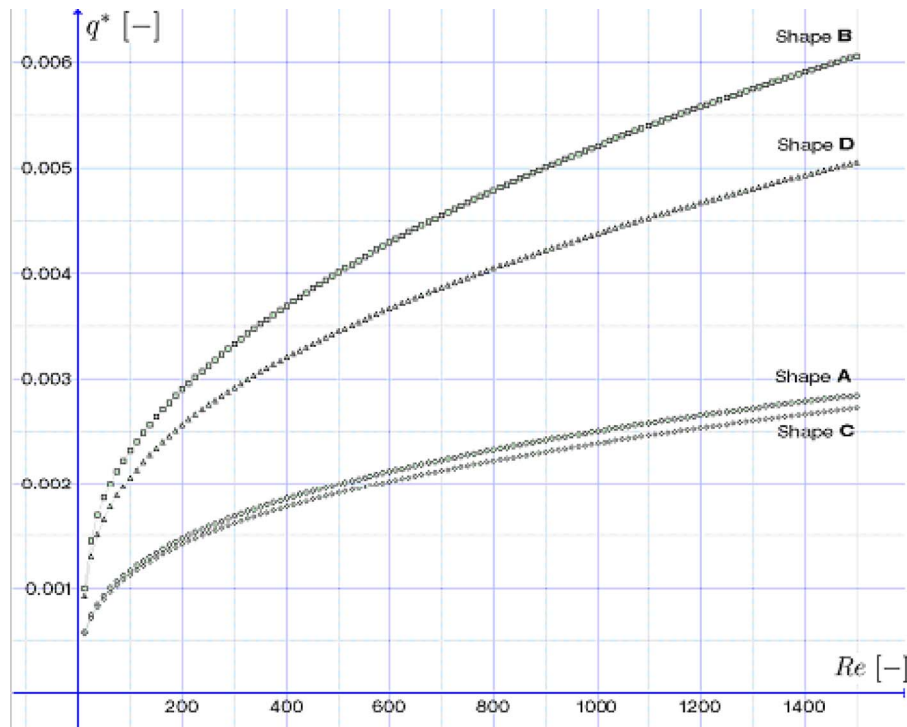


Fig. 32 Dimensionless conductance q^* in function of the Reynolds number Re : case $\theta=0.25$

one number, both q^* and Δp^* . The reference values consequently defined were q_{mA}^* as mean dimensionless conductance for a “shape A” geometry and $\theta=0.1$; Δp_{mA}^* as mean dimensionless loss of pressure for a “shape A” geometry and $\theta=0.1$. Both parameters were calculated in the whole Re range ($0 \div 1500$) investigated.

Successively it was possible to put the reference performances in relation to every other (i, j) th mean performance, q_{mij}^* , and Δp_{mij}^* ($i=1, 2, 3$ being in 1–1 correspondence to shapes B, C, D; $j=1, 2, 3$ being in 1–1 correspondence to $\theta=0.15, \theta=0.2, \text{ and } \theta=0.25$), as follows:

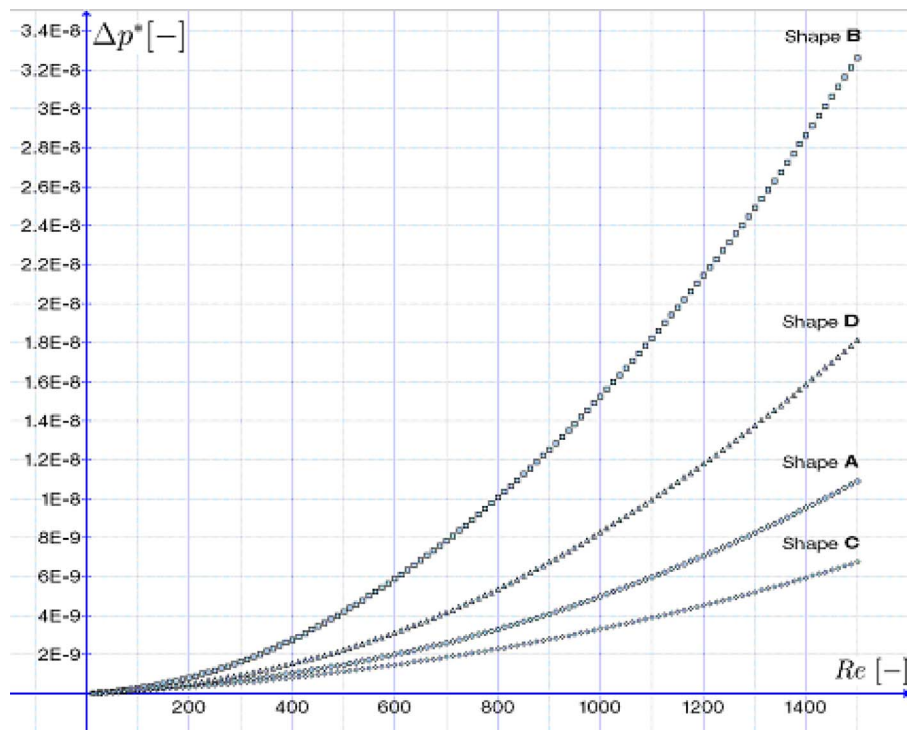


Fig. 33 Dimensionless loss of pressure Δp^* in function of the Reynolds number Re : case $\theta=0.25$

Table 2 Performance range in the cases study analyzed

Geometry	Performance	Shape	q^*	Shape	Δp^*
$\theta=0.1$	Best	D	1.23893×10^{-2}	C	5.09563×10^{-8}
	Worst	B	2.00877×10^{-3}	B	6.05452×10^{-7}
$\theta=0.15$	Best	B	1.08648×10^{-2}	C	2.95062×10^{-8}
	Worst	C	3.74803×10^{-3}	B	2.19689×10^{-7}
$\theta=0.2$	Best	B	7.46594×10^{-3}	C	1.22719×10^{-8}
	Worst	C	3.12374×10^{-3}	B	7.32821×10^{-8}
$\theta=0.25$	Best	B	6.05923×10^{-3}	C	6.75242×10^{-9}
	Worst	C	2.72589×10^{-3}	B	3.26172×10^{-8}

$$\tilde{q}_{mij} = \frac{q_{mij}^*}{q_{mA}^*}, \quad \Delta p_{mij} = \frac{\Delta p_{mij}^*}{\Delta p_{mA}^*} \quad (8)$$

where \tilde{q}_{mij} is mean dimensionless relative conductance (i th shape and j th θ) and Δp_{mij} is mean dimensionless relative loss of pressure (i th shape and j th θ). The values computed, case by case, were then to be inserted within the following formula, defining the novel overall optimization criterion, which this study introduces:

$$P_{ij} = \alpha \tilde{q}_{mij} + (1 - \alpha) \frac{1}{\Delta p_{mij}} \quad (9)$$

where P_{ij} is called the overall performance coefficient for the model with i th shape and j th θ , and α is called relevance, varying between 0 and 1, representing the weight of heat removal maximization with respect to loss of pressure minimization, depending on the context and on the use of the heat exchanger. In particular if α is set equal to 1 this means that, for the technical use requested, it is necessary to maximize heat removal, with less care on the losses of pressure: The overall performance coefficient will consequently point out which model is able to provide this result; on the contrary, if α is set equal to 0 this means that, for the use

requested, it is necessary to minimize the losses of pressure, with less care on heat removal: The overall performance coefficient will consequently point out which model is able to provide this result. Each value of relevance between 0 and 1 will describe intermediate needs. This novel criterion allows the operator to assess his technical priorities and then to choose the most suitable heat removing device. The performance trends reported in Fig. 34 display P_{ij} , as defined in Eq. (9), and refer to a direct comparison between the values obtained for every system tested and the reference one (REF: shape A, $\theta=0.1$). In Fig. 35 and in the following two ones, the dashed line (referred to as "REF" and still referred to as the case: shape A, $\theta=0.1$), used in addition to the four characteristic curves related to shapes A, B, C, and D, provides an immediate idea of how the latter systems improve the reference performance. So Fig. 34 reports the thermal fluid dynamics behavior of the four shapes investigated for a duct with $\theta=0.1$. If the interest on the losses of pressure is predominant ($\alpha=0$), then the system that maximizes the overall performance coefficient is that with Y fins located just at the bottom of the duct (shape C). In this case one obtains $P_{ij}=2.740275583$. Even when intermediate needs occur, i.e., when maximizing heat removal is considered to

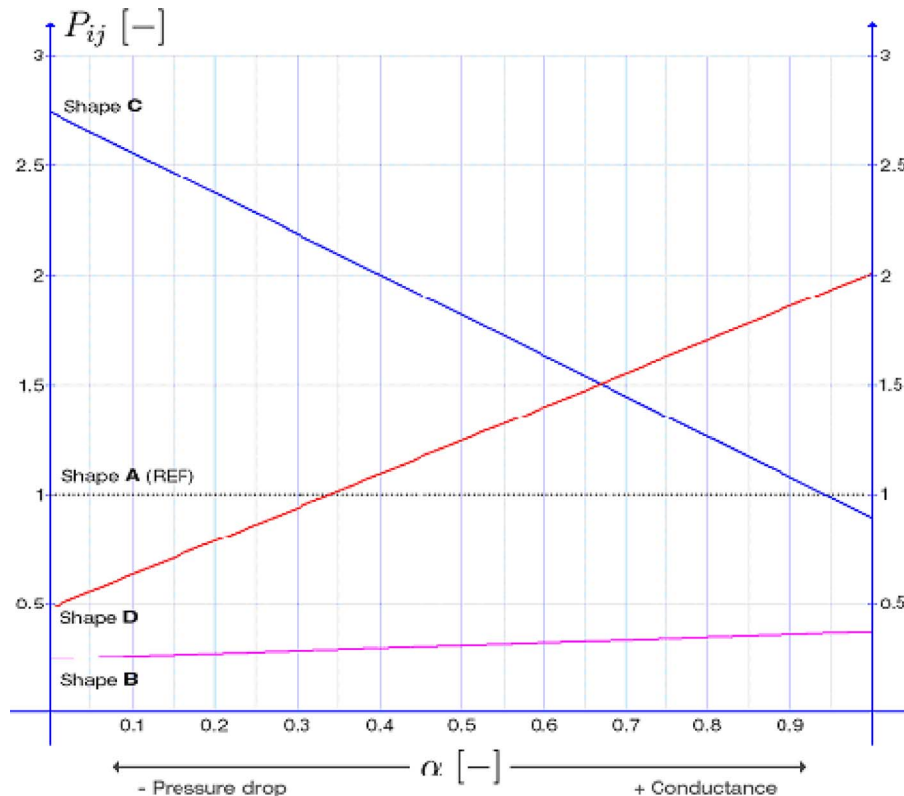


Fig. 34 Overall performance coefficient P_{ij} versus relevance α , case 1 ($\theta=0.1$)

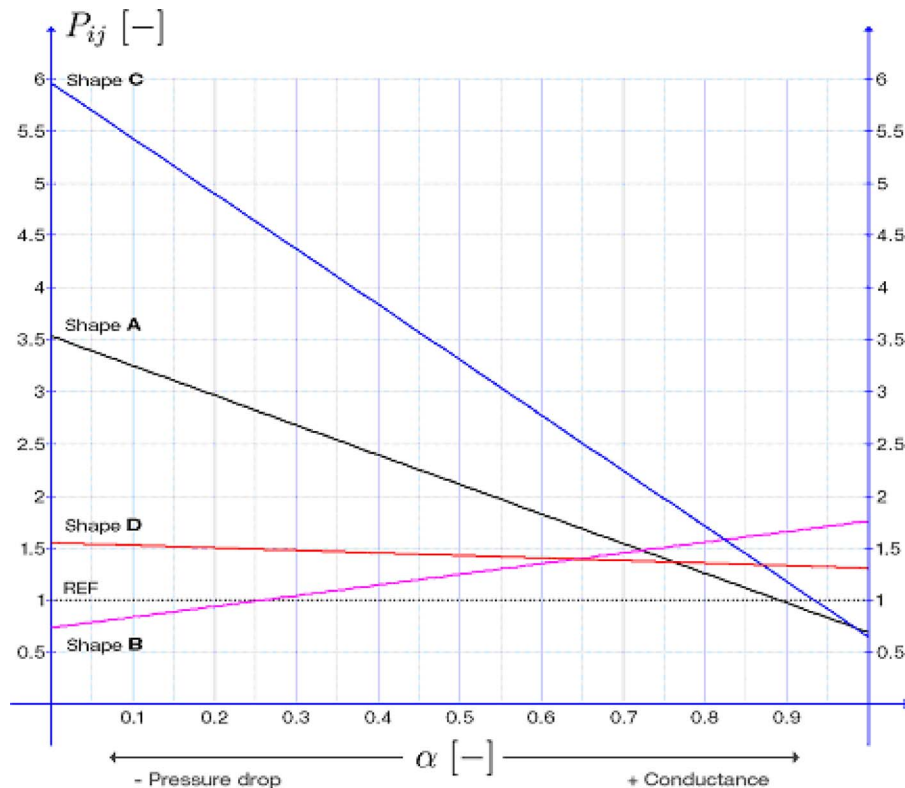


Fig. 35 Overall performance coefficient P_{ij} versus relevance α , case 2 ($\theta=0.15$)

be of the same importance as minimizing the losses of pressure and consequently $\alpha=0.5$, then shape C offers the highest value of P_{ij} : 1.81606626. But if relevance exceeds the limit of 0.67 (in the field where a high conductance is more important than a low loss of pressure), then the optimal system becomes that with shape D (Y fins distributed both at the bottom and at the top sides of the duct), and it keeps this privilege until $\alpha=1$, when heat removal is the only relevant option. For a relevance value of 1, the overall performance coefficient becomes equal to about 2 for shape D, and it drops to 0.891856938 for shape C. Shape B (I fins both at the bottom and at the top surface) is always pejorative with respect to the reference shape, while one can, in general, say that when Y fins are employed, the performance tends, as an average, to raise significantly in comparison with shape A, largely utilized in industry. The results of case 2 ($\theta=0.15$) are displayed in Fig. 35. It is evident that the trends change, especially for what concerns the “conductance maximization field” (i.e., for $\alpha \rightarrow 1$). Shape C still proves to be the best performing one in the “losses of pressure minimization field” (i.e., for $\alpha \rightarrow 0$), even reaching a value of 5.9621113, and in the “intermediate field” (i.e., for $\alpha \approx 0.5$), with $P_{ij}=3.306145963$, much higher than in the previous case. As anticipated, however, when α tends to 1, in particular for $\alpha > 0.8245$, shape B (I fins both at the bottom and at the top surface) becomes the best performing, with a top overall performance coefficient of 1.77013211, while shapes A and C tend to a P_{ij} common value of around 0.65, significantly lower than the reference one. Again, even in case 2, shape A systems do not provide particularly valuable performances if compared with the other possibilities shown involving novel shapes and modular combinations of such shapes. For what concerns case 3 ($\theta=0.2$), shape C remains the best performing option (see Figs. 36 and 37) for most of the independent variable fields, up to 0.9422, where it is overcome by shape B. The situation is quite similar to that of the previous case, where, anyway, the value of α making the performances of shapes B and C equal was slightly lower. In case attention is entirely to be put on the minimization of the losses of

pressure (i.e., for $\alpha=0$) the overall performance coefficient boasts a value of 13.74837034, the highest figure encountered up to now and, again, typical of a shape C model (Y fins just at the bottom of the duct). Instead, if the opposite need arises (attention entirely on the maximization of heat removal, i.e., for $\alpha=1$), shape B (I fins both at the bottom and at the top surface of the duct) is the best performing one, with $P_{ij}=1.24467078$, significantly lower than the homologous result in the previous case. Even in this case study, as just clarified, adopting other configurations than the reference one can lead to much better performances. Case 4 ($\theta=0.25$, see Figs. 38 and 39) confirms the predominance of shape C for an application mainly oriented on the losses of pressure reduction: for $\alpha=0$ one obtains $P_{ij}=24.36419796$, which is the highest value of overall performance coefficient met in the whole investigation. In this case study the value of α that realizes the same P_{ij} value for shapes B and C is equal to 0.9722, still closer to the area of exclusive interest for heat removal maximization. For $\alpha=1$, again, the best performing option is shape B, slightly overcoming the reference figure with $P_{ij}=1.012706786$. This represents the lowest value of overall performance coefficient found in the whole study for this condition, but it is not a surprise if one considers the relation between heat removal and the losses of pressure.

6 Conclusions

The performance of heat exchangers is not just a heat transfer problem but is also tightly linked to the power supplied for moving the coolant. This is especially true when finned surfaces are employed to augment heat exchange in forced convection. Both exigencies, maximizing heat removal or minimizing the power supplied to the fluid (i.e., the losses of pressure within the fluid), may become alternatively predominant depending on the particular technical application faced. Consequently, the present work considered optimization as an expression of the overall performance of a heat exchanger. Such approach, formulated on the

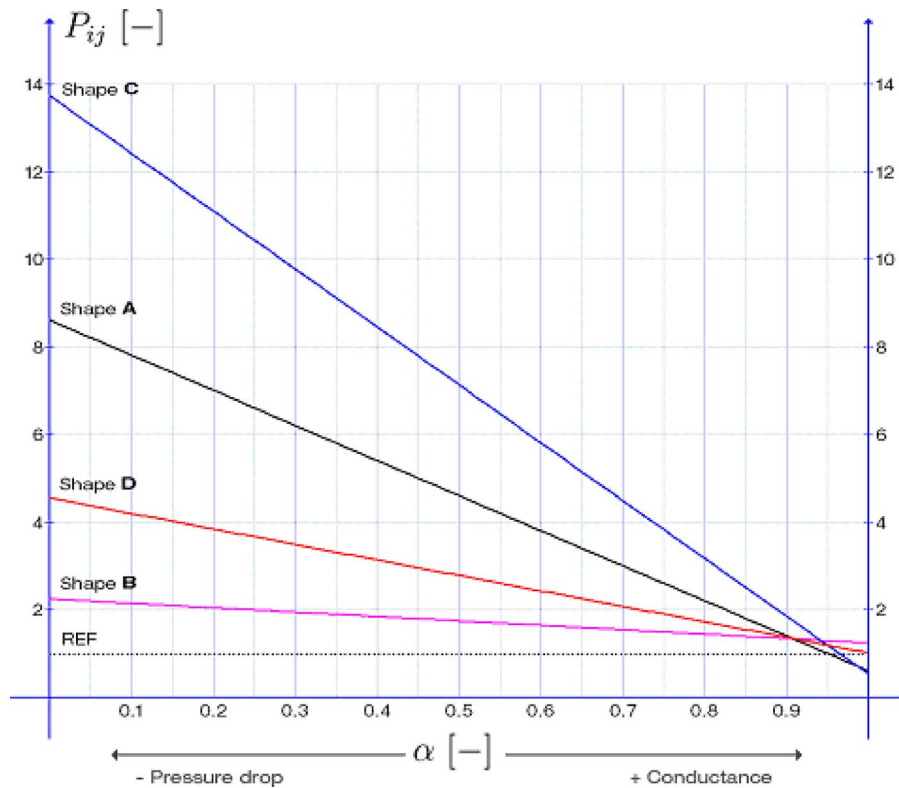


Fig. 36 Overall performance coefficient P_{ij} versus relevance α , case 3 ($\theta=0.2$)

strong basis of Bejan's Constructal theory, arrived at the definition of the overall performance coefficient P_{ij} . This definition was also based on a reference geometry (shape A, $\theta=0.1$), which is currently the most utilized in industrial applications of heat exchangers: It was, consequently, immediately possible to check how a

new option could improve the general performance with respect to the most common solution available. Such approach was utilized, air being the refrigerant fluid, to test different heat exchanging profiles and modules in forced convection and laminar flow conditions, with $Re < 1500$. The profiles tested: I fins (broadly em-

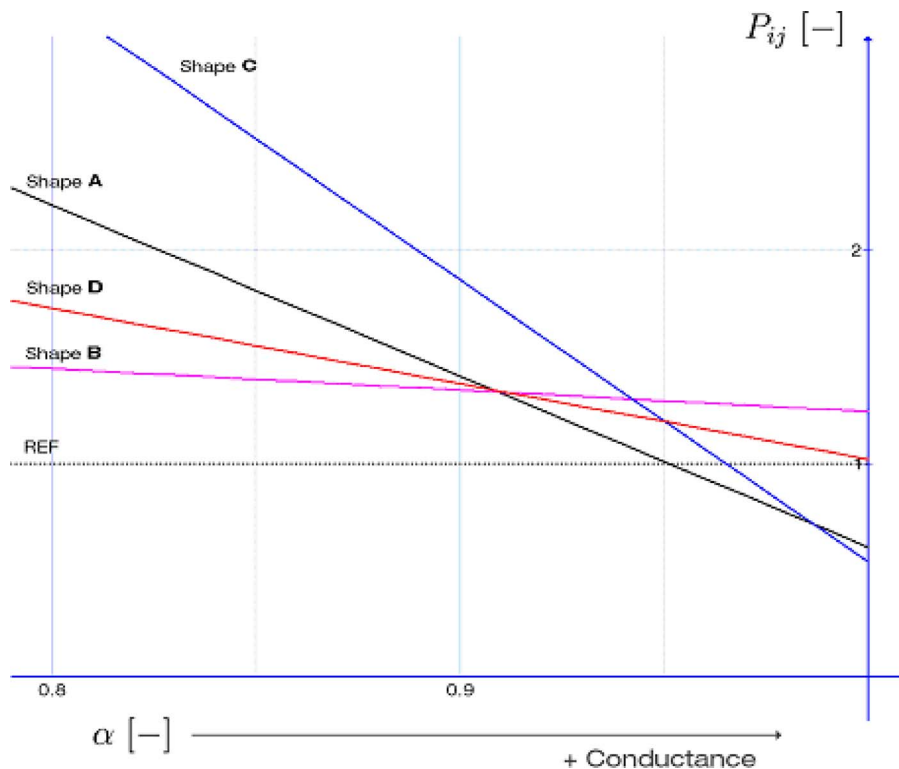


Fig. 37 Overall performance coefficient P_{ij} versus relevance α , case 3 ($\theta=0.2$): detail

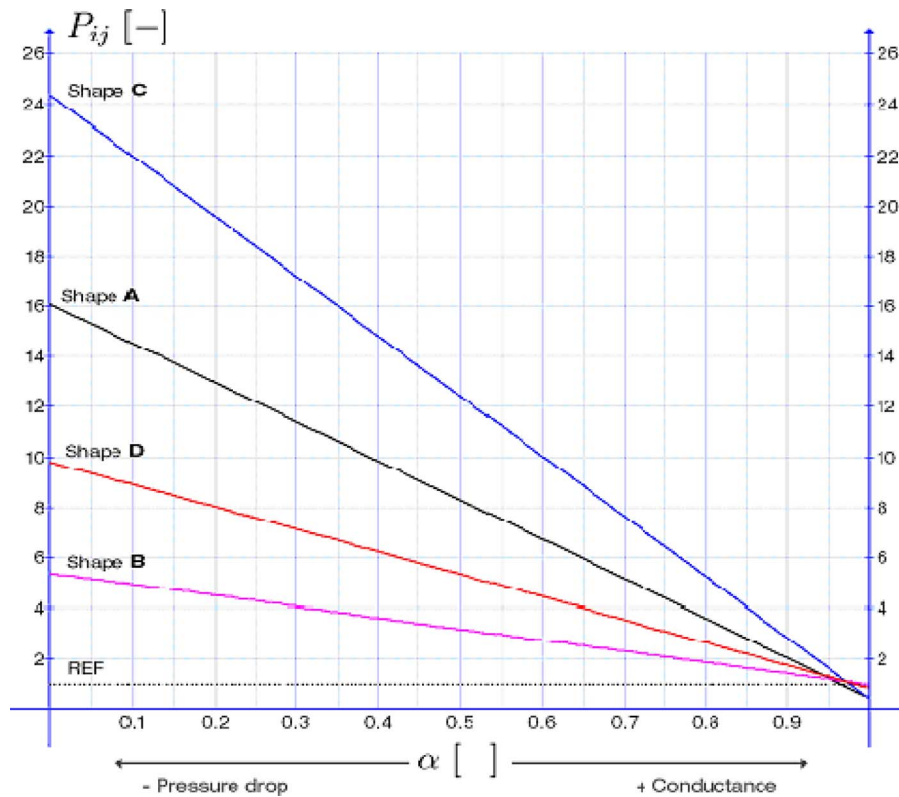


Fig. 38 Overall Performance Coefficient P_{ij} versus relevance α , case 4 ($\theta=0.25$)

ployed in industry) and Y fins (tested in recent research work by the same authors of this paper). The modules are the following (all characterized by the same cross-sectional area): modules of I fins located just at the bottom surface of the duct where the coolant flows (shape A); modules of I fins both at the bottom and at the

top surfaces of the duct (shape B); modules of Y fins just at the bottom surface of the duct (shape C); modules of Y fins both at the bottom and at the top surfaces of the duct (shape D). Moreover the introduction of four different shape ratios ($\theta=0.1, 0.15, 0.2,$ and 0.25), defined as ratio between the height and length of the duct

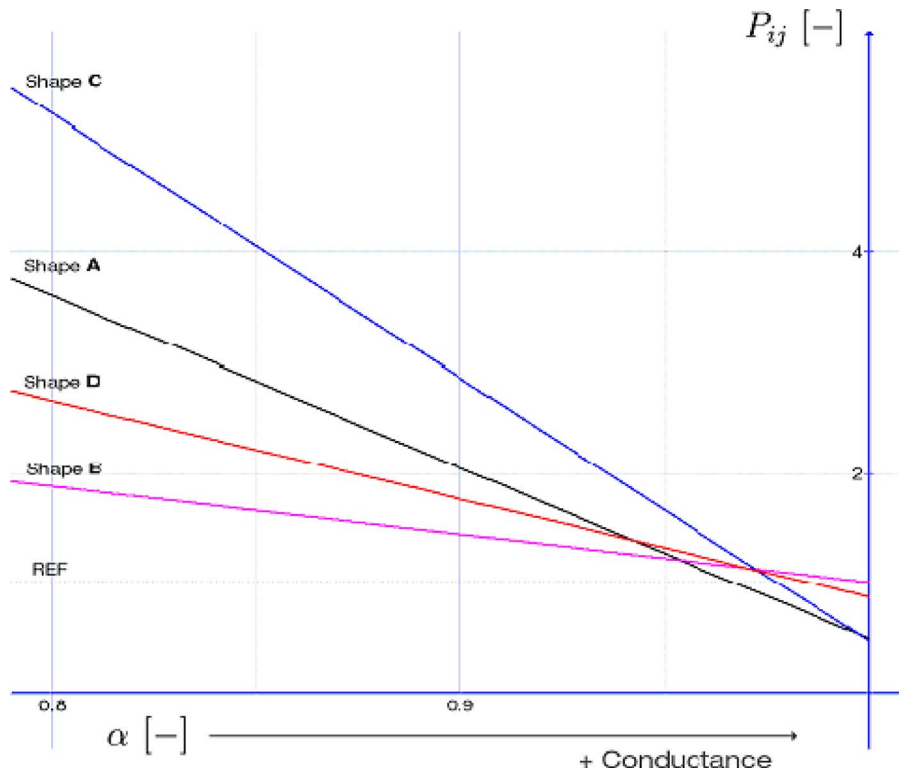


Fig. 39 Overall Performance Coefficient P_{ij} versus relevance α , case 4 ($\theta=0.25$): detail

tested, allowed for the investigation of manifold technical systems. The use of a novel overall performance evaluation criterion linking together heat removal maximization and losses of pressure minimization in association with a parameter called relevance (α), led to a set of results of general applicability able to describe processes characterized by (1) just heat removal maximization needed ($\alpha=1$); (2) just loss of pressure minimization needed ($\alpha=0$); (3) both requirements needed ($0<\alpha<1$). So, the results gained by the present investigation are able to show which heat exchanging configurations are to be chosen in which specific application. In particular, in Secs. 4 and 5 it was possible to highlight that the reference geometry (shape A, $\theta=0.1$) is very often less performing than the other options available and in particular those involving optimized Y fins, recently studied by the same authors of this paper. This performance enhancement becomes more evident when the loss of pressure minimization also becomes an important issue, but, in most cases, even just a “ $\alpha=1$ case study” proves that unconventional settings can provide better performances than traditional ones. Even θ proves to be an important variable, but this latter datum was somehow expected. In conclusion shape C (modules of Y fins located just at the bottom surface of the duct) is the best performing option, especially at low values of α .

Nomenclature

- a = dimensionless parameter, Eq. (3)
 A = fin cross-sectional area, Eq. (3) (m^2)
 B_I = fin width (I shape), Eq. (1) (m)
 B_Y = fin width (Y shape), Eq. (1) (m)
 D = characteristic length, Eq. (5) (m)
 H = duct height, Eq. (4) (m)
 H_I = fin height (I shape), Eq. (1) (m)
 H_Y = fin height (Y shape), Eq. (1) (m)
 k = thermal conductivity, Eq. (3) ($\text{W m}^{-1} \text{K}^{-1}$)
 L = optimized fin-module length, Fig. 4 (m)
 L_D = ($=3 \times L$) duct length, Eq. (4) (m)
 p = pressure (Pa)
 p_0 = atmospheric pressure, Eq. (7) (Pa)
 P_{cs} = duct cross-sectional perimeter, Eq. (6) (m)
 P_{ij} = overall performance coefficient, Eq. (9)
 p_{in} = mean inlet pressure, Eq. (7) (Pa)
 p_{out} = mean outlet pressure, Eq. (7) (Pa)
 Δp^* = dimensionless loss of pressure, Eq. (7)
 Δp_{mA}^* = mean dimensionless reference loss of pressure (shape A and $\theta=0.1$), Eq. (8)
 Δp_{mij}^* = mean dimensionless loss of pressure (i th shape and j th θ), Eq. (8)
 Δp_{mij}^{\sim} = mean dimensionless relative loss of pressure (i th shape and j th θ), Eq. (8)
 Pr = Prandtl number
 q^* = dimensionless conductance, Eq. (2)
 q_L = linear heat flux, Eq. (2) [W m^{-1}]
 q_{mA}^* = mean dimensionless reference conductance (shape A and $\theta=0.1$), Eq. (8)
 q_{mij}^* = mean dimensionless conductance (i th shape and j th θ), Eq. (8)
 q_{mij}^{\sim} = mean dimensionless relative conductance (i th shape and j th θ), Eq. (8)
 Re = Reynolds number, Eq. (5)
 S = duct cross-sectional area, Eq. (6) (m^2)
 T = temperature (K)
 T_R = fin root temperature, Eq. (2) (K)
 T_∞ = undisturbed flow inlet temperature, Eq. (2) (K)
 u = inlet velocity (x -component), Eq. (5) (m s^{-1})

Greek Symbols

- α = relevance, Eq. (9)

- η = dynamic viscosity, Eq. (5) ($\text{kg m}^{-1} \text{s}^{-1}$)
 θ = duct shape ratio, Eq. (4)
 ρ = volumic mass of the refrigerant fluid, Eq. (5) (kg m^{-3})

Subscripts

- i = fin type
 j = duct shape ratio

References

- [1] Nakayama, W., and Xu, L. P., 1983, “Enhanced Fins for Air-Cooled Heat Exchangers—Heat Transfer and Friction Correlations,” *Proceedings of the First ASME/JSME Thermal Engineering Joint Conference*, Vol. 1, pp. 495–502.
- [2] Upton, T. D., and Watt, D. W., 1997, “Experimental Study of Transient Natural Convection in an Inclined Rectangular Enclosure,” *Int. J. Heat Mass Transfer*, **40**(11), pp. 2679–2690.
- [3] Du, Y.-J., and Wang, C.-C., 2000, “An Experimental Study of the Airside Performance of the Superslit Fin-and-Tube Heat Exchangers,” *Int. J. Heat Mass Transfer*, **43**(24), pp. 4475–4482.
- [4] Sundén, B., and Heggs, P. J., 2000, *Recent Advances in Analysis of Heat Transfer for Fin Type Surfaces*, WIT, Boston, MA.
- [5] Alebrahim, A., and Bejan, A., 1999, “Constructal Trees of Circular Fins for Conductive and Convective Heat Transfer,” *Int. J. Heat Mass Transfer*, **42**(19), pp. 3585–3597.
- [6] Nuntaphan, A., Vithayasai, S., Kiatsiriroat, T., and Wang, C.-C., 2007, “Effect of Inclination Angle on Free Convection Thermal Performance of Louver Finned Heat Exchanger,” *Int. J. Heat Mass Transfer*, **50**(1–2), pp. 361–366.
- [7] Ben-Nakhi, A., and Chamkha, A. J., 2007, “Conjugate Natural Convection in a Square Enclosure With Inclined Thin Fin of Arbitrary Length,” *Int. J. Therm. Sci.*, **46**(5), pp. 467–478.
- [8] Wen, T., Xu, F., and Lu, T. J., 2007, “Structural Optimization of Two-Dimensional Cellular Metals Cooled by Forced Convection,” *Int. J. Heat Mass Transfer*, **50**(13–14), pp. 2590–2604.
- [9] Zhang, L.-Z., 2007, “Laminar Flow and Heat Transfer in Plate-Fin Triangular Ducts in Thermally Developing Entry Region,” *Int. J. Heat Mass Transfer*, **50**(7–8), pp. 1637–1640.
- [10] Biserni, C., Rocha, L. A. O., Stanesco, G., and Lorenzini, E., 2007, “Constructal H-Shaped Cavities According to Bejan’s Theory,” *Int. J. Heat Mass Transfer*, **50**(11–12), pp. 2132–2138.
- [11] Rocha, L. A., Lorenzini, E., and Biserni, C., 2005, “Geometric Optimization of Shapes on the Basis of Bejan’s Constructal Theory,” *Int. Commun. Heat Mass Transfer*, **32**(10), pp. 1281–1288.
- [12] Lorenzini, G., 1999, “A Numerical Approach to the Problem of Conjugate Heat Transfer in Turbulent Forced Convection for a Fluid in a Pipe With Internal Longitudinal Fins,” *Proceedings of the First International Conference on Engineering Thermophysics*, Beijing, China, pp. 194–203.
- [13] Horvat, A., and Catton, I., 2003, “Numerical Technique for Modeling Conjugate Heat Transfer in an Electronic Device Heat Sink,” *Int. J. Heat Mass Transfer*, **46**(12), pp. 2155–2168.
- [14] Kandasamy, R., and Subramanyam, S., 2005, “Application of Computational Fluid Dynamics Simulation Tools for Thermal Characterization of Electronic Packages,” *Int. J. Numer. Methods Heat Fluid Flow*, **15**(1), pp. 61–72.
- [15] Bar-Cohen, A. D., and Kraus, A., 1988, *Advances in Thermal Modelling of Electronic Components and Systems*, Vol. 4, ASME, New York.
- [16] Marthinuss, J., and Hall, G., and 2004, “Air Cooled Compact Heat Exchanger Design for Electronics Cooling,” *Electronics Cooling*, **10**(1), http://www.electronics-cooling.com/articles/2004/2004_february_a3.php
- [17] Belady, C. L., and Minichiello, A., 2003, “Effective Thermal Design for Electronic Systems,” *Electronics Cooling*, **9**(2), http://www.electronics-cooling.com/articles/2003/2003_may_a1.php
- [18] Jubran, B. A., Swiety, S. A., and Hamdan, M. A., 1996, “Convective Heat Transfer and Pressure Drop Characteristics of Various Array Configurations to Simulate the Cooling of Electronic Modules,” *Int. J. Heat Mass Transfer*, **39**(16), pp. 3519–3529.
- [19] Schmidt, R., 2004, “Challenges in Electronic Cooling—Opportunities for Enhanced Thermal Management Techniques—Microprocessor Liquid Cooled Minichannel Heat Sink,” *Heat Transfer Eng.*, **25**(3), pp. 3–12.
- [20] Webb, R. L., 2005, “Next Generation Devices for Electronic Cooling With Heat Rejection to Air,” *ASME J. Heat Transfer*, **127**(1), pp. 2–10.
- [21] Lall, P., Pecht, M., and Hakim, E., 1997, *Influence of Temperature on Microelectronics and System Reliability: A Physics of Failure Approach*, CRC, New York.
- [22] Lorenzini, G., and Moretti, S., 2007, “Numerical Analysis on Heat Removal From Y-Shaped Fins: Efficiency and Volume Occupied for A New Approach to Performance Optimisation,” *Int. J. Therm. Sci.*, **46**(6), pp. 573–579.
- [23] Lorenzini, G., and Moretti, S., 2007, “A CFD Application to Optimize T-Shaped Fins: Comparisons With Constructal Theory’s Results,” *ASME J. Electron. Packag.*, **129**(3), pp. 324–327.

- [24] Lorenzini, G., and Moretti, S., 2008, "Numerical Heat Transfer Optimization in Modular Systems of Y-Shaped Fins," *ASME J. Heat Transfer*, **130**(8), p. 081801.
- [25] Lorenzini, G., and Moretti, S., 2007, "Numerical Analysis of Heat Removal Enhancement With Extended Surfaces," *Int. J. Heat Mass Transfer*, **50**(3-4), pp. 746-755.
- [26] Bejan, A., and Almgobel, M., 2000, "Constructal T-Shaped Fins," *Int. J. Heat Mass Transfer*, **43**(12), pp. 2101-2115.
- [27] Bejan, A., and Gobin, D., 2006, "Constructal Theory of Droplet Impact Geometry," *Int. J. Heat Mass Transfer*, **49**(15-16), pp. 2412-2419.
- [28] 2007, Comsol Multiphysics Version 3.3, Users' Manuals.

Convective Heat Transfer Enhancement in a Circular Tube Using Twisted Tape

Zhi-Min Lin

Liang-Bi Wang

e-mail: lbwang@mail.lzjtu.cn

Department of Mechanical Engineering,
Lanzhou Jiaotong University,
Lanzhou,
Gansu 730070, P.R.C.

The secondary flow has been used frequently to enhance the convective heat transfer, and at the same flow condition, the intensity of convective heat transfer closely depends on the thermal boundary conditions. Thus far, there is less reported information about the sensitivity of heat transfer enhancement to thermal boundary conditions by using secondary flow. To account for this sensitivity, the laminar convective heat transfer in a circular tube fitted with twisted tape was investigated numerically. The effects of conduction in the tape on the Nusselt number, the relationship between the absolute vorticity flux and the Nusselt number, the sensitivity of heat transfer enhancement to the thermal boundary conditions by using secondary flow, and the effects of secondary flow on the flow boundary layer were discussed. The results reveal that (1) for fully developed laminar heat convective transfer, different tube wall thermal boundaries lead to different effects of conduction in the tape on heat transfer characteristics; (2) the Nusselt number is closely dependent on the absolute vorticity flux; (3) the efficiency of heat transfer enhancement is dependent on both the tube wall thermal boundaries and the intensity of secondary flow, and the ratio of Nusselt number with twisted tape to its counterpart with straight tape decreases with increasing twist ratio while it increases with increasing Reynolds number for both uniform wall temperature (UWT) and uniform heat flux (UHF) conditions; (4) the difference in the ratio between UWT and UHF conditions is also strongly dependent on the conduction in the tape and the intensity of the secondary flow; and (5) the twist ratio ranging from 4.0 to 6.0 does not necessarily change the main flow velocity boundary layer near tube wall, while Reynolds number has effects on the shape of the main flow velocity boundary layer near tube wall only in small regions. [DOI: 10.1115/1.3122778]

Keywords: thermal boundary condition, laminar convective heat transfer, secondary flow, twisted tape, numerical analysis

1 Introduction

In most science and engineering applications, heat convection means thermal transport through an interface when a fluid flows over it [1,2]. In this process, the value of the convective heat transfer coefficient h is commonly used to reflect the intensity of convective heat transfer, which depends on the details of both flow and temperature fields. At the same flow condition, convective heat transfer characteristics depend on the nature of the thermal boundary conditions imposed on the surface. In the numerical and experimental studies of the internal laminar convective heat transfer, two representative thermal boundary conditions, uniform wall temperature (UWT) and uniform heat flux (UHF), are frequently encountered. The significant difference between UWT and UHF conditions is that for the former, no tangent heat flux exists on the wall surface, while for the latter, tangent heat flux does exist.

The research results show that for all Prandtl numbers under the same flow condition convective heat transfer will have a larger Nusselt number when UHF is applied on the wall surface than when UWT is enforced [3]. For example, for laminar flow in a circular tube, the fully developed Nusselt numbers for both UHF and UWT conditions are 4.364 and 3.657, respectively [1,2], and this difference can be ascribed simply to the slightly different shapes of the temperature boundary layers [2]. For fully developed conditions in a circular tube, the ratio of Nusselt numbers for

the two cases decreases with increasing Reynolds numbers [3] and closely relates with the Prandtl number because of the effect of the Prandtl number on the distribution of thermal resistance. In addition, at a very low Prandtl number, thermal boundaries significantly affect the intensity of heat convection, while at higher Prandtl numbers, the effect is less significant [3]. Furthermore, the ratio is related to the cross-sectional shape of ducts [1,2]. For example, the ratio of the fully developed Nusselt numbers for UHF and UWT conditions is 1.193 and 1.249 for circular and equilateral triangle ducts, respectively.

Enhancement of convective heat transfer becomes increasingly important. To date, the secondary flow is frequently used to enhance the convective heat transfer. For example, one newly used method is to apply vortex generators (VGs) on fin surfaces to effectively improve the airside heat transfer performance of tube bank fin heat exchangers as discussed in related reports [4–8]. Experts know that the key point of heat transfer enhancement using this strategy is the secondary flow produced by VGs. For forced single-phase convective heat transfer inside tubes, a tube with helical ribs has been used as one of the passive heat transfer enhancement techniques and is the most widely used in several heat transfer applications, such as heat recovery processes, air conditioning and refrigeration systems, and chemical reactors [9–12]. The twisted tape placed inside a tube as one common technology has enjoyed widespread application for design and retrofit of the highly efficient and compact heat exchangers, since it offers significant increase in the heat transfer coefficient associated with a relatively small pressure-drop penalty, particularly at high Prandtl numbers [13–20]. Although in these reported literatures the correlation equations for a different thermal boundary of the tube wall surface and much useful information have been re-

Contributed by the Heat Transfer Division of ASME for publication in the JOURNAL OF HEAT TRANSFER. Manuscript received September 27, 2008; final manuscript received March 10, 2009; published online June 4, 2009. Review conducted by Louis C. Chow.

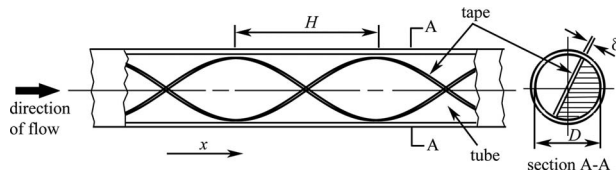


Fig. 1 Sketch of the twisted tape inserted in a circular tube

ported, researchers have not considered the effects of thermal conductivity of the tape and the thermal contact resistance between the tube wall and the tape.

In order to account for these facts and to further understand the intrinsic mechanism of heat transfer enhancement by using secondary flow, in this paper a commonly used secondary flow producer, a twisted tape placed inside a circular tube case, is considered, and the effects of thermal conductivity of the tape on the Nusselt number, the relationship between the absolute vorticity flux and the Nusselt number, the sensitivity of heat transfer enhancement to the thermal boundary conditions by using secondary flow, and the effects of secondary flow on flow boundary layer in laminar state are studied.

2 Physical Model and Mathematics Formulation

Figure 1 illustrates a circular tube containing a twisted tape. The tape has been twisted around its longitudinal axis. The width of the tape is usually about the same as the tube's internal diameter. As shown in Fig. 1, δ is the tape thickness, D is the tube's internal diameter, and H is the twist pitch length (i.e., the axial distance of the tape twisted with 180 deg). The twist ratio y is the ratio of the twist pitch length H to the tube diameter D (i.e., $y = H/D$).

In this study, we selected the circular tube fitted with straight tape as a reference case for studying the contribution of the secondary flow to heat transfer enhancement and the sensitivity of heat transfer enhancement to the thermal boundaries. To consider the conjugation of convective heat transfer in the flow field and conduction in the tape with a finite thermal conductivity, the simulation domain, which is half the region formed by the tube wall and the tape twisted with 360 deg, is divided into two regions as shown in Fig. 2. In the present calculation, water is the working fluid, several different thermal conductivities of the tape are considered (including the nonconducting tape), and the thermal contact resistance between the tube wall and the tape is also consid-

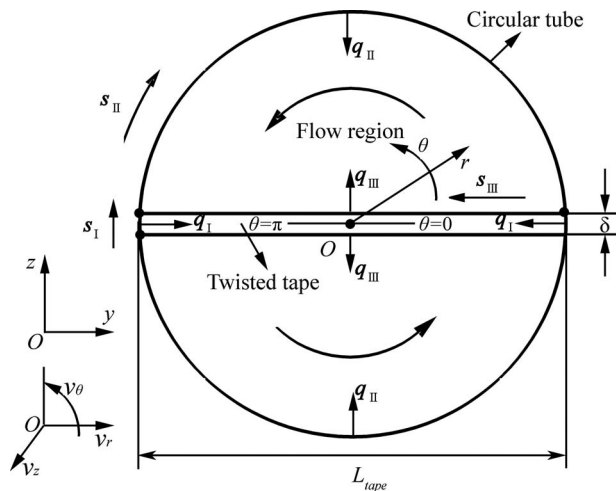


Fig. 2 Schematic view of heat transfer of the model, symmetric characteristic of temperature on tape surfaces and coordinates system

ered in the analysis. For the nonconducting tape case, the computational domain is only the flow region, which will result in a simplification of the thermal boundary on the interface of fluid-to-tape.

In developing the model, the following assumptions were made: (1) the physical properties of fluid and tape are constant; (2) the flow is limited as laminar, and the fluid is incompressible; (3) the flow and heat transfer are in steady state; and (4) the viscous dissipation is negligible. With these assumptions, in physical space the mathematical model can be written out.

2.1 In the Flow Region. The continuity equation,

$$\frac{\partial}{\partial x_i}(\rho u_i) = 0 \quad (1)$$

The momentum equation,

$$\frac{\partial}{\partial x_i}(\rho u_i u_k) = \frac{\partial}{\partial x_i} \left(\mu \frac{\partial u_k}{\partial x_i} \right) - \frac{\partial p}{\partial x_k} \quad (k = 1, 2, 3) \quad (2)$$

The energy equation,

$$\frac{\partial}{\partial x_i}(\rho c_p u_i T) = \frac{\partial}{\partial x_i} \left(\lambda_f \frac{\partial T}{\partial x_i} \right) \quad (3)$$

The boundary conditions are as follows.

At the inlet and outlet cross section, the periodicity boundary condition is adopted for both UWT and UHF conditions.

$$u(x, y, z)|_{in} = u(x, y, z)|_{out} \quad v(x, y, z)|_{in} = v(x, y, z)|_{out} \quad (4)$$

$$w(x, y, z)|_{in} = w(x, y, z)|_{out} \quad \Theta(x, y, z)|_{in} = \Theta(x, y, z)|_{out}$$

where Θ is the dimensionless temperature and is defined as follows.

For the UWT condition,

$$\Theta(x, y, z) = (T(x, y, z) - T_w) / (T_{bulk} - T_w) \quad (5)$$

For the UHF condition,

$$\Theta(x, y, z) = (T(x, y, z) - T_{bulk}) / (q_w D / \lambda_f) \quad (6)$$

where T_w is the tube wall temperature, q_w is the heat flux on the tube wall surface, and T_{bulk} is the average temperature at a cross section.

$$T_{bulk} = \frac{\int \int u(x, y, z) T(x, y, z) dy dz}{\int \int u(x, y, z) dy dz} \quad (7)$$

On the tube wall, the no-slip condition for velocity is applied for both the UWT and the UHF conditions.

$$u(x, y, z) = 0, \quad v(x, y, z) = 0, \quad w(x, y, z) = 0 \quad (8)$$

Uniform wall temperature T_w is specified on the tube wall for the UWT condition.

$$T = T_w \quad (9)$$

and uniform constant heat flux q_w is specified on the tube wall for the UHF condition.

$$-\lambda_f \frac{\partial T}{\partial n} \Big|_w = q_w \quad (10)$$

where n is the direction normal to the tube wall surface. On the tape surface, the no-slip condition for velocity is adopted for both the UWT and UHF conditions.

$$u(x, y, z) = 0, \quad v(x, y, z) = 0, \quad w(x, y, z) = 0 \quad (11)$$

The temperature on the tape surface for both the UWT and the UHF conditions is determined by

$$T|_f = T|_s, \quad \lambda_f \frac{\partial T}{\partial n} \Big|_f = \lambda_s \frac{\partial T}{\partial n} \Big|_s \quad (12)$$

where the subscripts f and s are representative of fluid and tape materials, respectively, and n is the direction normal to the tape surface, while for nonconducting tape cases, Eq. (12) can be simplified as follows:

$$\lambda_f \frac{\partial T}{\partial n} \Big|_f = 0$$

2.2 In the Tape Region. The energy equation,

$$\frac{\partial}{\partial x_i} \left(\lambda_s \frac{\partial T}{\partial x_i} \right) = 0 \quad (13)$$

The boundary conditions are as follows.

On both surfaces of the ends of the tape in the axial direction, the temperature distribution is obtained with linear interpolation using the neighboring nodal points in the axial direction, and then the periodic fully developed boundary of nondimensional temperature condition is enforced

$$\Theta(x, y, z)|_{\text{in}} = \Theta(x, y, z)|_{\text{out}} \quad (14)$$

where the definition of Θ is the same as Eqs. (5) and (6) for the UWT and the UHF conditions, respectively, but T_{bulk} in this definition is determined by

$$T_{\text{bulk}} = \int \int T(x, y, z) dy dz / \int \int dy dz \quad (15)$$

On the tape surfaces in contact with the tube wall, for the UWT condition:

$$T = T_w \quad (16)$$

For the UHF condition,

$$-\lambda_s \frac{\partial T}{\partial n} \Big|_w = q_w \quad (17)$$

On the tape surface in contact with fluid,

$$T|_f = T|_s, \quad \lambda_f \frac{\partial T}{\partial n} \Big|_f = \lambda_s \frac{\partial T}{\partial n} \Big|_s \quad (18)$$

It is assumed that two surfaces of the tape contacted with the tube wall have the same contact condition. Hence, the symmetric boundary conditions on temperature and heat flux shown in Fig. 2 are enforced and can be written as

$$T(x, y, \delta/2) = T(x, L_{\text{tape}} - y, -\delta/2) \quad (19)$$

$$\lambda_f \frac{\partial T(x, y, \delta/2)}{\partial n} \Big|_f = -\lambda_s \frac{\partial T(x, -y, -\delta/2)}{\partial n} \Big|_s \quad (20)$$

The Reynolds number and the friction factor are defined as

$$\text{Re} = \frac{\rho u_m D}{\mu}, \quad f = \frac{\Delta p D}{2\rho u_m^2 L} \quad (21)$$

where u_m is the average velocity at the inlet cross section based on an empty tube with a given mass flow rate. The local heat transfer coefficient and the local Nusselt number are determined by the following equations:

$$q_{\text{local}} = -\lambda \frac{\partial T}{\partial n} \Big|_w, \quad h_{\text{local}} = \frac{q_{\text{local}}}{(T(x, y, z)|_w - T_{\text{bulk}})} \quad (22)$$

$$\text{Nu}_{\text{local}} = \frac{h_{\text{local}} D}{\lambda_f}$$

where T_{bulk} is the average temperature at a cross section in the flow region, and h_{local} and Nu_{local} are only suitable for the tube

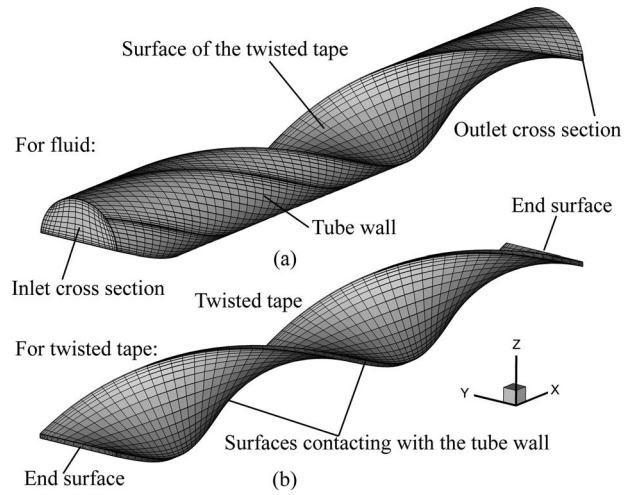


Fig. 3 Computational domain and grid system used in the simulation: (a) flow region and (b) tape region

wall surface in contact with fluid. The average Nusselt numbers are calculated as follows:

$$\text{Nu}_x = \frac{D \oint q_{\text{local}} dl / (\pi D - 2\delta)}{\lambda_f \left(\oint (T(x, y, z)|_w dl / \pi D - T_{\text{bulk}}) \right)}, \quad \text{Nu}_m = \frac{1}{2H} \int_0^{2H} \text{Nu}_x dx \quad (23)$$

3 Numerical Method

The simulation domain in the physical space (x - y - z coordinates) was transformed into a rectangular parallelepiped in the computational space (ξ - η - ζ coordinates) by using the transfinite interpolation algebraic method [21,22]. The schematic of the grid systems in the physical space are presented in Fig. 3. The governing equations shown above were then transformed into the computational space and were discretized there by using the control volume method. In addition, a power scheme approximation was used to discretize the convective terms, while the second order central difference schemes were employed for the viscous and source terms. A SIMPLE algorithm was used to handle the coupling of velocity and pressure [23], and a staggered grid arrangement was applied to overcome the decoupling between velocity and pressure.

Because the fluid properties were assumed constant, the continuity and the momentum equations in the flow region were first solved simultaneously to obtain the convergent velocity field. For the tape with finite thermal conductivity cases, the domain coupling method was adopted to solve the energy equations [24]. The convergent judgment is defined by the balance of energy in the tape region, the relative error of heat conducted from the tube wall to the tape, and the sum of the heat transferred from the tape to the fluid is less than 10^{-3} and 10^{-2} for UWT and UHF conditions, respectively. Because of the symmetric characteristic of heat transfer (as seen in Fig. 2), the expression of relative error can be written as

$$\varepsilon = \frac{\int \int q_{\text{I}} ds_{\text{I}} dx - \int \int q_{\text{III}} ds_{\text{III}} dx}{\int \int q_{\text{I}} ds_{\text{I}} dx} \quad (24)$$

Table 1 Results of the different grids tested

Twist ratio y	Grid Nos.	Nu, UWT	Nu, UHF	f
4.0	221 × 36 × (28+10)	14.069	13.861	0.1135
	221 × 46 × (34+12)	13.670	13.632	0.1133
	241 × 46 × (34+12)	13.689	13.644	0.1133
5.0	277 × 36 × (28+10)	13.019	13.143	0.1043
	277 × 46 × (34+12)	12.639	12.945	0.1043
	301 × 46 × (34+12)	12.650	12.955	0.1043
6.0	331 × 36 × (28+10)	12.204	12.438	0.09882
	331 × 46 × (34+12)	11.860	12.256	0.09871
	361 × 46 × (34+12)	11.869	12.264	0.09871

Three different grid numbers were selected and evaluated at $Re=600$, and $\delta=0.05D$ in perfect fitness with $\lambda_s/\lambda_f=56.6$ to identify the appropriate grid numbers for the three different twist ratio cases. The results of the independent grid evaluations are listed in Table 1, and the maximum variation in either the Nusselt number or the friction factor was observed to be within 3% for both the UWT and the UHF conditions. Then, the computational grids in ξ , η , and ζ directions were $221 \times 46 \times (34+12)$ for the $y=4$, $\delta=0.05D$ case; $277 \times 46 \times (34+12)$ for the $y=5$, $\delta=0.05D$ case; and $331 \times 46 \times (34+12)$ for the $y=6$, $\delta=0.05D$ case. Herein, grid number 34 was used for the flow region while grid number 12 was used for the tape region. For different δ , the grid number was adjusted.

4 Validation of Numerical Method

In the fully developed laminar swirl flow regime, the proposed correlation for friction factor by Manglik and Bergles [14] is shown as follows:

$$f = \frac{15.767}{Re} (1 + 10^{-6} Sw^{2.55})^{1/6} \left[1 + \left(\frac{\pi}{2y} \right)^2 \right] \times \left(\frac{\pi + 2 - 2\delta/D}{\pi - 4\delta/D} \right)^2 \left(\frac{\pi}{\pi - 4\delta/D} \right) \quad (25)$$

Equation (25) correlates friction factors for laminar swirl flows with $\pm 10\%$, a fairly large set of experimental data for a very wide range of flow conditions and tape geometry.

For the fully developed laminar swirl flow heat transfer under the UWT condition, the following equation presented in Ref. [14] was chosen for the comparison of the numerical results.

$$Nu = 0.106 Pr^{0.3} Sw^{0.767} (\mu_b/\mu_w)^{0.14} \quad (26)$$

Equation (26) correlates isothermal Nusselt numbers for laminar flow heat transfer within $\pm 15\%$ only when $Gr < Sw^2$, which determines secondary flow effects to be dominated. Under the UHF condition, Hong and Bergles [13] proposed the following correlation for the prediction of fully developed Nusselt numbers.

$$Nu = 5.172 \left[1 + 0.005484 Pr^{0.7} \left(\frac{\pi}{\pi - 4\delta/D} \cdot \frac{Re}{y} \right)^{1.25} \right]^{0.5} (\mu_b/\mu_w)^{0.14} \quad (27)$$

The comparison of friction factors is presented in Fig. 4. As shown in Fig. 4(a), with increasing Re at $\delta/D=0.05$, the friction factor decreases, and the deviation between numerical results and correlation is fairly small for different twist ratios, respectively, especially for $y=\infty$ (i.e., straight tape placed inside a circular tube) cases. The comparison of the numerical friction factors with correlation (including 70 sets of data) is depicted in Fig. 4(b); one can observe from this figure that numerical results agree very well with the correlation, and the maximum relative deviation reaches about 12.7%.

The comparison of numerical Nu with correlation is depicted in Fig. 5. As shown in Fig. 5(a), one can observe that the Nusselt

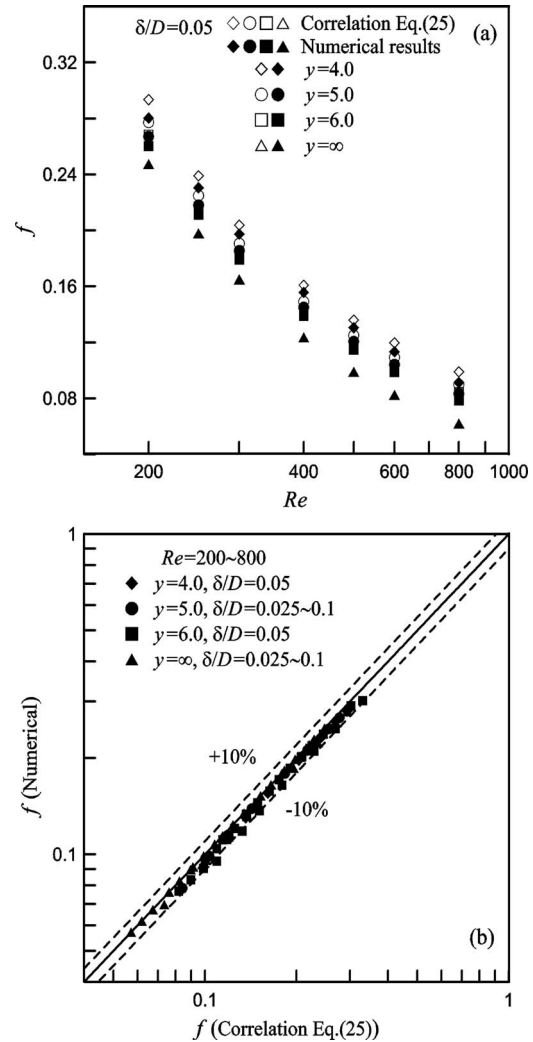


Fig. 4 Comparison of friction factor with the predictive correlations: (a) $f \sim Re$ and (b) $f(\text{numerical}) \sim f(\text{correlated})$

number Nu increases with increasing Re , and the deviation between numerical Nu and correlation changes with changing Re for both the UWT and UHF conditions, respectively. For the UWT condition, herein only Nu at $Re=400\sim 800$, $\delta/D=0.025\sim 0.1$, $y=4.0\sim 6.0$ are presented in Fig. 5(b), along with the consideration of the applicability of Eq. (26), i.e., $Gr < Sw^2$. Compared with the correlation, one can note that the majority of numerical results based on the conducting tape in perfect fitness with $\lambda_s/\lambda_f=56.6$ are within $\pm 15\%$, and the maximum relative deviation between the numerical results and about correlation is about 22.3%. For the UHF condition, the numerical results shown in Fig. 5(c) agree very well with the available correlation. The majority of numerical results based on the conducting tape in perfect fitness with $\lambda_s/\lambda_f=56.6$ are within $\pm 15\%$, and the maximum relative deviation between them is about 18.2%. The above comparisons indicate that numerical results in the present study are reliable.

5 Results and Discussion

5.1 The Effects of Tape Thermal Boundary Conditions on Nu. To clarify the effects of conduction in the tape on heat transfer performance, the numerical results on the basis of several different conductivities of the tape are presented together for comparison in Figs. 5(b) and 5(c). As for the consideration of thermal contact resistance between the tube wall and the tape, an equivalent thermal conductivity on the base of the tape was specified. In

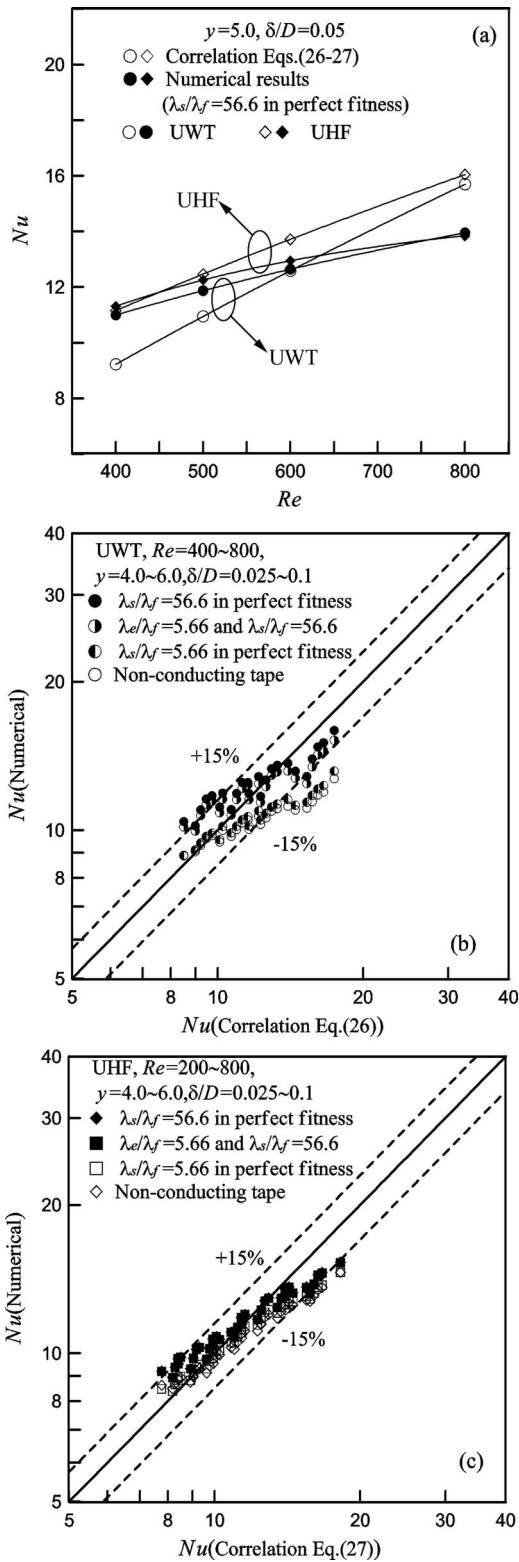


Fig. 5 Comparison of Nusselt number with the predictive correlations: (a) $Nu \sim Re$, (b) UWT: $Nu(\text{numerical}) \sim Nu(\text{correlated})$, and (c) UHF: $Nu(\text{numerical}) \sim Nu(\text{correlated})$

this study, the ratio of the width of the region with the equivalent thermal conductivity to the tube's internal diameter is about 1.79%, and the thermal conductivity in this region of the tape is assumed to be equal to $\lambda_e=0.1\lambda_s$ ($\lambda_e/\lambda_f=5.66$), and in another region of the tape, it is $\lambda_s/\lambda_f=56.6$. As shown in Fig. 5(b), when

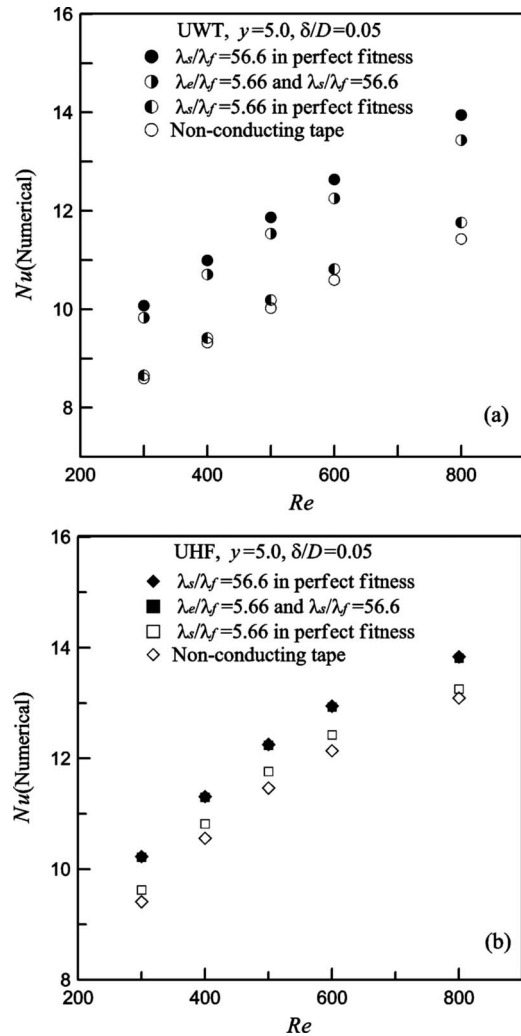


Fig. 6 Effect of conduction in the tape on numerical Nusselt number: (a) UWT and (b) UHF

the UWT condition was specified, the tape thermal boundaries can significantly affect numerical results, and a large difference exists between the conducting tape in perfect fitness with $\lambda_s/\lambda_f=56.6$ and the nonconducting tape cases. The reliability of numerical Nu is strongly dependent on the conduction of the tape; detailed information about this can be found in Ref. [25]. Figure 5(b) indicates that thermal contact resistance deteriorates the overall heat transfer performance, but the effect is not large because the lower thermal conductivity is specified in a very small width for the studied cases. For the UHF condition, however, one can observe from Fig. 5(c) that the effect of the conduction of the tape on average Nu is fairly small, as compared with that for the UWT condition, and the maximum relative deviation of Nu for the conducting tape in perfect fitness with $\lambda_s/\lambda_f=56.6$ and the nonconducting tape cases is about 9.4%; compared with the predictive correlation, even if the nonconducting tape was assumed during the simulation process, the maximum relative deviation between the numerical Nu and correlation is 19.7%. However, for both the UWT and the UHF conditions, the local Nu is affected by conduction in the tape, as will be discussed later.

At the same flow condition, the sensitivity of Nu for the UWT and the UHF conditions to the tape thermal boundary conditions is reflected in Fig. 6. As expected, Nu for the conducting tape in perfect fitness with $\lambda_s/\lambda_f=56.6$ is larger than that of the other three cases, and this results from the fin contribution of the tape. As shown in Fig. 6(a), Nu increases with increasing Re for the

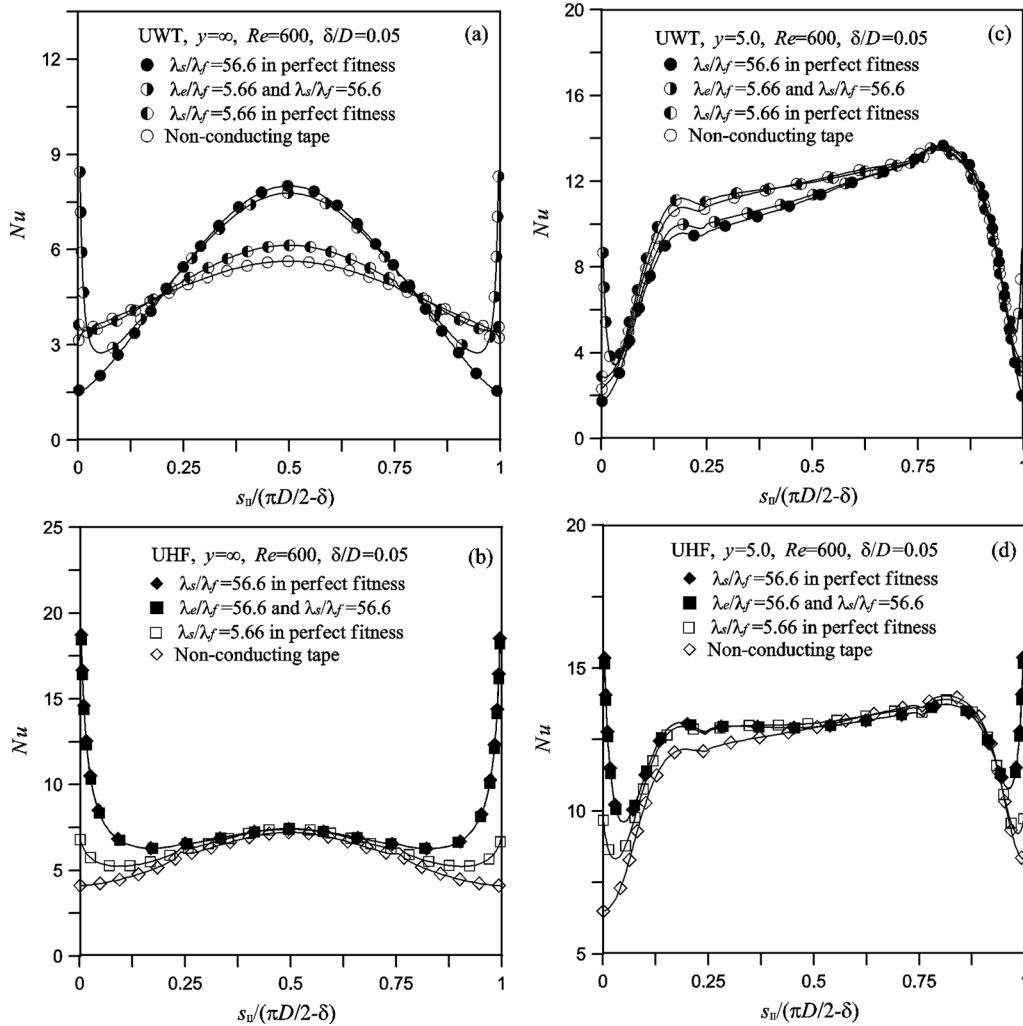


Fig. 7 Effect of conduction in the tape on the local Nusselt number at tube wall: (a) UWT: $\gamma = \infty$, (b) UHF: $\gamma = \infty$, (c) UWT: $\gamma = 5$, and (d) UHF: $\gamma = 5$

four different tape thermal boundaries, respectively. The evidence indicated that the rate of increase in Nu for the conducting tape in perfect fitness with $\lambda_s/\lambda_f = 56.6$ is larger than that of the other studied cases, which further indicates that the conduction in the tape obviously can affect the heat transfer performance when UWT is enforced. As shown in Fig. 6(b), however, the difference in Nu between different tape conductivities shows minimal change with increasing Re, and the thermal contact resistance has less effect on Nu for the UHF condition. The reason for the different effects of the condition in the tape with different tube thermal boundaries is related to the fin contribution of the tape. For example, when the conducting tape in perfect fitness with $\lambda_s/\lambda_f = 56.6$ at $\delta/D = 0.05$, and $\gamma = 5.0$ is considered, the heat transferred from the tape to fluid can reach more than 23% of the overall heat transferred for the UWT condition, while only 3.2% of the overall heat transferred for the UHF condition for the different Re studied.

The effect of conduction in the tape on local Nu along the local coordinate s_{II} , shown in Fig. 2, at $Re = 600$, $\delta/D = 0.05$ is reflected in Fig. 7. When no secondary flow exists on the cross section normal to the main flow direction (i.e., $\gamma = \infty$), the distribution of the local Nu at the tube wall is presented in Figs. 7(a) and 7(b) for the UWT and the UHF conditions, respectively. The tape thermal boundaries obviously affect the heat transfer performance of the tube. For the UWT condition, when the conducting tape in perfect fitness with $\lambda_s/\lambda_f = 56.6$ is considered, the heat flux is very large

on the tape to tube interface, as seen in Fig. 8(a), so a high temperature region is formed close to the tape and results in a lower local Nu in this region as compared with the nonconducting tape case. But for the $\lambda_s/\lambda_f = 5.66$ case, this phenomenon does not clearly exist, partly because of the shape of the corner close to the tape and the existence of the thermal contact resistance that leads to heat being transferred from the fluid to the tape as a result of a large local Nu existing in this region. For the UHF condition, the better conduction in the tape will lead to a low temperature region near the connection of the tape and tube. As an illustrative instance, heat is transferred from the fluid to the tape in this region, and then from the tape to the fluid in the other region for the conducting tape in perfect fitness with $\lambda_s/\lambda_f = 56.6$ case, as shown in Fig. 8(b). Therefore, the local Nu on the surface of the tube near the tape for the nonconducting tape case is lower than those of the other three cases, as shown in Fig. 7(b), and the thermal contact resistance has less effect on the local Nu on the tube wall. It is noted that the effect of the conduction in the tape on the local Nu is very strong, especially on the tube surface near the tape.

For $\gamma = 5$, the secondary flow reduces the effects of the conduction in the tape on the local Nu on the tube wall, except for the region near the tape when UHF is enforced, as shown in Figs. 7(c) and 7(d). This is mainly because the secondary flow promotes the mixture of hot and cold fluids in the flow region. For the UWT condition with better conduction in the tape, the difference between wall temperature (T_w) and the average temperature at cross

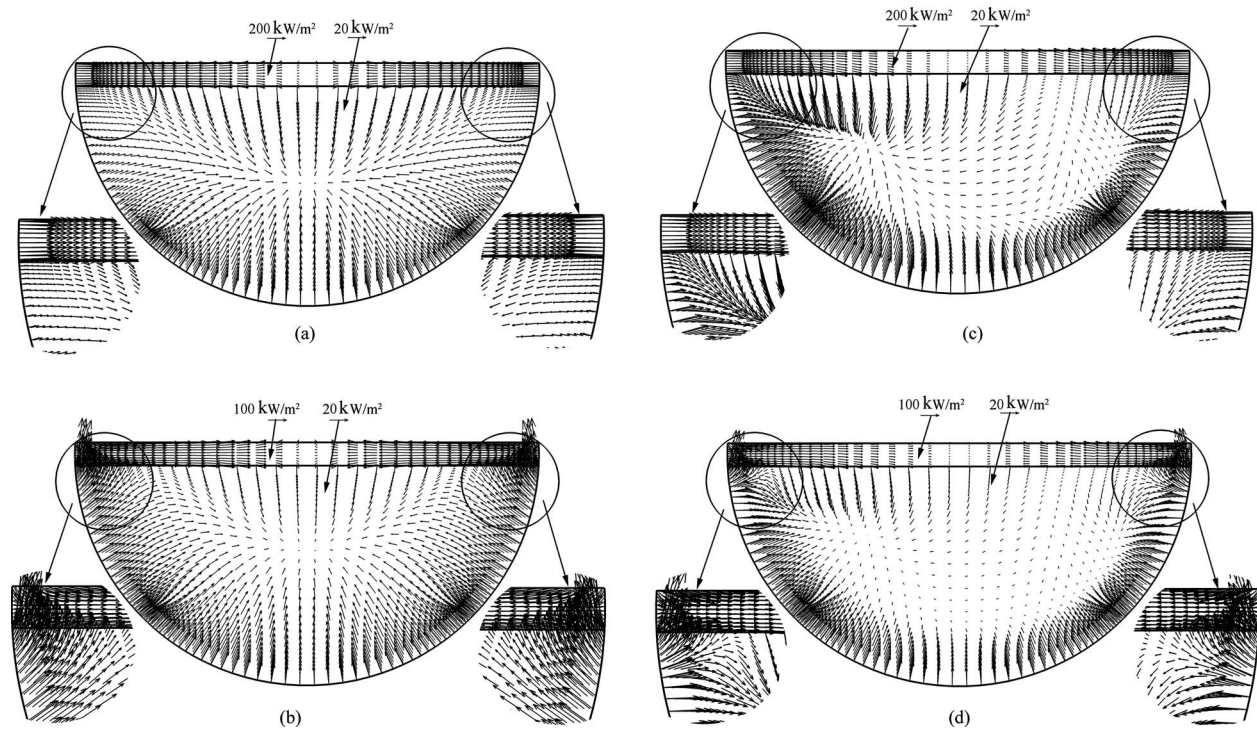


Fig. 8 Distribution of the heat flux vector on the cross section ($Re=600$, $\delta/D=0.05$) (a) UWT: $y=\infty$, (b) UHF: $y=\infty$, (c) UWT: $y=5$, (d) UHF: $y=5$

section (T_{bulk}) will necessarily decrease, due to the fin contribution of the tape; and in some regions, the local Nu is lower than that of the nonconducting tape case, as shown in Fig. 7(c). Because of the fin contribution of the tape discussed in Ref. [25] (about 5%, 18%, and 23% for the conducting tape in perfect fitness with $\lambda_s/\lambda_f=5.66$, the conducting tape considering the thermal contact resistance with $\lambda_e/\lambda_f=5.66$ in the contacting region and $\lambda_s/\lambda_f=56.6$ in the other region of the tape, and the conducting tape in perfect fitness with $\lambda_s/\lambda_f=56.6$, respectively), the overall heat transfer still can be enhanced, as shown in Fig. 6(a), and also is demonstrated by the fact that very large heat flux exists on the interface of the tape to the tube wall, as shown in Fig. 8(c). For the UHF condition, only approximately 3.2% fin contribution obviously cannot change the temperature difference mentioned above, but the better conduction in the tape can lead to a variation of the heat flux vector in the flow region, as shown in Fig. 8(d), which can strongly change the distribution of the local Nu , as shown in Fig. 7(d).

5.2 The Relationship Between J_{ABS}^n and Nu . The dimensionless swirl parameter Sw is commonly used to scale the intensity of the secondary flow induced by the twisted tape inserted into a tube. However, Sw is hard to define in other cases. Recently, our group numerically studied the quantitative relationship between the secondary flow and heat transfer enhancement [26–28]. Assuming that the secondary flow is the combination of many vortices and considering that the direction of overall heat transfer is along the main flow, a dimensional parameter, the absolute vorticity flux, can be used to specify the intensity of the secondary flow, in most cases, and to conveniently reevaluate the goodness of the arrangement of a secondary flow producer in real applications, which is defined as follows [26–28]:

$$J_{\text{ABS}}^n = \frac{1}{A} \int \int_A |\omega^n| dA \quad (28)$$

This equation denotes the average absolute vorticity flux of all of the vortices at the unit area of a cross section normal to the main

flow (n is the normal direction of this cross section). For the flow in a circular tube fitted with twisted tape, a linear relationship between J_{ABS}^n and the dimensionless swirl parameter Sw exists as follows [28]:

$$J_{\text{ABS}}^n = 0.106Sw - 4.708(1/s) \quad (29)$$

where the dimensionless swirl parameter Sw is calculated as [14]

$$Sw = \frac{Re}{y^{1/2}} \left(\frac{\pi}{\pi - 4\delta/D} \right) \left[1 + \left(\frac{\pi}{2y} \right)^2 \right]^{1/2} \quad (30)$$

According to the linear relationship between J_{ABS}^n and Sw indicated in Eq. (29), here we use the absolute vorticity flux J_{ABS}^n to describe the intensity of the secondary flow. The relationship of the intensity of the secondary flow and numerical Nu is depicted in Fig. 9. One can note from this figure that numerical Nu is closely dependent on the absolute vorticity flux J_{ABS}^n . The trend is clear, with increasing J_{ABS}^n , the numerical Nu increases for identical thermal boundaries, respectively. Obviously, the variety of Nu with J_{ABS}^n for the conducting tape in perfect fitness with $\lambda_s/\lambda_f=56.6$ cases is not as clear as in the nonconducting tape cases, which resulted from the different fin contributions of the tape to Nu under different tape thicknesses, as discussed in Ref. [25].

5.3 The Sensitivity of Heat Transfer Enhancement to Tube Thermal Boundary Conditions. The numerical results are based on the idealization of constant fluid properties; thus Nu does not change with increasing Re at $y=\infty$ (i.e., straight tape placed inside the circular tube) with the same configuration under the laminar flow condition. Herein we regarded it as a reference value to calculate the ratio of Nu/Nu_{ref} and to scale the sensitivity of the heat transfer enhancement to the tube thermal boundaries by using the secondary flow. For $\delta/D=0.05$ cases, these reference values and the ratio of Nu/Nu_{ref} are listed in Tables 2–5. For the same tape thermal boundary, the ratio of Nu/Nu_{ref} for the UWT condition is higher than that for UHF, and the ratio of Nu/Nu_{ref} is related to the tape thermal boundaries. The thermal contact resis-

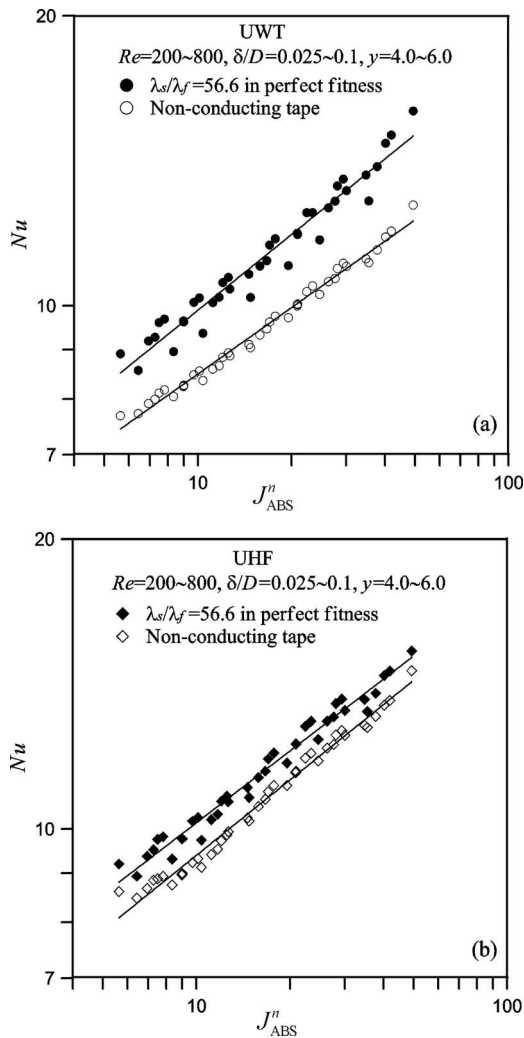


Fig. 9 Relationship of the intensity of secondary flow and numerical Nusselt number: (a) UWT and (b) UHF

tance considered for both the UWT and the UHF conditions does not obviously change the ratio of Nu/Nu_{ref} with identical other conditions. The better the thermal conduction in the tape is, the smaller the ratio of Nu/Nu_{ref} is for both the UWT and the UHF conditions.

The effect of twist ratio on the ratio of Nu/Nu_{ref} is presented in Fig. 10(a). The intensity of the secondary flow is closely dependent on the twist ratio; with decreasing twist ratio, the intensity of the secondary flow increases. One can note that, as the twist ratio is increased, the ratio of Nu/Nu_{ref} decreases, as shown in Fig. 10(a). The effect of Re on the ratio of Nu/Nu_{ref} is presented in Fig. 10(b). Re is the ratio of the inertial force to viscous force. With increasing Re , the intensity of the secondary flow also is enhanced, and the ratio of Nu/Nu_{ref} increases.

For the nonconducting tape, as shown in Fig. 10(a), the ratio of Nu/Nu_{ref} for the UWT condition is obviously higher than that for the UHF; the difference in the ratio of Nu/Nu_{ref} between the two cases does not change obviously with the changing twist ratio. However, for the conducting tape with finite thermal conductivities ($\lambda_s/\lambda_f=56.6$ and 5.66) and with an assumption of no thermal contact resistance between the tube wall and the tape, the difference becomes increasingly larger with decreasing twist ratio. These trends also exist in other studied Re cases, as shown in Tables 2–5. The comparison in this figure also indicates that the difference in the ratio of Nu/Nu_{ref} between the two different thermal boundaries is sensitive to the conduction in the tape.

For the nonconducting tape, as indicated in Fig. 10(b), the ratio of Nu/Nu_{ref} for the UWT is obviously larger than that for the UHF when Re ranged from 400 to 800, and the difference in the ratio of Nu/Nu_{ref} between the two cases does not obviously change with increasing Re . For the conducting tape with finite thermal conductivities ($\lambda_s/\lambda_f=56.6$ and 5.66) in perfect fitness cases, the difference in the ratio of Nu/Nu_{ref} between the two different tube thermal boundaries increases with increasing Re , but it does not change greatly when $Re < 600$.

The above discussion indicates that heat transfer enhancement using secondary flow is strongly dependent on the thermal boundary conditions of the tube wall, the conduction in the tape, and the intensity of secondary flow; the efficiency of heat transfer enhancement is better when UWT is enforced than when UHF is imposed, especially for the nonconducting tape cases.

Table 2 Ratio of Nu/Nu_{ref} at $\delta=0.05D$ (conducting tape in perfect fitness with $\lambda_s/\lambda_f=56.6$)

Thermal boundary	Nu_{ref}	y	Re						
			200	250	300	400	500	600	800
UWT	7.713	4.0	1.2500	1.3230	1.3981	1.5418	1.6649	1.7723	2.0658
		5.0	1.1915	1.2481	1.3061	1.4254	1.5387	1.6386	1.8083
		6.0	1.1556	1.2023	1.2473	1.3493	1.4440	1.5376	1.7072
UHF	7.979	4.0	1.2234	1.2975	1.3839	1.5367	1.6388	1.7098	1.9203
		5.0	1.1726	1.2235	1.2814	1.4178	1.5354	1.6236	1.7358
		6.0	1.1512	1.1921	1.2238	1.3380	1.4392	1.5373	1.6658

Table 3 Ratio of Nu/Nu_{ref} at $\delta=0.05D$ (conducting tape in perfect fitness with $\lambda_s/\lambda_f=5.66$)

Thermal boundary	Nu_{ref}	y	Re						
			200	250	300	400	500	600	800
UWT	5.377	4.0	1.5193	1.6129	1.7105	1.8927	2.0345	2.1451	2.4503
		5.0	1.4472	1.5209	1.5955	1.7513	1.8949	2.0120	2.1880
		6.0	1.3996	1.4631	1.5220	1.6535	1.7785	1.8968	2.0897
UHF	6.310	4.0	1.4415	1.5483	1.6690	1.8641	1.9881	2.0697	2.3129
		5.0	1.3701	1.4418	1.5251	1.7143	1.8641	1.9690	2.1002
		6.0	1.3421	1.3990	1.4422	1.6061	1.7435	1.8649	2.0180

Table 4 Ratio of Nu/Nu_{ref} at $\delta=0.05D$ (conducting tape with consideration of the thermal contact resistance between the tube wall and the tape, in the region in contact with the tube wall having 0.895% width of the tape $\lambda_e/\lambda_f=5.66$, in another region of the tape, $\lambda_s/\lambda_f=56.6$)

Thermal boundary	Nu_{ref}	y	Re						
			200	250	300	400	500	600	800
UWT	7.492	4.0	1.2563	1.3280	1.4016	1.5417	1.6593	1.7591	2.0311
		5.0	1.1991	1.2550	1.3121	1.4292	1.5398	1.6356	1.7936
		6.0	1.1638	1.2102	1.2545	1.3550	1.4480	1.5393	1.7012
UHF	7.949	4.0	1.2286	1.3021	1.3881	1.5405	1.6431	1.7121	1.9208
		5.0	1.1778	1.2280	1.2854	1.4215	1.5359	1.6264	1.7375
		6.0	1.1564	1.1966	1.2279	1.3416	1.4436	1.5403	1.6680

Table 5 Ratio of Nu/Nu_{ref} at $\delta=0.05D$ (nonconducting tape)

Thermal boundary	Nu_{ref}	y	Re						
			200	250	300	400	500	600	800
UWT	4.720	4.0	1.7462	1.8350	1.9309	2.1170	2.2610	2.3705	2.6956
		5.0	1.6769	1.7494	1.8208	1.9754	2.1237	2.2446	2.4212
		6.0	1.6285	1.6937	1.7514	1.8793	2.0047	2.1275	2.3279
UHF	5.745	4.0	1.5566	1.6574	1.7869	1.9928	2.1319	2.2327	2.5454
		5.0	1.5074	1.5618	1.6376	1.8381	1.9969	2.1149	2.2814
		6.0	1.4962	1.5387	1.5649	1.7296	1.8706	1.9999	2.1811

5.4 The Effects of Secondary Flow on the Flow Boundary Layer. The effects of twist ratio on the local distribution of velocity on the cross section normal to the main flow direction are presented in Fig. 11. As shown in this figure, the twist ratio has a small effect on the distribution of the main flow velocity for the studied cases, which implies that the velocity boundary layer does not obviously change as the twist ratio ranged from 4.0 to 6.0, as shown in Fig. 11(a). However, the intensity of the secondary flow (i.e., the values of v_θ and v_r , herein the v_{zm} is the same for different twist ratio cases) is closely dependent on the twist ratio, as shown in Figs. 11(b) and 11(c), which determines the intensity of heat transfer enhancement.

The effects of Re on the local distribution of velocity on the cross section normal to the main flow direction are presented in Fig. 12. As shown in Fig. 12(a), Re has effects on the distribution of the main flow velocity for the studied cases to some extent, but the effects of Re on the velocity boundary layer near the tube wall is also small, except for the region close to the twisted tape. As indicated in Figs. 12(b) and 12(c), the effects of Re on the relative intensity of the secondary flow (i.e., the local distributions of v_θ/v_{zm} and v_r/v_{zm}) are weaker compared with that of the twist ratio, as shown in Fig. 11(b) and 11(c), but the intensity of the secondary flow increases with increasing Re, which results in the enhancement of heat transfer. These facts show that the heat transfer enhancement might not come from a change in the velocity boundary layer; instead, they mainly come from the secondary flow, even though it is smaller in amplitude than the main flow.

6 Conclusion

We numerically analyzed the sensitivity of convective heat transfer enhancement to thermal boundaries in a circular tube by using the secondary flow generated by twisted tape. In order to account for the effects of conduction in the tape, several tapes with different conductivities are considered. The main points can be summarized as follows.

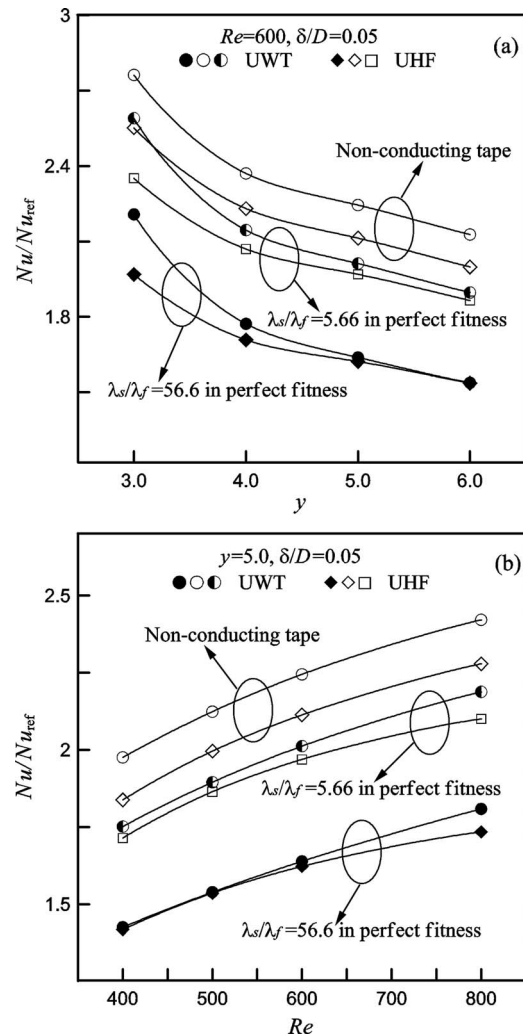


Fig. 10 Effects of twist ratio and Reynolds number on the ratio of Nu/Nu_{ref} : (a) twist ratio and (b) Reynolds number

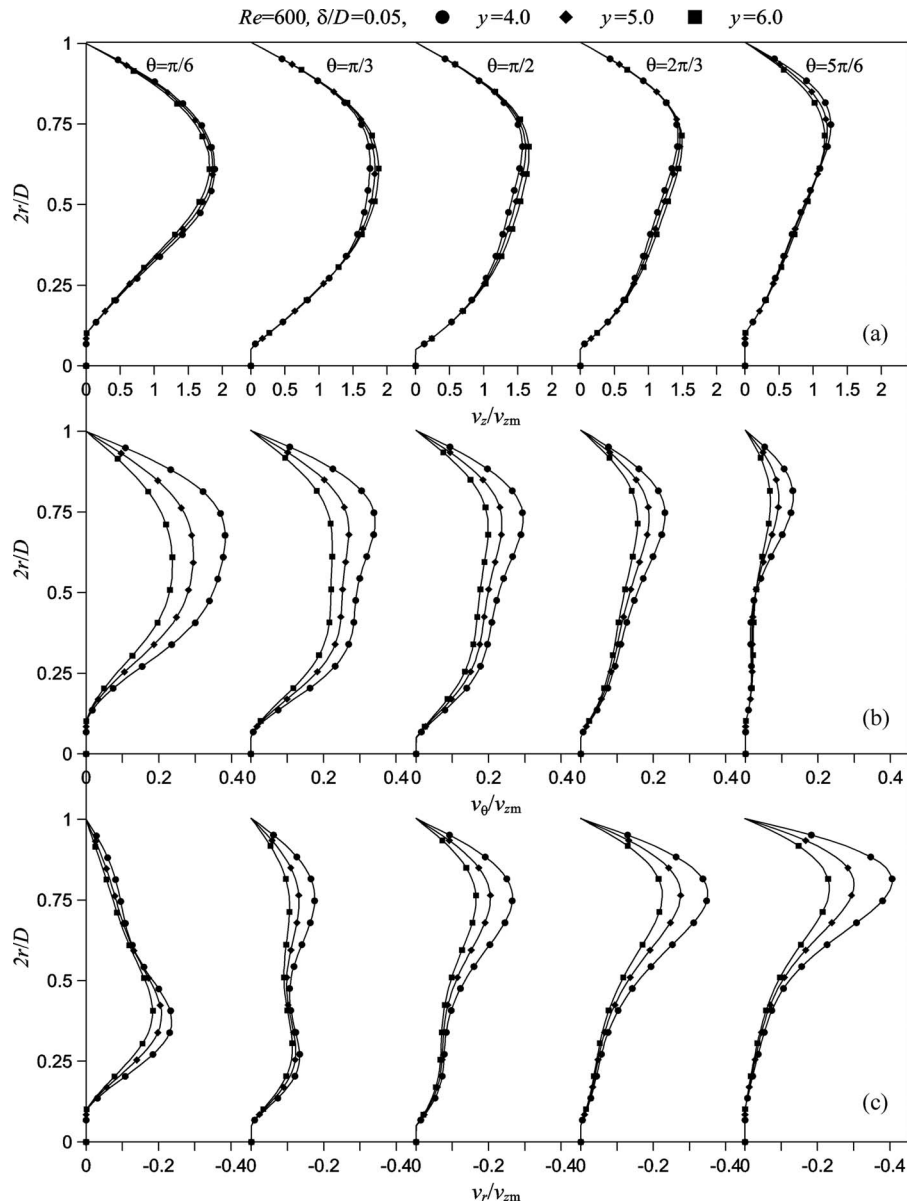


Fig. 11 Effect of twist ratio y on the local distribution of velocity on a cross section normal to the main flow direction

- (1) For fully developed laminar convective heat transfer, the thermal conduction in the tape obviously affects the overall heat transfer performance for the UWT condition, while having a small effect on that for the UHF condition (except for the $y=\infty$ cases), but it has great influence on the local Nusselt number on the tube surface.
- (2) Nu is closely dependent on the absolute vorticity flux J_{ABS}'' ; with increasing J_{ABS}'' , the Nu increases for a given thermal boundary condition. For different tape thicknesses, the different fin contributions of the tape to Nu will lead to a loose connection between Nu and J_{ABS}'' .
- (3) At the same conduction in the tape, when UWT is enforced on the tube wall, the efficiency of heat transfer enhancement is better than when UHF is imposed, especially for the nonconducting tape, and that is closely dependent on the intensity of the secondary flow. The ratio of Nu/Nu_{ref} decreases with an increasing twist ratio while it increases with an increasing Reynolds number. In addition, the difference in the ratio of Nu/Nu_{ref} between the UWT and

UHF conditions is strongly dependent on the conduction in the tape and the intensity of the secondary flow. For the nonconducting tape cases, the difference does not change greatly with the changing twist ratio and Re , while for the conducting tape cases, the difference becomes increasingly large with decreasing twist ratio. On the other hand, with the same twist ratio, the difference in the ratio of Nu/Nu_{ref} between the two different tube thermal boundaries increases with increasing Re , but it does not change greatly when $Re < 600$.

- (4) In a circular tube fitted with twisted tape, the twist ratio ranged from 4.0 to 6.0 and did not necessarily change the main flow velocity boundary layer, while Re has effects on the distribution of the main flow velocity to some extent in the studied cases but has a strong effect on the shape of the main flow velocity boundary layer near the tube wall only in the small region, which is near the connection of tape and tube.

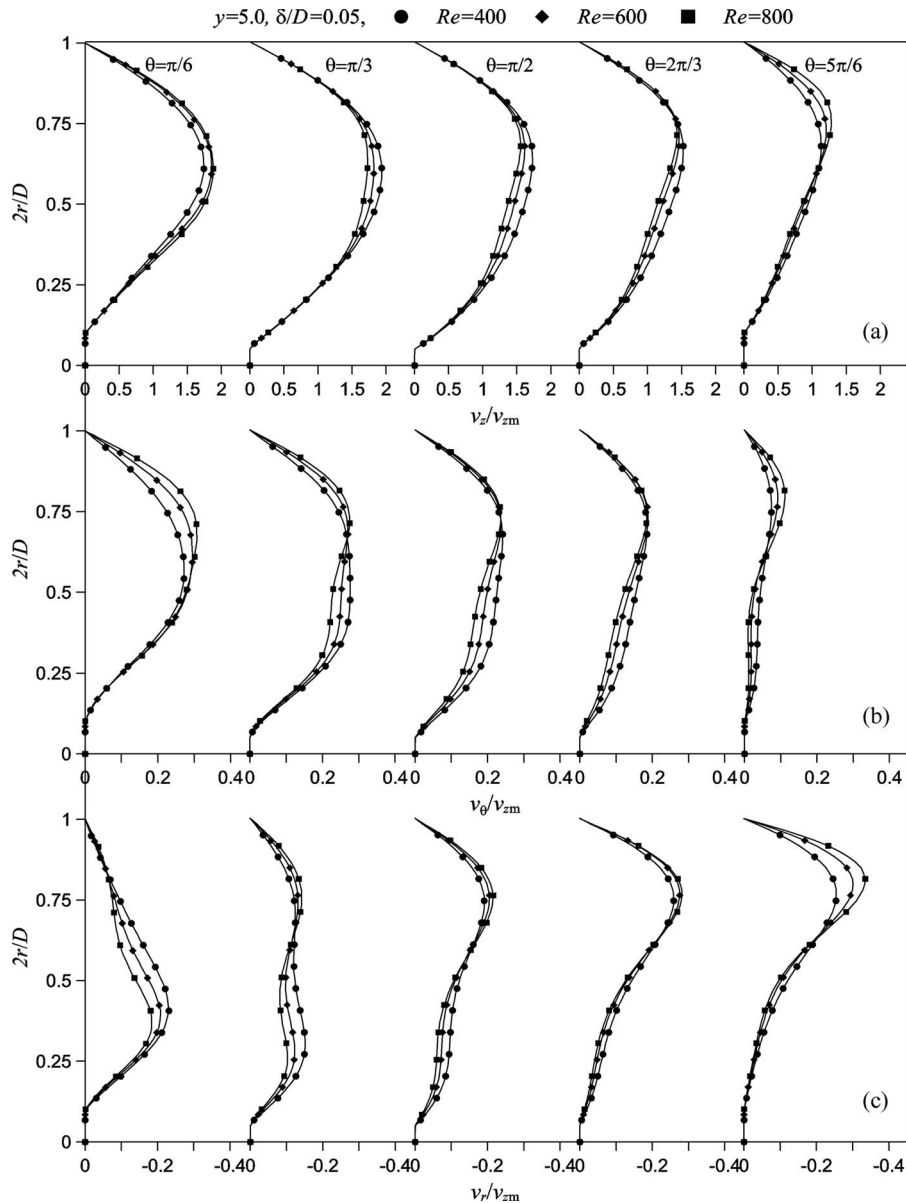


Fig. 12 Effect of the Reynolds number on the local distribution of velocity on a cross section normal to the main flow direction

Acknowledgment

L. B. Wang acknowledges the support from the National Natural Science Foundation of China (Contract No. 50876040).

Nomenclature

- A = area of cross section (m^2)
- c_p = specific heat capacity ($kJ/(kg\ K)$)
- D = tube internal diameter, hydraulic diameter (m)
- f = Fanning friction factor, $f = \Delta p D / (2\rho u_m^2 L)$
- h = convective heat transfer coefficient ($W/(m^2\ K)$)
- H = twist pitch length (m)
- J_{ABS}^n = absolute vorticity flux along the normal direction of cross section (s^{-1})
- L = axial tube length (m)
- L_{tape} = width of twisted tape (m)
- n = normal direction of the cross section or wall surface
- Nu = Nusselt number, $Nu = hD/\lambda$

- p = static pressure (Pa)
- Pr = Prandtl number, $Pr = \mu c_p / \lambda$
- q = heat flux (W/m^2)
- Re = Reynolds number, $Re = \rho u_m D / \mu$
- s = local coordinates (m)
- Sw = swirl parameter defined in Eq. (30)
- T = temperature (K)
- u_i, u, v, w = components of velocity vector (m/s)
- v_r, v_θ, v_z = components of velocity vector (m/s)
- u = velocity (m/s)
- y = twist ratio of the twisted tape: $y = H/D$
- x_i, x, y, z = components of coordinates axes (m)

Greek Symbols

- δ = tape thickness (m)
- ε = relative error defined in Eq. (24)
- η = coordinate (m)
- λ = thermal conductivity ($W/(m\ K)$)
- μ = viscosity Pa s
- ρ = density (kg/m^3)

Θ = dimensionless temperature
 Δp = pressure drop (Pa)
 ω = vorticity (s^{-1})
 ξ, ζ = coordinates axes (m)

Subscripts

bulk = cross average value
 e = equivalent value
 f = fluid
 in = inlet
 local = local value
 m = average value
 out = outlet
 ref = reference value
 s = solid or tape
 w = wall surface

References

- [1] Oosthuizen, P. H., and Naylor, D., 1999, *An Introduction to Convective Heat Transfer Analysis*, McGraw-Hill, New York.
- [2] Kays, W. M., Crawford, M. E., and Weigand, B., 2005, *Convection Heat and Mass Transfer*, 4th ed., McGraw-Hill, New York.
- [3] Sleicher, C. A., and Tribus, M., 1956, *Proceedings of Heat Transfer and Fluid Mechanics Institute*, Stanford University, Stanford, p. 59.
- [4] Fiebig, M., 1995, "Vortex Generators for Compact Heat Exchangers," *J. Enhanced Heat Transfer*, **2**(1–2), pp. 43–61.
- [5] Joardar, A., and Jacobi, A. M., 2005, "Impact of Leading Edge Delta-Wing Vortex Generators on the Thermal Performance of a Flat Tube, Louvered-Fin Compact Heat Exchanger," *Int. J. Heat Mass Transfer*, **48**(8), pp. 1480–1493.
- [6] Wang, L. B., Ke, F., Gao, S. D., and Mei, Y. G., 2002, "Local and Average Characteristics of Heat /Mass Transfer Over Flat Tube Bank Fin With Four Vortex Generators Per Tube," *ASME J. Heat Transfer*, **124**, pp. 546–552.
- [7] Biswas, G., Fujii, T. D., and Nishino, K., 1996, "Numerical and Experimental Determination of Flow Structure and Heat Transfer Effects of Longitudinal Vortices in a Channel Flow," *Int. J. Heat Mass Transfer*, **39**, pp. 3441–3451.
- [8] Wang, Q. W., Chen, Q. Y., Wang, L., Zeng, M., Huang, Y. P., and Xiao, Z. J., 2007, "Experimental Study of Heat Transfer Enhancement in Rectangular Narrow Channel With Longitudinal Vortex Generators," *Nucl. Eng. Des.*, **237**, pp. 686–693.
- [9] Webb, R. L., 2000, "Heat Transfer and Friction Characteristics of Internal Helical-Rib Roughness," *ASME J. Heat Transfer*, **122**, pp. 134–142.
- [10] Li, L. J., Cui, W. Z., Liao, Q., Xin, M. D., Jen, T. C., and Chen, Q. H., 2005, "Heat Transfer Augmentation in 3D Internally Finned and Microfinned Helical Tube," *Int. J. Heat Mass Transfer*, **48**(10), pp. 1916–1925.
- [11] Naphon, P., Nuchjapo, M., and Kurujareon, J., 2006, "Tube Side Heat Transfer Coefficient and Friction Factor Characteristics of Horizontal Tubes With Helical Rib," *Energy Convers. Manage.*, **47**, pp. 3031–3044.
- [12] Liao, Q., Jen, T. C., Chen, Q. H., Li, L. J., and Cui, W. Z., 2007, "Heat Transfer Performance in 3D Internally Finned Heat Pipe," *Int. J. Heat Mass Transfer*, **50**(7–8), pp. 1231–1237.
- [13] Hong, S. W., and Bergles, A. E., 1976, "Augmentation of Laminar Heat Transfer in Tubes by Means of Twisted Tape Inserts," *ASME J. Heat Transfer*, **98**, pp. 251–256.
- [14] Manglik, R. M., and Bergles, A. E., 1993, "Heat Transfer and Pressure Drop Correlations for Twisted-Tape Inserts in Isothermal Tubes: Part I—Laminar Flows," *ASME J. Heat Transfer*, **115**, pp. 881–889.
- [15] Agarwal, S. K., and Rajarao, M., 1996, "Heat Transfer Augmentation for the Flow of Viscous Liquid in Circular Tubes Using Twisted Tape Inserts," *Int. J. Heat Mass Transfer*, **39**, pp. 3547–3557.
- [16] Patil, A. G., 2000, "Laminar Flow Heat Transfer and Pressure Drop Characteristics of Power-Law Fluids Inside Tubes With Varying Width Twisted Tape Inserts," *ASME J. Heat Transfer*, **122**, pp. 143–149.
- [17] Date, A. W., 2000, "Numerical Prediction of Laminar Flow and Heat Transfer in a Tube With Twisted-Tape Insert: Effects of Property Variations and Buoyancy," *J. Enhanced Heat Transfer*, **7**, pp. 217–229.
- [18] Al-Fahed, S., Chamra, L. M., and Chakroun, W., 1998, "Pressure Drop and Heat Transfer Comparison for Both Microfin Tube and Twisted-Tape Inserts in Laminar Flow," *Exp. Therm. Fluid Sci.*, **18**(4), pp. 323–333.
- [19] Saha, S. K., Dutta, A., and Dhal, S. K., 2001, "Friction and Heat Transfer Characteristics of Laminar Swirl Flow Through a Circular Tube Fitted With Regularly Spaced Twisted-Tape Elements," *Int. J. Heat Mass Transfer*, **44**(22), pp. 4211–4223.
- [20] Manglik, R. M., and Bergles, A. E., 2003, "Swirl Flow Heat Transfer and Pressure Drop With Twisted-Tape Inserts," *Adv. Heat Transfer*, **36**, pp. 183–266.
- [21] Eriksson, L. E., 1985, "Practical Three-Dimension Mesh Generation Using Transfinite Interpolation," *SIAM (Soc. Ind. Appl. Math.) J. Sci. Stat. Comput.*, **6**(3), pp. 712–741.
- [22] Thompson, J. F., Warsi, Z. U. A., and Mastin, C. W., 1985, *Numerical Grid Generation, Foundation and Application*, North-Holland, New York, pp. 95–140.
- [23] Patankar, S. V., 1980, *Numerical Heat Transfer and Fluid flow*, Hemisphere, New York, pp. 330–351.
- [24] Tao, W. Q., 2001, *Numerical Heat Transfer*, 2nd ed., Xi'an Jiaotong University Press, Xi'an, China, pp. 485–488.
- [25] Lin, Z. M., Teng, S., and Wang, L. B., 2008, "Numerical Study of Conjugate Heat Transfer in a Tube With Twisted Tape Insert," *JP Journal of Heat and Mass Transfer*, **2**(3), pp. 279–302.
- [26] Chang, L. M., Wang, L. B., Song, K. W., Sun, D. L., and Fan, J. F., 2009, "Numerical Study of the Relationship Between Heat Transfer Enhancement and Absolute Vorticity Flux Along Main Flow Direction in Channel Formed by Flat Tube Bank Fin With Vortex Generators," *Int. J. Heat Mass Transfer*, **52**(7–8), pp. 1794–1801.
- [27] Song, K. W., Wang, L. B., and Sun, D. L., 2009, "Convective Heat Transfer and Absolute Vorticity Flux Along Main Flow in a Channel Formed by Flat Tube Bank Fins With Vortex Generators Mounted on Both Fin Surfaces," *J. Enhanced Heat Transfer*, **16**(2), pp. 123–139.
- [28] Lin, Z. M., Sun, D. L., and Wang, L. B., "The Relationship Between Absolute Vorticity Flux Along Main Flow and Convection Heat Transfer in a Tube Inserting a Twisted Tape," *Heat Mass Transfer*, submitted.

Characterization and Pool Boiling Heat Transfer Studies of Nanofluids

R. Kathiravan

Ravi Kumar

e-mail: ravikfme@iitr.ernet.in

Akhilesh Gupta

Department of Mechanical and Industrial
Engineering,
Indian Institute of Technology,
Roorkee 247 667, India

Ramesh Chandra

Institute Instrumentation Centre,
Indian Institute of Technology,
Roorkee 247 667, India

Copper nanoparticles with an average size of 10 nm are prepared by the sputtering method and are characterized using different techniques, viz., X-ray diffraction spectrum, atomic force microscopy, and transmission electron microscopy. The pool boiling heat transfer characteristics of 0.25%, 0.5%, and 1.0% by weight concentrations of copper nanoparticles dispersed in distilled water and in distilled water with 9.0 wt % of sodium dodecyl sulfate (SDS) are studied. Also the data for the boiling of pure distilled water and water with SDS are acquired. The above data are obtained using commercial seamless stainless steel tube heater with an outer diameter of 9.0 mm and an average surface roughness of 1.09 μm . The experimental results concluded that (i) critical heat flux (CHF) obtained in water with surfactant nanofluids gives nearly one-third of the CHF obtained by copper-water nanofluids, (ii) pool boiling heat transfer coefficient decreases with the increase in the concentration of nanoparticles in water base fluids, and (iii) heat transfer coefficient increases with the addition of 9.0% surfactant in water. Further addition of nanoparticles in this mixture reduces the heat transfer coefficient. (iv) CHF increases nearly 50% with an increase in concentration of nanoparticles in the water as base fluid and nearly 60% in the water with surfactant as base fluid.

[DOI: 10.1115/1.3111260]

Keywords: nanofluids, copper nanoparticles, critical heat flux, sputtering, pool boiling, and heat transfer coefficient

1 Introduction

Advances in the area of electronics, computers, nuclear energy, fossil energy, etc., have motivated the efforts for research in the area of enhancement of boiling heat transfer coefficient over the heated tubes (boiling is one of the most efficient means of heat transfer). The distinctive approaches considered to enhance pool boiling and critical heat flux (CHF) [1] are oxidation or selective fouling of a heater surface to increase the wettability of the liquid, vibration of heaters to promote the departure of bubbles from the heated surface, coating or extended heater surface to increase the heat transfer area, heater rotation to promote bubble departure from and liquid deposition onto the heater surface, fluid vibration to promote bubble departure and liquid supply, and application of electric fields to promote bubble departure from the surface by dielectrophoretic force to increase liquid renewal.

Besides, use of nanofluids is one of the promising methods. The small amount of solid particles of metals (average size of below 100 nm in diameter), suspended with base fluids like water, ethylene glycol, engine oil, etc., constitutes nanofluids. Choi [2] and Eastman et al. [3] prepared nanofluids by addition of particles with a size of 50 nm with base fluids and reported that the thermal conductivity of fluid increased by 40% and faced problem of sedimentation, abrasion, and clogging owing to their large size [1,4].

The main factor for the enhancement of thermal conductivity of fluid is the increase in the surface area by the addition of nanoparticles; also interactions and collisions among the particles increase the mixing fluctuation and turbulence of the fluid, as explained by Xuan and Li [4]. Das et al. [5] determined that nanofluids containing Al_2O_3 particles deteriorate boiling heat transfer. Vasallo et al. [6], using SiO_2 based nanofluid, showed

that the CHF was significantly increased due to deposition of silica over the heating surface, which increased the nucleation site density on the heated surface. However, the enhancement of CHF could not be quantified. Bang and Chang [7] found that the enhancement was nearly 32% and 13% for horizontal and vertical surfaces in a pool of water at high heat flux using alumina nanoparticle with water, which was in agreement with the findings of Vasallo et al. [6], which was due to change in surface roughness.

In fact, most of the experimental studies were related to CHF of nanofluids containing Al_2O_3 and SiO_2 . Further, most of the work was carried out over either a small diameter wire [2,3,6,8,9] or tubes having diameter of less than 20 mm [5] with the average size of the nanoparticles around 20–50 nm.

In order to understand the general behavior of nanofluid, it is imperative to investigate the boiling heat transfer of other nanofluids as well. Therefore, an experimental investigation has been carried out to study the pool boiling of nanofluid over a horizontal tube with different concentrations of copper in water and copper in water with a surfactant.

2 Preparation and Characterization of Nanofluids

The copper nanoparticles for the present investigation are generated using high pressure dc-magnetron sputtering process wherein the impact of an atom or ion on a surface produces sputtering of material from the surface due to momentum transfer. Unlike many other vapor phase techniques there is no melting of material in this process. The sputtering target is a pure copper disk of 50 mm diameter and 5 mm thickness. Cooling the substrate is done by continuously supplying liquid nitrogen, and the temperature is maintained around 100 K and the pressure was 10 mT of argon gas. Before the sputtering process started, the sputtering chamber has been maintained at a base pressure of 500 μTorr .

2.1 X-Ray Diffraction Spectra of Copper Nanoparticle. It is found that the copper nanoparticles are almost oriented with

Contributed by the Heat Transfer Division of ASME for publication in the JOURNAL OF HEAT TRANSFER. Manuscript received October 6, 2008; final manuscript received March 4, 2009; published online June 5, 2009. Review conducted by Patrick E. Phelan.

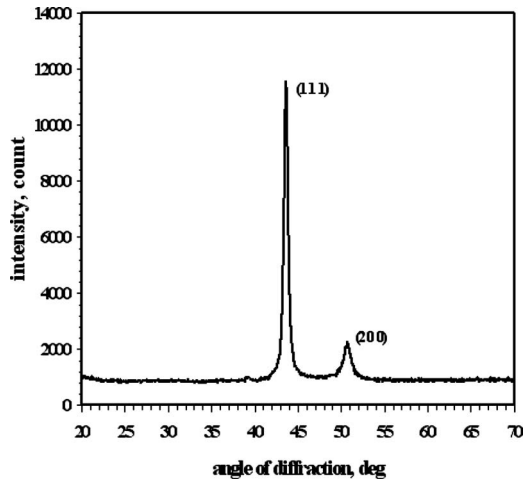


Fig. 1 Variation in intensity with angle of diffraction

Miller indices of [111]. The average size of the particles is determined by the following Scherrer formula [10] and is 10 nm:

$$t = \frac{0.9\lambda}{B \cos \theta} \quad (1)$$

Figure 1 depicts the X-ray diffraction (XRD) spectra of copper nanoparticles taking intensity, i.e., count of nanoparticles of abscissa and 2θ as ordinate. The atomic structure of majority of particles lies on the Miller indices of [1,1,1] and small amount of particles on the Miller indices of [2 0 0]. It is also found that the copper nanoparticles remained in pure copper state after generation.

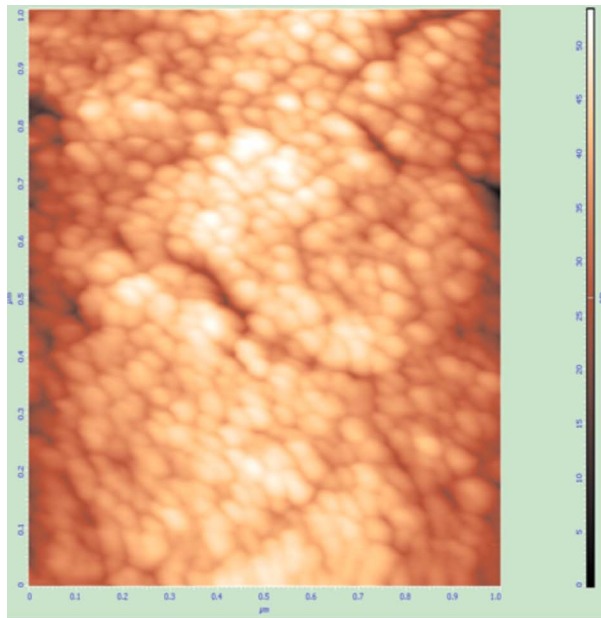
2.2 Atomic Force Microscopy Examination. Atomic force microscope in semicontact mode has been used to characterize the nanoparticles. Figure 2(a) shows that eight to ten nanoparticles measuring 100 nm are agglomerated and distributed over the glass substrate mounted inside the chamber during sputtering at 100 K. The [1,1,1] orientation of copper nanoparticles shows that they are

pure copper particles with a face-centered cubic (fcc) having an average size of 10–20 nm. No significant change in the particle size has been found by XRD at 100 K. However, the overall particle size shown by atomic force microscopy (AFM) is much higher as compared with that calculated from XRD because of the fact that the XRD gives the average mean domain size while AFM shows agglomeration of the particles. The XRD and AFM data can be reconciled by the fact that smaller primary particles have a larger surface free energy and would, therefore, tend to agglomerate faster and grow into larger grains. Figure 2(b) shows the variation in particle size when calculated from the AFM picture and plotted against the percentage volume. It shows that majority of particles come under the range of 20–40 nm due to agglomeration of particles.

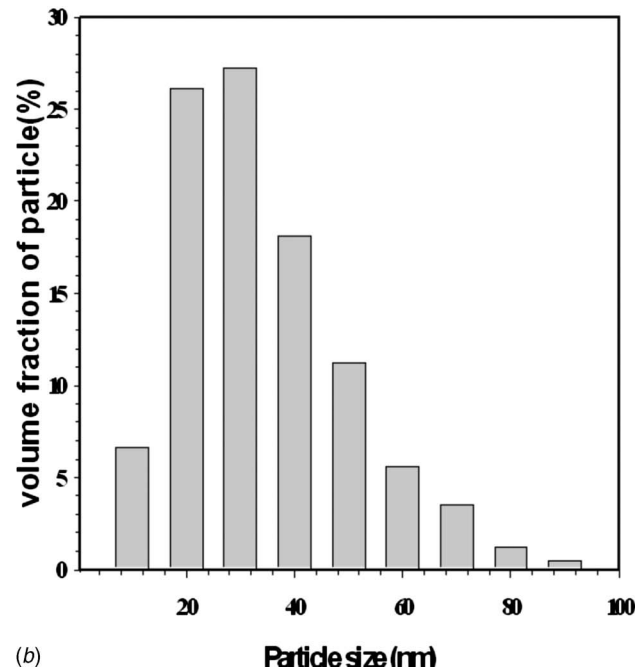
2.3 Transmission Electron Microscopy Examination. The reason for using copper nanofluid (water base) for boiling heat transfer studies is that it has superior heat transfer characteristics, stability, and uniformity. Nanofluids are found to be inert chemically with the base fluid, i.e., water. In order to ensure a stable and uniform suspension of nanoparticles in base fluid, the dispersed solution is subjected to vibration in an ultrasonic bath for 10 h, during which it is observed that there is an increase in the solution temperature, nearly 40°C above room temperature. Three different mass concentrations of copper nanofluids are prepared for the experiments by controlling the amounts of the particles in two different base fluids, i.e., water and water with 9.0% SDS anionic surfactant.

A high resolution transmission electron microscopy (TEM) is used to analyze the size and morphology of the nanoparticles. Figures 3(a) and 3(b) show the copper nanoparticles dispersed in the base fluid of water and its polycrystalline diffraction pattern, respectively. It has been approximated that the average size of these particles is 10 nm and is dispersed in water evenly even after 10 h of ultrasonic vibration. However, some of the particles agglomerate and form cluster due to the intermolecular attractive force, the average size of which is not more than 20 nm.

2.4 Physical Properties of Nanofluid. The physical properties of copper nanofluid can be determined using analytical methods [1,2,4], which depend on the size and shape of the nanopar-



(a)



(b)

Fig. 2 (a) AFM picture of copper nanoparticles and (b) variation in particle size with percentage volume

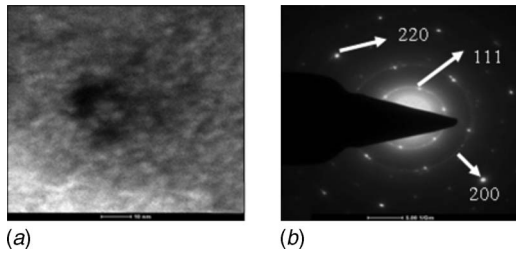


Fig. 3 TEM photographs of water-copper nanofluid: (a) dispersion of copper particles in water and (b) diffraction pattern

ticle and the involvement of surface molecules in heat transfer process. The shape and size of the particles are affected by the agglomeration. The flow phenomenon of a liquid-solid solution depends on the hydrodynamic force acting on the surface of solid particles. The following conversion formula has been used to compute the exact volume of nanoparticles:

$$\Phi_v = \frac{1}{\left(\frac{1 - \Phi_m}{\Phi_m}\right) \frac{\rho_p}{\rho_f} + 1} \quad (2)$$

From Eq. (2) the density of the nanofluid is derived, and the relation for heat capacity is [4]

$$\rho = \rho_f(1 - \Phi_v) + \rho_p\Phi_v \quad (3)$$

$$\rho C_p = \rho_f C_{pf}(1 - \Phi_v) + \rho_p C_{pp}\Phi_v \quad (4)$$

Applying the Hamilton and Crosser [11] model to copper nanoparticles in water, the effective thermal conductivity of the copper-water nanofluid is estimated by the following equation [1]:

$$\frac{k}{k_f} \approx 1 + n\Phi_v \quad (5)$$

where $n=3/\psi$, and ψ is the sphericity of the particle, defined as the ratio of the surface area of a sphere with a volume equal to that of the particle to the surface area of the particle. And n is the empirical shape factor. For spherical shape the sphericity value found by them was 0.3 and for the other shapes the n value is varied from 0.5 to 6.0.

Equation (5) is applicable only when there is significant increase in thermal conductivity with temperature. The effect of particle volume fraction and sphericity on the thermal conductivity ratio for a copper-water system is shown in Fig. 4. The sphericity of copper nanoparticles is 0.3; the thermal conductivity of water is enhanced by a factor of 1.003 at the low nanoparticle

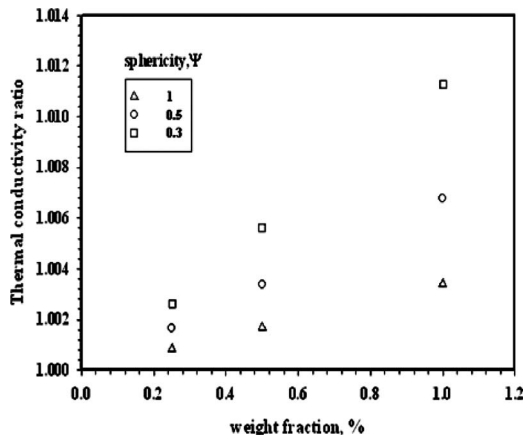


Fig. 4 Variation in thermal conductivity ratio with concentration of nanoparticles

Table 1 Major properties of nanofluids

Copper nanofluid	1	2	3
Φ_m (%)	0.2500	0.5000	1.0000
Φ_v (%)	0.0280	0.0560	0.1130
ρ/ρ_{fo}	1.0020	1.0040	1.0090
C_p/C_{po}	0.9980	0.9960	0.9830
k/k_o	1.0026	1.0056	1.0113
μ/μ_o	1.0007	1.0014	1.0028

weight fraction of 0.25%. This finding demonstrates that the copper nanoparticles are capable of increasing the thermal conductivity of water.

The following equation can be used for the prediction of viscosity of the nanofluid, as suggested by Brinkman [12]:

$$\mu = \mu_f(1 + 1.25\Phi_v) \quad (6)$$

Using the above equations, the thermophysical properties of copper nanofluids for various concentrations of copper nanoparticles in water have been determined and are shown in Table 1.

3 Experimental Setup and Procedure for Boiling Heat Transfer Studies

The schematic of pool boiling experimental setup is shown in Fig. 5, consisting of test-vessel (7) fabricated with a stainless steel sheet of 3 mm thickness. The vessel has a rectangular cross section of $100 \times 126 \text{ mm}^2$ and the height of 180 mm. In order to view the boiling of nanofluid inside the vessel, one of the longer sides of the vessel is fitted with a plain glass having 130 mm height, 70 mm width, and 5 mm thickness. The adjacent side of which is fitted with a sight glass (11) of 60 mm diameter for providing light into the test-vessel. The opposite side to the light is covered with a Teflon plate (2) to hold the test-section tube, i.e., test heater (10). The pressure gauge (4), drainage nut (13), and pipe lines for condenser (6) are mounted on the top of the vessel. The test-section tube (commercially available) is 115 mm long seamless stainless steel tube having inner diameter of 9.0 mm and wall thickness of 0.8 mm. One end of the tubes is plugged by a

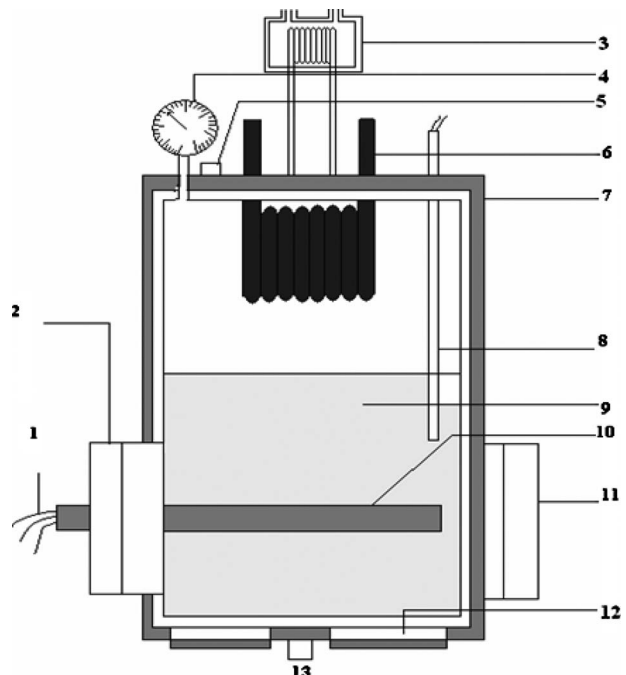


Fig. 5 Pool boiling experimental setup

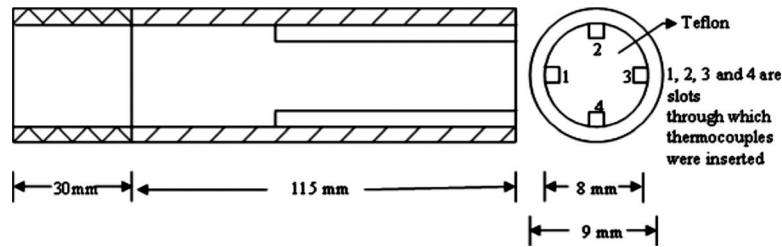


Fig. 6 Schematic of the heater tube

thin copper circular disk of diameter 9.0 mm. A preheater (12) is used in the bottom side of the vessel for initial heating of nanofluid. The schematic of the test-section tube is shown in Fig. 6.

The inner surface temperature of the test-section tube is measured using four ‘T’ type thermocouples placed at the top, bottom, and on either sides of the heater tube at the middle of the length. A water cooled condenser (6) having helical copper tube of 6.0 mm diameter is installed on the top portion of the vessel to condense and drain back the vapor generated during experimentation. The heating power is supplied to the test-section tube through a 10 kV A capacity step down transformer connected with dimmer stat for varying voltages.

The outer wall surface temperature of the heater tube at different locations T_w is determined by the following conduction equation:

$$T_w = \bar{T}_{in} - \left(\frac{q \ln\left(\frac{r_o}{r_i}\right)}{2\pi kL} \right) \quad (7)$$

where \bar{T}_{in} is the average of inner surface temperatures measured by the thermocouples placed at different locations, which is given by the following equation:

$$\bar{T}_{in} = \frac{T_t + T_{s1} + T_{s2} + T_b}{4} \quad (8)$$

where t , b , $s1$, and $s2$ are the locations of thermocouples at the top, bottom, and side positions, respectively. After determining the average outer surface temperature of the test-section tube, the average boiling heat transfer coefficient is evaluated using the following equation:

$$h = \frac{q}{T_w - T_s} \quad (9)$$

To begin the experiment, first, the cooling water supply to the condenser is switched on. The test-section is thermally stabilized by submerging the test-section in a pool of distilled water and heating the test-section for 12 h at a heat flux of 500 kW/m². Then the power to the heater is switched off, and the test-section is cooled down for another 12 h. In order to conduct the experiment, first, the preheater is switched on so that the temperature of the test fluid increases and is maintained at saturation temperature at the lowest heat flux of 50 kW/m². Initially, steam is allowed to pass through the vent to remove any dissolved gases in the test fluid and in the test-vessel. The vent is then closed and the test-liquid is boiled with tube heater at the heat flux of 50 kW/m² until the steady state is reached. The heat flux is then increased up to critical heat flux in steps of 50 kW/m². The data are acquired during steady state in each step. Thus, experiments are performed first for the boiling of water by varying heater heat flux from 50 kW/m² to just before the burn-out level in steps of 50 kW/m². The entire test is performed under atmospheric pressure. After the experiment, the pure water is replaced by the mixture of water and surfactant, and data are again acquired for the heat flux starting from 50 kW/m² to the CHF level. Similarly, data are acquired for the pool boiling of nanofluids with water

containing 0.25%, 0.5%, and 1.0% of copper nanoparticles by weight. The data are also acquired for the nanofluids containing 1.0% of copper by weight in the water and 9.0% surfactant mixture. The CHF for a test-section is the heat flux at which there is a rapid increase in surface temperature of the test-section. Hence all the data are acquired until this value to avoid the physical burn-out of the heater. After conducting experiment on each test fluid, the vessel and heater surfaces are cleaned with a water jet to ensure complete removal of nanoparticles from the system.

Although all precautions are taken to minimize the errors in experimentation, yet some errors are likely to creep. The error in measurement depends on the accuracy of the measuring instruments. Uncertainty analysis is carried out in the method of Kline and McClintock [13], which yields 0.24% for area, 0.43% for the heat energy supplied to the test surface, 0.49% for heat flux, 0.83% for outer wall temperature, 0.21% for inner wall temperature, and 4.62% for average heat transfer coefficient.

4 Results and Discussion

The data obtained from the boiling of distilled water over a plain horizontal tube have been analyzed in order to check the integrity of the experimental setup. These data shall also be used as reference data to assess the pool boiling characteristics of nanofluids. The results for the pool boiling of water have been compared with those predicted by Cornwell–Houston [14] correlation since it had good agreement with this model, given by the following equations:

$$Nu = 9.7P_c^{0.5}F_p Re^{0.67} Pr^{0.4} \quad (10)$$

$$F_p = 1.8P_r^{0.17} + 4P_r^{1.2} + 10P_r^{10} \quad (11)$$

where the pressure ratio $P_r = P/P_c$. Figure 7 shows the relation between experimental heat transfer coefficient and the predicted value. The agreement between them establishes the integrity of experimental setup. The data are acquired at different time intervals. Almost all the experimental data have remained in an error band of $\pm 15\%$.

The properties and behavior of nanofluids depend on a number of parameters including the properties of the base liquid and the dispersed phases, particle concentration, particle size, as well as the presence of dispersants or surfactants [15]. The boiling heat transfer of nanofluid is expected to be higher than that of water due to the fact that the thermal conductivity of the nanofluid is more than that of water. Figure 8 shows that for a given wall superheat of test-section the boiling heat transfer of nanofluids is lower than that for pure water as revealed by the right shift of boiling curve of pure water as the concentration on nanoparticles increases in the base fluid, i.e., water. This shows that the boiling heat transfer decreases with an increase in nanoparticle concentration. A possible reason for this shift may be the filling up of tube surface cavities by nanoparticles, thus reducing the number of nucleation sites on the test-section tube surface.

Although at a given wall superheat the heat flux for nanofluid is lower, the CHF is found to be higher. The CHF of nanofluids for different concentrations of copper is given in Table 2.

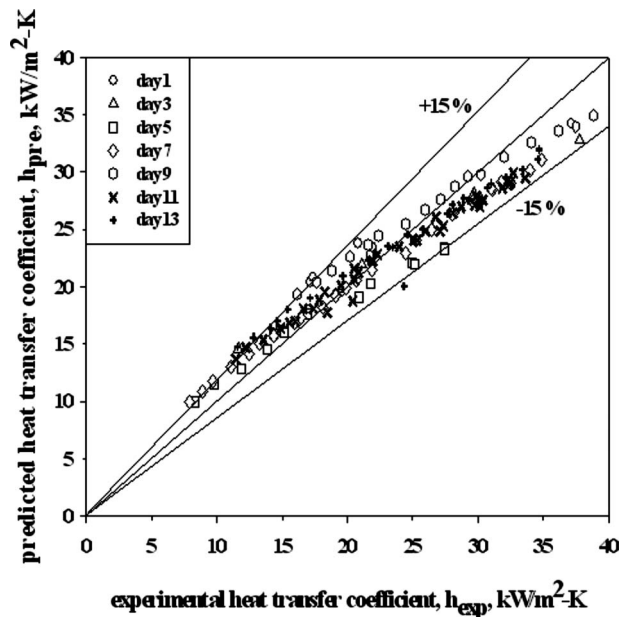


Fig. 7 Graph between experimental heat transfer coefficients with predicted heat transfer coefficient

Figure 9 shows that the influence of nanoparticles on boiling heat transfer coefficient is negligible for lower heat flux. But at higher heat flux the heat transfer coefficient reduces with an increase in the concentration of nanoparticles. This is due to the fact that at low heat flux only large cavities are activated. At higher

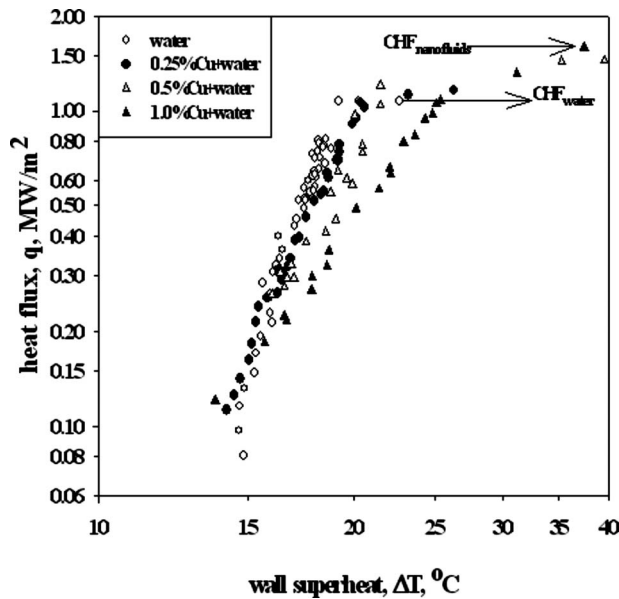


Fig. 8 Variation in heat flux with wall superheat

Table 2 CHF values for water and copper nanofluids

S. No	Test fluid	CHF (MW/m ²)	% increased
1	Water	1.070	-
2	0.25 wt % Cu-water nanofluid	1.160	8
3	0.5 wt % Cu-water nanofluid	1.450	36
4	1 wt % Cu-water nanofluid	1.592	49
5	Water with surfactant	0.224	-
6	1 wt % Cu-water-surfactant nanofluid	0.358	59

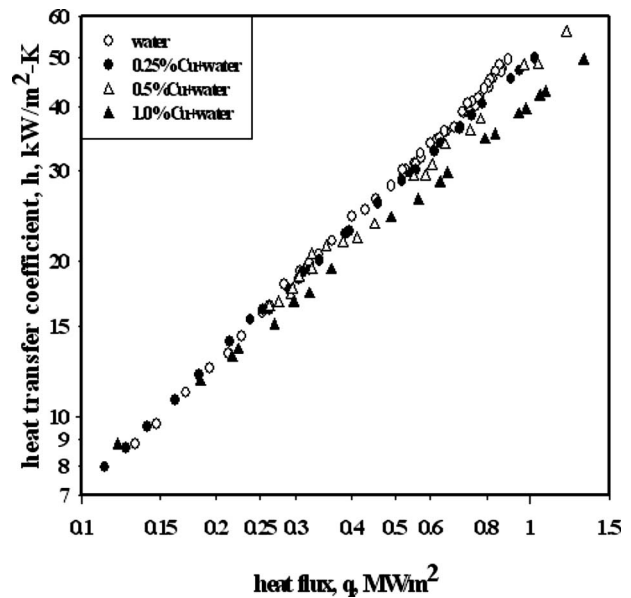


Fig. 9 Variation in heat flux with heat transfer coefficient

heat fluxes the smaller cavities are also activated for the boiling of pure water, but for nanofluid, these cavities are filled with nanoparticles, thus reducing the heat transfer coefficient.

In fact, the boiling phenomenon occurs in the three distinct regimes, viz., nucleate pool boiling, discrete bubble regime, and coalesced bubble regime. With the onset of nucleate boiling and at heat flux higher than 400 kW/m², more nucleation sites are activated on the heater surface. Similar phenomenon is observed by Bang and Chang [7] using Al₂O₃ nanofluid with water. However, they achieved the onset of nucleate boiling at the heat flux of 100 kW/m². This may be due to the varied heat transfer characteristics of nanofluid and surface roughness of the heating surface.

The boiling curves obtained are in a similar trend with Liu et al. [16]. They determined CHF of water-CuO nanofluids under different pressures with an increase in concentration from 0.1% to 2.0% and observed that the increase in CHF was due to the coating of nanoparticles over the heating surface. In the present work also a thin, smooth block coating layer is found over the heating surface after experimentation. This phenomenon changes the surface roughness of the test-section. The change in surface roughness before and after pool boiling experiments is found by using optical surface profilometer; the microphotographs are given in the Appendix.

The critical heat flux enhancement of nanofluids is nearly 73% for stainless steel wire with Al₂O₃, ZrO₂, and SiO₂ nanofluids [8]. The estimated surface roughness factor is 5.6 for alumina nanofluids [8], which is greater than unity. In the present investigation, the CHF enhancement is nearly 50%, and the surface roughness factor is 3.9 for 1.0% by weight copper nanofluids. The enhancement in CHF is due to the increase in effective contact area by deposition of nanoparticles over the heating surface. The nanoparticles generate a nanoporous layer on the test-section tube surface, thus reducing the contact angle between the fluid and heater surface [9]. Further, the existence of sorption layer enhances the trapping of liquid in the nanoporous sorption layer and prevents the vapor blanket formation. Therefore, the CHF increases with increasing sorption layer thickness at the low particle concentration range. When the particle concentration exceeds a certain value, the sorption layer thickness would not increase and therefore the CHF does not increase. Figure 10 shows the enhancement of critical heat flux with concentration of the nanoparticles in the water. Adaptation of the heater surface by the nanoparticle surface coating is dependent on the particle concentration of the nanofluids. In the case of nanofluids with the low particle concentration of

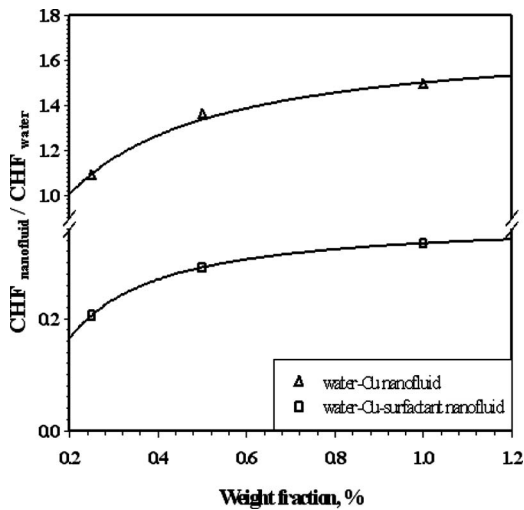


Fig. 10 Increase in critical heat flux with concentration of nanoparticles

0.25 wt %, the heating surface displays only a nominal change. However, as the concentration is increased, surface deposition of the nanoparticles is thickened and more microsized structures are formed on the heating surface. A similar phenomenon was also reported by Kim et al. [8] in their experiments of water-TiO₂ nanofluids under atmospheric pressure.

Properties of nanofluids, as given in Table 1, show that the thermal conductivity of water can be enhanced by a factor of 1.003 with a low nanoparticle concentration of 0.25% by weight. The most obvious reason behind the increase in thermal conductivity is the increased surface area due to particle size reduction. However, other factors are Brownian motion, interfacial liquid layering, ballistic transportation of energy carriers within nanoparticles, and formation of nanoparticle structure through fractal, clustering, and networking. It is observed that the heated surface, after the boiling tests, is smooth with metallic brilliancy and slightly oxidized. It is also observed that there exists a thin sorption or porous layer on the surface formed by nanoparticles. This was confirmed by the surface roughness test discussed in the Appendix. The sorption layer on the copper surface would decrease active nucleation sites and the contact angle [17]. Less active nucleation and the contact angle would delay the inception of boiling and generation of fewer bubbles at a given heat flux. In addition, the sorption layer increases the heat resistance between the metal surface and nanofluid.

Xuan and Li [4] found that the addition of SDS anionic surfactant (9.0% by weight), in water-nanoparticles, prevents the agglomeration and provides stable nanofluids for a longer time. In the present investigation also, no settlement has been found for the nanofluids with 9.0% surfactant even 36 h after the process of ultrasonic vibration. In fact, the surfactant behaves like an interfacial shell between the nanoparticles and base fluids. With the addition of surfactant to water the nucleate boiling curve shifts to the left, indicating enhancement in heat transfer. Surfactant modifies the surface tension and wettability of fluids, influencing boiling heat transfer in a significant manner [18–20]. In comparison to that of pure water, the boiling performance is enhanced significantly by the addition of surfactant, with an early onset of nucleate boiling. In fact, the enhancement in heat transfer is due to an early incipience, followed by a rapid departure of smaller-sized, regularly shaped bubbles from the heater surface in addition to an increase in the number of active nucleation sites. This is due to the fact that surfactant decreases the dynamic surface tension and increases the wettability of the surface [21]. The similar phenomenon has also been observed by Wasekar and Manglik [18]. The heat transfer coefficient of pure water has been found to be in-

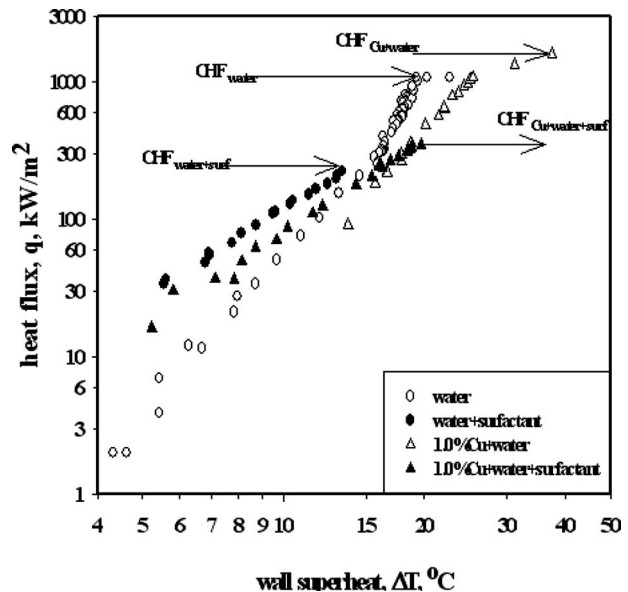


Fig. 11 Comparison of nanofluids with pure water and water with surfactant

creased up to 38% for a given heat flux because of the influence of surfactant. It is observed that irrespective of the presence of surfactants the heat transfer coefficient decreases in the copper-water nanofluid with an increase in the concentration of nanoparticles.

Figure 11 shows the variation in heat flux with wall superheat for pure water, water with surfactant, and nanofluid, which shows that the critical heat flux increases with an increase in the nanoparticle concentrations in water and water-surfactant as base fluid, but the values of CHF obtained in the case of water-surfactant nanofluids are nearly one-third of the nanofluids with water as base fluid. This is due to the unsteady porous agglutination formation over the heater surface due to surfactants, similar to Liu and Liao's [22] observations. The CHF obtained in the surfactant nanofluids is given in Table 2, and the maximum CHF percentage increase is 59% for the nanofluid of 1.0% by weight concentration of copper in comparison with water-surfactant nanofluid. Figure 12 shows that the heat transfer coefficient decreases with an increase in concentration of nanoparticles in water-surfactant nano-

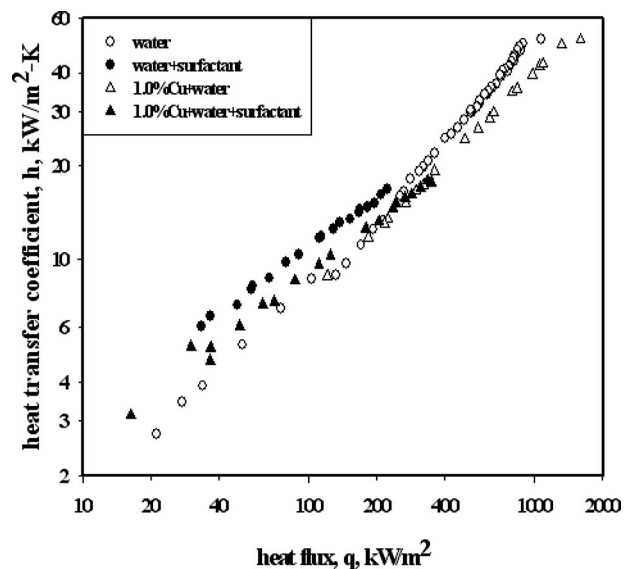


Fig. 12 Comparison between heat flux and heat transfer coefficient of nanofluids with pure water and water with surfactant

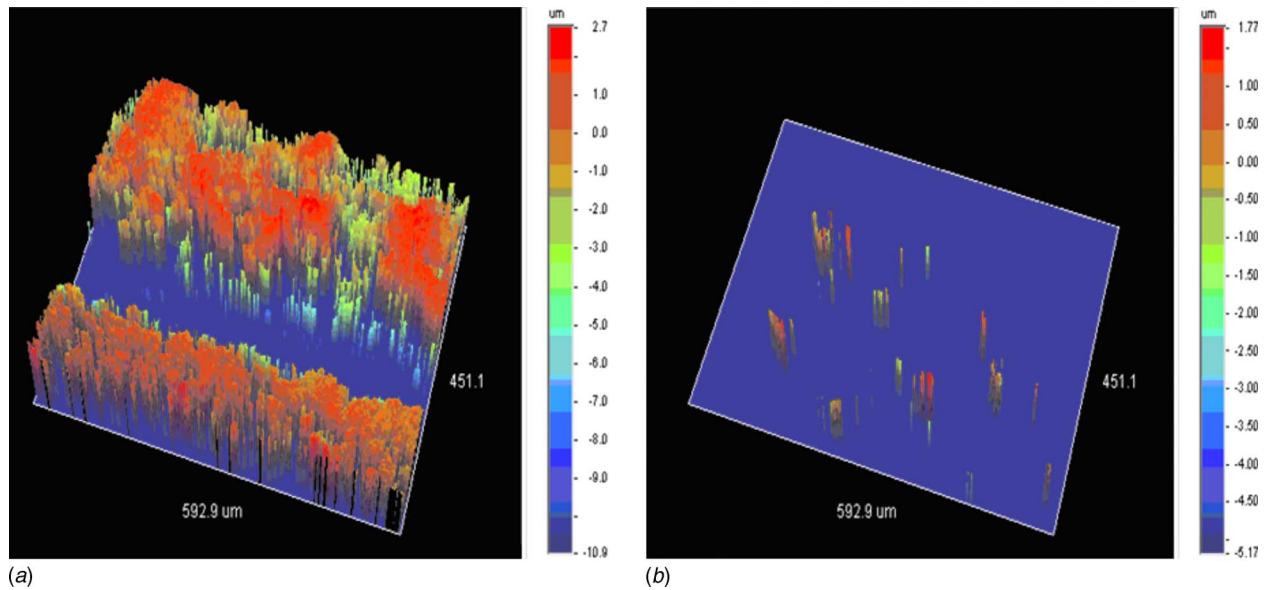


Fig. 13 Surface roughness of the heater: (a) before boiling and (b) after boiling

fluids, but when compared with water the heat transfer coefficient is always higher for a given heat flux. Therefore, the increase in heat transfer coefficient in the surfactant nanofluids is only due to the presence of surfactant, not due to the addition of nanoparticles.

Figure 10 shows the decrease in CHF with an increase in concentration of nanoparticles in copper-water nanofluid with 9.0% surfactant. However, with the increase in the concentration of nanoparticles the CHF increases and attains the highest value at 1.0% concentration of copper nanoparticles, which is only 34% of that of pure water. This is due to the early departure of bubbles growing in the water-surfactant nanofluids, which increases the wettability of the surface and decreases the dynamic surface tension [20].

5 Conclusions

The CHF of nanofluids for boiling over a horizontal test-section tube increases as the concentration of copper nanoparticles in the base fluid increases. The highest enhancement when compared with pure water is found to be 50% corresponding to a weight concentration of 1.0%. In the case of nanofluids containing surfactant, it has been found that the CHF enhancement is 60% corresponding to a weight concentration of 1.0% of water and 9.0% of surfactant.

Copper nanoparticles cause a decrease in pool boiling heat transfer coefficient with water as base fluid. The heat transfer coefficient decreases as the concentration of nanoparticle increases. However, for the water with 9.0% surfactant, the heat transfer coefficient increases by 30% for a given heat flux. This is purely due to the reduction in surface tension of water by surfactant.

Surface characteristics of the heater surface obtained after pool boiling CHF tests revealed that CHF enhancement of nanofluids is closely related to the surface microstructure and enhanced topography resulting from the deposition of nanoparticles on the tube surface. After boiling experiments with 1.0 wt % concentration, nanofluids show an increase in the surface roughness factor of 3.87.

Nomenclature

- A = heated surface area = πDL , m^2
 B = full width at half maximum (FWHM) intensity, rad
 C = surface-liquid combination factor

- D = diameter, m
 I = electric current, A
 L = length, m
 P = pressure, bar
 Pr = Prandtl number
 R_a = roughness parameter, μm
 Re_b = boiling Reynolds number, ($=qD/\mu_f h_{fg}$)
 R_q = roughness parameter, μm
 V = voltage, V
 h = heat transfer coefficient, $kW/m^2 K$
 k = thermal conductivity, $kW/m K$
 q = heat flux, kW/m^2
 r_i = inner radius of the heater tube, m
 r_o = outer radius of the heater tube, m
 t = size of the nanoparticle, nm

Greek Symbols

- Φ = fraction, %
 ρ = density, kg/m^3
 σ = surface tension, Pa m
 μ = dynamic viscosity, Pa s
 θ = maximum angle of reflection at which maximum intensity, in deg
 λ = wavelength of the X-ray target (for copper it is 1.54 Å)

Subscripts

- b = boiling
 c = critical
 f = fluid
 g = vapor
 m = mass
 p = particle
 v = volume
 w = wall

Appendix

The literature review reveals that increased surface roughness gives better heat transfer at a given wall superheat [22–24]. Webb and Pais [25] also showed the enhancement of boiling heat transfer coefficient of refrigerants by increasing the surface roughness of heaters. The surface characteristic of the stainless steel tube heater was studied using an optical profilometer. Figure 13 shows

Table 3 Roughness of heater before and after boiling for different places

No.	Before experiment (μm)		After experiment (nm)	
	R_a	R_q	R_a	R_q
1	0.877	1.35	513.5	659.54
2	1.31	1.79	660.57	990.87
3	1.22	1.58	774.38	1220
4	0.975	1.38	338.2	518.99

a 3D interactive display picture of surface roughness of the heater with a magnification of 10.43 in vertical scanning interferometry (VSI) measurement mode. The average surface roughness of the seamless stainless steel tube heater was found to be $1.09 \mu\text{m}$ before conducting the boiling experiment and 571.66 nm after boiling experiments. The average and root mean square values of surface roughness of the heater before and after the boiling experiments for various positions of the heater are given in Table 3.

References

- [1] Lee, S., Choi, U. S., Li, S., and Eastman, J. A., 1999, "Measuring Thermal Conductivity of Fluids Containing Oxide Nano Particles," *ASME J. Heat Transfer*, **121**, pp. 280–289.
- [2] Choi, S., 1998, "Nano Fluid Technology: Current Status and Future Research," The Second Korean-American Scientists and Engineers Association Research Trend Study, Vienna.
- [3] Eastman, J. A., Choi, U. S., Li, S., Yu, W., and Thompson, L. J., 2001, "Anomalously Increased Effective Thermal Conductivities of Ethylene Glycol-Based Nano Fluids Containing Copper Nano Particles," *Appl. Phys. Lett.*, **78**(6), pp. 718–720.
- [4] Xuan, Y., and Li, Q., 2000, "Heat Transfer Enhancement of Nano Fluids," *Int. J. Heat Fluid Flow*, **21**, pp. 58–64.
- [5] Das, S. K., Putra, N., Thiesen, P., and Roetzel, W., 2003, "Temperature Dependence of Thermal Conductivity Enhancement for Nanofluids," *ASME J. Heat Transfer*, **125**, pp. 567–574.
- [6] Vassallo, P., Kumar, R., and D'Amico, S., 2004, "Pool Boiling Heat Transfer Experiments in Silica-Water Nano Fluids," *Int. J. Heat Mass Transfer*, **47**, pp. 407–411.
- [7] Bang, I. C., and Chang, S. H., 2005, "Boiling Heat Transfer Performance and Phenomena of Al_2O_3 -Water Nanofluids From a Plain Surface in a Pool," *Int. J. Heat Mass Transfer*, **48**, pp. 2407–2419.
- [8] Kim, H., Kim, J., and Kim, M., 2006, "Experimental Study on CHF Characteristics of Water-TiO₂ Nano Fluids," *Nuclear Engineering and Technology: An International Journal of the Korean Nuclear Society*, **38**(1), pp. 61–68.
- [9] Kim, S. J., Bang, I. C., Buongiorno, J., and Hu, L. W., 2007, "Surface Wettability Change During Pool Boiling of Nanofluids and Its Effect on Critical Heat Flux," *Int. J. Heat Mass Transfer*, **50**, pp. 4105–4116.
- [10] Cullity, B. D., and Stock, S. R., 2001, *Elements of X-Ray Diffraction*, 3rd ed., Prentice-Hall, Englewood Cliffs, NJ, Chap. 5, p. 170.
- [11] Hamilton, R. L., and Crosser, O. K., 1962, "Thermal Conductivity of Heterogeneous Two-Component Systems," *I & EC Fundamentals*, Vol. 1, ACS Publications, pp. 187–191.
- [12] Brinkman, H. C., 1952, "The Viscosity of Concentrated Suspensions and Solutions," *J. Chem. Phys.*, **20**, pp. 571–581.
- [13] Kline, S. J., and Mc. Clintock, F. A., 1953, "Describing Uncertainties in Single-Sample Experiments," *Mech. Eng. (Am. Soc. Mech. Eng.)*, **75**, pp. 3–8.
- [14] Cornwell, K., and Houston, S. D., 1994, "Nucleate Pool Boiling on Horizontal Tubes: A Convection-Based Correlation," *Int. J. Heat Mass Transfer*, **37**, pp. 303–309.
- [15] Das, S. K., Putra, N., and Roetzel, W., 2003, "Pool Boiling Characteristics of Nano Fluids," *Int. J. Heat Mass Transfer*, **46**, pp. 851–862.
- [16] Liu, Z. H., Xiong, J. G., and Bao, R., 2007, "Boiling Heat Transfer Characteristics of Nanofluids in a Flat Heat Pipe Evaporator With Micro-Grooved Heating Surface," *Int. J. Multiphase Flow*, **33**, pp. 1284–1295.
- [17] Liu, Z. H., and Qiu, Y. H., 2007, "Boiling Heat Transfer Characteristics of Nano Fluids Jet Impingement on a Plate Surface," *Heat Mass Transfer*, **43**, pp. 699–706.
- [18] Wasekar, V. M., and Manglik, R. M., 2000, "Pool Boiling Heat Transfer in Aqueous Solutions of an Anionic Surfactant," *ASME J. Heat Transfer*, **122**(4), pp. 708–715.
- [19] Hetsroni, G., Gurevich, M., Mosyak, A., Rozenblit, R., and Segal, Z., 2004, "Boiling Enhancement With Environmentally Acceptable Surfactants," *Int. J. Heat Fluid Flow*, **25**, pp. 841–848.
- [20] Wen, D. S., Ding, Y. L., and Williams, R., 2006, "Pool-Boiling Heat Transfer of Aqueous Based TiO₂ Nanofluids," *J. Enhanced Heat Transfer*, **13**, pp. 231–244.
- [21] Wang, C. H., and Dhir, V. K., 1993, "Effect of Surface Wettability on Active Nucleation Site Density During Pool Boiling of Water on a Vertical Surface," *ASME J. Heat Transfer*, **115**, pp. 659–669.
- [22] Liu, Z. H., and Liao, L., 2008, "Sorption and Agglutination Phenomenon of Nanofluids on a Plain Heating Surface During Pool Boiling," *Int. J. Heat Mass Transfer*, **51**, pp. 2593–2602.
- [23] Kang, M. G., 2000, "Effect of Surface Roughness on Pool Boiling Heat Transfer," *Int. J. Heat Mass Transfer*, **43**, pp. 4073–4085.
- [24] Liu, Z. H., and Qiu, Y. H., 2002, "Enhanced Boiling Heat Transfer in Restricted Spaces of a Compact Tube Bundle With Enhanced Tubes," *Appl. Therm. Eng.*, **22**, pp. 1931–1941.
- [25] Webb, R. L., and Pais, C., 1992, "Nucleate Pool Boiling Data for Five Refrigerants on Plain, Integral-Fin and Enhanced Tube Geometries," *Int. J. Heat Mass Transfer*, **35**, pp. 1893–1904.

Magnetohydrodynamic Convective Heat and Mass Transfer Flow Due to a Rotating Disk With Thermal Diffusion Effect

Kh. Abdul Maleque

Associate Professor
Department of Mathematics,
American International University-Bangladesh,
House 53/B, 21 Kemal Ataturk Avenue,
Banani, Dhaka-1213, Bangladesh
e-mail: maleque@aiub.edu
e-mail: khmaleque@yahoo.com

Considering the importance of mass transfer in a magnetohydrodynamic (MHD) convective flow, a numerical solution is obtained for a steady three-dimensional MHD convective mass transfer flow in an incompressible fluid due to a rotating disk with thermal diffusion. The governing partial differential equations of the MHD convective mass transfer flow are reduced to nonlinear ordinary differential equations by introducing suitable similarity transformations. The nonlinear similarity equations are then solved numerically by Nachtsheim–Swigert iteration technique. The results of the numerical solution are then presented graphically in the form of velocity, temperature, and concentration profiles. The corresponding skin-friction coefficients, the Nusselt number, and the Sherwood number are also calculated and displayed in tables showing the effects of various parameters on them. A good comparison between the present numerical predictions and the previously published data (Sparrow, and Gregg, 1959, “Heat Transfer From a Rotating Disk to Fluids of Any Prandtl Number,” ASME J. Heat Transfer, 8, pp. 249–251; Benton, 1966, “On the Flow Due to a Rotating Disc,” J. Fluid Mech., 24, pp. 781–800) has been achieved. [DOI: 10.1115/1.3089555]

Keywords: MHD flow, heat and mass transfer, thermal diffusion, rotating disk

1 Introduction

The flow in the neighborhood of a rotating disk is of great practical importance, particularly in an infinite environment or in a housing, computer disk drives (see Ref. [1]), and film condensation (see Ref. [2]). In some applications, where the rotating object is a candidate for over heating and limitations exist on the allowable rotational speed, further heat removal is feasible by means of jet impingement. This is also a common cooling technique for some transmission gearing, where the mechanism bearings are subject to impingement, creating a complex but powerful flow capable of increasing heat transfer considerably. Interest in this subject has increased considerably over the past 20 years, and major gas-turbine manufacturers in Europe, the United States, and Japan are currently funding a large number of research projects. The solution of the Navier–Stokes equations is furnished by the flow around a flat disk, which rotates about an axis perpendicular to its plane with uniform angular velocity Ω , in a fluid otherwise at rest. The layer near the disk is carried by it through friction and is thrown outwards, owing to the action of centrifugal forces. This is compensated by particles, which flow in an axial direction toward the disk, to be in turn carried and ejected centrifugally. Thus the case is seen to be one of fully three-dimensional flows. The problem of flow over a rotating disk has a long history, with von Kàrmàn [3] originally describing similarity transformations that enable the Navier–Stokes equations for an isothermal impermeable rotating disk to be reduced to a system of coupled ordinary differential equations. Later, Cochran [4] obtained more accurate results by patching two series expansions. It is found that the disk acts like a centrifugal fan, the fluid near the disk being thrown

radially outwards. This, in turn, impules an axial flow toward the disk to maintain continuity. Benton [5] improved Cochran’s solution and extended the hydrodynamics problem to flow starting impulsively from rest. Subsequently comprehensive studies have been carried out on rotating disk flow by many researchers, some of them are Refs. [2,6–14]. Recently Maleque and Sattar [14] considered an implicit finite difference solution for an unsteady convective incompressible magnetohydrodynamic (MHD) flow due to an infinite rotating disk, taking into account heat absorption effect. More recently, the effects of variable properties and Hall current on steady MHD laminar flow of a compressible electrically conducting fluid on a porous rotating disk have been studied by Maleque and Sattar [15,16].

The effects of thermal diffusion on MHD convection of mass transfer flows have been considered by many investigators due to its important role, particularly in isotope separation and in mixtures between gases with very light molecular weight (H_2 and He) and medium molecular weight (N_2 and air) [17]. Considering these aspects, many papers have been published on the effects on thermal diffusion on MHD convective and mass transfer flow. Some of them are Refs. [18–20]. Recently Sattar and Alam [21] obtained an analytical solution on the free convection and mass transfer flow with thermal diffusion. Very recently Maleque and Sattar [22] obtained the numerical solution of MHD free-convective and mass transfer flow over an infinite vertical porous plate with thermal diffusion effects. Considering the importance of thermal diffusion of a MHD convective and mass transfer flow, in the present study a numerical solution is obtained for a steady three-dimensional MHD convective heat and mass transfer flow in an incompressible fluid due to a rotating disk with thermal diffusion. The governing partial differential equations of the MHD convective mass transfer flow are reduced to nonlinear ordinary differential equations by introducing suitable similarity transformations. The nonlinear similarity equations are then solved numerically by Nachtsheim–Swigert [23] iteration technique. The

Contributed by the Heat Transfer Division of ASME for publication in the JOURNAL OF HEAT TRANSFER. Manuscript received April 8, 2008; final manuscript received November 18, 2008; published online June 1, 2009. Review conducted by Frank Cunha.

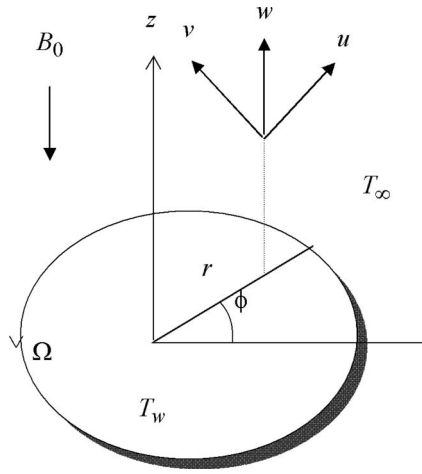


Fig. 1 The flow configuration and the coordinate system

results of the numerical solution are then presented graphically in the form of velocity, temperature and concentration profiles. The corresponding skin-friction coefficients, the Nusselt number and the Sherwood number, are also calculated and displayed in tables showing the effects of various parameters on them.

2 Governing Equations

Steady axially-symmetric incompressible flow of a homogeneous electrically conducting fluid with heat and mass transfer due to an infinite rotating disk has been considered, assuming that the fluid is infinite in extent in the positive z -direction. The disk rotates with constant angular velocity Ω and is placed at $z=0$, where z is the vertical axis in the cylindrical coordinates system, with r and ϕ as the radial and tangential axes, respectively. The components of the flow velocity are (u, v, w) in the directions of increasing r , ϕ , and z , respectively, the pressure is P , and the density of the fluid is ρ . T and C are the fluid temperature and concentration, respectively, and instantaneously the temperature of the surface of the rotating disk and concentration are raised to T_w and C_w , respectively, which are hereafter maintained constant. Far away from the surface, the freestream is kept at a constant temperature T_∞ , at a constant concentration C_∞ , and at a constant pressure P_∞ . The fluid is assumed to be Newtonian, viscous, and electrically conducting. The external uniform magnetic field is applied perpendicular to the surface of the disk and has a constant magnetic flux density B_0 , which is assumed unchanged by taking small magnetic Reynolds number ($Re_m \ll 1$). In addition, no electric field is assumed to exist and the Hall effect is negligible.

The physical model and geometrical coordinates are shown in Fig. 1. Due to axial symmetry, incompressible MHD laminar flow of a homogeneous fluid satisfies the following continuity, Navier-Stokes, energy, and mass equations:

$$\frac{\partial u}{\partial r} + \frac{u}{r} + \frac{\partial w}{\partial z} = 0 \quad (1)$$

$$u \frac{\partial u}{\partial r} - \frac{v^2}{r} + w \frac{\partial u}{\partial z} + \frac{\sigma B_0^2}{\rho} u + \frac{1}{\rho} \frac{\partial p}{\partial r} = \nu \left(\frac{\partial^2 u}{\partial r^2} + \frac{1}{r} \frac{\partial u}{\partial r} - \frac{u}{r^2} + \frac{\partial^2 u}{\partial z^2} \right) \quad (2)$$

$$u \frac{\partial v}{\partial r} + \frac{uv}{r} + w \frac{\partial v}{\partial z} + \frac{\sigma B_0^2}{\rho} v = \nu \left(\frac{\partial^2 v}{\partial r^2} + \frac{1}{r} \frac{\partial v}{\partial r} - \frac{v}{r^2} + \frac{\partial^2 v}{\partial z^2} \right) \quad (3)$$

$$u \frac{\partial w}{\partial r} + w \frac{\partial w}{\partial z} + \frac{1}{\rho} \frac{\partial p}{\partial z} = \nu \left(\frac{\partial^2 w}{\partial r^2} + \frac{1}{r} \frac{\partial w}{\partial r} + \frac{\partial^2 w}{\partial z^2} \right) \quad (4)$$

$$\rho c_p \left(u \frac{\partial T}{\partial r} + w \frac{\partial T}{\partial z} \right) = \kappa \left(\frac{\partial^2 T}{\partial r^2} + \frac{1}{r} \frac{\partial T}{\partial r} + \frac{\partial^2 T}{\partial z^2} \right) \quad (5)$$

$$\left(u \frac{\partial C}{\partial r} + w \frac{\partial C}{\partial z} \right) = D_M \left(\frac{\partial^2 C}{\partial r^2} + \frac{1}{r} \frac{\partial C}{\partial r} + \frac{\partial^2 C}{\partial z^2} \right) + \frac{D_M k_T}{T_M} \left(\frac{\partial^2 T}{\partial r^2} + \frac{1}{r} \frac{\partial T}{\partial r} + \frac{\partial^2 T}{\partial z^2} \right) \quad (6)$$

where κ is the thermal conductivity of heat, σ is the electrical conductivity, c_p is the specific heat with constant pressure, D_M is the molecular diffusivity, T_M is the mean fluid temperature, and k_T is the thermal diffusion ratio.

Appropriate boundary conditions for the present problem are given by

$$u = 0, \quad v = \Omega r, \quad w = 0, \quad T = T_w, \quad \text{and} \quad C = C_w \quad \text{at} \quad z = 0 \quad (7)$$

$$u \rightarrow 0, \quad v \rightarrow 0, \quad T \rightarrow T_\infty, \quad C \rightarrow C_\infty, \quad P \rightarrow P_\infty \quad \text{as} \quad z \rightarrow \infty$$

3 Mathematical Formulations

To obtain the nondimensional form of the above equations, we now introduce the following dimensionless variables:

$$R_1 = \frac{r}{L}, \quad Z_1 = \frac{z}{L}, \quad U = \frac{u}{\Omega L}, \quad V = \frac{v}{\Omega L}, \quad W = \frac{w}{\Omega L}$$

$$P = \frac{P - P_\infty}{\rho \Omega^2 L^2}, \quad \nu_1 = \frac{\nu}{\Omega L^2}, \quad \bar{T} = \frac{T - T_\infty}{T_w - T_\infty}, \quad \bar{C} = \frac{C - C_\infty}{C_w - C_\infty}$$

in Eqs. (1)–(5). We thus obtain the following dimensionless equations:

$$\frac{\partial U}{\partial R_1} + \frac{U}{R_1} + \frac{\partial W}{\partial Z_1} = 0 \quad (8)$$

$$U \frac{\partial U}{\partial R_1} - \frac{V^2}{R_1} + W \frac{\partial U}{\partial Z_1} + MU + \frac{\partial P}{\partial R_1} = \nu_1 \left(\frac{\partial^2 U}{\partial R_1^2} + \frac{1}{R_1} \frac{\partial U}{\partial R_1} - \frac{U}{R_1^2} + \frac{\partial^2 U}{\partial Z_1^2} \right) \quad (9)$$

$$U \frac{\partial V}{\partial R_1} + \frac{UV}{R_1} + W \frac{\partial V}{\partial Z_1} + MV = \nu_1 \left(\frac{\partial^2 V}{\partial R_1^2} + \frac{1}{R_1} \frac{\partial V}{\partial R_1} - \frac{V}{R_1^2} + \frac{\partial^2 V}{\partial Z_1^2} \right) \quad (10)$$

$$U \frac{\partial W}{\partial R_1} + W \frac{\partial W}{\partial Z_1} + \frac{\partial P}{\partial Z_1} = \nu_1 \left(\frac{\partial^2 W}{\partial R_1^2} + \frac{1}{R_1} \frac{\partial W}{\partial R_1} + \frac{\partial^2 W}{\partial Z_1^2} \right) \quad (11)$$

$$U \frac{\partial \bar{T}}{\partial R_1} + W \frac{\partial \bar{T}}{\partial Z_1} = \frac{\nu_1}{\text{Pr}} \left(\frac{\partial^2 \bar{T}}{\partial R_1^2} + \frac{1}{R_1} \frac{\partial \bar{T}}{\partial R_1} + \frac{\partial^2 \bar{T}}{\partial Z_1^2} \right) \quad (12)$$

$$U \frac{\partial \bar{C}}{\partial R_1} + W \frac{\partial \bar{C}}{\partial Z_1} = \frac{\nu_1}{\text{Sc}} \left(\frac{\partial^2 \bar{C}}{\partial R_1^2} + \frac{1}{R_1} \frac{\partial \bar{C}}{\partial R_1} + \frac{\partial^2 \bar{C}}{\partial Z_1^2} \right) + \nu_1 \text{So} \left(\frac{\partial^2 \bar{T}}{\partial R_1^2} + \frac{1}{R_1} \frac{\partial \bar{T}}{\partial R_1} + \frac{\partial^2 \bar{T}}{\partial Z_1^2} \right) \quad (13)$$

where length scale L disappears on simplification in dimensionless equations, $M = \sigma B_0^2 / \rho \Omega$ is the magnetic interaction parameter, which represents the ratio of the magnetic force to the fluid inertia force, $\text{Pr} = (\rho \nu c_p) / \kappa$ is the Prandtl number, $\text{Sc} = \nu / D_M$ is the Schmidt number, and $\text{So} = (\Delta T D_M k_T) / (\nu \Delta C T_M)$ is the Soret number, where $\Delta T = T_w - T_\infty$ and $\Delta C = C_w - C_\infty$.

The boundary condition (7) is obtained as

$$U=0, \quad V=R_1, \quad W=0, \quad \bar{T}=1.0, \quad \bar{C}=1 \quad \text{at} \quad Z_1=0 \quad (14)$$

$$U=0, \quad V=0, \quad \bar{T}=0, \quad \bar{C}=0, \quad P=0 \quad \text{as} \quad Z_1 \rightarrow \infty$$

Now, we introduce the following von Kàrmàn transformations to Eqs. (8)–(14):

$$U=R_1F'(\xi), \quad V=R_1G(\xi), \quad W=-2\nu_1^{1/2}F(\xi), \quad \bar{T}=\theta(\xi)$$

$$\bar{C}=\varphi(\xi), \quad Z_1=\xi\nu_1^{1/2}$$

where F' , G , θ , and φ are nondimensional functions of modified dimensionless vertical coordinate ξ . Using these transformations, the set of equations (9), (10), (12), and (13) take the form

$$\frac{d^3F}{d\xi^3} + 2F\frac{d^2F}{d\xi^2} - \left(\frac{dF}{d\xi}\right)^2 + G^2 - MF = 0 \quad (15)$$

$$\frac{d^2G}{d\xi^2} + 2F\frac{dG}{d\xi} - 2G\frac{dF}{d\xi} - MG = 0 \quad (16)$$

$$\frac{1}{Pr}\frac{d^2\theta}{d\xi^2} + 2F\frac{d\theta}{d\xi} = 0 \quad (17)$$

$$\frac{1}{Sc}\frac{d^2\varphi}{d\xi^2} + So\frac{d^2\theta}{d\xi^2} + 2F\frac{d\varphi}{d\xi} = 0 \quad (18)$$

The boundary condition (14) then becomes

$$F=0, \quad F'=0, \quad G=1, \quad \theta=1, \quad \varphi=1 \quad \text{at} \quad \xi=0 \quad (19)$$

$$F'=0, \quad G=0, \quad \theta=0, \quad \varphi=0 \quad \text{as} \quad \xi \rightarrow \infty$$

The solutions of Eqs. (15)–(18) subject to the above boundary conditions are now sought numerically.

4 Method of Solutions

Numerical solutions to the transformed set of coupled nonlinear differential equations (15)–(18) were obtained, utilizing a modification of the program suggested by Nachtsheim and Swigert. Within the context of the initial value method and the Nachtsheim–Swigert [23] iteration technique, the outer boundary conditions may be functionally represented by the first order Taylor's series as

$$F'(\xi_{\max}) = F'(X, Y, Z, t) \\ = F'_0(\xi_{\max}) + \Delta X F'_X + \Delta Y F'_Y + \Delta Z F'_Z + \Delta t F'_t = \delta_1$$

$$G(\xi_{\max}) = G(X, Y, Z, t) \\ = G_0(\xi_{\max}) + \Delta X G_X + \Delta Y G_Y + \Delta Z G_Z + \Delta t G_t = \delta_2$$

$$\theta(\xi_{\max}) = \theta(X, Y, Z, t) = \theta_0(\xi_{\max}) + \Delta X \theta_X + \Delta Y \theta_Y + \Delta Z \theta_Z + \Delta t \theta_t = \delta_3$$

$$\varphi(\xi_{\max}) = \varphi(X, Y, Z, t) \\ = \varphi_0(\xi_{\max}) + \Delta X \varphi_X + \Delta Y \varphi_Y + \Delta Z \varphi_Z + \Delta t \varphi_t = \delta_4$$

with the asymptotic convergence criteria given by

$$F''(\xi_{\max}) = F''(X, Y, Z, t) \\ = F''_0(\xi_{\max}) + \Delta X F''_X + \Delta Y F''_Y + \Delta Z F''_Z + \Delta t F''_t = \delta_5$$

$$G'(\xi_{\max}) = G'(X, Y, Z, t) \\ = G'_0(\xi_{\max}) + \Delta X G'_X + \Delta Y G'_Y + \Delta Z G'_Z + \Delta t G'_t = \delta_6$$

$$\theta'(\xi_{\max}) = \theta'(X, Y, Z, t) \\ = \theta'_0(\xi_{\max}) + \Delta X \theta'_X + \Delta Y \theta'_Y + \Delta Z \theta'_Z + \Delta t \theta'_t = \delta_7$$

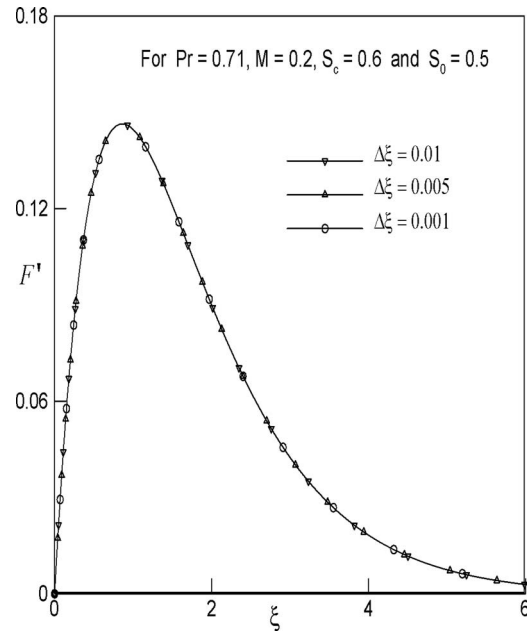


Fig. 2 Radial velocity profiles for different step sizes

$$\varphi'(\xi_{\max}) = \varphi'(X, Y, Z, t)$$

$$= \varphi'_0(\xi_{\max}) + \Delta X \varphi'_X + \Delta Y \varphi'_Y + \Delta Z \varphi'_Z + \Delta t \varphi'_t = \delta_8$$

where $X=F'(0)$, $Y=G'(0)$, $Z=\theta'(0)$, and $t=\varphi'(0)$ and X , Y , Z , and t subscripts indicate partial differentiation, e.g., $F_X = \partial F / (\partial F'(0))$. The subscript 0 indicates the value of the function at η_{\max} to be determined from the trial integration.

Solution of these equations in a least square sense requires determining the minimum value of $E = \delta_1^2 + \delta_2^2 + \delta_3^2 + \delta_4^2 + \delta_5^2 + \delta_6^2 + \delta_7^2 + \delta_8^2$ with respect to X , Y , Z , and t . To solve ΔX , ΔY , ΔZ , and Δt we require one to differentiate E with respect to X , Y , Z , and t , respectively. Thus adopting this numerical technique, a computer program was set up for the solutions of the basic nonlinear differential equations of our problem, where the integration technique was adopted as a six ordered Runge–Kutta method of integration. Various groups of the parameters M , Pr , Sc , and So were considered in different phases. In all the computations the step size $\Delta \xi = 0.01$ was selected, which satisfied a convergence criterion of 10^{-6} in almost all of the different phases mentioned above. Stating $\xi_{\infty} = \xi_{\max} + \Delta \xi$, the value of ξ_{∞} was found in each iteration loop. $(\xi_{\infty})_{\max}$, in each group of the parameters, has been obtained when the value of unknown boundary conditions at $\xi=0$ does not change to a successful loop with an error of less than 10^{-6} . However, different step sizes, such as $\Delta \xi = 0.01$, $\Delta \xi = 0.005$, and $\Delta \xi = 0.001$, were also tried, and the obtained solutions have been found to be independent of the step sizes, as observed in Fig. 2.

5 Solutions

Equations (15)–(18) are solved numerically under boundary condition (19) using the Nachtsheim–Swigert [23] iteration technique discussed shortly above. Thus adopting this numerical technique, a computer program was set up for the solutions of the basic nonlinear differential equations of our problem, where the integration technique was adopted as the six ordered Runge–Kutta method of integration. The results of this integration are then displayed graphically in the form of velocity, temperature, and concentration profiles in Figs. 2–10. In the process of integration, the local skin-friction coefficients and the local rates of heat and mass transfer to the surface, which are of chief physical interest, are also calculated out. From these solutions we may obtain derivatives of the G and F' functions at the disk surface ($\xi=0$), which

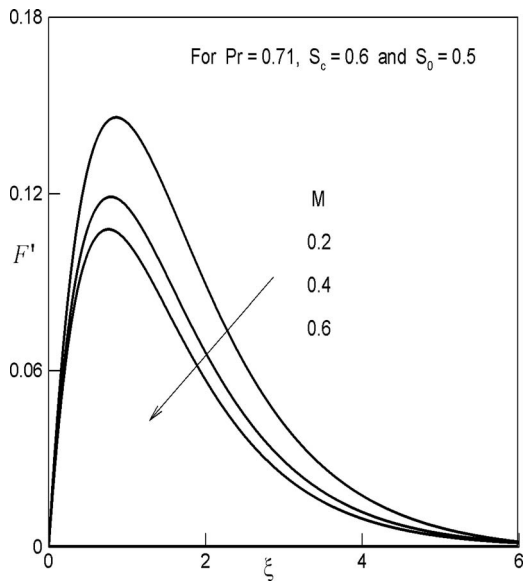


Fig. 3 Effect of M on the radial velocity profiles

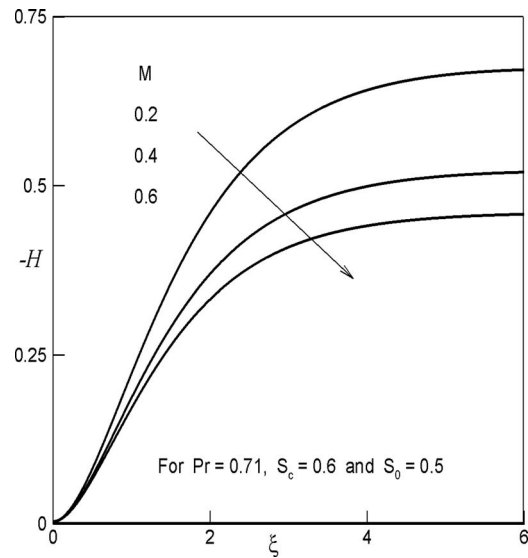


Fig. 5 Effect of M on the axial velocity profiles

are required for the calculation of the tangential shear stress τ_t and the radial shear stress τ_r . To find the tangential shear stress τ_t and the radial shear stress τ_r , we apply the Newtonian formulas

$$\tau_t = \mu \left(\frac{\partial v}{\partial z} + \frac{1}{r} \frac{\partial w}{\partial \phi} \right)_{z=0} \propto G'(0) \quad (20)$$

and

$$\tau_r = \left[\mu \left(\frac{\partial u}{\partial z} + \frac{1}{r} \frac{\partial w}{\partial \phi} \right) \right]_{z=0} \propto F''(0) \quad (21)$$

The heat flux (q_w) and the mass flux (M_w) at the surface are given by

$$q_w = -\kappa \left(\frac{\partial T}{\partial z} \right)_{y=0} = -\frac{\kappa \Delta T}{L} v_1^{1/2} \theta'(0) \quad \text{and}$$

$$M_w = -D_M \left(\frac{\partial C}{\partial z} \right)_{y=0} = -\frac{D_M \Delta C}{L} v_1^{1/2} \varphi'(0)$$

Hence the Nusselt number (Nu) and the Sherwood number (Sh) are obtained as

$$\text{Nu} = \frac{Lq_w}{\kappa \Delta T} = -\sqrt{v_1} \theta'(0) \quad \text{and} \quad \text{Sh} = \frac{LM_w}{D_M \Delta C} = -\sqrt{v_1} \varphi'(0)$$

Thus the heat and mass transfer coefficients are obtained as

$$\text{Nu}(v_1)^{-1/2} = -\theta'(0) \quad (22)$$

and

$$\text{Sh}(v_1)^{-1/2} = -\varphi'(0) \quad (23)$$

These above coefficients are then obtained from the procedure of the numerical computations and are sorted in Table 1. In the above equations, prime denotes derivative with respect to similarity variable ξ .

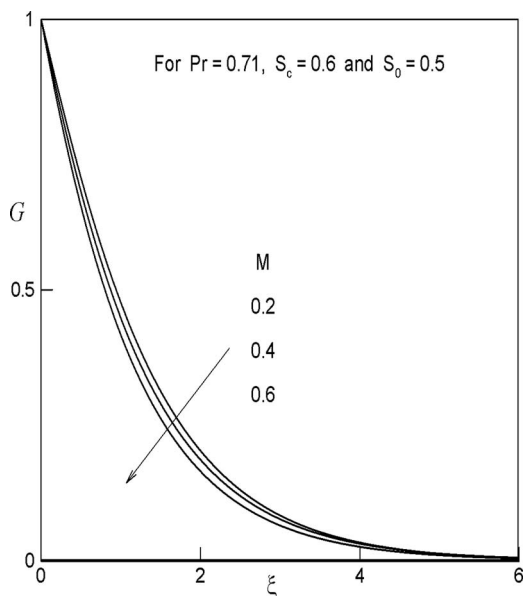


Fig. 4 Effect of M on the tangential velocity profiles

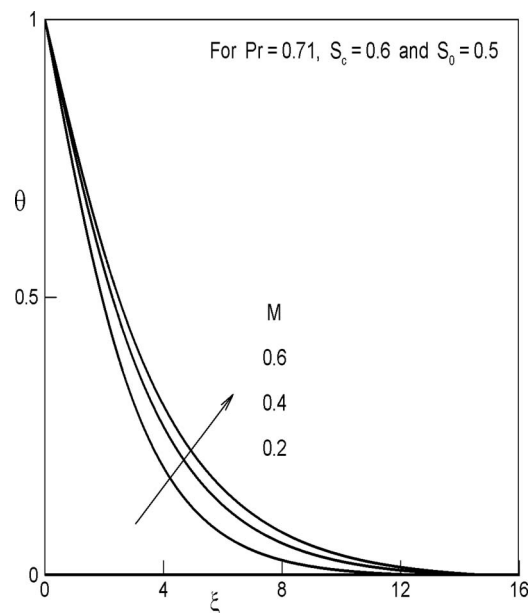


Fig. 6 Effect of M on the temperature profiles

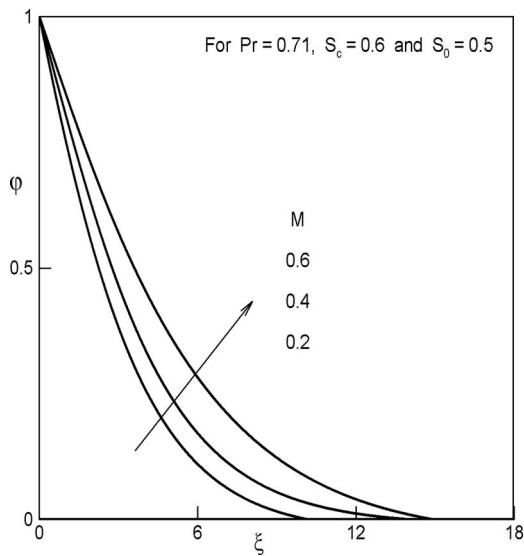


Fig. 7 Effect of M on the concentration profiles

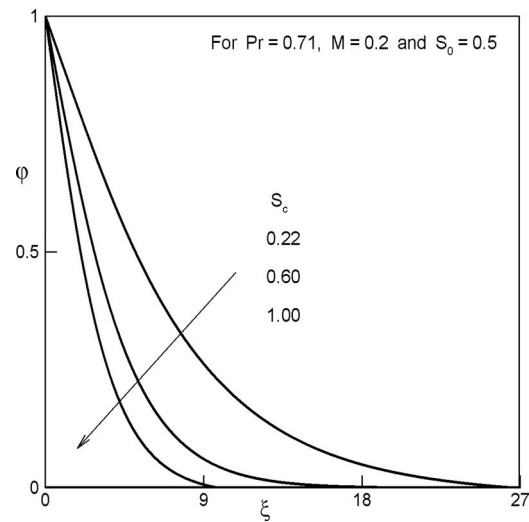


Fig. 9 Effect of Sc on the concentration profiles

6 Results and Discussions

The problem considered here involves a number of parameters, on the basis of which a wide range of numerical results have been derived. Of these results, a small section is presented here for brevity. The numerical results of the velocity profiles for r , ϕ , and z components of velocity, commonly known as radial, tangential, and axial velocities, are shown in Figs. 3–5.

The parameters entering into the fluid flow are magnetic parameter M , Prandtl number Pr , Schmidt number Sc , and Soret number So . It is, therefore, pertinent to inquire the effects of variation in each when the others are kept constant. The numerical results are thus presented for different values of M , Pr , Sc , and So . For Prandtl number Pr , three values, 0.71, 1.0, and 7.03, are considered ($Pr=0.71$ represents air at 20°C , $Pr=1.0$ corresponds to an electrolyte solution, such as salt water, and $Pr=7.03$ corresponds to water). In air ($Pr=0.71$) the diluting chemical species of most common interests have a Schmidt number in the range of 0.1–10.0. Therefore, three values, 0.22, 0.60, and 0.75, of the Schmidt number (Sc) are considered for they represent specific conditions

of the flow. In particular, 0.22 corresponds to hydrogen, while 0.6 corresponds to water vapor, which represents a diffusing chemical species of most common interest in air, and the value 0.75 represents oxygen. For water ($Pr=7.03$), the species, hydrogen, oxygen, and carbon dioxide, are the typical of the materials of most interest, in which the Schmidt number ranges from 100 to 500. Above values of Schmidt number Sc for different species are obtained from Ref. [20]. Three values of the magnetic parameter M (0.2, 0.4, and 0.6) are taken into account to encounter low magnetic field. In order to highlight the validity of the numerical computations adapted in the present investigation, some of our results (without thermal diffusion) have been compared with those of Sparrow and Gregg [2] and Benton [5], respectively, in Tables 2 and 3. The comparisons show excellent agreements, hence an encouragement for the use of the present numerical computations.

The representative velocity, temperature, and concentration profiles and the values of the physically important parameters, i.e., the local shear stress and the local rates of heat and mass transfer, are illustrated for uniform wall temperature and species concentration in Figs. 3–10 and in Table 3. In Figs. 3–5, the radial, tangential, and axial velocity profiles are shown, respectively, for

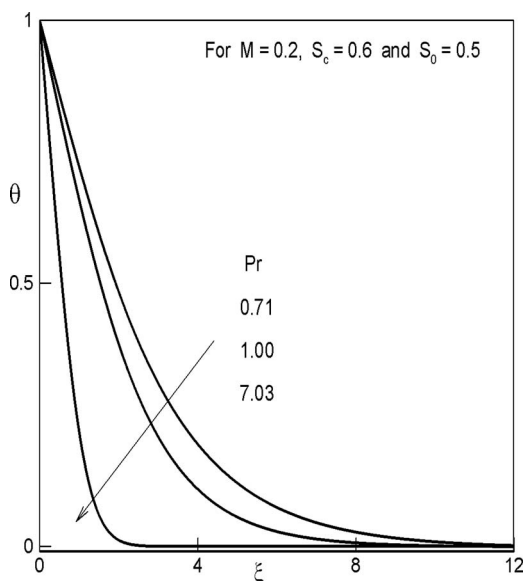


Fig. 8 Effect of Pr on the temperature profiles

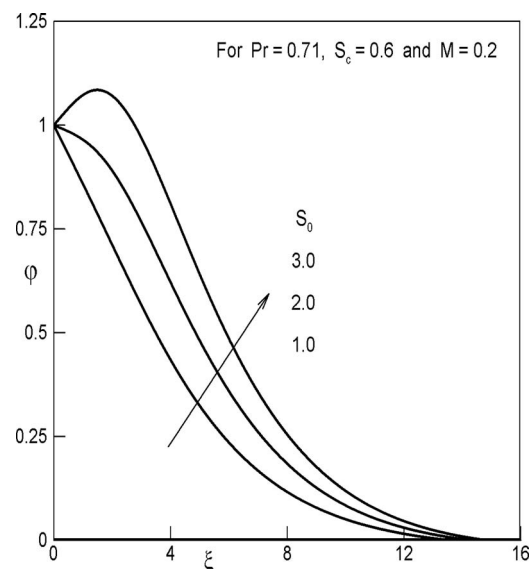


Fig. 10 Effect of So on the concentration profiles

Table 1 Numerical values of the radial shear stress τ_r , the tangential shear stress τ_b , Nusselt number Nu, and the Sherwood number Sh for the different values of M , Pr, Sc, and So: (a) for Pr=0.71, Sc=0.6, and So=0.5, (b) for $M=0.2$, Sc=0.6, and So=0.5, and (c) for Pr=0.71 and $M=0.2$

M	$F''(0)$	$-G'(0)$	$-\theta'(0)$	$-\varphi'(0)$
(a)0.0	0.510174	0.626143	0.385700	0.333941
0.1	0.480499	0.662260	0.306761	0.222261
0.2	0.453136	0.708770	0.283175	0.196607
0.3	0.428193	0.755623	0.263046	0.182197
0.4	0.405570	0.802362	0.243440	0.167397
0.5	0.387084	0.844112	0.227007	0.155794
Pr	$-\theta'(0)$		$-\varphi'(0)$	
(b)0.10	0.109091		0.270816	
0.71	0.283175		0.196607	
1.00	0.349565		0.182891	
2.00	0.511053		0.144306	
4.35	0.740694		0.085090	
7.03	0.913525		0.038137	
10.00	1.058404		-0.002268	
11.04	1.102125		-0.014604	
20.00	1.396383		-0.098859	
50.00	1.978522		-0.269185	
100.00	2.612601		-0.341351	
Sc	So		$-\varphi'(0)$	
(c)0.25	0.5		0.105908	
0.40	0.5		0.149389	
0.60	0.5		0.196607	
0.80	0.5		0.241491	
1.00	0.5		0.272331	
0.60	0.5		0.196607	
0.60	1.0		0.139508	
0.60	2.0		0.030292	
0.60	2.5		-0.025810	
0.60	3.0		-0.081929	

different values of M (0.2, 0.4, and 0.6). From these figures it is observed that the presence, as well as the increase in the magnetic field, leads to the decrease in the velocity field, indicating that the magnetic field retards the velocity field. In Figs. 6 and 7, we have plotted the temperature and concentration profiles for air (Pr = 0.71) at 20°C and at 1 atm, showing the effect of variation in magnetic parameter. It is thus apparent that the magnetic parameter M has increasing effects on temperature and concentration profiles. Imposition of a magnetic field to an electrically conducting fluid creates a draglike force called the Lorentz force. This force has the tendency to slow down the flow around the disk at the expense of increasing its temperature. This is depicted by the decreases in the radial, tangential, and axial velocity profiles and increases in the temperature profiles as M increases. In addition, the increases in the temperature and concentration profiles as M increases are accompanied by increases in the thermal and mass boundary layers.

Figure 8 presents the effect of Prandtl number Pr on the temperature profiles. From this figure, it is seen that the temperature profiles decrease with the increasing values of Pr. In the case of

Table 2 Comparison between the results of Sparrow and Gregg [2] (analytical) and the present work; heat transfer coefficients $-\theta'(0)$ for So=0, $M=0$, and Sc=0.22

Pr	Sparrow and Gregg	Present
1.0	0.39625	0.397991
10.0	1.1341	1.134531
100	2.6871	2.686091

water at 20°C (Pr=7.03), the thermal boundary layer shows a sharp decrease compared with the effects on electrolyte solution, such as salt water (Pr=1.0) and air (Pr=0.71) at 20°C. Figure 9 presents the effect of the Schmidt number Sc on the concentration profiles. From this figure, it is seen that the concentration profiles decrease with the increasing values of Sc.

The parameter So (Soret number) does not enter directly into the momentum and energy equations. Thus the effect of the Soret number on velocity and temperature profiles is not apparent. Figure 10 shows the variation in concentration profiles for different values of So. The parameter So has marked effects on the concentration profiles. It is observed that the concentration profiles increase with the increasing values of So. It is also observed from this figure that when So=1.0, that is, when the ratio between concentration and temperature gradient is very small, the concentration profile shows its usual trend of gradual decay. As the Soret number becomes large, the profiles overshoot the uniform concentration close to the boundary.

The radial and tangential skin frictions and the heat transfer and the mass transfer coefficients are tabulated in Table 1 for various values of M , Pr, Sc, and So. We observe in Table 1(a) that the radial skin-friction, heat, and mass transfer coefficients decrease, while the tangential skin friction increases with the increase in the magnetic parameter M . Table 1(b) shows that the heat transfer coefficient increases, whereas the mass transfer coefficient decreases with the increasing values of the Prandtl number Pr. Table 1(c) shows that the dimensionless Sherwood number increases with the increasing values of the Schmidt number Sc. It is also observed in Table 1(c) that as thermal diffusion (So) intensifies, the mass transfer coefficient decreases.

The step size in this case was selected to be $\Delta\xi=0.01$, which satisfied the convergence criterion of 10^{-6} . However, different step sizes, such as $\Delta\xi=0.01$, $\Delta\xi=0.005$, and $\Delta\xi=0.001$, were also tried, and the obtained solutions have been found to be independent of the step sizes observed in Fig. 2.

7 Conclusions

In this paper, a steady three-dimensional MHD convective heat and mass transfer flow in an incompressible fluid due to an infinite rotating disk is studied. The Nachtsheim–Swigert [23] iteration technique based on sixth order Runge–Kutta and shooting methods has been employed to complete the integration of the resulting solutions.

The following conclusions can be drawn as a result of the computations.

1. The effect of the Lorentz force or the usual resistive effect of the magnetic field on the velocity profiles is apparent. It is also apparent that the magnetic parameter M has increasing effects on temperature and concentration profiles.
2. It is observed that the temperature profiles decrease with the increasing values of Pr. In the case of water at 20°C (Pr = 7.03), the thermal boundary layer shows a sharp decrease compared with the effects in electrolyte solution, such as salt water (Pr=1.0) and air (Pr=0.71) at 20°C.
3. As for the effect of the Schmidt number Sc on the concentration profiles, it is seen that the concentration profiles decrease with the increasing values of Sc.
4. The parameter So has marked effects on the concentration profiles. It is observed that the concentration profiles increase with the increasing values of So.
5. We observe that the radial skin-friction, heat, and mass transfer coefficients decrease, while the tangential skin friction increases with the increase in the magnetic parameter M .
6. The heat transfer coefficient increases, whereas mass transfer coefficient decreases with the increasing values of the Prandtl number Pr.
7. It is observed that the dimensionless Sherwood number in-

Table 3 Comparison between the results of Benton [5] and the present work; the velocity field, its derivatives as a function of ξ

ξ	F'	G	$-H$	F''	G'
Present work for $M=0$, $Sc=0.6$, $Pr=0.71$, and $So=0$					
0.0	0.000000	1.000000	0.000000	0.510088	-0.616697
0.1	0.046261	0.938415	0.004790	0.416018	-0.612003
0.2	0.083989	0.877170	0.018091	0.332806	-0.599309
0.3	0.114365	0.816415	0.038641	0.259192	-0.580255
0.5	0.153206	0.708520	0.091087	0.147988	-0.533617
1.0	0.180279	0.478177	0.263261	-0.014211	-0.393658
1.5	0.157273	0.316419	0.430626	-0.067916	-0.272089
2.0	0.119400	0.201392	0.574235	-0.072951	-0.177531
2.5	0.084882	0.130455	0.674351	-0.060461	-0.116749
3.0	0.059054	0.083691	0.746181	-0.044941	-0.075884
4.0	0.028363	0.034390	0.829440	-0.021678	-0.031064
Results of Benton [5]					
0.0	0	1.0000	0	0.5102	-0.6159
0.1	0.0462	0.9386	0.0048	0.4163	-0.6112
0.2	0.0836	0.8780	0.0179	0.3380	-0.5987
0.3	0.1133	0.8190	0.0377	0.2620	-0.5803
0.5	0.1536	0.7076	0.0919	0.1467	-0.5321
1.0	0.1802	0.4766	0.2655	-0.0157	-0.3911
1.5	0.1559	0.3132	0.4357	-0.0693	-0.2677
2.0	0.1189	0.2033	0.5732	-0.0739	-0.1771
2.5	0.0848	0.1313	0.6745	-0.0612	-0.1153
3.0	0.0581	0.0845	0.7452	-0.0455	-0.0745
4.0	0.0257	0.0349	0.8251	-0.0216	-0.0309

creases with the increasing values of the Schmidt number Sc . It is also observed that as thermal diffusion (So) intensifies, the mass transfer coefficient decreases.

Acknowledgment

This work was supported by the American International University-Bangladesh.

Nomenclature

B_0 = applied magnetic field
 c_p = specific heat at constant pressure
 C = concentration of the fluid
 \bar{C} = dimensionless concentration of the fluid
 C_w = concentration of the fluid at the wall
 C_∞ = concentration of the fluid at infinity
 D_M = molecular diffusivity
 k_T = the thermal diffusion ratio
 L = length scale
 M = magnetic parameter
 Nu = Nusselt number
 Pr = Prandtl number
 p = pressure
 p_∞ = pressure at infinity
 (r, ϕ, z) = cylindrical polar coordinates
 R_1, Z_1 = dimensionless radial and axial coordinates
 Re = Reynolds number
 Sc = Schmidt number
 So = Soret number
 T = temperature of the flow field
 T_M = the mean fluid temperature
 \bar{T} = dimensionless temperature of the flow field
 T_∞ = temperature of the fluid at infinity
 T_w = temperature at the plate
 (u, v, w) = components of the velocity field
 (U, V, W) = dimensionless velocity components
 (F, G) = dimensionless similarity functions

Greek Symbols

θ = dimensionless temperature

φ = dimensionless concentration
 ξ = dimensionless similarity variable
 ν = kinematic viscosity
 ν_1 = dimensionless kinematic viscosity
 ρ = density of the fluid
 σ = electric conductivity
 κ = thermal conductivity
 Ω = angular velocity
 τ_r = radial shear stress
 τ_t = tangential shear stress
 μ = fluid viscosity

References

- [1] Herrero, J., Humphrey, J. A. C., and Giralt, F., 1994, "Comparative Analysis of Coupled Flow and Heat Transfer Between Co-Rotating Discs in Rotating and Fixed Cylindrical Enclosures," *HTD (Am. Soc. Mech. Eng.)*, **30**, pp. 111–121.
- [2] Sparrow, E. M., and Gregg, J. L., 1959, "Heat Transfer From a Rotating Disk to Fluids of Any Prandtl Number," *ASME J. Heat Transfer*, **8**, pp. 249–251.
- [3] von Kármán, T., 1921, "Ueber laminare und turbulente reibung," *Z. Angew. Math. Mech.*, **1**, pp. 233–255.
- [4] Cochran, W. G., 1934, "The Flow Due to a Rotating Disc," *Proc. Cambridge Philos. Soc.*, **30**, pp. 365–375.
- [5] Benton, E. R., 1966, "On the Flow Due to a Rotating Disc," *J. Fluid Mech.*, **24**, pp. 781–800.
- [6] Wagner, C., 1948, "Heat Transfer From a Rotating Disk to Ambient Air," *J. Appl. Phys.*, **19**, pp. 837–839.
- [7] Kuiken, H. K., 1971, "The Effect of Normal Blowing on the Flow Near a Rotating Disk of Infinite Extent," *J. Fluid Mech.*, **47**, pp. 789–798.
- [8] El-Mistikawy, T. M. A., and Attia, H. A., 1990, "The Rotating Disk Flow in the Presence of Strong Magnetic Field," *Proceedings of the Third International Congress of Fluid Mechanics*, Vol. 3, Cairo, Egypt, Jan. 2–4, pp. 1211–1222.
- [9] El-Mistikawy, T. M. A., Attia, H. A., and Megahed, A. A., 1991, "The Rotating Disk Flow in the Presence of Weak Magnetic Field," *Proceedings of the Fourth Conference on Theoretical and Applied Mechanics*, Cairo, Egypt, Nov. 5–7, pp. 69–82.
- [10] Hassan, A. L. A., and Attia, H. A., 1997, "Flow Due to a Rotating Disk With Hall Effect," *Phys. Lett. A*, **228**, pp. 246–290.
- [11] Attia, H. A., 1998, "Unsteady MHD Flow Near a Rotating Porous Disk With Uniform Suction or Injection," *Fluid Dyn. Res.*, **23**, pp. 283–290.
- [12] Kelson, N., and Desseaux, A., 2000, "Notes on Porous Rotating Disk Flow," *ANZIAM J.*, **42**, pp. C837–C855.
- [13] Yasuyuki, M., Noriyuki, F., and Masaya, K., 2002, "A Characteristic of the Flow Field on a Heated Rotating Disk," *Third International Symposium on Ultrasonic Doppler Methods for Fluid Mechanics and Fluid Engineering*, EPFL, Lausanne, Switzerland, Sept. 9–11, pp. 1–4.

- [14] Maleque, Kh. A., and Sattar, M. A., 2003, "Transient Convective Flow Due to a Rotating Disc With Magnetic Field and Heat Absorption Effects," *Journal of Energy, Heat and Mass Transfer*, **25**, pp. 279–291.
- [15] Maleque, Kh. A., and Sattar, M. A., 2005, "The Effects of Variable Properties and Hall Current on Steady MHD Compressible Laminar Convective Fluid Flow Due to a Porous Rotating Disc," *Int. J. Heat Mass Transfer*, **48**, pp. 4963–4972.
- [16] Maleque, Kh. A., and Sattar, M. A., 2005, "The Effects of Variable Properties on Steady Laminar Convective Flow Due to a Porous Rotating Disc," *ASME J. Heat Transfer*, **127**(12), pp. 1406–1409.
- [17] Eckert, E. R. G., and Drake, R. M., 1972, *Analysis of Heat and Mass Transfer*, McGraw-Hill, New York.
- [18] Jha, B. K., and Singh, A. K., 1990, "Soret Effects Free Convection and Mass Transfer Flow Over an Infinite Vertical Moving Plate," *Astrophys. Space Sci.*, **173**, pp. 251–255.
- [19] Kafoussias, N. G., 1992, "MHD Thermal-Diffusion Effects on Free-Convection and Mass Transfer Flow Over an Infinite Vertical Moving Plate," *Astrophys. Space Sci.*, **192**, pp. 11–19.
- [20] Alam, M. M., and Sattar, M. A., 1998, "Unsteady MHD Free Convection and Mass Transfer in a Rotating System With Thermal Diffusion," *J. Energy Heat Mass Transf.*, **20**, pp. 77–87.
- [21] Sattar, M. A., and Alam, M. M., 2001, "Analytical Solution of the Free Convection and Mass Transfer Flow With Thermal Diffusion," *Dhaka Univ. J. Sci.*, **49**(1), pp. 95–104.
- [22] Maleque, Kh. A., and Sattar, M. A., 2002, "Similarity Solution of MHD Free-Convection and Mass Transfer Flow Over a Vertical Porous Plate With Thermal Diffusion Effects," *The Aiub Journal of Science and Engineering (AJSE)*, **1**(1), pp. 44–55.
- [23] Nachtsheim, P. R., and Swigert, P., 1965, "Satisfaction of Asymptotic Boundary Conditions in Numerical Solution of System of Nonlinear of Boundary Layer Type," NASA Technical Report No. NASA-TN-D-3004.

Interactions Between Electromagnetic and Thermal Fields in Microwave Heating of Hardened Type I-Cement Paste Using a Rectangular Waveguide (Influence of Frequency and Sample Size)

P. Rattanadecho¹
e-mail: ratphadu@engr.tu.ac.th

N. Suwannapum
W. Cha-um

Research Center of Microwave Utilization in
Engineering (RCME),
Faculty of Engineering,
Thammasat University,
Pathumthani 10120, Thailand

Microwave heating-drying of hardened Type I-cement paste using a rectangular waveguide is a relatively new area of cement-based materials research. In order to gain insight into the phenomena that occur within the waveguide together with the temperature distribution in the heated cement paste samples, a detailed knowledge of absorbed power distribution is necessary. In the present paper, a three-dimensional finite difference time domain scheme is used to determine electromagnetic fields (TE_{10} -mode) and microwave power absorbed by solving transient Maxwell's equations. Two-dimensional heat transport within the cement paste located in rectangular waveguide is used to evaluate the variations of temperature with heating time at different frequencies and sample sizes. A two-dimensional heating model is then validated against experimental results and subsequently used as a tool for efficient computational prototyping.
[DOI: 10.1115/1.2993134]

Keywords: microwave heating, rectangular waveguide, numerical, type I-cement paste, hardened

1 Introduction

In the past decade, there are many successful examples of microwave application such as the heating and drying of foods, heating and drying of ceramics, heating and drying of cement paste, and vulcanizations of rubber. A number of other analyses of the microwave heating process have appeared in the recent literature [1–11].

The microwave heating process takes place inside the material, the penetrated depth of which governs how strongly the microwaves are absorbed. It is known that the heat dissipated from the microwave energy depends on many parameters, such as the configuration and geometry of the dielectric samples, the microwave power level, the microwave field distribution, and the dielectric properties of dielectric samples.

The use of alternative techniques for heating cement paste and concrete has been investigated sporadically in the past 20 years. Two of the main forms of alternative heating are Ohmic (or direct electric) heating and microwave heating. Watson [12] reported a research on microwave heating of concrete in 1968. However, very few additional works were reported over the next 20 years. Interest in microwave heating and curing of cement-based materials was again revived in the 1980s through the present [13–21]. The use of microwave heating and drying to process concrete

potentially covers the entire spectrum of the following [12,15,19,20]:

- preheating of concretes prior to the product casting or primary curing stage
- rapid (accelerated) curing and/or drying as a primary process stage
- drying as a secondary postcuring stage

These may be required individually or in combinations that are either applied sequentially or with some overlap.

In theoretical analysis, the microwave power absorbed generally is assumed to decay exponentially into the sample following Lambert's law. However, this assumption is valid for large dimension samples where the depth of sample is much larger than the penetration depth (all microwave energy, except the reflected wave from the upper surface of the sample, is dissipated within the sample). For small samples where the depth of sample is much smaller than the penetration depth, result heat in a faster rate by microwave due to the reflection and transmission components of microwave at each interface will contribute to the resonance of standing wave configuration inside the sample, whereas resonance is completely absent for greater length scales [1]. In perspective, Lambert's exponential decay law cannot predict resonance phenomenon. Therefore, the spatial variations of the electromagnetic field within small samples must be obtained by solution of the Maxwell's equations.

The two-dimensional models of the interactions between electromagnetic field and dielectric materials have been used previously to study numerous heating processes of materials in a variety of microwave applicator configurations such as rectangular

¹Corresponding author.

Contributed by the Heat Transfer Division of ASME for publication in the JOURNAL OF HEAT TRANSFER. Manuscript received May 16, 2007; final manuscript received June 27, 2008; published online June 1, 2009. Review conducted by Cholik Chan.

Table 1 Mix proportions of cement paste used

Water-to-cement ratio (w/c)	Portland cement Type I (kg/m^3)	Water (kg/m^3)
0.40	1394	558

waveguide and cavities [22,23,5–7,24]. Although most of the previous investigations considered simulations of microwave heating in solid sample, little effort has been reported on study of microwave heating of cement paste in a rectangular waveguide particularly full comparison between the mathematical simulations and experimental data. Due to the limited amount of theoretical and experimental work on microwave heating of porous media such as concrete or cement paste reported to date, the various effects are not fully understood and numbers of critical issues remain unresolved. These effects of irradiation time, working frequencies, and sample size on heating pattern have not been systematically studied.

In this work, the formulation of mathematical model for the microwave heating of hardened Type I-cement paste (henceforth “cement paste” will refer to hardened Type I-cement paste) inside a rectangular waveguide in which the microwave of TE_{10} mode operating at the specified frequencies is employed utilized three microwave frequencies of 1.5 GHz, 2.45 GHz, and 5.0 GHz in testing the model.

The mathematical models are solved numerically and compared with experimental data. In analysis, the effects of the irradiation time, working frequencies, and sample size on heating pattern are investigated in detail. The result presented here provides a basis for fundamental understanding of microwave drying of porous media such as cement paste and concrete.

2 Experimental Program

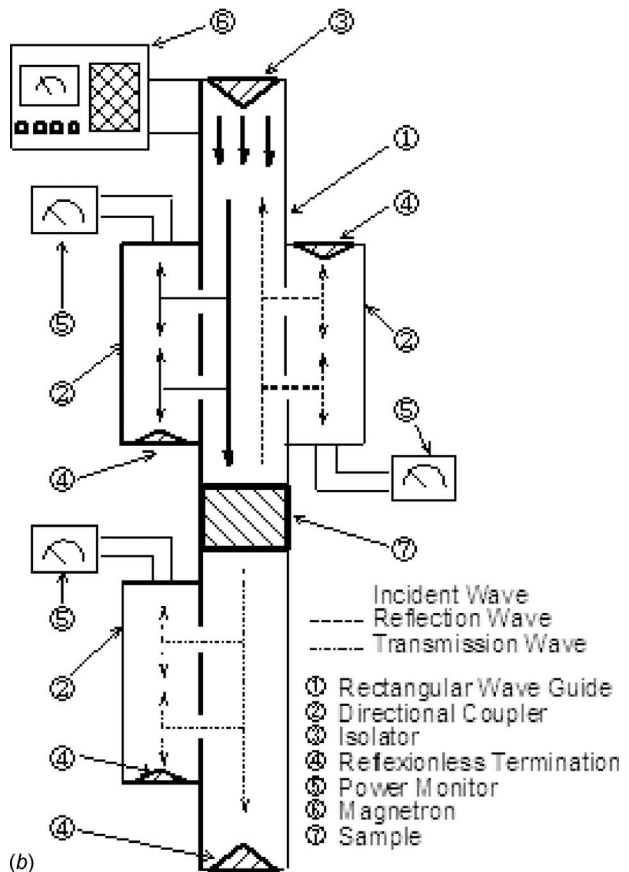
2.1 Sample Preparation. The samples studied were made with cement paste with different dimensions ($110 \text{ mm}(x) \times 54.61 \text{ mm}(y) \times 50 \text{ mm}(z)$ and $110 \text{ mm}(x) \times 54.61 \text{ mm}(y) \times 80 \text{ mm}(z)$). Portland cement type I (Blaine fineness of $3250 \text{ cm}^2/\text{g}$) is mixed with tap water ($\text{pH}=7.0$) following the ASTM C 305 Standard [25], the water-to-cement ratio (w/c) by weight was kept constantly equal to 0.4 in all experiments. The mixed proportions of cement paste used are shown in Table 1. After mixing and placing, the cement paste was put into mold, which was covered by plastic sheet to prevent moisture evaporation. After demolding at $23\frac{1}{2} \pm \frac{1}{2}$ h later, the samples were soaked in microwave energy.

2.2 Experimental Configuration. Figure 1(a) shows the experimental apparatus. The microwave system was a monochromatic wave of TE_{10} mode operating at a frequency of 2.45 GHz. Microwave was generated by a magnetron and transmitted along the z -direction of the rectangular waveguide, with an inner dimension of $110 \times 54.61 \text{ mm}^2$, toward a water load that was situated at the end of the waveguide (Fig. 1(b)). The water load (lower absorbing boundary) ensured that only a minimal amount of microwave was reflected back to the sample. The warm water load was circulated through the cooling tower to reduce the temperature in the water load system. The rectangular cement paste sample was arranged perpendicular to direction of irradiation via a rectangular waveguide. During the experiment, output of magnetron was adjusted at specified power (1000 W). The powers of incident, reflected, and transmitted waves were measured by a wattmeter using a directional coupler.

The temperature distributions within the cement paste sample were measured using fiber optic sensor (LUXTRON Fluoroptic Thermometer, Model 790, accurate to $\pm 0.5^\circ\text{C}$) (measured in



(a)



(b)

Fig. 1 Schematic of experimental facility: (a) equipment setup; (b) microwave measuring system

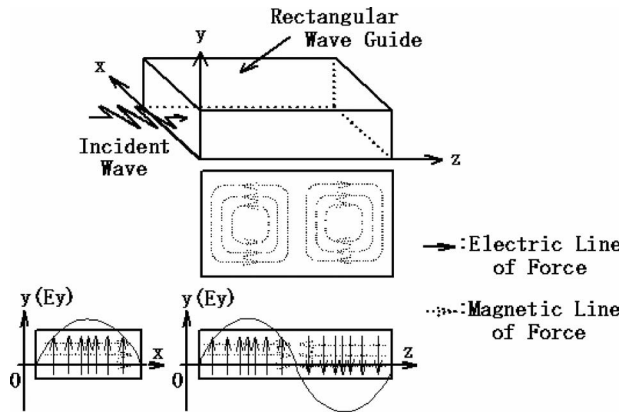


Fig. 2 Distribution of the electric field for TE₁₀ mode in a waveguide of dimensions a and b

symmetrical plane). An infrared camera was used to detect the temperature distribution at the surface of samples (x - z plane).

3 Analysis of Microwave Heating Using a Rectangular Waveguide

3.1 Physical Model. In our case, the fundamental mode, that is TE₁₀, is considered. Since microwave of TE₁₀ mode, which propagates in rectangular waveguide, is uniform in the y -direction, the three-dimensional electromagnetic field can be reduced to two-dimensional model on x - z plane (Fig. 2). Corresponding to electromagnetic field, temperature fields also can be considered in two-dimensional model. Figure 3 shows the physical model for the microwave heating of cement paste using rectangular waveguide. The model proposed is based on the following assumptions.

1. The absorption of microwave by air in rectangular waveguide is negligible.
2. The walls of rectangular waveguide are perfect conductors.
3. All materials, especially the cement paste samples, are non-magnetic.

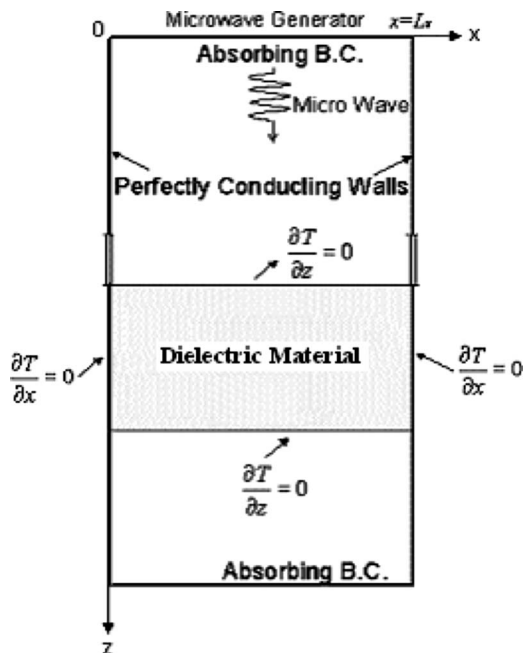


Fig. 3 Physical model

4. The effective dielectric loss factor and the effective loss tangent coefficient are assumed to vary with temperature during the heating process.
5. The effect of the sample container on the electromagnetic and temperature fields can be neglected.
6. The overall heating time is fast, and the moisture content is treated as constant throughout the numerical calculation of microwave heating process.

3.2 Maxwell's Equations. Under the assumption that microwave mode is TE₁₀, the governing equations for the electromagnetic field can be written in terms of the component notations of electric and magnetic field intensities [11]:

$$\frac{\partial E_y}{\partial z} = \mu \frac{\partial H_x}{\partial t} \quad (1)$$

$$\frac{\partial E_y}{\partial x} = -\mu \frac{\partial H_z}{\partial t} \quad (2)$$

$$-\left(\frac{\partial H_z}{\partial x} - \frac{\partial H_x}{\partial z}\right) = \sigma E_y + \varepsilon \frac{\partial E_y}{\partial t} \quad (3)$$

where E and H denote electric field intensity and magnetic field intensity, respectively. Subscripts x , y , and z represent x , y , and z components of vectors, respectively. Furthermore, permittivity or dielectric constant ε , magnetic permeability μ , and electric conductivity σ are given by

$$\varepsilon = \varepsilon_0 \varepsilon_r, \quad \mu = \mu_0, \quad \sigma = 2\pi f \varepsilon \tan \delta \quad (4)$$

In addition, if magnetic effects are negligible, which is true for most dielectric materials used in microwave heating applications, the magnetic permeability (μ) is well approximated by its value μ_0 in the free space.

Corresponding to the physical model, as shown in Fig. 3, boundary conditions can be given as follows.

- (a) *Perfectly conducting boundaries.* Boundary conditions on the inner wall surface of a rectangular waveguide are given by using Faraday's law and Gauss theorem:

$$E_t = 0, \quad H_n = 0 \quad (5)$$

- (b) *Continuity boundary condition.* Boundary conditions along the interface between different materials, for example, between air and dielectric material surfaces, are given by using Ampere's law and Gauss theorem:

$$E_t = E'_t, \quad H_t = H'_t, \quad D_n = D'_n, \quad B_n = B'_n \quad (6)$$

- (c) *Absorbing boundary condition.* At both ends of the rectangular waveguide, the first order absorbing conditions is applied:

$$\frac{\partial E_y}{\partial t} = \pm v \frac{\partial E_y}{\partial z} \quad (7)$$

Here, the symbol \pm represents forward or backward waves and v is the phase velocity of the microwave.

- (d) *Oscillation of the electric and magnetic field intensities by magnetron.* Incident wave due to magnetron is given by the following equations:

$$\begin{aligned} E_y &= E_{yin} \sin\left(\frac{\pi x}{L_x}\right) \sin(2\pi ft), \quad H_x \\ &= \frac{E_{yin}}{Z_H} \sin\left(\frac{\pi x}{L_x}\right) \sin(2\pi ft) \end{aligned} \quad (8)$$

Z_H is the wave impedance defined as

$$Z_H = \frac{\lambda_g Z_I}{\lambda_0} = \frac{\lambda_g}{\lambda_0} \sqrt{\frac{\mu_0}{\epsilon_0}} \quad (9)$$

The power flux associated with a propagating electromagnetic wave is represented by the Poynting vector:

$$S = \frac{1}{2} \text{Re}(E \times H^*) \quad (10)$$

The Poynting theorem allows the evaluation of the microwave power input. It is expressed as

$$P_{in} = \int_A S \cdot dA = \frac{A}{4Z_H} E_{yin}^2 \quad (11)$$

3.3 Heat Transport Equation. The temperature of cement paste exposed to incident wave is obtained by solving the heat transport equation with the microwave power included as a local electromagnetic heat generation term:

$$\frac{\partial T}{\partial t} = a \left(\frac{\partial^2 T}{\partial x^2} + \frac{\partial^2 T}{\partial z^2} \right) + \frac{Q}{\rho \cdot C_p} \quad (12)$$

where T is the temperature, a is the thermal diffusivity, ρ is the density, and C_p is the heat capacity at constant pressure. The local electromagnetic heat generation term Q directly depends on the electric field distribution defined as

$$Q = 2\pi \cdot f \cdot \epsilon_0 \cdot \epsilon_r(\tan \delta) E_y^2 \quad (13)$$

The initial condition of heating process is defined as $T=T_0$ at $t=0$. The boundary conditions for solving heat transport equation are shown in Fig. 3.

3.4 Dielectric Properties. In order to determine the functional temperature dependence of dielectric properties of cement paste, the theory surrounding mixing formulas is used throughout in this study. The volume fraction of water liquid and solid particle is considered as follows:

$$\epsilon_r(T) = (\epsilon_r'(T) - j\epsilon_r''(T)) \quad (14)$$

where

$$\epsilon_r'(T) = \phi \epsilon_{r'l}'(T) + (1 - \phi) \epsilon_{r'p}'(T) \quad (15)$$

$$\epsilon_r''(T) = \phi \epsilon_{r'l}''(T) + (1 - \phi) \epsilon_{r''p}''(T) \quad (16)$$

The effective loss tangent coefficient can be rewritten as

$$\tan \delta(T) = \frac{\epsilon_r''(T)}{\epsilon_r'(T)} \quad (17)$$

According to the above equations, the dielectric properties of liquid water are taken directly from Ref. [26] depend on temperature and those of solid particle (cement) are taken to be constant (see Table 3). According to the dielectric properties of materials, the penetration depth where the dissipated power is reduced to $1/e$ of the power entering the surface can be calculated by

$$D_p = \frac{1}{\frac{2\pi f}{v} \sqrt{\frac{\epsilon_r' \left(\sqrt{1 + \left(\frac{\epsilon_r''}{\epsilon_r'} \right)^2} - 1 \right)}{2}}} \quad (18)$$

$$= \frac{1}{\frac{2\pi f}{v} \sqrt{\frac{\epsilon_r' (\sqrt{1 + (\tan \delta)^2} - 1)}{2}}}$$

4 Numerical Technique

In order to predict the electromagnetic field, a finite difference time domain (FDTD) method is applied. In this study, the leapfrog scheme is applied to set of Maxwell's equations. The electric field

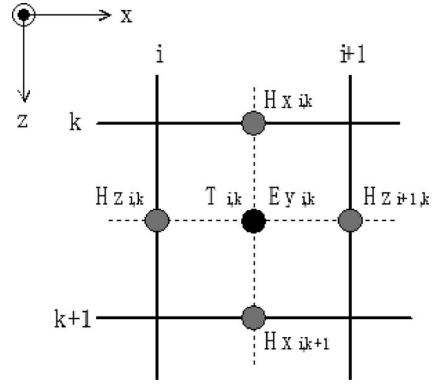


Fig. 4 Grid system configuration

vector components are offset one-half cell in the direction of their corresponding components, while the magnetic field vector components are offset one-half cell in each direction orthogonal to their corresponding components. The electric field and magnetic field are evaluated at alternative half time steps. For TE mode, the electric and magnetic field components are expressed in the total field FDTD equations as [11]

$$E_y^n(i, k) = \frac{1 - \frac{\sigma(i, k) \Delta t}{2\epsilon(i, k)}}{1 + \frac{\sigma(i, k) \Delta t}{2\epsilon(i, k)}} E_y^{n-1}(i, k) + \frac{1}{1 + \frac{\sigma(i, k) \Delta t}{2\epsilon(i, k)}} \frac{\Delta t}{\epsilon(i, k)} \times \left\{ \frac{-(H_z^{n-1/2}(i+1/2, k) - H_z^{n-1/2}(i-1/2, k))}{\Delta x} + \frac{(H_x^{n-1/2}(i, k+1/2) - H_x^{n-1/2}(i, k-1/2))}{\Delta z} \right\} \quad (19)$$

$$H_x^{n+1/2}(i, k+1/2) = H_x^{n-1/2}(i, k+1/2) + \frac{\Delta t}{\mu(i, k+1/2)} \left\{ \frac{E_y^n(i, k+1) - E_y^n(i, k)}{\Delta z} \right\} \quad (20)$$

$$H_z^{n+1/2}(i+1/2, k) = H_z^{n-1/2}(i+1/2, k) - \frac{\Delta t}{\mu(i+1/2, k)} \left\{ \frac{E_y^n(i+1, k) - E_y^n(i, k)}{\Delta x} \right\} \quad (21)$$

Furthermore, the heat transport equation (Eq. (12)) is solved by the finite difference method. The spatial and the temporal terms are approximated using finite difference equations for electromagnetic field and temperature field. Spatially, as shown in Fig. 4, Eqs. (21)–(23) and discretized heat transport equation are solved on this grid system. The choice of spatial and temporal resolutions is motivated by reasons of stability and accuracy [27–29].

To ensure stability of the time-stepping algorithm, Δt must be chosen to satisfy the Courant stability condition:

$$\Delta t \leq \frac{\sqrt{(\Delta x)^2 + (\Delta z)^2}}{v} \quad (22)$$

and the spatial resolution of each cell is defined as

$$\Delta x, \Delta z \leq \frac{\lambda_g}{10\sqrt{\epsilon_r}} \quad (23)$$

Corresponding to Eqs. (22) and (23), the calculation conditions are as follows.

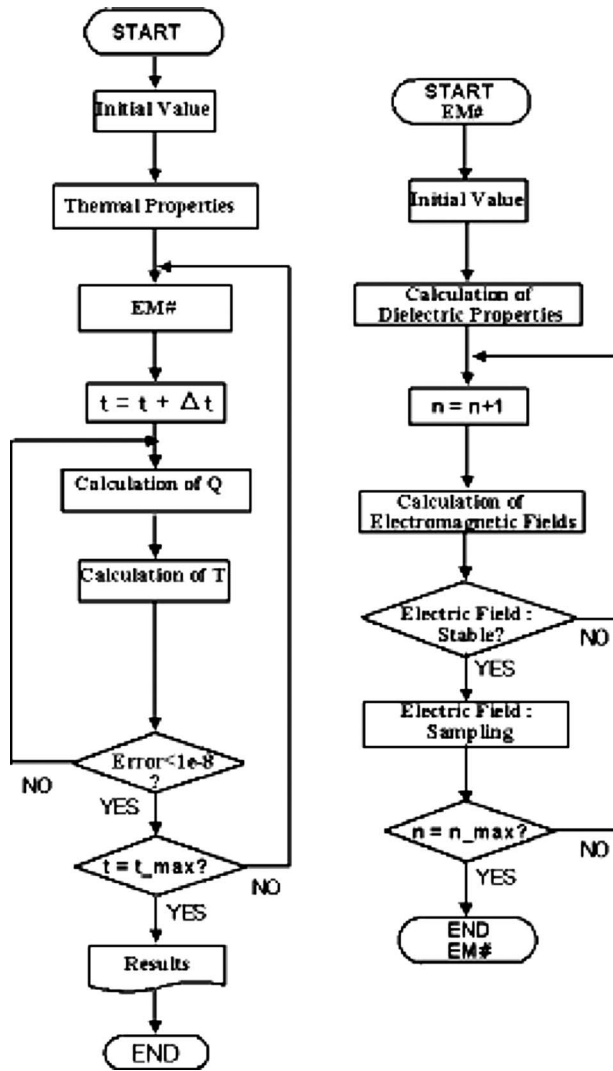


Fig. 5 Computational schemes

Table 2 Microwave power and electric field intensity relations in rectangular waveguide (1000 W)

Frequency (GHz)	Electric field intensity (V/m)
1.50	25,000
2.45	17,500
5.00	16,200

- (1) To ensure that each wavelength of the microwave in the computational domain for a frequency of 2.45 GHz has more than ten subdivisions in the numerical calculation, the computational domain is conservatively set such that the spatial resolution of each cell is $\Delta x = \Delta z \leq \lambda_{mg} / 10 \sqrt{\epsilon_r} \approx 1.0$ mm. Thus, the total of 110×250 cells in computational domain were used in the numerical calculation.
- (2) As the propagating velocity of microwave is very fast compared with the rate of heat transfer, the different time steps of $dt = 1$ ps and 1 s are used for the computation of the electromagnetic field and temperature field, respectively. The spatial step size is $dx = dz = 1$ mm.
- (3) The number of grid (N) is 110 (width) $\times 250$ (length).
- (4) The iteration procedure stops if relative errors are less than 10^{-8} .

5 The Iterative Computational Schemes

Since the dielectric properties of cement paste are temperature dependent, it is necessary to consider the coupling between electric field and temperature field in order to understand the influence of electromagnetic field on microwave heating realistically. For this reason, the iterative computational schemes are required to solve coupled nonlinear Maxwell's equations and heat transport equations.

The computational scheme is to first compute a local heat generation term by running an electromagnetic calculation with uniform properties, determined from initial temperature data. The electromagnetic calculation is performed until sufficient period is reached in which a representative average root-mean-square (rms) of the electric field at each spatial point is obtained, typically 30,000 time steps. The microwave power absorption at each point is computed and used to solve the time dependent temperature field. Using these temperatures, new values of the dielectric properties are calculated and used to recalculate the electromagnetic fields and microwave power absorption. All steps are repeated until the required heating time is reached. The details of computational scheme and strategy are illustrated in Fig. 5.

Table 3 Thermal properties and dielectric properties

$\epsilon_0 = 8.85419 \times 10^{-12}$ F/m	$\mu_0 = 4.0\pi \times 10^{-7}$ H/m	$\phi = 0.38$
$\epsilon_{ra} = 1.0$	$\epsilon_{rp} = 19.7$	
$\mu_{ra} = 1.0$	$\mu_{rp} = 1.0$	$\mu_{rl} = 1.0$
$\tan \delta_a = 0.0$	$\tan \delta_p = 0.29$	
$\rho_a = 1.205$ kg/m ³	$\rho_p = 2300$ kg/m ³	$\rho_l = 1000$ kg/m ³
$C_{pa} = 1.007$ kJ/kg K	$C_{pp} = 0.650$ kJ/kg K	$C_{pl} = 4.186$ kJ/kg K
$\lambda_a = 0.0262$ W/m K	$\lambda_p = 0.87$ W/m K	$\lambda_l = 0.610$ W/m K

Table 4 The ratio of penetration depth (Eq. (18)) versus sample thickness ($w/c = 0.40$)

Frequency f (GHz)	Temperature T (°C)	$\epsilon'_r(T)$	$\tan \delta(T)$	Penetration depth D_p (mm)	Penetration depth (D_p) /Sample thickness	
					$D_p/50$ mm	$D_p/80$ mm
1.50	30	35.63	0.136	51.0	1.020	0.638
	60	32.67	0.203	57.6	1.152	0.720
	90	29.97	0.195	62.7	1.254	0.784
2.45	30	35.63	0.221	31.1	0.622	0.389
	60	32.67	0.203	35.3	0.706	0.441
	90	29.97	0.195	38.4	0.768	0.481
5.00	30	35.63	0.221	15.2	0.304	0.190
	60	32.67	0.203	17.3	0.346	0.216
	90	29.97	0.195	18.8	0.376	0.234

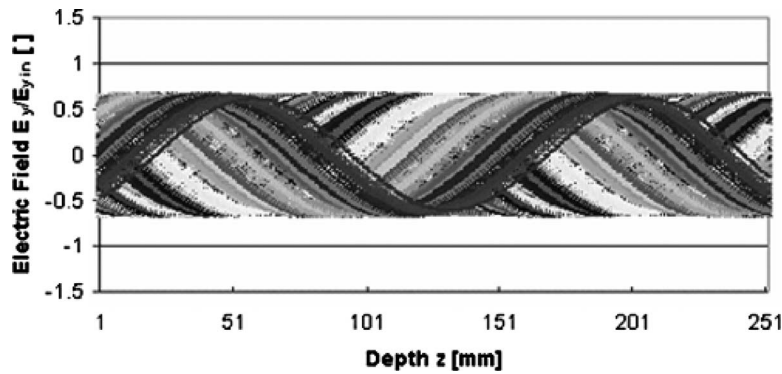


Fig. 6 The electric field distribution (Case 1)

6 Results and Discussion

In this study, the cement paste samples with a fixed water/cement ratio (w/c) of 0.4 and initial temperature of 25°C for all cases are used for analysis. Since the overall heating time is fast, the moisture content was treated as constant throughout the numerical calculation of microwave heating process. The effective dielectric loss factor and the effective loss tangent coefficient are assumed to vary with temperature during the heating process (Eqs. (14)–(17)). The output of magnetron was adjusted at specified power (1000 W) in all testing conditions. These powers can be converted into electric field intensity by using Eq. (11), as shown in Table 2. The thermal properties and dielectric properties are directly taken from Table 3. Table 4 shows the ratio of penetration depth (Eq. (18)) versus sample thickness, which can be used to provide the guidelines for discussion on the different regimes given in Figs. 11–18. In the microwave industry, only a few frequencies are available. Currently, three frequencies of 1.5 GHz, 2.45 GHz, and 5 GHz have been selected. The predicted results are then compared with experimental results for the microwave heating of cement paste. The influences of microwave frequencies and sample sizes on heating process are completely discussed in detail.

6.1 The Electric Field Distribution. To understand the electrical field distribution inside the rectangular waveguide and the cement paste sample during microwave heating, the simulation analysis is required. The simulations of the typical electric field of TE_{10} mode along the center axis ($x=54.61$ mm) of rectangular waveguide with fixed water and cement ratio (w/c) for various heating conditions are presented as follows.

- (1) Rectangular waveguide is empty; its dielectric constant is unity (which corresponds to that of air) (Case 1).
- (2) Rectangular waveguide is filled with cement paste sample operating microwave frequency of 2.45 GHz ($t=30$ s, $P=1000$ W, and size= 110 mm(x) \times 50 mm(z)) (Case 2).
- (3) Rectangular waveguide is filled with cement paste sample operating microwave frequency of 2.45 GHz ($t=30$ s, $P=1000$ W, and size= 110×80 mm²) (Case 3).
- (4) Rectangular waveguide is filled with cement paste sample operating microwave frequency of 5 GHz ($t=30$ s, $P=1000$ W, and size= 110×50 mm²) (Case 4).
- (5) Rectangular waveguide is filled with cement paste sample operating microwave frequency of 1.5 GHz ($t=30$ s, $P=1000$ W, and size= 100×50 mm²) (Case 5).

Figure 6 shows the stationary wave inside the rectangular waveguide with completely absorbed power at the end of the rectangular waveguide (Case 1). It is observed that the electric field distribution displays a wavy behavior with almost uniform amplitude along a rectangular waveguide without the sample.

Figures 7 and 8 show the electric field distribution inside a

rectangular waveguide when a sample of cement paste is inserted in the rectangular waveguide during microwave heating with a frequency of 2.45 GHz for Cases 2 and 3, respectively. Since cement paste considered as a high lossy material (as compared

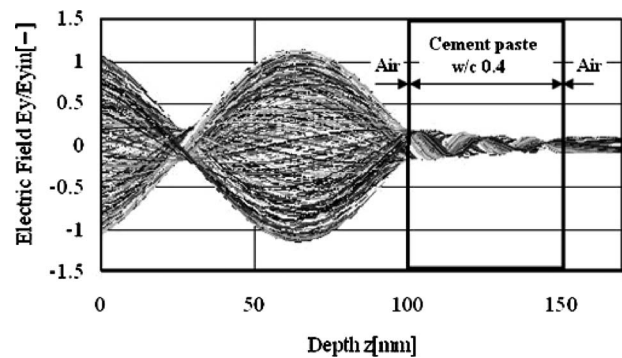


Fig. 7 The electric field distribution (Case 2)

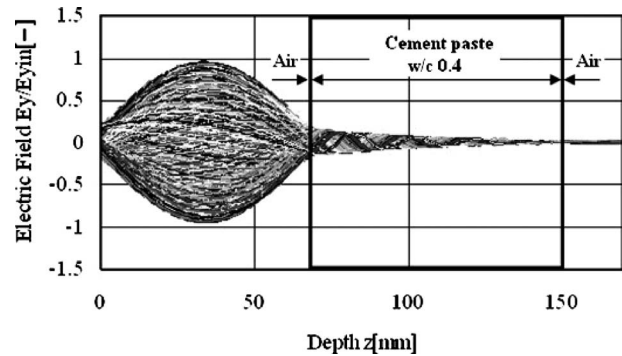


Fig. 8 The electric field distribution (Case 3)

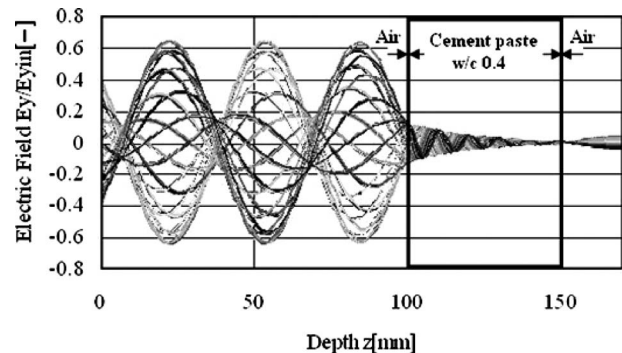


Fig. 9 The electric field distribution (Case 4)

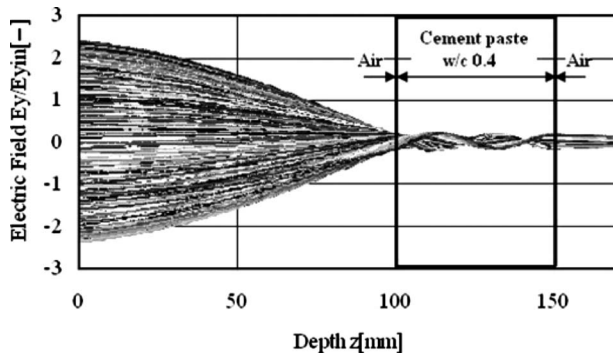


Fig. 10 The electric field distribution (Case 5)

with other materials such as wood and food stuff) has a short wavelength, which corresponds to a smaller penetration depth of microwave in comparison to the depth of sample (Table 4), larger part of microwaves is consequently absorbed by the sample. It is observed from the figures that the resonance of standing wave configuration inside the small sample (Case 2) is weak. Nevertheless, the resonance of standing wave configuration inside the large sample (Case 3) is absent due to all part of microwaves, except

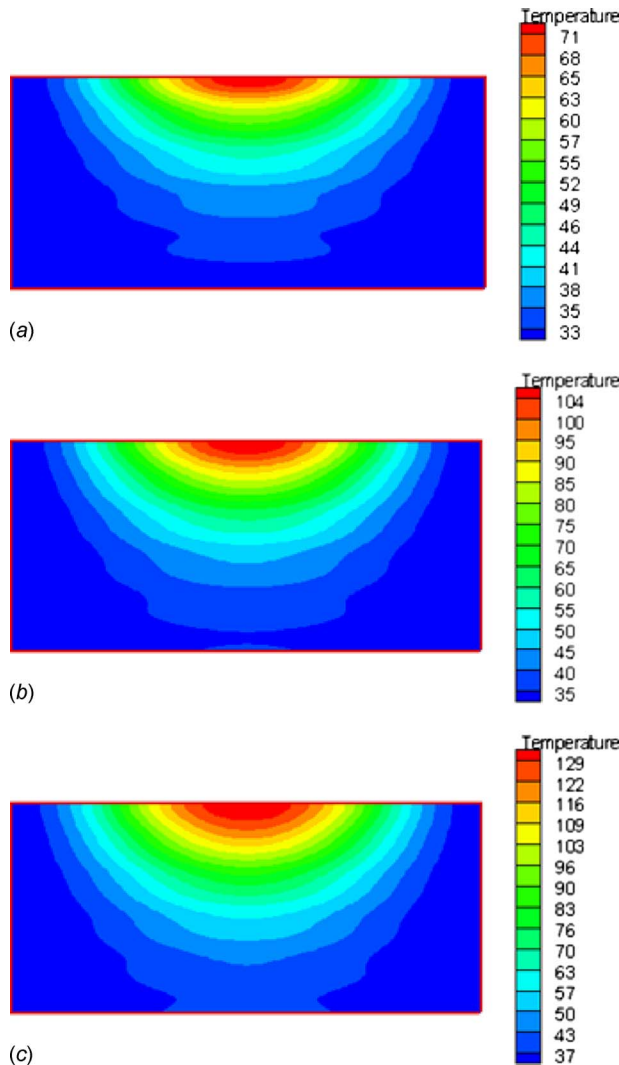


Fig. 11 Temperature distribution ($^{\circ}\text{C}$) at various heating times (Case 2): (a) 20 s; (b) 40 s; (c) 60 s

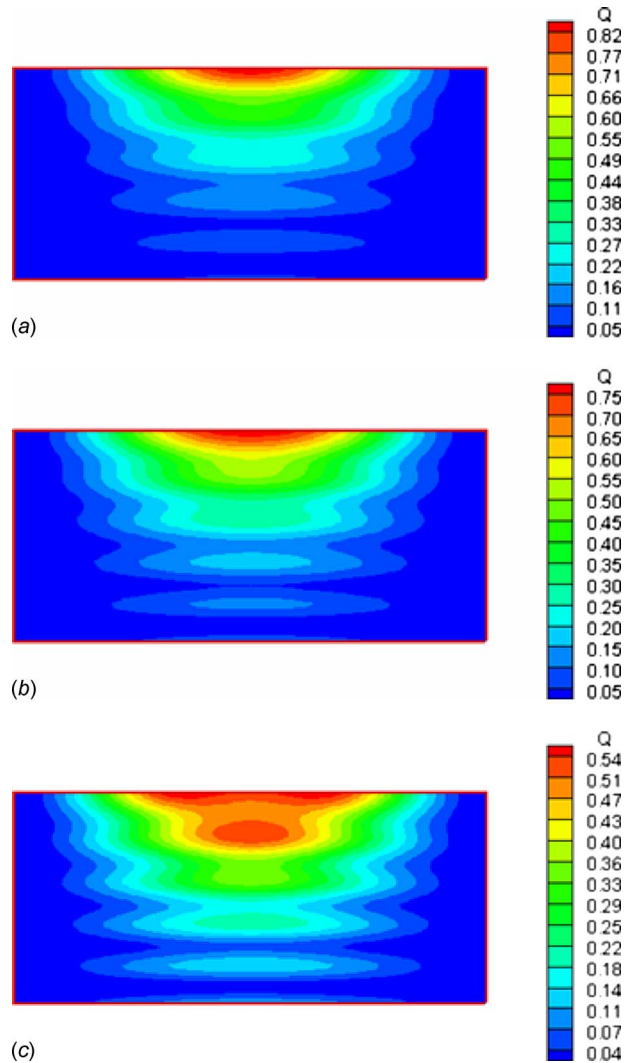
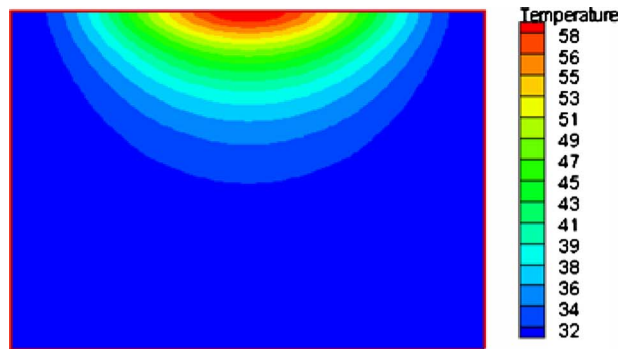


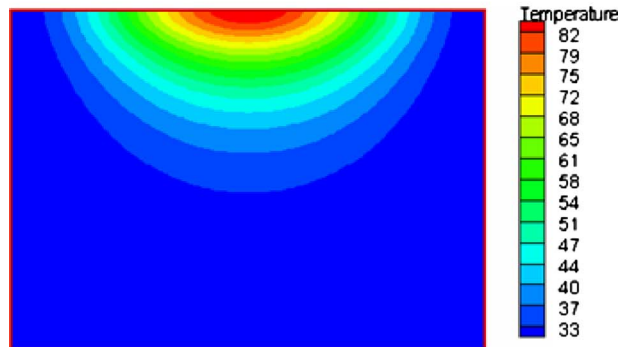
Fig. 12 Microwave power absorbed (MW/m^3) at various heating times (Case 2): (a) 20 s; (b) 40 s; (c) 60 s

the reflected wave from the upper surface of the sample that is absorbed by the sample. Focusing attention of electric field pattern inside the cavity (left hand side), a stronger standing wave with large amplitude is formed by interference between the incident and reflected waves from the surface of sample due to the different dielectric properties of materials (air and sample) at this interface. It is evident from the results that the electric field within the sample attenuates owing to energy absorption, and thereafter the absorbed energy is converted to the thermal energy, which increases the sample temperature.

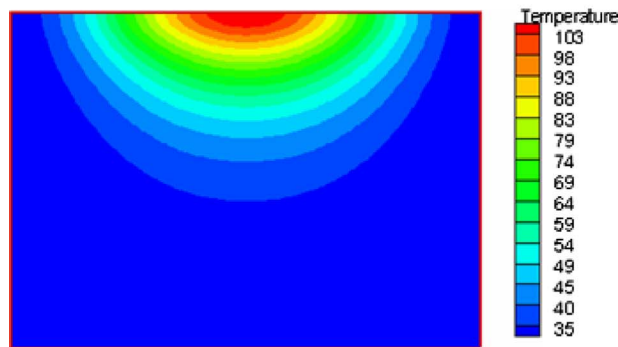
Figure 9 shows the electric field distribution when a sample of cement paste is inserted in the rectangular waveguide during microwave heating with a frequency of 5 GHz (Case 4). Since microwave operating at a high frequency has a short wavelength, which corresponds to a very small penetration depth in comparison to the depth of sample (Table 4), all microwaves, except the reflected wave from the upper surface of the sample, are consequently absorbed by the sample. It is found that the wave amplitude diminishes when z is larger the 30 mm, which results in a low microwave power absorbed. This phenomenon explains why the electric field and therefore the microwave power absorbed are the greatest at the surface exposed to incident microwaves and decay exponentially along the propagating direction with a very short wavelength. However, focusing attention of electric field



(a)



(b)



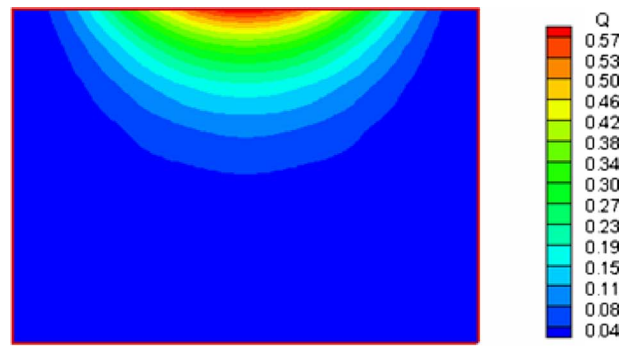
(c)

Fig. 13 Temperature distribution ($^{\circ}\text{C}$) at various heating times (Case 3): (a) 20 s; (b) 40 s; (c) 60 s

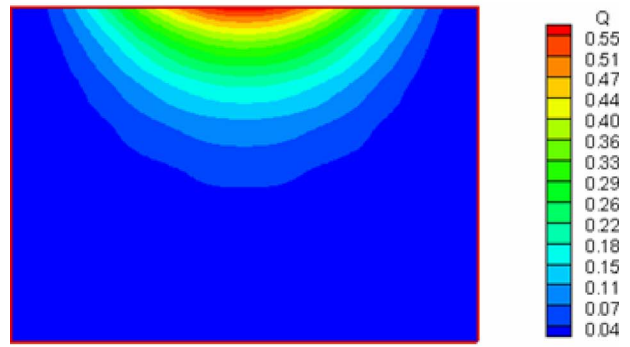
pattern inside the cavity (left hand side), a stronger standing wave with large amplitude is formed by interference between the incident and reflected waves from the surface of sample.

Figure 10 shows the electric field distribution when a sample of cement paste is inserted in the rectangular waveguide during microwave heating with a frequency of 1.5 GHz (Case 5). In this case, since microwave operating at a low frequency has a long wavelength, which corresponds to a larger penetration depth of microwave in comparison to the depth of sample (Table 4), a large part of microwaves are able to penetrate through the sample. The reflected wave will occur on each interface, air (cavity) to upper surface and lower surface of sample to air (cavity). The reflection and transmission components at each interface will contribute to the resonance of standing wave configuration inside the sample and give rise to a microwave absorption peak further from the surface exposed to incident microwaves.

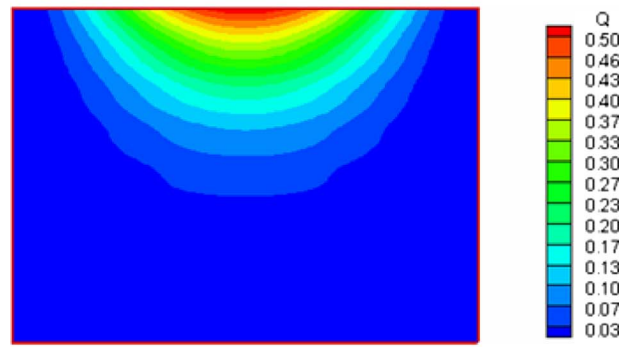
6.2 Temperature Distribution. The predictions of temperature and microwave power absorbed distributions for microwave heating of cement paste are shown in Figs. 11–20 and Fig. 22. The heating conditions correspond to Case 2, Case 3, Case 4, and Case



(a)



(b)



(c)

Fig. 14 Microwave power absorbed (MW/m^3) at various heating times (Case 3): (a) 20 s; (b) 40 s; (c) 60 s

5 as explained in the previous section.

For microwave heating of cement paste with microwave frequency of 2.45 GHz (Case 2), the predictions of temperature distribution are shown in Fig. 11. The temperature distributions correspond to the electric field distribution in the sample. This is because the electric field within the sample attenuates owing to energy absorption, and thereafter the absorbed energy is converted to the thermal energy, which increases the sample temperature. It is observed that the temperature distributions within the sample display a weak wavy behavior because the penetration depth of microwave drops dramatically and the wavelength is short. Since the reflected wave from the lower surface of the sample is almost negligible, a weak standing wave or resonance is formed within the sample. Therefore, the microwave power absorbed decreases sharply to a small value along the propagating direction (Fig. 12). Similar to the microwave power absorbed, the temperature distribution significantly varies from the maximum temperature to the minimum temperature in a short distance. The temperature distributions are shown for $t=20$ s, 40 s, and 60 s. The maximum temperature within the sample is approximately 129°C at $t=60$ s.

For microwave heating of cement paste with a large dimension

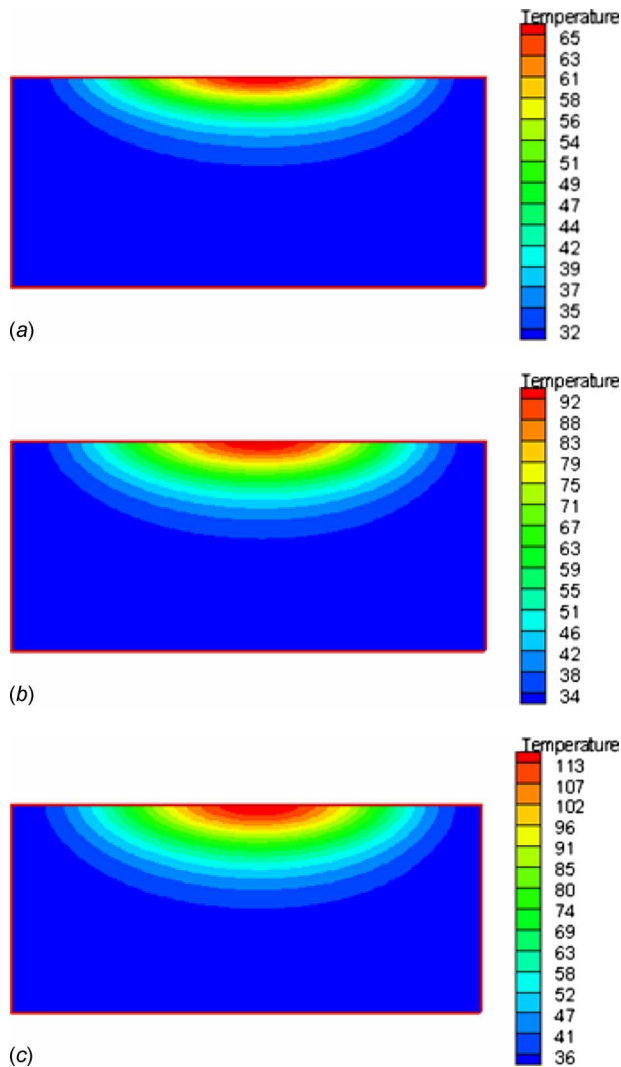


Fig. 15 Temperature distribution ($^{\circ}\text{C}$) at various heating times (Case 4): (a) 20 s; (b) 40 s; (c) 60 s

(Case 3), the predictions of temperature distribution and microwave power absorbed are shown in Figs. 13 and 14, respectively. In contrast to that case of a small sample size (Case 2), the wavy behavior within the sample is totally absent due to the negligible reflected wave from the lower surface of the sample. No standing wave or resonance is formed within the sample. This figure highlights that the larger sample has different heating characteristics in comparison with the smaller sample. The maximum power absorbed and maximum temperatures are lower as compared with Case 2 (Figs. 11 and 12). This is because the presence of the resonance has a substantial effect on the shape of the transient temperature distribution as well as microwave power absorbed. The temperature distributions are shown for $t=20$ s, 40 s, and 60 s. The maximum temperature within the sample is approximately 103°C at $t=60$ s.

For microwave heating of cement paste with microwave frequency of 5 GHz (Case 4), the predictions of temperature distributions are shown in Fig. 15. The temperature and microwave power absorbed distributions correspond to the electric field distribution in the sample (Fig. 9). It is observed that the wavy behavior of the temperature distributions within the sample is absent and it is totally different from those cases of smaller microwave frequency. This is because the reflected wave from the lower surface of the sample is negligible, and no standing wave or resonance is formed within the sample. Therefore, all microwaves,

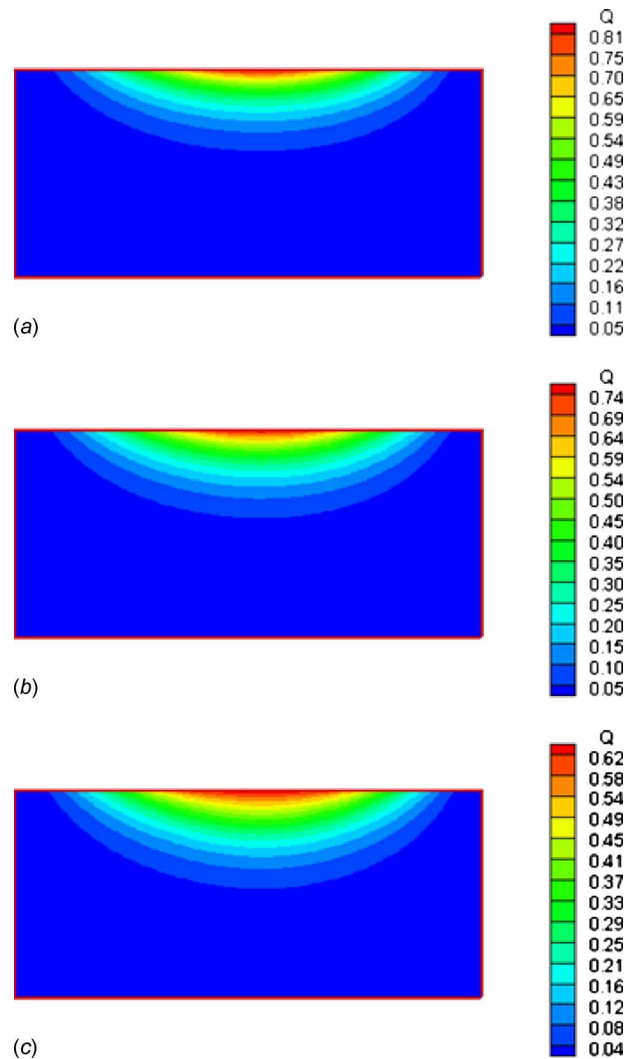


Fig. 16 Microwave power absorbed (MW/m^3) at various heating times (Case 4): (a) 20 s; (b) 40 s; (c) 60 s

except the reflected wave from the upper surface of the sample, are absorbed by the sample (Fig. 16). This phenomenon explains why the electric field and therefore the microwave power absorbed are the greatest at the surface exposed to incident microwaves and decay exponentially along the propagating direction with a very short wavelength, resulting in a thinner thermally stratified layer. In addition, the temperature distribution varies significantly from the maximum temperature to the minimum temperature in a short distance and, after $z > 25$ mm, the temperature distributions are almost unchanged within heating time of 20 s.

It is evident from the figure that there is only one peak appearing on the temperature distribution for this case. The maximum temperature within the sample is approximately 113°C at $t=60$ s.

For microwave heating of cement paste with a microwave frequency of 1.5 GHz (Case 5), the temperature profile within the sample (Fig. 17) displays a strong wavy behavior corresponding to the resonance of electric field (Fig. 10). This is because the electric field within the sample attenuates owing to energy absorption, and thereafter the absorbed energy is converted to the thermal energy, which increases the sample temperature. It is found that the temperatures decay slowly with a strong wavy behavior along the propagation direction following the absorption of microwave (Fig. 18).

Figures 19 and 20 show the predicted results and the experi-

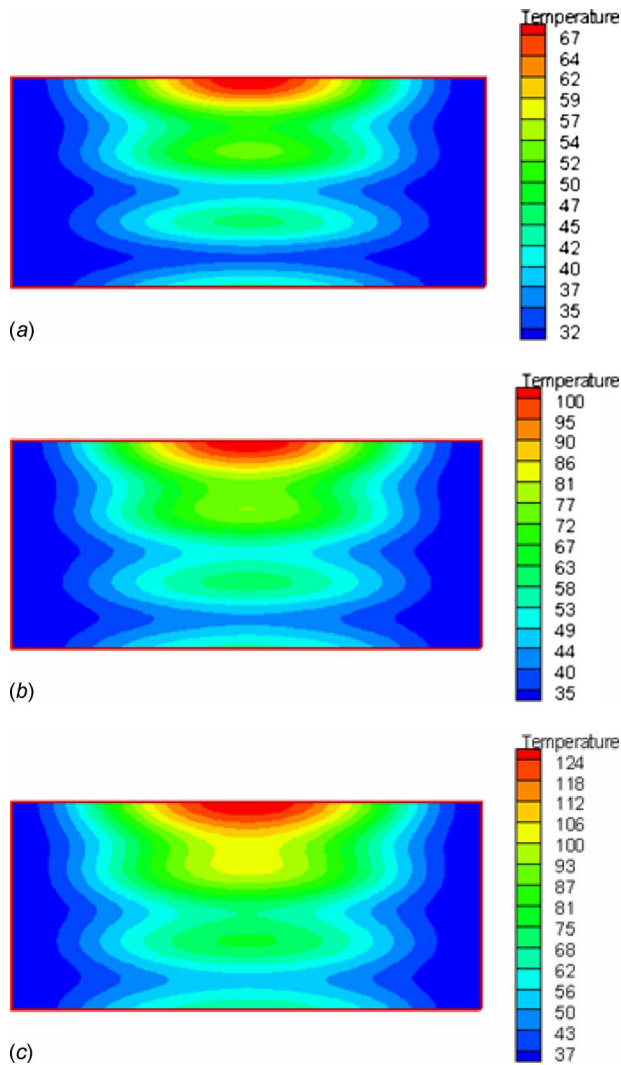


Fig. 17 Temperature distribution ($^{\circ}\text{C}$) at various heating times (Case 5): (a) 20 s; (b) 40 s; (c) 60 s

mental results (measured in symmetrical plane) of temperature distribution within the cement paste along with the horizontal axis of rectangular waveguide ($z=5$ mm) with different sample thicknesses (50 mm and 80 mm), which corresponds to the initial temperature of 25°C , microwave power level of 1000 W, and frequency of 2.45 GHz. The result shows the greatest temperature in the center of wood sample with the temperature decreasing toward the sidewalls of the sample. This phenomenon occurs because the TE_{10} field pattern displays a maximum electric field at the center of waveguide. It is shown that the predicted results agree well with the experimental result for the microwave heating of cement paste.

The prediction of temperature from mathematical model is compared with experimental data measured by infrared camera for microwave heating of cement paste, as shown in Fig. 21. It is shown that the predicted result agrees well with the experimental result for the microwave heating of cement paste particularly, the hot spot region. From the result, the capability of the mathematical model to correctly handle the field variations is shown. With further quantitative validation of the mathematical model, it is clear that the model can be used as an effective tool for investigating in detail this particular microwave heating of cement paste samples at a fundamental level.

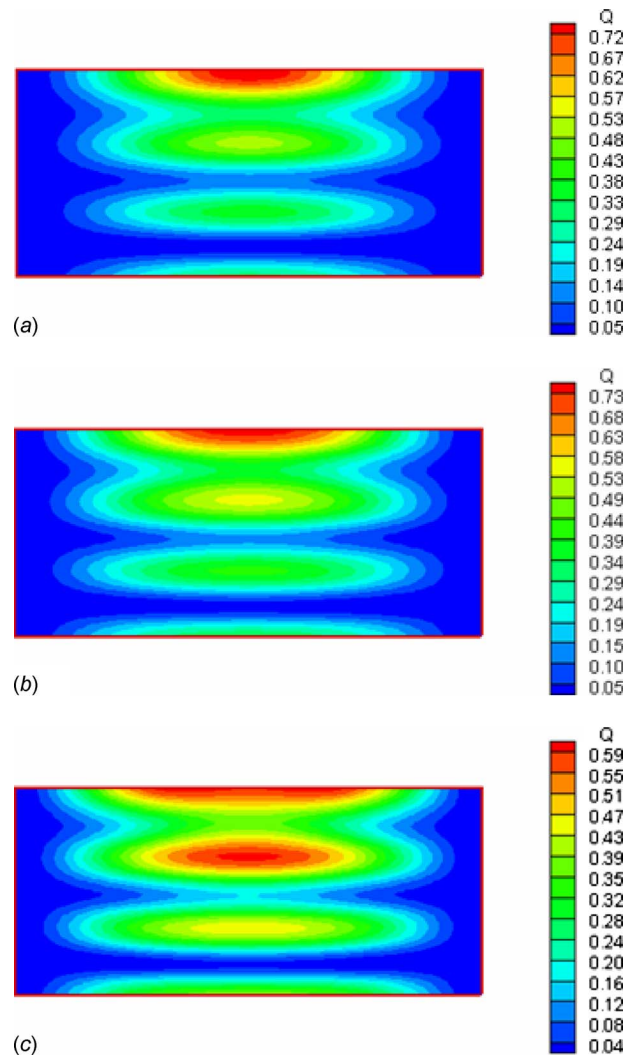


Fig. 18 Microwave power absorbed (MW/m^3) at various heating times (Case 5): (a) 20 s; (b) 40 s; (c) 60 s

7 Conclusions

The numerical analysis presented in this paper describes many important interactions within cement paste samples during microwave heating using a rectangular waveguide. The following paragraph summarizes the conclusions of this study.

- (1) A generalized mathematical model for microwave heating of cement paste is proposed. It is used successfully to describe the heating phenomena under various conditions.
- (2) The effects of irradiation times, working frequencies, and sample size on the microwave power absorbed and heating pattern that are developed within cement paste samples are clarified in detail. It can be concluded that the temperature distributions along the propagating wave show nonevidence of wavy behavior for Cases 3 and 4, which is inconsistent with what was exhibited for Cases 2 and 5. This result highlights that the working frequencies and sample size have significant effect on the heating characteristics. The simulated results for the temperature distributions within the cement paste samples rate are in agreement with experimental results. Figure 22 shows the generalized heating characteristics for Cases 2, 3, 4, and 5 for cement paste samples. The typical heating characteristics may be useful to provide guidance for optimal microwave processing of dielectric materials.

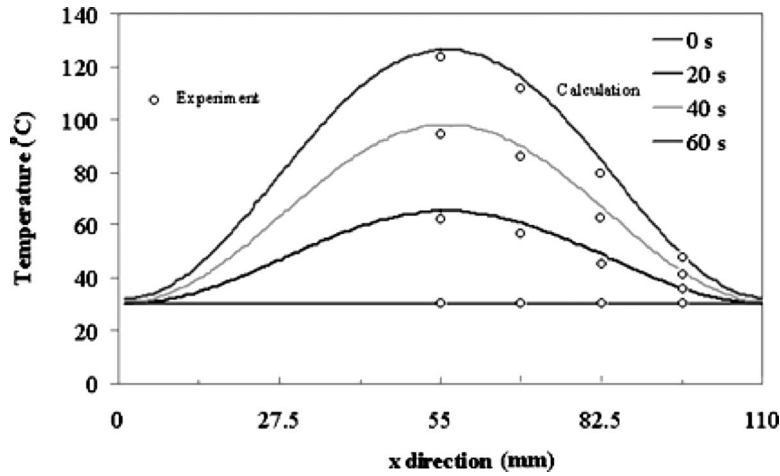


Fig. 19 Temperature distribution in cement paste along horizontal axis ($z=50$ mm) ($P=1000$ W, $f=2.45$ GHz, size= 110 mm (x) \times 50 mm(z))

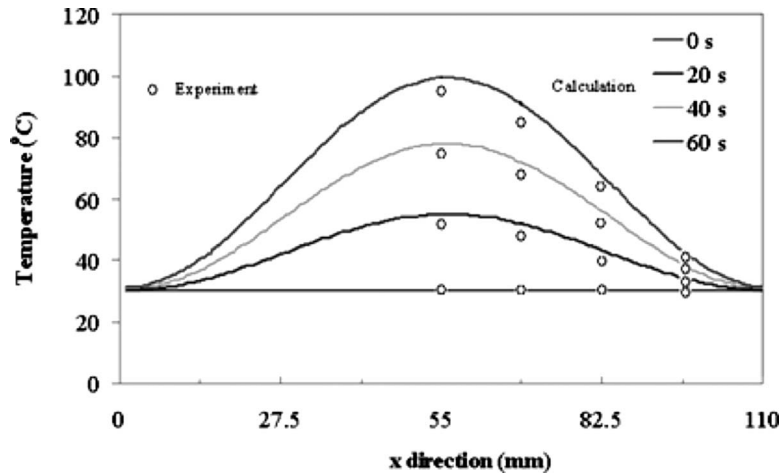


Fig. 20 Temperature distribution in cement paste along horizontal axis ($z=80$ mm) ($P=1000$ W, $f=2.45$ GHz, size= 110 mm (x) \times 80 mm(z))

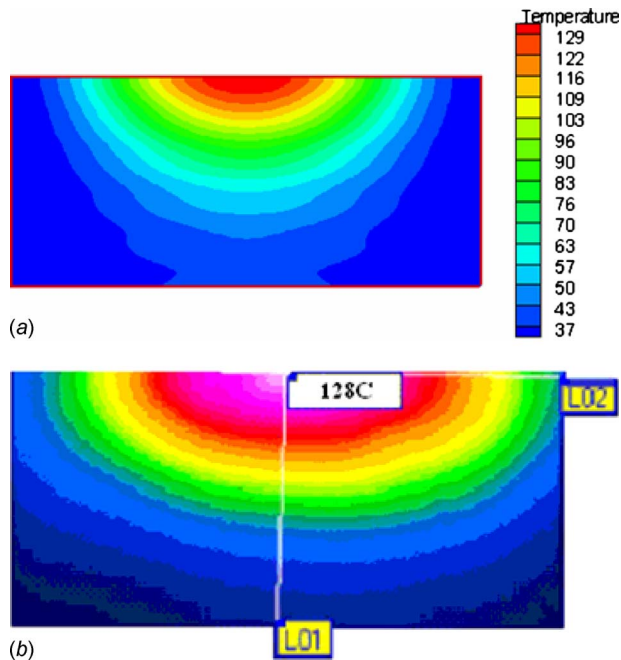


Fig. 21 The comparison of temperature distribution ($^{\circ}$ C) in wood sample: (a) simulated result and (b) experimental result

Acknowledgment

The authors are pleased to acknowledge Thailand Research Fund (TRF) for supporting this research work. The authors are also pleased to acknowledge Entech Associate Co., Ltd (Thailand) and Infra Tec GmbH (Germany) for providing thermographic measurement system.

Nomenclature

- A = area (m^2)
- B = magnetic flux density (Wb/m^2)
- C_p = specific heat capacity (J/kg K)
- D = electric flux density (C/m^2)
- E = electric field intensity (V/m)
- f = frequency of incident wave (Hz)
- H = magnetic field intensity (A/m)
- P = power (W)
- Q = local electromagnetic heat generation term (W/m^3)
- T = temperature ($^{\circ}$ C)
- t = time (s)
- $\tan \delta$ = loss tangent coefficient
- Z_H = wave impedance (Ω)
- Z_I = intrinsic impedance (Ω)









	(a) Case 2	(b) Case 3	(c) Case 4	(d) Case 5
Temperature Distribution				
Microwave Power Absorbed				
Conclusions	The optimal sample size and microwave frequency causes greater heating rates. A weak wavy behavior within the sample is formed	Heating pattern is not influenced by resonance. The wavy behavior within the sample is totally absent.	Heating pattern is not influenced by resonance and greater temperature takes place near the exposed surface. The wavy behavior within the sample is totally absent.	Heating pattern is influenced by resonance. The strong wavy behavior within the sample is formed.

Fig. 22 The heating characteristics for various heating conditions due to microwave energy for (a) case 2, (b) case 3, (c) case 4, (d) case 5. The darker shaded region represents the hot spot.

Greek Letters

- ϵ = permittivity (F/m)
- ϕ = porosity
- λ = wavelength (m)
- μ = magnetic permeability (H/m)
- v = velocity of propagation (m/s)
- ρ = density (kg/m^3)
- σ = electric conductivity (S/m)
- ω = angular frequency (rad/s)

Subscripts

- a = air phase
- l = liquid phase
- p = solid phase
- r = relative
- x, y, z = coordinates
- 0 = free space, initial condition

References

- [1] Ayappa, K. G., Davis, H. T., Crapiste, G., Davis, E. A., and Gordon, J., 1991, "Microwave Heating: An Evaluation of Power," *Chem. Eng. Sci.*, **46**, pp. 1005–1016.
- [2] Ayappa, K. G., Davis, H. T., Davis, E. A., and Gordon, J., 1992, "Two-Dimensional Finite Element Analysis of Microwave Heating," *AIChE J.*, **38**, pp. 1577–1592.
- [3] Saltiel, C., and Datta, A., 1997, "Heat and Mass Transfer in Microwave Processing," *Adv. Heat Transfer*, **30**, pp. 1–94.
- [4] Tada, S., Echigo, R., Kuno, Y., and Yoshida, H., 1998, "Numerical Analysis of Electromagnetic Wave in Partially Loaded Microwave applicator," *Int. J. Heat Mass Transfer*, **41**, pp. 709–718.
- [5] Ratanadecho, P., Aoki, K., and Akahori, M., 2001, "A numerical and Experimental Study of Microwave Drying Using a Rectangular Wave Guide," *Drying Technol.*, **19**, pp. 2209–2234.
- [6] Ratanadecho, P., Aoki, K., and Akahori, M., 2002, "Influence of Irradiation Time, Particle Sizes and Initial Moisture Content During Microwave Drying of Multi-Layered Capillary Porous Materials," *ASME J. Heat Transfer*, **124**, pp. 151–161.
- [7] Ratanadecho, P., Aoki, K., and Akahori, M., 2002, "Experimental Validation of a Combined Electromagnetic and Thermal Model for a Microwave Heating of Multi-Layered Materials Using a Rectangular Wave Guide," *ASME J. Heat Transfer*, **124**(5), pp. 992–996.
- [8] Basak, T., 2003, "Analysis of Resonances During Microwave Thawing of Slabs," *Int. J. Heat Mass Transfer*, **46**, pp. 4279–4301.
- [9] Basak, T., 2004, "Role of Resonances on Microwave Heating of Oil-Water Emulsions," *AIChE J.*, **50**, pp. 2659–2675.
- [10] Akkari, E., Chevallier, S., and Boillereaux, L., 2005, "A 2D Non-Linear 'Grey-Box' Model Dedicated to Microwave Thawing: Theoretical and Experimental Investigation," *Comput. Chem. Eng.*, **30**(2), pp. 321–328.
- [11] Ratanadecho, P., Aoki, K., and Akahori, M., 2002, "A Numerical and Experimental Investigation of the Modeling of Microwave Heating for Liquid Using a Rectangular Wave Guide (Effect of Natural convection and Electrical Conductivity)," *J. Turbomach.*, **26**(3), pp. 449–472.
- [12] Watson, A., 1968, "Curing of Concrete," *Microwave Power Engineering*, E. C. Okress, ed., Academic, New York.
- [13] Delia, G. B., Lai, S., and Pinna, M., 1994, "Microwaves for the Hyper-Accelerated Curing of Concretes," *Betonwerk Fertigteil-Tech./Concrete Pre-casting Plant and Technology*, **60**(12), pp. 87–93.
- [14] Dongxu, L., and Xuequan, W., 1993, "A Study on the Application of Vacuum Microwave Composite Dewatering Technique in Concrete Engineering," *Cem. Concr. Res.*, **24**, pp. 159–164.
- [15] Hutchison, J. T., Chang, H. M., Jennings, H. M., and Brodwin, M. E., 1991, "Thermal Acceleration of Portland Cement Mortars With Microwave Energy," *Cem. Concr. Res.*, **21**, pp. 795–799.
- [16] Leung, C. K., and Pheeraphan, T., 1995, "Very High Early Strength of Microwave Cured Concrete," *Cem. Concr. Res.*, **25**(1), pp. 136–146.
- [17] Leung, C. K., and Pheeraphan, T., 1995, "Microwave Curing of Portland Cement Concrete: Experimental Results and Feasibility for Practical Applications," *Constr. Build. Mater.*, **9**(2), 67–73.
- [18] Li, W., Ebadian, M. A., White, T. L., and Grubb, R. G., 1993, "Heat Transfer Within a Concrete Slab Applying the Microwave Decontamination Process," *ASME J. Heat Transfer*, **115**, pp. 42–50.
- [19] Mak, S. L., Sagoe-Crentsil, K. K., Taylor, A. H., and Ritchie, D., 1995, "Application of Microwave-Accelerated Processing in Cement and Concrete Technology," *Proceedings of 20th Conference on Our World in Concrete and Structures*, Vol. 15, C. T. Tan, ed., Otani, Singapore, Mar. 23–25, pp. 117–120.
- [20] Mak, S. L., Shapiro, O., and Son, T., 1998, "Accelerated Heating of Concrete With Microwave Curing," *Proceedings of the Fourth CANMET/ACI/JCI International Conference on Recent Advances in Concrete Technology*, Tokoshima, Japan, Jun. 7–11, pp. 531–542.
- [21] Wu, X., Dong, L., and Tang, M., 1987, "Microwave Curing Technique in Concrete Manufacture," *Cem. Concr. Res.*, **17**, pp. 205–210.
- [22] Perre, P., and Turner, W., 1997, "Microwave Drying of Softwood in an Oversized Waveguide," *AIChE J.*, **43**, pp. 2579–2595.
- [23] Zhao, H., and Turner, I. W., 2000, "The Use of a Coupled Computational Model for Studying the Microwave Heating of Wood," *J. Turbomach.*, **24**, pp. 183–197.
- [24] Ratanadecho, P., 2006, "The Simulation of Microwave Heating of Wood Using a Rectangular Wave Guide (Influence of Frequency and Sample Size)," *Chem. Eng. Sci.*, **61**(14), pp. 4571–4581.
- [25] American Society for Testing and Materials, 2006, *Annual Book of ASTM Standard Vol. 4, No. 02*, Philadelphia PA.
- [26] Von Hippel, A. R., 1954, *Dielectric Materials and Applications*, MIT, Boston.
- [27] Mak, S. L., Banks, R. W., Ritchie, D. J., and Shapiro, G., 2002, "Advances in Microwave Curing of Concrete," *Fourth World Congress on Microwave & Radio Frequency Applications*, Sydney, Australia, Sept. 22–26.
- [28] Ratanadecho, P., 2004, "The Theoretical and Experimental Investigation of Microwave Thawing of Frozen Layer Using Microwave Oven (Effects of Layered Configurations and Layered Thickness)," *Int. J. Heat Mass Transfer*, **47**, pp. 937–945.
- [29] Ratanadecho, P., Suwannapum, N., Chatveera, B., Atong, D., and Makul, N., 2008, "Development of Compressive Strength of Cement, Paste Under Accelerated Curing by Using a Continuous Microwave Belt Drier," *Mater. Sci. Eng., A*, **472**, pp. 299–307.

Full-Field Flow Measurements and Heat Transfer of a Compact Jet Impingement Array With Local Extraction of Spent Fluid

Andrew J. Onstad¹

e-mail: aonstad@stanford.edu

Christopher J. Elkins

Robert J. Moffat

John K. Eaton

Department of Mechanical Engineering,
Stanford University,
Stanford, CA 94305

Jet impingement cooling is widely used due to the very high heat transfer coefficients that are attainable. Both single and multiple jet systems can be used, however, multiple jet systems offer higher and more uniform heat transfer. A staggered array of 8.46 mm diameter impingement jets with jet-to-jet spacing of 2.34 D was examined where the spent fluid is extracted through one of six 7.36 mm diameter extraction holes regularly located around each jet. The array had an extraction area ratio (A_e/A_{jet}) of 2.23 locally and was tested with a jet-to-target spacing (H/D) of 1.18 jet diameters. Magnetic resonance velocimetry was used to both quantify and visualize the three dimensional flow field inside the cooling cavity at jet Reynolds numbers of 2600 and 5300. The spatially averaged velocity measurements showed a smooth transition is possible from the impingement jet to the extraction hole without the presence of large vortical structures. Mean Nusselt number measurements were made over a jet Reynolds number range of 2000–10,000. Nusselt numbers near 75 were measured at the highest Reynolds number with an estimated uncertainty of 7%. Large mass flow rate per unit heat transfer area ratios were required because of the small jet-to-jet spacing. [DOI: 10.1115/1.3109991]

Keywords: jet impingement cooling, heat transfer, magnetic resonance velocimetry, spent fluid

1 Introduction

Jet impingement cooling is widely used in applications ranging from paper manufacturing to the cooling of gas turbine blades because of the very high local heat transfer coefficients that are possible. Recently, interest has grown in the use of impingement cooling for high power electronics. While the use of single jet impingement results in nonuniform cooling, higher and more uniform mean heat transfer coefficients may be attained by dividing the total cooling flow among an array of smaller jets. Problems arise because the fluid, which has already impacted the target surface, or the “spent” fluid, from the central jets in the array interacts with the array’s outer jets producing a situation referred to as crossflow. The development of crossflow will reduce the outer jet’s cooling ability, decreasing the average heat transfer coefficient for the entire array. Kercher and Tabakoff [1] proposed a mean Nusselt number correlation for arrays of jets as a function of the Reynolds number, hole geometry, and the effect of spent fluid. Their analysis, however, involved graphical determination of the correlation coefficients. Florschuetz et al. [2] proposed another correlation in 1981 for both staggered and inline jet arrays. This correlation was of similar form to that of Kercher and Tabakoff [1], yet it included a parameter to account for the effect of crossflow.

The degradation of heat transfer due to crossflow is avoided in impingement cooled turbine blades by removing the spent fluid from the cooling cavity through film cooling holes located in the cooled target surface as shown in Fig. 1(a). This approach is not feasible in most other cooling applications including electronics cooling.

In this paper, an alternative approach is examined where the

spent fluid is removed locally to a plenum through extraction holes placed on the same surface as the exit of the impingement jets as shown in Fig. 1(b).

There is a large database of literature encompassing over 50 years of research on impingement heat transfer. In addition, several reviews exist examining both single and multiple jet impingements: most notably Martin [3], followed by Downs and James [4], Jambunathan et al. [5], Viskanta [6], and Han and Goldstein [7]. Although a large amount of literature does exist on both single and multiple jet impingements, relatively little published research has been done regarding multiple jet impingement with local extraction of the spent air.

Hollworth and co-workers [8,9] used thermocouples to examine the removal of spent fluid through holes located on an isothermal target surface similar to the gas turbine blade geometry shown in Fig. 1(a). They found by using the exhaust holes that they could increase the average heat transfer rate by 20–30% over the same array of impingement jets with no local extraction. Using a similar geometry, Rhee et al. [10] examined the effect of the exhaust hole pattern on the target surface using a naphthalene sublimation method. They concluded the geometric configuration with the largest ratio of exhaust area to jet area (A_e/A_{jet}) consistently achieved higher heat transfer coefficients at every separation distance (H/D) tested.

The second possible location for the exhaust holes is on the surface of the impingement jet exit (Fig. 1(b)). In 1994, Huber and Viskanta [11] examined the effect of separation distance (H/D) on this type of geometry by a thermochromic liquid crystal technique. The average heat transfer rate for a square array was found to increase approximately 10% over an array with no local extraction for small separation distances ($0.25 \leq H/D \leq 1$). Although their heat transfer rates were similar for an extracted and a non-extracted array near $H/D=1$, they conceded that increased heat transfer would be expected at separation distances less than 2 ($H/D \leq 2$) for larger arrays where crossflow will develop. Rhee

¹Corresponding author.

Manuscript received August 18, 2008; final manuscript received February 18, 2009; published online June 4, 2009. Review conducted by Minking Chyu.

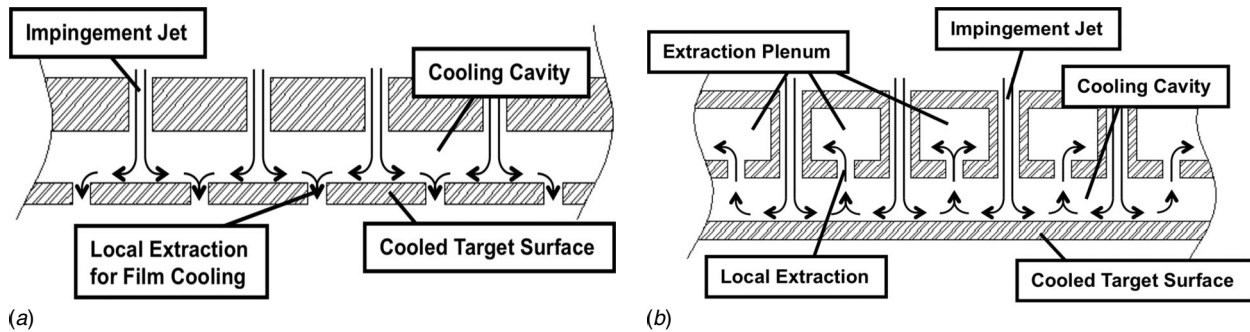


Fig. 1 Two different types of impingement cooling with local extraction of spent fluid

et al. [12] also studied the effects of separation distance on a staggered geometry in 2003 by naphthalene sublimation. They found for separation distances less than 2 that the average transport coefficient increased when local extraction was implemented. They reported a 20% increase in mean transport at $H/D=1$, and nearly a 60% increase at $H/D=0.5$. The effect of jet-to-jet spacing on local and mean transport coefficients was also studied by Huber and Viskanta [13]. They found the mean transport coefficient increased with decreasing jet-to-jet spacing for the three configurations tested ($Z_n/D=4,6,8$) although the smallest spacing required the greatest mass flow rate at the same Reynolds number.

Very high heat flux electronics cooling applications are likely to require impingement geometries, which are very compact thereby increasing the array's overall ability to carry away heat. This can be accomplished by reducing the interjet spacing (Z_n/D), which maximizes the number of jets impacting the target surface. The geometry studied by Rhee et al. [12] had an interjet spacing of 6, which is too large for high heat flux applications. Huber and Viskanta [11,13] studied the effect of jet-to-jet spacing, however, their study stopped at $Z_n/D=4$.

The performance of very compact arrays with small jet-to-jet spacing is expected to be significantly degraded by crossflow. Thus a geometry, which incorporates local extraction with a large exhaust area ratio (A_e/A_{jet}), is preferred to maintain a high average transport coefficient. With this in mind, the purpose of this research is to experimentally visualize and quantify the mean flow field of a compact impingement geometry ($Z_n/D=2.34$) with local extraction on the impingement plane ($A_e/A_{jet}=2.23$) by way of magnetic resonance velocimetry (MRV). The average convective heat transfer coefficient is also measured in the same flow geometry as a function of the jet Reynolds number ranging from $Re_D=2000$ to $Re_D=10,000$.

2 Experimental Apparatus and Techniques

2.1 Description of Geometry.

The present injection and extraction hole geometries are illustrated in Fig. 2. The working fluid is injected through a staggered array of 36 8.46 mm diameter injection holes with a jet-to-jet spacing of 2.34 diameters ($Z_n/D=2.34$). Around each interior injection hole are 6 regularly spaced 7.29 mm diameter extraction holes giving a ratio of exhaust area to jet area of 2.23 ($A_e/A_{jet}=2.23$) when calculated on a repeating unit cell. This hole geometry allows for local extraction in the geometric center between any two adjacent injection holes in the array. A target distance of 1.18 injection diameters was used ($H/D=1.18$).

The apparatus consists of three major components: inlet manifold, impingement array, and extraction plenum. Figure 3(a) illustrates the entire geometry where the working fluid enters from a 0.5 m long and 50.8 mm diameter development pipe into the inlet manifold. The inlet manifold serves two purposes. First, it changes the 50.8 mm diameter circular cross section to a square (152×152 mm²) cross section. Second, the manifold serves to

turn the flow 90 deg and distribute the flow across the injection array. To create a uniform flow distribution, the upper wall of the manifold is tapered, as shown in Fig. 3(b). The idea is that a uniform pressure distribution is established along the tapered wall resulting in a uniform flow distribution across the entire array of injection holes, which lie directly under the inlet manifold. Upon entering the injection holes, the flow travels 28.6 mm through the extraction manifold in individual tubes exiting in the cooling cavity as an array of jets. Figure 4 schematically illustrates how the jets pass through the extraction plenum into the cooling cavity. The jets impinge on the target surface producing a primary stagnation zone under each jet. As a consequence of the stagnation, the flow turns away from the jet centerline producing an axisymmetric radial wall jet. This wall jet then interacts with the wall jets from the adjacent impingement jets in the array resulting in a secondary annular stagnation region on the target surface surrounding each impingement jet. The stagnation pressure in this region pushes the fluid up and through the extraction holes located between the injection holes into the extraction plenum. In this plenum, the extracted fluid then flows around the cylindrical tubes of the impingement jets and makes its way to one of four 25.4 mm diameter tubes located at the corners of the plenum. These four extraction tubes converge and the working fluid is exhausted through a 31.8 mm diameter tube.

2.2 Magnetic Resonance Velocimetry.

MRV was used to measure the 3D mean velocity field within an array of staggered impingement jets with local extraction. MRV is a noninvasive

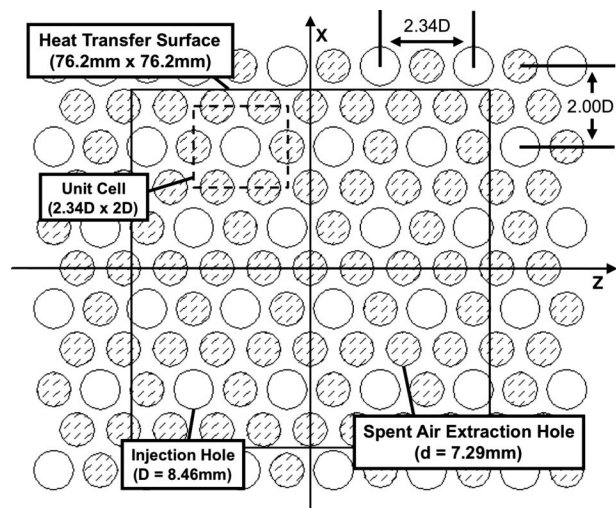


Fig. 2 View of the jet impingement geometry from the jet impingement exit plane. The geometry is a staggered array of 36 8.46 mm diameter injection holes surrounded by 6 7.29 mm diameter extraction holes.

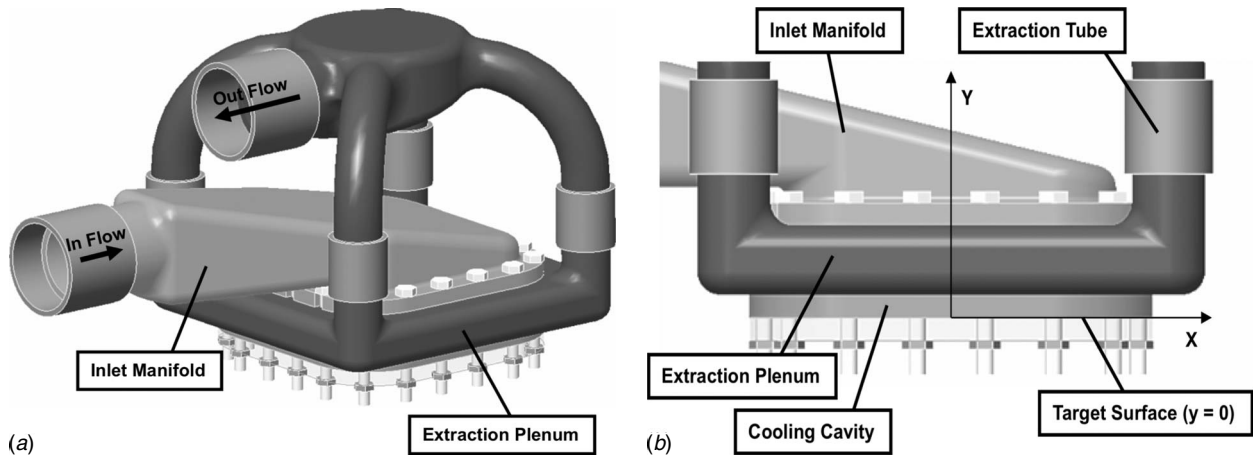


Fig. 3 Impingement apparatus. The working fluid enters through the inlet manifold and progresses through the impingement array. The fluid leaves the array entering the extraction plenum where it passes through one of four tubes before it is exhausted.

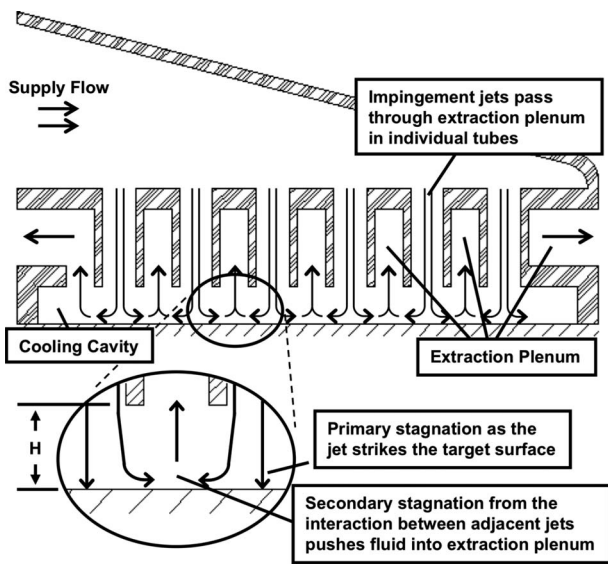


Fig. 4 Cross section of the jet impingement geometry. The impinging jets pass in tubes through the extraction plenum striking the target surface creating primary stagnation regions. The fluid turns radially outward and interacts with adjacent jets creating a secondary stagnation zone. The fluid is then exhausted through spent fluid holes into the extraction plenum.

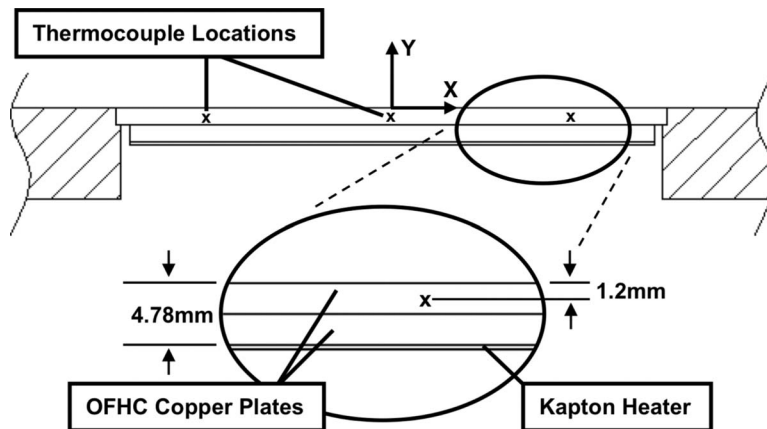


Fig. 5 Cross-sectional view of the heat transfer surface

experimental technique, which makes use of the nuclear magnetic resonance (NMR) properties of hydrogen atoms bound in water. The technique is capable of measuring the three-component mean velocity field inside of complex geometries without the use of flow tracers or requiring optical access [14].

The impingement apparatus was manufactured by stereolithography (SLA) to facilitate measurements in a 1.5T General Electric Signa CV/i magnetic resonance imaging (MRI) system. Water was used as the working fluid. To increase the water's signal strength, a gadolinium-based contrast agent (Omniscan, Nycomed, Inc., Zurich, Switzerland) was added at 0.5% concentration. A centrifugal pump (TE-6MD-HC, Little Giant, Oklahoma City, OK) moved the water from a large holding tank through the impingement apparatus, located inside the magnet bore, and back to the tank where the volume flow rate was measured by a paddle wheel flow meter with estimated uncertainty of 4%. The experimental setup is restricted due to the MRI's large magnetic field and its sensitivity to radio frequency (RF) noise. The pump was placed approximately 3 m from the magnet, and no metallic parts were used in the flow loop. The MR images were checked and found to have negligible RF noise produced by the pump.

The mean velocity field was determined by averaging 16 separate experiments at $Re_D=2600$ (37.5 ± 1.5 l/min) and $Re_D=5300$ (76 ± 3 l/min). The measurements were taken with an imaging volume of $240 \times 64 \times 240$ mm³ (x, y, z) and a spatial reso-

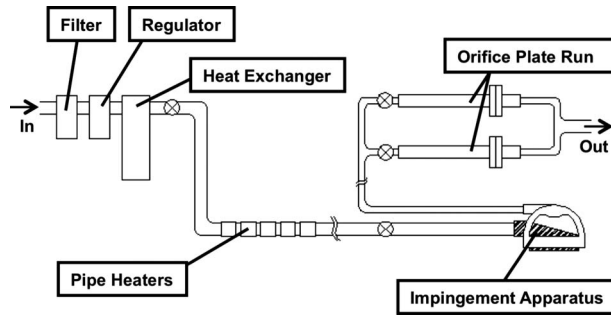


Fig. 6 Laboratory air supply schematic

lution of approximately 1 mm^3 . Based on previous studies by the authors, the maximum uncertainty in individual mean velocity vector measurements is less than 10% [15].

2.3 Average Heat Transfer. Average heat transfer measurements were carried out on the same flow geometry with the addition of a heat transfer surface used to supply a constant wall temperature at the target surface plane ($y=0$). The heat transfer surface (Fig. 5) consisted of a $76.2 \times 76.2 \times 2.4 \text{ mm}^3$ oxygen-free high thermal conductivity (OFHC) copper plate mounted in a Plexiglas frame. Five k -type thermocouples were epoxied into holes drilled from the backside of the plate to 1.2 mm beneath the target surface plane with high conductivity epoxy. One thermocouple was located in the center of the plate ($x=0, z=0$) and the other four were in each of the four quadrants surrounding the origin ($x = \pm 25.7 \text{ mm}, z = \pm 24.8 \text{ mm}$). A kapton heater (Omega, KH-303/10), fixed to a second OFHC copper plate measuring $72.4 \times 72.4 \times 2.4 \text{ mm}^3$, was attached to the back of the first copper plate to supply the necessary heat flux to the heat transfer surface. Power is supplied to the heater by a 110V variable AC transformer. Heater voltage drop is measured by a digital multimeter (8842A, Fluke, Everett, WA) and the current measured using a wattmeter (2101, Valhalla Scientific, San Diego, CA), which measures both the transformer voltage and current, wired in series with the load.

Air from a rotary screw compressor (SSR-XF-400, Ingersoll Rand, Montvale, NJ) is used as the working fluid for the heat transfer measurements and is fed from a large holding tank to the test cell via the route shown in Fig. 6. The air passes through a filter (F18-C00-A3DA, Norgren, Littleton, CO) and a pressure regulator (R18-C00-RNXA, Norgren, Littleton, CO) before encountering two subsystems used to control the mainstream inlet temperature. A chilled water shell-and-tube heat exchanger (1383, CMS Heat Transfer Division Inc., Bohemia, NJ) was followed by a series of pipe heaters (STB3A1J6, Watlow, Los Gatos, CA) powered by a 110 V variable ac transformer. During operation, the chilled water flow rate and the power to the heaters were controlled to hold inlet temperature fluctuations to within $\pm 0.1^\circ\text{C}$ of the desired inlet temperature.

The air passed through a 0.5 m long and 50.8 mm diameter development pipe and into the inlet manifold of the impingement apparatus. The air inlet temperature T_{in} was measured immediately upstream of the inlet manifold by a 1.57 mm diameter k -type thermocouple (KMQSS-062E-6, Omega Engineering, Stamford, CT) immersed parallel to the flow. The air temperature was assumed to be uniform at this inlet station because the flow passed through several meters of isothermal supply pipe and multiple flow turning and control elements. Upon leaving the impingement apparatus the air exit temperature T_{exit} was measured with a similar k -type thermocouple immersed in the flow. The air mass flow rate was then measured by one of two identical 52.5 mm bore orifice plate meters plumbed in parallel. A combination of three different square-edged orifice plates was used (19.05 mm, 25.40 mm, and 35.00 mm) to achieve a range of Reynolds numbers from

$Re_D=2000$ to $Re_D=10,000$. Uncertainty in the mass flow rate and Reynolds number were both estimated to be less than 0.5% based on a 95% confidence interval using the method described by Kline and McClintock [16].

At each Reynolds number tested, the inlet temperature was stabilized to 23°C and power was supplied to the heat transfer surface to raise the wall temperature 30°C above the inlet temperature. The wall temperature T_{wall} was determined by averaging the five individual heat transfer surface thermocouples. During the experiment, these five individual thermocouples were found to deviate less than 0.5°C , thus the average was believed to be a good representation of the mean wall temperature. Once steady, 50 temperature measurements were made at each thermocouple. In order to accomplish these measurements, each thermocouple was connected to a GPIB controlled multiplexor (3497A, Hewlett Packard, Palo Alto, CA) where the voltage was read by a GPIB controlled digital multimeter (8842A, Fluke, Everett, WA). Each thermocouple measurement was referenced to an ice bath with an assumed temperature of 0.01°C . The uncertainty in the temperature measurements, utilizing a 95% confidence interval, was approximated at $\pm 0.2^\circ\text{C}$.

The Nusselt number Nu in Eq. (1) was used to assess the heat transfer performance of the impingement apparatus.

$$Nu = \frac{(\dot{q} - \dot{q}_{loss})D}{k_{Air}A_{HT}(T_{wall} - T_{in})} \quad (1)$$

The entire apparatus was wrapped in 25.4 mm of fiberglass insulation to minimize heat losses. The heater power lost through conduction, \dot{q}_{loss} in Eq. (1), was estimated by a transient experiment under normal experimental conditions. The apparatus was stabilized at $Re_D=10,000$, simultaneously the air supply and the heater power were turned off and the heat transfer surface temperature T_{wall} was measured in time. A numerical time derivative of the wall temperature was computed by a central difference approximation. The value of the derivative is used at short times in conjunction with Eq. (2) to estimate the power lost through conduction.

$$\dot{q}_{loss} = (\rho_{HT}V_{HT})C_{p,HT} \frac{dT_{wall}}{dt} \quad (2)$$

The transient experiment was repeated multiple times resulting in a conduction loss estimate of 2 W or 5% of the input power at $Re_D=10,000$. The wall temperature is consistent throughout all of the heat transfer experiments, thus, it is assumed the conduction losses are also constant. Uncertainty in the conduction loss is estimated conservatively at $\pm 50\%$, resulting in a loss estimate of $2 \text{ W} \pm 1 \text{ W}$. Subsequently, uncertainty in the Nusselt number, determined by the method described by Kline and McClintock [16], was estimated at 7% based on a 95% confidence interval.

3 Results and Discussion

3.1 Magnetic Resonance Velocimetry. The three-component mean velocity field for the impingement apparatus was measured using MRV at $Re_D=2600$ and $Re_D=5300$. Although two separate Reynolds numbers were tested, no significant difference in the structure of the mean velocity field was measured. Subsequently, only results from the higher Reynolds number $Re_D=5300$ will be shown.

A full-field cross section of the impingement array is shown in Fig. 7. Time averaged velocity magnitude contours (in m/s) are illustrated for the (z - y) plane taken near the center of the array ($x=-8.46 \text{ mm}$). The flow started at the top of the frame in the inlet manifold, accelerating into the injection tubes to a peak velocity in the vena-contracta near 1 m/s. At the entrance of the outer jets, a small flow separation region was present as the flow accelerates into the injection tube. Shortly downstream, the flow in each injection tube decelerated and a well mixed jet exited into

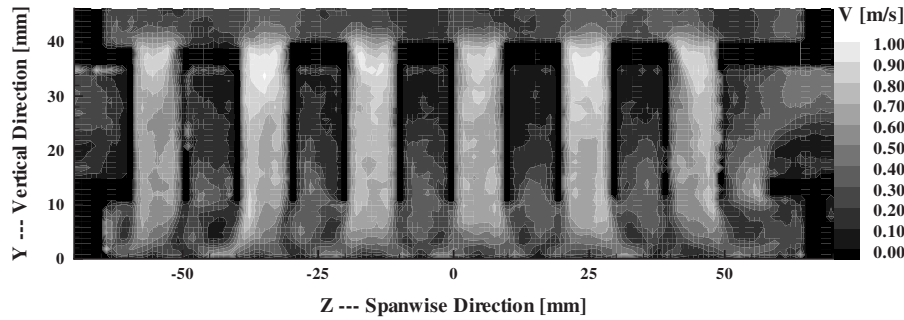


Fig. 7 Velocity magnitude contours (in m/s) illustrating the full array spanwise cross section (y - z) at $Re_D=5300$

the cooling cavity at $y=10$ mm. Once the jets emerged into the cooling cavity they began to spread and eventually impacted the target surface at $y=0$.

A magnified view of the flow within the cooling cavity is shown in Fig. 8. Contours of velocity magnitude (m/s) and the in-plane (z - y) velocity vectors are displayed for the identical plane shown in Fig. 7. Here, the jet was clearly spreading until it impacted the target surface forming the primary stagnation on the jet centerline. A radial wall jet formed on the target surface and accelerated away from the jet centerline. This wall jet then interacted with the adjacent wall jet and created a secondary stagnation zone directly between the two impingement jets. These secondary stagnation regions created an upwelling of the fluid forcing it out of the cooling cavity through the extraction hole located between the two impingement jets. In this plane, there was little sign of a vortical structure around the jet. The flow transitioned very smoothly from the jet to the extraction plenum.

This smooth transition is not present in Fig. 9. Here, the jet shown at $z=5$ mm in Fig. 8 is shown in an orthogonal plane (x - y). Again, the jet emerged at $y=10$ mm and impacted the target surface at $y=0$ mm, however, the primary stagnation was not found on the jet centerline but was shifted approximately 2 mm in the negative x direction. A small counterclockwise rotating vortex is clearly visible on the positive x side of the jet. On the opposite side, a larger clockwise rotating vortex was present. Upon further inspection, this structure of two counter-rotating vortices in the x - y plane was present around each jet in the array. The vortices

are attributed to a slight crossflow, which developed in the cooling cavity. The mean crossflow velocity to the jet velocity ratio was calculated at 8%. The crossflow is a consequence of the taper of the inlet manifold ending in a radius (Figs. 3(b) and 4) and not simply tapering to zero. This radius resulted in a higher static pressure at the downstream (positive x) jet locations inducing a higher mass flow rate in those respective jets. Figure 10 illustrates the variation by plotting the nondimensional mass flow rate through each of the 36 jets in symbols, and the spanwise mean in a solid line versus the streamwise array location. The inlet flow enters from the $-x$ direction and the inlet manifold radius is located at $x=76$ mm. The figure shows higher jet mass flow rates on the downstream side of the array. The jet mass flow rate decreases with decreasing streamwise location and the variation is estimated at 15% of the bulk average mass flow rate. The downstream jets also show less spanwise variation in mass flow rate than the slower upstream jets. The spanwise variation in the slower upstream jets is attributed to two large vortices present in the inlet manifold. Figure 11 illustrates the two vortices in an x - z plane, 10 mm above the start of the impingement jet tubes. The strength of the vortices was examined by comparing the dynamic pressure of the recirculating fluid to the dynamic pressure lost by the fluid due to acceleration through the jets. The vortical dynamic pressure was found to be 11% of the pressure lost due to jet acceleration. The presence of these structures does influence the jet mass flow rate on the upstream side of the array as seen in the spanwise variation, yet they are not strong enough to significantly

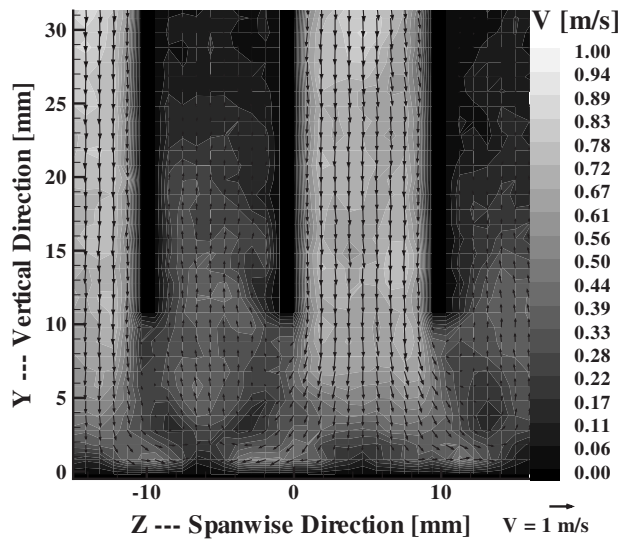


Fig. 8 Velocity magnitude contours in m/s and in-plane, (z - y), velocity vectors zoomed in to show the flow structure inside the cooling cavity at $Re_D=5300$

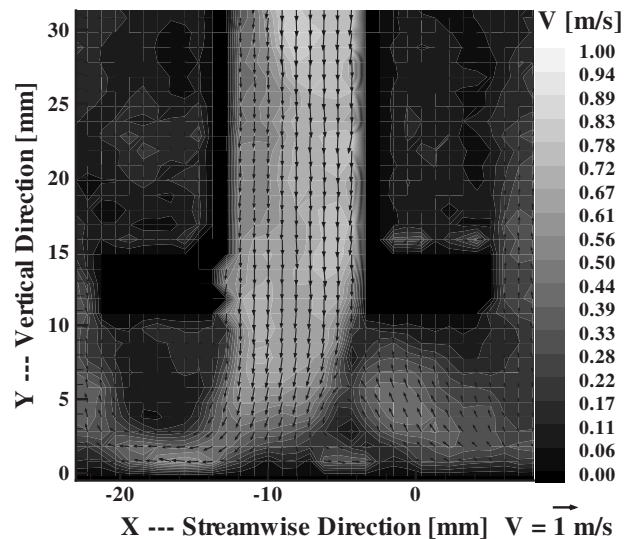


Fig. 9 Velocity magnitude contours in m/s and in-plane (x - y), velocity vectors shown for the plane orthogonal to that shown in Fig. 8

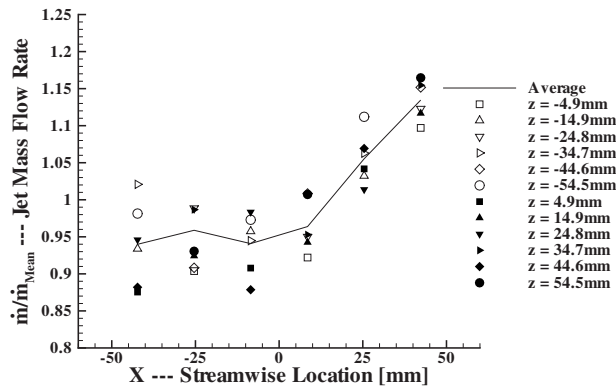


Fig. 10 Nondimensional mass flow rate through each individual jet. Jets located at identical z locations are plotted as a group with the same symbol indicating the spanwise variation in jet mass flow rate.

alter the jet mass flow rates.

Figures 12–14 illustrate contours of mean velocity magnitude (m/s) in flow planes (x - z) parallel to target plane at $Re_D=5300$. Figure 12 was measured at $y=9.5$ mm ($y/H=0.95$) or immediately beneath where the jets enter the cooling cavity. The jet velocities were fairly uniform in the spanwise (x) direction with magnitudes near 0.7 m/s. The figure shows the slight nonuniformity in jet velocity in the streamwise (x) direction. Figure 12 does not show the full 15% variation because it is showing the flow field only above the heat transfer surface, which lies inside the outermost rows of impingement jets, where the effect is most prevalent.

In between the jets, local regions of higher velocity (0.2–0.3 m/s) were measured. The velocity in this location is in the opposite direction as that of the impingement jets and corresponds to the location of the extraction holes. This region of moderate velocity is also present in Fig. 8 where it shows the spent fluid entering the extraction plenum.

The velocity magnitude in Fig. 13 was measured at $y=5$ mm ($y/H=0.5$), or midway between the target surface and the start of the impingement jets. Here, each jet has begun to spread out as well as slow down to approximately 0.5 m/s as can be seen in Fig.

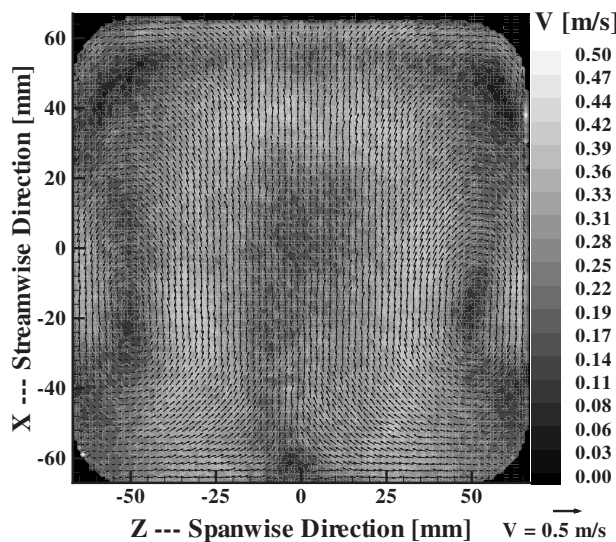


Fig. 11 Contours of velocity magnitude (m/s) and in-plane x - z vectors showing the flow field 10 mm upstream of the impingement jets

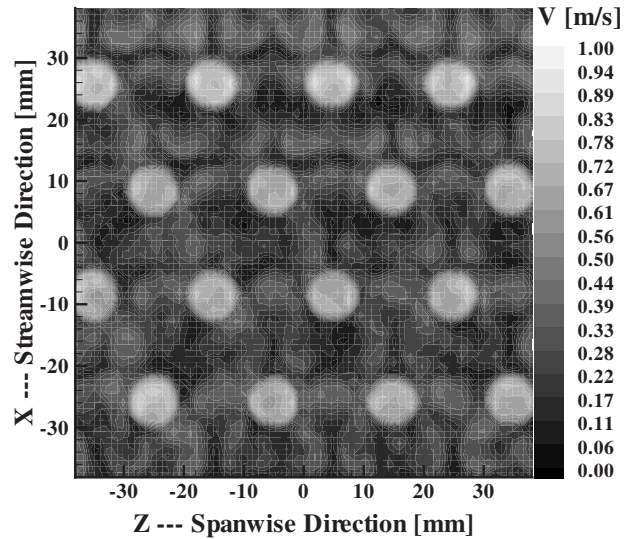


Fig. 12 Contours of velocity magnitude (m/s) in the x - z plane measured at $y=9.5$ mm, or at the start of the impingement jets

8. Regions of nearly quiescent flow can be seen around each jet, while an interconnected region of faster moving flow separates each jet. This interconnected region is moving in the opposite direction of the jet and is the result of the interaction of the jets as they spread out on the target surface. In addition, the jet shape has become elliptical. This change in shape is attributed to the variation in mass flow rate introduced by the inlet manifold.

The flow immediately above the target surface ($y/H=0.05$) is shown in Fig. 14. The primary stagnation region can be readily seen where each jet impacts the target surface. Around each primary stagnation, a nearly axisymmetric radial wall jet is established along the target surface. The effect of the crossflow is not easily noticed in the shape of the wall jets although it is easily visible a few millimeters away (Fig. 13). The wall jet accelerates outward to a velocity near 0.5 m/s and subsequently decelerates to form a secondary stagnation region. The secondary stagnation region surrounds each jet in a region closely resembling a hexagon. This stagnation creates the upwelling of flow seen in Fig. 13.

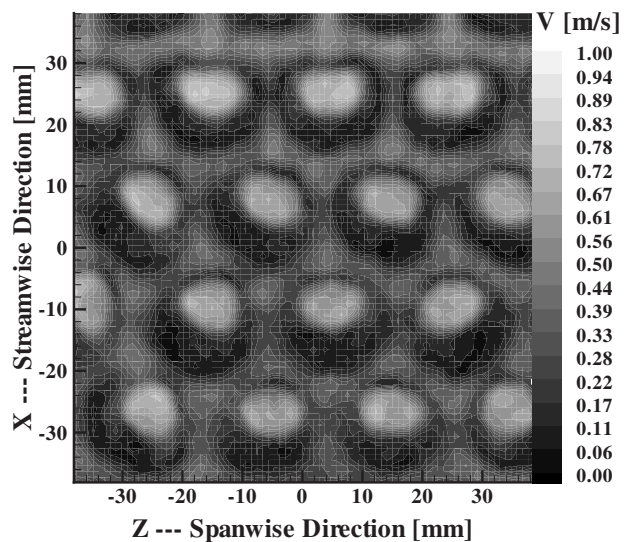


Fig. 13 Contours of velocity magnitude (m/s) in the x - z plane measured at $y=5$ mm, or at the midplane of the impingement jet

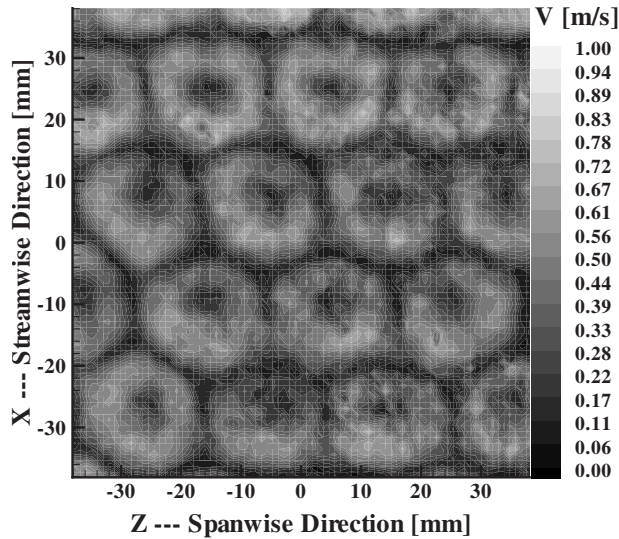


Fig. 14 Contours of velocity magnitude (m/s) in the x - z plane measured immediately above the target surface

3.2 Average Heat Transfer. Average heat transfer measurements were made for jet Reynolds numbers ranging from 2000 to 10,000. Figure 15 shows the average Nusselt number as a function of jet Reynolds number for the array along with a power law approximation to the data. The measured Nusselt number is also compared with correlations provided by Florschuetz et al. [2] and Martin [3]. The correlation by Martin [3] considers the geometry, however it does not account for any crossflow. Florschuetz et al. [2] considered both the geometry and crossflow and are shown for three different crossflow-to-jet velocity ratios: 0%, 7.5%, and 15%.

At low Reynolds numbers, the correlation of Florschuetz et al. [2] using a crossflow-to-jet ratio of 7.5–15% does a reasonable job of capturing the mean Nusselt number. The crossflow-to-jet velocity ratio for the array tested was calculated at 8%. With increasing Reynolds number, however, the correlation increases too quickly resulting in an overprediction of the measured Nusselt number,

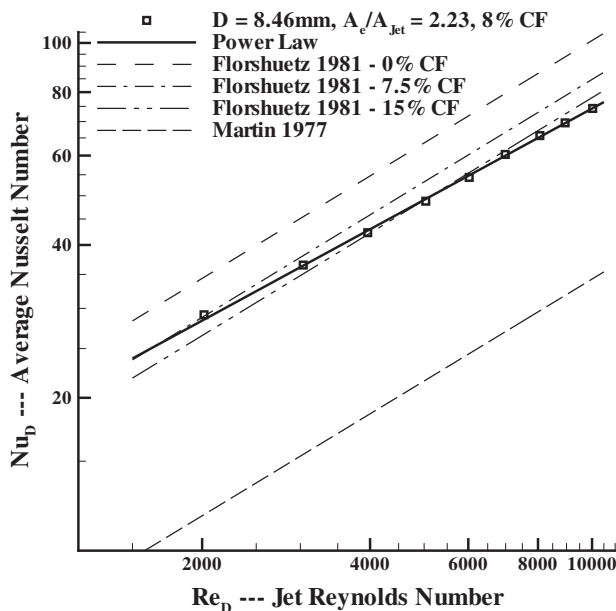


Fig. 15 Average Nusselt number as a function of the jet Reynolds number

nearly 15% at $Re_D=10,000$. Although the Reynolds number dependence of the correlation is a bit strong, it does suggest the heat transfer rates measured could be increased by nearly 20% if the inlet manifold was redesigned to eliminate the cooling cavity crossflow, as illustrated by the 0% crossflow ratio curve.

Martin's [3] correlation underpredicts the Nusselt number throughout the range of the Reynolds numbers tested. In addition, its functional relationship with Reynolds number increases to a similar power to that of Florschuetz et al. [2], which is greater than the 0.6 power for the tested array. The geometry tested does not fit within the range of geometric parameters provided by Martin [3], $0.004 \leq A_{jet}/A_{HT,Unit} \leq 0.04$ and $2 \leq H/D \leq 12$, or in the jet spacing parameters provide by Florschuetz et al. [2], $5 \leq Z_n/D \leq 10$ and $4 \leq X_n/D \leq 8$. Because the geometry lies outside of the range of validity for the two correlations, it is not expected they would capture the behavior of very compact impingement arrays.

The small interjet spacing ($Z_n/D=2.34$) continued the trend reported by Huber and Viskanta [13] of an increasing mean Nusselt number with decreasing jet-to-jet spacing. This configuration showed an estimated 10% improvement in Nusselt number over their most compact array ($Z_n/D=4$). The ratio of jet area to heat transfer surface area (A_{jet}/A_{HT}) of this array, however, has increased by nearly a factor of 3 over the array tested by Huber and Viskanta [13]. At $Re_D=10,000$, this increase in jet area results in a mass flow rate requirement per heat transfer area of nearly two times that of their most compact geometry.

Decreasing the jet-to-jet spacing has been shown to decrease the peak local Nusselt number in the primary stagnation region [13]. However, decreasing the jet-to-jet spacing also increases the mean Nusselt number of the entire array by increasing the area for primary stagnation heat transfer and decreasing the area under the wall jets establishing more uniform heat transfer across the entire array.

4 Conclusion

We have shown quantitative flow measurements of the full 3D mean velocity field within a compact array of impinging jets with local extraction. Although the spatially resolved flow field was measured at two different Reynolds numbers, little difference was measured in the structure of the flow field. An appreciable crossflow, a crossflow-to-jet velocity ratio of 8%, was measured inside the cooling cavity of the array. This crossflow established asymmetric counter-rotating vortices upstream and downstream, relative to the crossflow direction, of each impingement jet. In the transverse direction, no indication of the presence of the vortical structure was measured, a smooth transition from the jet through the cooling cavity was observed. The presence of the crossflow displaced the center of the primary stagnation region from the jet centerline. The presence of the crossflow was not easily seen very close ($y \sim 1$ mm ($y/H=0.05$)) to the target surface. However its presence was clear at greater distances, approximately 2–4 mm ($y/H=0.2$ to $y/H=0.4$).

The mean Nusselt number was obtained as a function of jet Reynolds number. The small jet-to-jet spacing of the impingement array enabled a large Nusselt number by increasing the area encompassed by primary stagnation heat transfer. This had two effects: (1) The mass flow requirement per heat transfer area at a given Reynolds number increased because more jets are used to cool the surface, and (2) although peak Nusselt numbers decrease with decreasing jet-to-jet spacing [13], the mean Nusselt number improves because, locally, the heat transfer is more uniform. Comparison to previous empirical work by Florschuetz et al. [2] suggests improvement in heat transfer rates is possible through the elimination of the cooling cavity crossflow.

Nomenclature

A_e = exhaust area, m^2
 A_{jet} = jet area, m^2

A_{HT} = heat transfer surface area, m^2
 H = jet impingement length, mm
 D = impingement jet diameter, mm
 d = extraction hole diameter, mm
 Z_n = jet-to-jet spacing, mm
 X_n = streamwise row-to-row jet spacing, mm
 Re_D = Reynolds number based on the jet diameter,
 $\rho V_{jet} D / \mu$
 V_{jet} = bulk jet velocity, m/s
 ρ = bulk fluid material density, kg/m^3
 ρ_{HT} = bulk heat transfer surface density, kg/m^3
 μ = bulk material dynamic viscosity, Pa s
 y = vertical direction, normal to the target surface,
mm
 x = streamwise direction, along the target surface,
mm
 z = spanwise direction, along the target surface,
mm
 T_{in} = fluid temperature measured at the apparatus
inlet, $^{\circ}C$
 T_{exit} = fluid temperature measured at the apparatus
exit, $^{\circ}C$
 T_{wall} = average heat transfer surface temperature, $^{\circ}C$
 Nu = average Nusselt number on the heat transfer
surface, hD/k
 \dot{q} = heat flux supplied to the heat transfer surface,
W
 \dot{q}_{loss} = heat flux lost from the heat transfer surface by
conduction, W
 k = thermal conductivity, W/mK
 V_{HT} = volume of the heat transfer surface, m^3
 $C_{p,HT}$ = Specific heat capacity of the heat transfer sur-
face, J/kgK

References

- [1] Kercher, D. M., and Tabakoff, W., 1970, "Heat Transfer by a Square Array of Round Air Jets Impinging Perpendicular to a Flat Surface Including the Effect of Spent Air," *ASME J. Eng. Power*, **92**(1), pp. 73–82.
- [2] Florschuetz, L. W., Truman, C. R., and Metzger, D. E., 1981, "Streamwise Flow and Heat Transfer Distributions for Jet Array Impingement With Cross-flow," *ASME J. Heat Transfer*, **103**, pp. 337–342.
- [3] Martin, H., 1977, "Heat and Mass Transfer Between Impinging Gas Jets and Solid Surfaces," *Adv. Heat Transfer*, **13**, pp. 1–60.
- [4] Downs, S. J., and James, E. H., 1987, "Jet Impingement Heat Transfer — A Literature Survey," *ASME Paper No. 87-HT-35*.
- [5] Jambunathan, K., Lai, E., Moss, M. A., and Button, B. L., 1992, "A Review of Heat Transfer Data for Single Circular Jet Impingement," *Int. J. Heat Fluid Flow*, **13**(2), pp. 106–115.
- [6] Viskanta, R., 1993, "Heat Transfer to Impinging Isothermal Gas and Flame Jets," *Exp. Therm. Fluid Sci.*, **6**(2), pp. 111–134.
- [7] Han, B., and Goldstein, R. J., 2001, "Jet-Impingement Heat Transfer in Gas Turbine Systems," *Ann. N. Y. Acad. Sci.*, **934**, pp. 147–161.
- [8] Hollworth, B. R., and Berry, R. D., 1978, "Heat Transfer From Arrays of Impinging Jets With Large Jet-to-Jet Spacing," *ASME J. Heat Transfer*, **100**, pp. 352–357.
- [9] Hollworth, B. R., and Dagan, L., 1980, "Arrays of Impinging Jets With Spent Fluid Removal Through Vent Holes on the Target Surface, Part 1: Average Heat Transfer," *ASME J. Eng. Power*, **102**, pp. 994–999.
- [10] Rhee, D. H., Choi, J. H., and Cho, H. H., 2003, "Heat (Mass) Transfer on Effusion Plate in Impingement/Effusion Cooling Systems," *J. Thermophys. Heat Transfer*, **17**(1), pp. 95–102.
- [11] Huber, A. M., and Viskanta, R., 1994, "Convective Heat Transfer to a Confined Impinging Array of Air Jets With Spent Air Exits," *ASME J. Heat Transfer*, **116**(3), pp. 570–576.
- [12] Rhee, D. H., Yoon, P. H., and Cho, H. H., 2003, "Local Heat/Mass Transfer and Flow Characteristics of Array Impinging Jets With Effusion Holes Ejecting Spent Air," *Int. J. Heat Mass Transfer*, **46**(6), pp. 1049–1061.
- [13] Huber, A. M., and Viskanta, R., 1994, "Effect of Jet-Jet Spacing on Convective Heat-Transfer to Confined, Impinging Arrays of Axisymmetric Air Jets," *Int. J. Heat Mass Transfer*, **37**(18), pp. 2857–2869.
- [14] Elkins, C. J., and Alley, M. T., 2007, "Magnetic Resonance Velocimetry: Applications of Magnetic Resonance Imaging in the Measurement of Fluid Motion," *Exp. Fluids*, **43**(6), pp. 823–858.
- [15] Elkins, C. J., Markl, M., Iyengar, A., Wicker, R., and Eaton, J. K., 2004, "Full-Field Velocity and Temperature Measurements Using Magnetic Resonance Imaging in Turbulent Complex Internal Flows," *Int. J. Heat Fluid Flow*, **25**(5), pp. 702–710.
- [16] Kline, S. J., and McClintock, F. A., 1953, "Describing Uncertainty in Single-Sample Experiments," *Mech. Eng. (Am. Soc. Mech. Eng.)*, **75**(1), pp. 3–8.

Heat Transfer and Thermodynamic Analyses of Some Typical Encapsulated Ice Geometries During Discharging Process

David MacPhee¹

e-mail: david.macphee@uoit.ca

Ibrahim Dincer

e-mail: ibrahim.dincer@uoit.ca

Faculty of Engineering and Applied Science,
University of Ontario Institute of Technology,
2000 Simcoe Street North,
Oshawa, ON, L1H 7K4, Canada

This study deals with the process of melting in some typical encapsulated ice thermal energy storage (TES) geometries. Cylindrical and slab capsules are compared with spherical capsules when subjected to a flowing heat transfer fluid (HTF). The effect of inlet HTF temperature and flow rate as well as the reference temperatures are investigated, and the resulting solidification and melting times, energy efficiencies, and exergy efficiencies are documented. Using ANSYS GAMBIT and FLUENT 6.0 softwares, all geometries are created, and the appropriate boundary and initial conditions are selected for the finite volume solver to proceed. Sufficient flow parameters are monitored during transient solutions to enable the calculation of all energy and exergy efficiencies. The energetically most efficient geometric scenario is obtained for the slab geometry, while the spherical geometry energetically achieves the highest efficiencies. The difference between the two results is mainly through the accounting of entropy generation and exergy destroyed, and the largest mode of thermal exergy loss is found to be through entropy generation resulting from heat transfer accompanying phase change, although viscous dissipation is included in the analysis. All efficiency values tend to increase with decreasing HTF flow rate, but energetically the best scenario appears to be for the spherical capsules with low inlet HTF temperature. Energy efficiency values are all well over 99%, while the exergy efficiency values range from around 72% to 84%, respectively. The results indicate that energy analyses, while able to predict viscous dissipation losses effectively, cannot correctly quantify losses inherent in cold TES systems, and in some instances predict higher than normal efficiencies and inaccurate optimal parameters when compared with exergy analyses. [DOI: 10.1115/1.3111262]

Keywords: latent heat storage, heat transfer, efficiency, energy, exergy, encapsulated, ice, discharging, sphere, cylinder, slab, temperature

1 Introduction

Due to the current and increasing world demand for energy, the storage of energy is becoming a viable technology to attempt to help alleviate costs and environmental impact. Since most sources of sustainable energy, for example, solar and geothermal, do not offer themselves at a constant rate, there is an obvious advantage in the storage of solar, wind, and tidal energies, so that they may be used in times of need. Although there are many types of energy storage that services society today, including electrical, mechanical, and chemical, thermal energy storage (TES) presents one of the easiest and cost efficient means to store energy. For example, solar hot water heaters are garnering increased attention as of late, due to the ease in installation and maintenance, as well as the cost reductions in heating and decreased greenhouse gases (GHGs) when compared with natural gas or oil heaters. Many recent studies, for example, Ref. [1], have focused on heat exchanger types to most efficiently transmit heat to and from latent sources. Although a comprehensive review of the many latent TES applications for space heating is exhaustive, there are nonetheless many

recent and ongoing studies to find uses for latent heat storage in solar heat capture [2] and electronics cooling [3], to name a few. Cold TES, on the other hand, has not received as much attention, and it is becoming an excellent option in warmer areas, where space cooling costs and electricity demands are becoming increasingly high.

The main focus of this paper is concerned with encapsulated ice TES. This is due to a number of factors, including its low cost and attractive economic and environmental benefits. The utilization of encapsulated ice TES, along with other modes of TES, reduces both electricity demand and cost, and ultimately lowers GHG emissions through a lowered energy demand.

Encapsulated ice TES utilizes a heat transfer fluid (HTF), which is usually a glycol solution, to freeze de-ionized water encapsulated in plastic capsules (usually made of polyvinyl chloride (PVC), due to its low cost, nonvolatility, and high durability). The capsules are typically made in a spherical shape, but other geometries including rectangular prism, cylindrical, and annular shapes are also possible. These capsules are contained in a large storage tank, and the HTF mainly serves as a medium to deliver the cooling load from the storage tank to the building. It can be cooled via many techniques, but a vapor compression refrigeration cycle is primarily used. During night times, electricity is usually much cheaper, and chillers cool the heat transfer fluid, which in turn freezes the encapsulated water. During peak electricity times, the cost can be as much as five times that in the night [4], so the HTF

¹Corresponding author.

Contributed by the Heat Transfer Division of ASME for publication in the JOURNAL OF HEAT TRANSFER. Manuscript received October 16, 2008; final manuscript received January 13, 2009; published online June 5, 2009. Review conducted by Ali Ebdian.

is used to extract the heat from the ice storage tank and deliver the cooling load to the building. This has an immense cost benefit, and some case studies have shown payback periods of as little as 2–7 years [5]. In addition to this, utilizing cold TES can help reduce the peak electricity demand since it effectively shifts electricity loads from peak to off-peak times. This eliminates the need for more generating plants to satisfy the peak demand and, ultimately, acts to lower greenhouse gases, which have been a major concern for environmentalists and scientists alike.

There are many literature works that have direct applications to encapsulated ice TES and these are either concerned with packed bed flows or single capsule analyses. The wealth of information regarding packed bed investigations is immense; however, most are concerned with high velocity gas flowing through a bed with particles of small diameter, for example, Refs. [6,7]. These studies, although helpful, usually have applications in reactor beds [8] or adsorption beds. Due to the small particle diameters, they cannot correctly analyze the important phenomena that are inherent to encapsulated packed bed TES. For these larger capsules, a number of studies have been undertaken in order to analyze thermal dispersion [9] and viscous dissipation [10]. A critical review of the thermal dispersion in various packed beds was performed in Ref. [11].

In a recent work [12] more aligned with the principles of encapsulated ice TES, an analytical technique is presented to simulate flow in a packed bed of larger spheres. The method, which includes porous medium concepts, takes into consideration fluid-to-capsule convection, conduction and radiation, as well as one-dimensional radial conduction inside particles. They achieve good results when compared with numerical and experimental data when a free-convection heat transfer configuration is employed.

Another relevant usage of the porous medium concept [13] proposes a cylindrical storage tank, packed with spherical capsules, and using the integral approach assuming a linear transverse temperature profile, as well as heat leakage from the ambient, a HTF temperature profile is obtained. The resulting energy and exergy efficiencies, along with the exergy destructions, are evaluated when the flow rates and inlet temperatures are varied during charging. It was found that when using larger flow rates and inlet temperatures close to that of the solidification temperature, the exergy efficiency was maximized and the destroyed exergy was minimized.

Though there are a few other analytical studies concerned with modeling encapsulated ice TES system, most of the wealth of research into this subject is concerned with numerical studies and simulations of the charging and discharging of the storage module. In Ref. [14], an existing TES system is replicated using a two-dimensional axisymmetric model, and the role of free convection on the heat transfer performance of the tank is addressed. Another similar work can be found in Ref. [15], where a two-dimensional transient analysis of a cylindrical storage tank is performed, with the storage tank filled with uniformly sized spherical capsules. The capsules are filled with paraffin wax and are packed randomly into the storage module, exchanging heat with air acting as the HTF.

Furthermore, some studies combine both porous medium concepts with a numerical solution, as in Ref. [16]. Here, a two-dimensional approach is used to solve for the temperature field in a cylindrical container containing spherical capsules used for ice storage. Density variations within the HTF were considered, and the system was run in both the vertical and horizontal positions. It was determined that the optimal case occurred with the tank in the vertical position when the natural convective currents coincide with forced convection currents.

Though encapsulated ice TES shows many promising benefits in industrial cooling, the literature is somewhat lacking in the particular area of this paper since many studies either consider encapsulated paraffin for warm TES purposes or simply provide case studies of existing systems. This research paper goes beyond

what is found in the literature in the sense that the inner flow fields between capsules are simulated using numerical techniques, and the dependence of performance on factors such as capsule geometry, HTF temperature and flow rate, as well as ambient conditions is examined. It is believed that only when these inner flow fields are properly treated can better efficiencies, lower costs, and better sustainability be realized by designers.

2 Analysis

Before specifying the equations used in both the heat transfer analysis and the thermodynamic analysis, an outline of the numerical study and computational domains will be addressed. In most encapsulated ice storage tanks, the capsules are either of the spherical, cylindrical, or rectangular (slab) geometry. The spherical geometry is far more common in industrial applications due to its ease of manufacturing and packing. There are other geometries that have been used, but for the purpose of this analysis, only the spherical, slab, and cylindrical capsules are considered. For a better understanding of the storage tank and capsule relationship for the three geometries, see Fig. 1. The present analysis will consider one capsule of each type in a bed of like capsules, and simulate the ice discharging or melting process, while varying many factors as described above.

Each capsule will have a PVC shell with a thickness of 5 mm. This material is chosen due to its durability and flexibility and should provide a good approximation to the various plastics used for capsule shells in the industry. Before continuing any further, the assumptions used in this analysis are as follows:

- negligible radiation effects
- constant thermophysical properties for both HTF and PVC
- piecewise constant thermophysical properties for the phase change material (PCM)
- incompressible materials with constant density
- negligible storage tank wall effect
- negligible heat penetration into storage tank, and
- negligible potential (gravitational) energy effects

The slab capsules are considered to have a heat transfer fluid stream thickness equal to half the slab thickness.

The material thermophysical properties used in the analysis are given in Table 1. The properties for water and ice are taken constant at temperatures of 275 K and 269 K, respectively, since this is an acceptable mean temperature at which these substances will be experiencing. The properties of the heat transfer fluid—an ethylene glycol solution (30% by mass)—are obtained from Ref. [17].

Now that the above general guidelines and domain descriptions are set, the computational procedure for the solutions can be addressed. Afterward, a detailed explanation of the computational domains is presented so that the performance criteria can be examined according to the various inputs.

2.1 Heat Transfer and Fluid Flow Analysis. For the whole of the numeric simulations, ANSYS FLUENT and GAMBIT 6.3 softwares are used to create the domains, split them into finite volumes, and set boundary and initial conditions. These domains have been split up into a finite number of volumes (or cells), and the relationships between adjacent cells are computed over their joining faces (or facets). The actual solver employed in this analysis is a pressure-based solver; since all of the materials used in this problem are assumed incompressible, the flow is governed solely by pressure differentials. In this case, the pressure-based solver uses an algorithm that belongs to a general class of methods called projection methods [18]. In this method, the conservation of mass, or continuity, is achieved by solving a pressure correction equation. This equation is derived from the continuity and momentum equations in such a way that the pressure/velocity field satisfies the continuity equation. Since the differential equations that must be satisfied are nonlinear by nature and coupled, the solution must

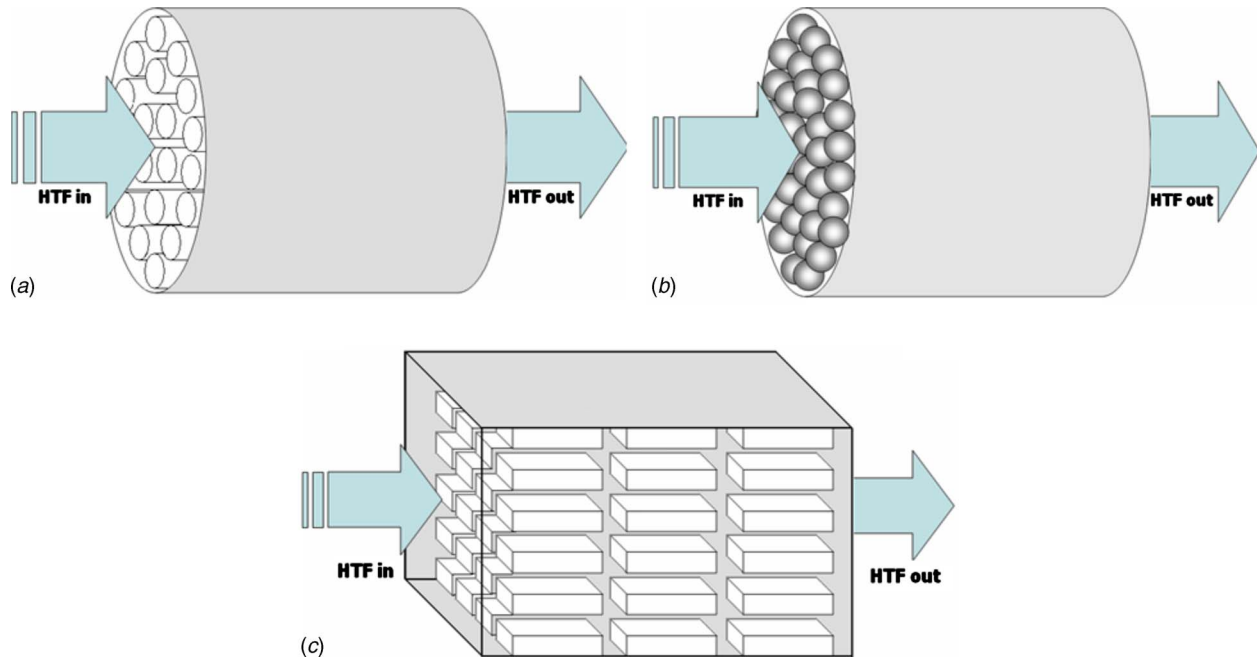


Fig. 1 Storage tank schematic for (a) cylindrical capsules, (b) spherical capsules, and (c) slab capsules

be iterated in a closed loop until the solution converges within the required tolerances.

Though the actual solution procedure used in ANSYS software can be very complex, it is nonetheless more important, from an engineering or designing perspective, to outline the governing equations and boundary conditions necessary for these numerical solutions to take place. In all cases, there will be three separate sections where governing equations change: the inner capsule (henceforth referred to as the PCM), the capsule shell (or PVC), and the flowing HTF. FLUENT works in Cartesian (or x - y - z) coordinates, and each material will have its own governing equations and boundary and initial conditions, which are to be presented next.

2.1.1 The PCM. Due to the aforementioned assumptions, the PCM becomes conduction dominated and contains no flow terms. The energy equation for the phase change material is then as follows:

$$\rho_{\text{PCM}} \frac{DH_{\text{PCM}}}{Dt} = k_{\text{PCM}} \nabla^2 T \quad (1)$$

The substantial derivative, seen in the first term of the above equation, for any variable γ , is defined as

$$\frac{D\gamma}{Dt} = \frac{d\gamma}{dt} + u \frac{d\gamma}{dx} + v \frac{d\gamma}{dy} + w \frac{d\gamma}{dz} \quad (2)$$

where u , v , and w are the x , y , and z components of the velocity vector. The del (∇) operator, seen in the last term of the energy equation above, is a vector quantity, though in this case due to its

multiplication it becomes a scalar. Nonetheless, it is used throughout the analysis, and it is shown below:

$$\nabla = \left(\frac{\partial}{\partial x} \vec{i} + \frac{\partial}{\partial y} \vec{j} + \frac{\partial}{\partial z} \vec{k} \right) \quad (3)$$

where \vec{i} , \vec{j} , and \vec{k} are the unit vectors in the x , y , and z directions, respectively. Continuing on with the energy equation, it is known that a phase change will occur in this medium. Therefore, the enthalpy of the PCM, H , will be computed as the sum of the sensible enthalpy, h , and the latent heat portion, H_l . Due to the assumption of constant thermophysical properties, this enthalpy can be written as a function of temperature as follows:

$$H_{\text{PCM}}(T) = h_{\text{PCM},o} + C_{\text{PCM}}(T - T_o) + H_l \quad (4)$$

where $h_{\text{PCM},o}$ and T_o are the arbitrary reference enthalpy value and temperature; since only the change in enthalpy is required for analysis, these values will drop out in all calculations.

There are many methods of numerically simulating the process of solidification; however, FLUENT uses the enthalpy/porosity method [19–21]. In lieu of a solver that produces a specific melt interface position, this method is often chosen to solve problems in more complex geometries. Instead of tracking this interface position explicitly, a quantity called the liquid fraction is solved, which computes the fraction of the cell that is in liquid form. The liquid fraction is then solved each iteration in order to correctly define the temperature field. This liquid fraction, β , is defined to vary between $\beta=0$ if $T < T_{\text{sf}}$ (melting temperature) and $\beta=1$ if $T > T_{\text{sf}}$. Any cells that have a liquid fraction between 0 and 1 will have a temperature of $T=T_{\text{sf}}$, and the liquid fraction will depend on the amount of latent heat stored. Once the cell has received all of its latent heat, it will continue to heat as a liquid.

In order to continue with the governing equations, the latent heat portion, H_l , must be written in terms of the latent heat of the material, L , such that $H_l = \beta L$.

The PCM temperature field and liquid fraction, defined by the above equations, can only be solved once one of the initial and boundary conditions is specified. The first condition is the initialization temperature $T_{\text{ini,PCM}}$; at time $t=0$ the PCM is set at a temperature of 271 K to indicate a subcooled solid. The second

Table 1 Material properties used in the analysis

Substance	C (J/kg K)	ρ (kg/m ³)	K (W/m K)	μ (kg/m s)
Water (liquid)	4200	1000	0.5576	0.001519
Water (solid)	2106	917.4	2.108	N/A
Ethylene glycol 30%	3574	1053.1	0.4220	0.00503
PVC	900	1380	0.16	N/A

condition required for the solution to proceed is the wall boundary condition, which is satisfied by the temperature condition at the PVC/PCM interface. Since there should be no discontinuities in the temperature field, the temperatures are set equal at both sides of the interface. The exact wall temperatures on the facets themselves are automatically interpolated linearly by FLUENT software.

2.1.2 The Capsule Shell (PVC). The PVC capsule is a solid structure, and since the PCM density changes and gravity effects were neglected, the energy equation is similar in the PVC medium to the PCM medium. Thus, the energy equation in the PVC medium is as follows:

$$\rho_{PVC} \frac{Dh_{PVC}}{Dt} = k_{PVC} \nabla^2 T \quad (5)$$

where the specific enthalpy, h , is defined as was done in Eq. (4), minus the latent heat portion. Again, in order to successfully solve the above equation, boundary conditions on both the inner and outer surfaces of the PVC are required. The inner boundary condition was already satisfied by the wall condition already addressed in the PCM/PVC interface; thus the outer boundary condition must now be addressed. This boundary condition is very similar to the one in the PCM/PVC interface. In order to keep a more continuous temperature profile, the temperatures at the outer PVC wall and the HTF next to the PVC wall must be equal. The exact temperatures on the facets themselves are once again interpolated linearly by FLUENT software.

As with the PCM domain, the PVC domain will be initialized at the same temperature so that the capsules begin simulations at a constant temperature throughout the PCM and PVC. The PVC and PCM domains now need only the heat transfer fluid temperature distributions to be fully solved, and this is done in Sec. 2.1.3 concerning the heat transfer fluid domain, which is the most complicated of all three.

2.1.3 The HTF. The heat transfer fluid will need to satisfy a number of governing equations due to the complex flow conditions within the domain. To begin with, since there is moving fluid, the energy equation for the heat transfer fluid becomes more complex due to viscous dissipation. A number of new variables must be introduced, and the energy equation is shown below.

$$\rho_{HTF} \frac{Dh_{HTF}}{Dt} = \frac{Dp}{Dt} + k_{HTF} \nabla^2 T + \Phi \quad (6)$$

The last term on the right hand side of the above equation involves viscous stresses and is customarily called the dissipation function. By the governing assumptions, we obtain the following for the dissipation function, Φ :

$$\Phi = \mu \left[2 \left(\frac{\partial u}{\partial x} \right)^2 + 2 \left(\frac{\partial v}{\partial y} \right)^2 + 2 \left(\frac{\partial w}{\partial z} \right)^2 + \left(\frac{\partial v}{\partial x} + \frac{\partial u}{\partial y} \right)^2 + \left(\frac{\partial w}{\partial y} + \frac{\partial v}{\partial z} \right)^2 + \left(\frac{\partial u}{\partial z} + \frac{\partial w}{\partial x} \right)^2 \right] \quad (7)$$

This term, when inserted into the energy equation, becomes the viscous stress term, which addresses the pressure energy transformed into heat due to the shear stress in the fluid.

Since the above equation now must be solved to include pressure and velocity terms, many more equations must be introduced, along with their boundary conditions, before transient solutions can take place. First, the continuity equation must be fulfilled, and since the heat transfer fluid is assumed incompressible, the continuity equation becomes

$$\nabla \cdot \vec{V} = 0 \quad (8)$$

The above equation, put simply, ensures that the mass fluxes across adjacent cells are conserved. Next, the momentum equations, known as the Navier–Stokes equations, must also be conserved:

$$\rho_{HTF} \frac{D\vec{V}}{Dt} = -\nabla p + \mu \nabla^2 \vec{V} \quad (9)$$

So, the momentum conservation equations depend primarily on the velocity vectors and pressure differential within the velocity field. The change in velocity at any point in the fluid depends on the pressure gradient at that point, ∇p as well as the viscous dampening effects, denoted by $\mu \nabla^2 \vec{v}$.

Since there are some new equations introduced here with many more variables, in order to fully solve for the flow fields there will need to be a few more initial and boundary conditions. To begin with, before the solution is initialized, the temperature of the heat transfer fluid is patched into the HTF domain so that the HTF has a temperature equal to its inlet temperature for ease of computations. The velocity of the heat transfer fluid is set to zero before transient solutions but is instantaneously switched to a specified velocity, uniform over the inlet, afterward. The flow direction is in the z -direction so that $V(t=0)=0$ and $V_{in}(t>0)=w_{in}$. For the geometries that have a non-PCM bounded wall, for example, the spherical and slab capsule geometries, there will be a boundary type that can be set as a zero shear stress wall. This is done in order to more precisely model a real-world scenario; there will be an axis of symmetry between capsule bunches, and the following attempts to model these:

$$\frac{d\vec{V}}{d\vec{n}} (\vec{f} \in W_{ns}) = 0$$

The above equation is explained as such; for the wall facets, \vec{f} , which are part of the “no shear” symmetric wall points, W_{ns} , the derivative of the velocity with respect to the vector normal to the wall facet, \vec{n} , will be zero. This ensures that no viscous dissipation is encountered in these zones and is an important proponent to the solution if the flow fields are to be solved far away from the capsule tank wall. Conversely, for the wall facets not on the no shear facets (in other words, all other “real” walls), there is a no-slip condition

$$\vec{V} (\vec{f} \notin W_{ns}) = 0$$

So, the velocity vectors on all wall facets not in the “no-slip” regime are set to zero for all cases.

For the outflow zones, there is no need to define any conditions at these boundaries since FLUENT extrapolates the required information from the interior of the domain. There are, however, a few aspects of this boundary condition type to note before proceeding; first, FLUENT assumes a zero diffusion flux for all flow variables at the outlet. In other words,

$$\frac{d\gamma}{dz} (\vec{f} \in W_{out}) = 0$$

Here, the symbol γ can be any of the velocity, temperature, or temperature vectors, and the above equation simply states that the flow is fully developed at the outlet in the z direction, which is streamwise and normal to the outlet. The reader should note that the accuracy of the above assumption is entirely dependent on the far-field boundary condition and the placement of the outlet. This is why there must be some consideration taken when building the computational zones and placing the outlet boundaries, which will be addressed when performing far-field boundary independence tests in Sec. 2.2.

The second outlet consideration that must be highlighted is the overall continuity correction. Since the continuity equation (8) must be conserved, the mass flow inlet and mass flow outlet must carry the same amount of mass:

$$\left[\rho \sum_{k=1}^n w|A_k| \right]_{\text{inlet}} = \left[\rho \sum_{k=1}^n w|A_k| \right]_{\text{outlet}}$$

So, the density, which is constant, multiplied by the summation of all streamwise velocities at each facet k , multiplied by the area of each facet, will equal the mass flow rate at the inlet/outlet. These two values must be conserved to ensure that the continuity equation is fulfilled.

Now that the governing equations have been addressed, the algorithm is able to solve the temperatures, flow, and pressure fields to within desired tolerances; in this case they are set to 1.0×10^{-3} for continuity, as well as the x , y , and z velocities, and 1.0×10^{-6} for energy.

2.2 Thermodynamic Analysis. In addition to the heat transfer and fluid flow computational analyses, the thermodynamic aspects of the solidification and melting processes must be examined. Thermodynamic analyses are very helpful in determining system performance, including efficiency values and losses. There are usually two bases to perform a thermodynamic analysis, and these are usually called the energy and exergy analyses, and will be introduced and discussed next.

2.2.1 Energy Analysis. An energy balance on either the solidification or melting process results in the following:

$$\Delta E_{\text{sys}} = E_{\text{in}} - E_{\text{out}} \quad (10)$$

In other words, the total energy change in the computational domain during the entire process must balance the difference between the inlet and outlet energy flows. This is known as the conservation of energy principle or the first law of thermodynamics. By the assumptions of negligible kinetic and potential effects, as well as constant densities, the flow energy difference can be rewritten as follows:

$$E_{\text{in}} - E_{\text{out}} = U_{\text{in}} - U_{\text{out}} = H_{\text{in}} - H_{\text{out}} + V(P_{\text{in}} - P_{\text{out}}) \quad (11)$$

Here, U denotes the internal energy, H represents the enthalpy, V is the total volume of the heat transfer fluid used in the process, and P is the average total pressure of the heat transfer fluid.

The change in energy of the system is defined as the energy change in each of the components of the system:

$$\Delta E_{\text{sys}} = \Delta E_{\text{HTF}} + \Delta E_{\text{PCM}} + \Delta E_{\text{PVC}} \quad (12)$$

where $\Delta E_{\text{HTF}} = m_{\text{HTF}} C_{\text{HTF}} (\Delta \bar{T}_{\text{HTF}})$, $\Delta E_{\text{PVC}} = m_{\text{PVC}} C_{\text{PVC}} (\Delta \bar{T}_{\text{PVC}})$, and $\Delta E_{\text{PCM}} = m_{\text{PCM}} [L + C_w (\Delta \bar{T}_{\text{PCM},w}) + C_i (\Delta \bar{T}_{\text{PCM},i})]$.

Here, the HTF and PVC zones undergo a change in sensible enthalpy only, while the PCM undergoes a change in sensible enthalpy in both the solid and liquid phases, along with a change in enthalpy associated with phase change. Now that the proper energy balance equations have been addressed, it is necessary to introduce the energy efficiency; the ratio of the desired energy output to the total energy input is as follows:

$$\eta = \frac{\text{desired energy output}}{\text{total energy input}} = \frac{E_{\text{des}}}{E_{\text{tot}}} \quad (13)$$

Since the purpose of the discharging process is to obtain the cool energy back from the control volume, the desired energy output is defined as the change in enthalpy for the flows between the inlet and outlet:

$$\begin{aligned} E_{\text{des}} = H_{\text{in}} - H_{\text{out}} = & m_{\text{PCM}} [L + C_w (\bar{T}_{f,\text{PCM}} - T_{\text{sf}}) + C_i (T_{\text{sf}} - \bar{T}_{\text{ini},\text{PCM}})] \\ & + V(P_{\text{out}} - P_{\text{in}}) + m_{\text{PVC}} C_{\text{PVC}} (\bar{T}_{f,\text{PVC}} - \bar{T}_{\text{ini},\text{PVC}}) \\ & + m_{\text{HTF}} C_{\text{HTF}} (\bar{T}_{\text{ini},\text{HTF}} - \bar{T}_{f,\text{HTF}}) \end{aligned} \quad (14)$$

The above was arrived at by combining Eqs. (10)–(12) so that the enthalpy difference could be rewritten in terms of the other variables for ease of calculations.

The total energy input is given by the required energy needed

for a process to occur. Therefore, this will be equal to the amount of cool energy stored in the control volume before the melting process begins.

$$\begin{aligned} E_{\text{tot}} = & m_{\text{PCM}} [L + C_i (T_{\text{sf}} - \bar{T}_{\text{ini},\text{PCM}}) + C_w (\bar{T}_{f,\text{PCM}} - T_{\text{sf}})] \\ & + m_{\text{PVC}} C_{\text{PVC}} (\bar{T}_{f,\text{PVC}} - \bar{T}_{\text{ini},\text{PVC}}) + m_{\text{HTF}} C_{\text{HTF}} (\bar{T}_{\text{ini},\text{HTF}} - \bar{T}_{f,\text{HTF}}) \end{aligned} \quad (15)$$

Now that the proper required and desired energy contents have been identified, the energy efficiencies for the charging and discharging processes are easily calculated using Eq. (13). After analyzing the systems, however, it became apparent that the energy efficiencies were very high, all of which being over 99% efficient. While this phenomenon will be addressed in the discussion of the results, the normalized energy efficiency is introduced next in order to inspect the efficiency differences in this last percentile.

$$\bar{\eta} = \left(\frac{\eta - 0.99}{0.0001} \right) \quad (16)$$

2.2.2 Exergy Analysis. An exergy balance on any system undergoing any process is written as follows:

$$\Delta \Xi_{\text{sys}} = \Xi_{\text{in}} - \Xi_{\text{out}} - \Xi_d \quad (17)$$

The above exergy balance is quite similar to the energy case, but it contains one extra term, the exergy destroyed Ξ_d . The exergy destroyed results from irreversibilities within the system and represents the exergy which becomes unrecoverable during the process.

As with the energy case, the exergy change in the system is a result of the exergy changes associated with each material within the system:

$$\Delta \Xi_{\text{sys}} = \Delta \Xi_{\text{HTF}} + \Delta \Xi_{\text{PVC}} + \Delta \Xi_{\text{PCM}} \quad (18)$$

where

$$\Delta \Xi_{\text{HTF}} = m_{\text{HTF}} C_{\text{HTF}} \left[\bar{T}_{f,\text{HTF}} - \bar{T}_{\text{ini},\text{HTF}} - T_{\infty} \ln \left(\frac{\bar{T}_{f,\text{HTF}}}{\bar{T}_{\text{ini},\text{HTF}}} \right) \right]$$

and

$$\Delta \Xi_{\text{PVC}} = m_{\text{PVC}} C_{\text{PVC}} \left[\bar{T}_{f,\text{PVC}} - \bar{T}_{\text{ini},\text{PVC}} - T_{\infty} \ln \left(\frac{\bar{T}_{f,\text{PVC}}}{\bar{T}_{\text{ini},\text{PVC}}} \right) \right]$$

In the above equations, the change in exergy for the HTF and the PVC was obtained due to the incompressibility assumption. However, for the PCM, the exergy change is not as straightforward. Since there is both a sensible and a latent exergy change within the PCM, the total change in exergy will be the sum of the exergy change in the water and ice states, which are evaluated similar to the above, plus the exergy change due to the solidification of the PCM. So, for the charging and discharging states, this becomes

$$\begin{aligned} \Delta \Xi_{\text{PCM}} = & m_{\text{PCM}} C_i \left[T_{\text{sf}} - \bar{T}_{\text{ini},\text{PCM}} - T_{\infty} \ln \left(\frac{T_{\text{sf}}}{\bar{T}_{\text{ini},\text{PCM}}} \right) \right] \\ & + m_{\text{PCM}} C_w \left[\bar{T}_{f,\text{PCM}} - T_{\text{sf}} - T_{\infty} \ln \left(\frac{\bar{T}_{f,\text{PCM}}}{T_{\text{sf}}} \right) \right] \\ & + m_{\text{PCM}} L \left(1 - \left(\frac{T_{\infty}}{T_{\text{sf}}} \right) \right) \end{aligned} \quad (19)$$

In the above equations, the latent exergy term was arrived at by noticing that, for any incompressible substance,

$$\Delta \Xi = \Delta E - T_{\infty} \Delta S$$

And, the change in entropy for the solidification process is determined by the *entropy of fusion* equation

$$\Delta S_{\text{fus}} = m_{\text{PCM}} \frac{L}{T_{\text{sf}}} \quad (20)$$

Now that the system energy change over the process has been evaluated, the inlet, outlet, and destroyed exergy terms must be addressed. The simplest way to achieve this is to first observe or calculate the exergy destruction in Eq. (17). Once this term is evaluated, the exergy flow difference is easily solved.

The exergy destruction equation is written as follows:

$$\Xi_d = T_\infty S_{\text{gen}} \quad (21)$$

As mentioned earlier, this is a result of irreversibilities or losses within the system. Since the exergy destruction depends on the entropy generation, an entropy balance must now be performed on the system:

$$\Delta S_{\text{sys}} = S_{\text{in}} - S_{\text{out}} + S_{\text{gen}} \quad (22)$$

The entropy, S , is a measurement of the degree of randomness of a substance. It is always increasing due to irreversibilities in the system. This is a corollary of the second law of thermodynamics. However, if the system is taken as the capsule region *plus* the total amount of HTF, and since there is no heat loss to/from the system, the generated entropy occurs as a result of two separate phenomena: viscous dissipation losses and entropy generation from heat transfer to the capsules.

$$S_{\text{gen}} = S_{\text{gen,diss}} + S_{\text{gen,trans}} \quad (23)$$

The entropy generated from viscous dissipation (from Ref. [22]) will depend on the bulk fluid temperature of the HTF, the total mass of heat transfer fluid in the process, and the average pressure drop within the HTF:

$$S_{\text{gen,diss}} = \frac{M_{\text{HTF}}(P_{\text{in}} - P_{\text{out}})}{\rho_{\text{HTF}} \bar{T}_{b,\text{HTF}}} \quad (24)$$

Here, the bulk heat transfer fluid temperature $\bar{T}_{b,\text{HTF}}$ is the temperature at which viscous heat is added to the flow. It is estimated to be the average between the initial and final states. Since the heat transfer fluid, on average, does not undergo a large temperature change, this assumption should be regarded as accurate to within at least a few hundredths of a percentile:

$$\bar{T}_{b,\text{HTF}} = \frac{\bar{T}_{\text{ini,HTF}} + \bar{T}_{f,\text{HTF}}}{2}$$

In addition to the viscous dissipation, entropy is also generated from heat transfer to the capsules. The equation for this mode of generation is given by the summation of all entropy changes within the insulated system, which arises as a result of pure heat transfer (and not viscous dissipation):

$$S_{\text{gen,trans}} = M_{\text{HTF}} C_{\text{HTF}} \ln\left(\frac{T_{\text{in}} + \Delta T}{T_{\text{in}}}\right) + \Delta S_{\text{PVC}} + \Delta S_{\text{PCM}} \quad (25)$$

where

$$\Delta S_{\text{PVC}} = m_{\text{PVC}} C_{\text{PVC}} \ln\left(\frac{\bar{T}_{f,\text{PVC}}}{\bar{T}_{\text{ini,PVC}}}\right)$$

and

$$\Delta S_{\text{PCM}} = m_{\text{PCM}} \left[-\frac{L}{T_{\text{sf}}} + C_i \ln\left(\frac{\bar{T}_{\text{ini,PCM}}}{T_{\text{sf}}}\right) + C_w \ln\left(\frac{T_{\text{sf}}}{\bar{T}_{f,\text{PCM}}}\right) \right]$$

Here, ΔT is the change in temperature that is brought about by heat transfer, which changes the total system energy:

$$\Delta T = \frac{\Delta E_{\text{sys}}}{M_{\text{HTF}} C_{\text{HTF}}}$$

So, the above equations, in conjunction with Eq. (20), finally allow the destroyed exergy to be calculated. However, in Eqs. (24)

and (25), the total mass of HTF must be evaluated. To do this, the overall solidification time for each process Δt is multiplied by the mass flow rate of the entering heat transfer fluid. Since the inlet velocity of the fluid is specified, the total mass of heat transfer fluid used in each trial is very easily calculated under the constant density assumption:

$$M_{\text{HTF}} = \rho_{\text{HTF}} V_{\text{in}} A_{\text{cross}} \Delta t \quad (26)$$

where A_{cross} is the cross-sectional area of the inlet.

The exergy balance equation can now be solved in full. The intention for the current analysis is to define the exergy efficiency, which is similar to the energy case, in that it is simply the ration of the desired to required exergy contents. It is given as follows, and to avoid cumbersome equations it will depend on the terms already outlined in this section.

$$\psi = \frac{\text{desired exergy output}}{\text{total exergy input}} = \frac{\Xi_{\text{des}}}{\Xi_{\text{tot}}} \quad (27)$$

where

$$\begin{aligned} \Xi_{\text{des}} &= \Delta \Xi_{\text{HTF}} + \Delta \Xi_{\text{PCM,dis}} + \Delta \Xi_{\text{PVC}} - \Xi_d \quad \text{and} \quad \Xi_{\text{tot}} = \Delta \Xi_{\text{HTF}} \\ &+ \Delta \Xi_{\text{PCM,dis}} + \Delta \Xi_{\text{PVC}} \end{aligned}$$

Now that the thermodynamic analysis of the system has been attended to, the charge for the remainder of the analysis is to see what effect the inlet heat transfer velocity and temperature, capsule geometry, as well as the dead-state temperature has on the following system performance criteria:

- solidification and melting times
- energy efficiency
- exergy efficiency, and
- exergy destruction

However, before these criteria can be calculated, the various cases studied must be outlined, including the domain descriptions and grid structuring procedures for each.

2.3 Domain Description. The capsules that will be considered here will be of spherical, cylindrical, and slab shapes, and each will contain an equal amount of phase change material. For the cases investigated here, the PCM volume is set at 268.1 cm³, a value that was chosen to be quite close to capsule sizes used in the industry today [23]. In addition to this, each capsule will be enclosed by a PVC shell with a wall thickness of 0.5 cm. This is again chosen to be close to the industry standard, though most companies keep shell material and dimensions a secret.

The capsules will then be tested according to geometry. The spherical capsules will be compared with cylindrical and slab capsules, each with an aspect ratio of 5, in order to determine the dependence of geometry on performance. For the cylindrical capsules, the aspect ratio is defined as the (streamwise) length to diameter ratio. Likewise, for the slab capsule, the aspect ratio is defined as the (streamwise) length to thickness ratio. For the slab capsule, the cross-stream length is assumed to be equal to the streamwise length, so the slab capsules are essentially a square-topped capsule with side length equal to five times the inner capsule height. Note that for all geometries, the aspect ratios are defined according to the inner boundaries of the PVC, not the outer. The dimensions of all capsules can be found in Table 2.

The spherical capsule domain, as seen in Fig. 2, will be defined as a square cylinder, containing parts of four adjacent and touching PCM capsules. This is done to more correctly model the interactions between spheres stacked in a large storage tank. The eight corners of the square cylinder will be located at the centers of eight far-field capsules to ensure that far-field considerations are minimal. The velocity outlet is analogously defined.

The spherical domain was constructed using GAMBIT software, and special consideration was taken when creating the grids. First, since the gradients are usually strongest along the no-slip walls of

Table 2 Geometric dimensions of the capsules used in this analysis

	Sphere	
Inner radius (R_{inner}) (cm)		4.0
Outer radius (R_o) (cm)		4.5
	Slab	
Length (Le_s) (cm)		11.025
Inner height ($H_{t,s,inner}$) (cm)		2.205
Outer height ($H_{t,s,o}$) (cm)		3.205
	Cylinder	
Length (Le_c) (cm)		20.435
Inner diameter (D_{inner}) (cm)		4.087
Outer diameter (D_o) (cm)		5.087

a surface, the heat transfer fluid grids were created first, with special care taken on the boundaries of the outer PCM walls. A tetrahedral/hybrid element type was used for all elements in the domain, including the heat transfer fluid due to the spherical nature of the PCM capsules. The PCM and PVC zones were made with a much more even distribution of volumes due in part to the

negating of convection within the PCM and to the unknown liquid-solid interface location.

For the cylindrical capsules, the computational domain is similarly defined. The domain is again a square cylinder, but in this case it will contain one-quarter of four adjoining cylindrical capsules. This is again done to more precisely model a packed bed of touching cylindrical PCM capsules. The heat transfer fluid inlet and outlet is then defined to be the area between capsules. The geometric layouts for this domain can be seen in Fig. 3. Notice that similar to the spherical capsule case, the inlet flow channel has again been elongated in order to eliminate far-field boundary effects.

The slab capsules were somewhat more difficult to envision since there is no universally accepted gap thickness between capsules for the HTF flow field. However, since thinner capsules will need less heat flux through their surfaces to achieve solidification, it was decided that the spacing should be proportional to the thickness of the capsule itself. Therefore, the gap spacing is set to half that of the outer capsule thickness for the main reason that it was noticed that this thickness was large enough not to affect boundary layer interaction between upper and lower slabs. For more of a visual interpretation, the slab capsule domain is pictured in the same way as was done for the other geometries in Fig. 4.

Once again, the grid construction procedures were done while

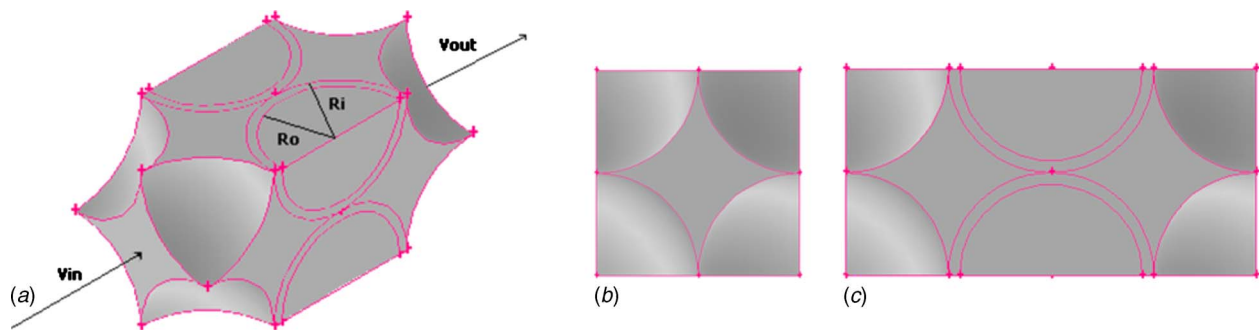


Fig. 2 Auxiliary (a), front (b), and side (c) views of the spherical capsule domain

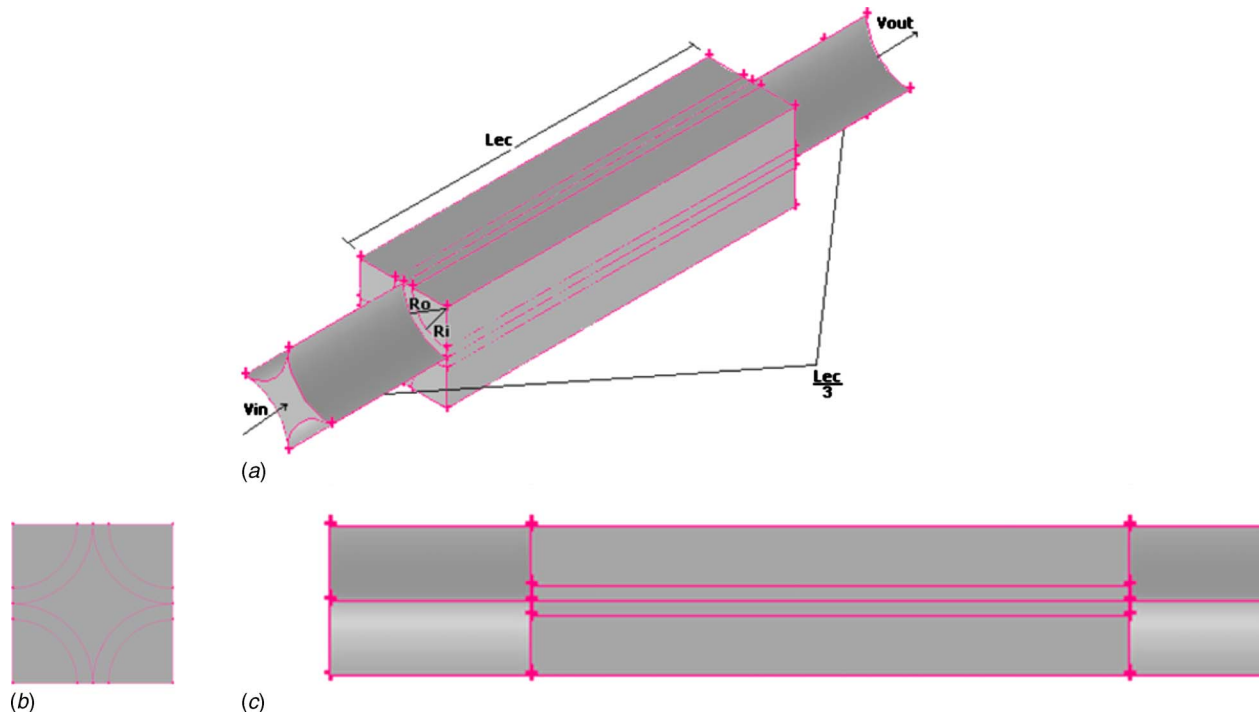


Fig. 3 Auxiliary (a), front (b), and side (c) views of the cylindrical capsule domain

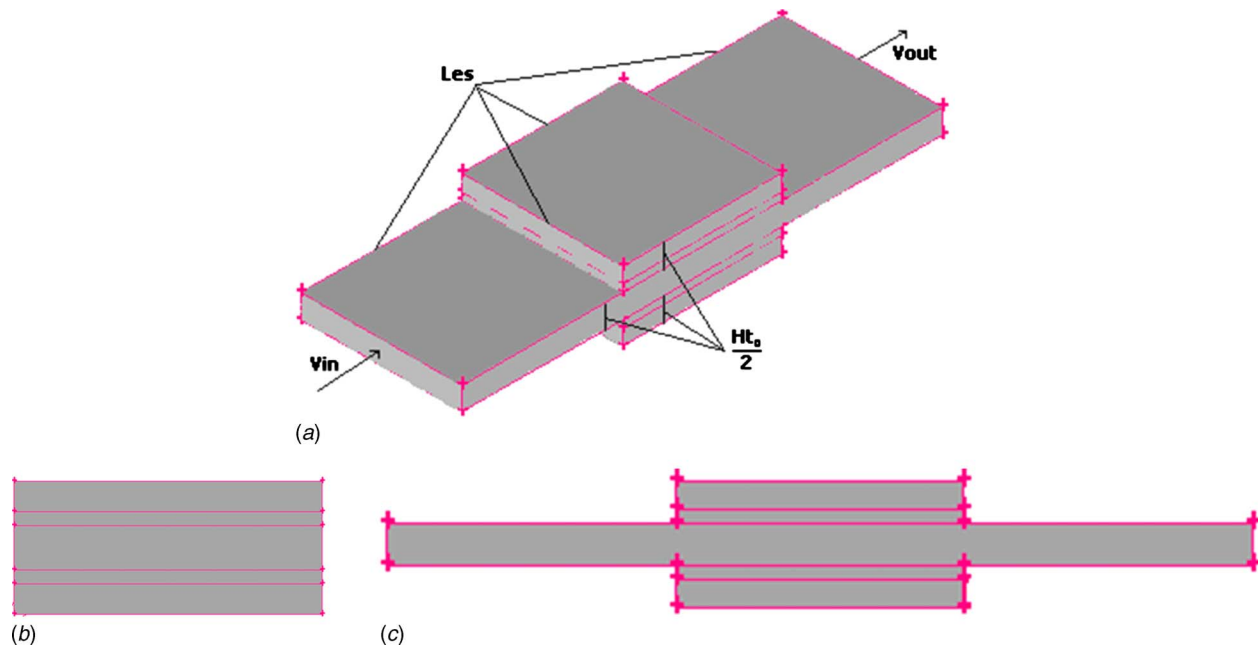


Fig. 4 Auxiliary (a), front (b), and side (c) views of the rectangular prism (slab) capsule domain

taking attention to the PVC walls surrounding the heat transfer fluid. As a result, the boundary layers were created with a significant cell density in the boundary layer area of the flow field. The heat transfer fluid grids were made with a hexahedron type cell, as were all other zones, due to their rectangular prism shape. The inlet flow channel is somewhat differently sized than the cylindrical capsule domain, but far-field independence is nonetheless satisfied and will be addressed in Sec. 2.4.

2.4 Model Independence Testing. As noted earlier, before the results of the simulations can be taken seriously, a careful investigation of the dynamics of the model must be undertaken. Sensitivity tests, including grid sensitivity, time step independence, and far-field boundary independence tests, must be completed and the model must perform in a satisfactory way for the results to be meaningful. However, due to the longevity of producing these results, the reader is referred to Ref. [24] for further details, where a complete sensitivity analysis was completed on the exact model used herein. The results of this test indicate almost complete independence of grid size, orientation, time step, and far-field boundary conditions, which is why the geometries were constructed in this way initially. In summary, and to avoid cumbersome presentation of the many independence tests required for a study of this magnitude, it can be said that the model behaves in an appropriate manner to be used in a numerical study of this magnitude, and once again the much more detailed report in Ref. [24] should suffice in lieu of presenting the results here.

The solutions obtained in this study were done so using 20 hp workstation xw8000 computers in a computing laboratory at the University of Ontario Institute of Technology. Each workstation computer featured one 3.20 GHz Intel Xeon processor, equipped with 4.0 Gbytes of PC2100 DDR SD RAM. Though these computers are quite powerful, the computational times for the various trials were considerable, and typical computational times for each trial were between 3 h and 5 h, depending on the geometry and HTF characteristics.

3 Results and Discussion

Before charging into the results, a model validation must be performed to ensure that the model is a viable simulation of real-world processes. A similar experiment to the one here has been performed by Ettouney et al. [25]. In this study, the process of

both solidification and melting is observed in a small copper sphere. The experiment was run with air as the HTF and paraffin wax as the PCM. The properties of the paraffin wax given in this study are outlined in Table 3. It should be noted that, since density effects are assumed negligible, the average density was again taken as the PCM density in the numerical solutions.

The experimental process in this study occurs as follows: The air enters a cylindrical duct, initially at 296 K, which contains a small copper sphere with an inner diameter of 3 cm. The capsule has a wall thickness of 1.2 mm and contains the paraffin wax PCM. The air has an inlet temperature of 333 K and an inlet velocity of 10 m/s. Thermocouples are placed at different angles with respect to the inlet flow direction along the inner diameter of the sphere, and the transient temperature profiles are recorded. A small opening is left on the top of the sphere to allow for PCM expansion.

Once total melting of the PCM has occurred, and the temperatures are close enough to the flow temperature (at $t=1120$ s), the inlet temperature is changed abruptly back to 296 K until complete resolidification is observed. The results can be seen in Figs. 5–7 for angles of 0° , 90° , and 180° , respectively, for the experimental and numerical solutions.

In viewing Figs. 5–7, it can be observed that the numerical and experimental temperature profiles do not exactly match, and this might be due to a number of factors, including contact resistance, small effects produced by the thermocouples embedded in the PCM, and possibly convection effects in the PCM. However, the

Table 3 Thermophysical properties of the paraffin used in the model validation

Solidification temperature (K)	321.51
Latent heat L (kJ/kg)	210
Solid density ρ (kg/m ³)	860
Liquid density ρ (kg/m ³)	780
Solid specific heat C (kJ/kg K)	2.9
Liquid specific heat C (kJ/kg K)	2.1
Dynamic viscosity μ (kg/m s)	0.15

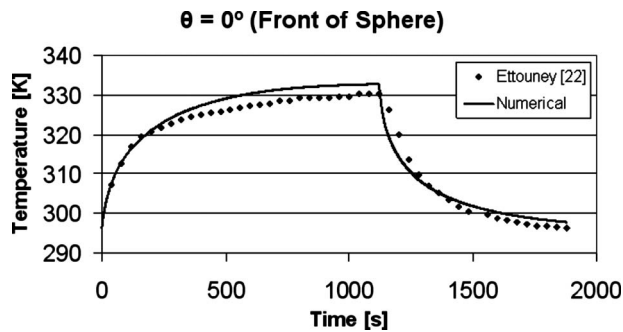


Fig. 5 Numerical and experimental temperature profiles at the front of the sphere ($\theta=0$ deg)

solidification and melting times, as well as the overall heat transfer rates, were of utmost importance to inspect, and the following results can be summarized.

- The time required for the PCM to completely melt was very close in both the experimental and numerical cases. Complete melting was reached in 600 s experimentally, while in the numerical solutions complete melting was reached in 615 s, within 97.6% of the expected melting time.
- Once solidification was initiated in the experimental unit, an additional 280 s was required to complete solidification. This is again very close to the numerical value of 285 s, to within 98.2%.

These similarities between numerical and experimental results are encouraging since the purpose of this paper is not to inspect the melt front but to simulate the heat transfer and viscous forces between the PCM capsule and the flowing HTF.

Because there are no experimental validations known to the author that track the solidification and melting times in cylindrical

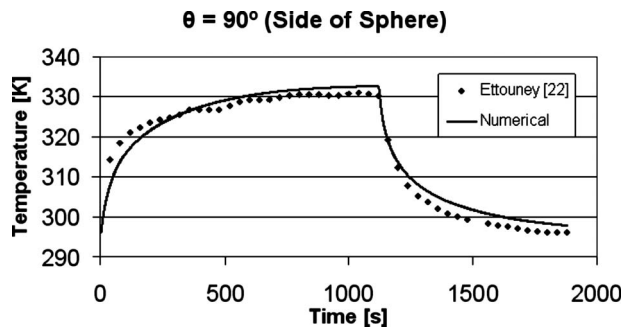


Fig. 6 Numerical and experimental temperature profiles at the side of the sphere ($\theta=90$ deg)

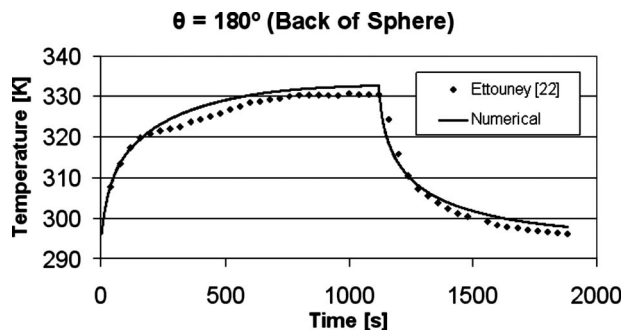


Fig. 7 Numerical and experimental temperature profiles at the back of the sphere ($\theta=180$ deg)

and rectangular capsules in a cross flow, the other geometries cannot be similarly validated. However, since the numeric procedures in all cases are identical, and since the experimental and numerical solution temperatures, solidification times, and melting times are very close, the model should be assumed accurate for all geometries explored in this study. With this in mind, and now that the model has been properly validated, the results of the solutions for the discharging processes can now be examined in full.

For the discharging process in question, the algorithm was run until the liquid fraction $\beta=1$ everywhere in the PCM. Note that the reference temperature T_∞ is set at 298 K to simulate cold storage in a warmer region. While the reference temperature will remain constant at this value for the bulk of the analysis, the effect of varying this reference temperature on the performance of the charging and discharging processes will be discussed in due time.

Three separate flow rates are used in this study:

- $Q_1=8.7 \times 10^{-4} \text{ m}^3/\text{s}$
- $Q_2=1.74 \times 10^{-3} \text{ m}^3/\text{s}$
- $Q_3=2.61 \times 10^{-3} \text{ m}^3/\text{s}$

These flow rates were chosen to be small enough so that they could easily be attained in a storage tank of like capsules. If the algorithm flow rates were too high, they would not be a reasonable estimate of the pumping requirements of a real-world storage system. It is summarized that these three flow rates, when set into rows of a hundred capsules or so, would generate a required pumping flow rate of around 8.7–26.1 l/s, which is not unreasonable for large pump flow rates with relatively small pressure heads.

Aside from the flow rates, the inlet HTF temperatures are also varied and were chosen to vary between 275 K and 279 K. Since heat will be transferring to the capsules during this process, there will inevitably be a large variation in the HTF temperature, and the heat transfer fluid is likely to vary within these ranges at some point in the storage tank. The temperatures used here are attempting to duplicate real scenarios; at the storage tank outlet, the HTF temperature will most likely be much closer to the solidification temperature of water due to the cooling effect of the capsules on the HTF. Since the remainder of the inlet and boundary conditions has been met, the results of the charging process for all flow rates, inlet HTF temperatures, and geometries were simulated. With three flow rates, three geometries, and five inlet temperatures, this amounts to 45 total simulations.

3.1.1 Discharging Times. The easiest and most explainable observations of the processes are the discharging times. For each simulation, the total time taken for the liquid fraction to reach a value of 1 was monitored, and the results are displayed in Table 4, with the shortest and longest times highlighted.

Upon inspection of Table 4, three main findings can easily be addressed. The first is the impact of inlet temperature on solidification time; as the inlet temperature increases, the solidification time decreases. This is due to the larger temperature gradients that exist between the capsule and the HTF when the inlet temperature is lowered. This is as expected since Newton's law of cooling states that the rate of heat transfer between an object and a convective flow is proportional to the difference between the surface temperature and the flow temperature. The second main finding is the fact that the flow rate, Q , has little relative effect on the discharging times. It was expected that, when increasing the flow rate, the convective heat transfer coefficient between the HTF and the ice capsules would greatly increase. However, even after doubling and tripling the flow rate from Q_1 to Q_2 and Q_3 , the overall charging times lowered, but not by any significant amount. The effects of flow rate on other system properties, including efficiency and destroyed exergy, will be more apparent, but will be discussed in more detail with the results of the performance investigations. The last note to discuss when assessing the charging times is the effect of geometry. It can be seen above that the

Table 4 Discharging times for all geometries, according to geometry, flow rate, and inlet HTF temperature

Geometry	Flow rate	Inlet HTF temperature (K)				
		275	276	277	278	279
Spherical	Q1	1782.5	1412.0	1226.5	1116.0	1037.5
	Q2	1756.0	1395.0	1215.0	1106.0	1028.5
	Q3	1724.0	1384.5	1210.0	1102.0	1025.5
Cylindrical	Q1	1130.4	924.3	803.3	722.3	663.8
	Q2	1076.4	882.9	769.5	693.9	639.5
	Q3	1048.5	861.8	752.0	678.6	626.0
Slab	Q1	899.0	706.5	594.5	522.0	469.0
	Q2	882.5	694.5	584.0	514.5	462.0
	Q3	874.5	689.0	579.5	510.0	458.5

fastest solidification times occurred with the slab capsule, followed by the cylindrical and lastly the spherical capsule. This effect points out an important note about surface area when dealing with convective heat transfer. The spherical capsule, which has the least amount of surface area, has the least desirable heat transfer characteristics. Since the heat transfer between any two bodies depends on the temperature difference (addressed above) and the area connecting the two bodies, it is expected that these phenomena occur.

3.1.2 Energy Efficiency. One of the more important articles to be addressed following numerical solutions is the overall energy efficiency. However, before assessing the values, a few remarks must be made. First, it was noticed that the energy efficiencies are extremely high; all efficiency values, regardless of geometry, inlet HTF temperature, or flow rate, are well above 99%. Though these values are indeed quite high, they are certainly not unexpected. The energy efficiency is, by definition, the ratio of the desired to the required energy amounts. However, the difference between these two values is a sole result of the viscous dissipation in the

fluid. This value, which is analogous to a pressure loss within the fluid, is important when designing systems like these; however, it is quite insignificant when compared with the thermal energy stored in the water and in the PCM, which explains the remarkably high efficiency values. The reason why the normalized energy efficiencies were adopted was so that a closer inspection of the differences can be observed.

It is also important to note that real-world systems may have a lower efficiency value due to heat leakage into the storage tank from the ambient. However, the flow fields inside the system, and the resulting head loss due to interior flows, are equally important to designers. The comparisons are made in this study to determine the best possible conditions for storage and retrieval of latent thermal energy when the capsule tank is sufficiently insulated. The energy efficiencies were then calculated according to the prescribed equations and can be seen in Fig. 8 for the three flow rates.

Other than the very high efficiencies resulting from these solutions, it should be apparent that efficiency decreases when chang-

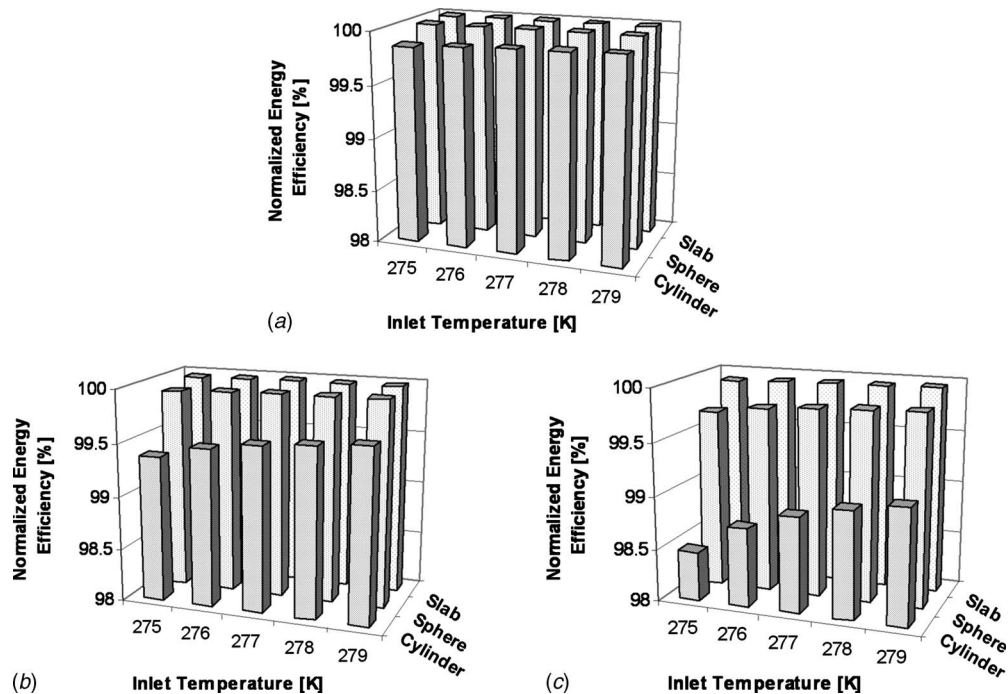


Fig. 8 Normalized energy efficiency values (in percent) for flow rates of (a) $Q_1 = 8.7 \times 10^{-4} \text{ m}^3/\text{s}$, (b) $Q_2 = 1.74 \times 10^{-3} \text{ m}^3/\text{s}$, and (c) $Q_3 = 2.61 \times 10^{-3} \text{ m}^3/\text{s}$

Table 5 Inlet velocities for the three geometries according to flow rate

	Q_1 velocity (m/s)	Q_2 velocity (m/s)	Q_3 velocity (m/s)
Spherical	0.050	0.100	0.150
Slab	0.049	0.098	0.148
Cylindrical	0.157	0.313	0.470

ing geometry from slab to sphere to cylinder, that efficiencies decrease along with increased HTF flow rate, and that they increase when inlet HTF temperature is increased. All of these phenomena can be attributed to viscous heating effects since this is the only energy loss occurring during the discharging process.

The viscous heating effect, or viscous dissipation, is a result of shear stresses in the fluid domain. When there are velocity differences in a fluid, there will always be friction between adjacent molecules traveling at different speeds, which give rise to heat generation. However, due to the first law of thermodynamics, heat cannot simply be generated without an energy transfer across system boundaries; it must be transferred from existing energy sources. This is why the pressure decreases along any duct or pipe flow.

For faster moving flows, this shear stress becomes much larger, just as brake pads on an automobile develop more frictional heat during high-speed stops. Geometry plays a factor as well; for ducts or flow channels that are highly irregular and change the momentum of a fluid considerably, such as pipe elbows or valves, the velocity gradients and hence frictional heating can increase significantly. However, it is the flow speed that gives rise to the greatest efficiency changes, and inspection of Table 5 further proves this argument.

It is quite apparent that the inlet HTF velocities increase with increased flow rate and that they increase from the slab capsule to the spherical to the cylindrical capsules. This shows why viscous heating is greater (and why efficiencies are less) when changing geometry and flow rate.

When comparing efficiency across HTF inlet temperatures, the trends are similarly explained. From Eqs. (14) and (15), it can be summarized that the greater the volume of HTF flow that is used in the discharging process, the greater the viscous dissipation term. Therefore, the inlet HTF temperatures, which achieve complete melting in the lowest times (see Table 4), will realize the lowest amount of viscous dissipation. Therefore, the higher inlet temperatures experience the highest energy efficiency values.

3.1.3 Exergy Efficiency. Exergy analyses can be more helpful than energy in a number of ways since they assess both the quantity and the usefulness of energy. Cold exergy is an excellent example since exergy analyses treat “cold” as a useful commodity due to the inclusion of ambient temperature effects.

The term “cold energy” seems somewhat contradictory. The change in energy from a solid to a liquid state in water is inherently negative, while the change in exergy (given a reference temperature higher than the solidification temperature) is actually positive. This is due to the usefulness of the stored energy. If the temperature of the thermal storage strays farther away from the ambient, the change in exergy is positive since it becomes more useful. Analogously, if its change in temperature moves toward the ambient, the exergy change is deemed negative. This is an interesting and certainly useful impact of the exergy analysis. For example, a block of ice at 0°C, placed in a room at 20°C, certainly has cooling potential in both the energy and the exergy sense. However, if the room temperature is reduced to 1°C, the exergy content of the block of ice would greatly decrease since the potential for the thermal storage has lessened. However, in the energy sense, the block of ice would have the exact same amount of latent energy to receive from the ambient, which can be mis-

leading, since the cooling potential of the block of ice is only useful in the 0–1°C temperature range. It is for this reason why exergy analysis for cold TES is more useful. They can provide much more insight into the actual performance of the system by treating cold as a useful quantity. So, the exergy efficiencies, like the energy efficiencies, were calculated for each flow rate, inlet temperature, and geometry, and the results can be seen in Fig. 9, once again grouped by flow rate.

When looking at Figs. 8 and 9, a number of differences can be seen: The first major difference is the efficiency values; although all energy efficiencies are well over 99%, the exergy efficiencies attained are much lower, ranging from around 72% to just over 84%. The reasons for the much lower exergetic efficiency are twofold: because of the decrease in storage quantity and because of the increase in losses when compared with the analogous energy quantities.

Equation (19) can explain why the required content is much less in the exergy sense than in the energy sense. For the discharging process, the required content is simply the cold energy (or exergy) contained in the PCM and PVC, most of which is contained in the cold ice region. From comparing Eqs. (19) and (12), it is most apparent that the exergetic content for the cold PCM is much less due to the inclusion of the ambient temperature in the equations. This inclusion allows for the thermal store to be evaluated on both quantitative and qualitative bases. The losses in the system are also much greater in an exergy sense than in an energy one, and this can be proved by viewing Eqs. (21)–(25). In the energy sense, the only loss the system incurs is due to viscous heating, as in the right hand side of Eq. (11). However, in the exergy analysis, there is another mode of loss—entropy generation due to heat transfer and phase change. Whenever exergy is transferred from a high quality source to a lower one, exergy is destroyed. This is due to the difference in exergy between the initial and final states and, simply put, means that the ice store is at a higher exergy state than the mass of heat transfer fluid and capsule after discharging. It is analogous to the case where a cube of ice is allowed to melt in a glass of lukewarm water. Although the water is somewhat colder after melting, the overall exergy content is less afterward, which can be linked to irreversibility. These ice melting processes are not reversible in that the ice cannot be recreated without the addition of work or a heat sink to the glass. So, a loss of exergy is incurred, which cannot be explained through energy analyses alone, and this is the main reason why exergetic efficiencies for melting processes like this are much lower than their energetic counterparts.

Other than the much lower exergy efficiencies, a few other points can be inferred from Fig. 9, some of which are in stark contrast to the energy efficiency results in Fig. 8. The first major difference is that exergy efficiency decreases with increased inlet HTF temperature, which is the opposite effect of that shown by energy analyses in Fig. 8. The second is that efficiency values do not vary in the same way when compared by geometry, and the third note about Fig. 9 is that exergy efficiencies tend to decrease with increased flow rate. All of the above are readily explained once the exergy destroyed terms are inspected since the only terms in Eq. (27), which will change by any significant amount when the above variables are changed, are the destroyed exergy terms.

When inlet HTF temperature increases, the destroyed exergy is decreased due to a significant decrease in entropy generation. Since there are essentially two modes of entropy generation that lead to destroyed exergy, one will undoubtedly be the dominant term, and in this case it is always the entropy generated from heat transfer and phase change. When the inlet HTF temperature is lowered, Eq. (25) becomes much lower, meaning that these lower inlet temperatures are able to extract more high quality exergy due to the average change in temperature of the HTF, which increases its quality. When the HTF inlet temperature is lowered closer to that of the solidification temperature of water, more mass is re-

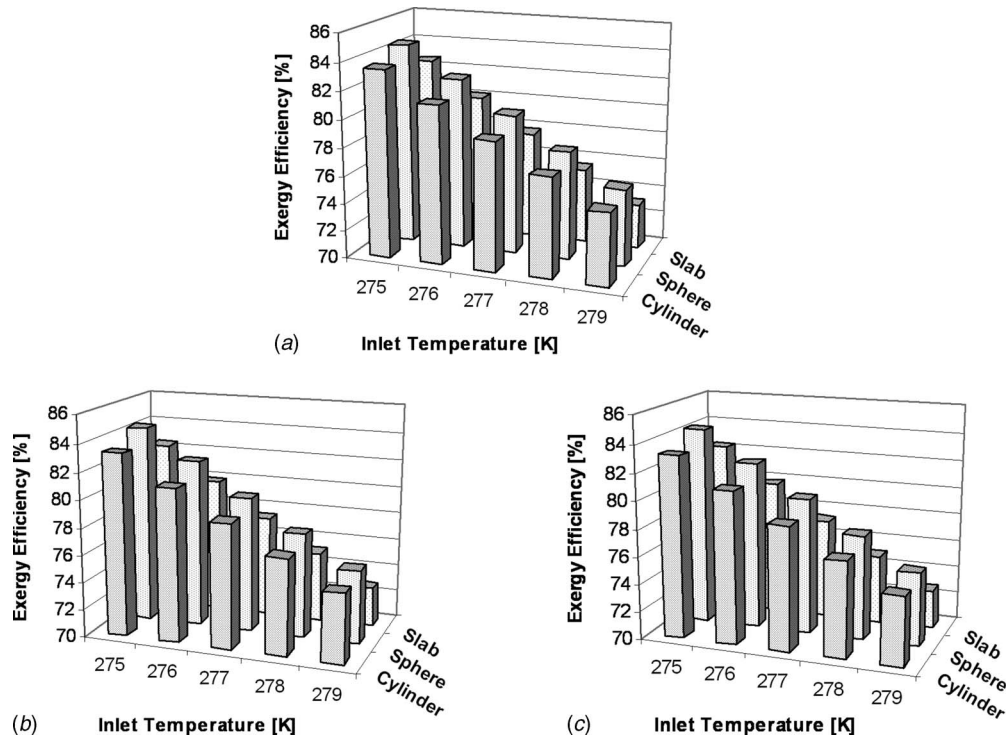


Fig. 9 Exergy efficiency values (in percent) for flow rates of (a) $Q_1=8.7 \times 10^{-4} \text{ m}^3/\text{s}$, (b) $Q_2=1.74 \times 10^{-3} \text{ m}^3/\text{s}$, and (c) $Q_3=2.61 \times 10^{-3} \text{ m}^3/\text{s}$

quired to extract the cold exergy contained in the PCM, and the quality of the HTF is increased as well due to the nature of Eq. (25). Since the inlet temperature is lowered, the temperature difference of the HTF has more of an effect, which raises the exergy gain of the HTF. In short, this result suggests that melting of a solid in a superheated liquid is more efficient when the liquid temperature is lower or closer to the solidification temperature.

When the HTF flow rate is increased, the exergy efficiency decreases as well due to the same reasons as discussed when addressing HTF temperature. The overall mass of HTF used in Eq. (25) is greatly increased; however, the temperature difference observed by the HTF is decreased, and the exergy gain is not as effective. So, although the captured exergy by the HTF can seem to be greater because of the increased mass of HTF, it is actually less because the HTF flow temperature difference is much lower.

Finally, when compared across geometry, it can be inferred that the spherical capsules are the most efficient exergetically, followed by the cylindrical and lastly the slab capsules. Although the exergy destroyed through viscous dissipation is much greater for the spherical and cylindrical capsules than for the slab capsules, this mode of loss is once again much less than the losses incurred through entropy generation. By viewing Table 4, it is quite apparent that the most desirable geometry in terms of charging times is the slab capsule. However, due to the nature of Eq. (25), in order to capture as much exergy as possible from the capsule, either the temperature difference of the HTF or the total mass of the HTF must be increased. By viewing the exergetic results of Fig. 9, it is shown that the total mass of HTF is more dominant. For example, the slab capsules have the lowest charging times, suggesting that they have the greatest HTF temperature difference, while for the spherical capsules, which attain the highest charging times, the HTF temperature difference would be quite small comparatively. Since the spherical capsules attain the highest exergy efficiency values, it is clear that it is more desirable to melt slower, which lessens the quality gain in the mass of HTF. This suggests that, at least in this case, it is more desirable to melt ice using a larger mass of HTF than a smaller mass, which would achieve a greater

temperature difference.

Another important criterion, which must be taken into consideration, is the variance in exergy efficiency when ambient conditions change. Since ambient temperatures are intrinsic to the exergy analysis, it is always interesting to note how these values are affected when the dead state or ambient temperature is changed. So, as an example, the spherical capsules were chosen with flow rate Q_3 , and the exergy efficiencies were monitored while the ambient temperature was varied from 275 K to 320 K. The results can be seen in Fig. 10. One immediately notices that the energy efficiency remains unchanged when the ambient temperature is changed, and this is a result of the independence of the energy analyses on the ambient conditions. However, in cold TES exergy analyses, the reference temperature is actually very important since it governs the potential of thermal storage. Figure 10 accurately reflects this, and as dead-state temperatures increase, the exergy efficiencies increase along with it. This is due to the fact that the stored exergy content becomes much larger for larger dead-state temperatures, while the destroyed exergy content is

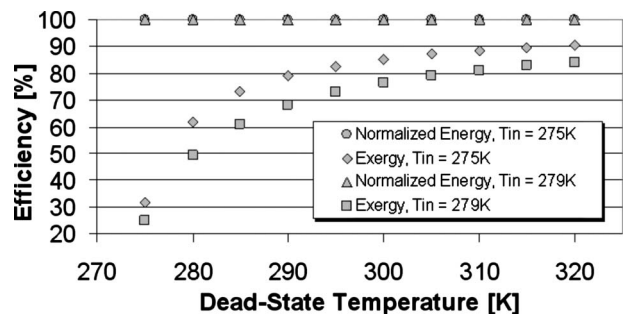


Fig. 10 Effect of dead-state temperature on exergy and normalized energy efficiencies for the spherical geometry with a flow rate of $Q_3=2.61 \times 10^{-3} \text{ m}^3/\text{s}$

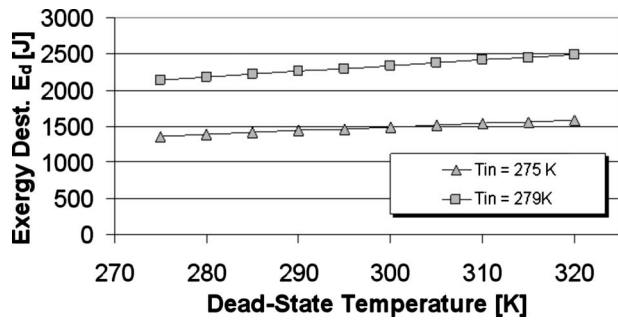


Fig. 11 Exergy destruction with respect to the dead-state temperature; the spherical geometry with a flow rate of $Q_3=2.61 \times 10^{-3} \text{ m}^3/\text{s}$ is shown

largely unaffected (see Fig. 11).

At first glance, it may be compelling to dismiss the destroyed exergy amounts as quite small since their values are only in the order of a few thousand joules. However, these losses can add up, and it helps to consider what kinds of losses can be expected in a storage tank of a few thousand capsules for a modest daily cooling load. To illustrate this, the cylindrical geometry was chosen with a flow rate of Q_3 , and destroyed exergy contents for storage tanks with capsules of either 1000 or 5000 are shown in Fig. 12. In inspection of Fig. 12, it is quite apparent that the destroyed exergy contents do indeed become quite for larger storage tanks. It is for this reason why exergy analyses should be implemented during design and before building systems since large system losses can be avoided by choosing the correct inlet HTF temperatures, flow rates, and capsule geometries.

In summary, the most important factor regarding exergy efficiency was found to be the inlet HTF temperature. By regulating the temperature—and hence quality—of the entering HTF fluid, large gains in efficiency can be realized. In addition, it was also found that having a slower HTF flow rate also increased the efficiency in all cases, though the efficiency gains were not as large as when the inlet temperatures were varied. The spherical capsules were found to be the most efficient exergetically, and one final note should be made about this particular geometry. Spherical capsules have been used in the encapsulated ice TES industry for a number of years and have many advantages in storage systems. They can be manufactured to be of any size, require no internal structure, and can be packed fairly efficiently at random. Even though energetically the slab capsules proved to be the most efficient, the quality of the thermal storage is not taken into effect, and the spherical capsule geometries should remain most efficient for discharging processes such as these.

4 Conclusions

In this paper, the process of melting in some common encapsulated ice TES geometries has been modeled and simulated using

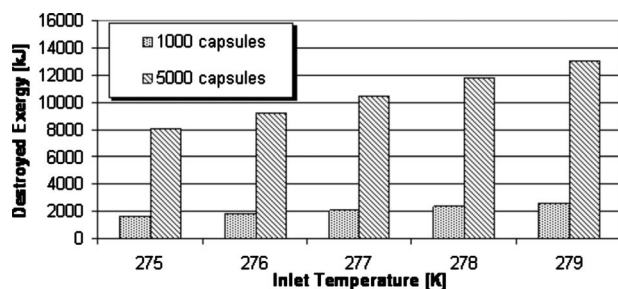


Fig. 12 Exergy destroyed contents for the cylindrical geometry, experiencing a flow rate of $Q_3=2.61 \times 10^{-3} \text{ m}^3/\text{s}$ in a bed of 1000 or 5000 capsules.

the commercially available FLUENT 6.0 software for computational fluid mechanics and heat transfer. Spherical, slab (rectangular), and cylindrical capsules were investigated and modeled to be in a packed bed of like capsules. The model was validated and found to be in good agreement with experimental results. Following this validation, simulations were performed while varying the inlet HTF temperature, flow rate, and reference temperature. The inlet HTF temperature was varied from 275 K to 279 K, the flow rate was varied from 0.87 l/s to 2.61 l/s, and the reference temperature was varied from 275 K to 320 K.

A detailed analysis was then performed after an adequate amount of data was obtained to facilitate calculations. Performance criteria that were observed include melting times, energy efficiency, and exergy efficiency, and the following relationships were concluded.

- Discharging times tended to decrease along with increased inlet heat transfer fluid temperatures.
- The slab capsule, followed by the cylindrical and lastly the spherical capsule, experienced the lowest discharging time.
- Flow rate has little effect on charging times when compared with the effects seen by changing inlet HTF temperature, but higher flow rates produced lower charging times.
- Increased heat transfer fluid temperatures corresponded to increased energy efficiencies, but decreased exergy efficiencies.
- Increased flow rates correspond to decreased energy and exergy efficiencies.
- The slab capsule was most efficient energetically, followed by the spherical and lastly the cylindrical capsule.
- Exergetically, the most efficient geometry was the sphere, followed by the cylindrical and slab capsules.
- All energy efficiencies were over 99.98%, while exergy efficiencies varied from 72.75% to 84.45%.
- Energetically, the most efficient scenario was realized by the slab capsule, with a flow rate of Q_1 and an inlet HTF temperature of 279 K, which produced an efficiency of well over 99.99%.
- Exergetically, the best scenario was the spherical capsule, with a flow rate of Q_1 and an inlet HTF temperature of 275 K, which attained an efficiency of 84.45%.
- The least efficient capsule energetically was the cylindrical capsule, with a flow rate of Q_3 and an inlet HTF temperature of 275 K, which attained a minimum efficiency value of just over 99.98%. Exergetically, the least efficient capsule was the slab capsule, with a flow rate of Q_3 and an inlet HTF temperature of 279 K, corresponding to a minimum exergy efficiency of 72.75%.
- The destroyed exergy due to viscous dissipation was far less than the exergy destroyed due to entropy generation resulting from heat transfer accompanying phase change.

Lastly, the effect of the dead-state (or reference) temperature is very interesting to note. It was noticed that while the reference temperature had absolutely no effect on the energy efficiency, the exergy efficiency was drastically improved by increasing the dead-state temperature. The opposite effect was also true; a lowering of the reference temperature produced much lower exergy efficiencies. This is due to the quality of the latent storage. For higher reference temperatures, the latent heat storage is much higher, which produces much higher efficiencies since the exergy destroyed term is largely unaffected by reference temperature in comparison.

In summary, in any cold thermal energy storage analysis, it is clearly more advantageous to consider exergy analysis to correctly determine the system performance. Using energy analyses alone, designers may not seek to improve design since all processes may appear to be over 99.9% efficient. However, using exergy analysis this has proved to be false and, in fact, a great deal of losses can be observed by varying something as simple as the inlet flow rate

or temperature of the HTF. For these reasons, only when exergy and energy analyses are used together can a better picture of the system dynamics be realized.

Acknowledgment

The authors acknowledge the support provided by the Natural Sciences and Engineering Research Council of Canada.

Nomenclature

C = specific heat capacity (J/kg K)
 D = diameter (m)
 E = total energy (J)
 \tilde{f} = wall facet
 h = sensible enthalpy (J/kg)
 H = total specific enthalpy (J/kg)
 Ht = height (m)
 \vec{i} = unit normal vector in the x -direction
 \vec{j} = unit normal vector in the y -direction
 k = thermal conductivity (W/m K)
 \vec{k} = unit normal vector in the z -direction
 L = Latent heat (J/kg)
 Le = length (m)
 M = mass (kg)
 \vec{n} = normal vector
 p = static pressure (kg/m s²)
 p^* = guessed pressure field
 \bar{P} = average pressure (kg/m s²)
 P = total pressure (kg/m s²)
 R = radius (m)
 S = entropy (J/K)
 t = time (s)
 T = temperature (K)
 \bar{T} = average temperature (K)
 u = x -velocity (m/s)
 U = internal energy (J/kg)
 v = y -velocity (m/s)
 V = velocity (m/s)
 \bar{V} = volume (m³)
 \vec{V} = velocity (m/s)
 w = z -velocity (m/s)

Greek Letters

β = liquid fraction
 γ = dummy variable
 Δ = "change in"
 η = energy efficiency
 $\bar{\eta}$ = normalized energy efficiency
 μ = dynamic viscosity (kg/m s)
 Ξ = total exergy (J)
 ρ = density (kg/m³)
 Φ = dissipation function
 ψ = exergy efficiency
 ∇ = differential "del" operator
 \in = "is an element of"
 \notin = "is not an element of"

Subscripts

∞ = dead-state
 b = bulk
 c = centroid
 C = cylinder
 ch = charging
 $cross$ = cross-sectional
 cyl = cylinder
 d = destroyed

D = diameter
 des = desired
 dis = discharging
 $diss$ = from viscous dissipation
 f = final
 gen = generated
 HTF = heat transfer fluid
 i = ice
 in = inlet
 ini = initial
 $inner$ = inner
 l = latent portion
 ns = no shear
 O = reference environment
 out = outlet
 PCM = phase change material
 PVC = polyvinyl chloride
 S = slab
 sf = solidification
 $slab$ = slab (rectangular capsule)
 sys = system
 tot = total
 $trans$ = from heat transfer
 w = water
 wa = wall

References

- [1] Balikowski, J., and Mollendorf, J., 2007, "Performance of Phase Change Materials in a Horizontal Annulus of a Double Pipe Heat Exchanger in a Water Circulating Loop," *ASME J. Heat Transfer*, **129**, pp. 265–272.
- [2] Lee, W., Chen, B., and Chen, S., 2006, "Latent Heat Storage in a Two-Phase Thermosiphon Solar Water Heater," *ASME J. Sol. Energy Eng.*, **128**, pp. 69–76.
- [3] Saha, S., Srinivasan, K., and Dutta, P., 2008, "Studies on Optimum Distribution of Fins in Heat Sinks Filled With Phase Change Materials," *ASME J. Heat Transfer*, **130**, p. 034505.
- [4] IESO, 2008, "Ontario Demand and Market Prices, August 8, 2008," http://www.ieso.ca/imoweb/siteShared/demand_price.asp?sid=ic.
- [5] Dincer, I., and Rosen, M. A., 2001, "Energetic, Environmental and Economic Aspects of Thermal Energy Storage Systems for Cooling Capacity," *Appl. Therm. Eng.*, **21**, pp. 1105–1117.
- [6] Wen, D., and Ding, Y., 2006, "Heat Transfer of Gas Flow Through a Packed Bed," *Chem. Eng. Sci.*, **61**, pp. 3532–3542.
- [7] Dekhtyar, R. A., Sikovsky, D. P., Gorine, A. V., and Mukhin, M., 2002, "Heat Transfer in a Packed Bed at Moderate Values of the Reynolds Number," *High Temp.*, **40**, pp. 693–700.
- [8] Yee, S. S., and Kamiuto, K., 2002, "Effect of Viscous Dissipation on Forced-Convection Heat Transfer in Cylindrical Packed-Beds," *Int. J. Heat Mass Transfer*, **45**, pp. 461–464.
- [9] Nakayama, A., Kuwahara, F., and Kodama, Y., 2006, "An Equation for Thermal Dispersion Flux Transport and Its Mathematical Modeling for Heat and Fluid Flow in a Porous Medium," *J. Fluid Mech.*, **563**, pp. 81–96.
- [10] Lin, H. J., and Horvath, S., 1981, "Viscous Dissipation in Packed Beds," *Chem. Eng. Sci.*, **36**, pp. 47–55.
- [11] Delgado, J. M. P. Q., 2006, "A Critical Review of Dispersion in Packed Beds," *Heat Mass Transfer*, **42**, pp. 279–310.
- [12] Laguerre, O., Amara, S. B., Alvarez, G., and Flick, D., 2008, "Transient Heat Transfer by Free Convection in a Packed Bed of Spheres: Comparison Between Two Modeling Approaches and Experimental Results," *Appl. Therm. Eng.*, **28**, pp. 14–24.
- [13] MacPhee, D., and Dincer, I., 2009, "Thermal Modeling of a Packed Bed Thermal Energy Storage System During Charging," *Appl. Therm. Eng.*, **29**, pp. 695–705.
- [14] Kerslake, T. W., and Ibrahim, M. B., 1994, "Two-Dimensional Model of a Space Station Freedom Thermal Energy Storage Canister," *ASME J. Sol. Energy Eng.*, **116**(2), pp. 114–121.
- [15] Benmansour, A., Hamdan, M. A., and Bengueudach, A., 2006, "Experimental and Numerical Investigation of Solid Particles Thermal Energy Storage Unit," *Appl. Therm. Eng.*, **26**, pp. 513–518.
- [16] Kousksou, T., Bédécarrats, J. P., Dumas, J. P., and Mimet, A., 2005, "Dynamic Modeling of the Storage of an Encapsulated Ice Tank," *Appl. Therm. Eng.*, **25**, pp. 1534–1548.
- [17] ASHRAE, 1997, *ASHRAE Fundamentals Handbook*, American Society of Heating, Refrigerating and Air-Conditioning Engineers, Inc., Atlanta, GA, Chap. 20.
- [18] Chorin, A. J., 1968, "Numerical Solution of Navier-Stokes Equations," *Math. Comput.*, **22**, pp. 745–762.
- [19] Voller, V. R., and Prakash, C., 1987, "A Fixed-Grid Numerical Modeling Methodology for Convection-Diffusion Mushy Region Phase-Change Prob-

lems," *Int. J. Heat Mass Transfer*, **30**, pp. 1709–1720.

- [20] Voller, V. R., 1987, "Modeling Solidification Processes," *Mathematical Modeling of Metals Processing Operations Conference*, American Metallurgical Society.
- [21] Voller, V. R., Brent, A. D., and Reid, K. J., 1987, "A Computational Modeling Framework for the Analysis of Metallurgical Solidification Process and Phenomena," *Conference for Solidification Processing*.
- [22] Sahin, A. Z., 1999, "The Effect of Variable Viscosity on the Entropy Generation and Pumping Power in a Laminar Fluid Flow Through a Duct Subjected to Constant Heat Flux," *Heat Mass Transfer*, **35**, pp. 499–506.
- [23] Lenotre, C., 2003, "Sub-Zero Thermal Energy Storage for Process Cooling," *Kansas City Technical Program (Seminar 16: Emerging Technologies in the Refrigeration Industry)*, Cristopia Thermal Energy Storage, Inc., San Dimas, CA.
- [24] MacPhee, D., 2008, "Performance Investigation of Various Cold Thermal Energy Storages," MS thesis, University of Ontario Institute of Technology, Oshawa, ON, Canada.
- [25] Ettouney, H., El-Dessouky, H., and Al-Ali, A., 2005, "Heat Transfer During Phase Change of Paraffin Wax Stored in Spherical Shells," *ASME J. Sol. Energy Eng.*, **127**, pp. 357–365.

Modeling Electron-Phonon Nonequilibrium in Gold Films Using Boltzmann Transport Model

Arvind Pattamatta

e-mail: ap65@eng.buffalo.edu

Cyrus K. Madnia¹

e-mail: madnia@eng.buffalo.edu

Department of Mechanical and Aerospace
Engineering,
University at Buffalo,
Buffalo, NY 14260-4400

Ultrashort-pulsed laser irradiation on metals creates a thermal nonequilibrium between electrons and the phonons. Previous computational studies used the two-temperature model and its variants to model this nonequilibrium. However, when the laser pulse duration is smaller than the relaxation time of the energy carriers or when the carriers' mean free path is larger than the material dimension, these macroscopic models fail to capture the physics accurately. In this paper, the nonequilibrium between energy carriers is modeled via a numerical solution of the Boltzmann transport model (BTM) for electrons and phonons, which is applicable over a wide range of lengths and time scales. The BTM is solved using the discontinuous Galerkin finite element method for spatial discretization and the three-step Runge–Kutta temporal discretization. Temperature dependent electron-phonon coupling factor and electron heat capacity are used due to the strong electron-phonon nonequilibrium considered in this study. The results from the proposed model are compared with existing experimental studies on laser heating of macroscale materials. The model is then used to study laser heating of gold films, by varying parameters such as the film thickness, laser fluence, and pulse duration. It is found that the temporal evolution of electron and phonon temperatures in nanometer size gold films is very different from the macroscale films. For a given laser fluence and pulse duration, the peak electron temperature increases with a decrease in the thickness of the gold film. Both film thickness and laser fluence significantly affect the melting time. For a fluence of 1000 J/m², and a pulse duration of 75 fs, gold films of thickness smaller than 100 nm melt before reaching electron-phonon equilibrium. However, for the film thickness of 2000 nm, even with the highest laser fluence examined, the electrons and phonons reach equilibrium and the gold film does not melt. [DOI: 10.1115/1.3111258]

1 Introduction

The physics of short-pulse laser heating of metallic films is very complex and has been the subject of many investigations [1–9]. During pulsed laser irradiation of metal films such as gold, the electron-photon interaction time is very short, on the order of femtoseconds, compared with electron-phonon interaction time, which is on the order of picoseconds. Due to this, it has been assumed that the incident photon energy of the laser beam is absorbed instantaneously by the free electrons of the metal and is confined close to the surface. Hence, a strong nonequilibrium between the energy carriers, namely, the electrons and phonons, is created in this process [1,4]. The thermal energy possessed by these “hot” electrons diffuses deeper into the film while colliding with the phonons and subsequently transferring a portion of their energy to the lattice through inelastic electron-phonon collisions. However, when the laser pulse duration is smaller than the relaxation time of the energy carriers or when the carriers' mean free path (MFP) is larger than the material dimension, the macroscopic models fail to accurately capture the nonequilibrium between the energy carriers [1,2,10,11]. Kaganov et al. [12] was the first to theoretically evaluate the thermal coupling between electrons and phonons by considering separate electron and lattice temperatures in metals. A phenomenological parabolic two-step heat conduction model was pioneered by Anisimov et al. [13] and advanced later by Fujimoto et al. [14]. The two-temperature model has been validated by experiments for gold films [3,14,15]. Qiu and Tien [1]

derived a more rigorous hyperbolic two-step radiation heating model based on quantum mechanics. But in this model, phonons act only as a reservoir and do not transport energy. To incorporate the contribution of phonons to thermal transport, Chen and Beraun [6] extended the model of Qiu and Tien [1] to include the relaxation behavior of phonons by solving a hyperbolic conduction equation for phonon transport. Although, this model incorporates the contributions of both the charge carriers to heat transport, it does not include the dynamics of interaction between the charge carriers. Therefore, the phenomenological models based on either the Fourier or Cattaneo equations cannot be used to describe heat transfer in highly nonequilibrium situations, as seen in the case of nanometer thin metallic films irradiated with laser pulse durations comparable to the electron-phonon relaxation time. In order to model this nonequilibrium accurately, the interaction between the energy carriers have to be captured by solving the coupled Boltzmann transport equations (BTEs) for the electrons and phonons [10,11]. The BTE can be used to model heat transport over a wide range of lengths and time scales. In most of the previous studies of pulsed laser interactions with gold films, a constant value of electron-phonon coupling factor has been used [2,4,6]. However, recent numerical and experimental studies [9,16] suggest that the applicability of the constant electron-phonon coupling may be limited to low electron temperatures corresponding to low laser fluences in noble metals. Lin et al. [16] also showed that in gold for electron temperatures higher than 3000 K the electron heat capacity does not follow a linear temperature dependence due to the participation of *d*-band electrons. The increase in electron-phonon coupling factor with temperature and the deviation of electron heat capacity from the linear approximation for gold are computed by Lin et al. [16]. The main objective of the present study is to model the laser heating of gold films by solving coupled BTEs describing the electron and phonon energy densi-

¹Corresponding author.

Manuscript received August 28, 2008; final manuscript received February 25, 2009; published online June 5, 2009. Review conducted by Patrick E. Phelan. Paper presented at the 2008 ASME International Mechanical Engineering Congress (IMECE2008), Boston, MA, October 31–November 6, 2008.

Table 1 Characteristic length and time scales

λ (nm)	Λ (nm)	L (nm)	Kn	t_p (ps)	τ_{e-e} (ps)	τ_{p-p} (ps)
0.5	20	20–2000	1–0.01	0.05–10	0.04	0.8

ties. Emphasis is placed on studying strong nonequilibrium created during the interaction of femtosecond pulse duration laser with nanometer size films. The temperature dependent electron heat capacity and electron-phonon coupling factor of Lin et al. [16] are used. A parametric study is conducted for gold films to study the effect of film thickness, laser pulse duration, and fluence on the electron-phonon nonequilibrium characteristics.

2 Theory

In this section, the problem description, details of the Boltzmann transport model, calculation of electron and phonon thermal properties, and the computational methodology are discussed.

2.1 Problem Description. The electron-phonon interactions are studied by applying a laser beam with a wide range of pulse durations and fluences to a gold film with thicknesses in the range of nano- to micrometers. The laser beam diameter is much larger than the optical and electron penetration depths, and hence a one-dimensional model can describe the physical problem [1]. The mathematical expression for the laser heat source is given as [1,6]

$$S(x, t) = \sqrt{\frac{\beta}{\pi}} \frac{1-R}{t_p \delta_s} \phi \cdot e^{-(x/\delta_s) - \beta(t - 2t_p)/t_p)^2} \quad (1)$$

where ϕ is the fluence carried by the laser pulse, R is the reflectivity, t_p is the laser pulse duration defined as full width at half maximum of the laser pulse shape, δ_s is the optical penetration depth, x is the depth measured from the front surface, $\beta = 4 \ln(2)$. For gold, the typical value of δ_s for visible light of wavelength 550 nm is 15.3 nm. The reflectivity of gold is dependent on the film thickness and is calculated from the expression for reflectivity of thin films given by Abelès [17]. From Eq. (1), the peak of the laser intensity occurs at time $t = 2t_p$.

Table 1 shows the characteristic length and time scales involved in the problem. These are the physical scales that affect energy transfer between the carriers. For metal thicknesses less than the phonon wavelength λ , wave effects may play a dominant role, which are neglected by the Boltzmann transport model. The regimes of heat transport can be classified based on the phonon Knudsen number Kn defined as the ratio of phonon mean free path to the metal film thickness. Thus, a Kn of 1 indicates nanoscale regime while a Kn of 0.01 indicates the macroscale or Fourier regime. The electron-electron collision time $\tau_{e-e} = 40$ fs [6] is comparable with the femtosecond laser pulse duration. On the other hand, the phonon-phonon relaxation time $\tau_{p-p} = 0.8$ ps [6] is comparable with the picosecond pulse duration. The cases with large Kn and femtosecond pulse duration represent strong nonequilibrium between the energy carriers.

2.2 Boltzmann Transport Model. The electron-phonon interaction in gold film is modeled via the Boltzmann transport model (BTM) consisting of two coupled BTEs, one each for electrons and phonons. The BTEs are formulated in the relaxation time approximation to describe the energy densities of electrons and phonons denoted by u_e and u_p , respectively. The electron or phonon energy density is defined as the flux of energy per unit volume and per unit solid angle in the direction s . The electron energy density u_e is related to its distribution function, f_e

$$u_e(\mathbf{r}, s, t) = \int (E - E_f) f_e(\mathbf{r}, s, t) D_e(E) dE \quad (2)$$

where \mathbf{r} denotes the position vector, $(E - E_f)$ is the electron band energy relative to the Fermi energy, and $D_e(E)$ is the electron density of states per unit volume. The equilibrium distribution of electrons is represented by the Fermi-Dirac distribution [18]. Similarly, the phonon energy density u_p is related to its distribution function f_p [19] as follows:

$$u_p(\mathbf{r}, s, t) = \sum \int \hbar \omega f_p(\mathbf{r}, s, t) D_p(\omega) d\omega \quad (3)$$

where \hbar is the Planck's constant divided by 2π , ω is the phonon frequency, $D_p(\omega)$ is the phonon density of states per unit volume and the summation is over the three phonon polarization modes. The equilibrium distribution of phonons is represented by the Bose-Einstein distribution [20].

The frequency independent BTM for coupled electron and phonon energy intensities can be expressed as [21,22]

$$\frac{\partial u_e}{\partial t} + v_e \left(\mu \frac{\partial u_e}{\partial x} \right) = \frac{u_{eq(e)} - u_e}{\tau_{(e-e)}} - \frac{G(T_e - T_p)}{4\pi} + \frac{S(x, t)}{4\pi} \quad (4)$$

$$\frac{\partial u_p}{\partial t} + v_p \left(\mu \frac{\partial u_p}{\partial x} \right) = \frac{u_{eq(p)} - u_p}{\tau_{(p-p)}} + \frac{G(T_e - T_p)}{4\pi} \quad (5)$$

Here the subscript e and p denote the electron and phonon, respectively. The equilibrium energies are given by

$$u_{eq(e)} = \frac{1}{4\pi} \int_{-1}^1 \int_0^{2\pi} u_e d\Omega \quad \text{and} \quad u_{eq(p)} = \frac{1}{4\pi} \int_{-1}^1 \int_0^{2\pi} u_p d\Omega \quad (6)$$

where μ is the x -direction cosine. In Eqs. (4) and (5), G is the electron-phonon coupling parameter and represents the inelastic scattering that drives the electrons and phonons to equilibrium. In gold films, the value of G is nearly constant up to temperatures of approximately 3000 K and significantly increases at higher temperatures [16]. This is due to the participation of d -band electrons in gold, which increases the number of carriers that can collide with the lattice and transfer energy, thus increasing the electron-phonon coupling factor at higher electron temperatures. The electron-phonon coupling factor of gold as a function of temperature obtained from the electron density of states by Lin et al. [16] is used in the present simulations to accurately model the cases with strong electron-phonon interactions.

2.3 Electron and Phonon Properties. The solution to the BTM requires knowledge of electron and phonon relaxation times, group velocities, thermal conductivities, and heat capacities. For gold film, at high laser fluence, the electron temperature can be of the order of its Fermi temperature of 64,200 K. At such high electron temperatures, the assumption of linear dependence of electron thermal conductivity on temperature does not hold anymore. Therefore, a general expression to evaluate the electron thermal conductivity K_e , which is valid over a wide range of electron temperatures, is considered here [23]

$$K_e = \chi \frac{(\vartheta_e^2 + 0.16)^{5/4} (\vartheta_e^2 + 0.44) \vartheta_e}{(\vartheta_e^2 + 0.092)^{1/2} (\vartheta_e^2 + \eta \vartheta_l)} \quad (7)$$

where $\vartheta_e = \kappa_b T_e / E_f$, $\vartheta_l = \kappa_b T_l / E_f$, $\chi = 353 \text{ W m}^{-1} \text{ K}^{-1}$, and $\eta = 0.16$ for gold. For high electron temperatures $\vartheta_e \gg 1$, the above equation results in the well-known dependence $K_e T_e^{5/2}$, which is valid for low density plasma. In the low-temperature limit $\vartheta_e \ll 1$, the equation for K_e reduces to the standard expression $K_e = 315 T_e / T_l$ for gold. The temperature dependent electron heat capacity calculated by Lin et al. [16] is used instead of the linear

relation $C_e=70T_e$. The electron relaxation time is assumed to be constant and is given in Table 1. The electron velocity is calculated from the kinetic relation $K_e=C_e v_e^2 \tau_{(e-e)}/3$. The values of total thermal conductivity for gold ranging from room temperature to the melting temperature are obtained from Refs. [24,25]. The temperature dependent phonon thermal conductivity is calculated to be 1% of the total thermal conductivity and the phonon specific heat is calculated based on the Debye model. The relaxation time for phonons is given in Table 1. The phonon velocity is obtained from a similar kinetic relation expressed for electrons.

2.4 Computational Methodology. The coupled BTEs for electrons and phonons are solved numerically using the Runge–Kutta discontinuous Galerkin (RKDG) method [26–28]. The RKDG method incorporates the local conservation property of the finite volume schemes and the higher order accuracy of finite element methods [26]. The DG methods have some attractive properties that make them good alternatives to existing methods for problems described using hyperbolic equations such as those encountered in fluid flows or thermal radiation. These properties include high-order local approximation using polynomials, ease of parallelization, elementwise conservation, and geometric flexibility of conventional finite elements. High resolution temporal discretization is achieved using a four stage Runge–Kutta time stepping scheme that allows the RKDG method to be numerically stable [27].

The RKDG scheme using piecewise constant Legendre polynomials as basis functions is developed by the authors for the BTEs for electrons and phonons [21]. Two Legendre bases involving the piecewise constant and piecewise linear functions are used for higher order spatial discretization. The angular discretization of the BTEs is achieved using the “finite volume” method extended to the angular space [29]. This allows for exact analytical evaluation of the integrals in the BTEs without the use of quadratures.

A detailed spatial, angular, and temporal resolution study has been performed to test for grid independence of the solution [21]. It is found that a spatial grid with 50 elements and an angular decomposition with 30 elements provide the best resolution of the temperature profiles. A temporal resolution study has also been performed and a value of Courant number equal to 0.2 is found to ensure accurate transient solution using the RK time stepping.

During the very short duration of laser heating, heat losses from the front and back surfaces of the metal are found to be negligible and hence treated as adiabatic. These surfaces are modeled as specularly reflecting boundaries on which the following conditions on electron and phonon thermal intensities are imposed:

$$u_e(0, \mu, t) = u_e(0, -\mu, t), \quad u_e(L, -\mu, t) = u_e(L, \mu, t) \quad (8)$$

$$u_p(0, \mu, t) = u_p(0, -\mu, t), \quad u_p(L, -\mu, t) = u_p(L, \mu, t) \quad (9)$$

where μ is the x -direction cosine.

The initial energy densities for electrons and phonons are assumed to be constants and are calculated at $T=300$ K. The energy densities obtained from solving the BTEs are used to determine the electron and phonon temperatures from

$$\int_0^{T_e} C_e dT = u_e(x, \theta) \Delta\Omega \quad \int_0^{T_p} C_p dT = u_p(x, \theta) \Delta\Omega \quad (10)$$

where $\Delta\Omega=4\pi \sin \theta \sin(0.5\Delta\theta)$ is the volume of the “finite angle.” The integrals in the equation above are evaluated using trapezoidal rule and the temperatures are obtained iteratively using the bisection method. At nanoscales, the temperature, as such, has no physical meaning except that it is an indicator of the local energy density of the system.

3 Results and Discussion

The BTM is verified with the experimental result of Qiu et al. [2], involving a 20 nm thick gold film, heated with a 100 fs laser

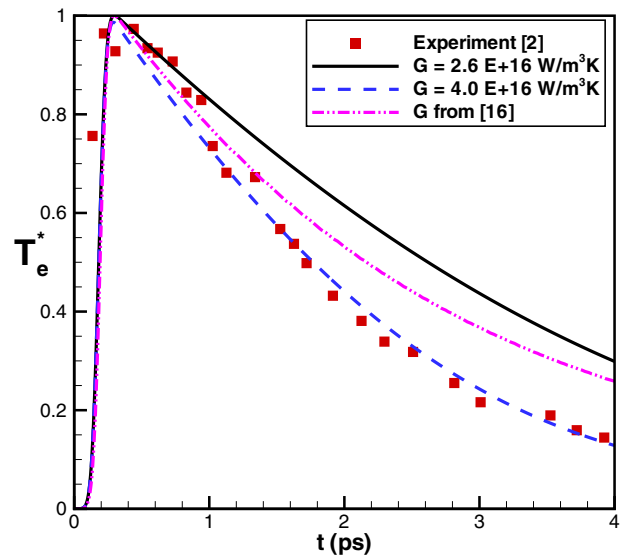


Fig. 1 Nondimensional electron temperature profiles at the front surface of a gold film for $L=20$ nm and $\phi=13.4$ J/m²

pulse having a fluence of 13.4 J/m². Figure 1 depicts the calculated electron temperature profiles at the front surface compared with the experimental data for different values of electron-phonon coupling parameter G . The electron temperature is nondimensionalized with its maximum value. The commonly used value of $G=2.6 \times 10^{16}$ W m⁻³ K⁻¹ for bulk gold is compared with the value of 4.0×10^{16} W m⁻³ K⁻¹ and with the temperature dependent value for G obtained from Ref. [16]. The best agreement of electron temperature profile with the experiment is obtained for the value of $G=4.0 \times 10^{16}$ W m⁻³ K⁻¹. A similar value of G has been obtained experimentally for thin gold films [30]. Hence, for cases with low laser fluences corresponding to electron temperatures less than 3000 K, a constant coupling factor of 4.0×10^{16} W m⁻³ K⁻¹ is used while the temperature dependent value of G from Ref. [16] is used for electron temperature above 3000 K.

The BTM is applied to the problem of laser heating of gold film by varying different parameters and studying their impact on the thermal transport in gold. The categories considered for the parametric study are summarized in Table 2. The values of film thickness, laser fluence, and laser pulse duration have been chosen to span a wide range of lengths and time scales over which BTM can be applied. Three categories are considered. For each category several simulations are performed. In Category 1, the effect of film thickness in the range of 20–2000 nm is studied, keeping the laser pulse duration and the fluence fixed at 75 fs and 1000 J/m², respectively. In Category 2, the effect of laser pulse duration in the range of 0.05–10 ps is studied, keeping the thickness and the fluence fixed at 20 nm and 1000 J/m², respectively. The total input energy obtained through the time integration of the laser source in Eq. (1), is the same for both Categories 1 and 2. In Category 3, the laser fluence is varied while maintaining the film thickness and pulse duration fixed at 20 nm and 75 fs, respectively. The pulse duration of 75 fs is comparable to the electron-

Table 2 Summary of parameters

Category	L (nm)	t_p (ps)	ϕ (J/m ²)	R
1	20–2000	0.075	1000	0.54–0.93
2	20	0.05–10	1000	0.54
3	20	0.075	10–1000	0.54

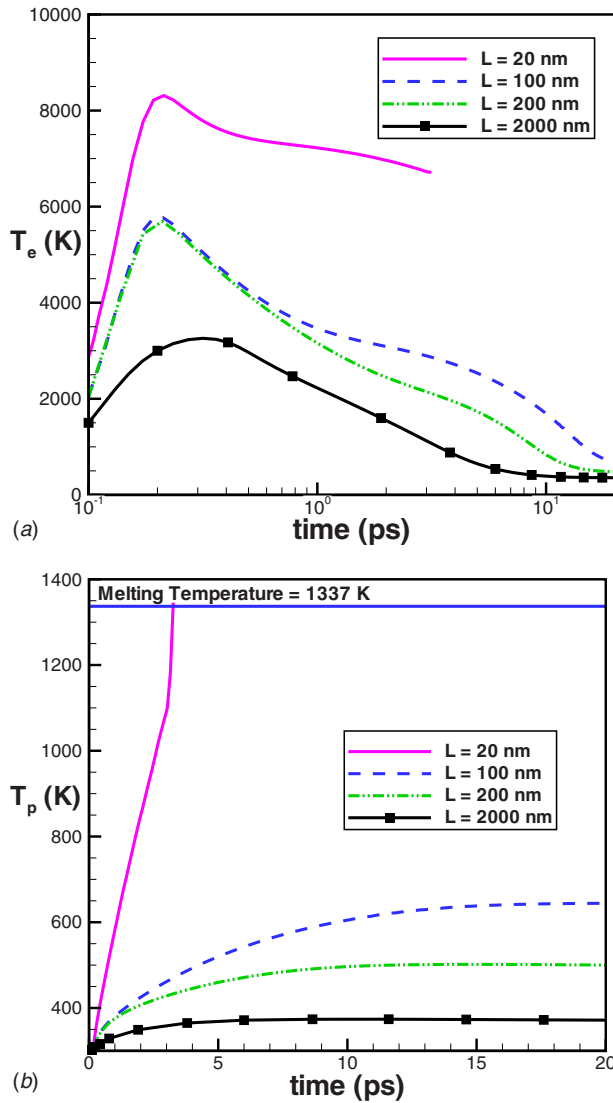


Fig. 2 Temporal variation of temperature at the front surface with film thickness for (a) electrons and (b) phonons; $t_p = 75$ fs and $\phi = 1000$ J/m²

electron collision time. The short-pulse duration and the high fluence used in this study are chosen to create a strong nonequilibrium between the energy carriers. The values of reflectivity R , shown in Table 2, obtained from the expression of Abelès [17], is between 0.54 and 0.93 depending on the gold film thickness. The value of R for a film of thickness of 20 nm is 0.54 as compared with 0.93 for $L = 2000$ nm.

3.1 Temporal Characteristics of Electron-Phonon Nonequilibrium. Figure 2 shows the temporal evolution of electron and phonon temperatures at the front surface of the gold film for varying film thicknesses (Category 1 of Table 2). It can be observed from Fig. 2(a) that due to the small heat capacity of electrons as compared with the phonons, peak temperatures of several thousand Kelvin is attained. For thicknesses smaller or comparable to the electron mean free path of 20 nm, where diffusion is negligible, the electron transport is almost entirely ballistic inside the gold film. Also, for film thicknesses comparable to the laser penetration depth of 15 nm, the entire film is heated up uniformly. Therefore, it is observed from Fig. 2(a) that the peak electron temperature approaches values in excess of 8000 K for the smallest thickness and decreases with increasing film thickness. For the metal thicknesses less than 100 nm, the electron

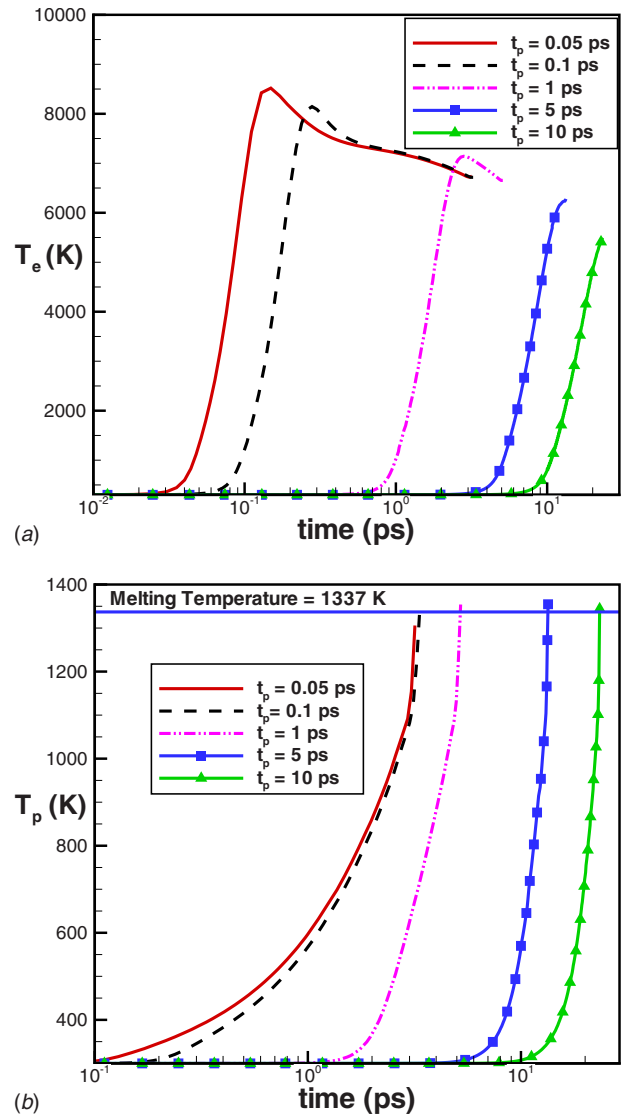


Fig. 3 Temporal variation of temperature at the front surface with pulse duration for (a) electrons and (b) phonons; $L = 20$ nm and $\phi = 1000$ J/m²

temperature decays very slowly in time. This is primarily due to the ballistic nature of electron transport. For these cases, the phonon temperature rises rapidly due to electron-phonon collisions and approaches the melting temperature of 1337 K [4], as seen in Fig. 2(b). Whereas, for thicknesses in the macroscale range, for example, for $L = 2000$ nm, the electron temperature approaches the phonon temperature without the melting of the gold film. This may be attributed to the faster rate of energy exchange due to electron-electron collisions when the diffusion effects are dominant. Figure 2(b) shows that phonon temperature increases very rapidly for thin films. The kink in the phonon temperature profile for $L = 20$ nm case may be attributed to enhanced electron-phonon interactions thereby increasing the slope of the phonon temperature before melting.

Figure 3, corresponding to Category 2 in Table 2, shows the effect of varying the laser pulse duration on electron and phonon temperatures when irradiated with a fluence of 1000 J/m². In all these simulations, the metal thickness is kept constant at 20 nm. For pulse durations shorter than the electron-phonon relaxation time and comparable to the electron-electron relaxation time, a strong nonequilibrium is created between the electrons and phonons. Thus, for laser pulse durations shorter than or equal to 1

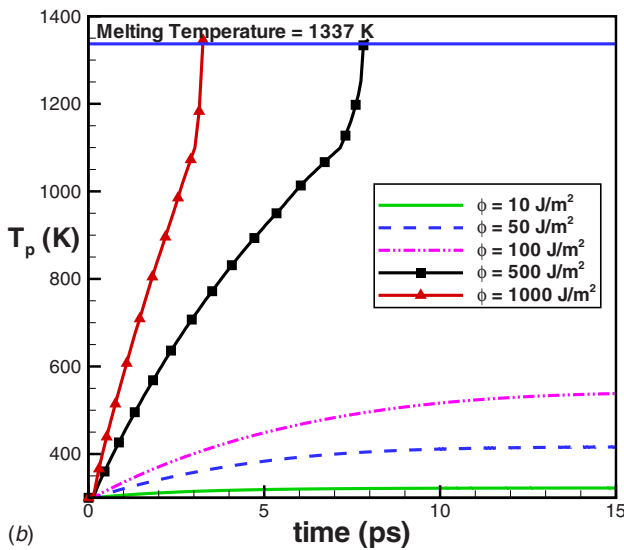
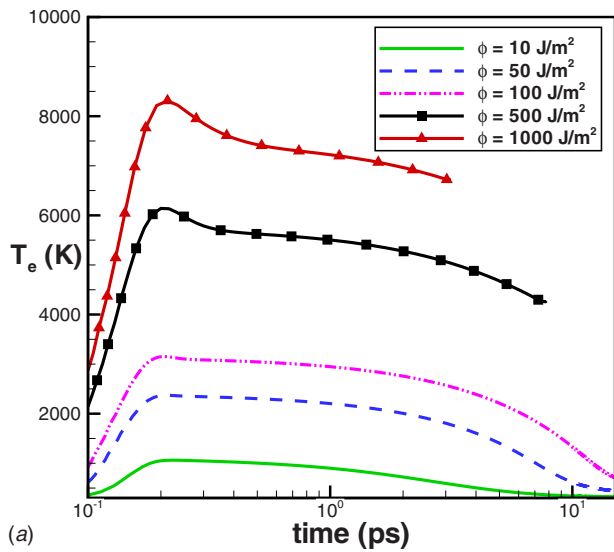


Fig. 4 Temporal variation of temperature at the front surface with laser fluence for (a) electrons and (b) phonons; $L = 20$ nm and $t_p = 75$ fs

ps, the electron temperature plotted in Fig. 3(a) decays slowly before melting. The electron-phonon collisions significantly increase for simulations with t_p longer than 1 ps. This causes hot electrons to transfer their energy directly to the phonons, which leads to the melting of the film. From Fig. 3(b), it is seen that increasing the pulse duration delays the increase in phonon temperature similar to that observed for the electron temperature in Fig. 3(a). The high phonon temperatures obtained with the laser fluence of 1000 J/m^2 leads to the melting of the gold film for all values of laser pulse durations.

The effect of varying the laser intensity on the electron and phonon temperatures, Category 3 in Table 2, is shown in Fig. 4. Larger values of fluence imply higher total energy input and therefore contribute to higher electron temperatures as seen in Fig. 4(a). This figure shows that for fluence of 1000 J/m^2 the maximum electron temperature increases beyond 8000 K , whereas for a low fluence of 10 J/m^2 the maximum temperature only reaches 1000 K . Also, for laser fluences less than 500 J/m^2 , the electron temperature reaches equilibrium with the phonon temperatures without the melting of the gold film. From Fig. 4(b), it is seen that the phonon temperature increases with the laser fluence due to the coupling with electron temperature. The kinks in the phonon tem-

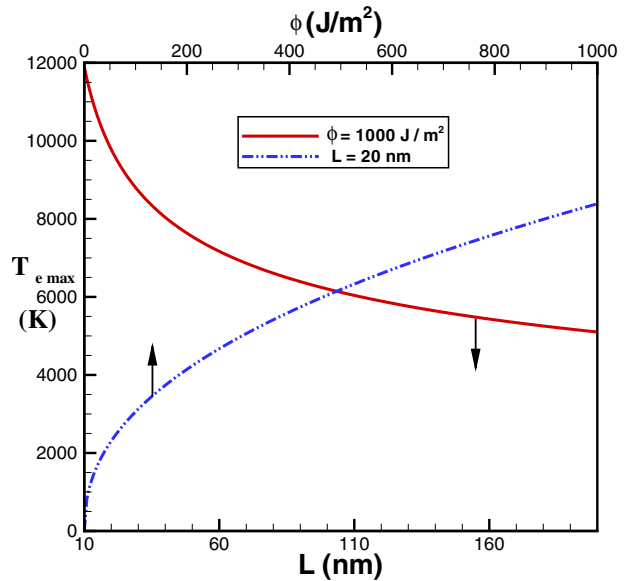


Fig. 5 Variation of maximum electron temperature with laser fluence and film thickness for a pulse duration of 75 fs

perature, similar to that seen in Fig. 2(b) is observed for fluences higher than 100 J/m^2 , whereas they are absent for the low fluence cases. From this figure, it can be seen that the 20 nm thick gold film melts when irradiated with a femtosecond pulse duration laser of fluence greater than or equal to 500 J/m^2 .

The maximum electron temperature $T_{e_{\max}}$ is plotted as a function of the thickness as well as the laser fluence in Fig. 5. The maximum electron temperature varies between 800 K to 9000 K depending on the thickness and the fluence. Increasing the metal thickness, while keeping the fluence fixed at 1000 J/m^2 causes $T_{e_{\max}}$ to decrease. For a thickness of 20 nm , the effect of increasing fluence is to increase the maximum electron temperature.

For thicknesses less than 100 nm , $t_p = 75$ fs and $\phi = 1000 \text{ J/m}^2$, the gold film melts before reaching electron-phonon equilibrium. However, for thicker films the electron and phonon temperatures reach a constant value at equilibrium. The phonon Knudsen number for a thickness of 2000 nm is 0.01 , which corresponds to the Fourier heat conduction regime. The equilibrium time t_{eq} is defined as the time when the relative difference between the electron and phonon temperatures becomes less than 1% . For $L = 2000 \text{ nm}$, it is found that the smallest values of t_{eq} are achieved for the short-pulse duration and low fluence cases.

3.2 Spatial Characteristics of Electron-Phonon Nonequilibrium. Figure 6 shows the spatial variation of electron and phonon temperatures at time instants corresponding to the initial transient and the time before melting. The temperatures are compared for film thicknesses of 20 nm and 200 nm , respectively, irradiated with a 75 fs laser pulse at a fluence of 1000 J/m^2 . The time instant of 200 fs is the same for both film thicknesses, while the time instants 1 ps and 9 ps are for thicknesses corresponding to 20 nm and 200 nm , respectively. For the 20 nm film, at both time instants, the electron and phonon temperatures show a smaller variation inside the film when compared with the 200 nm film. For film thicknesses comparable or smaller than the laser penetration depth, the laser energy is deposited uniformly inside the gold film as seen from Eq. (1). Also, for film thickness of 20 nm , which is comparable or smaller than the mean free path of the charge carriers, the heat transport occurs ballistically. However, for the 200 nm thick gold film, both ballistic and diffusive effects contribute to the heat transport. At a time instant of 0.2 ps , hot electrons dominate near the front surface of the 200 nm thick film. Since the film thickness is much larger than the laser penetration

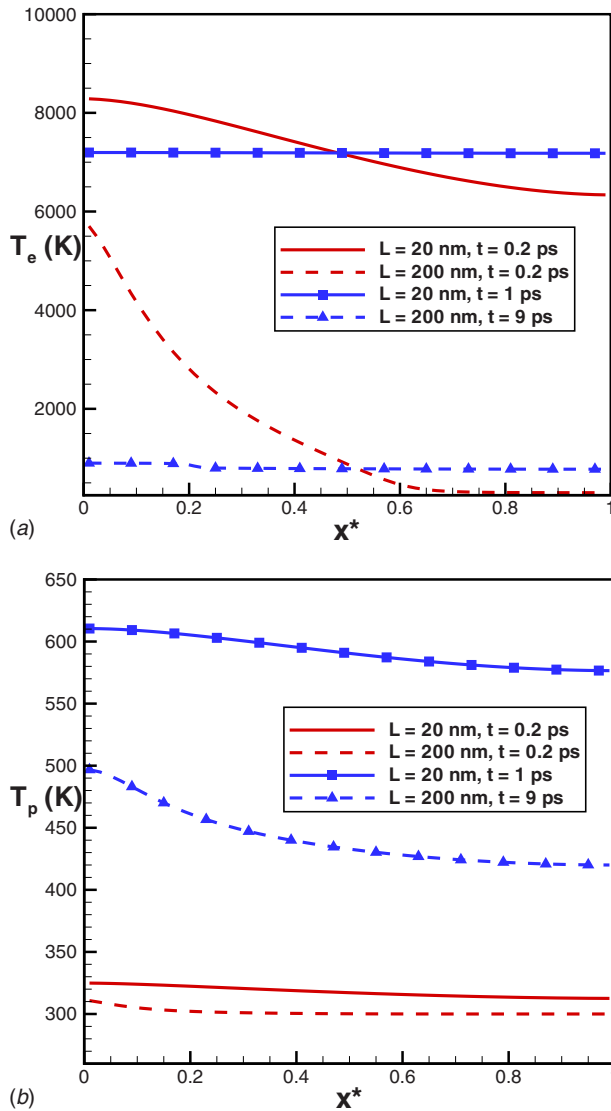


Fig. 6 Spatial variation of (a) electron temperature and (b) phonon temperature for $t_p=75$ fs and $\phi=1000$ J/m²

depth, the electron temperature at the rear surface is not affected by the laser. At this time, the phonon temperature is close to 300 K. From Fig. 6(a), it is observed that for $L=200$ nm, at a time instant of 9 ps, the electron temperature shows a kink near the nondimensional location of 0.2, corresponding to 40 nm. For axial locations less than 40 nm the ballistic effects are dominant. However, for axial locations larger than 40 nm, the energy of the hot electrons is depleted due to diffusion and hence less of it is transferred to the phonons resulting in a slower rate of decrease in the phonon temperature as seen in Fig. 6(b). At this time, the electrons thermalize rapidly resulting in a near uniform electron temperature inside the gold film. For the 20 nm film shown in Fig. 6, melting occurs before the electrons and phonons reach equilibrium.

3.3 Melting Threshold Fluence. For laser microstructuring applications that require high precision, determination of the melting threshold fluence ϕ_m is of importance. For that reason, the dependence of the absorbed threshold fluence on the film thickness and laser pulse duration is shown in Fig. 7. The melting threshold fluence is defined as the value of laser fluence at which the phonon temperature reaches the melting temperature of gold. Figure 7(a) shows the variation in melting threshold fluence with the film thickness and the pulse duration for a laser pulse width of

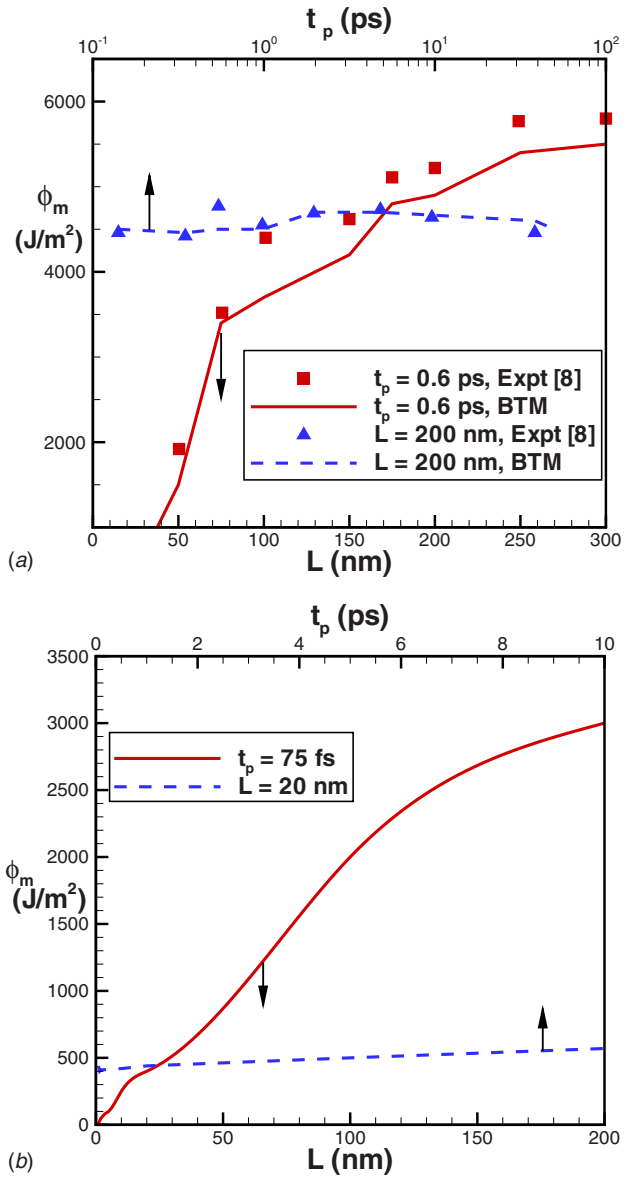


Fig. 7 (a) Comparison of melting fluence threshold with experiments; (b) melting threshold fluences for $t_p=75$ fs and $L=20$ nm

0.6 ps and film thickness of 200 nm, respectively. The melting threshold fluence calculated using the BTM is in good agreement with the experimental data of Stuart et al. [8]. From Fig. 7, it is observed that the value of laser fluence required to melt the gold film decreases with decreasing thickness. Unlike the strong variation of melting threshold with metal thickness, the variation with pulse duration is relatively small. This behavior can be explained from Fig. 3, where it was observed that irrespective of the laser pulse durations used, the gold film melts for the fluence of 1000 J/m². Figure 7(b) shows the plot of melting threshold for highly nonequilibrium cases. The variation of melting threshold with metal thickness and pulse duration is plotted for a pulse width of 75 fs and for a film size of 20 nm, respectively. It is seen from Fig. 7(b) that for the film thickness of 20 nm the melting threshold values are smaller than the values of 200 nm film thickness shown in Fig. 7(a). This may be due to an increase in the electron-phonon nonequilibrium that causes the gold film to melt at smaller values of ϕ_m . Unlike for the 200 nm thick film case, the 20 nm case shows a slight increase in melting threshold with increasing laser pulse duration.

4 Conclusions

The electron-phonon nonequilibrium due to laser heating of metal films has been previously studied using the “two-temperature” model and its variants. However, when the laser pulse duration is smaller than the relaxation time of the energy carriers or when the carriers’ mean free path is larger than the material dimension, these macroscopic models fail to capture the physics accurately. In this study, the BTM has been introduced to study the electron-phonon nonequilibrium due to short pulsed laser interaction with thin gold films. The BTM results are compared with the previous experimental results of Qiu and Tien [1] corresponding to a laser fluence of 13.4 J/m^2 and the best agreement is obtained for a constant electron-phonon coupling factor of 4×10^{16} . Thus for electron temperatures less than 3000 K, this value of the coupling factor is used with the BTM while at higher temperatures, the temperature dependent coupling factor calculated by Lin et al. [16] is used. The BTM is then applied to perform a parametric study of the effect of the gold film thickness, laser pulse duration, and fluence on the nonequilibrium between the energy carriers. The film thickness is varied between 20 nm and 2000 nm, and the laser pulse duration and fluence are varied between 50 fs to 10 ps and $10\text{--}1000 \text{ J/m}^2$, respectively. The smallest film thicknesses considered are comparable to the laser penetration depth of 15.3 nm for gold and the phonon mean free path of 20 nm. Thickness dependent reflectivity from the expression of Abelès [17] is used in the laser source term. The pulse duration of the order of femtoseconds is comparable to the electron-electron relaxation time of 40 fs. The parametric study reveals that the temporal evolution of electron and phonon temperatures in nanometer size gold films is very different from the macroscale films. The maximum electron temperature increases with a decrease in the thickness of the gold film. With the laser fluence of 1000 J/m^2 and pulse duration of 75 fs, for gold films thinner than 100 nm, the phonon temperature reaches the melting value of 1337 K. However, for the film thicknesses above 100 nm, with the highest laser fluence examined, the electrons and phonons reach equilibrium and the gold film does not melt. The melting threshold fluence calculated using the BTM for the case of 200 nm gold film irradiated by picosecond pulse width laser are found to compare well with the experimental data of Stuart et al. [8]. The threshold fluence values required to melt a 20 nm gold film are found to be smaller than that required to melt a 200 nm film. It is found that for the 20 nm thick film with t_p smaller than 1 ps, the electron temperature attains its peak before melting occurs. Both the metal thickness and fluence are found to strongly affect the melting time in gold films.

Nomenclature

C_e	= electron volumetric heat capacity ($\text{J/m}^3 \text{ K}$)
C_p	= phonon volumetric heat capacity ($\text{J/m}^3 \text{ K}$)
D_e	= electron density of states per unit volume (m^{-3})
D_p	= phonon density of states per unit volume (m^{-3})
E	= electron band energy (J)
E_f	= electron Fermi energy (J)
f_e	= Fermi–Dirac distribution function
f_p	= Bose–Einstein distribution function
G	= electron-phonon coupling parameter ($\text{W m}^{-3} \text{ K}^{-1}$)
κ_b	= Boltzmann constant (J/K)
K_e	= electron thermal conductivity (W/m K)
K_p	= phonon thermal conductivity (W/m K)
Kn	= Knudsen number (Λ/L)
L	= film thickness (nm)
m	= mass of free electron (kg)
n	= number density of free electron (m^{-3})
p	= phonon polarization mode

R	= reflectivity
\mathbf{r}	= position vector
\mathbf{s}	= direction vector
S	= laser energy source (Wm^{-3})
T_e	= electron temperature (K)
T_e^{\max}	= maximum electron temperature (K)
T_e^*	= nondimensional electron temperature, $(T_e - 300)/(T_e^{\max} - 300)$
T_p	= phonon temperature (K)
t	= time
t_{eq}	= equilibrium time
t_m	= melting time
t_p	= laser pulse duration
u_e	= electron energy density per unit solid angle ($\text{J m}^{-3} \text{ sr}^{-1}$)
u_p	= phonon energy density per unit solid angle ($\text{J m}^{-3} \text{ sr}^{-1}$)
$u_{\text{eq}(e)}$	= electron equilibrium energy density (J m^{-3})
$u_{\text{eq}(p)}$	= phonon equilibrium energy density (J m^{-3})
v_e	= average electron group velocity (m/s)
v_p	= average phonon group velocity (m/s)
x	= coordinate
x^*	= nondimensional x -coordinate (x/L)
δ_s	= optical penetration depth
θ	= polar angle (rad)
Λ	= phonon mean free path
λ	= phonon wavelength
μ	= x -directional cosine
$\tau_{(e-e)}$	= electron relaxation time
$\tau_{(p-p)}$	= phonon relaxation time
ϕ	= laser fluence (J m^{-2})
ϕ_m	= melting fluence (J m^{-2})
ω	= phonon frequency (Hz)
Ω	= solid angle (sr)

References

- [1] Qiu, T. Q., and Tien, C. L., 1993, “Heat Transfer Mechanisms During Short-Pulse Laser Heating of Metals,” *ASME J. Heat Transfer*, **115**, pp. 835–841.
- [2] Qiu, T. Q., Juhasz, T., Suarez, C., Bron, W. E., and Tien, C. L., 1994, “Femtosecond Laser Heating of Multi-Layer Metals—II. Experiments,” *Int. J. Heat Mass Transfer*, **37**, pp. 2799–2808.
- [3] Qiu, T. Q., and Tien, C. L., 1994, “Femtosecond Laser Heating of Multi-Layer Metals—I. Analysis,” *Int. J. Heat Mass Transfer*, **37**, pp. 2789–2797.
- [4] Wellershoff, S., Hohlfeld, J., Guddé, J., and Matthias, E., 1999, “The Role of Electron-Phonon Coupling in Femtosecond Laser Damage of Metals,” *Appl. Phys. A: Mater. Sci. Process.*, **69**, pp. S99–S107.
- [5] Al-Nimr, M. A., and Arpaci, V. S., 2000, “The Thermal Behavior of Thin Metal Films in Hyperbolic Two-Step Model,” *Int. J. Heat Mass Transfer*, **43**, pp. 2021–2028.
- [6] Chen, J. K., and Beraun, J. E., 2001, “Numerical Study of Ultrashort Laser Pulse Interactions With Metal Films,” *Numer. Heat Transfer, Part A*, **40**, pp. 1–20.
- [7] Chen, J. K., Tzou, D. Y., and Beraun, J. E., 2006, “A Semiclassical Two-Temperature Model for Ultrasfast Laser Heating,” *Int. J. Heat Mass Transfer*, **49**, pp. 307–316.
- [8] Stuart, B., Feit, M. D., Herman, S., Rubenchik, A. M., Shore, B. W., and Perry, M. D., 1996, “Optical Ablation by High Power Short-Pulse Lasers,” *J. Opt. Soc. Am. B*, **13**, pp. 459–468.
- [9] Hopkins, P. E., and Norris, P. M., 2007, “Substrate Influence in Electron-Phonon Coupling Measurements in Thin Au Films,” *Appl. Surf. Sci.*, **253**, pp. 6289–6294.
- [10] Tien, C., Majumdar, A., and Gerner, F., 1997, *Microscale Energy Transport*, Taylor & Francis, New York.
- [11] Chen, G., Borca-Tasciuc, D., and Yang, R., 2004, “Nanoscale Heat Transfer,” *Encyclopedia of Nanoscience and Nanotechnology*, Vol. 17, H. S. Nalwa, ed., American Scientific Publishers, pp. 429–459.
- [12] Kaganov, M. I., Lifshitz, I. M., and Tanatarov, L. V., 1957, “Relaxation Between Electrons and Crystalline Lattices,” *Sov. Phys. JETP*, **4**, pp. 173–178.
- [13] Anisimov, S. I., Kapeliovich, B. L., and Perel’man, T. L., 1974, “Electron Emission From Metal Surfaces Exposed to Ultrashort Laser Pulses,” *Sov. Phys. JETP*, **39**, pp. 375–377.
- [14] Fujimoto, J. G., Liu, J. M., and Ippen, E. P., 1984, “Femtosecond Laser Interaction With Metallic Tungsten and Non-Equilibrium Electron and Lattice Temperature in Thin Gold Film,” *Phys. Rev. Lett.*, **53**, pp. 1837–1840.

- [15] Brorson, S. D., Fujimoto, J. G., and Ippen, E. P., 1987, "Femtosecond Electronic Heat-Transfer Dynamics in Thin Gold Film," *Phys. Rev. Lett.*, **59**, pp. 1962–1965.
- [16] Lin, Z., Zhigilei, L. V., and Celli, V., 2008, "Electron-Phonon Coupling and Electron Heat Capacity of Metals Under Conditions of Strong Electron-Phonon Nonequilibrium," *Phys. Rev. B*, **77**, p. 075133.
- [17] Abelès, F., 1967, "Optics of Thin Films," *Advanced Optical Techniques*, A. C. S. Van Heel, ed., North-Holland, Amsterdam.
- [18] Ashcroft, N. W., and Mermin, N. D., 1976, *Solid State Physics*, Holt, Rinehart and Winston, New York.
- [19] Joshi, A., and Majumdar, A., 1993, "Transient Ballistic and Diffusive Phonon Heat Transport in Thin Films," *J. Appl. Phys.*, **74**, pp. 31–39.
- [20] Ziman, J. M., 1960, *Electrons and Phonons*, Oxford University Press, London, UK.
- [21] Pattamatta, A., and Madnia, C. K., 2009, "A Comparative Study of Two-Temperature and Boltzmann Transport Models for Electron-Phonon Nonequilibrium," *Numer. Heat Transfer, Part A*, **55**(7), pp. 611–633.
- [22] Pattamatta, A., and Madnia, C. K., 2009, "Modeling Heat Transfer in $\text{Bi}_2\text{Ti}_3\text{-Sb}_2\text{Te}_3$ Nanostructures," *Int. J. Heat Mass Transfer*, **52**, pp. 860–869.
- [23] Anisimov, S. I., and Rethfeld, B., 1997, "On the Theory of Ultrashort Laser Pulse Interaction With Metal," *Proc. SPIE*, **3093**, pp. 192–203.
- [24] Touloukian, Y. S., Powell, R. W., Ho, C. Y., and Klemens, P. G., 1970, "Thermal Conductivity," *Thermophysical Properties of Matter*, Plenum, New York, 1, pp. 132–137.
- [25] Touloukian, Y. S., and Buyco, E. H., 1970, "Specific Heat," *Thermophysical Properties of Matter*, Plenum, New York, 4, pp. 83–86.
- [26] Cockburn, B., Karniadakis, G. E., and Shu, C.-W., 2000, *Discontinuous Galerkin Methods: Theory, Computation and Applications*, Springer-Verlag, Berlin.
- [27] Cockburn, B., and Shu, C.-W., 2001, "Runge–Kutta Discontinuous Galerkin Methods for Convection-Dominated Problems," *J. Sci. Comput.*, **16**(3), pp. 173–261.
- [28] Cui, X., and Li, B. Q., 2004, "A Discontinuous Finite-Element Formulation for Internal Radiation Problems," *Numer. Heat Transfer, Part B*, **46**, pp. 223–242.
- [29] Chai, J. C., Lee, H. S., and Patankar, S. V., 1994, "Finite Volume Method for Radiation Heat Transfer," *J. Thermophys. Heat Transfer*, **8**(3), pp. 419–425.
- [30] Hostetler, J. L., Smith, A. N., Czajkowsky, D. M., and Norris, P. M., 1999, "Measurement of the Electron-Phonon Coupling Factor Dependence on Film Thickness and Grain Size in Au, Cr, and Al," *Appl. Opt.*, **38**(16), pp. 3614–3620.

Natural Convection Heat Transfer From Horizontal Rectangular Inverted Notched Fin Arrays

Sanjeev D. Suryawanshi¹

Department of Mechanical Engineering,
SSVPS's BSD Polytechnic,
Dhule (MS) 424 005, India
e-mail: sanjeev_suryawanshi@yahoo.co.in

Narayan K. Sane

Department of Mechanical Engineering,
J.S. College of Engineering,
Pune 28 (MS) 411 028, India
e-mail: narayan_sane@yahoo.co.in

The variables for natural convection cooling with the help of finned surfaces are orientation and geometry. In lengthwise short array ($L/H \sim 5$), where single chimney flow pattern is present, a stagnant zone is created at the central bottom portion of fin array channel and hence it does not contribute much in heat dissipation. Hence it is removed in the form of inverted notch at the central bottom portion of fin to modify its geometry for enhancement of heat transfer. An experimental setup is developed for studying the investigation on normal and inverted notched fin arrays (INFAs). Fin spacing, heater input, and percentage of area removed in the form of inverted notch are the parameters. For few spacing, it is verified by computational fluid dynamics analysis (Course Notes on Introduction to Commercial CFD of Tridiagonal Solutions, Pune), and the results are well matching. It is found that the average heat transfer coefficient for INFAs is nearly 30–40% higher as compared with normal array. [DOI: 10.1115/1.3109993]

Keywords: heat transfer enhancement, natural convection, inverted notched fins, single chimney flow

1 Introduction

The current trend in industry is microminiaturization of electronic packages. The thermal design problem is recognized as one of the factors limiting achievement of higher packaging densities. Because of reduction in surface area available for heat dissipation, optimization of fin surface area and geometry becomes very important in natural convection heat transfer. In lengthwise short array ($L/H \sim 5$), where the single chimney flow pattern is present, as shown in Fig. 1, near the central bottom portion of the fin channel, the stagnant zone that is created becomes ineffective because no air stream passes over this part. In this central portion, a rectangular notch is cut, as shown in Fig. 2, and its effect on heat transfer characteristics and flow is studied.

The problem of natural convection heat transfer from fin arrays has been studied both experimentally and theoretically by a number of investigators. It was investigated experimentally by Starner and McManus [1], Harahap and McManus [2], Jones and Smith [3], and Mannan [4]. Sane and Sukhatme [5] considered the situation of an isothermal rectangular fin array on a horizontal surface. For the first time, governing differential equations were solved by finite difference method. They obtained good agreement with experimental data. In addition, flow visualization study was carried out by Schlieren shadowgraph in order to depict the zone in which the single chimney flow pattern occurs, which was very effective in natural convection heat transfer viewpoint. Horizontal base fin array with notch was investigated experimentally by Sane et al. [6,7].

A systematic theoretical investigation of the effects of fin spacing, fin height, fin length, and temperature difference between fin and surroundings on the free convection heat transfer from horizontal fin arrays was carried out by Baskaya et al. [8]. It has been concluded that it is not possible to obtain optimum performance in terms of overall heat transfer by concentrating only on one or two

parameters. The interactions among all the design parameters must be considered. The results are presented in a graphical form together with optimum values and correlation.

The present work is an experimental investigation of effects of various parameters such as fin spacing, heater input, and percentage of area removal in the form of inverted notch, on heat transfer characteristics. The experimental results are validated by computational fluid dynamics (CFD) analysis.

2 Experimentation

For experimental setup, fin flats and spacers are cut from 3 mm and 1 mm thick rolled aluminum sheet and assembled together to form the required fin array. Figure 3 shows the arrangement of assembled horizontal fin array. Four cartridge heaters are placed in the base portion of the fin array. An assembled array is placed in an insulating brick cavity up to base portion to minimize heat loss by conduction through base and sides of the fin array. The array is placed in a sufficiently large enclosure to provide natural convection condition. Calibrated thermocouples with temperature indicator are used to measure temperatures at various locations of fin array. A calibrated wattmeter is connected to measure heater input.

3 Methodology

Experiments are performed and steady-state observations are recorded. Fin spacing, heater input, and percentage of area removed are the parameters of experimental study. Table 1 summarizes the parameters included in the experimentation. Radiation loss is accounted suitably by the predetermined values of emissivity, which are 0.5 for nonblackened and 1 for black array.

4 Numerical Model

The natural convection flow under investigation is modeled by a set of elliptic partial differential equations describing the conservation of mass, momentum, and energy in three rectangular Cartesian coordinates. The numerical model is based on control volume finite difference formulation. The set of equations are integrated over each control volume to obtain discretized linear algebraic equations, termed as finite volume equations. These equations are solved by commercial CFD package, like FLUENT [9].

¹Corresponding author.

Contributed by the Heat Transfer Division of ASME for publication in the JOURNAL OF HEAT TRANSFER. Manuscript received July 26, 2008; final manuscript received January 24, 2009; published online June 3, 2009. Review conducted by Ali Ebadian.

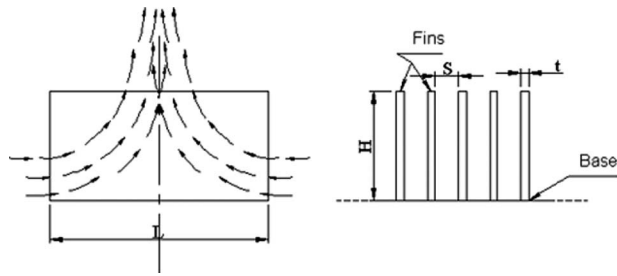


Fig. 1 Single chimney flow pattern for normal fin

The infinite number of fins with negligible thickness is assumed. The fin surfaces with base are assumed as a source and held at uniform temperature. Laminar natural convection is the mechanism for heat transfer from the fin array. Radiation heat loss

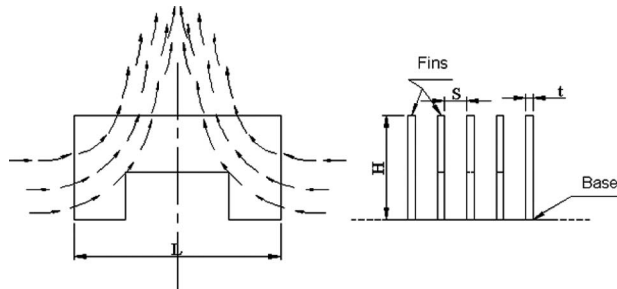


Fig. 2 Single chimney flow pattern for INFA

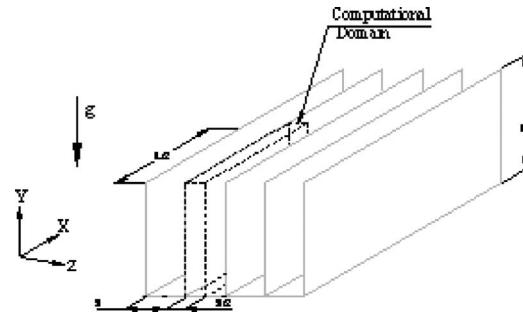


Fig. 4 Quarter channel of fin array under investigation

is not considered. The schematic drawing of fin array under investigation with isothermal fin surface with base is shown in Fig. 4, with an actual simulated part of one fin. As shown in Fig. 5, the computational domain is reduced to one-quarter of fin channel. Table 2 summarizes the parameters for numerical analysis. The temperature differences are up to 130°C; hence the Boussinesq approximation is not employed.

4.1 Validation. The computer code used in the present CFD analysis is validated for a 2D problem of isothermal heated vertical plate and the local heat transfer coefficients are in agreement with correlation values [10] within 8%.

4.2 Boundary Conditions. In natural convection flows, there is no information regarding the velocity and temperature fields before the start of calculations. Since governing equations are invariably coupled, the temperature field causes the velocity field

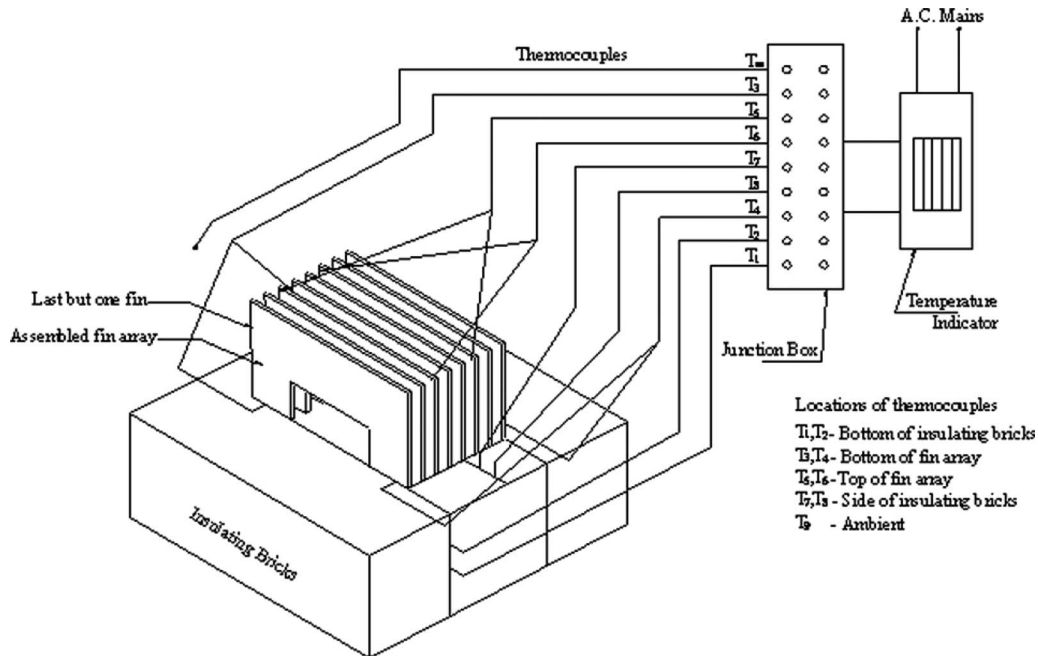


Fig. 3 Experimental setup with thermocouple locations

Table 1 Parameters for experimentation

Length of fin array, L (mm)	150				
Height, H (mm)	75				
Spacing, S (mm)	4	5	6	9	13
No. of fins	15	13	12	9	7
Notched portion (%)	10	20	30	40	
Heater input (W)	50	100	150	200	

Lamp black coating on fin surface (9 mm and 13 mm spacing)

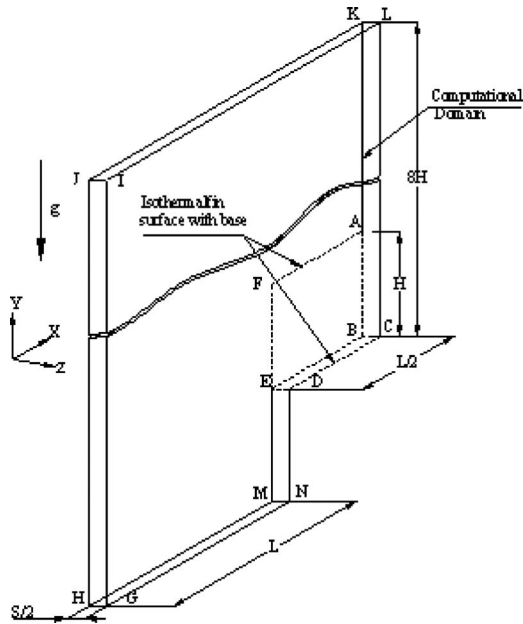


Fig. 5 Computational domain with extended boundaries and heat source

to develop and in turn the velocity field affects the temperature field, with the promotion of convective heat transfer. Because of symmetry only one-quarter of fin channel is investigated. It is realistic to extend computational domain beyond actual dimensions of the fin array in order to meet ambient condition.

The imposed boundary conditions are as shown in Fig. 5. The fin surface and base are held at a constant temperature T_s ($ABEFA$ and $BCDEB$ surfaces). The symmetry boundary conditions are applied at $AFEMHJKA$, $BCLKAB$, $EDNME$, and $LCDNGIL$ surfaces. All the remaining boundaries are assigned as pressure outlets where air enters or leaves the channel at the ambient temperature T_∞ and corresponding density ρ_0 . Here the ambient pressure is used as stagnation boundary condition with the incoming mass having the ambient temperature.

The static pressure is assumed equal to the pressure of surrounding atmosphere. Molecular (laminar) transport boundary conditions are applied to the fin walls to simulate the effects of laminar friction and heat transfer, known as no-slip boundary conditions.

4.3 Convergence. In iterative process, convergence is used as the monitor of achievement of the final solution. The criterion of convergence of numerical solution is based on the absolute normalized residuals of the equations that are summed for all cells in the computational domain.

There are five residuals to be monitored in natural convection problem that is continuity, x , y , and z velocities, and energy. The default convergence criteria are 1×10^{-03} for all four of the above, i.e., continuity and velocities and 1×10^{-06} for energy. Same values are used for the first order scheme. Once solution is converged in first order, during second order the convergence criteria are

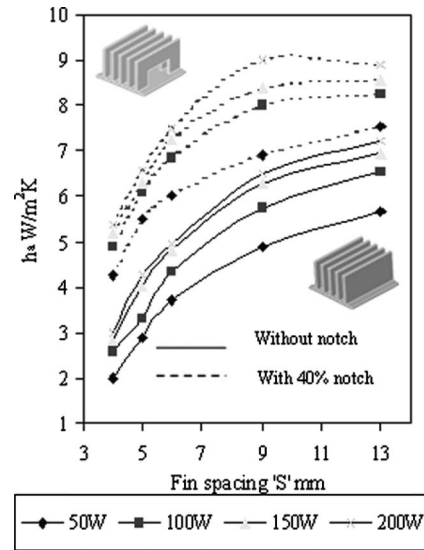


Fig. 6 Variation of h_a with fin spacing

shifted to 1×10^{-05} for three velocities and the remaining are the same. Iterative convergence is also checked by terminating the solution only when progressive single cell values showed little change per iteration as the calculation progressed.

4.4 Grid Independency. Grid independency checks are made and final simulations are achieved with cell count ranging from 80,000 to 110,000 over entire computational domain.

4.5 Domain Size Independency. For natural convection problem, domain is extended from actual size of experimental model for ensuring ambient conditions. Domain size is varied from $2H$ to $25H$ in the Y direction and from $1H$ to $5H$ in the X direction, where H is the height of fin. Finally, $8H$ is the domain height and $3H$ is the domain width, since negligible change in results is recorded by further extension. The results obtained from numerical analysis are given in Sec. 5.2.

5 Results and Discussion

5.1 Experimental Investigation. The results are obtained in terms of h_a , h_b , Nu_a , Nu_b , and Gr_H . Figure 6 shows the effect of fin spacing on h_a with heater input as the parameter for normal and 40% INFAs. From the figure, it is clear that as the fin spacing increases, h_a increases asymptotically as expected. The increasing trend is to steep up spacing to about 9 mm; after that there is a gradual rise. This may be attributed to choking of flow at smaller fin spacing and wider spacing causes less lateral boundary layer interference. The notched configurations yield 50–55% higher values compared with the unnotched fin. This is mainly because of the removal of surface area from the stagnant zone of fin channel, thus indicating superiority of INFAs. It is also observed that the values of h_a are higher at higher heater input as expected.

Figure 7 shows the variation of h_a against the percentage of area removed for 6 mm fin spacing with heater input as a param-

Table 2 Parameters for numerical analysis

Length of fin array, L (mm)	150				
Height, H (mm)	75				
Spacing, S (mm)	-	-	-	9	13
No. of fins	-	-	-	9	7
Notched portion (%)	10	20	30	40	
Heater input (W)	50	100	150	200	

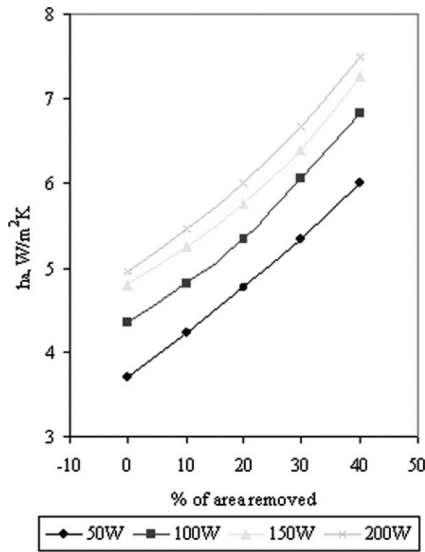


Fig. 7 Variation of h_a with different percentage of area removed for 6 mm spacing

eter. It is concluded that values of h_a for INFAs are more than normal arrays as expected. It is also concluded that h_a increases as the percentage of area removed increases. At higher heater input, the values of h_a are higher.

Figure 8 shows the effect of fin spacing on Nu_b for normal and 40% INFAs. The values of Nu_b increases as fin spacing decreases. It reaches a maximum value at fin spacing of about 6 mm, indicating optimum zone. This can be attributed to choking of flow at very low fin spacing. Beyond the optimum zone, the total surface area is reduced and Nu_b shows a decreasing trend.

Figure 9 shows the variation of heater input against ΔT with percentage of area removed as the parameter for normal and INFAs. From the figure, it is clear that for particular temperature difference ΔT the heat transfer rate of INFAs is higher than that of normal fin arrays. It is also concluded that 40% INFA gives higher heat transfer rate for particular temperature difference. From the figure, it is observed that to dissipate 200 W, ΔT for 40% INFA is 101.88 °C and 107.10 °C for normal array indicating the superiority of INFAs.

Figure 10 shows the effect of Nu_b for different fin configura-

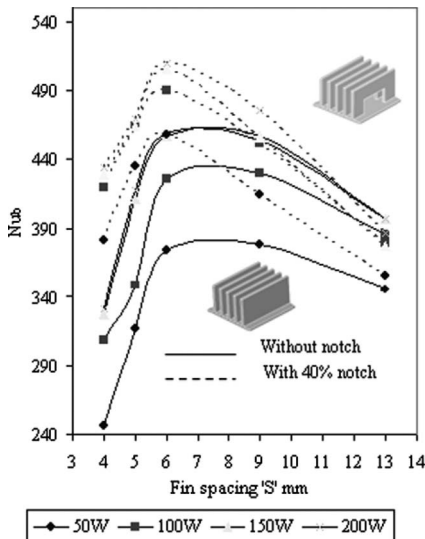


Fig. 8 Variation of Nu_b with fin spacing

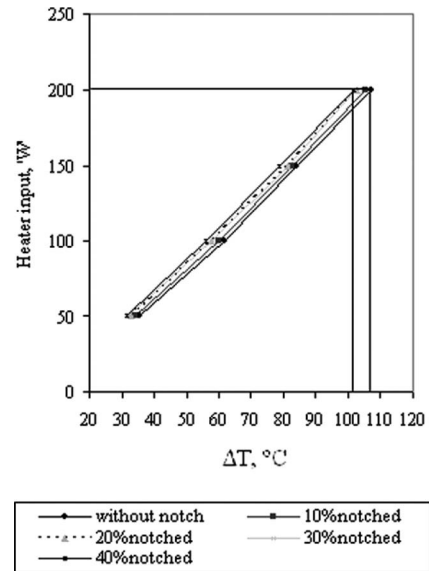


Fig. 9 Effect of inverted notch on surface temperature

tions. The values of Nu_b are higher for higher heater input. It is observed that values of Nu_b are higher for INFAs and highest for 40% INFA.

5.2 Numerical Analysis. Figure 11 shows the variation of heat flux (q/A) against the percentage of area removed for 9 mm fin spacing with heater input as a parameter. From the figure, it is observed that experimental and CFD results are well matching, and the variation is within 7% for experimental investigation of relatively polished surface of normal and INFAs. For blackened normal and INFAs, the variation is around -9% in reference with CFD results. It is also concluded that as the percentage of area removed increases, heat dissipation rate increases, which is the outcome of experimental investigation.

6 Correlation

Finally, an attempt is made to correlate the results obtained in the present study. The correlation curve is proposed in Fig. 12. The average Nusselt number (Nu_a) is correlated with the other

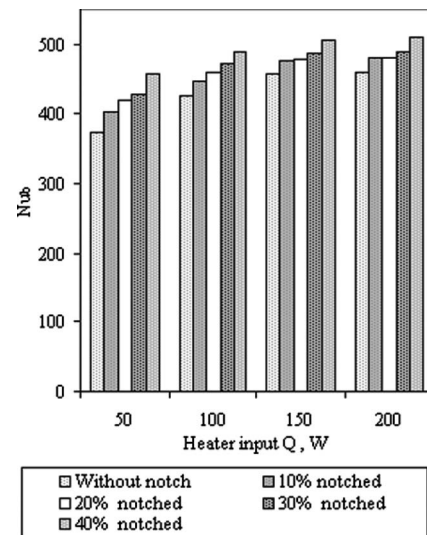


Fig. 10 Variation of Nu_b for different configurations

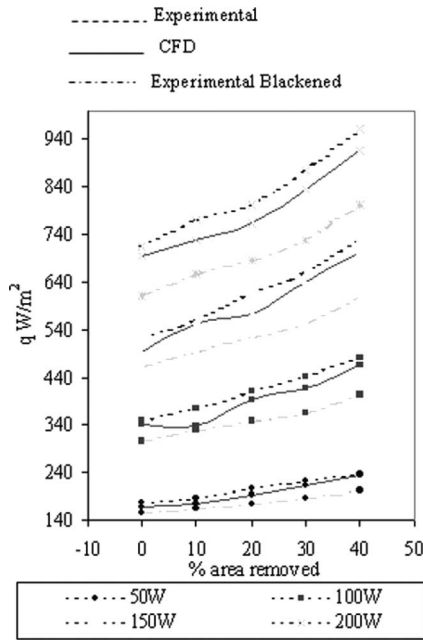


Fig. 11 Comparison of experimental and CFD results for 9 mm fin spacing; effect of percentage area removed on $q_{\text{convection}}$

relevant governing parameters of fin array, namely, the Grashof number Gr_H , the spacing to height ratio (S/H), and the ratio of exposed area of normal to INFAs (A_e/A_n).

The following correlation is obtained:

$$Nu_a = 17.49 \ln[Gr_H(S/H)(A_e/A_n)] - 188.8$$

The correlation is only valid for $Pr=0.7$, 200 W heater input, for values of S/H and (A_e/A_n) are less than 0.1733 and 1.4, respectively. The value of correlation coefficient, R^2 , is 89%. Same correlation can be obtained for remaining heater input.

7 Flow Visualization

Figure 13 shows the photographs of flow visualization by simple smoke technique using for normal and 30% INFAs. From photographs, it is concluded that coalescing of two streams at less height from fin bottom in normal fin array whereas it is at more height in INFAs, giving wider chimney and enhancing the heat transfer rate.

8 Conclusion

The values of h_a are 50–55% higher for INFAs giving better performance. For smaller spacing, increment in h_a is small due to the flow constriction effect. The value of h_a increases with spacing

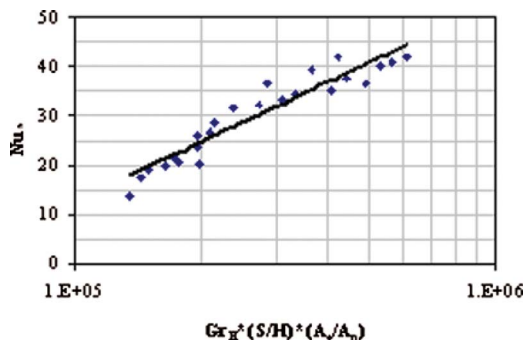


Fig. 12 The proposed horizontally oriented INFAs correlation

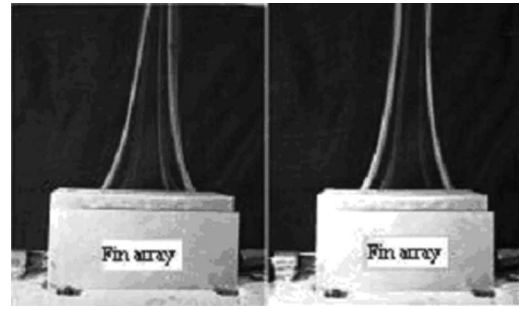


Fig. 13 Photographs showing flow visualization by simple smoke technique

giving an optimum value at about $S=6$ mm. This is in agreement in other investigators. Single chimney flow pattern is retained in INFAs also with a wider chimney zone, which is the possible reason for heat transfer enhancement. When single chimney flow pattern is present, in midchannel stagnant bottom portion becomes ineffective. The modified array is designed in inverted notched form and that has proved to be successful retaining single chimney together with the removal of ineffective fin flat portion. This is the main contribution of present paper. Limited CFD solutions obtained are in good agreement with experimental work. Radiation contribution is also important and needs further investigation.

Acknowledgment

The numerical analysis with CFD is supported by Tridiagonal Solutions, Pune. The authors would like to acknowledge the assistance of Mr. Ashish A. Kulkarni and Sandeepak G. Natu from Tridiagonal Solutions.

Nomenclature

- A = area, m^2
- $Gr_H = g \times \beta \times \Delta T \times H^3 / \nu^2$, Grashof number
- $h_a = (q_{\text{convection}}/A_e \times \Delta T)$, average heat transfer coefficient, $W m^{-2} K^{-1}$
- $h_b = (q_{\text{convection}}/A_b \times \Delta T)$, base heat transfer coefficient, $W m^{-2} K^{-1}$
- H = height of fin array, mm
- K = thermal conductivity, $W m^{-2} K^{-1}$
- L = length of fin array, mm
- $Nu_a = h_a \times L / K$, average Nusselt number
- $Nu_b = h_b \times L / K$, base Nusselt number
- q = heater input, W
- $q_{\text{convection}} = q - (q_{\text{conduction}} + q_{\text{radiation}})$, W
- $q_{\text{conduction}}$ = heat loss by conduction, from fin array, W
- $q_{\text{radiation}}$ = heat loss by radiation, from fin array, W
- Pr = Prandtl number
- S = fin spacing, mm
- T = thickness of the fin, mm
- u, v, w = velocity components, $m s^{-1}$
- X, Y, Z = Cartesian coordinates

Greek Symbols

- ρ = density, $kg m^{-3}$
- β = coefficient of thermal expansion, K^{-1}
- ν = kinematic viscosity, $m^2 s^{-1}$
- ΔT = temperature difference, $^{\circ}C$

Subscripts

- a = average
- b = base
- e = total exposed area for convective heat transfer for normal fin array

n = total exposed area for convective heat transfer for INFA
 s = surface average
 ∞ = ambient

References

- [1] Starmer, K. E., and McManus, H. N., 1963, "An Experimental Investigation of Free Convection Heat Transfer From Rectangular Fin Arrays," *Trans. ASME, Ser. C: J. Heat Transfer*, **85**, pp. 273–278.
- [2] Harahap, F., and McManus, H. N., 1967, "Natural Convection Heat Transfer From Horizontal Rectangular Fin Arrays," *Trans. ASME, Ser. C: J. Heat Transfer*, **89**, pp. 32–38.
- [3] Jones, C. D., and Smith, L. F., 1970, "Optimum Arrangement of Rectangular Fins on Horizontal Surface for Free Convection Heat Transfer," *ASME Paper No. 69-HT-44*.
- [4] Mannan, K. D., 1970, "An Experimental Investigation of Rectangular Fins on Horizontal Surface," Ph.D. thesis, Ohio State University, Columbus, OH.
- [5] Sane, N. K., and Sukhatme, S. P., 1974, "Natural Convection Heat Transfer From Short Horizontal Rectangular Fin Arrays," *Fifth International Heat Transfer Conference, Tokyo, Sept.*
- [6] Sane, N. K., Kittur, M. B., and Magdum, J. D., 1995, "Natural Convection Heat Transfer From Horizontal Rectangular Fin Arrays With a Rectangular Notch at the Center," *Seventh ISHMT Conference, Suratkal.*
- [7] Sane, N. K., Tikekar, A. N., and Morankar, K. P., 2000, "Natural Convection Heat Transfer From Vertical Arrays With Rectangular Notched Fins," *ME thesis, Shivaji University, Kolhapur, India.*
- [8] Baskaya, S., Sivrioglu, M., and Ozek, M., 2000, "Parametric Study of Natural Convection Heat Transfer From Horizontal Rectangular Fin Arrays," *Int. J. Therm. Sci.*, **39**, pp. 797–805.
- [9] *Course Notes on Introduction to Commercial CFD of Tridiagonal Solutions, Pune.*
- [10] Ostrach, S., 1953, "An Analysis of Laminar Free Convection Flow and Heat Transfer About a Flat Plate Parallel to the Direction of Generating Body Force," *NACA Report No. 1111.*

Flow and Heat Transfer of Natural Convection in Horizontal Annulus With a Heating Element on Inner Cylinder

C. S. Yang¹

Department of Computer Science and Information Engineering,
Far East University,
Hsin-Shih, Tainan County 744, Taiwan

D. Z. Jeng

U. H. Tang

C. Gau¹

e-mail: gauo@mail.ncku.edu.tw

Institute of Aeronautics and Astronautics and
Center for Micro/Nano Science and Technology,
National Cheng Kung University,
Tainan 70101, Taiwan

Experiments have been performed to study natural convection flow and heat transfer in a horizontal annulus when a square heating element is positioned at different locations on the inner insulated cylinder. The annulus is filled with water and has cylinder to cylinder diameter ratio of 3. The square heating element is small and has the width to annulus gap width ratio of 1/6. The range of Rayleigh number studied is approximately from 1.9×10^6 to 3.3×10^7 . It has been found that the flow pattern, the temperature distribution around the inner cylinder wall, and the local heat transfer rate around the outer cylinder are very sensitive to the location of the heating element. The heating element Nusselt numbers at various locations on the inner cylinder are obtained and well correlated against the Rayleigh number to the 1/3 powers. A maximum in the correlation parameter C is obtained when the heating element is placed 90 deg from the bottom.

[DOI: 10.1115/1.3109995]

Keywords: natural convection in annulus, natural convection heat transfer, localized heating, avionics cooling

1 Introduction

The study of natural convection heat transfer and fluid flow in enclosures has received considerable attention because of the fundamental importance in practical applications [1–5]. Natural convection between annulus has been studied extensively in the past [6–10]. It has been well recognized that in a horizontal annulus the heat transfer and fluid motion are determined and correlated primarily by the Rayleigh number and the Prandtl number [11,12].

However, much of the attention has been concentrated on eccentricity of the inner cylinder on the natural convection flow and heat transfer process. Both numerical and experimental studies [13,14] have indicated that the position or the eccentricity of the inner cylinder can have a significant effect on the natural convection heat transfer and fluid motion. The downward positioning of the inner cylinder results in an increase in heat transfer because of the augmentation in the convection and the increase in the conduction of heat. The eccentricity effects on the local heat transfer around the inner cylinder and the outer cylinder were also presented. Chao et al. [15] indicated that the horizontal eccentricity of the inner cylinder causes a decrease in the heat transfer because of the suppression of natural convection. Sparrow et al. [16] studied natural convection heat transfer in a relatively large cylinder with an inner cylinder having cylinder to outer cylinder diameter ratio of 0.2, and indicated that inner body Nusselt number is independent of the position of the inner body and even the orientation of the outer cylinder. Both the inner and the outer cylinders have a length-diameter ratio of unity. For a wider eccentricity range ($0 \leq e < 1$), the flow and thermal fields in eccentric cylinders ($R_o/R_i=2.36$) was studied numerically and compared with the experimental results [17].

For narrow gap annulus with outer cylinder to inner cylinder diameter ratio of 1.05–1.2, the natural convection flow may be-

come three dimensional due to the flow instability or end wall effects at relatively low Rayleigh number range (1500–3000) [18–20]. Three-dimensional supercritical states occur and the existence of four such states is established. These four states are characterized by the orientations and directions of rotation of counter-rotating rolls that form in the upper part of the annulus owing to thermal instability, and exhibit (i) transverse rolls, (ii) transverse rolls with reversed directions of rotation, (iii) longitudinal rolls in combination with transverse rolls, and (iv) longitudinal rolls with reversed directions of rotation in combination with transverse rolls, respectively. The occurrence of different flow patterns leads to significant difference in the heat transfer process. With the presence of a porous geometric perturbation in the annulus, the heat transfer can be either significantly enhanced or retarded [21] depending on the ratio of the conductivity of the porous material to that of the fluid.

The present study was motivated by the practical interest to determine the location where the electronic module (or the heating element) should be placed on the plastic (or the adiabatic) inner wall of the horizontal annulus in order to have a maximum cooling rate, due to the internal natural convection heat transfer, to avoid the overheating of the electronics. The geometry has a practical application in the cooling of avionics in a flight vehicle. The heating element is used to simulate a module. The findings up to the present could not provide a physical explanation and the correlation of the natural convection heat transfer in a horizontal annulus when a heating element is attached at different positions around the inner insulated cylinder. No relevant work has been found in the literature. Therefore, experiments with flow visualization, temperature distribution, and heat transfer measurements were conducted and used to provide a physical understanding and heat transfer data for the configuration of interest.

2 Experiments

2.1 Apparatus. A horizontal annulus having a gap of 6 cm and a length of 30 cm was made, as shown in Fig. 1, with the inner wall being insulated and the outer wall serving as a heat sink. The inner cylinder having an outside diameter of 6 cm was made of 5

¹Corresponding author.

Contributed by the Heat Transfer Division of ASME for publication in the JOURNAL OF HEAT TRANSFER. Manuscript received August 15, 2008; final manuscript received December 3, 2008; published online June 4, 2009. Review conducted by Giulio Lorenzini.

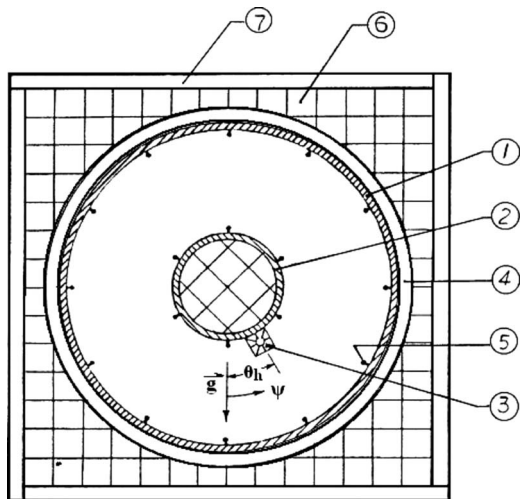


Fig. 1 Schematic of test apparatus: (1) outer cylinder, (2) inner cylinder, (3) heating element, (4) cooling coil, (5) thermocouples, (6) insulation, and (7) plexiglass box

mm thick plexiglass. Therefore, the current annulus has a diameter ratio of 3. The outer cylinder having an inside diameter of 18 cm was made of 5 mm thick aluminum plate. Around the outside cylinder wall, a small copper tube was wrapped tightly through which coolant was circulated inside with a constant temperature bath and was used to control the outer cylinder surface temperature. A square heating element having a cross section of $1 \times 1 \text{ cm}^2$ (i.e., the ratio of the width of the heating element to the annulus gap is 1/6), and a length of 30 cm was made of aluminum and was epoxied axially on the plexiglass wall. The Nichrome electric resistance was wired inside the element uniformly along the axial direction and was used with a dc power supply to provide a uniform and desired heat flux.

The horizontal annulus was situated inside a plexiglass box that had inside dimensions of $25 \times 25 \text{ cm}^2$ in cross section, 30 cm in length, and a wall thickness of 10 mm. The cylinders were bolted on both the end walls of the box. On the top of the aluminum cylinder, two holes having a diameter of 5 mm were drilled separately near the end walls to allow water to be siphoned into the annulus. The remaining space inside the box and the inner cylinder was filled with insulation. The inner cylinder together with the heating element was allowed to rotate with a 30 deg increment for each experiment. The selection of thin plexiglass inner cylinder as insulated wall was due to the fact that it has the thermal conductivity a factor of 1/3 less than that of water. Therefore, the circumferential heat conduction along the inner cylinder wall may be negligible small.

A total of 67 K-type thermocouples having a wire diameter of 0.5 mm were used to measure all the temperature. On the outer cylinder wall near the central region, 12 equally spaced holes having a diameter of 1.5 mm were drilled circumferentially, while on the inner cylinder six holes were drilled. A total of 18 thermocouples were inserted individually into each hole and the centers of the thermocouple beads were positioned 2 mm above the surface. It has been found [13,22,23] that the temperature distribution within 1/30 of the gap thickness, which in our case is within 2 mm, is nearly linear for Rayleigh number up to 10^8 and outer cylinder to inner cylinder diameter ratio of 2–3. Therefore, with the given temperature on the wall, the local temperature gradient, the heat flux, and the local heat transfer coefficient on the wall of the outer cylinder can be readily calculated. The wall temperatures were measured and averaged with a total of 42 thermocouples that were embedded closed to the surface. The temperatures on the heating element were measured with seven thermocouples. A closer space was arranged for the thermocouples near the end

walls to estimate the heat loss from the end walls to the outside environment. During the experiment 10 mm thick pieces of insulation were attached to both the end walls to reduce the heat loss. The axial (or circumferential) temperature distribution along the outer cylinder wall, the inner cylinder, and heating element were found to be very uniform. The heat loss to the environment was evaluated from the axial temperature gradient of the heating element at the ends, and was found within 5% of the total power input. A two dimensional heat transfer process in the annulus was, therefore, expected.

2.2 Experimental Procedure and Data Reduction. Before the experiments, a small amount of fish scales was mixed into the water to trace the fluid motion. In the front of the test cell, a filament lamp was used for illumination. The fluid was kept stagnant initially. Once the uniform temperature in the water was reached, both the coolant circulation around the outer cylinder and the power supplied to the heating element were switched on. Usually it takes 4–6 h to reach steady state. The temperature measurements were calibrated within $\pm 0.05^\circ\text{C}$ and the results were recorded. During fluid visualization experiment, the insulations attached to the end walls were removed. Both photographs were taken and fluid motion was traced with a pencil. For heating element at different positions on the inner cylinder wall, each experiment was restarted from the same initial state when fluid was stagnant and temperature in the fluid was uniform.

With the power supply calculated from the measured electric voltage and current across the Nichrome thin resistance and subtracted by the heat loss from the ends, the average heat transfer coefficient and Nusselt number from the heating element to the outer cylinder are evaluated with

$$h = Q/A_h(T_h - T_o), \quad \text{Nu} = hL_c/k \quad (1)$$

The Nusselt number is correlated against the Rayleigh number with the relationship that $\text{Nu} = C \text{Ra}^n$. Within the range of Rayleigh number studied, the value of n is found very close to 1/3 and is insensitive to the positions of the heating element. The local heat flux q_ψ on the outer cylinder was calculated by the temperature difference, which was between the outer cylinder wall and the thermocouple, which was 2 mm above the cylinder wall, divided by the distance 2 mm and multiplied by the thermal conductivity of water. Therefore, the local heat transfer coefficient and local Nusselt number are evaluated from

$$h_\psi = q_\psi/(T_h - T_o), \quad \text{Nu}_\psi = h_\psi L_c/k \quad (2)$$

The accuracy of the local heat flux measurements depends on the accuracy of the temperature measurements around the outer cylinder wall and the ones 2 mm above, and is estimated within $\pm 2\%$. For a given wall temperature, the local heat transfer rate or the local heat transfer coefficient is actually proportional to the water temperature measured 2 mm above the wall. The accuracy of the current measurement can be checked by integrating the local heat flux measured around the outer cylinder and seeing if the total heat transfer from the heating element to the bulk fluid is equal to the total heat transfer from the bulk flow into the outer cylinder. It is found that the total heat transfer from the bulk flow to the outer cylinder is approximately 5% less than the total heat transfer from the heating element to the bulk fluid. This is attributed to the heat loss from the bulk fluid to the ambient through the end walls. The error analysis for the Nusselt number is performed by following the procedures described in Ref. [24]. The maximum uncertainty for the heating element Nusselt number is 5.6%, and for the local Nusselt number around the outer cylinder is 7.5%.

3 Results and Discussion

3.1 Flow Visualization. Experiments were performed to visualize the fluid motion and flow structures with the heating element being placed at different positions. Different flow structures were visualized and photographed for the heating element at different

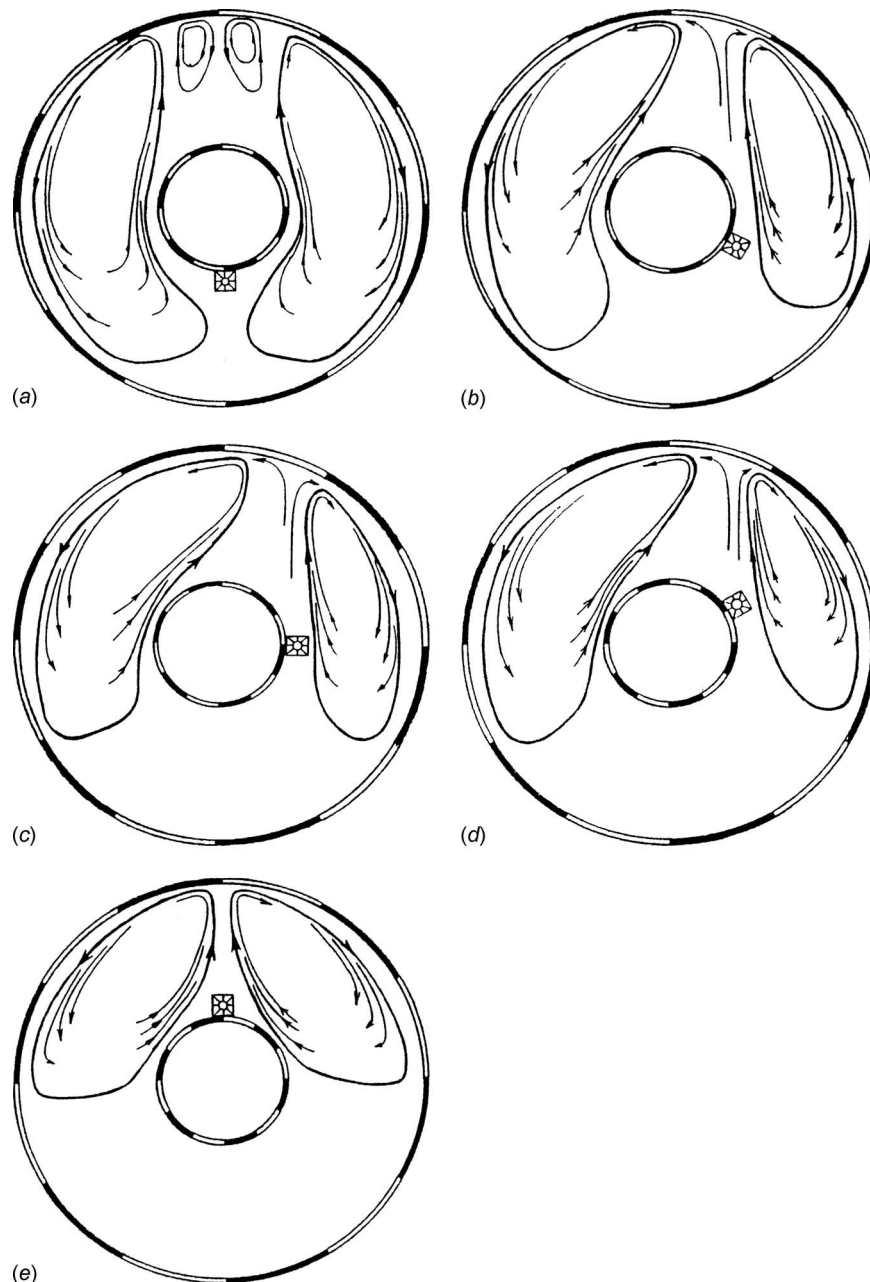


Fig. 2 Flow pattern with heating element positioned at different angles: (a) $\theta_h=0$, (b) $\theta_h=60$ deg, (c) $\theta_h=90$ deg, (d) $\theta_h=120$ deg, and (e) $\theta_h=180$ deg for $Ra=1.113 \times 10^6$

positions on the inner cylinder. Unfortunately, the photograph quality has been very poor; thus only the flow patterns traced with pencil are shown in Figs. 2(a)–2(e). In general, the flow velocity in the upper region of the annulus is relatively high and fluid motion was readily traced, while in the lower region the flow motion is small and in some situations the flow motion is so slow that the particle tracing became very difficult especially for flow near the edge of the stagnant region.

When the heating element is at the bottom on the inner cylinder, the heated flow around the heating element due to buoyancy force ascends along the inner cylinder wall. However, the heated flow close to the inner cylinder do not separate from the wall at the top of cylinder (as for the case with heated inner cylinder) but separated at an earlier stage, as shown in Fig. 2(a), when the separation angle is $\psi=150$ deg and $\psi=210$ deg. The heated flow on either side of inner cylinder symmetrically impinges on the outer cylinder wall and forms two flow streams. The two upward flow

streams meet at the central top of the cylinder and formed two small circulation cells, while downward flow streams moving along the outer cylinder wall gradually slow down and turn back toward the central region, and finally form two symmetric large circulation cells. The flow motion in the circulation core is relatively slow.

As the heating element is located at 60 deg from the bottom or above, only two unsymmetric circulation cells appear. The one on the heating element side shrinks and is smaller than the one on the other side. As the heating element is positioned further upward, both the circulation cells in the lower region shrink, and a nearly stagnant region near the bottom of the annulus can be observed and grow in size. Fluid stratification can be expected and cause the shrinking of the convection cell. When the heating element is located at $\theta_h > 120$ deg, a rise of the convection cell, on the heating element side, with the upward positioning of the heating element can be expected. When the heating element is at the top of

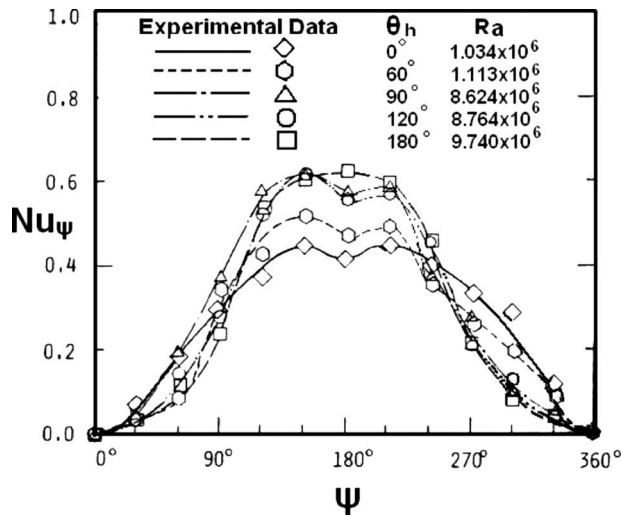


Fig. 3 Local Nusselt number around the outer cylinder with heating element positioned at different angles

the inner cylinder, the convection cells become symmetric and appear only in the upper region. The rising flow is only in the central region. The stagnant fluid in the lower region has the largest area and is so stable that it is not affected at all by the upper circulation flow.

3.2 Temperature Distribution and Local Heat Transfer.

Significant difference in flow structure causing difference in temperature distribution and local heat transfer rate can be expected. However, the buoyancy induced flow causes in general that the fluid temperature in the upper region is higher than in the lower region. As a result, a higher heat transfer rate or a higher local Nusselt number around the outer cylinder, as shown in Fig. 3, occurs in the upper region. The maxima in local Nusselt number are found at the place where the hot stream impinges the wall. As the hot stream gradually moves downward along the outer cylinder, it reduces in temperature gradually due to the heat transfer to the outer cylinder. As a result, the local heat transfer rate or the local Nusselt number around the outer cylinder is reduced. Near the bottom region, the heat transfer is smaller when natural convection does not occur or when conduction of heat is dominant in the annulus. Similar findings were reported for natural convection in a horizontal annulus [11].

When the heating element is at the bottom, the local Nusselt number is distributed symmetrically and has a local minimum, as shown in Fig. 3, in the upper part of the Nu curves. The relative minimum is caused by the flow separation from the top of the outer annulus wall. As the heating element is positioned upward, the local Nusselt number distribution become unsymmetric and is caused by the unsymmetric convection cells. The maximum heat transfer rate having the largest value, as shown in Fig. 3, which occurs and remains at $\psi=150$ deg, is caused by impingement by the relatively hot stream (Figs. 2(b) and 2(c)) that rises from the region near the heating element. As the heating element moves upward with $\theta_h > 120$ deg, the maximum Nusselt number having a higher value moves upward and toward the top of the cylinder due to the rise of the convection cell on the heating element side. When the heating element is at 180 deg from the bottom, the hot streams from both convection cells merge and impinge the top of the wall and cause a bell-like maximum in Nusselt number, as shown in Fig. 3. Near the bottom region, the local Nusselt number distribution along the wall reduces gradually and is nearly linear as the case when the heating element is at 60 deg from the bottom. The fluid stratification in the lower region may be deduced as we have observed.

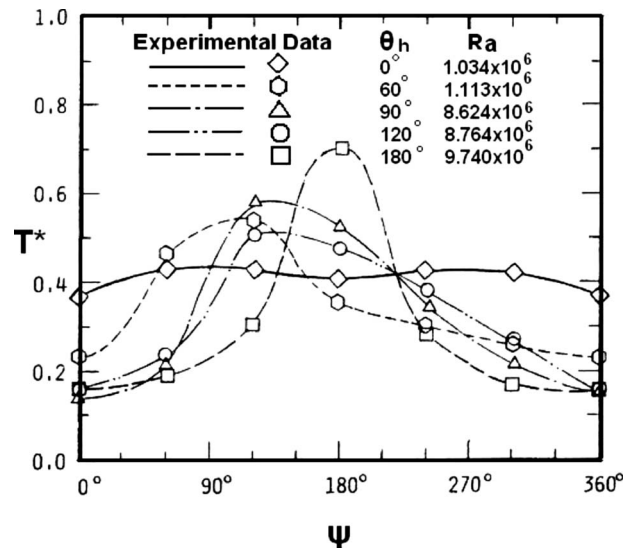


Fig. 4 Temperature distribution around the inner cylinder with heating element positioned at different angles

The temperature distribution around the inner cylinder wall, as shown in Fig. 4, is very uniform, when the heating element is at the bottom. The finding implies that the heat transfer rate from the hot stream to the heating element or even the central core region is negligible because of the very narrow size of hot stream, which behaves like a plume. As the heating element moves upward, a peak in temperature is found, as shown in Fig. 4, and is caused by the hot stream moving along the inner cylinder wall. A decrease in temperature occurs when the hot stream separates from the inner cylinder wall and moves toward the outer cylinder. On the opposite side of the heating element as the flow stream along the inner cylinder moves upward, a moderate increase in flow stream temperature can be observed. The increase in temperature is due to the fact that the temperature in the upper region of the bulk fluid is, in general, higher than in the lower region. This is a clear effect of fluid stratification. As the heating element moves further upward, the peak in temperature also moves upward and eventually becomes symmetric when the heating element is at the top. No significant increase in temperature is found around the inner cylinder for ψ within 120 deg and between 240 deg and 360 deg since the fluid in the region below is stagnant.

3.3 Heat Transfer From the Heating Element. The average heat transfer coefficient from the heating element, positioned at each specific location, to the outer cylinder was well correlated. The typical result for the average Nusselt number against the Rayleigh number for the heating element positioned at $\theta_h=120$ deg is presented in Fig. 5. A total of 19 data points have been fitted with a least-squares method with $n=1/3$. For heating element at different locations, a general correlation equation can be obtained as follows:

$$Nu = C Ra^{1/3} \quad (3)$$

where C is a correlation parameter, which depends on the angular location of the heater, and is 0.102 for $\theta_h=120$ deg with a maximum deviation of $\pm 4.24\%$ for Rayleigh number in the range from 10^6 to 10^8 . Different values of the correlation parameter C for the heating element at different locations are summarized in Table 1. A maximum in C is obtained and is about 20% higher when the heating element is at 90 deg from the bottom. Figure 6 shows that when $\theta_h < 60$ deg the Nusselt number is insensitive to the position of the heating element. The heat transfer rate increases for $\theta_h > 60$ deg and reaches a maximum at $\theta_h=90$ deg. Further increase in the heater's angle θ_h causes a gradual reduction in the

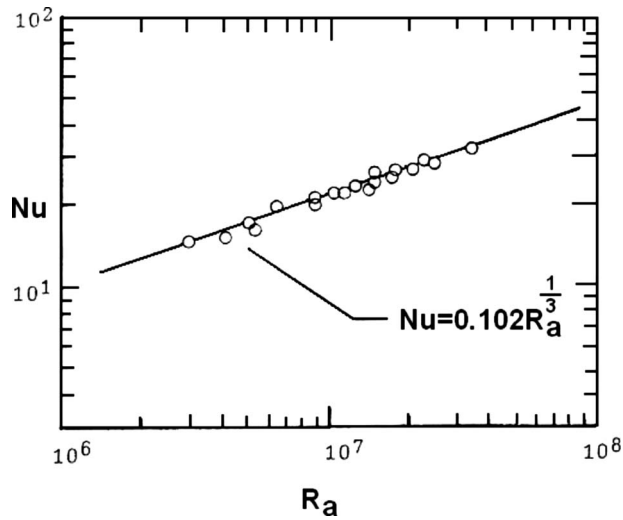


Fig. 5 Nusselt number results and correlation against Rayleigh number with heating element at $\theta_h = 120$ deg

heat transfer. The finding is surprisingly different from that of Sparrow et al [16] in a somewhat different configuration that without an insulated inner cylinder, the heating body Nusselt number in a horizontal cylinder is insensitive to the position of the heating body. Even the orientation of the outer cylinder does not affect the heating body Nusselt number. With the flow visualization experiment, the variation in the heating element Nusselt number may be explained by the fact that the total heat transfer rate depends on the ability of the hot stream to bring heat from the heating element to the outer cylinder. This has been determined by the length the hot stream travels around the outer cylinder and the local heat transfer rate of the hot stream. However, the local heat transfer and the hot stream path around the outer cylinder are significantly affected by the flow structures (Figs. 2 and 3) and therefore by the position of the heat element. An integration of the local heat transfer rate around the outer cylinder indicates that a maximum total heat transfer rate is indeed found when the heating element is at

Table 1 Data correlated with $Nu = C Ra^{1/3}$

θ_h	Ra	No. ^a	C	(%)
0	$1.926 \times 10^6 - 2.758 \times 10^7$	18	0.096	5.87
60	$2.228 \times 10^6 - 3.331 \times 10^7$	18	0.094	5.52
90	$2.228 \times 10^6 - 1.665 \times 10^7$	18	0.119	7.40
120	$2.825 \times 10^6 - 3.093 \times 10^7$	19	0.102	4.24
180	$4.006 \times 10^6 - 2.837 \times 10^7$	18	0.088	10.91

^a“No.” represents the number of data points.

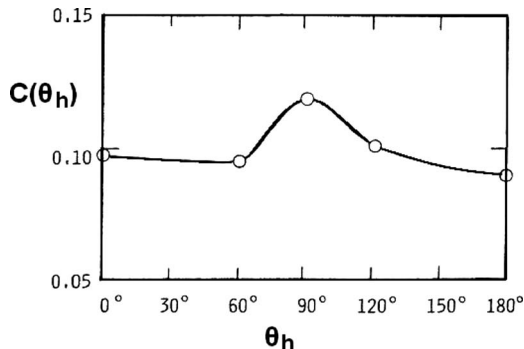


Fig. 6 Effect of the heating element position on the heat transfer correlation parameter C

Table 2 Data correlated with $Nu = C Ra^{1/4}$

θ_h	Ra [*]	No. ^a	C	(%)
0	$2.151 \times 10^7 - 7.972 \times 10^8$	18	0.172	5.68
60	$2.666 \times 10^7 - 1.001 \times 10^9$	18	0.170	5.45
90	$3.528 \times 10^7 - 5.027 \times 10^8$	18	0.202	7.12
120	$3.815 \times 10^7 - 9.866 \times 10^8$	19	0.180	3.41
180	$5.565 \times 10^7 - 7.640 \times 10^8$	18	0.162	10.68

^a“No.” represents the number of data points.

90 deg from the bottom. An optimal in hot stream travel length and its local heat transfer rate may have been achieved when the heating element is at 90 deg. Further upward positioning of the heating element reduces the size of convection cells or alternatively the length that the hot stream travels around the cylinder wall. As a result a reduction in the heat transfer from the heating element to the outer cylinder wall is obtained. For $\theta_h > 120$ deg, the heating element Nusselt number is almost insensitive to the position of the heating element. The lowest heat transfer rate is found when the heating element is at the top.

The Rayleigh number defined above is based on the temperature difference between the heating element and the outer cylinder. The Rayleigh number can also be defined based on the heat flux generated in the heating element. In this case, the Nusselt number can also be correlated with this modified Rayleigh number. One can obtain a similar kind of correlation as Eq. (3) except that the power of the modified Rayleigh number, n , is 1/4. The correlation parameter C obtained is summarized in Table 2.

4 Conclusion

Flow visualization experiments have provided detailed flow information that has been used to explain the results from the temperature distribution and local heat transfer measurements. Different flow patterns have been observed for the heating element at different positions. Four symmetric cells with two large and two small ones have been found when the heating element is at the bottom. As the heating element is positioned upward, only two unsymmetric cells appear and gradually shrink in the lower region where a stagnant and stratified region gradually forms at the bottom.

Significant difference in flow structure causes difference in temperature distribution and local heat transfer rate. The maximum in local heat transfer occurs at the place where the hot stream impinges the cylinder wall. The hot stream passing through the inner cylinder wall can cause a higher wall temperature. However, the locations for the maximum heat transfer, the values of the heat transfer rate, and the occurrence of a high temperature distribution around the inner cylinder are significantly affected by the position of the heating element.

The heating element average Nusselt number has been well correlated against the Rayleigh number to the 1/3 powers or the modified Rayleigh number to the 1/4 powers, for the heating element at different angles. Due to the differences in flow structures and resulting difference in local heat transfer along the outer cylinder, the maximum in the heating element Nusselt number is found when the heating element is at 90 deg from the bottom. The Nusselt number is almost insensitive to the positions of the heating element when θ_h is less than 60 deg or greater than 120 deg.

Nomenclature

- A_h = surface area of the heating element exposed to the fluid
- C = heat transfer correlation parameter
- D = diameter of cylinder
- g = acceleration of gravity

h = average heating element heat transfer coefficient
 k = thermal conductivity
 L_c = characteristic length, $(D_o - D_i)/2$
 Nu = heating element Nusselt number
 Nu_{ψ} = local Nusselt number on the outer cylinder
 Pr = Prandtl number
 q = heat flux generated on the heating element
 q_{ψ} = local heat flux on the outer cylinder
 Q = total heat transfer
 Ra = Rayleigh number, $g\beta(T_h - T)L_c^3 / \nu\alpha$
 Ra^* = modified Rayleigh number, $g\beta q L_c^4 / \nu\alpha$
 T_h = temperature on the heating element
 T_o = temperature on the outer cylinder wall
 T^* = dimensionless temperature, $(T - T_o) / (T_h - T_o)$

Greek Symbols

α = thermal diffusivity
 β = coefficient of thermal expansion
 ρ = density
 ν = kinematic viscosity
 θ_h = circumferential position of heating element
 ψ = circumferential coordinate
 δ = standard deviation

Subscripts

i = inner cylinder
 o = outer cylinder
 h = heating element

References

- [1] Kennedy, K. J., and Kanehl, J., 1983, "Free convection in Tilted Enclosures," *Heat Transfer in Electronic Equipment*, Vol. 28, S. Oktay and A. BarCohin, eds., ASME, New York, pp. 43–47.
- [2] Ha, M. Y., Jung, M. J., and Kim, Y. S., 1999, "Numerical Study on Transient Heat Transfer and Fluid Flow of Natural Convection in an Enclosure With a Heat-Generating Conducting Body," *Numer. Heat Transfer, Part A*, **35**, pp. 415–433.
- [3] Gebhart, B., Yaluria, Y., Mahajan, R. L., and Sammakia, B., 1988, *Buoyancy-Induced Flows and Transport*, Hemisphere, Washington, DC.
- [4] Yang, K. T., 1987, "Natural Convection in Enclosures," *Handbook of Single Phase Convection Heat Transfer*, Wiley, New York.
- [5] Ostrach, S., 1988, "Natural Convection in Enclosures," *ASME J. Heat Transfer*, **110**, pp. 1175–1190.
- [6] Fant, D. B., Prusa, J., and Rothmayer, A. P., 1990, "Unsteady Multicellular Natural Convection in a Narrow Horizontal Cylindrical Annulus," *ASME J. Heat Transfer*, **112**, pp. 379–387.
- [7] Kuehn, T. H., and Goldstein, R. J., 1976, "An Experimental and Theoretical Study of Natural Convection in the Annulus Between Horizontal Concentric Cylinders," *J. Fluid Mech.*, **74**, pp. 695–719.
- [8] Yoo, J.-S., 1996, "Dual Steady Solutions in Natural Convection Between Horizontal Concentric Cylinders," *Int. J. Heat Fluid Flow*, **17**(6), pp. 587–593.
- [9] Castrejon, A., and Spalding, D. B., 1988, "An Experimental and Theoretical Study of Transient Free-Convection Flow Between Horizontal Concentric Cylinders," *Int. J. Heat Mass Transfer*, **31**, pp. 273–284.
- [10] Charrier-Mojtabi, M. C., Mojtabi, A., and Caltagirone, J. P., 1979, "Numerical Solution of a Flow Due to Natural Convection in Horizontal Cylindrical Annulus," *ASME J. Heat Transfer*, **101**, pp. 171–173.
- [11] Kuehn, T. H., and Goldstein, R. J., 1976, "Correlating Equation for Natural Convection Heat Transfer Between Horizontal Circular Cylinders," *Int. J. Heat Mass Transfer*, **19**, pp. 1127–1134.
- [12] Kays, W. M., Crawford, M. E., and Weigand, B., 2004, *Convective Heat and Mass Transfer*, 4th ed., McGraw-Hill, New York.
- [13] Kuehn, T. H., and Goldstein, R. J., 1978, "An Experimental Study of Natural Convection Heat Transfer in Concentric and Eccentric Horizontal Cylindrical Annuli," *ASME J. Heat Transfer*, **100**, pp. 635–640.
- [14] Prusa, J., and Yao, L. S., 1983, "Natural Convection Heat Transfer between Eccentric Horizontal Cylinders," *ASME J. Heat Transfer*, **105**, pp. 108–116.
- [15] Chao, C. H., Chang, K. S., and Park, K. H., 1982, "Numerical Simulation Natural Convection in Concentric and Eccentric Horizontal Cylindrical Annuli," *ASME J. Heat Transfer*, **104**, pp. 624–630.
- [16] Sparrow, E. M., Stryker, P. C., and Ansari, M. A., 1984, "Natural Convection in Enclosures With Off-Center Innerbody," *Int. J. Heat Mass Transfer*, **27**, pp. 49–56.
- [17] Guj, G., and Stella, F., 1995, "Natural Convection in Horizontal Eccentric Annuli: Numerical Study," *Numer. Heat Transfer, Part A*, **27**(1), pp. 89–105.
- [18] Dyko, M. P., and Vafai, K., 2001, "Three-Dimensional Natural Convective States in a Narrow-Gap Horizontal Annulus," *J. Fluid Mech.*, **445**, pp. 1–36.
- [19] Dyko, M. P., Vafai, K., and Mojtab, A. K., 1999, "Numerical and Experimental Investigation of Stability of Natural Convective Flows Within a Horizontal Annulus," *J. Fluid Mech.*, **381**, pp. 27–61.
- [20] Dyko, M. P., and Vafai, K., 2002, "On the Presence of Odd Transverse Convection Rolls in Narrow-Gap Horizontal Annuli," *Phys. Fluids*, **14**, pp. 1291–1294.
- [21] Iyer, S. V., and Vafai, K., 1999, "Passive Heat Transfer Augmentation in a Cylindrical Annulus Utilizing Multiple Perturbations on the Inner and Outer Cylinders," *Numer. Heat Transfer*, **35**, pp. 567–586.
- [22] Padilla, E. L. M., and Silveira-Neto, A., 2008, "Large-Eddy Simulation of Transition to Turbulence in Natural Convection in a Horizontal Annular Cavity," *Int. J. Heat Mass Transfer*, **51**, pp. 3656–3668.
- [23] Tsui, Y. T., and Tremblay, B., 1984, "On Transient Natural Convection Heat Transfer in the Annulus Between Concentric Horizontal Cylinders With Isothermal Surfaces," *Int. J. Heat Mass Transfer*, **27**, pp. 103–111.
- [24] Kline, S. J., and McClintock, F. A., 1953, "Describing Uncertainties in Single-Sample Experiments," *Mech. Eng. (Am. Soc. Mech. Eng.)*, **75**, pp. 3–12.

Effect of Wick Characteristics on the Thermal Performance of the Miniature Loop Heat Pipe

Randeep Singh

e-mail: randeep.singh@rmit.edu.au

Aliakbar Akbarzadeh

Energy Conservation and Renewable Energy
Group,
School of Aerospace, Mechanical and
Manufacturing Engineering,
RMIT University,
P.O. Box 71,
Bundoora East Campus,
Bundoora, Victoria 3083, Australia

Masataka Mochizuki

R&D Department,
Thermal Technology Division,
Fujikura Ltd.,
1-5-1 Kiba, Koto-Ku,
Tokyo 135-8512, Japan

Two phase heat transfer devices based on the miniature version of loop heat pipe (LHP) can provide very promising cooling solutions for the compact electronic devices due to their high heat flux management capability and long distance heat transfer with minimal temperature losses. This paper discusses the effect of the wick properties on the heat transfer characteristics of the miniature LHP. The miniature model of the LHP with disk-shaped evaporator, 10 mm thick and 30 mm disk diameter, was designed using copper containment vessel and water as the working fluid, which is the most acceptable combination in electronic cooling applications. In the investigation, wick structures with different physical properties including thermal conductivity, pore radius, porosity, and permeability and with different structural topology including monoporous or biporous evaporating face were used. It was experimentally observed that copper wicks are able to provide superior thermal performance than nickel wicks, particularly for low to moderate heat loads due to their low heat conducting resistance. With monoporous copper wick, maximum evaporator heat transfer coefficient (h_{ev}) of 26,270 W/m² K and evaporator thermal resistance (R_{ev}) of 0.06–0.10 °C/W were achieved. For monoporous nickel wick, the corresponding values were 20,700 W/m² K for h_{ev} and 0.08–0.21 °C/W for R_{ev} . Capillary structure with smaller pore size, high porosity, and high permeability showed better heat transfer characteristics due to sufficient capillary pumping capability, low heat leaks from evaporator to compensation chamber and larger surface area to volume ratio for heat exchange. In addition to this, biporous copper wick structure showed much higher heat transfer coefficient of 83,787 W/m² K than monoporous copper wick due to improved evaporative heat transfer at wick wall interface and separated liquid and vapor flow pores. The present work was able to classify the importance of the wick properties in the improvement of the thermal characteristics for miniature loop heat pipes.

[DOI: 10.1115/1.3109994]

Keywords: miniature loop heat pipe, pore size, permeability, porosity, effective thermal conductivity, biporous wick, monoporous wick

1 Introduction

Thermal control of the electronic devices has achieved significant improvement with the development in the heat pipes based on two phase cooling technology. Heat pipe is an efficient two phase heat transfer device [1] that utilizes latent heat of vaporization of working fluid pumping under capillary pressure to transport waste heat from the hot source to the remotely located heat sink. However, the applications of conventional heat pipes in electronic cooling are mainly limited to transfer heat over relatively shorter distances with the evaporator and condenser mostly at same horizontal levels. These drawbacks on the part of the heat pipe are mainly related to the major pressure losses associated with liquid flow through the porous wick structure, present along the entire length of the heat pipe, and viscous interaction between the vapor and liquid phases, also called entrainment losses [2].

Loop heat pipe (LHP) is an improved version of a heat pipe [3,4] that addresses these limitations of the conventional heat pipe by completely separating the liquid and vapor phases from each other and localizing the capillary structure in the evaporator section only. LHPs possess all the main advantages of conventional heat pipes and are additionally capable of transferring large heat loads for distances up to several meters in any orientation in the

gravity field. These devices are one of the most promising thermal control technologies for ground based [5] as well as space applications [6]. In the electronics cooling, LHPs can be considered as potential alternatives [7–10] to the convectional heat pipes due to the high heat transport capacity of their evaporator and wickless transportation lines that can be easily bent for installation inside device cabinet.

The evaporator is the most critical and main structural element of the loop heat pipe. It consists of the evaporation section and the integrated liquid reservoir (also known as compensation chamber), which are hydraulically and thermally connected via wick structure. The wick is an integral part of the loop heat pipe evaporator and provides the necessary capillary forces to the working fluid for its continuous circulation in the loop. As a connecting link between the evaporator and compensation chamber, the wick is also expected to perform as a thermal and hydraulic barrier to minimize back flow of heat and vapor from the evaporation zone to the compensation chamber. Use of fine pore wicks in LHPs helps to provide the necessary high capillary pressure to inhibit the migration of vapor from the evaporation zone to the compensation chamber. The problem of back conduction of heat through liquid saturated wick is very critical in the proper functioning of the loop evaporator and to a large extent dictates the thermal behavior of the LHP. Unlike conventional heat pipes, the wick structure used in the LHPs should not have excessively high effective thermal conductivity to avoid heat leaks to the liquid present in the compensation chamber. It should be noted that there

Contributed by the Heat Transfer Division of ASME for publication in the JOURNAL OF HEAT TRANSFER. Manuscript received August 4, 2008; final manuscript received February 14, 2009; published online June 4, 2009. Review conducted by Louis C. Chow.

is a need for compromise between back conduction problem and the desire for good thermal conductivity of wick to promote efficient heat exchange in the evaporating zone.

Miniature designs of the loop heat pipes have been investigated by different researchers [11–15] for the cooling of compact electronic equipment like laptops. The main restriction in the development of the small scale loop heat pipes is imposed on the down scaling of evaporator thickness, which is the diameter for the cylindrical evaporators and overall thickness for the flat evaporators. This is directly related to the heat leakage issue that is more dominating in the miniature loop heat pipes (mLHPs) due to the smaller wick thickness [16]. As a result, the thermal performance of the miniature LHPs is lower than the larger size loop systems, which have wick structures of considerable thickness.

Within the framework of the evaporator, there is considerable scope to address the thermal performance issues for miniature LHP by optimizing the structure topology, geometric parameters, and thermal characteristics of the wick. The choice of wick material and its physical properties like pore size, porosity, and permeability has considerable effect on the operational characteristics of the loop system. The capillary structure can be made from plastic or metal. Plastic wicks made from thermoplastic polymeric like polypropylene [17], Teflon [18], and polyethylene [19] have been successfully used as capillary pumps in LHPs. These plastic wicks present very low thermal conductivity, which is desirable for the efficient LHP operation, but there exists a limit on the maximum value of the porosity of these wicks. In most cases, the porosity of these wicks is less than 50%, which imposes a limit on the maximum heat transfer capacity of the LHPs. A comprehensive study done by Singh et al. [20] on the determination of the physical properties of polyethylene wicks shows that such wicks generally exhibit a porosity value of less than 38% for a pore size in the range of 8–20 μm . Also, the permeability for these wicks, of the order 10^{-14} m^2 , is quite low that increases the pressure drop through the porous structure. In addition to this, operational regime of the plastic wicks is limited by their maximum allowed operation temperature. For example, maximum permissible temperature for polyethylene is 120°C and for Teflon is 250°C .

Contrary to this, sintered metal wicks can be easily obtained with an effective pore radius as small as 2 μm , high porosity of 55–75%, and permeability in the range of 10^{-12} – 10^{-13} m^2 by using developed techniques [21,22]. In the category of sintered metal wicks, nickel wicks [23] are widely used in LHPs due to their low thermal conductivity and ability to be formed in fine pore sizes with high porosity. Titanium [24,25], stainless steel [26], and copper [8] are the other frequently used LHP wick materials with desirable properties as a capillary structure. The wick structures as discussed above showed quite efficient performance in loop heat pipes and are mostly used as monoporous wicks, i.e., their pore size distribution is similar to the Poisson distribution and they are characterized by single average pore size. To improve the performance of the evaporator at very high heat fluxes, a porous medium with two characteristic capillary pore radii known as biporous structure has been proposed [27]. In the biporous capillary structure, the size of the large pores is an order of magnitude greater than in monoporous ones. Thus a biporous wick includes bidispersed media that are made from large porous particles, which have small pores in/on them. Chernysheva et al. [28] proposed a mathematical model to predict the intensity of heat exchange process inside the LHP evaporation zone. It was concluded that the character and intensity of heat exchange depend considerably on the structural characteristics of capillary porous material. Tests conducted by Yeh et al. [29] on miniature LHP showed a low total thermal resistance of 0.31°C/W at 200 W with biporous wick as compared with 0.53°C/W at 125 W for monoporous wick. Maydanik et al. [30] utilized the concept of bidisperse wicks and organized an efficient three step vapor removal channel inside the LHP evaporator. It was confirmed through experimentation that use of biporous layer was able to

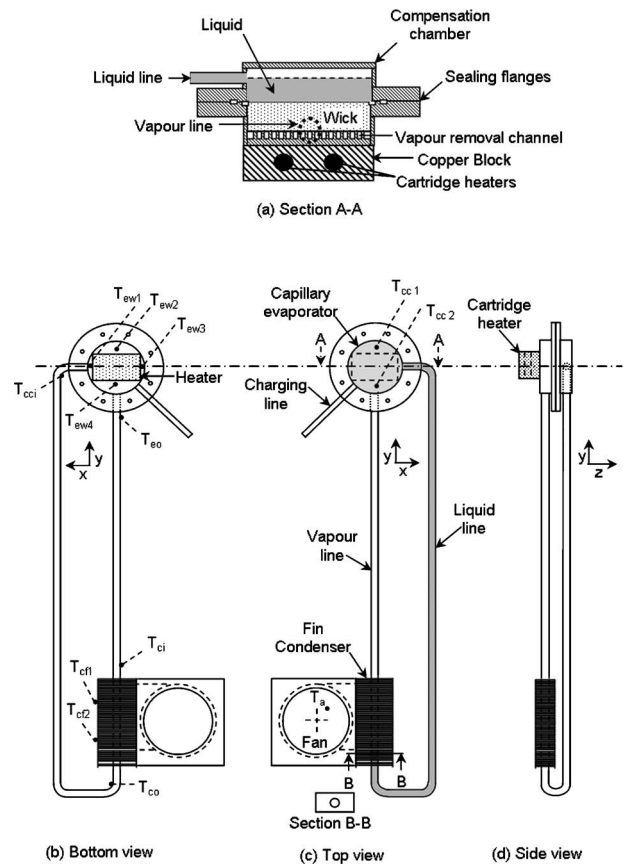


Fig. 1 Schematics of the mLHP experimental prototype and details of the test setup showing the temperature measurement points and locations of condenser fan and heater

improve the heat transfer characteristics in the LHP evaporator irrespective of the device orientation in the gravity field.

Considering the possible options, appropriate choice of the thermal conductivity and the flow properties of the wick structure can help in the design of a suitable wick configuration that can improve heat transfer efficiency of the miniature LHP. In the present investigation, different types and grades of wick structures were developed and tested in the designed prototype of miniature loop heat pipe with an intention to classify the effect of the wick structure on the mLHP performance and to improve the acceptability of the mLHP for electronic cooling. Wick structures made from copper or nickel material and different physical properties were used in the present research.

2 Experimental Prototype

In order to investigate the effect of the wick characteristics on the LHPs, a miniature scale prototype of LHP, as shown in Fig. 1, with the flat disk shaped evaporator, 30 mm in diameter and 10 mm in total thickness, was designed. LHPs for cooling compact electronic equipment like notebooks need to be extremely compact and easy to install inside the object to be cooled. In this regard, flat evaporator can be considered as an optimum choice due to ease of interfacing with heat source and integration inside the cabinet enclosure. The thickness of the evaporator consists of the vapor removal channels, wick structure, and the compensation chamber, as presented in Fig. 1(a). Unlike the conventional heat pipe, the evaporation section in the LHP is arranged quite differently with respect to the location of the vapor flow passage and evaporation zone. In the present design, 15 longitudinal grooves with an individual cross section of 0.9 mm width \times 1 mm depth were machined on the inside of the active heating zone, which

behaves as vapor removal channels and also provides heat to the wick structure through conduction process. In the LHP evaporator, the evaporation zone is formed at the interface of the wick with the internal wall of the heating zone. In principle, the capillary structure of a LHP is localized in the heat supply zone. On one hand, this approach helps to minimize the length of the liquid flow path through the porous structure, while on the other hand, it enables the use of fine pore wicks with high capillary pressure to enable the operation of the device at adverse tilt angles. The upper face of the capillary wick is the absorbing one, while the bottom face serves as the evaporating surface. For capillary pumping of working fluid, different types of wick structures made by sintering copper or nickel powder of different grades (i.e., powder size and shape) were used. It should be noted that the thickness of the wick structure, which was 3 mm, was the same for all the wick configurations. The compensation chamber was 4 mm thick and basically covered the entire liquid absorbing face of the wick, which guarantees continual wetting of the wick. As shown in Fig. 1(a), in LHP the compensation chamber is collocated with the evaporator and helps to accommodate the displaced liquid from the loop components during loop startup and variation in heat loads. Hence, optimum sizing of the compensation chamber is a very important consideration in the design of the loop heat pipe. If the liquid chamber is oversized, it will increase the system thermal mass and thus response time to changing heat loads, whereas being undersized it will not be able to perform its intended functions of liquid storage and continual wetting of the wick. In the designed mLHP, the compensation chamber was large enough to contain all the liquid charge. For dissipating heat transferred from the evaporator section, remotely located fin-and-tube type condenser with the total length of 50 mm and fin cross section of $10 \times 20 \text{ mm}^2$ was used. The heat transport zone (i.e., vapor line) of the mLHP was 150 mm in length and 2 mm in internal diameter. For the return of the condensate to the evaporator, a liquid return line with the total length of 290 mm and internal diameter of 2 mm was used. mLHP body was made from high conductive copper material. The evaporator structure was hermetically sealed by using an O-ring seal between the sealing flanges fastened by nut and screw arrangement. Rubber packing was also provided around the wick periphery to avoid any vapor bypass to the compensation chamber and to apply uniform pressure on the wick for proper thermal contact with the vapor channels top.

Proper care was taken to clean the mLHP before it was charged with the working fluid. First the LHP components were heated in a furnace at a temperature of around 150°C for 30 min to remove any organic as well as inorganic impurities from the process of manufacturing. Then cleaning using acetic acid was performed, followed by rinsing in boiling water, and then cleaning using compressed air. This process was repeated three to four times to remove any residual cleaning agent. Wettability test was performed on each wick sample before it was installed inside the evaporator. In the case of poor wetting with the working fluid or evidence of contamination/oxidation based on visual inspection, the wick structure was resintered at low temperature in reduced atmosphere. In all the tests, the loop was charged with distilled, deionized, and degassed water equal to 70% of its internal volume [31].

3 Test Procedure

The thermal characteristics of the designed miniature LHP were studied by applying uniform heat load to the evaporator active face using a heater with a thermal footprint of $25 \times 15 \text{ mm}^2$, as shown in Fig. 1. In this case, the heat load simulator was in the form of a copper block with two embedded cylindrical cartridge heaters. For testing, the heater block was attached symmetrically to the center of the evaporator active zone. A digital wattmeter with a precision of $\pm 0.1 \text{ W}$ was used to measure and control the input heat load to the heat simulator. During testing, the input power to the heat simulator was increased in a step of 5 W. Condenser cooling was accomplished by forced convection provided

Table 1 Description of the powder used for each wick sample

Sample	Material	Powder size (mesh size)	Powder type
Sample A	Nickel	-200	Monoporous
Sample B	Copper	-200	Monoporous
Sample C	Copper	100–200	Monoporous
Sample D	Copper	-200 (monoporous) 50–140 (biporous)	Monoporous (first layer) Biporous (second layer)

by a centrifugal fan using ambient air with a controlled temperature of $24 \pm 2^\circ\text{C}$. The maximum flow rate of the fan was $0.1 \text{ m}^3/\text{min}$ under 5 V and 0.1 A power supply. In order to measure the temperature at different locations, T-type thermocouples were used. Figures 1(b) and 1(c) show the placement of the thermocouples on the mLHP prototype. The thermocouples were calibrated in a narrow range by using precise temperature bath with an accuracy of $\pm 0.2^\circ\text{C}$. Data from thermocouples were acquired and recorded every 10 s using a Keyence data acquisition system.

For the applied heat load, the steady state heat transfer effectiveness of each wick configurations used in the mLHP was measured on the basis of the saturation vapor temperature (T_v), evaporator thermal resistance (R_{ev}), and evaporator heat transfer coefficient (h_{ev}). Equations (1) and (2) were used to calculate these parameters.

Evaporator thermal resistance

$$R_{ev} = \frac{(T_{ew} - T_v)}{\dot{Q}_a} \quad (1)$$

Evaporator heat transfer coefficient

$$h_{ev} = \frac{\dot{Q}_a}{A_{ew}(T_{ew} - T_v)} \quad (2)$$

In the above equations, T_{ew} is the external temperature of the evaporator active zone, which was measured by averaging the temperatures of the thermocouples fixed on the evaporator heating face (i.e., T_{ew1} , T_{ew2} , T_{ew3} , and T_{ew4}). The vapor temperature (T_v) was taken to be equal to the temperature at the evaporator outlet (T_{eo}), as indicated in Fig. 1(b). It should be noted that the T_{eo} provides quite accurate prediction of the true vapor temperature inside the evaporation zone. In order to confirm that T_{eo} is not biased by the conduction heat transfer along the vapor line, it was compared with the condenser inlet temperature (T_{ci}), which due to the thermal insulation of the vapor line was very close to the evaporator outlet temperature (T_{eo}). In this case, temperature difference of less than 0.5°C was noted between T_{eo} and T_{ci} , which was predominately due to the pressure drop along the vapor line. The maximum uncertainties in the calculation of h_{ev} and R_{ev} were 12.5% and 6.5%, respectively.

4 Wick Analysis

The necessary hydraulic and thermal analysis was performed on the wick samples to measure their physical properties, which helped to confirm their suitability to perform as a capillary pump for the designed mLHP and further provided grounds to explain the outcomes of the experiment.

4.1 Capillary Structure Types. In the experiment, four types of porous structures, which differed with respect to the material (nickel or copper), powder size (mesh size of 100–200 or -200), and powder type (monoporous or biporous), were used. It should be noted that mesh size specifies the range of the granule sizes that are contained in the given powder sample. For example, 100–200 mesh size powder means that granules with size in the range of 100–200 mesh number are contained in the given sample. The -200 mesh size means that powders with granule sizes less than 200 mesh number are present in the sample. Table 1 gives the

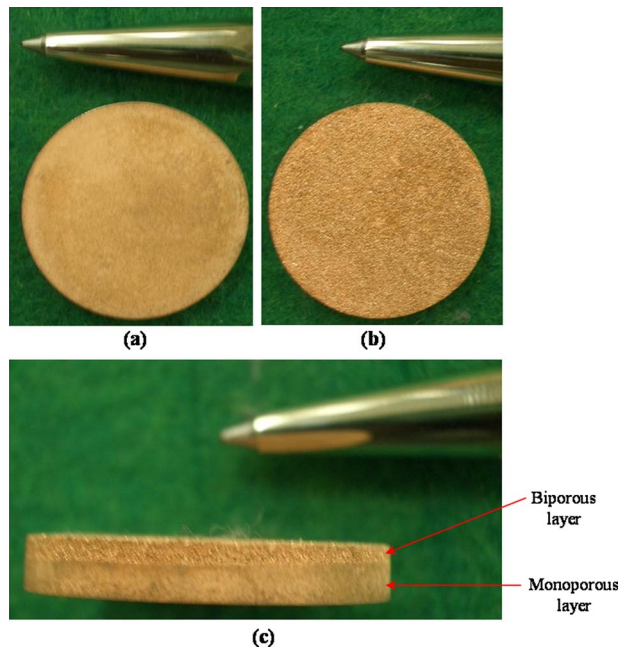


Fig. 2 Combined copper wick sample showing the (a) monoporous layer as a liquid absorbing face, (b) biporous layer as an evaporating face, and (c) side view showing the layers

details of the powder used for each wick sample. The first three samples were single layered monoporous wicks, whereas the fourth sample was double layered combined wick with a monoporous and a biporous layer, as shown in Fig. 2. It should be noted that the dimensions of each sample were the same, i.e., 28 mm diameter and 3 mm thickness. The magnified structural detail of the monoporous and biporous copper wicks used in the current testing is shown in Fig. 3.

4.2 Flow Property Measurement. In order to predict the thermal performance of the loop heat pipes with different wick structures, information on the flow properties of the porous structure including permeability, porosity, and pore radius is required. The following simple laboratory techniques were developed to establish these properties. Reference [14] covers these techniques in more detail.

4.2.1 Permeability. The permeability of the porous structure determines their ability to transport liquid under applied pressure head. In order to measure the permeability, a constant hydrostatic head was maintained across the wick specimen by using a liquid

reservoir with an overflow arrangement. At steady flow conditions under constant pressure head, the mass of water flowing through the porous matrix in a given time interval was measured by using weighing technique. This information is used with Darcy law [32] to calculate the specific permeability at different pressures as given by Eq. (3). The maximum uncertainty in the measurement of permeability was $\pm 6.17\%$.

$$k_p = \frac{V_l \mu_l t_w}{A_w \Delta P_w} \quad (3)$$

4.2.2 Porosity. Porosity is defined as the ratio of the porous volume to the total volume of the wick structure. Two methods were used to measure the porosity of the wick structures. In the first approach, known as density method, the porosity was calculated from the measured density (ρ_w) of the wick, which was determined from the volume and weighing of the dry sample. As the density (ρ_{wm}) of the wick material (copper or nickel) is known in the nonporous state, porosity (ϵ_w) of the specimen can be calculated as follows:

$$\therefore \epsilon_w = 1 - \frac{\rho_w}{\rho_{wm}} \quad (4)$$

The second method, known as the soaking method, measures the quantity of the liquid absorbed by the dry wick sample to estimate its porous volume. Out of the two methods, the density method gave accurate results when compared with the manufacturer's specifications due to problems of closed spaces and improper wetting of the wick substrate by the working fluid in the soaking method. In the present study, results from the density method were used, which were subjected to a maximum error of $\pm 2.12\%$.

4.2.3 Pore Radius. The pore radius of the wick structure was obtained by using U-tube bubble point method, as explained in Ref. [20]. The uncertainty in the determination of the pore radius was $\pm 2.5\%$. It should be noted that the bubble point approach gave the estimation on the largest pore size in the given porous specimen, which is very important for validating the successful operation of the loop heat pipe. Unlike convective heat pipes, the capillary pressure generating capacity of the LHP wicks should be accessed on the basis of the largest pore size in the wick structure and not from the mean pore radius. It is expected that the dryout of the largest pore will supersede the smaller pores due to its low capillary pumping limit. Local dryout of the porous structure will create bypass for vapor flow to the compensation chamber, thereby hampering the performance of the complete system. On this basis, it can be argued that the capillary limit of the capillary evaporator calculated from the mean pore radius will overestimate the thermal capacity of the LHP, which can be a serious design issue in electronic cooling.

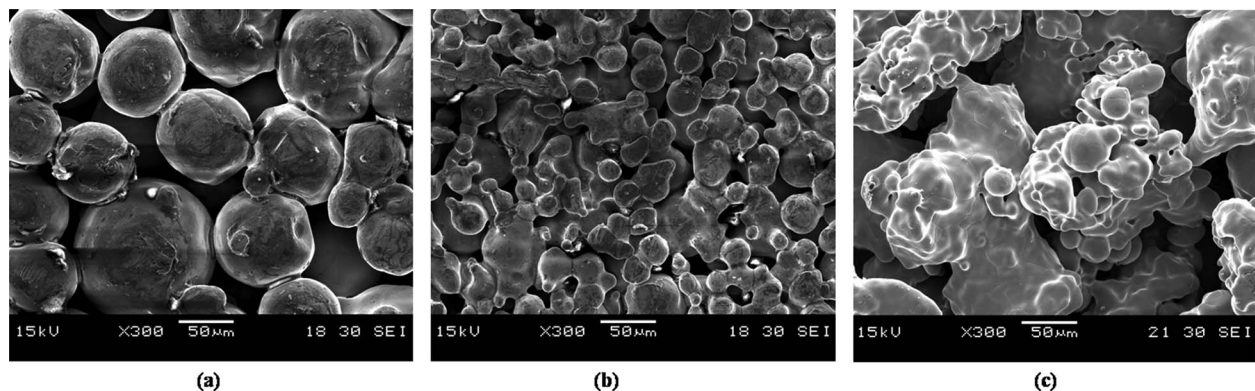


Fig. 3 Structure of the (a) monoporous copper sample made from 100–200 mesh size powder, (b) monoporous copper sample made from -200 mesh size powder, and (c) biporous copper sample at $\times 300$ magnification

Table 2 Experimental and predicted values for effective thermal conductivity of water saturated wick (powder: monoporous, copper, 100–200 mesh size)

Method	k_e (W/m K)
Experimental value	31.77–32.54 (~32)
Dunn and Reay [1]	188.09
Volume averaging technique [1]	228.27
Alexander correlation [33]	65

4.3 Wick Effective Thermal Conductivity. The effective thermal conductivity of the wick is a very important parameter to be considered during the selection of the wick material and design of the capillary evaporator. A simple experiment based on the one-dimensional conduction heat transfer was developed to determine the effective thermal conductivity of the sintered copper wick saturated with water. The test setup consisted of a sealed rectangular copper container with water saturated sintered copper wick, 43% porous, and made from 100–200 mesh size powder, such that the bottom face of the sample is provided with uniform heat flux, while the top face is cooled using fin heat exchanger with air flow arrangement. Experimental data were substituted in Eq. (5) to calculate the effective thermal conductivity of the wick. The experimental uncertainty for effective thermal conductivity (k_e) was 5.7%.

$$k_e = \frac{Q_s^* t_s}{(T_{bf} - T_{tf}) A_s} \quad (5)$$

The experimentally determined k_e was compared with prediction made on the basis of different correlations available in the literature as given below.

Dunn and Reay [1] proposed the following correlation to calculate the effective thermal conductivity k_e of the isotropic wick structure,

$$k_e = k_w \left(\frac{2 + (k_l/k_w) - 2\varepsilon[1 - (k_l/k_w)]}{2 + (k_l/k_w) + \varepsilon[1 - (k_l/k_w)]} \right) \quad (6)$$

Effective thermal conductivity of the wick can also be obtained by volume averaging technique [1] as stated below:

$$k_e = k_w(1 - \varepsilon) + \varepsilon k_l \quad (7)$$

Alexander [33] derived a correlation for calculating the effective conductivity of the homogeneous wick structure as

$$k_e = k_l \left(\frac{k_l}{k_w} \right)^{-(1 - \varepsilon)^\alpha} \quad (8)$$

where α is a constant equal to 0.59.

Table 2 lists the values for k_e obtained from the experiment and theoretical correlations discussed above. It can be seen from comparison that correlations largely overpredict the value of k_e . The effective thermal conductivity obtained from the Dunn and Reay correlations and volume averaging technique is more than 5.8 and 7 times of the experimental value of 32 W/m K, respectively. However, the k_e value predicted by Alexander's equation (~65 W/m K) was better than other correlations. The difference in experimental conditions and setup as compared with those used while deriving the correlations, experimental uncertainties in porosity (~2.1%) and effective thermal conductivity (~5.7%), possible imperfections in test sample like improper thermal contact between container wall and wick, and incomplete wetting of wick are some of the sources that can account for discrepancies between measured and predicted results.

4.4 Pressure Criterion. The main condition that needs to be satisfied for the proper operation of the LHP is the same as for any other heat pipe and relates to the balance of the capillary pressure

Table 3 Results of the pressure analysis on each wick sample

Sample	Capillary pressure (Pa)	Pressure drop (at T_v and 60 W input) (Pa)
A	8163.18	503.22
B	8081.98	444.91
C	3231.56	386.87
D	8362.4	647.91

generated by the porous structure on the working fluid and the total pressure drop in the loop. In other words, the wick structures used in the present experiments must be able to generate enough capillary pressure to keep the working fluid in continuous circulation. This criterion can be stated mathematically as follows:

$$\Delta P_{\text{cap}} \geq \Delta P_v + \Delta P_l + \Delta P_g = \Delta P_t \quad (9)$$

where ΔP_{cap} is the generated capillary pressure and ΔP_t is the total pressure drop in the loop, which includes pressure loss due to vapor flow (ΔP_v), pressure loss incurred due to the liquid flow (ΔP_l), and hydrostatic pressure loss due to the unfavorable slopes of the device in the gravity field (ΔP_g).

The maximum capillary pressure, which depends on the surface tension coefficient (σ_l) of the liquid working fluid and pore radius (r_m) of the porous structure, is given by the Young–Laplace equation [1] as

$$\Delta P_{\text{cap}} = \frac{2\sigma_l}{r_m} \quad (10)$$

The pressure drop due to friction losses in liquid and vapor flows through the loop (for laminar or turbulent flows, circular or non-circular pipes, and smooth or rough surfaces) is given by the Darcy–Weisbach equation [34] as

$$\Delta P = f \frac{L}{D_h} \frac{\rho U^2}{2} \quad (11)$$

where f , Darcy friction factor, is a dimensionless quantity and function of Reynolds number. For perfectly smooth pipes/channels, the friction factor (f) is given by

$$f = \frac{64}{\text{Re}} \quad \text{Re} < 2300 \text{ (laminar flow)} \quad (12)$$

$$f = \frac{0.316}{\text{Re}^{0.25}} \quad \text{Re} > 2300 \text{ (turbulent flow)} \quad (13)$$

A suitable wick structure must satisfy the pressure criterion for the successful operation of the loop as expressed below:

$$\Delta P_{\text{cap}} \geq \Delta P_t \quad (14)$$

Table 3 presents data on the capillary pressure generated by different wick structures as calculated on the basis of largest pore size and the associated total pressure drop inside the mLHP for each case. These results are reported at the maximum heat load applied in the experiments. It is evident that the capillary pressure provided by each wick structure was quite large as compared with the pressure losses. In other words, the capillary limit was not reached in any of the test run.

5 Results and Discussion

The results of the experimentation on the mLHP prototype using different types of wicks are now presented.

5.1 Effect of Wick Material. Sintered metal wicks made from nickel and copper were used to study the effect of the thermal conductivity on the mLHP performance. For the two wick types, the physical characteristics were approximately the same with the maximum pore radius of less than 15 μm and a porous

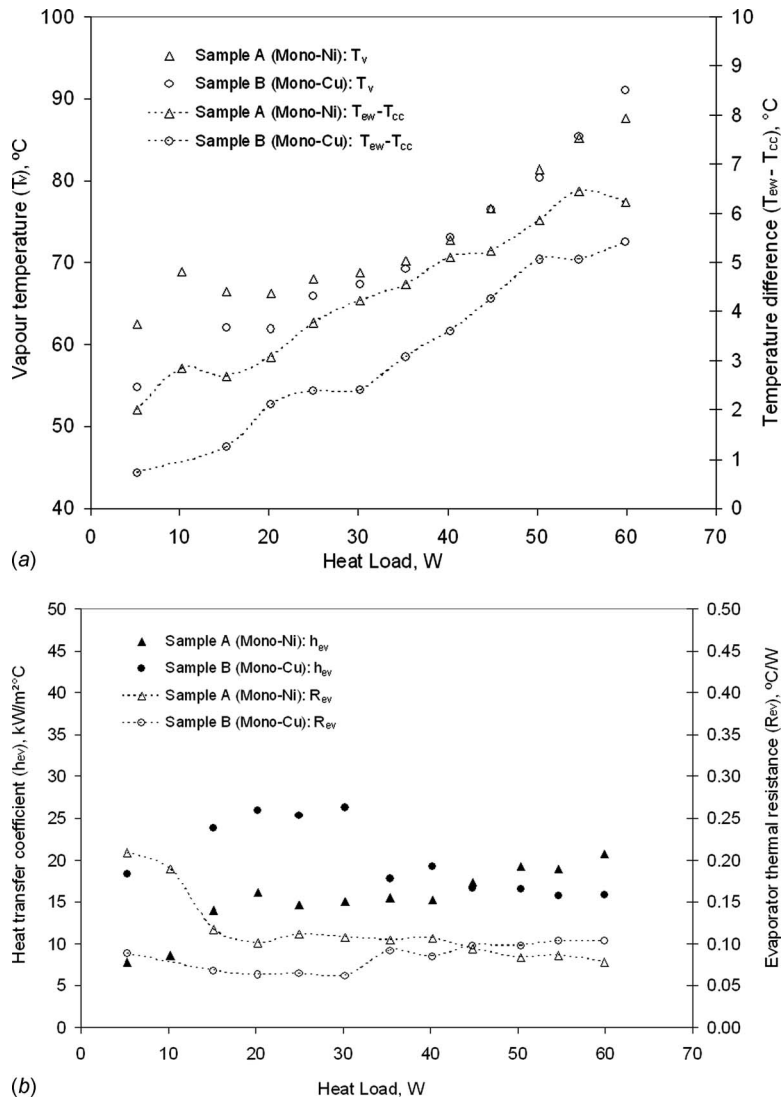


Fig. 4 Heat load dependence of (a) vapor temperature (T_v) and temperature difference between evaporator and compensation chamber wall ($T_{ew}-T_{cc}$) and (b) heat transfer coefficient (h_{ev}) and evaporator thermal resistance (R_{ev}) for wick samples A and B

volume of 45–50%. The thermal conductivities of the copper material and nickel material used to fabricate these samples were 400 W/m K and 90 W/m K, respectively, which correspond to the effective thermal conductivities of 55.68 W/m K and 16.9 W/m K, respectively, as calculated from Eq. (8). The thickness of the wick structure was restricted to 3 mm with an absorbing face area of 616 mm². Figure 4(a) shows the heat load dependence of the vapor temperature with two types of wick material.

It can be seen from the graph that for a heat load of less than 45 W, the evaporator saturation temperature for the mLHP with copper wick is lower than with the nickel wick. This is the result of the efficient heat exchange in the evaporation zone with the copper wick, as shown in Fig. 4(b). With the copper wick overall heat transfer coefficient from the evaporator wall to the vapor was as high as 26,270 W/m² K. These higher values of the heat transfer coefficient were obtained because of the high thermal conductivity of copper, which helped to transfer heat efficiently to the evaporating menisci in the capillary structure by conduction through the wick skeleton. An abrupt decrease in the heat transfer coefficient with the copper wick was experienced at approximately 30 W, possibly due to the formation of dissociated pores near the heating

wall as the heat load increases. Here, the desiccated or dried out pores introduced additional thermal resistance in the evaporation zone, as is clearly shown in Fig. 4(b) for heat loads greater than 30 W. In the case of nickel wick, the maximum heat transfer coefficient value achieved was 20,700 W/m² K.

For the copper wick mLHP, as shown in Fig. 4(b), low values of 0.06–0.10 $^{\circ}\text{C/W}$ for evaporator thermal resistance (R_{ev}) from the evaporator wall to the evaporator outlet were achieved over the range of applied heat load. R_{ev} with nickel wick was found to be between 0.08 $^{\circ}\text{C/W}$ and 0.21 $^{\circ}\text{C/W}$. For the copper wick, the lowest value of R_{ev} is achieved at low heat load, whereas with nickel wick R_{ev} is lowest at maximum applied heat load, i.e., 60 W. This fact helps to differentiate the operational regime and heat transfer characteristics of copper and nickel wicks. The high thermal conductivity of copper wick is an advantage in organizing efficient heat exchange between heated wall and working fluid inside the evaporation zone. In this case, heat transfer augmentation is performed by copper wick by improving conduction heat flow along the evaporating face of the porous structure via highly conductive wick matrix. Positively, this helps to address the cold state startup problems faced by the mLHPs at low heat loads [35].

Table 4 Measured flow properties of the monoporous copper wicks

Property	Measurement method/principle	Sample B	Sample C
Maximum pore radius (μm)	Bubble point testing	12–15	30–37
Porosity (%)	Density method	44–46	40–43
Permeability (m^2)	Darcy law	7.21×10^{-12}	1.79×10^{-11}

However, high conductance of copper also increases the thermal diffusion in the wick thickness that increases the heat leaks from the evaporation zone to the compensation chamber particularly at high heat loads. As a result, the saturation temperature for the mLHP with copper wick was slightly higher than that of the nickel wick mLHP beyond 45 W. Figure 4(a) also plots the temperature difference across the capillary structure calculated by deducting the average evaporator wall temperature from the mean compensation chamber wall temperature. A low temperature difference signifies lower thermal resistance and thus high rate of heat flow across the wick. It is evident from the graph that heat leaks with copper wick are higher than nickel wick. As a result, nickel wick performs better at high heat loads but worst at low input powers due to its 4.4 times lower thermal conductivity than copper.

At high heat loads (above 35 W), it is noted that the same incremental rise in the input load produced higher increase in evaporator temperature for both wick structures. Such behavior is very typical for LHPs and depicts the constant conductance mode of loop operation in contrast to the variable conductance mode that is presented at low heat loads. The variable mode of operation is characterized by auto regulation of the evaporator temperature within certain range and is associated with the filling of the compensation chamber by displaced liquid from condenser with the progressive increase in the input power. In the present case, variable mode is presented below 35 W heat load. Once the compensation chamber is fully occupied with liquid, the constant conductance mode commences in which the operational characteristics of LHP are similar to the conventional heat pipe. As an outcome of this experiment, it can be concluded that capillary structures made

from a highly conductive material like copper can be effectively used in a miniature LHP for thermal control of electronic equipment without any major performance degradation. This is made possible by the use of a fine pore wick with a highly conductive porous matrix that is occupied by working fluid with relatively low thermal conductivity.

5.2 Effect of Wick Flow Properties. Apart from the material characteristics like thermal conductivity, physical properties of the wick structure like porosity, permeability, and pore configuration also play an important role in determining its operational characteristics. In order to study the effect of the physical properties on the mLHP operation, two samples of the monoporous copper wick with different physical properties were tested as capillary pump in the designed mLHP. The first sample was sintered from copper powder with –200 mesh size, while in the second sample copper powder 100–200 mesh size was used. The geometrical properties of these samples, as measured experimentally using approach outlined in Sec. 4.2, are presented in Table 4.

The results of the experiment are presented in Fig. 5 as a heat load dependence of the evaporator saturation temperature for the two samples. It is evident from the graph that the performance of the mLHP with sample B is much superior to sample C. The physical properties of sample B are optimum to provide necessary vapor and heat flow barrier from the evaporation zone to the compensation chamber. The maximum capillary pressure provided by the wick structure is decided on the basis of the effective radius of the largest through-pore, which is much higher in the case of sample C ($\sim 37 \mu\text{m}$). At higher heat loads a pore can dryout, thereby permitting vapor flow from the evaporating surface of the wick to the compensation chamber. For sample B, the value of the maximum pore radius (≤ 15) was low enough to guarantee vapor locking in the given range of heat load, as verified by the loop pressure analysis given in Table 3. With both wick samples, the evaporator did not show any symptoms of capillary structure dry-out like vapor back flow or sudden elevation in evaporator temperature. Although the pressure analysis for both samples supports sufficient pumping capability of the wicks in the range of applied heat load, chances of local dryout for sample C at high heat loads are more than for sample B due to large pore sizes. Such a dryout can be recoverable but manifests itself by displaying relative rise

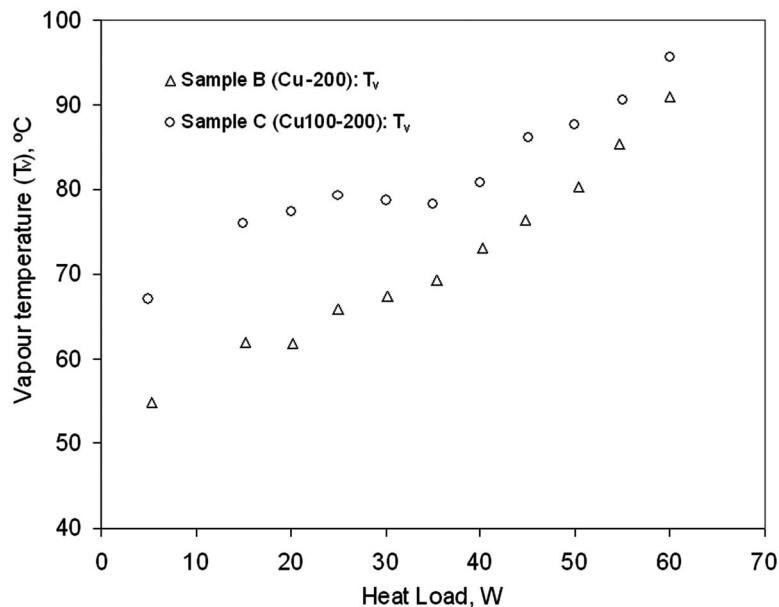


Fig. 5 Heat load dependence of vapor temperature (T_v) and temperature difference between evaporator and compensation chamber wall ($T_{ew} - T_{cc}$) for wick samples B and C

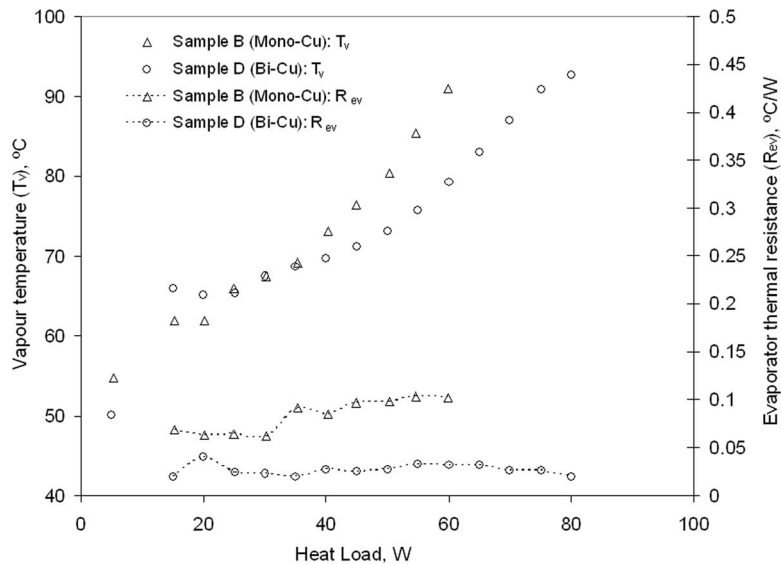


Fig. 6 Heat load dependence of vapor temperature (T_v) and evaporator thermal resistance (R_{ev})

in evaporator temperature.

The porosity of the wick affect the parasitic heat leaks from the evaporator zone to the compensation chamber and thus take part in providing thermal barrier. From Table 4, it is evident that the porosity of sample B (46%) is larger than sample C (43%). As the effective thermal conductivity of the wick structure has strong inverse dependence on the porosity of the capillary structure, back heat conduction through sample C was higher than sample B, which is evident from the higher evaporator saturation temperature with sample C, as presented in Fig. 5. The effective thermal conductivities for samples B and C as calculated by Eq. (8) were $55.68 \text{ W/m}^2 \text{ K}$ and $64.4 \text{ W/m}^2 \text{ K}$, respectively, that supports the observed temperature trend. It should be noted that due to larger pore size in sample C, the measured permeability of the sample is higher than sample B which results in lower liquid pressure losses through sample C as confirmed by pressure drop values in Table 3. In the context of LHP, the wick must possess sufficient permeability such that its capillary pumping limit is not compromised due to the liquid pressure losses through it, which is true for both the samples.

Sample B was sintered from powder with low mesh size as compared with sample C. The powder size affects the surface area to volume ratio of the wick sample, which is higher for specimen fabricated from powder with smaller size granular. As a result, evaporating heat transfer area for sample B was larger than sample C, which provides better thermal performance for sample B.

5.3 Effect of Wick Structure. In this experiment, two samples of a sintered copper wick, one based on the principle of single pore distribution (monoporous structure) and another based on the double pore distribution (biporous structure), respectively, were made. Sample B was the same as in previous case, i.e., monoporous copper wick made from -200 mesh size powder and 46% porous. For the second sample, as shown in Fig. 2, a double layered wick structure with a combination of a monoporous and a biporous layer was used. The biporous copper layer has a high porosity of 65% and was made from biporous copper powder with a granular of 50–140 mesh size. Due to the possibility of vapor breaking through the large pores of the biporous media into the compensation chamber, an additional backing layer of a monoporous material (the same as that used in sample B) was sintered attached to it. The biporous portion of the wick formed the evapo-

rating face, while the monoporous portion acted as an absorbing face (Fig. 2). The total thickness of both samples was the same at 3 mm.

Figure 6 presents the relation between saturation vapor temperature and applied heat load for mLHP testing with the monoporous and combined wick structure. It is noted from the graph that the combined wick structure presented superior thermal performance to that of the monoporous wick, particularly at high heat loads. This can be explained by looking into the details of the heat transfer processes in the evaporation zone with two types of wick configuration. In the wick with a monoporous distribution, the vapor phase in the capillary structure volume along the heating wall is absent at low to moderate heat loads. This is because the liquid superheat is not sufficient to boil the working fluid in the pores. It should be noted that the presence of vapor phase inside the porous matrix along the heated wall is beneficial in providing large surface area for evaporation. For the biporous capillary structure due to the presence of two characteristic pore sizes, the value of superheat at which one can observe liquid boiling in large pores is smaller than in monoporous wicks. In this case, the combination of randomly distributed large and small pores provides sufficient nucleation sites as well as necessary temperature difference to initiate boiling and thus clearing of liquid from larger pores. The resultant outcome is the availability of the larger surface area for evaporative heat transfer. Therefore in the bidispersed wick portion, heat transfer is enhanced in the nucleate boiling regime by the increasing surface area from which thin film evaporation can take place. The biporous wick also allows the liquid and vapor phases to have separate flow paths, the liquid through the small pores and the vapor through the large pores. Unlike the monoporous wick, this helps to avoid any vapor blanket formation at the heating wall due to desiccation of the pores at high heat fluxes, which can introduce additional thermal resistance.

For low heat loads ($<30 \text{ W}$) in Fig. 6, there is no clear distinction between the performance of the two wick types due to the absence of vapor phase inside the porous structure along the heated wall. In this case, for both wicks, the bulk of the porous structure is saturated with the liquid, which provides approximately equivalent evaporating face area and thus comparable performance. However, biporous wick is able to provide much better performance than monoporous wicks at high heat fluxes.

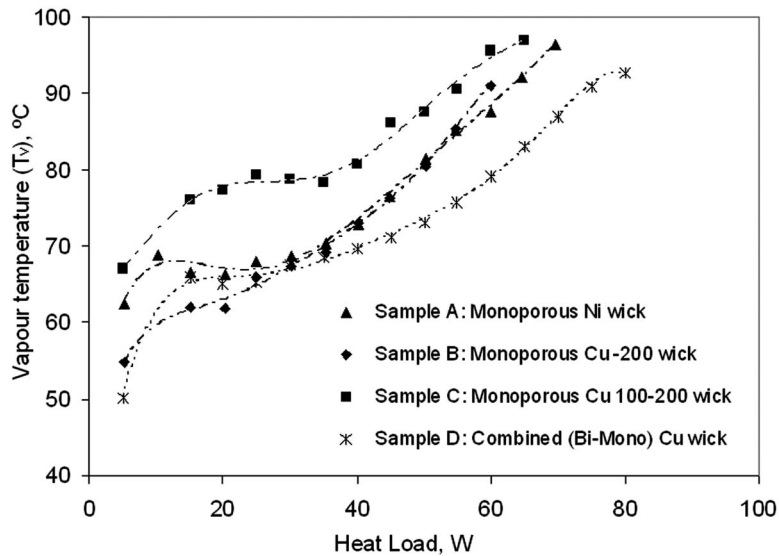


Fig. 7 Relation between vapor temperature (T_v) and applied heat load for the four wick samples tested in mLHP

mLHP with biporous wick presented low rate of increase in vapor saturation temperature with applied heat load due to the high evaporator heat transfer coefficient. In the range of applied power, maximum heat transfer coefficient values of $83,787 \text{ W/m}^2 \text{ K}$ and $26,270 \text{ W/m}^2 \text{ K}$ were achieved with biporous wick and monoporous wick, respectively. Figure 6 also presents the evaporator thermal resistance of two wick types. The evaporator thermal resistance using biporous wick was within $0.019\text{--}0.04^\circ\text{C/W}$ as compared with $0.06\text{--}0.10^\circ\text{C/W}$ for monoporous wick.

For the sake of comparison, Fig. 7 presents the vapor saturation temperature versus heat load trend for each wick configuration. Out of the tested configuration, biporous wick showed best thermal performance with more than 12% improvement over monoporous wick in the mLHP operating temperature.

6 Conclusions

The outcomes of this paper can be summarized as follows.

- The thermal characteristics of the miniature loop heat pipe evaporator with capillary structures of different materials, flow properties, and porous structures have been studied to improve the efficiency of the heat exchange process inside the evaporation zone.
- It was experimentally demonstrated that high conductive copper wick showed superior performance than nickel wick and provided heat transfer coefficient (h_{ev}) of $26,270 \text{ W/m}^2 \text{ K}$ and evaporator thermal resistance (R_{ev}) of $0.06\text{--}0.10^\circ\text{C/W}$ as compared to h_{ev} of $20,700 \text{ W/m}^2 \text{ K}$ and R_{ev} of $0.08\text{--}0.21^\circ\text{C/W}$ for nickel wick. However, the heat leaks from the evaporator to the compensation chamber due to heat conduction through porous matrix are larger for copper wick.
- The flow properties of the wick are very detrimental in the proper functioning and acceptable heat transfer performance of the capillary evaporator. High porosity is required to minimize the parasitic heat leaks from the evaporator zone to the compensation chamber. High permeability of the wick helps to reduce the pressure losses through the porous media. Apart from this, the wick should be able to generate sufficient capillary head, as calculated on the basis of the largest pore size, to keep the fluid in continuous circulation.
- Heat transfer characteristics of the biporous wick were better than monoporous wicks tested in the experiment. In the

biporous wick, the presence of the two characteristic pore sizes (i.e., large pores and small pores) increases evaporative heat transfer from the wick wall interface and at the same time provides separate flow paths for the liquid (through small pores) and vapor (through large pores). Maximum heat transfer coefficient of $83,787 \text{ W/m}^2 \text{ K}$ for biporous wick and of $26,270 \text{ W/m}^2 \text{ K}$ for monoporous wick was attained.

Nomenclature

A	= area, m^2
D	= diameter, m
f	= friction factor
h	= heat transfer coefficient, $\text{W/m}^2 \text{ K}$
k	= thermal conductivity, W/m K
k_p	= specific permeability of the porous structure, m^2
L	= length, m
ΔP	= pressure difference/pressure drop, Pa
Q	= heat load, W
R	= thermal resistance, $^\circ\text{C/W}$ or K/W
r	= pore radius, m
Re	= Reynolds number
t	= thickness, m
T	= temperature, $^\circ\text{C}$ or K
U	= flow velocity, m/s
V	= volumetric flow rate, m^3/s

Greeks Symbols

ρ	= density, kg/m^3
ε	= porosity, %
σ	= surface tension, N/m
μ	= viscosity, Pa s

Constants

$$\alpha = 0.59 \text{ (as per Eq. (8))}$$

Subscripts

a	= applied
bf	= bottom face
cap	= capillary
cc	= compensation chamber
cci	= compensation chamber inlet

cf = condenser fin
 ci = condenser inlet
 co = condenser outlet
 e = effective
 eo = evaporator outlet
 ev = evaporator
 ew = evaporator wall
 g = gravity
 h = hydraulic
 l = liquid
 m = maximum
 s = specimen
 t = total
 tf = top face
 v = vapor
 w = wick
 wm = wick material

References

- [1] Dunn, P. D., and Reay, D. A., 1994, *Heat Pipes*, Pergamon, London.
- [2] Faghri, A., 1995, *Heat Pipe Science and Technology*, Taylor & Francis, London.
- [3] Maydanik, Y. F., and Fershtater, Y. G., 1997, "Theoretical Basis and Classification of Loop Heat Pipes and Capillary Pumped Loops," *Proceedings of the Tenth International Heat Pipe Conference*, Stuttgart, Germany, Sept. 21–25.
- [4] Ku, J., 1999, "Operating Characteristics of Loop Heat Pipes," *Proceedings of the 29th International Conference on Environmental Systems*, Denver, CO, Jul. 12–15, SAE Paper No. 1999-01-2007.
- [5] Maydanik, Y. F., 2005, "Loop Heat Pipes," *Appl. Therm. Eng.*, **25**(5–6), pp. 635–657.
- [6] Swanson, T. D., 2004, "Thermal Control Technologies for Complex Spacecraft," *Proceedings of the 13th International Heat Pipe Conference*, Shanghai, China, Sept. 21–25, pp. 1–11.
- [7] Maydanik, Y. F., 2004, "Miniature Loop Heat Pipes," *Proceedings of the 13th International Heat Pipe Conference*, Shanghai, China, Sept. 21–25, pp. 24–37.
- [8] Maydanik, Y. F., Vershinin, S. V., Korukov, M. A., and Ochterbeck, J. M., 2005, "Miniature Loop Heat Pipes—A Promising Means for Cooling Electronics," *IEEE Trans. Compon. Packag. Technol.*, **28**(2), pp. 290–296.
- [9] Singh, R., Akbarzadeh, A., Dixon, C., Mochizuki, M., and Riehl, R. R., 2007, "Miniature Loop Heat Pipe With Flat Evaporator for Cooling Computer CPU," *IEEE Trans. Compon. Packag. Technol.*, **30**(1), pp. 42–49.
- [10] Singh, R., Akbarzadeh, A., Dixon, C., and Mochizuki, M., 2006, "Thermal Characteristics of the Miniature Loop Heat Pipe With Water as the Working Fluid," *Proceedings of the Eighth International Heat Pipe Symposium*, Kumamoto, Japan, Sept. 24–27, pp. 191–196.
- [11] Hoang, T. T., O'Connell, T. A., Ku, J., Butler, C. D., and Swanson, T. D., 2003, "Miniature Loop Heat Pipes for Electronic Cooling," *ASME Paper No. 35245*.
- [12] Bienert, W. B., Krotiuk, W. J., and Nikitkin, M. N., 1999, "Thermal Control With Low Power Miniature Loop Heat Pipes," *Proceedings of the 29th International Conference on Environmental Systems*, Denver, CO, Jul. 12–15, SAE Paper No. 1999-01-2008.
- [13] Kiseev, V. M., Nepomnyashy, A. S., Gruzdova, N. L., and Kim, K. S., 2003, "Miniature Loop Heat Pipes for CPU Cooling," *Proceedings of the Seventh International Heat Pipe Symposium*, Jeju, Korea.
- [14] Singh, R., 2006, "Thermal Control of High-Powered Desktop and Laptop Microprocessors Using Two-Phase and Single-Phase Loop Cooling Systems," Ph.D. thesis, RMIT University, Melbourne, Australia.
- [15] Singh, R., Akbarzadeh, A., Dixon, C., Mochizuki, M., Nguyen, T., and Riehl, R. R., 2007, "Miniature Loop Heat Pipes With Different Evaporator Configurations for Cooling Compact Electronics," *Proceedings of the 14th International Heat Pipe Conference*, April 22–27, Florianopolis, Brazil, pp. 176–181.
- [16] Singh, R., Akbarzadeh, A., Dixon, C., and Mochizuki, M., 2007, "Novel Design of a Miniature Loop Heat Pipe Evaporator for Electronic Cooling," *ASME J. Heat Transfer*, **129**(10), pp. 1445–1452.
- [17] Boo, J. H., and Chung, W. B., 2005, "Thermal Performance of a Loop Heat Pipe Having Propylene Wick in a Flat Evaporator," *Proceedings of the ASME Heat Transfer Conference*, San Francisco, CA, Jul. 17–22.
- [18] Kobayashi, T., Ogushi, T., Haga, S., Ozaki, E., and Fujii, M., 2003, "Heat Transfer Performance of a Flexible Looped Heat Pipe Using R134a as a Working Fluid: Proposal for a Method to Predict the Maximum Heat Transfer Rate of FLHP," *Heat Transfer Asian Res.*, **32**(4), pp. 306–318.
- [19] Riehl, R. R., and Dutra, T., 2005, "Development of an Experimental Loop Heat Pipe for Application in Future Space Missions," *Appl. Therm. Eng.*, **25**, pp. 101–112.
- [20] Singh, R., Akbarzadeh, A., Dixon, C., and Mochizuki, M., 2004, "Experimental Determination of the Physical Properties of a Porous Plastic Wick Useful for Capillary Pumped Loop Applications," *Proceedings of the 13th International Heat Pipe Conference*, Shanghai, China, Sept. 21–25.
- [21] Reimbrecht, E. G., Fredel, M. C., Bazoo, E., and Pereira, F. M., 1999, "Manufacturing and Microstructural Characterization of Sintered Nickel Wicks for Capillary Pumps," *Mater. Res.*, **2**(3), pp. 225–229.
- [22] Li, Q., and Xuan, Y., 2003, "Development of High Performance Sintered Wicks for CPLs," *Proceedings of the Seventh International Heat Pipe Symposium*, Jeju, South Korea, Oct.
- [23] Maydanik, Y. F., Fershtater, Y. G., and Pastukhov, V. G., 1992, "Development and Investigation of Two Phase Loops With High Pressure Capillary Pumps for Space Applications," *Proceedings of the Eighth International Heat Pipe Conference*, Beijing, China.
- [24] Pastukhov, V. G., Maydanik, Y. F., and Chernyshova, M. A., 1999, "Development and Investigation of Miniature Loop Heat Pipes," *Proceedings of the 29th International Conference on Environmental Systems*, Denver, CO, Paper No. 1999-01-1983.
- [25] Baumann, J., and Rawal, S., 2001, "Viability of Loop Heat Pipes for Space Solar Power Applications," *American Institute of Aeronautics and Astronautics Paper No. 2001-3078*.
- [26] Khrustalev, D., and Semenov, S., 2003, "Advances in Low Temperature Cryogenic and Miniature Loop Heat Pipes," *Proceedings of the 14th Spacecraft Thermal Control Workshop*, El Segundo.
- [27] Wang, J., and Catton, I., 2004, "Vaporization Heat Transfer in Biporous Wicks of Heat Pipe Evaporators," *Proceedings of the International Heat Pipe Conference*, Shanghai, China, Sept. 21–25.
- [28] Chernysheva, M. A., Maydanik, Y. F., and Vershinin, S. V., 1999, "Heat Exchange in the Evaporator of a Loop Heat Pipe With a Biporous Capillary Structure," *Proceedings of the 11th International Heat Pipe Conference*, Tokyo, Japan.
- [29] Yeh, C. C., Liu, B. H., and Chen, Y. M., 2008, "A Study of Loop Heat Pipe With Biporous Wicks," *Heat Mass Transfer*, **44**, pp. 1537–1547.
- [30] Maydanik, Y. F., Vershinin, S. V., and Fershtater, Y. G., 1997, "Heat Transfer Enhancement in a Loop Heat Pipe Evaporator," *Proceedings of the Tenth International Heat Pipe Conference*, Stuttgart, Germany, Sept. 21–25.
- [31] Singh, R., Akbarzadeh, A., and Mochizuki, M., 2008, "Operational Characteristics of a Miniature Loop Heat Pipe With Flat Evaporator," *Int. J. Therm. Sci.*, **47**(11), pp. 1413–1562.
- [32] Scheidegger, A. E., 1974, *The Physics of Flow Through Porous Media*, University of Toronto, Toronto.
- [33] Alexander, E. G., 1972, "Structure-Property Relationships in Heat Pipe Wick-ing Materials," Ph.D. thesis, North Carolina State University, Raleigh, NC.
- [34] Cengel, Y. A., and Turner, R. H., 2001, *Fundamentals of Thermal-Fluid Sciences*, McGraw-Hill, New York, Chaps. 18 and 19.
- [35] Maydanik, Y. F., Solodovnik, N., and Fershtater, Y., 1995, "Investigation of Dynamic and Stationary Characteristics of a Loop Heat Pipe," *Proceedings of the Ninth International Heat Pipe Conference*, Albuquerque, NM, pp. 1002–1006.

Experimental Determination and Modeling of the Radiative Properties of Silica Nanoporous Matrices

Sylvain Lallich

Centre de Thermique de Lyon,
UMR CNRS 5008,
Institut National des Sciences Appliquées,
20 Avenue Albert Einstein,
F-69621 Villeurbanne Cedex, France
e-mail: sylvainlallich@yahoo.fr

Franck Enguehard¹

CEA/Le Ripault,
BP 16,
F-37260 Monts, France
e-mail: franck.enguehard@cea.fr

Dominique Baillis

Centre de Thermique de Lyon,
UMR CNRS 5008,
Institut National des Sciences Appliquées,
20 Avenue Albert Einstein,
F-69621 Villeurbanne Cedex, France
e-mail: dominique.baillis@insa-lyon.fr

Superinsulating materials are currently of interest because the heating and cooling of houses and offices are responsible for an important part of CO₂ emissions. In this study, we aim at modeling the radiative transfer in nanoporous silica matrices that are the principal components of nanoporous superinsulating materials. We first elaborate samples from different pyrogenic amorphous silica powders that slightly differ one from another in terms of specific surface, nanoparticle diameter, and composition. The various samples are optically characterized using two spectrometers operating on the wavelength range (250 nm; 20 μm). Once the hemispherical transmittance and reflectance spectra are measured, we deduce the radiative properties using a parameter identification technique. Then, as the considered media are made of packed quasispherical nanoparticles, we try to model their radiative properties using the original Mie theory. To obtain a good agreement between experiment and theory on a large part of the wavelength range, we have to consider scatterers that are up to five times larger than the primary nanoparticles; this is attributed to the fact that the scatterers are not the nanoparticles but aggregates of nanoparticles that are constituted during the fabrication process of the powders. Nevertheless, in the small wavelength range (λ smaller than 1 μm), we can never get a satisfactory agreement using the Mie theory. This disagreement is attributed to the fact that the original Mie theory does not take into account the nanostructure of the aggregates. So we have developed a code based on the discrete dipole approximation that improves the modeling results in the small wavelength range, basing our computations on aggregates generated using the diffusion-limited cluster-cluster aggregation algorithm in order to ensure a fractal dimension close to what is usually found with aggregates of silica nanoparticles. [DOI: 10.1115/1.3109999]

1 Introduction

Nanoporous superinsulating materials are currently the subject of much attention because of their awesome thermal insulation properties: up to five times better than air, generally regarded as an excellent thermal insulator, when they are placed under primary vacuum. These materials are essentially made of a nanoporous matrix of amorphous silica nanoparticles (more than 90% of the solid volume fraction) that provides the main thermal properties to these superinsulating materials. In addition to the matrix, we typically find two other types of components:

- micrometric scale fibers that are expected to provide mechanical reinforcement;
- micrometric particles that improve opaqueness in the infrared wavelength region.

The porosity of these superinsulating materials is close to 90%. A more detailed description of their microstructure can be found in Ref. [1].

Several studies have focused on the thermal properties of these materials. Since the middle of the 1980s, the interest for vacuum insulating materials (among which the silica aerogels) has been increasing [2–4]. Most of the earlier studies concerning these materials deal with combined conductive and radiative heat transfers. As far as the solid conductivity is concerned, Kamiuto [3] treated

it as an effective thermal conductivity that only depends on the porosity. Heinemann et al. [4] corrected the conductivity of solid materials (SiO₂) with a geometrical factor evaluated from the measured heat transfer coefficient at low temperature. Concerning the radiative transfer, it is computed from the Mie theory or experimentally determined. In the latest years, as the knowledge of the nanostructure of the material increases, the studies aim at taking it into account and uncouple the radiative and conductive transfers. Recently, Rochais et al. [5] developed a model enabling to study the transient or steady-state conductive heat transfer through a fractal representation of a nanoporous material in order to compute the thermal conductivity of these materials. At the same time, Enguehard [1] modeled the radiative heat transfer in these highly porous materials using the Rosseland approximation and the Mie theory. Coquard and Quenard [6] proposed a model for steady-state heat transfer that combines conductive and radiative transfers: The conduction is treated with Fourier's law on a theoretical representation of the network formed by the nanoparticles, and the radiative transfer is computed with the Rayleigh scattering theory. As far as the order of magnitude of the thermal conductivity in superinsulating materials is concerned, Caps and Fricke [7] measured effective conductivities close to 3–4 mW m⁻¹ K⁻¹ on silica matrices with opacifiers at room temperature. They evaluated the value of the solid thermal conductivity at ~2 mW m⁻¹ K⁻¹. This value is consistent with the computations of Rochais et al. [5] that indicate a thermal conductivity of the solid phase of 2.5 mW m⁻¹ K⁻¹ on 3D fractal structures that are representative of the nanostructure of the material. Lastly, Enguehard [1] evaluated the radiative conductivity at 300 K between 0.7 mW m⁻¹ K⁻¹ and 1.7 mW m⁻¹ K⁻¹, depending on the opaci-

¹Corresponding author.

Contributed by the Heat Transfer Division of ASME for publication in the JOURNAL OF HEAT TRANSFER. Manuscript received June 25, 2008; final manuscript received February 9, 2009; published online June 1, 2009. Review conducted by He-Ping Tan.

Table 1 Properties of the silica powders used to make the samples

	Wacker HDK-T30	Cabot Cab-O-Sil EH5	Degussa Aerosil COK84
Composition (% in weight)	$\geq 99.8\%$ SiO ₂	$\geq 99.8\%$ SiO ₂	84% SiO ₂ and 16% Al ₂ O ₃
B.E.T. specific surface	300 m ² g ⁻¹	380 m ² g ⁻¹	180 m ² g ⁻¹
Characteristic aggregate length	120 nm	200–300 nm	
Diameter of nanoparticles	9 nm	7 nm	13.5 nm
Silanol surface density	2 nm ⁻²	3.5–4.5 nm ⁻²	
Water contents	~2%	~8%	~3.5%

fiers (composition and size of the microparticles), whereas the value of the radiative conductivity without any opacifiers was found to be close to 6.6 mW m⁻¹ K⁻¹. It is worthy to note that if we add the values of the solid [5] and the radiative [1] conductivities for silica nanoporous matrices with opacifiers, we retrieve the effective conductivity value indicated in Ref. [7]. These results prove that even at 300 K, the radiative transfer is far from being negligible in superinsulating materials, since the radiative conductivity is of the order of 30% of the effective thermal conductivity. It is therefore of great interest to study and model the radiative transfer in such nanostructures, in order to better understand the radiative transfer phenomena and optimize such materials.

We aim at determining experimentally and modeling the radiative properties of such nanoporous materials, which are semitransparent media in the considered wavelength range. The matrix being the most influential ingredient on the thermal properties of these materials, we only consider the nanoporous matrix in the current approach. In order to study the influence of the matrix on the thermal radiative properties, nanoporous superinsulating materials are especially elaborated without the two other components (fibers and micrometric particles).

We first present the characteristics of the samples and the way we used to get their optical properties. Then, after a brief review of the radiative transfer equation (RTE) and of the parameter identification technique that we have used, we discuss the radiative property spectra obtained from transmittance and reflectance hemispherical measurements. These experimental spectra are compared with the predictions of the original Mie theory including dependent scattering in a first step. Because of discrepancies observed in the short wavelength region between the Mie and experimental spectra that are attributed to limitations inherent in the original Mie theory, we use in a second step the discrete dipole approximation. This modeling technique leads to a better agreement between the computed spectra and the experimental ones.

2 Experimental Determination of the Radiative Properties of the Nanoporous Matrices

2.1 Characteristics of the Studied Silica Powders.

The studied materials are silica nanoporous matrices obtained by packing hydrophilic pyrogenic silica nanoparticles. Different silica powders from three different manufacturers were used to elaborate our samples (see Table 1). The silica nanoparticles are precised to be hydrophilic: Their surface chemistry mainly depends on the presence of silanol groups Si–OH. The concentration of silanols at the silica nanoparticle surface governs its moisture adsorption capacity. If the samples are subject to a moist atmosphere, the equilibrium between the samples and the atmosphere is reached within a few minutes; so adsorption is a very fast process. If we wanted to cast off the presence of water in our samples, we should dry them at temperatures higher than 200 °C. Nevertheless, after the drying process, we would have to work under controlled atmosphere to prevent the samples from rehydrating; such conditions are inconceivable. So in the results presented below, we will work with hydrated samples. Table 1 presents the properties of the different powders we used to make our samples. Apart from the nanoparticle diameter that was computed

from the specific surface and the density of the bulk material ($d_p = 6 / (S_{\text{spe}} \rho)$), all these data are stemmed from the suppliers's booklets [8–10]. Here it is important to underline that isolated primary nanoparticles do not exist in the powders. During the fabrication process of these powders, nanoparticles fuse together to form larger units called aggregates. This aggregate structure can be observed on the electron micrograph of Figs. 1 and 2. With transmission electron microscopy (TEM) images, we checked that the observed diameter of the primary nanoparticles was consistent with the specific surface values announced by the various suppliers. The nanoporous matrix samples were made by isostatic com-

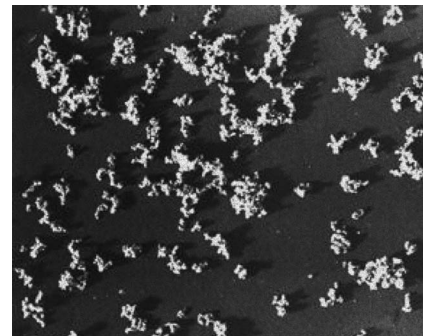


Fig. 1 Figure stemmed from Ref. [43]: Electron micrograph of the Cab-O-Sil fumed silica, which has been shadowed with vaporized gold to highlight the three dimensional random branching of the aggregates. Final magnification 50,000 \times .

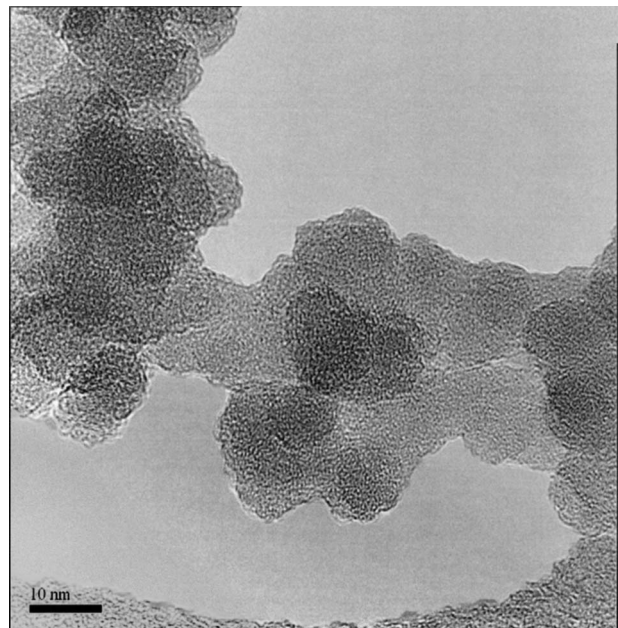


Fig. 2 TEM micrograph of the Wacker HDK-T30 powder

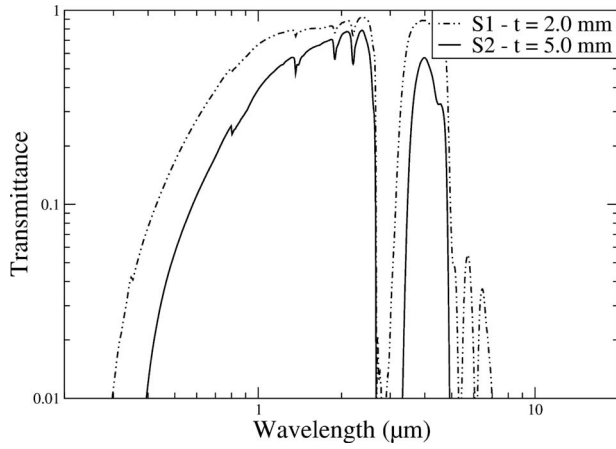


Fig. 3 Hemispherical transmittance spectra obtained for two samples (S1 and S2) of different thicknesses t made of the same HDK-T30 powder

pression of the silica powders at a pressure close to 60 bars. The samples are highly porous ($\sim 90\%$) and have different thicknesses ranging between 2.0 and 10.5 mm.

2.2 Transmittance and Reflectance Measurements. The samples are then optically characterized using two different spectrometers covering an overall spectral band of (250 nm; 20 μm): a Varian Cary grating spectrometer on the (250 nm; 2.5 μm) spectral band and a Bruker IFS66V Fourier transform infrared (FTIR) spectrometer on the wavelength range (1.6 μm ; 20 μm). The measured quantities are the hemispherical transmittance and reflectance properties: For these measurements, the two spectrometers are equipped with integrating spheres made of polytetrafluoroethylene (PTFE) for the Varian Cary and of gold for the Bruker that collect hemispherically the radiation traveling through or reflected by the samples.

Figures 3 and 4 show the spectra obtained for two samples of thicknesses 2.0 mm and 5.0 mm made of the Wacker HDK-T30 powder. These spectra are in accordance with what we expect. As far as the transmittance is concerned, we can point out that this quantity decreases as the sample thickness increases, which is quite consistent. In the neighborhood of the 3 μm wavelength, the transmittance almost vanishes: This large absorption spectral zone is attributed to the presence of water within the pores and/or at the surface of the silica nanoparticles. Above 8 μm , the trans-

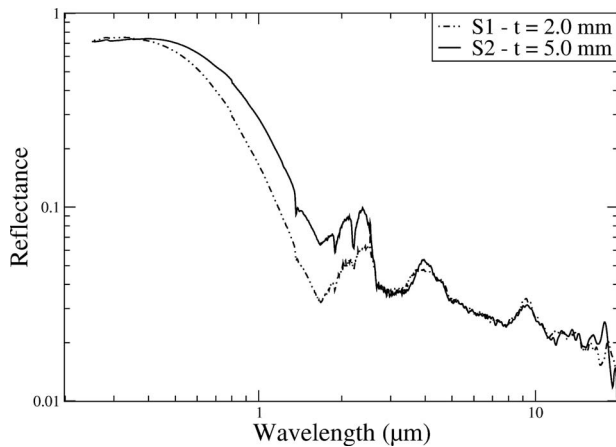


Fig. 4 Hemispherical reflectance spectra obtained for two samples (S1 and S2) of different thicknesses t made of the same HDK-T30 powder

mittance is nil because of the bulk absorption of silica that strongly increases in this wavelength range. With regard to the reflectance, we note that this quantity increases with the sample thickness: This behavior is consistent and finds its explanation in the fact that the quantity of backscattered photons increases with the sample thickness. Above 8 μm , the reflectance does not depend anymore on the sample thickness: silica being very absorbing in this wavelength range, even the thinnest sample can be considered as optically thick.

2.3 RTE Solution Model and Parameter Identification.

In this part we aim at identifying the radiative properties of the samples from the experimental data derived from optical measurements using a parameter identification technique.

To compute the theoretical data used in the parameter identification process, we have to solve the RTE. The assumptions of our model are as follows:

- one-dimensional radiative transfer within a homogeneous semitransparent absorbing and scattering medium;
- azimuthal isotropy;
- the self-emission term is neglected.

Under these conditions, the RTE can be written as follows

$$\frac{\mu}{\beta_\lambda} \frac{\partial I_\lambda(z, \mu)}{\partial z} + I_\lambda = \frac{\omega_\lambda}{2} \int_{-1}^1 I_\lambda(z, \mu') \phi_\lambda(\mu', \mu) d\mu' \quad (1)$$

where I_λ is the space and direction dependent intensity field, z is the spatial coordinate (lying between 0 and the thickness t of the sample), μ is the cosine of the polar angle of the scattering direction, and μ' is the cosine of the polar angle of the incident direction. β_λ is the extinction coefficient, ω_λ is the scattering albedo, and ϕ_λ is the phase function. These properties are the effective radiative properties of the studied sample, i.e., the properties of the equivalent homogeneous medium in terms of radiative transport.

As we have only two experimental data for each wavelength (hemispherical transmittance and reflectance), we can determine the values of only two physical quantities using the parameter identification. As the data that we are interested in are the extinction coefficient and the albedo, we choose the phase function as isotropic, i.e., $\forall \lambda, \forall \mu, \forall \mu', \phi_\lambda(\mu, \mu') = 1$. Doing so, the data we determine with the parameter identification technique are not the real extinction coefficient β_λ and albedo ω_λ of the medium, but the radiative properties β_λ^* and ω_λ^* of an equivalent medium that scatters radiation isotropically. This procedure is known as the isotropic scaling [11] or the transport approximation [12,13]. The isotropic scaling data β_λ^* and ω_λ^* are related to the real data β_λ and ω_λ according to

$$\beta_\lambda^* = \beta_\lambda (1 - \omega_\lambda g_\lambda) \quad (2)$$

$$\omega_\lambda^* = \frac{\omega_\lambda (1 - g_\lambda)}{(1 - \omega_\lambda g_\lambda)} \quad (3)$$

where g_λ is the asymmetry factor of the medium. The two modeling techniques we use hereafter (the original Mie theory and the discrete dipole approximation) permit us to compute β_λ , ω_λ , and g_λ . So in order to be able to compare these values with the experimental radiative properties, the computed data are corrected using the isotropic scaling technique. Consequently, until the end of the current paper, when we consider extinction coefficients or albedos, we will actually deal with the isotropic scaling properties, i.e., the radiative properties of the equivalent homogeneous medium that scatters radiation isotropically.

Our samples being very porous ($\sim 90\%$), the refraction index contrast at their boundaries is very weak. So, there are no reflections at the interfaces and we can use the following boundary conditions:

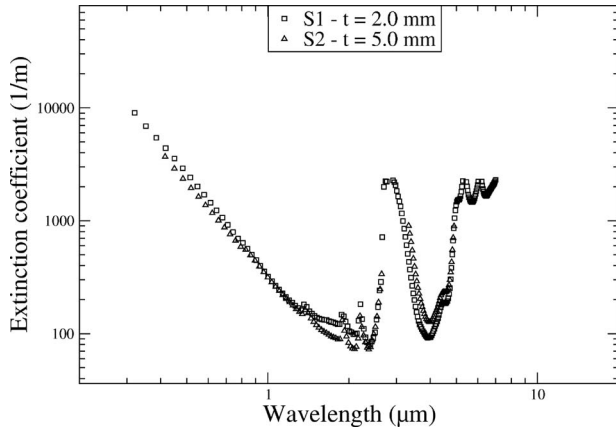


Fig. 5 Extinction coefficient spectra obtained by parameter identification for two samples of different thicknesses t made of the same HDK-T30 powder

$$I_{\lambda}(z=0, \mu) = \begin{cases} \Psi_{\lambda}(\mu) & \text{when } \mu_0 \leq \mu \leq 1 \\ 0 & \text{when } 0 \leq \mu \leq \mu_0 \end{cases} \quad (4)$$

$$I_{\lambda}(z=t, \mu) = 0 \quad \text{at } \mu \leq 0 \quad (5)$$

where Ψ_{λ} is the direction and wavelength dependent illumination function. The value μ_0 is close to 1 and indicates a directional illumination. As the thickness t of the sample is known, the phase function ϕ_{λ} is assumed to be isotropic ($\phi_{\lambda} \equiv 1$), and the boundary conditions are clearly expressed; if we know β_{λ} and ω_{λ} , we can solve the RTE (1) and compute the intensity field, I_{λ} , using the discrete ordinates method [14]. From that field, the hemispherical transmittance and reflectance can be quantified from the expressions

$$T_{\lambda}^h = \frac{\int_0^1 I(t, \mu) \mu d\mu}{\int_{\mu_0}^1 \Psi_{\lambda}(\mu) \mu d\mu}, \quad R_{\lambda}^h = \frac{-\int_{-1}^0 I(0, \mu) \mu d\mu}{\int_{\mu_0}^1 \Psi_{\lambda}(\mu) \mu d\mu} \quad (6)$$

The whole procedure described above, which allows the evaluation of the hemispherical transmittance and reflectance of our samples from the knowledge of their radiative properties, must be regarded as the direct problem; the inverse problem is numerically solved using a method based on the Newton–Raphson algorithm.

The radiative property spectra obtained that way for the samples made of the HDK-T30 powder are shown in Figs. 5 and 6. Here, we can point out the importance of the water contribution in the extinction coefficient spectra. The extinction peaks at $1.4 \mu\text{m}$, $1.95 \mu\text{m}$, $2.9 \mu\text{m}$, and $6.0 \mu\text{m}$ are attributed to the water molecule [15]. Above $7 \mu\text{m}$, since the silica is very absorbing [16], the transmittance is too weak so that we use these spectra in the parameter identification procedure. Hence, we do not present the results of the radiative property spectra above $7 \mu\text{m}$. The two last peaks at $2.2 \mu\text{m}$ and $5.3 \mu\text{m}$ are, respectively, associated with Si–OH [15] and Si–H [17] bonds.

3 Modeling of the Radiative Properties of the Silica Nanoporous Matrices

One of the main goals of this work is to be able to predict the radiative behavior of our silica nanoporous matrix materials on the basis of their morphological descriptions. As our samples are made of packed quasispherical nanoparticles, the first idea that comes in mind is to compare the experimentally determined radiative properties to the ones computed with the well-known Mie theory [18]. In a second step, we propose working on an alterna-

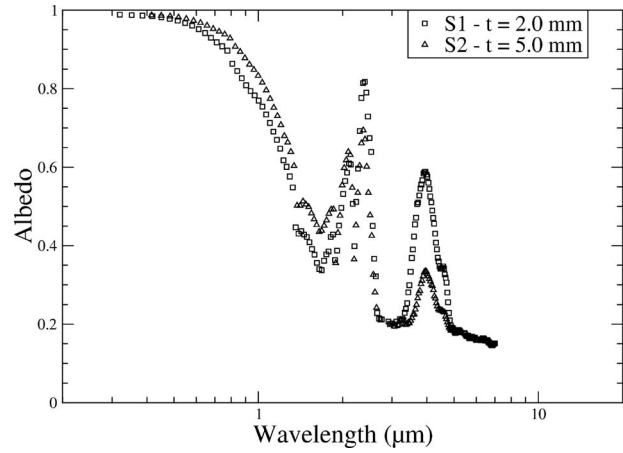


Fig. 6 Albedo spectra computed by parameter identification for two samples of different thicknesses t made of the same HDK-T30 powder

tive modeling technique based on the discrete dipole approximation (DDA) that takes finely into account the nanostructures of our media and the dependent scattering effects between the nanoparticles.

3.1 Comparison Between the Experimental Results and the Original Mie Theory

3.1.1 Using the Standard Mie Theory Including Dependent Scattering. As the studied materials are made of packed quasispherical nanoparticles, we first try to use the Mie theory [18] to predict the radiative properties of our samples. This very classical modeling tool allows the computation of the interaction (scattering and absorption) between an electromagnetic wave and a sphere (or a spherical particle cloud) [19].

In this section, we take into account the water contribution using the Maxwell–Garnett mixing rule. The water mass fraction is chosen so that we respect the data indicated by the various suppliers: $\sim 2\%$ for the HDK-T30, $\sim 8\%$ for the EH5, and $\sim 3.5\%$ for the COK84.

We have first computed the radiative properties of our media neglecting the dependent scattering effects that may occur. The results presented in Figs. 7 and 8 concern the HDK-T30 powder; if we assume that the size of the scatterer is the same as the one of

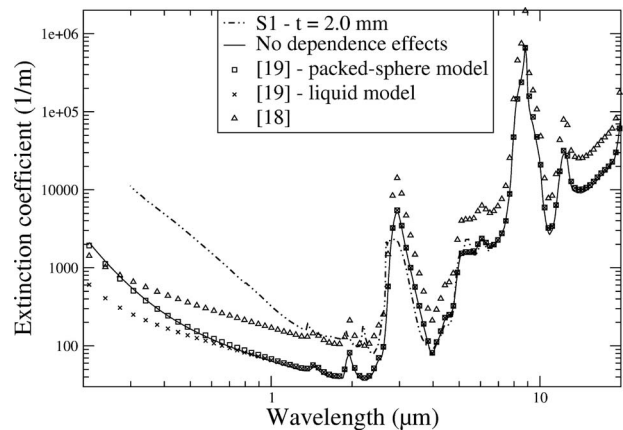


Fig. 7 Comparison of the HDK-T30 powder of an experimental extinction coefficient spectrum (S1) with those obtained using the Mie theory for 9 nm diameter scatterers. Various correlations are applied to the Mie theory in order to account for dependent scattering effects.

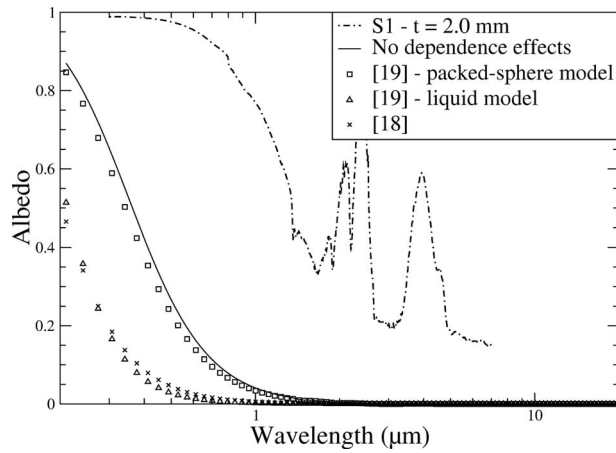


Fig. 8 Same as Fig. 1, but for albedo spectra

the primary nanoparticle (~ 9 nm), we see that the radiative properties we obtain are far from the experimentally determined ones whatever the quantity we consider: The Mie albedo spectrum is very distant from the experimental one on the whole wavelength range; as far as the extinction coefficient is considered, the agreement between the Mie and experimental ones is satisfactory for wavelengths above $2.5 \mu\text{m}$, whereas below this value, the divergence between the Mie results and the experimental ones can reach more than one order of magnitude.

Due to the observed discrepancies, we have decided to inquire about the influence of the dependent scattering. First, if we locate our problem on the well-known scattering regime map of size parameter versus volume fraction published by Tien and Drolen [20], we see that we clearly lie in the dependent scattering regime ($f_v \sim 0.13$; size parameter ≤ 0.11). In order to determine if the observed discrepancies might be attributed to dependent scattering effects alone, we have tried various correlations. As we aim at determining the radiative properties over a wide range of size parameter ($1.4 \times 10^{-3} \leq x \leq 0.11$), we have first made sure that we lie in the Rayleigh scattering regime over the whole wavelength range, computing the relative error between the Rayleigh formulas and the general Mie formulas results: We have concluded that the maximum relative error is below 1% over the wavelength range whatever the cross section (absorption or scattering) we look at. So to take into account the correlated radiative transfer in our media, we have used the correlations developed in Refs. [21–23] that apply to Rayleigh sized particles. These models account for the interparticle effects on the radiative characteristics of densely packed systems.

- The correlation developed in Ref. [21] is based on the assumption of a Percus–Yevick pair distribution function to describe the spatial organization of the particles. This correlation depends on the volume fraction alone. It is important to notice that the use of this model is suggested for volume fractions ≤ 0.1 .
- In Ref. [22], the authors derived their model for various distribution functions: the gas model (especially adapted for volume fractions ≤ 0.1), the packed-sphere model (especially adapted for volume fractions ≥ 0.1), and the liquid model that incorporates the gas and the packed-sphere model.
- Prasher [23] derived the effective field approximation (EFA) and the quasicrystalline approximation (QCA) for the Rayleigh regime. The EFA assumes independent scattering, so it only takes into account the multiple scattering, whereas the QCA accounts for the multiple scattering effects and for the dependent scattering.

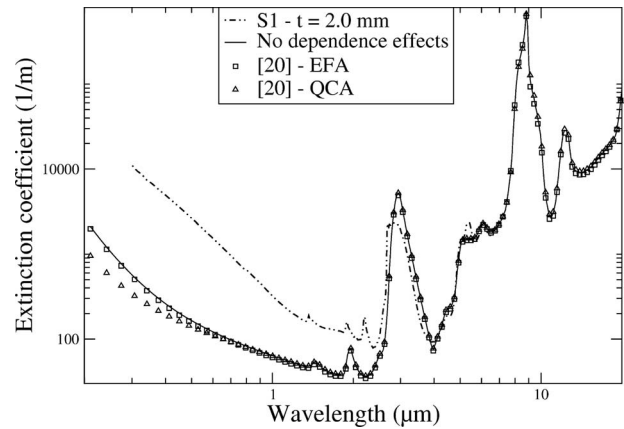


Fig. 9 Comparison of the HDK-T30 powder of an experimental extinction coefficient spectrum with those obtained using the Mie theory for 9 nm diameter scatterers. The results obtained using the correlations developed in Ref. [23] are presented to appreciate the impact of multiple and dependent scattering.

Figures 7 and 8 show the results we get with the three following dependent scattering correlations: the relation of Ref. [21] (even if the solid volume fractions of our samples are quite slightly than 0.1) and the packed-sphere and the liquid models presented in Ref. [22]. The radiative property spectra computed with the gas model are not presented because this model yields negative scattering efficiencies, which is quite unphysical. Figures 9 and 10 show the radiative property spectra we compute using the EFA and the QCA.

As we can see, whatever the model we consider, the use of these correlations does not improve the agreement between the Mie results and the experimental ones. Focusing on the albedo spectra, we see that the dependent scattering tends to decrease the scattering and so the albedo, while the experimental albedo spectrum is already superior to the one computed with the Mie theory without taking into account dependent scattering. If we now consider the extinction coefficient spectra, we observe a decrease in this coefficient for wavelengths below 800 nm when we wish an increase in this extinction coefficient in order to bring the Mie results including dependent scattering closer to the experimental ones. The only correlation that improves the agreement in the small wavelength region is the model developed in Ref. [21], but as it multiplies almost the whole extinction coefficient spectrum by a constant value, this model severely decreases the concordance between computed and experimental results for wave-

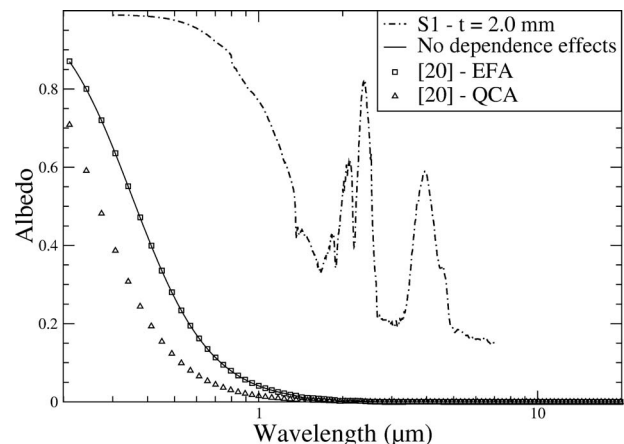


Fig. 10 Same as Fig. 9, but for albedo spectra

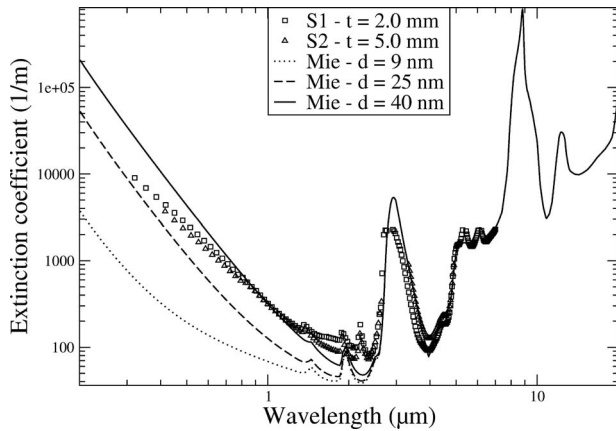


Fig. 11 Comparison of the HDK-T30 powder of two experimental extinction coefficient spectra with those obtained using the Mie theory for three different scatterer diameters. The model we use to include the contribution of water is the coated sphere model.

lengths above $2 \mu\text{m}$.

None of the correlations we tried brought the Mie radiative property spectra closer to the experimental ones in a convincing way, so the differences observed between the radiative property spectra computed with the Mie theory and the experimental ones cannot be imputed to the dependent scattering alone.

3.1.2 Application of the Coated Sphere Model. To reduce the discrepancies observed above, we thought about using a model that is more realistic with regard to the water adsorption by the silica nanoparticles. The Maxwell–Garnett mixing rule consists in homogenizing the water and the silica, building an effective material in which water is homogeneously mixed with silica. Actually the water molecules are located at the surface of the nanoparticle and are not dispersed in the volume, so we tried the coated sphere model described in Ref. [19] to represent the geometry of the nanoparticle more realistically. We chose a coating thickness that respects the water mass fraction that is indicated by the various suppliers.

Assuming 9 nm diameter scatterers (the same diameter as the one of the nanoparticles), the radiative property spectra we obtain with the coated sphere model (Figs. 11 and 12) superimpose per-

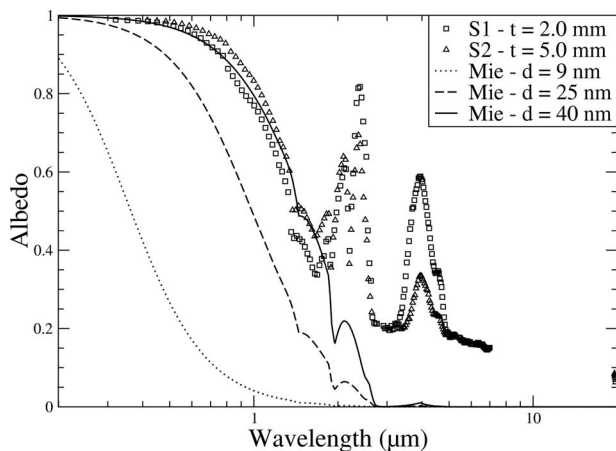


Fig. 12 Comparison of the HDK-T30 powder of two experimental albedo spectra with those obtained using the Mie theory with the same parameters as in Fig. 11

flectly with the results we obtain with the Maxwell–Garnett mixing rule and so, do not improve the agreement between the Mie results and experimental ones.

3.1.3 Introduction of the Notion of Representative Scatterer. Having failed to model the radiative properties of our media with the Mie theory using a scatterer diameter equal to the diameter of the nanoparticles, we decided to try to determine an effective diameter of a representative scatterer that yields the best agreement between the Mie results and the experimental radiative property spectra. A straightforward way to shift to higher wavelengths the transition between the scattering regime and the absorptive regime in order to improve the agreement between the experimental results and those obtained using the Mie theory is to increase the diameter of the scatterer in the Mie calculations. It turns out that, if we choose a diameter of the scatterers of 25 nm, it improves the agreement not only for the albedo as expected, but also for the extinction coefficient. We keep on increasing the scatterer diameter until we obtain satisfactory agreement between the albedos. It is interesting to notice that the agreement of the extinction coefficient improves the same way. The best agreement is found for a scatterer diameter of 40 nm. Although this value is significantly different from the one of the diameter of the primary particles, it makes sense: Indeed, during the silica powder fabrication process, the primary nanoparticles of 9 nm diameter fuse together to form aggregates of approximately 120 nm hydrodynamic equivalent-sphere diameter [8]. If we assume that the porosity of these aggregates is close to the one of the nanoporous matrix, the volume of silica contained in such an aggregate is equivalent to the volume of a dense silica sphere of 50 nm diameter.

We have checked that our analysis regarding the HDK-T30 powder remained valid with the other two pyrogenic silica powders that we have used to make the various samples. In the case of the Cab-O-Sil EH5 powder, to get a good agreement between the experimentally determined radiative properties and the ones predicted by the Mie theory, we had to increase the diameter up to 40 nm. The same observation was made with the Aerosil COK84 samples: A satisfactory agreement between the experimental radiative properties and the Mie ones was obtained with 65 nm diameter scatterers.

Hence, we observe that the nanoporous matrix scatters radiation as a cloud of scatterers, which are not the primary nanoparticles but aggregates obtained by collision of primary nanoparticles during the production process of the pyrogenic silica powder. For each type of powder considered, as we have a nice agreement of the experimentally determined radiative properties between the various samples, the size of the representative scatterer determined with the procedure described above seems to depend only on the nature of the powder used. This is an information of great interest: Fitting the experimental spectra (especially the albedo one) permits us to determine the volume of silica contained in the representative aggregate for each type of pyrogenic silica powder. This way, the Mie theory appears to be quite predictive on a wide part of the spectrum. Nevertheless, in the wavelength range (250 nm ; $1 \mu\text{m}$), we still observe a behavior of the slope of the experimental extinction coefficient spectrum that is significantly different from the predicted one. This slope observed difference may be interpreted as nanostructure effects and tends to show the limit of the original Mie theory: As long as the wavelength is superior to $1 \mu\text{m}$, the interaction between the wave and the scatterer is not sensitive to the shape of the scatterer because the latter is significantly smaller than the wavelength; on the contrary, when the wavelength is below $1 \mu\text{m}$, the wavelength and the size of the aggregate are of the same order of magnitude, so the scattering properties become aggregate shape sensitive. The original Mie theory cannot take into account the nanostructure of these aggregates; nevertheless the general Mie theory [24] is successfully applied to calculations for very complex particles. To model more accurately the radiative properties of the aggregates, we have chosen to use a modeling approach called the discrete dipole approxi-

mation. In Sec. 3.2, we present an overview of this method and the way we applied it to our silica nanoporous matrices.

3.2 Application of the DDA to Silica Nanoporous Matrices

3.2.1 The Discrete Dipole Approximation: Overview of the Method. The DDA, initially proposed in Ref. [25], is a flexible method that allows computation of the absorption and scattering properties of irregular targets (particles of complex shapes and clusters of spheres) approximated by arrays of point dipoles. The DDA calculations require a detailed description of the scatterer: the locations \mathbf{r}_j of the dipoles in space and the evaluation of their polarizabilities (we discuss the choice of a polarizability prescription in Sec. 3.2.2). As we only deal with isotropic materials, the polarizability, a tensor in the most general case, reduces to a scalar quantity α_j . Each dipole j has a dipole moment \mathbf{P}_j expressed as [26,27]

$$\mathbf{P}_j = \alpha_j \mathbf{E}_{\text{loc},j} \quad (7)$$

where $\mathbf{E}_{\text{loc},j}$ is the local electric field at \mathbf{r}_j due to the incident wave $\mathbf{E}_{\text{inc},j}$ and to the contributions of the $(N-1)$ neighboring dipoles $\mathbf{E}_{\mathbf{k},j}$. So we can write N simultaneous complex vector equations of the form

$$\mathbf{P}_j = \alpha_j \left\{ \mathbf{E}_{\text{inc},j} + \sum_{\mathbf{k} \neq j} \mathbf{E}_{\mathbf{k},j} \right\} \quad (8)$$

The electric field $\mathbf{E}_{\mathbf{k},j}$ at \mathbf{r}_j due to the presence of the oscillating dipole $\mathbf{P}_{\mathbf{k}}$ at $\mathbf{r}_{\mathbf{k}}$ can be expressed as [28]

$$\mathbf{E}_{\mathbf{k},j} = \frac{\exp(ikr_{jk})}{4\pi\epsilon_0 r_{jk}^3} \{ k^2 r_{jk}^2 [(\mathbf{n} \times \mathbf{P}_{\mathbf{k}}) \times \mathbf{n}] + (1 - ikr_{jk}) [3(\mathbf{n} \cdot \mathbf{P}_{\mathbf{k}})\mathbf{n} - \mathbf{P}_{\mathbf{k}}] \} \quad (9)$$

where $k=2\pi/\lambda$, $r_{jk}=|\mathbf{r}_j-\mathbf{r}_{\mathbf{k}}|$, and $\mathbf{n}=(\mathbf{r}_j-\mathbf{r}_{\mathbf{k}})/r_{jk}$. We can rewrite Eq. (9) under a matrix form

$$\mathbf{E}_{\mathbf{k},j} = -\mathbf{A}_{\mathbf{k},j} \mathbf{P}_{\mathbf{k}} = \frac{\exp(ikr_{jk})}{4\pi\epsilon_0 r_{jk}^3} \left[(k^2 r_{jk}^2 + ikr_{jk} - 1) \begin{pmatrix} 1 & 0 & 0 \\ 0 & 1 & 0 \\ 0 & 0 & 1 \end{pmatrix} + (3 - 3ikr_{jk} - k^2 r_{jk}^2) \begin{pmatrix} n_x^2 & n_x n_y & n_x n_z \\ n_x n_y & n_y^2 & n_y n_z \\ n_x n_z & n_y n_z & n_z^2 \end{pmatrix} \right] \begin{pmatrix} P_{k_x} \\ P_{k_y} \\ P_{k_z} \end{pmatrix} \quad (10)$$

Injecting the expression of $\mathbf{E}_{\mathbf{k},j}$ in Eq. (8), we obtain

$$\mathbf{P}_j = \alpha_j \left\{ \mathbf{E}_{\text{inc},j} - \sum_{\mathbf{k} \neq j} \mathbf{A}_{\mathbf{k},j} \mathbf{P}_{\mathbf{k}} \right\} \quad (11)$$

Noting $\mathbf{A}_{jj}=(1/\alpha_j)\mathbf{Id}$, where \mathbf{Id} is the 3×3 identity matrix, we can transform Eq. (11) to

$$\sum_{\mathbf{k}=1}^N \mathbf{A}_{\mathbf{k},j} \mathbf{P}_{\mathbf{k}} = \mathbf{E}_{\text{inc},j} \quad (12)$$

We can reduce these N vector equations to a single vector equation of size $3N$: $\tilde{\mathbf{A}}\tilde{\mathbf{P}}=\tilde{\mathbf{E}}$. The unknown vector $\tilde{\mathbf{P}}$ is solved numerically using a conjugate gradient technique. Once the dipole moment vectors \mathbf{P}_j are known for one polarization, we can compute the extinction, scattering, and absorption cross sections of the scatterer with the following formulas [26,27]:

$$C_{\text{ext}} = \frac{k}{\epsilon_0 E_0^2} \sum_{j=1}^N \text{Im}\{\mathbf{E}_{\text{inc},j}^* \cdot \mathbf{P}_j\} \quad (13)$$

$$C_{\text{sca}} = \frac{k^4}{(4\pi\epsilon_0)^2 E_0^2} \int_{4\pi} \left\| \sum_{j=1}^N \mathbf{n} \times \mathbf{P}_j \exp(-ik\mathbf{n} \cdot \mathbf{r}_j) \right\|^2 d\Omega \quad (14)$$

$$C_{\text{abs}} = \frac{k}{\epsilon_0 E_0^2} \sum_{j=1}^N \left(\text{Im}((\alpha_j^*)^{-1}) - \frac{k^3}{6\pi\epsilon_0} \right) \mathbf{P}_j \cdot \mathbf{P}_j^* \quad (15)$$

When working with unpolarized light (which is the case in this survey), we have to solve the problem for two orthogonal polarizations of the incident wave and then to calculate the arithmetic average of the cross sections computed for these two polarization states. Noting m the complex index of refraction, the validity criterion that is commonly used [26,27] for the discrete dipole approximation technique is

$$|m|kd \leq 1 \quad (16)$$

Relation (16) expresses the fact that the electric field must be constant in terms of amplitude and phase over the whole volume element associated with the dipole of characteristic length d . It implies that the characteristic length d must be small compared with the wavelength and to the attenuation length within the material.

3.2.2 Choice of a Polarizability Prescription. As far as the polarizability is concerned, it depends on the problem we are dealing with. In literature, it is almost always made use of the lattice dispersion relation (relation developed in Ref. [29] so that an infinite lattice of polarizable points has the same dispersion relation as a continuous medium of the same refractive index), referenced to as the LDR hereafter, unless they have to compute the scattering properties of clusters of spheres that are small compared with the wavelength. In this particular case, some authors [30–32] used what is commonly named the a_1 -term method. The expression of this polarizability depends on a_1 , the first term of the Mie series; i , which is equal to $\sqrt{-1}$; and k , the wave number ($2\pi/\lambda$).

$$\alpha = i \frac{3a_1}{2k^3} \quad (17)$$

Initially introduced in Ref. [33], this method allows treating each particle as a single dipole. Okamoto [31] compared the LDR and the a_1 -term prescription for the same target (two touching spheres, each sphere being replaced with a single dipole) with a refractive index $m=1.33+0.01i$. His survey points out that the a_1 -term prescription is always superior to the LDR and yields errors within 10% for sphere size parameters up to 1.4 and while the errors with the LDR become larger than 100% for a sphere size parameter larger than 1.2. The limiting cases of this polarizability expression are a size parameter of the aggregate of the order of 100 and a size parameter of the particles making up the aggregate close to 1.

In our survey, as we deal with media made of packed particles of diameter smaller than 20 nm, and as the wavelengths of interest are greater than 250 nm, we are clearly in the domain of applicability of the a_1 -term prescription. This is the polarizability expression that we use afterwards.

3.2.3 Modeling of the Nanostructure. As explained above, the DDA requires a detailed geometrical description of the scatterer. So we have to generate material structures on which the DDA calculations are performed, and these material structures must be representative of our nanoporous matrix in terms of porosity ($\sim 90\%$), specific surface (between $170 \text{ m}^2 \text{ g}^{-1}$ and $300 \text{ m}^2 \text{ g}^{-1}$) and fractal dimension (~ 1.8 according to literature) [34].

To this end, we have generated numerical structures with the help of the diffusion-limited cluster-cluster aggregation (DLCCA) algorithm [35,36], which is known to produce clusters of fractal dimensions close to 1.8. We have integrated the water contribution (and the alumina contribution for the samples made of the Degussa Aerosil COK84 powder) in the relative dielectric permittivity function and hence in the polarizability function of the particles with the help of the Maxwell–Garnett mixing rule.

Knowing the volume of silica contained in the representative aggregate, thanks to the procedure explained in Sec. 3.1.3 and the diameter of the primary nanoparticles, we deduce the number of

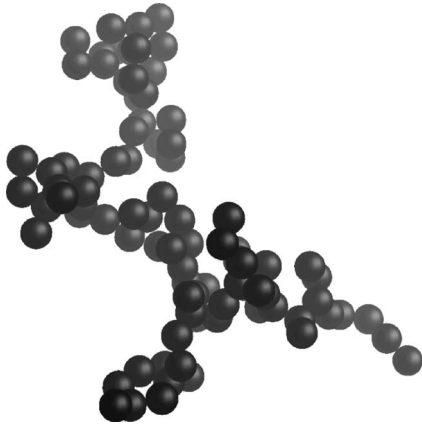


Fig. 13 Example of aggregate generated using the DLCCA algorithm and made of 87 nanoparticles of 9 nm diameter; this aggregate is representative of our HDK-T30 powder samples

particles forming the representative scatterer for the various powders we used. This scatterer is found to be made up of 87 particles for the HDK-T30 powder, 186 for the Cab-O-Sil EH5 powder, and 88 for the Aerosil COK84 powder. A typical aggregate representative of the HDK-T30 powder is presented in Fig. 13.

3.2.4 Comparison of the DDA and Mie Results to the Experimental Ones. The DDA computations are based on the aggregates obtained using the procedure explained above, and are achieved over a hundred directions of the incident beam covering 2π sr. As the DDA radiative property spectra depend on the incidence of the illumination, we present the arithmetic mean and the extreme (maximum and minimum) value spectra. With regard to the albedo spectra, we only show the mean values because the albedo was found to be quasi-insensitive to the incidence of the illumination in our computations.

The radiative property spectra derived from our DDA computations are shown in Fig. 14 (extinction coefficient) and Fig. 15 (albedo) with regard to the HDK-T30 powder based nanoporous matrix. Figures 16 and 17 on the one hand, and Figures 18 and 19 on the other hand deal, respectively, with the EH5 and the COK84

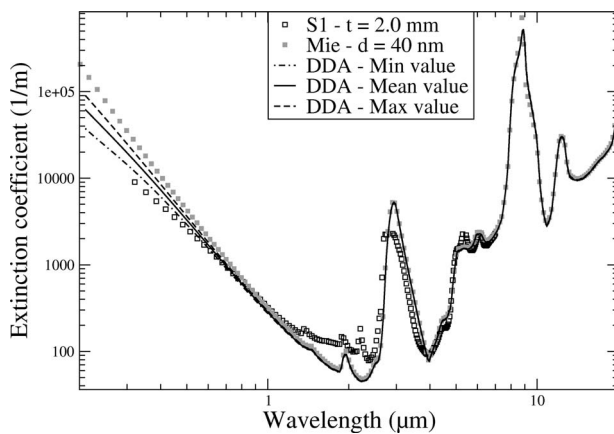


Fig. 14 Comparison of the HDK-T30 powder of an experimental extinction coefficient spectrum to the spectra obtained using the Mie theory on the one hand and using the DDA on the aggregate of Fig. 13 on the other hand. Concerning the DDA results, we present the minimum, the arithmetic mean, and the maximum values yielded by the computations over 100 target orientations.

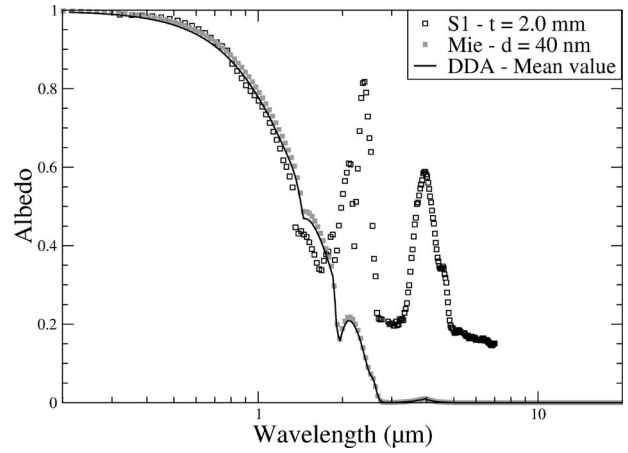


Fig. 15 Comparison of the HDK-T30 powder of an experimental albedo spectrum to the spectra obtained using the Mie theory on the one hand and using the DDA on the aggregate of Fig. 13 on the other hand. Concerning the DDA results, we present the minimum, the arithmetic mean, and the maximum values yielded by the computations over 100 target orientations.

powder based nanoporous matrices.

For the discussion of these figures, we will split the wavelength range in two parts: the wavelength range (250 nm; 1 μ m) and the one beyond 1 μ m.

If we first focus on the wavelength range beyond 1 μ m, whatever the pyrogenic silica we consider (Figs. 14–19), the computed radiative properties using the DDA and those obtained with the Mie theory stack to perfection in this wavelength range. This means that the radiative properties are insensitive to the structure of the aggregate in this region. This is a consistent result, because in this region the wavelength is clearly larger than the size of the aggregate, so the wave perceives it as a pointlike obstacle.

This result being expected, the interest of the DDA lies in the (250 nm; 1 μ m) wavelength range over which the wavelength is of the same order of magnitude as the diameter of the aggregate. We first focus on the HDK-T30 silica (Figs. 14 and 15). In Fig. 15, which shows the albedo spectra, we see that the results are very slightly influenced by the computation technique. This seems

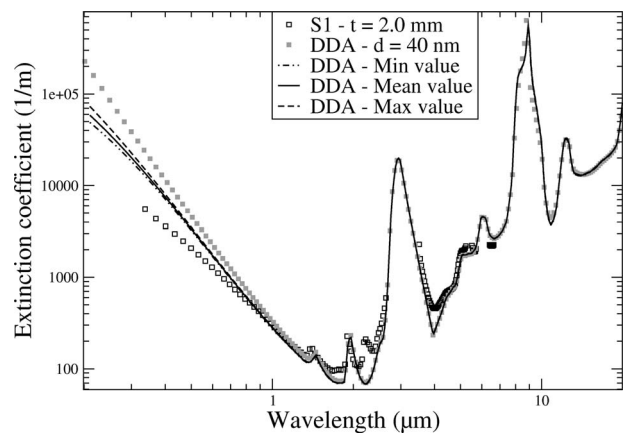


Fig. 16 Comparison of the EH5 powder of an experimental extinction coefficient spectrum to the spectra obtained using the Mie theory on the one hand and using the DDA on a DLCCA representative aggregate on the other hand. For the results obtained with the DDA, we present the minimum, the arithmetic mean, and the maximum values of the computations over 100 target orientations.

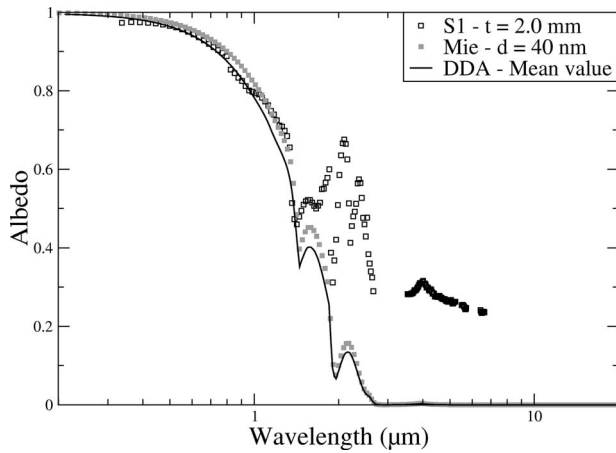


Fig. 17 Comparison of the EH5 powder of an experimental albedo spectrum to the spectra obtained using the Mie theory on the one hand and using the DDA on a DLCCA representative aggregate on the other hand. For the results obtained with the DDA, we present the minimum, the arithmetic mean, and the maximum values of the computations over 100 target orientations.

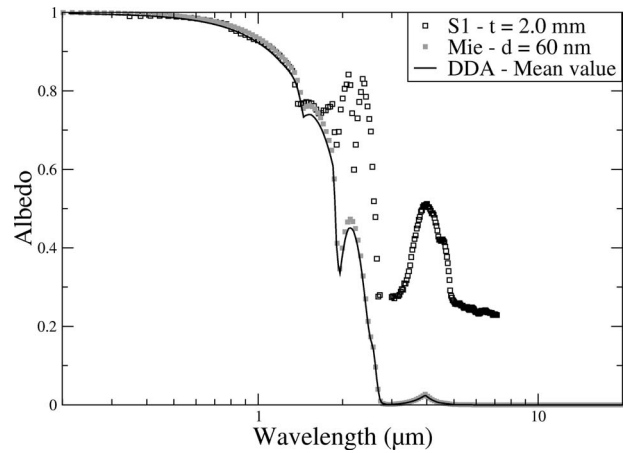


Fig. 19 Comparison of the COK84 powder of an experimental albedo spectrum to the spectra obtained using the Mie theory on the one hand and using the DDA on a DLCCA representative aggregate on the other hand. For the results obtained with the DDA, we present the minimum, the arithmetic mean, and the maximum values of the computations over 100 target orientations.

to mean that the albedo does not depend on the structure of the scatterer. On the other hand, the extinction coefficient spectrum (Fig. 14) does. Whatever the results (extreme or mean values of the extinction coefficients computed using the DDA) we examine, the DDA results are in better agreement with the experimental ones than the Mie results, even in the least favorable case. Moreover, in the most favorable case (the minimum values of the extinction coefficient), the results almost stack with the experimental data. Consequently, it is shown quite clearly here that the DDA approach leads to an improved ability of prediction of the radiative properties of nanostructures in the small wavelength range as compared with the Mie theory applied to aggregates: The DDA reproduces in a much better way the slope shown by the experimental extinction coefficient spectrum for wavelengths below $1 \mu\text{m}$ than the Mie theory.

The observations we have made above with the HDK-T30 pyrogenic silica sample also apply to the other two silica powders

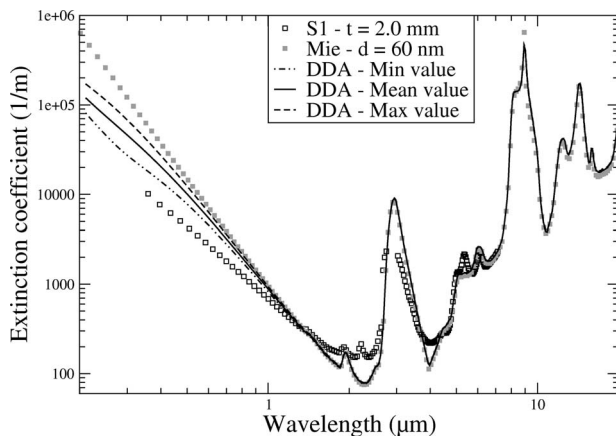


Fig. 18 Comparison of the COK84 powder of an experimental extinction coefficient spectrum to the spectra obtained using the Mie theory on the one hand and using the DDA on a DLCCA representative aggregate on the other hand. For the results obtained with the DDA, we present the minimum, the arithmetic mean, and the maximum values of the computations over 100 target orientations.

(Figs. 16 and 17 for the EH5 and Figs. 18 and 19 for the COK84). We always observe that the DDA improves the agreement of the computed results with the experiment.

Although the DDA results agree fairly well with the experimental ones, there are still two issues that we cannot answer yet. First, what about the validity of the complex index of refraction of silica? The index we have used is taken from Ref. [16]; it has been experimentally determined on amorphous bulk silica, and we may reasonably wonder if the refraction index is the same for 10 nm diameter particles as for bulk materials. In Ref. [37], the phonon mean free path is estimated to be 6 \AA , which tends to prove that the size effects can be neglected. Moreover, in the various figures, we see that in the wavelength range neighboring $2 \mu\text{m}$, the agreement between the experimental results and the computed ones is not very good. In this region, the complex index of refraction is known to depend on the type of silica: The presence of silanol groups, which is a powder dependent parameter, affects the refraction index [38,13]. Our silica powders presenting many silanol groups at the nanoparticle surfaces, this may explain the poor agreement for wavelengths close to $2 \mu\text{m}$. Finally, what might be the influence of the nanostructure? Until now we have based our computations on aggregates that are presumed to be representative. Nevertheless, if we take the liberty to generate an aggregate ignoring the very little we know about the real medium, we can get DDA results that superimpose perfectly over the whole wavelength range with the experimental results. This point implies that the radiative properties of our particulate media are very much dependent on the spatial organization of the nanoparticles within them, especially at wavelengths “probing” this spatial arrangement. We hope in the near future to be able to perform microtomography on our samples in order to refine the representations that we have proposed for our media.

3.3 Parameter Sensitivity. It is well founded to worry about the sensitivity of the results to some of the parameters we use, namely, the size of the representative scatterer determined using the Mie theory (that will imply a variation in the number of nanoparticles making the aggregate), the size of the primary nanoparticles, and the spatial organization of these nanoparticles.

First, as far as the diameter of the representative scatterer is considered, we focus on Fig. 20 that shows the experimental albedo spectra we obtain for the samples made of the HDK-T30 powder and the ones that we compute with the Mie theory for various diameters of the scatterer: 36 nm, 38 nm, 40 nm, 42 nm,

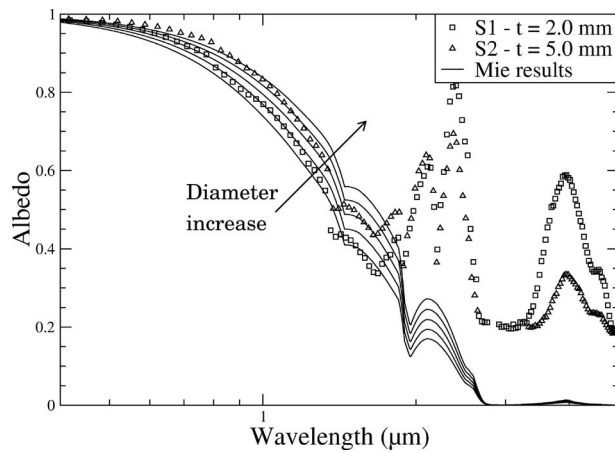


Fig. 20 Comparison of the HDK-T30 powder of two experimental albedo spectra with those obtained using the Mie theory for uniform distributions of scatterer diameters equal to 36 nm, 38 nm, 40 nm, 42 nm, and 44 nm

and 44 nm. We recall that the criterion that seems to be the most suitable for the evaluation of the scatterer diameter is the transition between the scattering regime and the absorptive regime; in our experiments, this transition occurs at wavelengths around $1.3 \mu\text{m}$. Considering this criterion, we see that the two extreme values are not acceptable. Regarding the three others, each value is appropriate, the three spectra lying in the zone defined by the two experimental albedo spectra. Consequently, this figure allows us to say that the determination of the diameter of the equivalent scatterer from the albedo spectrum is quite precise, since we are able to determine this diameter with an error of 1 nm or 2 nm, which is a relative error below 5%.

The second parameter we use is the diameter of the nanoparticles. As written earlier, it is deduced from the values of the specific surface and the density of the powder used to make the samples. Moreover, we consider a uniform distribution of the particle diameters; but we clearly observe the following on the TEM micrograph of Fig. 2.

- The nanoparticles do not look perfectly spherical.
- The diameters of the nanoparticles seem to vary between typically 9 nm and 15 nm. If we were dealing with dense smooth nanoparticles, the specific surface should be smaller than the experimental one indicated by powders suppliers. So, we explain the high value of the specific surface with the surface roughness of the nanoparticles and decide to keep on working with smooth nanoparticles.

The geometrical shape of the nanoparticles is not expected to affect the radiative properties because the wavelength is much larger than the diameter of the nanoparticles. Concerning the diameter of the nanoparticles, which is considered as uniform in our computations, its influence on the radiative properties is not very tangible. So we have computed for HDK-T30 samples the radiative property spectra for aggregates made of, respectively, 5 nm, 7 nm, 9 nm, 11 nm, 13 nm, and 15 nm diameter particles, keeping the volume of silica making the aggregates constants (so the examined aggregates were, respectively, made of 512, 187, 87, 48, 29, and 19 nanoparticles). Figure 21 shows the extinction coefficient spectra obtained for three different nanoparticle diameters (5 nm, 9 nm, and 15 nm) on the wavelength range (250 nm; $3 \mu\text{m}$). We can observe that for wavelengths above 800 nm, the size of the nanoparticles does not impact the radiative properties; that is why we only show the spectra below $3 \mu\text{m}$. Below the value of 800 nm, the smaller the nanoparticle diameter, the lower the extinction coefficient. The relative deviation between the two extreme values can reach more than 100% of the smallest value

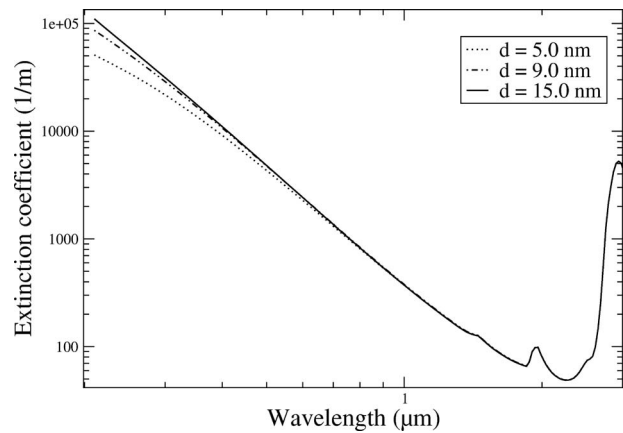


Fig. 21 Evolution of the DDA extinction coefficient spectrum in relation to the diameter of the nanoparticles constituting the DLCCA representative aggregate

(obtained for the cluster made of the smallest particles). So the impact of the diameter of the nanoparticles can be significant and it might be interesting to use a distribution of the diameters; nevertheless, as the nanoparticles are fused to each other, we cannot obtain this real distribution from classical granulometry measurements. TEM images might be exploited, but it would be a very laborious work because of the trouble to define the diameter for a nonperfectly spherical particle and of the difficulty to define the edge of each nanoparticle.

The last questionable point is the use of the DLCCA algorithm to generate the nanostructures on which the DDA computations are performed. This algorithm has been chosen because the fractal dimension of the resulting structure is very close to the fractal dimensions that are reported in literature on silica aggregates [39,40,34], even if other values lying between 1.5 and 2.6 can also be found [41,34]. Nevertheless, it must not be lost of sight that the correlation length of the fractal dimension is only a few nanoparticle diameters [41], so we can raise doubts about the legitimacy of this model to generate representative nanostructures. Thus we have tried to model the nanostructure with another well-known algorithm: the diffusion-limited aggregation (DLA) algorithm [42], in which freely moving particles are added, one at a time. The resultant fractal dimension of DLA aggregates is close to 2.5. The aggregates we obtain this way look quite different from those we obtain with the DLCCA algorithm. Nonetheless, the variations in terms of radiative properties seem to be negligible in our preliminary computations. The results obtained on a DLA aggregate are plotted in Fig. 22. These results must be compared with those of Fig. 16 (DLCCA aggregate). Comparing these results, we see that the impact of the choice of the algorithm that is used to generate the aggregates on the mean radiative properties is quite minor. The influence of the algorithm is more conspicuous as far as the extreme values of the DDA extinction coefficient spectra in the short wavelength region (below 400 nm in the case of the EH5 powder that is presented here) are considered. Because of the anisotropy of the cluster that is more pronounced in the case of the DLA algorithm than in the case of the DLCCA one, the extreme values of the extinction coefficient spectrum are slightly more spread when the DDA computations are performed on the DLA aggregate.

4 Conclusion

We have determined the spectral radiative properties of silica nanoporous matrices from reflectance and transmittance measurements using a parameter identification technique based on the radiative transfer equation inversion. The experimental radiative properties have been compared with their counterparts derived

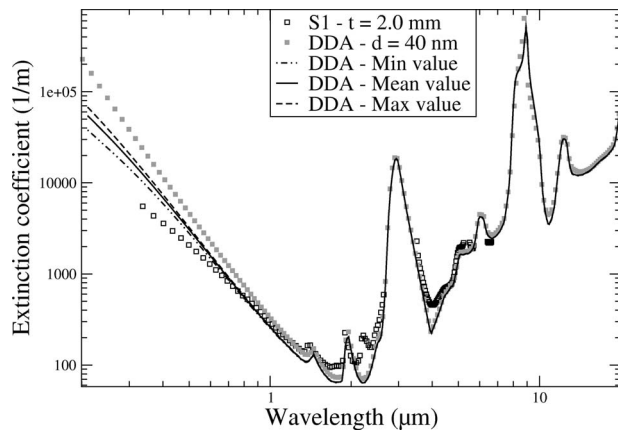


Fig. 22 Same as Fig. 16, but here the DDA computations are performed on an aggregate generated using the DLA algorithm

from the Mie theory assuming a uniform diameter distribution of spheres having the same diameter as the nanoparticles. The results being unsatisfactory at wavelengths below $2 \mu\text{m}$ on the one hand, and the experimental albedo spectra presenting quite elevated scattering to absorption transition wavelengths on the other hand, we have looked for scatterer apparent diameters yielding good agreements between the experimental values and the Mie theory. Nevertheless, the correspondence of the extinction coefficient spectra at low wavelengths remained unsatisfactory. So we have proposed the interpretation that the nanoporous matrix scatters radiation as a cloud of representative scatterers, the representative scatterer being here the aggregate obtained during the powder production process; and the poor agreement below $1 \mu\text{m}$ has been attributed to the impact of the spatial distribution of matter within these aggregates. In order to confirm this hypothesis, we have developed a code based on the discrete dipole approximation. The simulations are performed on computer generated structures that have fractal dimensions close to what is usually found in literature for aggregates of silica nanoparticles. The satisfactory correspondence between the experimental and simulated radiative property spectra using the DDA is quite encouraging, and is a first step toward a reasonable representation of the material organization within our nanoporous matrices. Besides, the very good agreement between the results of the Mie theory on the one hand and of the DDA on the other hand for wavelengths above $2 \mu\text{m}$ at ambient temperature allows us to affirm that it is possible with the Mie theory to study the impact of the composition of the matrix on the radiative transfer within the nanoporous superinsulating materials as long as the size of the nanoparticles and the size of the aggregates of nanoparticles are significantly smaller than the wavelength. This is of interest because, the opacifier microparticles being in very low volume fraction, assuming that the two populations of particles scatter independently, the Mie theory can be up to get the order of magnitude of the performance of nanoporous superinsulating materials of various compositions.

Nomenclature

C	= optical cross section
D_f	= mass fractal dimension
\mathbf{E}	= electric field
I	= intensity of radiation
\mathbf{P}	= dipole moment
R	= reflectance
S_{spe}	= specific surface
T	= transmittance
a_1	= first term of the Mie series
d	= characteristic length associated with a dipole
d_p	= primary particle diameter

f_v	= volume fraction
g	= asymmetry factor
i	= $\sqrt{-1}$
k	= wave number
m	= complex refractive index, $m=n+i\kappa$
x	= size parameter, $x=\pi d_p/\lambda$

Greek Symbols

α	= polarizability
β	= extinction coefficient
β^*	= weighted extinction coefficient
ϕ	= scattering phase function
λ	= wavelength
μ	= cosine of the polar angle
ρ	= density
ω	= scattering albedo
ω^*	= weighted scattering albedo

Subscripts and Superscripts

abs	= absorption
ext	= extinction
inc	= incident
sca	= scattering
h	= hemispherical (transmittance or reflectance)

References

- [1] Enguehard, F., 2007, "Multi-Scale Modelling of Radiation Heat Transfer Through Nanoporous Superinsulating Materials," *Int. J. Thermophys.*, **28**(5), pp. 1693–1717.
- [2] Büttner, D., and Fricke, J., 1985, "Thermal Conductivity of Evacuated Highly Transparent Silica Aerogel," *Int. J. Sol. Energy*, **3**(2), pp. 89–94.
- [3] Kamiuto, K., 1990, "Combined Conductive and Radiative Heat Transfer Through Evacuated Silica Aerogel Layers," *Int. J. Sol. Energy*, **9**(1), pp. 23–33.
- [4] Heinemann, U., Caps, R., and Fricke, J., 1996, "Radiation-Conduction Interaction: An Investigation on Silica Aerogels," *Int. J. Heat Mass Transfer*, **39**(10), pp. 2115–2130.
- [5] Rochais, D., Domingues, G., and Enguehard, F., "Numerical Simulation of Thermal Conduction and Diffusion Through Nanoporous Superinsulating Materials," *Proceedings of the European Conference on Thermophysical Properties*, Bratislava, Slovak Republic.
- [6] Coquard, R., and Quenard, D., "Modeling of Heat Transfer in Nanoporous Silica," *Proceedings of the Eighth International Vacuum Insulation Symposium*, Würzburg, Germany.
- [7] Caps, R., and Fricke, J., 2000, "Thermal Conductivity of Opacified Powder Filler Materials for Vacuum Insulations," *Int. J. Thermophys.*, **21**(2), pp. 445–452.
- [8] Wacker's Booklet, http://www.wacker.com/internet/webcache/de_DE/_Downloads/Basis_en.pdf.
- [9] Cab-o-sil eh5 Brochure, [http://www.cabot-corp.com/cws/product.nsf/PDSKEY/~EH5/\\$file/CAB-O-SIL_EH-5.pdf?OpenElement](http://www.cabot-corp.com/cws/product.nsf/PDSKEY/~EH5/$file/CAB-O-SIL_EH-5.pdf?OpenElement).
- [10] Aerosil cok84 Booklet, <http://www.aerosil.com>.
- [11] McKellar, B. H. J., and Box, M. A., 1981, "The Scaling Group of the Radiative Transfer Equation," *J. Atmos. Sci.*, **38**, pp. 1063–1068.
- [12] Davison, B., 1957, *Neutron Transport Theory*, Oxford University Press, London.
- [13] Dombrovsky, L. A., 1996, *Radiation Heat Transfer in Disperse Systems*, Begell House, New York.
- [14] Modest, M. F., 2003, *Radiative Heat Transfer*, 2nd ed., Academic, New York.
- [15] Davis, K. M., and Tomozawa, M., 1996, "An Infrared Spectroscopic Study of Water-Related Species in Silica Glasses," *J. Non-Cryst. Solids*, **201**, pp. 177–198.
- [16] Palik, E. D., ed., 1991, *Handbook of Optical Constants of Solids*, Academic, Boston, MA.
- [17] Pankove, J. I., Zanzucchi, P. J., Magee, C. W., and Lucovsky, G., 1985, "Hydrogen Localization Near Boron in Silicon," *Appl. Phys. Lett.*, **46**(4), pp. 421–423.
- [18] van de Hulst, H. C., 1957, *Light Scattering by Small Particles*, Wiley, New York.
- [19] Bohren, C. F., and Huffman, D. R., 1983, *Absorption and Scattering of Light by Small Particles*, Wiley, New York.
- [20] Tien, C. L., and Drolen, B. L., 1987, "Thermal Radiation in Particulate Media With Dependent and Independent Scattering," *Annu. Rev. Numer. Fluid Mech. Heat Transfer*, **1**, pp. 1–32.
- [21] Chu, H. S., Stretton, A. J., and Tien, C. L., 1988, "Radiative Heat Transfer in Ultra-Fine Powder Insulations," *Int. J. Heat Mass Transfer*, **31**(8), pp. 1627–1634.
- [22] Kumar, S., and Tien, C. L., 1990, "Dependent Absorption and Extinction of Radiation by Small Particles," *ASME J. Heat Transfer*, **112**, pp. 178–185.
- [23] Prasher, R., 2007, "Thermal Radiation in Dense Nano- and Microparticulate

- Media," J. Appl. Phys., **102**, p. 074316.
- [24] Mishchenko, M., Travis, L., and Lacis, A., 2006, *Multiple Scattering of Light by Particles: Radiative Transfer and Coherent Backscattering*, Cambridge University Press, New York.
- [25] Purcell, E., and Pennypacker, C. R., 1973, "Scattering and Absorption of Light by Nonspherical Dielectric Grains," *Astrophys. J.*, **186**, pp. 705–714.
- [26] Draine, B. T., 1988, "The Discrete-Dipole Approximation and Its Application to Interstellar Graphite Grains," *Astrophys. J.*, **333**, pp. 848–872.
- [27] Draine, B. T., and Flatau, P. J., 1994, "Discrete-Dipole Approximation for Scattering Calculations," *J. Opt. Soc. Am. A Opt. Image Sci. Vis.*, **11**(4), pp. 1491–1499.
- [28] Jackson, J. D., 1999, *Classical Electrodynamics*, 3rd ed., Wiley, New York.
- [29] Draine, B. T., and Goodman, J., 1993, "Beyond Clausius-Mossotti: Wave Propagation on a Polarizable Point Lattice and the Discrete-Dipole Approximation," *Astrophys. J.*, **405**, pp. 685–697.
- [30] Dungey, C. E., and Bohren, C. F., 1991, "Light Scattering by Nonspherical Particles: A Refinement to the Coupled-Dipole Method," *J. Opt. Soc. Am. A*, **8**, pp. 81–87.
- [31] Okamoto, H., 1995, "Light Scattering by Clusters: The A1-Term Method," *Opt. Rev.*, **2**(6), pp. 407–412.
- [32] Okamoto, H., and Xu, Y., 1998, "Light Scattering by Irregular Interplanetary Dust Particles," *Earth, Planets Space*, **50**, pp. 577–585.
- [33] Doyle, W. T., 1989, "Optical Properties of a Suspension of Metal Spheres," *Phys. Rev. B*, **39**(14), pp. 9852–9858.
- [34] Legrand, A. P., 1998, *The Surface Properties of Silicas*, Wiley, New York, Chap. 2, pp. 83–143.
- [35] Meakin, P., 1983, "Formation of Fractal Clusters and Networks by Irreversible Diffusion-Limited Aggregation," *Phys. Rev. Lett.*, **51**(13), pp. 1119–1122.
- [36] Kolb, M., Botet, R., and Jullien, R., 1983, "Scaling of Kinetically Growing Clusters," *Phys. Rev. Lett.*, **51**(13), pp. 1123–1126.
- [37] Chen, G., 1996, "Nonlocal and Nonequilibrium Heat Conduction in the Vicinity of Nanoparticles," *ASME J. Heat Transfer*, **118**, pp. 539–545.
- [38] Petrov, V. A., and Stepanov, S. V., 1975, "Radiation Characteristics of Quartz Glasses Spectral Radiating Power," *Teplofiz. Vys. Temp.*, **13**(2), pp. 335–345.
- [39] Ehrburger, F., and Jullien, R., 1988, "Studies of Surface Science and Catalysis," *Characterization of Porous Solids I*, Vol. 39, K. K. Unger, J. Rouquerol, K. S. W. Sing, and H. Karl, eds., Elsevier, Amsterdam, pp. 441–449.
- [40] Hurd, A. J., Schaefer, D. W., and Martin, J. E., 1987, "Surface and Mass Fractals in Vapor-Phase Aggregates," *Phys. Rev. A*, **35**(5), pp. 2361–2364.
- [41] Freltoft, T., Kjems, J. K., and Sinha, S. K., 1986, "Power-Law Correlations and Finite-Size Effects in Silica Particle Aggregates Studied by Small-Angle Neutron Scattering," *Phys. Rev. B*, **33**(1), pp. 269–275.
- [42] Witten, T. A., and Sander, L. M., 1981, "Diffusion-Limited Aggregation, a Kinetic Critical Phenomenon," *Phys. Rev. Lett.*, **47**(19), pp. 1400–1403.
- [43] 1993, "Untreated Fumed Silica: Properties and Functions," Cabot Corporation brochure.

Correlations of Wave Characteristics for a Liquid Film Falling Down Along a Vertical Wall

Yasuo Koizumi¹

Department of Functional Machinery and
Mechanics,
Division of Creative Engineering,
Faculty of Textile Science and Technology,
Shinshu University,
3-15-1 Tokida, Ueda-shi,
Nagano 386-8567, Japan
e-mail: koizumi@shinshu-u.ac.jp

Ryou Enari

Nippon PMAC Co., Ltd.,
3150 Iiyama, Atsugi-shi,
Kanagawa 243-0213, Japan
e-mail: ryou_enari@pmac.co.jp

Hiroyasu Ohtake

Department of Mechanical Engineering,
Kogakuin University,
2665-1 Nakano-machi, Hachioji-shi,
Tokyo 192-0015, Japan
e-mail: at10988@ns.kogakuin.ac.jp

The behavior of a liquid film that flows down countercurrently along the inner surface of a circular pipe was examined. In the experiments of the present study, silicone oils of 500 cS, 1000 cS, and 3000 cS, as well as water, were used as the liquid phase. The gas phase was air. The vertically oriented test section was a circular pipe of 30 mm in inner diameter and 5.4 m in length. The substrate thickness of the silicone films, the film Reynolds numbers of which were quite low, was close to the mean film thickness, while the water film substrate was much thinner than the mean film thickness. Waves were observed on the substrate. Waves of a certain amplitude were confirmed to exist, even on the silicone films near the flooding occurrence, where the film Reynolds number was quite low. The mean film thicknesses of the silicone films, as well as that of the water film, were well expressed by applying the universal velocity profile to the film flow. When the film Reynolds number was lower than 600, the wave velocity was well predicted as the velocity of small perturbation waves on a laminar film. As the film Reynolds number became large, the wave velocity became slower than the small perturbation wave velocity. The correlation for the wavelength was developed based on the present experimental results. Combining this correlation with the Nosoko correlations and modifying the constants and exponents of the parameters in the equations, new correlations for the wave velocity and maximum film thickness were proposed. These new correlations were used to predict the wave velocity and the maximum film thickness to an accuracy of within 15%. [DOI: 10.1115/1.3084133]

Keywords: falling film, film thickness, waves, wave height, wave velocity, wavelength

1 Introduction

When the critical heat flux or the dry-out of a falling film on a heated wall is considered, the characteristics of waves on the film surface become important. Koizumi et al. [1] visually observed a film flow on a heated wall. Near the critical heat flux condition, they noticed bubble bursting in the film flow at many locations. Dry areas or dry patches were left at some locations after bubble bursting. While the dry patches were rewetted by the successive film flow, the wall temperature did not increase and the critical condition was not reached. When the dry patches were not erased by the film flow, the number of dry patches gradually increased until the dry area covered a substantial portion of the wall. The wall temperature then began to increase until the critical heat flux condition was reached. Based on this observation, they developed the correlation for the critical heat flux by considering whether the dry patch that remained after bubble bursting was eliminated by the film flow. The proposed correlation predicted well the critical heat flux data. This suggests that the interaction between the film flow and the dry patch is important when considering the critical heat flux.

The criteria as to whether the dry patch created in the film flow on the wall remains is known as the minimum wetting rate of the film flow. The minimum wetting rate has been investigated extensively, as reviewed by Hewitt and Hall-Taylor [2] and Ueda [3].

For example, in the adiabatic condition, decreasing the flow rate of the film flow, the film flow eventually reaches a limiting state, in which dry patches generated on the wall can exist stably or the film disintegrates into rivulets. The minimum film flow rate at which the liquid film can flow on the wall as a continuum film is called the minimum wetting rate. Hartley and Murgatroyd [4] assumed that the dynamic pressure of the film balanced the upward component of the surface tension at the front edge of the permanent dry patch, and they then derived the correlation for the minimum wetting rate. However, the minimum wetting rate calculated with the correlation was considerably larger than the measured values.

Koizumi et al. [5] carefully conducted minimum wetting rate experiments on an adiabatic falling film flow. They confirmed that the wave motion on the falling film is key in the formation of a stable dry patch. The contact angle of the film at the top edge of the stable dry patch varied periodically in a range synchronous with the arrival of the waves. When the contact angle exceeded the maximum advancing contact angle at the arrival of the large wave, the top edge of the dry patch began to move downward, i.e., rewetting of the dry patch was initiated. When this wave motion effect was incorporated into the Hartley and Murgatroyd model, the overprediction of the model was resolved and the minimum wetting rate was expressed well by the modified model.

The wave characteristics, such as wave height, wave velocity, wave frequency, and wavelength, are essential when considering the critical heat flux condition of the film flow, including the annular flow of the forced convection flow boiling. The present paper is an attempt to provide fundamental information about wave characteristics on the falling liquid film.

In the falling-film-heated system, the countercurrent flow con-

¹Corresponding author.

Contributed by the Heat Transfer Division of ASME for publication in the JOURNAL OF HEAT TRANSFER. Manuscript received January 13, 2008; final manuscript received January 11, 2009; published online June 5, 2009. Review conducted by Louis C. Chow. Paper presented at the 2005 ASME International Mechanical Engineering Congress (IMECE2005), Orlando, FL, November 5–11, 2005.

dition, in which generated vapor flows upward countercurrently to the falling film, is quite usual. In this system, countercurrent flow limiting (CCFL) or flooding is critical to safe operation. The characteristics of waves on the film surface are essential in examining the occurrence of the flooding.

In the advanced waste furnace, ash is melted to avoid dioxin production. Ash is also melted in the coal gasification system. Molten ash is highly viscous; the viscosity is 1000 to 3000 times higher than that of water. In these molten ash systems, some accidents/problems have been reported by Inumaru et al. [6]. Entrained droplets of molten ash deposited on the wall, interfering with the smooth flow of gas, and the flow path was choked in some cases. The entrained mechanism is closely related to the characteristics of the waves on the film flow. In order to address these problems, the characteristics of waves on a film of highly viscous fluid must be clarified.

The characteristics of waves on a falling film have been investigated extensively. However, most of these studies examined the waves of water or of fluids that have physical properties similar to water. In the present paper, the behavior of falling liquid films of water and highly viscous fluids in the countercurrent flow condition is examined.

The characteristics of waves on a thin film that flowed down along a vertical pipe were studied by Telles and Dukler [7], and the statistical aspects of waves on the film were discussed.

Takahama and Kato [8] examined the flow characteristics of the water film falling down along the outer wall of a circular tube without concurrent gas flow. The wave motion on the film was measured using needles and the electric capacitance method. They reported data on the wave velocity and the wave peak height.

Karapantsios et al. [9] studied the characteristics of water films flowing down inside a vertical pipe. They focused on very high Reynolds number film flow and reported mean film thickness data and wave amplitudes.

Nosoko et al. [10] conducted falling-film experiments producing well regulated waves on a water film that flowed down along a flat plate. They proposed correlations for the wave velocity and the peak wave height. Since the wave separation was artificially controlled, the wavelength information is required in their correlations.

Takamasa et al. [11,12] measured the characteristics of waves of a water film that flowed down along the inner wall of a vertical pipe by a sophisticated method using a laser focus displacement meter. Data of the wave velocities and the maximum, minimum, and average film thicknesses were reported.

Koizumi et al. [5,13,14] investigated falling films of water and R-113 along the outer wall of vertical pipes. Wave motion was measured using the visual technique and the electric capacitance method. The wave velocity, the minimum, maximum, and mean film thicknesses, and the wavelength were reported.

In the present paper, the behavior of a film that falls down along the inner surface of a vertical pipe in the countercurrent flow condition is examined. Water and highly viscous fluids of silicone oils of 500 cS, 1000 cS, and 3000 cS, are used as the liquid phase. The gas phase is air. Considering that the characteristics of waves on the film should be determined by only the superficial conditions, such as the mass flow rate of liquid and the flow path dimension, new general correlations that cover a wide range of fluid property conditions from water to highly viscous fluid are proposed for wavelength, wave velocity, and maximum film thickness.

2 Experiments

2.1 Experimental Apparatus and Procedures. The experimental apparatus used in the present study is shown schematically in Fig. 1. Air was used as the gas phase. Silicone oils of 500 cS, 1000 cS, and 3000 cS were used as the liquid phase. For comparison, water was also used as the liquid phase. The experiments

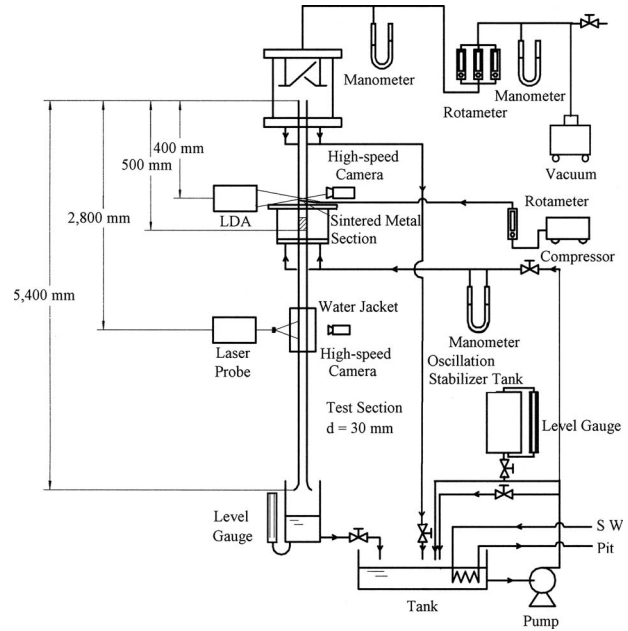


Fig. 1 Experimental apparatus

were conducted at room temperature and atmospheric pressure.

The test section was a 5.4-m-long vertical circular Plexiglas pipe with an inner diameter of 30 mm. The wall thickness was 5 mm. Liquid was supplied through a rotameter to the liquid inlet section by a circulation pump. The liquid then flowed into the test section through a 200 μ sintered metal mesh. The length, inner diameter, and outer diameter of the sintered metal were 80 mm, 30 mm, and 40 mm, respectively. Liquid flowed down gravitationally along the inner wall of the test section as a film. A vacuum was connected to the top of the test flow channel. Air was sucked from the bottom of the test flow channel. The bottom entrance of the test flow channel had a bell mouth configuration to allow for smooth inflow of air into the test flow channel.

The flow rate of water for the air-water experiments was measured by the rotameters, which were calibrated prior to experiments. In the air-silicone experiments, the pressure drop of the silicone flow along a horizontal circular pipe was measured using a Hg manometer, and the flow rate of the silicone was then derived from the measured pressure drop using the Hagen–Poiseuille law. Details are provided in the Appendix. The draining liquid flow rate from the test pipe was obtained by measuring the liquid level variation in a draining liquid catch tank. The air flow rate to the test flow channel was measured using rotameters between the outlet of the test flow channel and the vacuum.

The rotameters were calibrated prior to the experiments. The uncertainty of the rotameters was 0.1%. The uncertainty of the silicone flow rate measurement was also confirmed prior to the experiments. In the confirmation experiments, the volume flow rate of silicone was obtained by catching a certain amount of flow with a graduated cylinder during a certain period of time. The measured volumetric flow rate was compared with the flow rate derived from the pressure-drop measurement and the Hagen–Poiseuille law method. The uncertainty was less than 1%. The drainage flow rate from the bottom of the test pipe was not used in the present study but was recorded for use in flooding experiments; the results of which will be reported elsewhere.

Experiments were performed for the film Reynolds number of $Re_f = 6 \times 10^{-2} - 9 \times 10^3$ using the 3000 cS, 1000 cS, and 500 cS silicone oils and water. The upward air flow rate was from 0 m/s through the flooding initiation velocity. The flooding initiation was the condition whereby part of the liquid film flow began to flow upward.

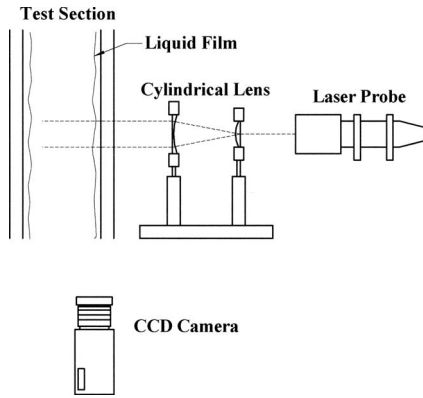


Fig. 2 Measurement of film thickness

2.2 Measurements of Wave Properties

2.2.1 Film Thickness. The countercurrent flow of the falling film and the upward air flow were formed in the test flow channel. Fluorescent dye (Rhodamine B) was dissolved into liquid in the experiments. An Ar laser ray sheet of 5 W was emitted toward the flow so as to be parallel to and toward the centerline of the test pipe, as shown in Fig. 2, at 2400 mm below the liquid inlet point. The dye in the liquid then fluoresced along the laser ray. Images were captured by a charge coupled device (CCD) video camera and a high-speed video camera with a frame rate of 500 frame/s. The luminous plane in the image corresponded to the film on the wall.

Images recorded with the high-speed video camera were used to derive the variation in the film thickness with time. The film thickness at a fixed position on an image that was enlarged on a monitor was measured frame by frame.

Images recorded with the CCD video camera were used to obtain the average, minimum, and maximum film thicknesses. The image of one frame was divided into ten sections in the axial direction. The heights of the film at these divided ten locations were measured on the image. The average, the minimum, and maximum heights were obtained for the frame. Scores of continuous frames were randomly selected from the recorded images for measurement. The average of the average film thicknesses, the minimum among the minimum film thicknesses, and the maximum among the maximum film thicknesses of the selected frames were determined as the average, minimum, and maximum film thicknesses for the test condition.

A water jacket that had flat outer surfaces and that was filled with water was attached to the emitting location of the laser ray sheet in order to minimize the effect of refraction. The refraction was also corrected for the recorded images. The thickness of the laser ray sheet was 0.5 mm. The laser ray sheet was emitted toward the pipe center and was perpendicular to the outer wall of the water jacket. Thus, the reflection effect was negligible. The uncertainty of the film thickness measurement was less than 0.1 mm.

2.2.2 Wave Velocity. One frame of the video captured by the CCD video camera that contained a wave peak was selected. Then, several frames were sent from that frame. The distance traveled by the peak of the wave while the frames were passed was measured on the images. The velocity of the wave was determined from the distance and the time interval between the frames. This procedure was performed for a number of frames that were selected randomly. The average of the values derived in this manner was defined as the wave velocity for this experimental condition. The uncertainty of the measured wave velocity was less than approximately 0.001 m/s.

2.2.3 Wavelength. As in the wave velocity derivation, a frame

of a video that contained a wave peak was selected. When two peaks were in the frame, the distance between the peaks was measured as the wavelength. When two peaks were not captured in the same frame, frames were passed until the next peak appeared on the frame. The wavelength was then calculated using the velocity of the peak, which was obtained in a manner similar to that described in Sec. 2.2.2, and the time interval until the next peak appeared. More than 50 data were obtained. The average of the values derived in this manner was defined as the wavelength for this experimental condition. The uncertainty of the wavelength was less than 0.01 m.

3 Experimental Results and Discussions

3.1 Wave Profile. The film thicknesses measured in the present experiments are presented in Figs. 3 and 4. The air velocity is zero in these cases. Figure 3 shows the data for water, and Fig. 4 shows the data for 500 cS silicone. The film thicknesses are plotted with respect to time in Figs. 3(a) and 4(a). In Figs. 3(b) and 4(b), the horizontal axes are converted into the axial length using the wave velocity. The dotted lines in the figures denote the mean film thickness.

The film thickness varies with periodically time in Fig. 3. Large waves are found to occur on the thin substrate.

Periodical variations are also observed in Fig. 4. However, the number of large waves is less than for water. The thickness of the substrate is approximately equal to the mean film thickness. There are a few small waves between the large waves, and the wave surface is smooth.

3.2 Film Thickness. The mean, maximum, and minimum film thicknesses of water and silicone films are plotted with respect to the film Reynolds number:

$$\text{Re}_f = \frac{4\Gamma}{\mu} \quad (1)$$

in Figs. 5 and 6. Here, Γ is the film flow rate per unit width, and μ is the viscosity of the liquid. The air velocity is zero in Fig. 5. The condition of Fig. 6 is near the onset of flooding.

In the countercurrent flow condition, the upward air flow rate was increased stepwise, while maintaining the liquid flow rate constant. As the air flow rate was increased, part of liquid that flowed into the test pipe through the sintered metal section was suddenly initiated to flow upward above the liquid inlet and out from the top of the test pipe. In the present study, the initiation of this upward flow of liquid from the liquid inlet was defined as the initiation of flooding. The air flow rate at the flooding initiation took a different value, depending on the test condition of the liquid flow rate. The film thicknesses presented in Fig. 6 were measured just before the initiation of flooding.

The dashed lines in Figs. 5 and 6 are the values of the Nusselt film thickness correlation for the laminar falling film [3,15]:

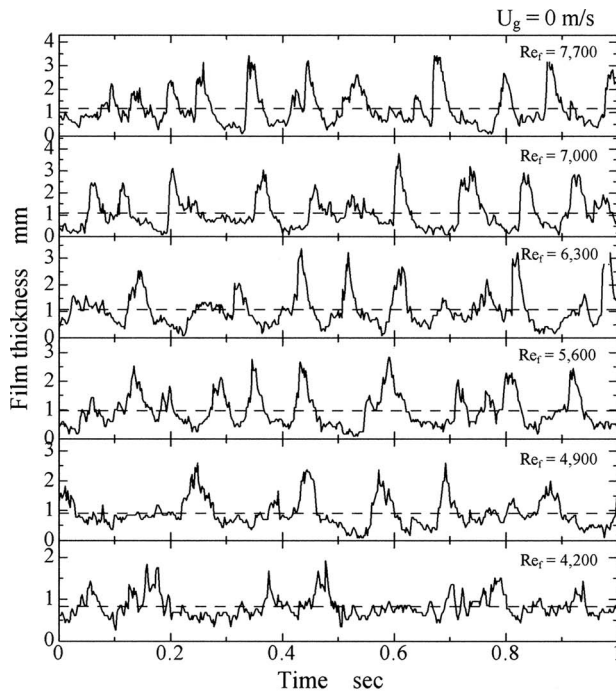
$$y_{iN}^* = (3/4)^{1/3} \text{Re}_f^{1/3}, \quad y_{iN}^* = y_{iN}(g/\nu^2)^{1/3} \quad (2)$$

where y_{iN} is the Nusselt film thickness, g is the gravitational acceleration, and ν is the kinematic viscosity. In addition, y_i^* is the nondimensional film thickness $= y_i(g/\nu^2)^{1/3}$. In deriving Eq. (2), the interfacial shear stress was set to zero.

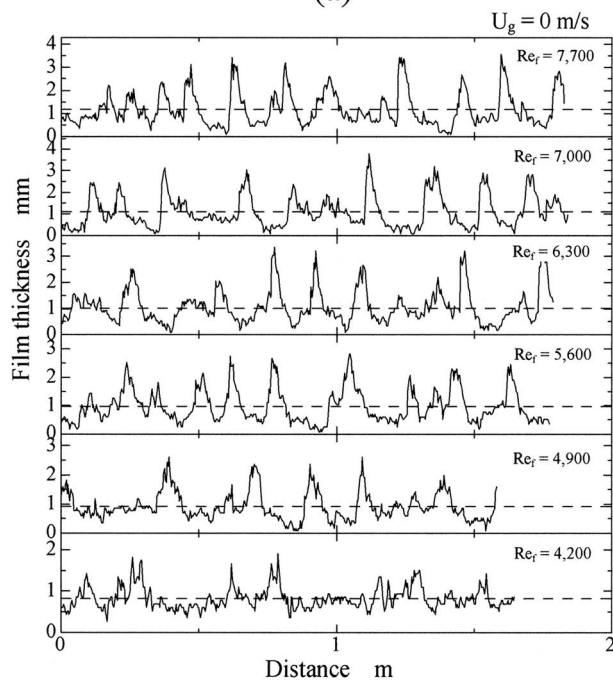
The solid lines in Figs. 5 and 6 denote the film thicknesses calculated by the following equations:

$$\begin{aligned} \text{Re}_f &= 2(y_i^+)^2, & y_i^+ &\leq 5 \\ \text{Re}_f &= 50 - 32.2y_i^+ + 20y_i^+ \ln y_i^+, & y_i^+ &\leq 30 \\ \text{Re}_f &= -256 + 12y_i^+ + 10y_i^+ \ln y_i^+, & y_i^+ &> 30, \end{aligned} \quad (3)$$

where $y_i^+ = (y_i/\nu)\sqrt{\tau_w/\rho}$ and y_i is the film thickness. The symbol τ_w is the wall shear stress, and ρ is the liquid density. Equation (3) is derived by applying the Karman universal velocity profile for a



(a)

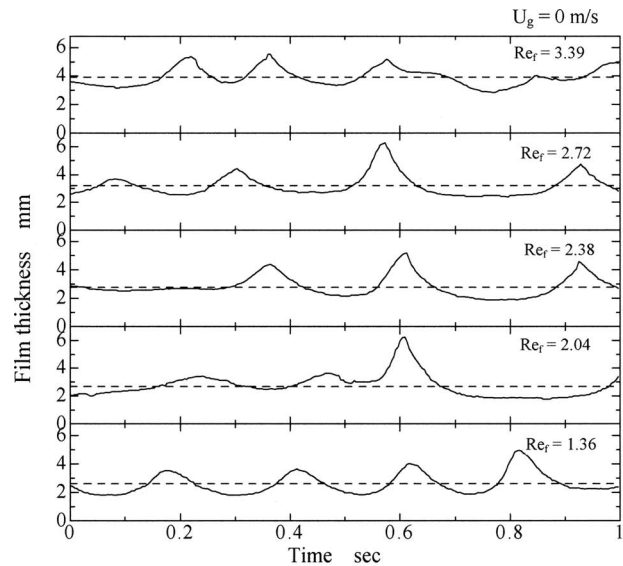


(b)

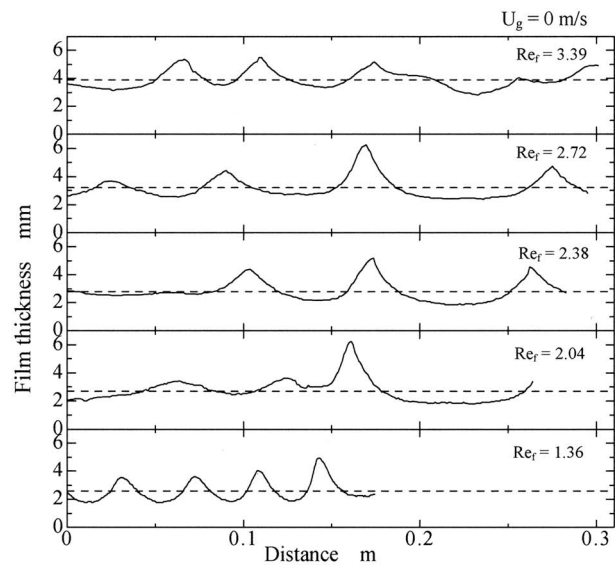
Fig. 3 Variation in film thickness (water film)

single-phase flow to the falling-film flow [3,15,16]. When the film thickness is thinner than the viscous sublayer thickness, the first equation of Eq. (3) is applied. When the film thickness is in the region of the buffer layer or the turbulent region, the second or third equation, respectively, is applied. If the shear stress at the wall $\tau_w = \rho g y_i$ is assumed in the falling film, then y_i^+ is related to y_i^* as $(y_i^+)^2 = (y_i^*)^3$. The dashed lines in Figs. 5 and 6 were calculated in this manner.

The mean film thicknesses are well expressed by Eqs. (2) and



(a)



(b)

Fig. 4 Variation in film thickness (silicone 500 cS film)

(3) in Figs. 5 and 6, although Eq. (3) gives slightly better results. Note that the agreement between the measured and predicted film thicknesses is not affected by the existence of the air flow until the occurrence of flooding. This suggests that the upward air flow has little effect on the film thickness before the initiation of flooding.

When there is no air flow, Fig. 5, the maximum film thicknesses of the water film and the 500 cS and 1000 cS silicone films are much larger, 1.5–3 times larger than the mean film thicknesses. This suggests that there are large waves on the film. However, in the case of 3000 cS silicone, there are no waves on the film.

At the condition just before flooding initiation shown in Fig. 6, the amplitudes of the waves of water and the 500 cS and 1000 cS silicone films are slightly larger than those in Fig. 5 of no air flow case, but the differences are not too much. Note that waves appear even in the case of the 3000 cS silicone film, which proves that the flooding is triggered by the interaction between the upward air flow and the wave motion on the film.

3.3 Wave Velocity. If a laminar falling film with a smooth-flat surface on a vertical wall is assumed, the velocity profile in

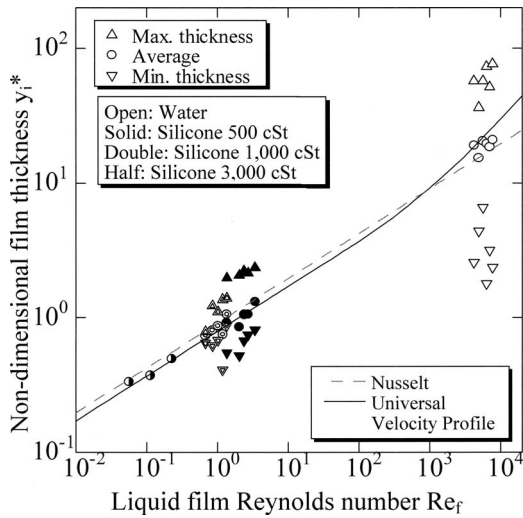


Fig. 5 Film thickness ($U_g=0$)

the film is derived from Newton's law. This is the Nusselt falling film, the film thickness y_{iN} of which is given in nondimensional form by Eq. (2). The film velocity u_{iN} at the surface y_{iN} and the mean film velocity u_{mN} , respectively, are expressed as follows:

$$u_{iN} = \frac{1}{2} \frac{\rho g}{\mu} y_{iN}^2 \quad (4)$$

$$u_{mN} = \frac{2}{3} u_{iN} \quad (5)$$

When small perturbation waves on the film surface are considered, the velocity of the small perturbation waves u_{spw} [17] is

$$u_{spw} = 2u_{iN} = 3u_{mN} \quad (6)$$

Here, μ is the viscosity of the film.

Considering the nondimensional form of the wave velocity u_w , $N_{u_w} = u_w / (g\nu)^{1/3}$. Thus, the expression for the surface velocity of the Nusselt film is

$$(N_{u_w})_{iN} = \left(\frac{1}{2}\right) \left(\frac{3}{4}\right)^{2/3} Re_f^{2/3} \quad (7)$$

and the expression for the velocity of the small perturbation waves on the Nusselt film is

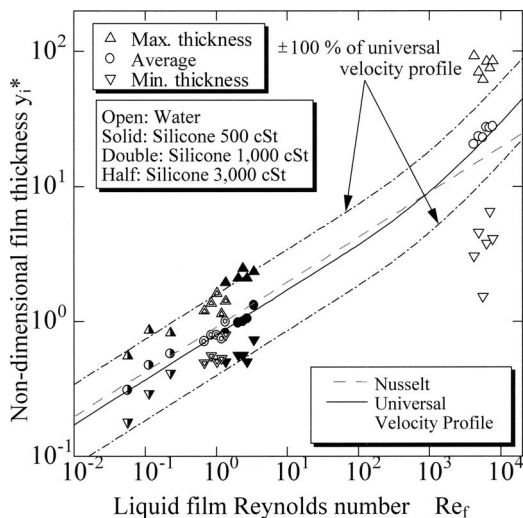


Fig. 6 Film thickness (U_g : near onset of flooding)

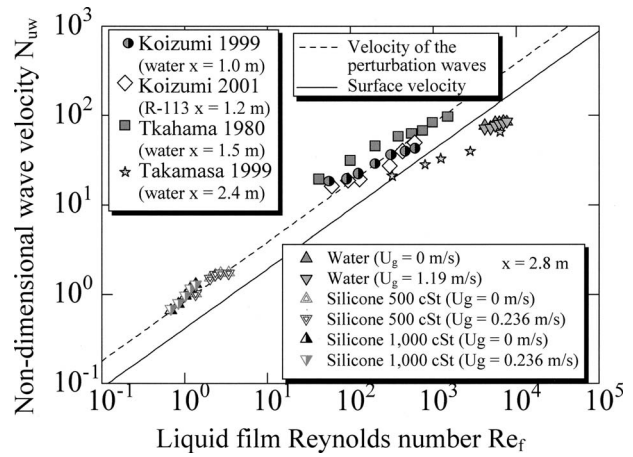


Fig. 7 Wave velocity

$$(N_{u_w})_{spw} = 2(N_{u_w})_{iN} \quad (8)$$

The wave velocities obtained in the present experiments are shown in nondimensional form in Fig. 7. The values calculated by Eqs. (7) and (8) are included in the figure for comparison. The data of Koizumi et al. [5,14] for the film on the outer wall of the vertical pipes for water and R-113, the data of Takahama and Kato [8] for the water film on the outer wall of a vertical pipe, and the data of Takamasa et al. [11,12] for the water film on the inner wall of a vertical pipe are also plotted in the figure.

When the film Reynolds number is low, $Re_f \leq 600$, the wave velocities of either water or R-113 are well expressed by Eq. (8) for the small perturbation waves on the smooth film (the Nusselt film). It is suggested that the waves are on the laminar falling film of the smooth surface of the Nusselt film and behave like small perturbation waves of sine-wave form.

When the film Reynolds number is large, i.e., $Re_f > 600$, the wave velocity becomes slower than the Nusselt film surface velocity. As discussed in Fig. 3, large waves existed on the substrate of the film. The substrate is much thinner than the Nusselt film. The film velocity at the substrate thickness is much slower than the Nusselt film surface velocity. Thus, it is natural that the wave velocity on the substrate is slower than the Nusselt film surface velocity.

3.4 Wavelength. The wavelengths for water and silicone measured in the present experiments are plotted with respect to the film Reynolds number in Fig. 8. It is difficult to say that the wavelength is a function only for the film Reynolds number.

Dimensional analysis revealed that the wavelength is expressed

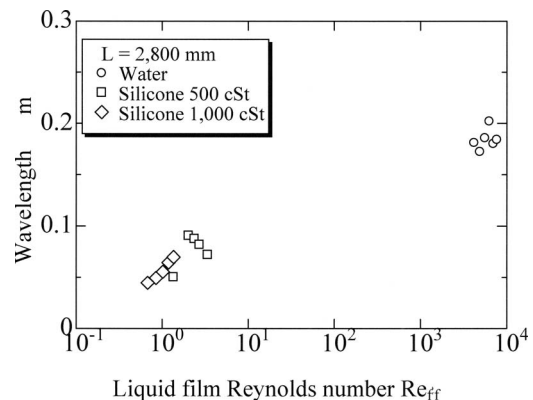


Fig. 8 Wavelength

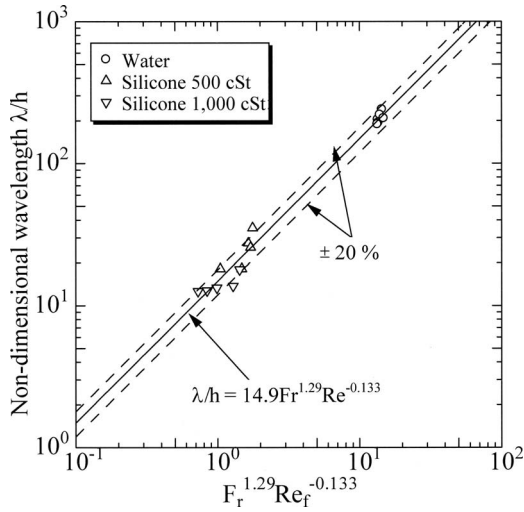


Fig. 9 Correlation of wavelength

by the following nondimensional parameters.

For nondimensional wavelength,

$$N_\lambda' = \frac{\lambda}{h} \quad (9)$$

For Froude number,

$$Fr = \frac{u_w}{\sqrt{gh}} \quad (10)$$

and the film Reynolds number (given in Eq. (1)), where h is the mean film thickness, u_w is the wave velocity, and λ is the wavelength. For the present experimental results,

$$N_\lambda' = 14.9 Fr^{1.29} Re_f^{-0.133} \quad (11)$$

is obtained as the best fit form. The values predicted by Eq. (11) are compared with the experimental results in Fig. 9, and good agreement is observed between the experimental results and the predicted values.

3.5 Correlations of Wave Properties. When nondimensional analysis of the wave properties of the wave velocity u_w and the maximum film thickness h_p is performed using the Buckingham π theorem, five nondimensional parameters are derived.

a. Nondimensional velocity

$$N_{u_w} = \frac{u_w}{(\nu g)^{1/3}} \quad (12)$$

b. Nondimensional maximum film thickness

$$N_{h_p} = h_p \left(\frac{g}{\nu^2} \right)^{1/3} \quad (13)$$

c. Nondimensional wavelength

$$N_\lambda = \lambda \left(\frac{g}{\nu^2} \right)^{1/3} \quad (14)$$

d. Morton number

$$K_F = \frac{\rho^3 \nu^4 g}{\sigma^3} \quad (15)$$

e. Film Reynolds number (given in Eq. (1)), where σ is the surface tension.

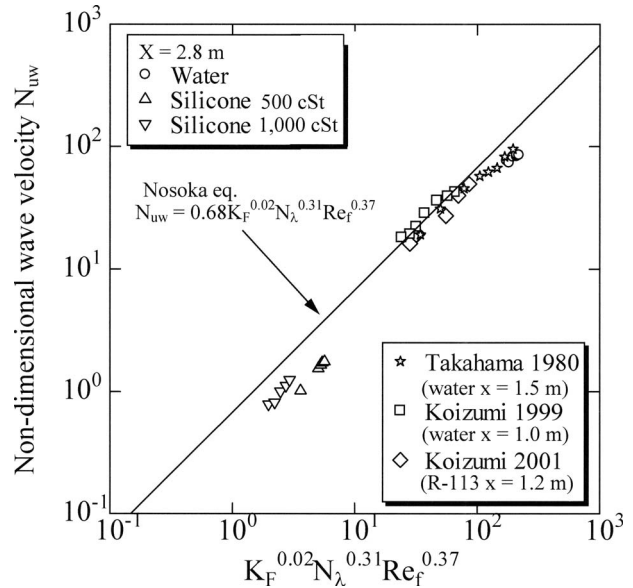


Fig. 10 Nosoko correlation of wave velocity

3.5.1 Comparison With the Nosoko Correlations. Nosoko et al. [10] proposed the following correlations for the wave velocity and the maximum film thickness based on the nondimensional parameters:

$$N_{u_w} = 0.68 K_F^{0.02} N_\lambda^{0.31} Re_f^{0.37} \quad (16)$$

$$N_{h_p} = 0.26 K_F^{0.044} N_\lambda^{0.39} Re_f^{0.46} \quad (17)$$

The data of the present study are compared with the Nosoko correlations, Eqs. (16) and (17), in Figs. 10 and 11. For comparison, the data of Takahama and Kato [8] for a falling film on the outer wall of a vertical pipe and the data of Koizumi et al. [5,14] for falling films of water and R-113 on the outer wall of a vertical pipe are also presented in the figures. Measured wavelengths were used in the calculation of the correlations.

In Fig. 10, The Nosoko correlation predicted the wave velocity slightly faster at the low film Re_f region of the silicone films (please refer to Fig. 7 for the film Re_f). In the intermediate Re_f region, where the correlation was developed, good agreement is

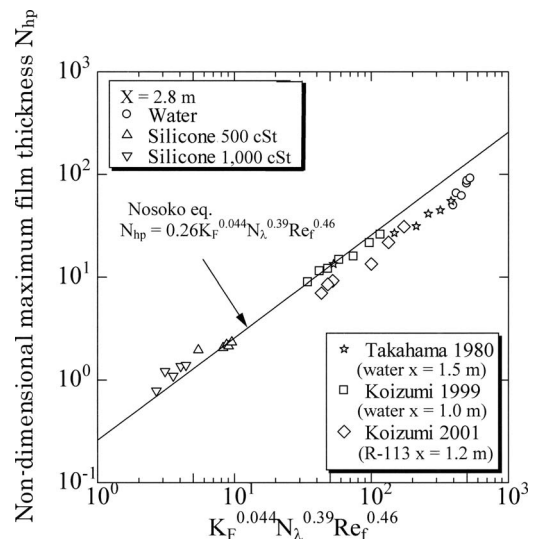


Fig. 11 Nosoko correlation of maximum film thickness

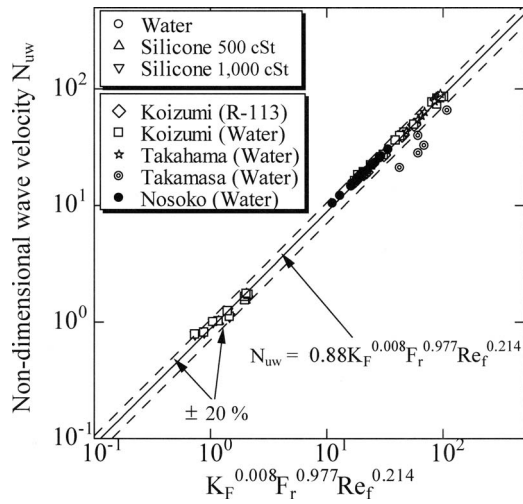


Fig. 12 New correlation of wave velocity

observed between the prediction and obtained data. At high Re_f , approximately $Re_f \geq 600$, the data plots start to deviate from the Nosoko line. Koizumi et al. [5,14] reported that the film becomes disturbed and takes on the appearance of a turbulent flow when $Re_f \geq 600$. This region is outside of the Nosoko experimental range.

The maximum film thickness is well predicted by the Nosoko correlation in Fig. 11 when $Re_f < 600$. Again, the data plots in the figure begin to deviate from the Nosoko line when the film begins to take on the characteristics of a turbulent flow at $Re_f \geq 600$.

3.5.2 Development of New Correlations. The Nosoko correlations require knowledge of the wavelength. The correlations are not closed in this context. Actually, there is no way to predict the wave velocity and the maximum film thickness using the Nosoko correlations. It is desirable that the wave velocity and the maximum film thickness be evaluated only from the film flow rate and the physical dimensions. Therefore, in the present study, new correlations were derived. The proposed correlations require only the film flow rate that is given at the boundary, the physical dimensions, and the physical parameters.

The wavelength correlation was developed in Sec. 3.4 using the present results, as shown in Fig. 9. An attempt was made to incorporate the wavelength correlation into the Nosoko correlations. When Eq. (11) was substituted into Eqs. (16) and (17), some scatterings of the data plots were observed. Then, the constants and exponents were adjusted to provide better results. The final forms were obtained as follows:

$$N_{u_w} = 0.88 K_F^{0.008} Fr^{0.977} Re_f^{0.214} \quad (18)$$

$$N_{h_p} = 1.09 K_F^{0.021} Fr^{0.316} Re_f^{0.424} \quad (19)$$

Figures 12 and 13 provide a comparison of Eqs. (18) and (19) with experimental values. In these figures, the data of Takahama and Kato [8] for water films, the data of Nosoko et al. [10] for water films, the data of Takamasa et al. [11,12] for a water film, and the data of Koizumi et al. [5,14] for water and R-113 films are also shown. The correlations could predict the experimental values to an accuracy of within 20%.

In Sec. 3.5.1, it was mentioned that the films of Figs. 10 and 11 tend to show different behaviors when the film Reynolds number Re_f exceeded 600. Thus, it is physically better to develop correlations for each region separately. Therefore, the following correlations were derived for each region:

$$N_{u_w} = 0.86 K_F^{0.013} Fr^{0.582} Re_f^{0.429} \quad (Re_f \leq 600) \quad (20)$$

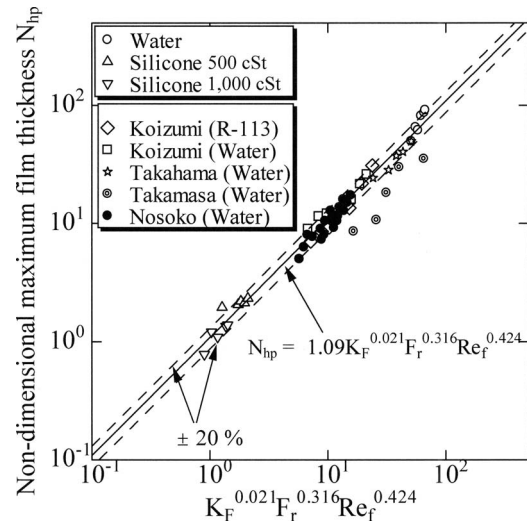


Fig. 13 New correlation of maximum film thickness

$$N_{h_p} = 1.11 K_F^{0.019} Fr^{0.693} Re_f^{0.229} \quad (Re_f \leq 600) \quad (21)$$

$$N_{u_w} = 3.97 K_F^{0.008} Fr^{0.348} Re_f^{0.255} \quad (Re_f > 600) \quad (22)$$

$$N_{h_p} = 0.18 K_F^{0.031} Fr^{1.15} Re_f^{0.381} \quad (Re_f > 600) \quad (23)$$

The values predicted by these correlations are compared with measured values in Figs. 14–17. The results are slightly better than Eqs. (18) and (19). Note that the data of Takamasa et al. [11,12] show a different trend from the other data. The reason for

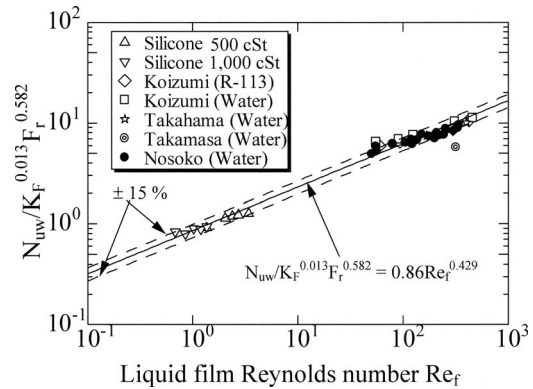


Fig. 14 New correlation of wave velocity ($Re_f \leq 600$)

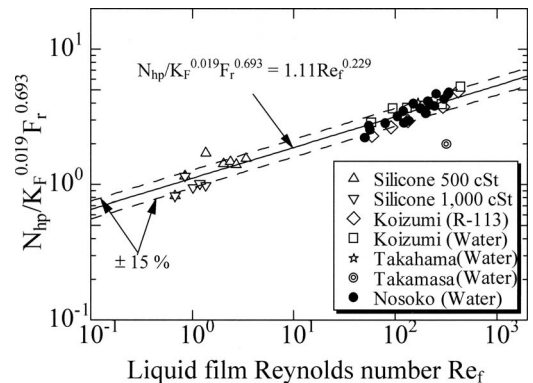


Fig. 15 New correlation of maximum film thickness ($Re_f \leq 600$)

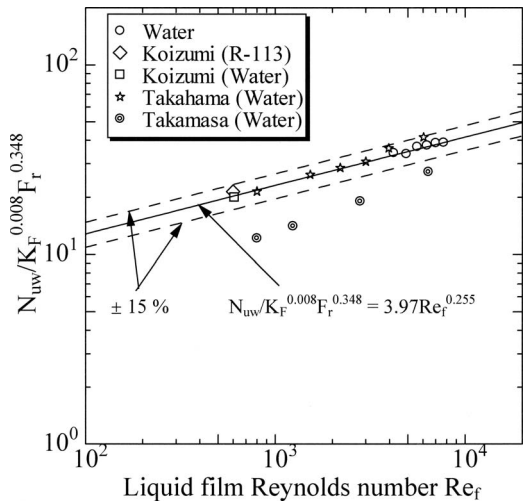


Fig. 16 New correlation of wave velocity ($Re_f > 600$)

this is not clear. They adopted the laser focus displacement method to obtain the wave characteristics. In this method, most of the waves, including small ripples on the surface, were detected. In other studies, the wave characteristics were mainly obtained visually. Naturally, the small ripples were excluded in the visual data acquisition process. This may be the reason for the discrepancy in the figures. Finally, note that large waves are important when phenomena such as the critical heat flux are considered.

4 Conclusions

The behavior of the liquid film flowing down along the inner surface of a vertical pipe of 30 mm inner diameter (ID) was examined. In the experiments of the present study, highly viscous fluids of silicone oils of 500 cS, 1000 cS, and 3000 cS, as well as water, were used as the liquid phase. The gas phase was air. The following conclusions were obtained.

1. The substrate thickness of the silicone film, where the film Reynolds number was quite low, was close to the mean film thickness, while the water film substrate was much thinner

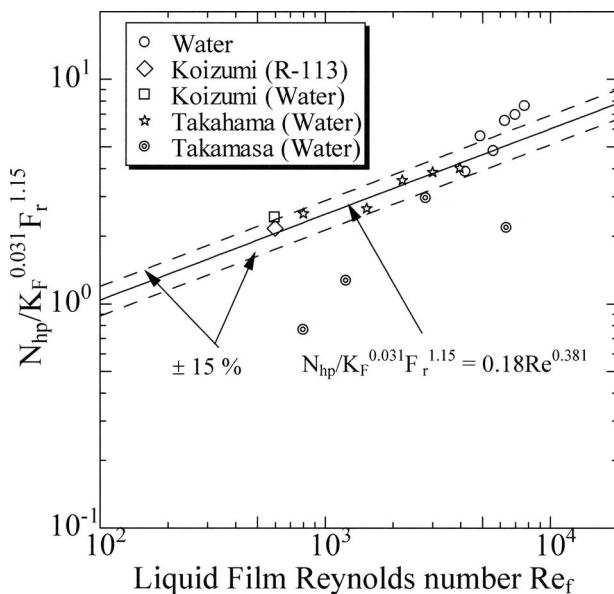


Fig. 17 New correlation of maximum film thickness ($Re_f > 600$)

than the mean film thickness. The wave surface on the silicone film was smooth. However, there were several small ripples on the wave surface of the water film.

2. The mean film thicknesses of the silicone films, as well as the water film, were well expressed by applying the universal velocity profile to the film flow. Waves of a certain height were confirmed to exist, even on the silicone films, where the film Reynolds number was quite low near the flooding occurrence.
3. When the film Reynolds number was lower than 600, the wave velocity was well predicted as the velocity of small perturbation waves on the laminar film. As the film Reynolds number became large, the wave velocity became slower than the small perturbation wave velocity.
4. Nosoko correlations for the wave velocity and the maximum film thickness were compared with the present experimental results. The correlations provided reasonable prediction for the present experimental results, although some deviations were observed. However, the correlations require knowledge of the wavelength and are not closed.
5. The correlation for the wavelength was developed based on the present experimental results. Combining this correlation with the Nosoko correlations and modifying the constants and exponents of the parameters in the equations, new correlations for the wave velocity and maximum film thickness were proposed. The correlations could be used to predict the wave velocity and maximum film thickness to an accuracy of within 15%.

Nomenclature

- Fr = Froude number = u_w / \sqrt{gh}
 g = gravitational acceleration (m/s^2)
 h = mean film thickness (m)
 h_p = maximum film thickness (m)
 K_F = Morton number = $\rho^3 \nu^4 g / \sigma^3$
 N_{h_p} = nondimensional maximum film thickness = $h_p (g / \nu^2)^{1/3}$
 N_{u_w} = nondimensional wave velocity = $u_w / (\nu g)^{1/3}$
 N_λ = nondimensional wavelength = $\lambda (g / \nu^2)^{1/3}$
 N'_λ = nondimensional wavelength = λ / h
 Re_f = film Reynolds number = $4\Gamma / \mu$
 y = distance from wall surface (m)
 y_i^* = nondimensional film thickness = $y_i (g / \nu^2)^{1/3}$
 y^+ = nondimensional distance = $(y / \nu) \sqrt{\tau_w / \rho}$
 U_g = upward superficial air velocity (m/s)
 u = velocity (m/s)

Greek Symbols

- Γ = film flow rate per unit width (kg/ms)
 λ = wavelength (m)
 μ = liquid viscosity (Pa s)
 ν = kinematic viscosity (m^2/s)
 ρ = liquid density (kg/m^3)
 σ = surface tension (N/m)
 τ_w = wall shear stress (N/m^2)

Subscripts

- i = falling-film surface
 m = mean value
 N = Nusselt film
 spw = small perturbation wave
 w = wave

Appendix: Silicone Flow Rate Measurement

The pressure drop ΔP of the flow in a circular pipe of length L is expressed as follows:

$$\Delta P = \frac{1}{2} \lambda \frac{L}{D} \rho u^2 \quad (\text{A1})$$

where D is the pipe inside diameter and u is the average velocity in the pipe. Greek symbols λ and ρ are the friction factor defined based on the pipe inside diameter and the fluid density, respectively. When the flow is laminar, the friction factor is

$$\lambda = \frac{64}{\text{Re}} \quad (\text{A2})$$

Here, Re is the Reynolds number that is expressed as

$$\text{Re} = \frac{uD}{\nu} \quad (\text{A3})$$

where ν is the kinematic viscosity.

Combining Eqs. (A1)–(A3), the following equation is obtained:

$$u = \frac{1}{32} \frac{D^2}{\rho \nu L^2} \Delta P \quad (\text{A4})$$

Then, the volumetric flow rate V in the pipe is based on the velocity u in the pipe

$$V = \frac{\pi}{4} D^2 u \quad (\text{A5})$$

It was also confirmed that when silicone oil was used as the test fluid in the present experiments, the flow in the flow rate measurement pipe was laminar.

References

- [1] Koizumi, Y., Matsuo, T., Miyota, Y., and Ueda, T., 1998, "Dry-Out Heat Flux of Falling Film and Low-Mass Flux Upward-Flow in Heated Tubes," *JSME*, **64**(624), pp. 2578–2585.
- [2] Hewitt, G. F., and Hall-Taylor, N. S., 1970, *Annular Two-Phase Flow*, Pergamon, Oxford, pp. 127–135.
- [3] Ueda, T., 1981, *Two-Phase Flow and Heat Transfer*, Yokendo Co., Tokyo, pp. 125–127, 128–132, and 202–219.
- [4] Hartley, D. E., and Murgatroyd, W., 1964, "Criteria for the Break-Up of Thin Liquid Layers Flowing Over Solid Surfaces," *Int. J. Heat Mass Transfer*, **7**, pp. 1003–1015.
- [5] Koizumi, Y., Ohtake, H., and Ueda, T., 1999, "A Study on the Minimum Wetting Rate of Isothermal Films Flowing Down on Outer Surface of Vertical Pipes," ASME Paper No. AJTE996426.
- [6] Inumaru, J., Ohtaka, M., and Watanabe, H., 2000, "Droplet Entrainment of High-Viscosity Liquid in Counter-Current Annular Flow With Large Diameter Pipe," *Proceedings of the 37th National Heat Transfer Symposium of Japan*, Vol. 3, pp. 751–752.
- [7] Telles, A. S., and Dukler, A. E., 1970, "Statistical Characteristics of Thin, Vertical, Wavy, Liquid Films," *Ind. Eng. Chem. Fundam.*, **9**(3), pp. 412–421.
- [8] Takahama, H., and Kato, S., 1980, "Longitudinal Flow Characteristics of Vertical Falling Liquid Films Without Concurrent Gas Flow," *Int. J. Multiphase Flow*, **6**, pp. 203–215.
- [9] Karapantsios, T. D., Paras, S. V., and Karabelas, A. J., 1989, "Statistical Characteristics of Free Falling Films at High Reynolds Number," *Int. J. Multiphase Flow*, **15**(1), pp. 1–21.
- [10] Nosoko, T., Yoshimura, P. N., Nagata, T., and Oyakawa, K., 1996, "Characteristics of Two-Dimensional Waves on a Falling Film," *Chem. Eng. Sci.*, **51**, pp. 725–732.
- [11] Kurabayasi, M., Kobayasi, K., and Takamasa, T., 1999, "Velocity Measurement of Interfacial Waves on a Film Flowing Down a Vertical Tube Inner Wall Using an Image-processing Method and Laser Focus Displacement Meters," *Proceedings of the 18th Multiphase Flow Symposium '99*, pp. 111–112.
- [12] Takamasa, T., and Kobayashi, K., 2000, "Measuring Interfacial Waves on Film Flowing Down Tube Inner Wall Using Laser Focus Displacement Meter," *Int. J. Multiphase Flow*, **26**, pp. 1493–1507.
- [13] Koizumi, Y., Ohtake, H., and Ikeda, S., 2000, "Characteristics of a Falling Liquid Film on the Outer Surface of a Vertical Pipe (Minimum Wetting Rate and Waves on the Film)," *Proceedings of the 2000 ASME International Mechanical Engineering Congress and Exposition*, ASME, New York, HTD-Vol. 2, pp. 197–203.
- [14] Koizumi, Y., Ohtake, H., and Ikeda, S., 2001, "Characteristics of an R-113 Falling Liquid Film on the Outer Surface of a Vertical Pipe, Fourth International Conference on Multiphase Flow, CD-ROM EF1.
- [15] Kandlikar, S. G., Shoji, G., and Dhir, V. K., 1999, *Handbook of Phase Change: Boiling and Condensation*, Taylor & Francis, Philadelphia, pp. 342–345.
- [16] Whalley, P. B., 1987, *Boiling, Condensation, and Gas-Liquid Flow*, Oxford University Press, New York, pp. 29–31.
- [17] Carey, V. P., 1992, *Liquid-Vapor Phase-Change Phenomena*, Hemisphere, Bristol, PA, pp. 106–113.